Contribution to the simulation of low-velocity compressible two-phase flows with high pressure jumps using homogeneous and two-fluid approaches

David Iampietro

UNIVERSITÉ AIX-MARSEILLE
U.F.R. des Sciences
ÉCOLE DOCTORALE DE MATHÉMATIQUES ET D'INFORMATIQUE (E.D 184)

THÈSE

pour obtenir le grade de

DOCTEUR DE L'UNIVERSITÉ AIX-MARSEILLE

Spécialité doctorale "Mathématiques Appliqués"

présentée et soutenue publiquement par

David IAMPIETRO

le 8 Novembre 2018

Contribution à la simulation d'écoulements diphasiques compressibles à faible vitesse en présence de sauts de pression par approches homogène et bifluide

Directeur de thèse : **Jean-Marc HÉRARD**
Encadrant industriel : **Frédéric DAUDE**

devant le jury composé de:

Mme Edwige Godlewski,	Professeur, Université Pierre et Marie Curie (Paris 6)	Rapporteur
Mme Marie-Hélène Vignal,	Maître de conférences, Université Paul Sabatier (Toulouse 3)	Rapporteur
M. Christophe Berthon,	Professeur, Université de Nantes	Examinateur
Mme Raphaèle Herbin,	Professeur, Université Aix-Marseille	Examinateur
M. Siegfried Müller,	Professeur, RWTH Aachen University	Examinateur
M. Khaled Saleh,	Maître de conférences, Université Claude Bernard (Lyon 1)	Examinateur
M. Frédéric Daude,	Ingénieur chercheur, EDF R&D	Encadrant
M. Jean-Marc Hérard,	Ingénieur chercheur sénior, EDF R&D	Directeur de thèse

Remerciements

Bien au delà d'un travail personnel, ce manuscrit est avant tout le fruit du soutien constant et protéiforme prodigué par une foultitude de personnalités. Aussi, avant de commencer les choses sérieuses, je profite de ce bref intermède pour saluer chaleureusement chacun de ces hommes et de ces femmes.
Donc..
Merci à Julie A. pour cette présentation de la thèse CIFRE que tu as faite à l'ENSTA et qui m'a donnée l'étincelle pour me lancer également dans ce vaste projet.
Merci à Frédéric P. pour ta spontanéité, ton état d'excitation constant ainsi que ta très grande générosité envers autrui ; générosité qui je pense est une qualité indispensable pour le "mieux vivre ensemble".
Merci à Élodie R. pour nos diverses divagations sur le sens de la vie ; divagations systématiquement teintées d'une touche de Rock'n roll pour les rendre légèrement acidulées. Ta capacité d'écoute m'a fait le plus grand bien dans les moments difficiles.
Merci à Victor G. pour ces séances de fractionné où tu voulais nous pousser, selon ton expression "jusqu'à la galette" ! À tes côtés, j'ai aiguisé ma combativité et ma persévérance. De plus ton honnêteté intellectuelle dans nos conversations a toujours été fort appréciable.
Merci à Amine A. Bien que je doute qu'il en ait conscience, il constitue pour moi un modèle de confiance et de brio intellectuel complété par un remarquable engagement dans les sciences. J'espère un jour pouvoir te ressembler sur ces aspects là.
Merci à Aurélien J. pour ces innombrables conversations sur la psychologie humaine et plus particulièrement sur la façon de penser du bavarois. Ta passion pour l'industrie ainsi que ton travail sur le banc d'essai que tu as construit au cours de ta thèse m'inspirent pour la suite..
Merci à l'équipe Aster et plus particulièrement à Guillaume D. (avec qui je partage un mouton en trombones) pour leur bonne humeur, leur professionnalisme et les saluts en Polonais du mardi matin.
Merci à Mouhammadou D. pour ces conversations sur nos carrières futures et sur nos volontés de créer un monde hors du plateau de Saclay. Je reste persuadé que nous pourrions ouvrir un "business" au Sénégal pour y faire fortune.
Merci à Patrick V. qui par son témoignage sur ces expériences canadiennes m'a fait prendre un certain recul sur les déambulations de la vie ainsi que sur l'immensité des possibles. Tu as su m'insuffler une part de confiance dans l'avenir.
Merci à Charles D. mon frère de thèse et à présent bon ami. Nos discussions sur les modèles diphasiques vont me manquer ; de même que ce congrès mémorable passé à tes côtés à Lille. Je te souhaite par ailleurs beaucoup de succès dans tes œuvres musicales.
Merci à Samuel K. dont la passion pour les sciences, la curiosité intellectuelle et l'extrême gentillesse me donnent, encore aujourd'hui, l'envie de travailler avec lui.
J'en viens à présent à mes encadrants, Jean-Marc H. et Frédéric D. Merci à vous deux pour votre implication dans ma thèse, pour votre patience et votre grande bienveillance. À vos côtés j'ai pu développer un réel amour des sciences. Vous avez été mes mentors pendant 3 ans . Auprès de vous j'ai beaucoup appris. Et je tenais à vous dire que, non comptant d'avoir fait de moi un docteur, vous avez surtout hérité aujourd'hui d'un ami. Parlant d'amitié, je tenais aussi à remercier Pierre D., Edward B. ainsi que Marion C. dont la présence et l'empathie m'ont permis de tenir bon dans cette épreuve.
Enfin, j'aimerais rendre hommage à mes parents, Joseph et Michèle ainsi qu'à mes frères Vincent et Thomas pour l'amour dont ils ont su m'entourer depuis que je suis tout petit et qui me donne, encore aujourd'hui, l'énergie d'avancer en Science comme dans ma vie.

Résumé

Les travaux de la thèse sont axés sur le développement de méthodes numériques pour les écoulements diphasiques, compressibles, à faible vitesse, prenant en compte l' apparition soudaine de forts gradients de pression. La vitesse matérielle de chacune des phases étant très petite devant la vitesse du son associée aux ondes acoustiques, l'écoulement étudié est caractéristique d'un régime dit à faible nombre de Mach. Beaucoup de travaux de la littérature se basent sur une analyse asymptotique en faisant tendre le nombre de Mach vers zéro pour aboutir à des modèles dits incompressibles. Dans le cadre de la thèse, la compressibilité de chacune des phases sera systématiquement prise en compte. Néanmoins, que celle-ci soit analytique ou tabulée, la loi d'état contient toujours une information relative à la raideur thermodynamique mesurant la plus ou moins grande compressibilité de la phase considérée. Ainsi, dans le cadre d'écoulements eau-vapeur, la phase liquide est très faiblement compressible. D'un point de vue dynamique, la faible compressibilité de l'eau peut produire un régime d'écoulement particulier où des sauts de pression importants apparaissent même si le nombre de Mach est très faible. Ceci est régulièrement observé et mesuré dans le cadre de l'étude de transitoires rapides appelés coups de bélier. La première partie de la thèse s'est focalisée sur un modèle diphasique dit homogène-équilibré. Les deux phases de l'écoulement ont alors la même vitesse, pression, température ainsi que le même potentiel chimique. On observe alors l'évolution de l'écoulement uniquement à travers des variables dites de mélange. Dans ce contexte, un premier travail a été dédié à la construction et à l'évaluation de solveurs de Riemann approchés dits tout-nombre-de-Mach. Lors qu'aucun transitoire rapide ne vient perturber l'écoulement, ces solveurs ont la capacité de baser leur contrainte de pas de temps sur la vitesse des ondes matérielles lentes et restent donc précis pour suivre les fronts associés à ces ondes. En revanche, lorsqu'une onde de choc, caractérisée par un saut de pression important et une vitesse de propagation élevée traverse l'écoulement, ces solveurs s'adaptent automatiquement pour capturer la bonne position du choc ainsi que les bons niveaux de pression de part et d'autre du front. La seconde partie de la thèse s'est focalisée sur la prise en compte du couplage convection-source dans le cadre des modèles en approche bi-fluides. Dans ces modèles, les deux phases de l'écoulement possèdent leur propre jeu de variables pression, vitesse, température et taux de présence. Contrairement au modèle homogène, la valeur des trois premières variables ainsi que du potentiel chimique peut a priori différer entre les deux phases. Aussi, les modèles bi-fluides incluent généralement la présence de termes sources de relaxation afin de garantir un retour rapide vers l'équilibre mécanique et thermodynamique. Le cadre de travail a été le modèle simplifié à cinq équations appelé Baer-Nunziato isentropique au sein duquel seules les relaxations en pression et en vitesse sont considérées. Un schéma implicite à mailles décalées, basé sur l'influence des termes sources dans des problèmes de Riemann linéaires, a été proposé pour ce modèle. De plus, une analyse sur la prise en compte de l'équilibre asymptotique dans la partie convective des modèles bi-fluides a été également conduite.

Mots clés : Méthodes numériques, Écoulements basse vitesse compressibles, Écoulements diphasiques, Sauts de pression, Relaxation, Modèles bi-fluides.

Abstract

The present work focuses on the development of numerical methods for low-material velocity compressible two-phase flows with high pressure jumps. In this context, the material velocity of both phases is small compared with the celerity of the acoustic waves. The flow is said to be a low-Mach number flow. By making the Mach number tend towards zero, many authors in the literature perform an asymptotic analysis of the conservation laws at stake. Incompressible models are then derived. In this work, compressibility of both phases is systematically considered. Nevertheless, either analytical or tabulated, the equation of state always contains information related to the thermodynamical stiffness of the fluid. Such a stiffness can be seen as a measure of the compressibility of the considered phase. Thus, for two-phase flows involving sub-cooled liquid water and over-heated vapor, the liquid phase is known to be slightly compressible. When sudden events occur such as valve closures, the low-compressibility of liquid water may lead to fast transients in which high pressure jumps are produced even if the flow Mach number is low. This is often observed experimentally through the study of water hammer events. The first part of this work has leaned on two-phase homogeneous-equilibrium models. Thus, both phases have the same velocity, pressure, temperature as well as the same chemical potential. The evolution of the flow is observed only through mixture variables. The construction and the evaluation of what is called an all-Mach-number approximate Riemann solver has been conducted. When no fast transients come through the flow, the above solvers enable computations with CFL conditions based on low-material velocities. As a result, they remain accurate to follow slow material interfaces, or subsonic contact discontinuities. However, when fast shock waves associated with high pressure jumps propagate, these solvers automatically adapt in order to capture the position of the shock front as well as the right pressure levels. The second part of the thesis has been dedicated to the design of numerical methods enhancing the coupling between convection and relaxation in two-fluid models. In such models, both phases have their own set of variables : velocity, pressure, temperature and void fraction. Contrary to homogeneous models, the mechanical and thermodynamical equilibriums are not imposed, and the value of velocity, pressure, temperature and chemical potential between both phases may differ. Convergence towards equilibrium is ensured by adding relaxation source terms in these models. For the sake of simplicity, the framework has been restricted to the isentropic Baer-Nunziato model with velocity-pressure relaxations. A time-implicit staggered scheme, based on the influence of relaxation source terms on linear Riemann problems has been proposed. What is more, an asymptotic analysis dealing with the integration of relaxation source terms into the convective part of the two-phase flow model has been carried out.

Key words : Numerical methods, Low-velocity compressible flows, Two-phase flows, Pressure jumps, Relaxation, Two-fluid models.

Table des matières

Introduction générale

Cette thèse a pu être menée dans le cadre du contrat EDF-CIFRE 0561-2015. Elle s'est déroulée au sein du département ERMES sur le site d'EDF lab Saclay, en collaboration avec le départment MFEE du site EDF lab Chatou. Les ressources informatiques ont été fournies par le groupe EDF.

Sommaire

1.1 Contexte industriel

Les travaux présentés ici sont à mettre en lien avec différents types d'écoulements eau-vapeur présents à l'intérieur de certaines conduites des *réacteurs à eau pressurisée* (REP). On identifie en particulier deux configurations d'intérêt.

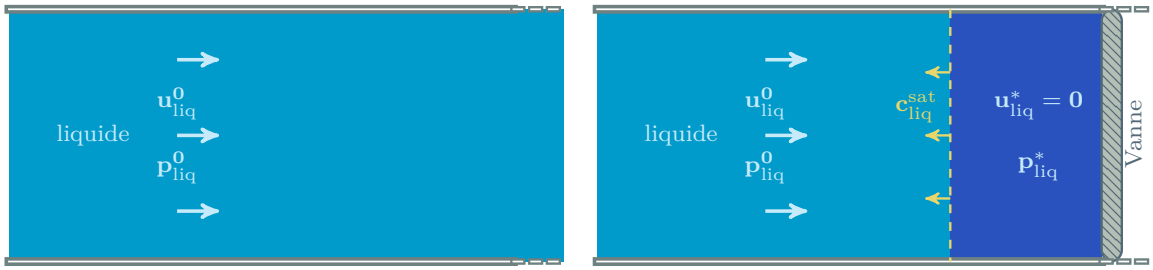

(a) Régime nominal monophasique liquide (b) Coup de bélier mécanique

FIGURE 1.1 – Transition : écoulement nominal, coup de bélier mécanique

La première, illustrée en FIGURE 1.1, représente un écoulement *monophasique* liquide dans une conduite *en charge* (conduite pleine) du circuit secondaire. Sur la FIGURE 1.1a, le régime d'écoulement est nominal à pression constante p^0_{liq} et vitesse constante u^0_{liq}. Comme décrit en FIGURE 1.1b, lors de la brusque fermeture d'une vanne d'arrêt présente sur le circuit, la colonne d'eau est violemment stoppée. Si l'on introduit ρ_{liq} la densité de l'eau liquide, on peut définir la quantité de mouvement en régime nominal comme $\rho_{\mathrm{liq}}\, u^0_{\mathrm{liq}}$. À la fermeture de la vanne, cette

dernière tend soudainement vers zero. Par conservativité, une telle chute se traduit par une augmentation significative de la pression qui passe de p_{liq} à p^*_{liq}. L'inertie de la colonne d'eau, due à la forte densité de l'eau liquide ρ_{liq}, implique que alors que le saut de pression relatif $\left(p^*_{liq} - p^0_{liq}\right)/p^0_{liq}$ peut être largement supérieur à un. Par la suite, une onde associée à ce saut de pression de grande amplitude remonte le long de la conduite et peut causer des dégâts sur sa structure. Ce type de scénarios est appelé *coup de bélier hydraulique* [9, 43, 53].

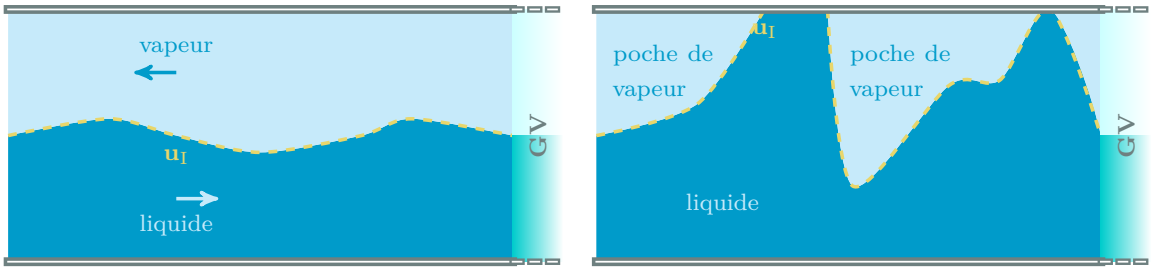

(a) Écoulement stratifié eau-vapeur (b) Écoulement eau-vapeur de type "slug"

FIGURE 1.2 – Transition : écoulement stratifié, écoulement de type "slug"

La deuxième configuration, représentée en FIGURE 1.2 décrit un écoulement eau-vapeur *stratifié* [15, 54, 55] localisé au niveau de la branche froide du circuit secondaire alimentant le *générateur de vapeur* (GV). Lors de certains régimes de fonctionnement dits *hors-charge*, un filet de vapeur peut remonter le long du circuit secondaire. Les deux phases circulent alors *à contre-courant* l'une de l'autre. Dans ce contexte, on définit u_I, la vitesse matérielle associée à l'interface eau-vapeur. Sous l'effet des forces de cisaillement, cette interface eau-vapeur se déforme progressivement et une instabilité de type Kelvin-Helmholtz [62] se développe. Comme illustré sur la FIGURE 1.2b, pour des échelles de temps suffisamment longues, l'écoulement stratifié peut se transformer en écoulement de type "slug" [15, 54, 55] où des poches de vapeurs se retrouvent piégées au sein de l'écoulement d'eau liquide. Par la suite, la condensation brutale de ces poches peut générer des ondes de choc appelées coups de bélier de condensation dont l'impact sur les structures peut engendrer des déformations, des fissures ou même des brèches.

Outre la spécificité inhérente à l'aspect diphasique des écoulements présentés ci-dessus, on peut également identifier d'autres particularités relatives aux ordres de grandeur de certaines quantités d'importance. En effet, des mesures expérimentales révèlent que :

$$|u_I| \approx 1\, m.s^{-1},\ \left|u^0_{liq}\right| \approx 1\, m.s^{-1},\ \left|u^*_{liq}\right| = 0\, m.s^{-1}. \tag{1.1}$$

Par ailleurs, on peut également introduire :

$$c^{sat}_{vap} = 481\, m.s^{-1},\ c^{sat}_{liq} = 909\, m.s^{-1}, \tag{1.2}$$

les vitesses du son de la phase vapeur et de la phase liquide sur la courbe de saturation à température $T^{sat} = 300°\,C$. Définissant $c_I = \min\left(c^{sat}_{vap}, c^{sat}_{liq}\right)$, on constate alors que pour l'ensemble des écoulements présentés ci-dessus :

$$M_I = \frac{|u_I|}{c_I} \ll 1,\ M_{liq} = \frac{\left|u^0_{liq}\right|}{c^{sat}_{liq}} \ll 1,\ M^* = \frac{\left|u^*_{liq}\right|}{c^{sat}_{liq}} = 0. \tag{1.3}$$

La faible valeur du nombre de Mach dans chacune de ces configurations, assortie au fait que les phases considérées sont *systématiquement* dotées d'une équation d'état thermodynamique, sont des caractéristiques des écoulements dits *compressibles à faible vitesse.*

Par ailleurs deux échelles de temps t_{ref} différentes peuvent être associées aux phénomènes présentés ci-dessus. La première, commune à l'écoulement stratifié FIGURE 1.2a et au régime nominal FIGURE 1.1a, se base sur la dynamique des ondes matérielles dont les vitesses sont u_I et

u^0_{liq} :

$$t^{\text{I}}_{\text{ref}} = \frac{\text{L}}{|u_{\text{I}}|} \approx t^0_{\text{ref}} = \frac{\text{L}}{\left|u^0_{\text{liq}}\right|}, \tag{1.4}$$

où L est une longueur caractéristique de la conduite (par exemple son diamètre). La deuxième échelle de temps caractéristique est rattachée à la propagation du coup de bélier de la FIGURE 1.1b. Le front de discontinuité entre les zones de pression p^0_{liq} et p^*_{liq} se déplace alors à une vitesse proche de $c^{\text{sat}}_{\text{liq}}$. On peut donc écrire :

$$t^*_{\text{ref}} = \frac{\text{L}}{c^{\text{sat}}_{\text{liq}}}. \tag{1.5}$$

Un grand écart relatif existe donc entre les dynamiques des phénomènes étudiés puisque $t^0_{\text{ref}}/t^*_{\text{ref}} = 1/\text{M}_{\text{liq}} \gg 1$. On peut enfin souligner une différence importance quant aux variations de pression relevées dans chacun des scénarios présentés. En effet, dans le cadre de l'écoulement stratifié ou au cours du régime nominal précédant la fermeture de la vanne, les fluctuations de pression dans la phase vapeur ou la phase liquide sont très faibles. En revanche, celles associées au coup de bélier mécanique sont, pour un fluide aussi *dense* et aussi *peu compressible* que l'eau liquide, très importantes.

Les phénomènes physiques décrits dans les exemples industriels précédents sont à la croisée des chemins entre plusieurs domaines des mathématiques appliqués à la mécanique des fluides compressibles. Tout d'abord, l'interaction entre l'eau et sa vapeur dans la configuration 1.2 relève de la *modélisation diphasique des écoulements*. Ensuite, dans le cadre des scénarios 1.2a et 1.1a, la prépondérance des ondes matérielles combinée à l'absence de sauts de pression de *grande* amplitude appellent à faire le parallèle avec les écoulements *à faible nombre de Mach* (où en général la densité est faible et la compressibilité importante). Enfin, dans le cadre de la configuration 1.1b, l'apparition et la propagation d'un saut de pression de grande amplitude dans un écoulement uniformément à faible vitesse requiert l'étude d'un régime asymptotique particulier propre aux coups de bélier.

Par la suite, chacun de ces différents axes sont présentés en regard de la littérature déjà existante.

1.2 Contexte scientifique

Conformément aux thèmes évoqués dans les éléments de contexte, on aborde ici successivement les notions de *modélisation diphasiques des écoulements*, la convergence asymptotique des équations d'Euler compressible vers le système d'Euler *incompressible* ainsi que celle vers un autre modèle asymptotique appelé *système d'Allievi*.

1.2.1 Modélisation diphasique des écoulements à phases compressibles

La modélisation diphasique des écoulements à phases compressibles est un domaine en plein essor depuis une cinquantaine d'années. Comme proposé dans les ouvrages [36, 54, 55], le point de départ consiste à représenter ces écoulements comme un ensemble de domaines monophasiques séparés par des interfaces mobiles. Au sein de chacune des régions délimitées par ces interfaces, la phase en présence vérifie les équations de Navier-Stokes. Les interfaces sont quant à elle modélisées par des lois algébriques et leur évolution prend en compte les multiples échanges mécaniques, thermiques et chimiques entre les différents domaines délimités.

Du point de vue de la simulation numérique, la prise en compte de l'ensemble des échelles spatiales définies par les interfaces suppose d'utiliser des méthodes de suivi dites *Lagrangiennes*. Ces dernières peuvent se révéler inadaptées lorsque l'échelle caractéristique des bulles ou des gouttes présentes dans l'écoulement est bien plus petite que la taille de maille considérée. De

plus, lorsque le nombre d'interfaces à suivre augmente considérablement, ces méthodes peuvent s'avérer coûteuses en temps de calcul.

Dans ce contexte, deux alternatives basées sur des méthodes *Eulériennes* peuvent être mentionnées. Il s'agit de la modélisation diphasique par approche *homogène* et par approche *bifluide*. Ces techniques reposent sur un principe de *moyennisation* temporelle, spatiale ou statistique (voir [35, 54]) permettant de remplacer les interfaces *discontinues*, introduites initialement entre les phases, en interfaces *diffuses*. Les spécificités relatives à chacune de ces méthodes de modélisation sont décrites ci-dessous.

Approche homogène

Dans le cadre de la modélisation diphasique par approche homogène, les deux phases sont décrites comme un seul et même fluide. Dans le cas plus spécifique du *modèle homogène équilibré* (HEM en anglais) [20], des équilibres en vitesse, pression, température ainsi qu'en potentiel chimique sont supposés entre les deux phases. On suit alors l'évolution du fluide à travers une densité ρ, une quantité de mouvement $\rho\mathbf{u}$ ainsi qu'une énergie totale ρe de mélange. Le système d'équations aux dérivées partielles (EDP) vérifié par ces variables est alors très similaire au système d'Euler compressible :

$$\partial_t \rho + \underline{\nabla} \cdot (\rho \mathbf{u}) = 0, \tag{1.6a}$$

$$\partial_t (\rho \mathbf{u}) + \underline{\nabla} \cdot (\rho \mathbf{u} \otimes \mathbf{u} + p \mathbf{I}) = \mathbf{0}, \tag{1.6b}$$

$$\partial_t (\rho e) + \underline{\nabla} \cdot ((\rho e + p) \mathbf{u}) = 0, \tag{1.6c}$$

$$e = \frac{|\mathbf{u}|^2}{2} + \varepsilon, \ \varepsilon = \varepsilon^{\mathrm{EOS}}\left(\rho, p\right). \tag{1.6d}$$

L'équation d'état présentée en (1.6d) relie l'énergie interne du mélange ε à la densité et la pression. Dans le cadre d'écoulements diphasiques, cette dernière peut être approximée par une loi d'état tabulée [50, 91]. Une autre alternative est basée sur la résolution d'un problème de maximisation sous contrainte pour l'entropie du mélange [7]. Si l'hypothèse d'équilibre en potentiel chimique est relâchée, une équation supplémentaire sur le titre massique doit être ajoutée. On obtient alors un modèle dit *homogène relaxé* (HRM en anglais) [12, 34]. Enfin, le déséquilibre en vitesse entre les deux phases peut être également ré-introduit à travers une loi de fermeture à l'intérieur du flux de quantité de mouvement et éventuellement d'un des flux de masse. On parle alors de modèle de *dérive* ("drift-flux model" en anglais) [38, 47, 93].

La nature des modèles présentés ci-dessus est telle que ces derniers sont plutôt adaptés aux écoulements diphasiques dispersés [15, 54] présentant une certaine uniformité spatiale (distribution homogène de bulles de vapeur au sein d'un écoulement d'eau liquide). Leur formalisme basé sur une écriture *conservative* des flux permet par ailleurs de poser un cadre mathématique rigoureux. Du point de vue de la simulation numérique, ceci se traduit par une certaine robustesse des solveurs développés notamment pour les écoulements dans le coeur des REP (code THYC d'EDF [67], code FLICA du CEA [90]).

Ils sont nettement moins appropriés lorsqu' apparaissent des phénomènes thermodynamiquement hors-équilibre comme la métastabilité [16]. Ces modèles peuvent également manquer de précision dans des configurations d'écoulements stratifiés où les vitesses de chaque phase peuvent être fortement décorrélées.

Approche bifluide

Contrairement aux modèles homogènes, la modélisation diphasique par approche bifluide considère les phases comme deux fluides distincts. En accord avec la notion d'interfaces diffuses, cette approche repose sur un processus de moyennisation des lois de conservation vérifiées par chacune des phases $k \in \{1, 2\}$. Ces lois de conservation sont au préalable pondérées par une fonction couleur qui spécifie la présence ou l'absence de la phase k dans le domaine d'étude.

Dans le cas le plus général, chaque phase admet donc une EDP relative à sa propre densité moyenne $\alpha_k \rho_k$, quantité de mouvement moyenne $\alpha_k \rho_k \mathbf{u}_k$ et énergie totale moyenne $\alpha_k \rho_k e_k$. La variable α_k représente le *taux de présence* moyen de la phase k au sein du domaine considéré. La dynamique de cette variable est souvent modélisée par une équation de transport (appelée également équation topologique) impliquant une vitesse interfaciale $\mathbf{u}_\mathrm{I}$. Par ailleurs, une pression interfaciale p_I intervient également dans la partie convective de ces modèles.

Qui plus est, les variables thermodynamiques de chaque phase sont liées par une loi d'état indépendante des variables de l'autre phase. Aucun équilibre entre les vitesses, les pressions, les températures ou les potentiels chimiques des deux phases n'est donc *a priori* supposé. De ce fait, l'approche bifluide contient intrinsèquement une plus grande richesse quant à la gamme d'écoulements diphasiques qu'elle peut représenter.

En contrepartie, de nombreuses lois de fermeture doivent être spécifiées. Ces dernières modélisent notamment les échanges mécaniques et thermodynamiques entre les phases mais caractérisent également la vitesse et la pression interfaciales. Encore à l'heure actuelle, aucun consensus clair n'existe quant aux critères de détermination de ces lois de fermeture. Différents travaux fondamentaux de modélisation diphasique par approche bifluide sont donc présentés ci-dessous.

Un des premiers modèles bifluides à deux vitesses et deux pressions appliqués aux écoulements eau-vapeur a été introduit par Ransom et Hicks [79]. On peut aussi mentionner le modèle à une seule pression de Stewart et Wendroff [87]. Dans le cadre de scénarios de combustion de matériaux granulaires baignant dans une phase de gaz brûlés, le modèle de Baer et Nunziato [5] a été également pionnier. Ce dernier a largement été repris pour le même type d'applications par Kapila *et al.* [60, 61] mais aussi pour des écoulements eau-vapeur [42, 45].

Une version *isentropique* et monodimensionnelle du modèle de Baer et Nunziato sera étudiée dans le cadre de la deuxième partie de cette thèse. Aussi, il nous paraît important de présenter, au préalable, le système d'EDP général (*i. e.* avec équations d'énergie) de ce modèle. Dans un formalisme multidimensionnel, ce dernier s'écrit donc :

$$
\begin{array}{lcccccl}
\partial_t \alpha_k & + & \mathbf{u}_\mathrm{I} \cdot \underline{\nabla} \alpha_k & & & = & (-1)^{k+1} \Phi_\alpha, \\
\partial_t m_k & + & \underline{\nabla} \cdot (m_k \mathbf{u}_k) & & & = & (-1)^{k+1} \Phi_m, \\
\partial_t m_k \mathbf{u}_k & + & \underline{\nabla} \cdot \left(m_k \mathbf{u}_k \otimes \mathbf{u}_k + \alpha_k p_k \mathbf{I} \right) & - & p_\mathrm{I} \underline{\nabla} \alpha_k & = & (-1)^{k+1} \Phi_{mu}, \\
\partial_t m_k e_k & + & \underline{\nabla} \cdot \left((m_k e_k + \alpha_k p_k) \mathbf{u}_k \right) & - & p_\mathrm{I} \mathbf{u}_\mathrm{I} \cdot \underline{\nabla} \alpha_k & = & (-1)^{k+1} \Phi_{me}, \\
\multicolumn{7}{l}{\text{avec : } m_k = \alpha_k \rho_k,\ e_k = \dfrac{|\mathbf{u}_k|^2}{2} + \varepsilon_k,\ \varepsilon_k = \varepsilon_k^{\mathrm{EOS}} \left(\rho_k, p_k \right).}
\end{array}
\tag{1.7}
$$

Les termes à droite des égalités modélisent les échanges mécaniques, chimiques et thermiques entre les deux phases. Dans le cadre des travaux présentés dans [52, 71], une proposition de lois de fermeture est faite pour chacun de ces termes. Elle s'appuie sur le principe d'augmentation de l'entropie de *mélange* des deux phases. D'autres approches basées sur l'augmentation des entropies *phasiques* sont explorées dans [42, 75].

Par ailleurs, on remarque que la vitesse et la pression interfaciales $\left(\mathbf{u}_\mathrm{I},\ p_\mathrm{I} \right)$ interviennent en facteur du gradient du taux de présence. On constate alors que dans les régions où α_k est constant, ces termes *non-conservatifs* disparaissent et le système (1.7) est similaire à deux systèmes d'Euler compressibles découplés. Dans le cas non constant, ces termes sont cruciaux car ils modélisent l'interaction entre les deux phases à travers une onde de *couplage*. Plusieurs fermetures pour le couple $\left(\mathbf{u}_\mathrm{I},\ p_\mathrm{I} \right)$ ont été proposées dans la littérature [44, 79, 82]. On peut également mentionner [1] où des fermetures discrètes sont proposées. On peut notamment distinguer les travaux de Coquel *et al.* [21] et Gallouët *et al.* [40] qui proposent des formes admissibles de vitesse interfaciale afin d'assurer le caractère linéairement dégénéré de l'onde de couplage entre les deux phases. Ce faisant, les produits non-conservatifs présents dans le système (1.7) peuvent être complètement définis au sens faible. Une fois u_I définie, la pression interfaciale p_I est également déduite à l'aide du critère portant sur le bilan d'entropie de mélange du système.

Au delà des modèles de type Baer-Nunziato, l'approche bifluide est très utilisée pour développer certains codes industriels dans le domaine du nucléaire. On peut mentionner le code CA-

THARE [11] développé par le CEA, NEPTUNE_CFD [46] dans le cadre du consortium EDF-CEA-IRSN-AREVA, mais aussi les codes RELAP5 [66] et RELAP7 [10] pour le nucléaire américain.

Les approches homogène et bifluide présentées ci-dessus permettent à présent de justifier les choix de modélisation effectués dans cette thèse afin de traiter les configurations (1.1) et (1.2) introduites dans les éléments de contexte industriel. En effet, la configuration présentée en (1.2a) correspond à un écoulement stratifié eau-vapeur en conduite où la déformation de l'interface est engendrée par le déséquilibre en vitesse entre les deux phases. L'approche bifluide, basée sur un modèle monodimensionnel de type Baer-Nunziato isentropique incluant des termes sources de relaxation en pression et en vitesse sera donc privilégiée pour ce type de scénario. Il convient de remarquer que la condensation brutale des poches de vapeurs au sein du régime de type "slug" n'entre pas dans le cadre de ces travaux de thèse. Un modèle de type Baer-Nunziato avec équations d'énergie et effets de relaxation en pression, vitesse, potentiel chimique et température aurait été requis pour étudier un tel phénomène.

En revanche, aucun déséquilibre eau-vapeur n'est la cause de la transition entre le régime d'écoulement nominal et le coup de bélier mécanique présentés en (1.1a), (1.1b). Par ailleurs, le caractère monophasique liquide de l'écoulement pousse à adopter l'approche homogène pour ce type de scénario.

1.2.2 Amplitude des sauts de pression pour les écoulements à phases compressibles à faible vitesse

Comme cela a été brièvement mentionné dans les éléments de contexte, le mécanisme à l'origine des coups de bélier mécaniques relève de la conversion brutale de l'énergie cinétique en énergie interne du fluide considéré. Ce transfert s'effectue à travers la loi d'état et son ordre de grandeur dépend de la compressibilité du fluide mis en jeu. Rappelons par ailleurs que cet événement particulier se développe au sein d'un écoulement compressible à basse vitesse. Deux analyses asymptotiques formelles, menées lorsque le nombre de Mach tend vers zéro, permettent alors de rendre compte de la présence ou de l'absence d'importants sauts de pression liés à l'occurrence de ce phénomène.

Ces analyses sont présentées ci-dessous.

Limite asymptotique vers le modèle Euler incompressible

Beaucoup de travaux de la littérature sur les écoulements à faible nombre de Mach [27, 33, 48, 49, 65, 74] traitent de la convergence formelle des solutions du système d'Euler compressible (1.6) vers celles issues du système d'Euler *incompressible*. Des résultats théoriques rigoureux ont par ailleurs été établis dans les travaux de Klainerman et Majda [63, 64] pour le système d'Euler isentropique ainsi que ceux de Schochet et Métivier [73, 83] pour le système d'Euler complet.

Nous ne soulignons ici que les hypothèses clefs utilisées au cours de ces analyses et commentons la compatibilité du modèle asymptotique obtenu avec la propagation d'un saut de pression de grande amplitude au sein d'un écoulement d'eau liquide.

L'analyse asymptotique repose sur l'adimensionnement du système (1.6). Le temps de référence t_{ref} associé aux dérivées partielles temporelles est alors construit à l'aide d'une vitesse matérielle de référence u_{ref} ainsi qu'une longueur de référence l_{ref} :

$$t_{\text{ref}} = \frac{l_{\text{ref}}}{u_{\text{ref}}}. \tag{1.8}$$

Les estimations des temps caractéristiques proposées en (1.4) et (1.5) permettent dors et déjà de remarquer que l'adimensionnement par t_{ref} convient davantage au régime nominal (1.1a) qu'à la propagation d'un coup de bélier (1.1b).

Un second point d'importance concerne l'adimensionnement du gradient de pression. Considérons ρ_{ref}, p_{ref} et c_{ref} une densité, pression et vitesse du son de référence propres au fluide étudié.

Dans de nombreux travaux, ces quantités sont reliées par la relation :

$$p_{\text{ref}} = \rho_{\text{ref}}\, c_{\text{ref}}^2. \tag{1.9}$$

La pertinence de cette égalité peut être discutée suivant le niveau de *compressibilité* du fluide considéré. En effet, on peut remarquer que

$$\begin{aligned} &\rho_{\text{ref}}\, c_{\text{ref}}^2 = \frac{1}{\beta_{\text{ref}}}, \\ &\text{avec } \beta = -\frac{1}{\tau}\frac{\partial \tau}{\partial p}_{|s}, \ \tau = 1/\rho, \end{aligned} \tag{1.10}$$

le coefficient de compressibilité isentropique. On peut alors relever de très grandes variations de valeur de β_{ref} entre de l'air compressible à température et pression ambiante et de l'eau très peu compressible circulant dans le circuit secondaire d'un REP. Dans le premier cas cela conduit à un ordre de grandeur de p_{ref} cohérent. Dans le second cas la valeur obtenue surestime largement les données expérimentales. En effet, pour de l'eau liquide circulant dans le circuit secondaire d'un REP à une pression de l'ordre de 150 bar et une température de 300° C on obtient une valeur de p_{ref} de l'ordre de 10^4 bar.

Dans tous les cas, on peut définir le nombre de Mach de référence de l'écoulement comme : $\mathrm{M} = u_{\text{ref}}/c_{\text{ref}}$. L'analyse asymptotique basée sur les égalités (1.8), (1.9) conduit alors à une décomposition de la pression adimensionnée de la forme :

$$p(x,\, t) = p^0(t) + \mathrm{M}^2\, \pi(x,\, t) + \mathrm{O}\left(\mathrm{M}^3\right). \tag{1.11}$$

Dans l'égalité (1.11), $p^0(t)$ est une pression *thermodynamique* déterminée à l'aide des conditions limites aux bords du domaine d'étude. L'expression $\pi(x,\, t)$ désigne quant à elle une pression *hydrodynamique* qui n'est plus reliée à la densité et à l'énergie interne à travers la loi d'état. Cette dernière modélise les forces de pression dans le système d'Euler incompressible :

$$\partial_t \rho + \mathbf{u}\cdot\underline{\nabla}\rho = 0, \tag{1.12a}$$

$$\partial_t \mathbf{u} + \mathbf{u}\cdot\underline{\nabla}\mathbf{u} + \tau\underline{\nabla}\pi = \mathbf{0}, \tag{1.12b}$$

$$\underline{\nabla}\cdot\mathbf{u} = 0. \tag{1.12c}$$

La décomposition (1.11) indique par ailleurs que les fluctuations spatiales de la pression totale adimensionnée sont de l'ordre de M^2. Dans le cadre d'un écoulement compressible à faible vitesse, $\mathrm{M}^2 \ll 1$ et ces variations sont donc infinitésimales. Ceci contraste avec l'amplitude du saut de pression relatif observée lors d'un coup de bélier. L'étude asymptotique menant au modèle (1.12) n'est donc pas satisfaisante pour traiter correctement l'apparition et la propagation des coups de bélier mécaniques.

Une autre analyse asymptotique permettant de mieux prendre en compte ces phénomènes est présentée ci-dessous.

Limite asymptotique vers le modèle d'Allievi

L'étude asymptotique présentée ici mène au modèle d'Allievi [2]. Bien que les lois de conservation linéaires de ce dernier soient très simples, il fournit néanmoins des estimations précises sur les sauts de pression lors de coups de bélier mécanique pour de l'eau liquide à température constante. Ce modèle peut, par ailleurs, être enrichi afin de prendre en compte les sauts de section ainsi que l'interaction fluide-structure (IFS) dans les conduites où le coup de bélier se propage [9, 43].

Le point de départ de l'analyse est le système d'Euler compressible à température constante. Contrairement à la technique d'adimensionnement précédente, le temps de référence associé à l'opérateur temporel est construit sur les vitesses d'ondes acoustiques :

$$t_{\text{ref}} = \frac{l_{\text{ref}}}{c_{\text{ref}}}. \tag{1.13}$$

De plus la pression de référence s'écrit maintenant comme :

$$p_{\text{ref}} = \rho_{\text{ref}}\, c_{\text{ref}}\, u_{\text{ref}}. \tag{1.14}$$

Cette définition est en accord avec les niveaux de pression caractéristiques d'un écoulement en conduite d'eau liquide à une vitesse de l'ordre du mètre par seconde et dont la température ne dépasserait pas les 179° C (température de saturation pour un niveau de pression de l'ordre de la dizaine de bar). Réécrit en variables pression-vitesse, les solutions régulières du modèle sans dimension vérifient alors formellement à l'ordre zéro :

$$\partial_t\, p + \rho\, c^2\, \underline{\nabla} \cdot \mathbf{u} = 0, \tag{1.15a}$$
$$\partial_t\, \mathbf{u} + \tau\, \underline{\nabla}\, p = \mathbf{0}. \tag{1.15b}$$

En supposant que la densité et la vitesse du son de l'eau varient très peu autour d'un couple $\left(\rho^0,\, c^0\right)$ constant à température donnée, le modèle d'Allievi s'écrit alors :

$$\partial_t\, p + \underline{\nabla} \cdot \left(\rho^0\, (c^0)^2\, \mathbf{u}\right) = 0, \tag{1.16a}$$
$$\partial_t\, \mathbf{u} + \underline{\nabla}(\tau^0\, p) = \mathbf{0}. \tag{1.16b}$$

Les valeurs propres de ce modèle hyperbolique linéaire sont $\pm c^0$. L'application des relations de Rankine-Hugoniot aux équations (1.16) pour un écoulement monodimensionnel permettent alors d'écrire les relations de saut de Joukowski [59] :

$$\left[p\right] = \pm \rho^0\, c^0\, \left[u\right], \tag{1.17}$$

où $\left[\phi\right]$ symbolise le saut associé à la variable ϕ à travers une discontinuité. Cette relation fait écho à l'adimensionnement (1.14) et permet d'estimer les bons niveaux de sauts de pression associés à la propagation d'un coup de bélier mécanique pour un écoulement d'eau liquide en conduite [85].

1.3 Objectifs des travaux

L'objectif de ce travail de thèse est de proposer des méthodes numériques nouvelles pour la simulation de deux scénarios de transition d'écoulements diphasiques relatifs aux FIGURE 1.1, 1.2 :

(I) Transition rapide d'un régime d'écoulement nominal monophasique liquide à l'apparition et la propagation d'un coup de bélier mécanique.

(II) Évolution d'un écoulement stratifié eau-vapeur vers un écoulement eau-vapeur de type "slug".

À la lumière des éléments introductifs présentés ci-dessus il s'avère que les écoulements au sein des scénarios (I) et (II) sont compressibles et à basse vitesse matérielle.

Par ailleurs, les différents régimes d'écoulement associés au point (I) peuvent être modélisés par une approche homogène. Qui plus est, lorsque le nombre de Mach tend vers zéro, deux modèles asymptotiques distincts sont sous-jacents à ce scénario de transition. Les très faibles fluctuations de pression observées lors du régime d'écoulement nominal suggèrent une proximité avec le modèle d'Euler incompressible. En revanche, la propagation rapide d'un saut de pression de grande amplitude liée au coup de bélier appelle à considérer le modèle d'Allievi et les relations de sauts de Joukowski.

Le régime d'écoulement de type "slug" du point (II) résulte d'une déformation de l'interface eau-vapeur due à un écart de vitesse entre les deux phases. Ce scénario de transition sera donc modélisé avec une approche bifluide.

1.4 Synthèse des travaux

Faisant écho aux scénarios de transition présentés en (I) et (II) , les travaux de thèse sont séparés en deux parties. La première propose d'aborder les difficultés relatives aux point (I) sous l'angle des méthodes numériques dites *multi-régimes*. La seconde se focalise sur le développement d'un nouveau schéma numérique pour un modèle de type Baer-Nunziato isentropique. Sa ligne directrice repose sur la prise en compte du couplage entre opérateur de convection et opérateur de relaxation pour ce type de modèle bifluide.

1.4.1 Partie I : Écoulements compressibles à faible vitesse et brusques sauts de pression

Comme annoncé précédemment, la première partie de ce travail se focalise sur le développement d'une méthode numérique dite *multi-régimes* [17] pour des modèles diphasiques homogènes. Le jeu d'équations aux dérivées partielles (EDP) étudié est alors similaire au système d'Euler compressible (1.6).

Rappelons que dans ce système, ρ, $\mathbf{u}$, p et e désignent respectivement la densité, le vecteur vitesse, la pression ainsi que l'énergie totale spécifique de la phase de mélange étudiée. Comme précisé en (1.6d), l'énergie totale spécifique est composée de la somme de l'énergie cinétique et de l'énergie interne spécifique ε. Cette dernière est reliée à la densité et à la pression via l'équation d'état générale décrite également en (1.6d). Par la suite on introduit aussi

$$c\left(\rho, p\right), \tag{1.18}$$

la vitesse du son associée au système d'Euler compressible.

Contexte

Au sein de ce travail, la notion d'écoulement compressible *multi-régimes* fait référence à trois types de configuration :

(i) L'écoulement est tel que le nombre de Mach moyen est supérieur ou égal à un. La compressibilité du fluide considéré permet alors l'apparition d'ondes de choc et d'ondes de raréfaction associées à de fortes variations de pression.

(ii) L'écoulement est tel que le nombre de Mach maximal sur le domaine d'étude est très petit devant un. De plus, le fluide considéré est suffisamment peu *dense* pour admettre une équation d'état telle que le saut de pression relatif, au travers d'une onde de choc, est borné devant le nombre de Mach. Il en résulte que seules des variations de pression de *petite amplitude* peuvent traverser l'écoulement.

(iii) De manière similaire à la configuration précédente, le nombre de Mach maximal de l'écoulement est très petit devant un. En revanche, le fluide considéré est très *dense* et possède une équation d'état qualifiée de "raide" ce qui signifie une *faible compressibilité*. Des ondes non-linéaires associées à des variations de pression de *grande amplitude* peuvent alors se propager à travers le domaine d'étude ; ceci *même si le nombre de Mach de l'écoulement est très petit devant un*.

À titre d'illustration on pourra donner, dans le cas de la configuration (i) , l'exemple d'un écoulement d'air autour du profil d'aile d'un avion se déplaçant à la vitesse du son [26]. Parmi l'immense variété d'écoulements eau-vapeur en conduite auxquels pourrait correspondre la configuration (ii) , on peut mentionner la déformation progressive de l'interface eau-vapeur au sein d'un écoulement stratifié menant progressivement à un régime de type "slug" [54]. Enfin, la configuration (iii) fait écho à des phénomènes transitoires violents tels que les *coups de bélier* d'origine mécanique [43]. On pourra notamment mentionner l'expérience due à Simpson [85] impliquant un écoulement d'eau liquide en conduite et où la brusque fermeture d'une vanne provoque des variations de pression de 15 bar, se propageant à 1280 mètres par seconde dans un écoulement dont la vitesse matérielle reste de l'ordre du mètre par seconde.

Le développement d'une méthode numérique "multi-régimes", au sens de la définition donnée dans [17], implique que deux objectifs sont atteints quelle que soit la configuration d'écoulement rencontrée. Ces objectifs sont les suivants :

1. La discrétisation spatiale de la méthode proposée doit être capable de capturer précisément les ondes d'intérêt du régime rencontré.
2. Considérons $\mathscr{C}$, le nombre de Courant basé sur les valeurs propres associées aux ondes d'intérêt du régime étudié. La zone de stabilité du schéma numérique développé doit contenir des valeurs de $\mathscr{C}$ proches de l'unité.

Précisons que dans le cadre des régimes d'écoulement (i) et (iii) l'attention se porte *a priori* sur les ondes de choc et de raréfaction associées aux champs vraiment non-linéaires. Les vitesses caractéristiques de ces ondes sont alors $|\mathbf{u}|+c$ pour la configuration (i) et $|\mathbf{u}|+c \approx c$ pour (iii) . Le régime d'écoulement (ii) se focalise quant à lui sur la propagation des ondes matérielles ou plus généralement sur les ondes de contact associées au champ linéairement dégénéré du système (1.6). Leur vitesse caractéristique est donnée par $|\mathbf{u}|$ qui, par définition d'un écoulement à faible nombre de Mach, est très petite devant c.

La méthode numérique multi-régimes résultant des chapitre 2 et chapitre 3 est construite pas à pas. Dans le chapitre 2, la structure générale de l'approche ainsi que les éléments théoriques clefs sont présentés et étudiés. Ces concepts se traduisent alors par un schéma volumes-finis dont l'intégration *explicite* en temps permet de traiter, au sens des objectifs 1. et 2. , des régimes d'écoulement proches de (i) et (iii) . Les lignes directrices ayant déjà été posées, le chapitre 3 modifie le schéma numérique précédent en y proposant une intégration en temps semi-implicite. Ce chapitre s'attache alors à montrer que la méthode développée est capable de remplir les objectifs 1. et 2. lors de *scénarios de transition* entre les régimes (ii) et (iii) . Précisons enfin que, dans le cadre du chapitre 3, la méthode numérique développée afin de traiter convenablement le régime d'écoulement (ii) ne se focalise que sur l'obtention des objectifs 1. et 2. . En particulier, la propriété de *préservation de l'asymptotique* du système d'Euler *incompressible* démontrée dans de nombreux travaux [27, 33, 49] n'a pas fait l'objet d'une étude dédiée dans ce chapitre.

Chapitre 2 : Splitting d'opérateur dépendant du nombre de Mach pour le système d'Euler

Inspiré des travaux de Baraille *et al.* [6] et Klein [65], ce chapitre propose d'aborder la problématique des écoulements multi-régimes en introduisant un splitting au sein du système (1.6). On met alors en évidence un opérateur dit *convectif* responsable des phénomènes de transport à vitesse matérielle et un opérateur *acoustique* à l'origine des variations de pression au sein de l'écoulement. Ces deux opérateurs sont alors associés à deux sous-systèmes d'équations aux dérivées partielles $\mathcal{C}$ (pour l'opérateur convectif) et $\mathcal{A}$ (pour l'opérateur acoustique) donnés par :

$$\mathcal{C} : \begin{cases} \partial_t \rho + \underline{\nabla} \cdot (\rho \mathbf{u}) = 0, \\ \partial_t (\rho \mathbf{u}) + \underline{\nabla} \cdot \left(\rho \mathbf{u} \otimes \mathbf{u} + \mathscr{E}_0^2(t)\, p \mathbf{I}\right) = \mathbf{0}, \\ \partial_t (\rho e) + \underline{\nabla} \cdot \left((\rho e) + \mathscr{E}_0^2(t)\, p\right) \mathbf{u}\big) = 0, \end{cases} \tag{1.19}$$

$$\mathcal{A} : \begin{cases} \partial_t \rho = 0, \\ \partial_t (\rho \mathbf{u}) + \underline{\nabla} \cdot \left((1 - \mathscr{E}_0^2(t))\, p \mathbf{I}\right) = \mathbf{0}, \\ \partial_t (\rho e) + \underline{\nabla} \cdot \left((1 - \mathscr{E}_0^2(t))\, p \mathbf{u}\right) = 0. \end{cases} \tag{1.20}$$

Il est important de remarquer qu'un paramètre temporel $\mathscr{E}_0(t)$ apparaît dans ces sous-systèmes conservatifs. On comprend alors qu'au cours du temps, l'évolution de $\mathscr{E}_0(t)$ peut engendrer un splitting de nature différente. Dans ce chapitre, le paramètre $\mathscr{E}_0(t)$ est une fonction du nombre de Mach maximal instantané de l'écoulement dans le domaine d'étude Ω. On le définit comme :

$$\begin{aligned} &\mathscr{E}_0(t) \propto \max\left(\mathscr{E}_{inf}, \min\left(\mathrm{M}_{max}(t), 1\right)\right), \\ &\mathrm{M}_{max}(t) = \sup_{x \in \Omega} \left(\mathrm{M}(x,t) = \frac{|\mathbf{u}(x,t)|}{c(x,t)}\right), \; 0 < \mathscr{E}_{inf} \ll 1. \end{aligned} \tag{1.21}$$

Par construction, ce paramètre prend ces valeurs dans $]0,1]$. Ainsi, les écoulements dont le nombre de Mach maximal à l'instant t est supérieur ou égal à un seront associés à l'asymptotique $\mathscr{E}_0(t) \to 1$. On peut alors remarquer que le sous-système $\mathcal{C}$ converge formellement vers le système d'Euler complet pendant que le sous-système $\mathcal{A}$ dégénère en un système stationnaire. En revanche, si le nombre de Mach maximal de l'écoulement est très petit devant un, $\mathscr{E}_0(t) \to 0^+$ et les termes liés au gradient de pression disparaissent totalement de $\mathcal{C}$ pour ré-apparaître dans $\mathcal{A}$. On tend alors vers un découplage complet des phénomènes convectifs et de la production d'ondes acoustiques.

Par la suite, la méthode numérique proposée est basée sur une approche à pas fractionnaires qui résout successivement, par le biais d'un schéma de type volumes-finis, le sous-système $\mathcal{C}$ et le sous-système $\mathcal{A}$. Ceci requiert au préalable d'étudier le système d'EDP relatif à chacun de ces deux nouveaux sous-systèmes. Ce chapitre se focalise en particulier sur l'hyperbolicité, la structure des champs (Proposition 2.2.1) ainsi que la positivité de la densité et de l'énergie interne spécifique (Section 2.2.2) pour des lois d'état de type gaz raide. Sous réserve de positivité de la pression, les deux sous-systèmes sont hyperboliques et deux nouvelles célérités $c_{\mathcal{C}}^2 > 0$ et $c_{\mathcal{A}}^2 > 0$ telles que,

$$(c_{\mathcal{C}})^2 + \left(1 - \mathscr{E}_0^2\right)(c_{\mathcal{A}})^2 = c^2, \tag{1.22}$$

interviennent respectivement au sein de chacun d'eux. Les valeurs propres de chacun de ces sous-systèmes s'écrivent :

$$\begin{aligned} &\lambda_1^{\mathcal{C}} = u - \mathscr{E}_0\, c_{\mathcal{C}} && \leq \lambda_2^{\mathcal{C}} = u \leq \lambda_3^{\mathcal{C}} = u + \mathscr{E}_0\, c_{\mathcal{C}}, \\ &\lambda_1^{\mathcal{A}} = -\left(1 - \mathscr{E}_0^2\right) c_{\mathcal{A}} && \leq \lambda_2^{\mathcal{A}} = 0 \leq \lambda_3^{\mathcal{A}} = \left(1 - \mathscr{E}_0^2\right) c_{\mathcal{A}}. \end{aligned} \tag{1.23}$$

Qui plus est, les champs 1 et 3 associés à ces ondes sont vraiment non-linéaires alors que les champs 2 sont linéairement dégénérés.

La structure hyperbolique des sous-systèmes $\mathcal{C}$ et $\mathcal{A}$ suggère un choix de discrétisation impliquant des solveurs de Riemann approchés. Notons tout d'abord que la dépendance en temps du paramètre $\mathscr{E}_0(t)$ ne perturbe pas la résolution du problème de Riemann général associé à chacun des sous-systèmes. En effet, au niveau discret, la fonction $t \to \mathscr{E}_0(t)$ est remplacée, avant chaque résolution, par sa valeur prise au pas de temps précédent. Le paramètre $\mathscr{E}_0$ est donc constant au cours de la résolution des sous-systèmes $\mathcal{C}$ et $\mathcal{A}$. Dans ce chapitre, afin de contourner la difficulté relative à la prise en compte des champs vraiment non-linéaires, un schéma de *relaxation* [13, 23, 58] de type *Suliciu* [88] est appliqué à chacun des sous-systèmes. Comme mentionné dans les éléments de contexte, dans ce chapitre, les deux sous-systèmes font l'objet d'une intégration explicite en temps. Par ailleurs, sous réserve d'une condition *sous-caractéristique* [92] légèrement modifiée, et avec un pas de temps discret basé sur les vitesses d'onde du système d'Euler, le Lemma 2.3.1 et le Lemma 2.3.2 assurent la positivité de la densité ainsi que de l'énergie interne spécifique obtenues avec l'approche à pas fractionnaires proposée.

Comme expliqué ci-dessus, dans le cadre du régime d'écoulement (i) , les valeurs discrètes du paramètre $\mathscr{E}_0$ sont proches de un. Le schéma de relaxation associé au sous-système $\mathcal{C}$ tend alors formellement vers un schéma de relaxation de type Suliciu pour le système d'Euler complet. L'intégration explicite en temps des termes liés au gradient de pression implique alors que, sous une condition CFL de la forme

$$\Delta t = \mathscr{C}\, \frac{\Delta x}{\sup\limits_{\Omega} (|\mathbf{u}| + c)}, \quad 0 < \mathscr{C} < 1/2, \tag{1.24}$$

le schéma proposé est stable et capture précisément les ondes liées aux champs vraiment non-linéaires. Les objectifs 1. et 2. sont donc remplis.

Le régime (iii) présente, quant à lui, une difficulté supplémentaire intrinsèquement liée à la discrétisation spatiale des schémas de type Godunov approchés. Comme expliqué dans [29–31], cette difficulté est en réalité à mettre en relation avec une problématique plus générale d'incompatibilité entre ce type de solveur et l'espace des *solutions incompressibles*. Dans le cadre de l'ap-

proche à pas fractionnaires proposée dans ce chapitre, cela se traduit par une diffusion numérique prohibitive associée à l'équation de moment. En effet, pour des maillages grossiers et dans la configuration (iii) , l'ordre de grandeur de cette dernière peut s'écrire comme

$$\nu^{\text{num}} = \mathrm{O}\left(\frac{\Delta x}{\mathrm{M}}\right), \quad \Delta x \gg \mathrm{M},\ \mathrm{M} \ll 1. \tag{1.25}$$

Adaptant la démarche présentée dans [17, 18], une analyse sur l'erreur de troncature relative aux schémas de relaxation de chacun des sous-systèmes puis sur celle produite par l'approche à pas fractionnaires globale est menée. On montre alors que l'application d'une θ-*correction* similaire à celle proposée dans [31, 39, 80] sur la partie décentrée du flux de quantité de mouvement du sous-système $\mathcal{A}$ permet de réduire la diffusion numérique de l'approche à

$$\nu^{\text{num},\theta} = \mathrm{O}\left(\frac{\theta\Delta x}{\mathrm{M}}\right) \approx \mathrm{O}\left(\Delta x\right), \quad \Delta x \gg \mathrm{M},\ \mathrm{M} \ll 1. \tag{1.26}$$

La méthode à pas fractionnaires proposée dans ce chapitre est par la suite comparée à une approche de type *Lagrange-Projection* décrite dans [17] et dont le splitting a été proposé dans [22]. Les deux schémas sont testés sur une série de tube à choc de type Sod [86] en faisant varier le nombre de Mach maximal de l'écoulement M_{max} ainsi que la raideur de l'équation d'état du fluide étudié. Le régime d'écoulement (i) correspond alors à des tubes à choc dont le fluide est peu dense et doté d'une loi d'état de type gaz parfait. Les cas tests associés au régime (iii) , quant à eux, utilisent un fluide dense et une loi d'état de type gaz raide. Il s'avère que dans le cadre du régime (i) , l'approche proposée est aussi précise et aussi efficace que la méthode de type Lagrange-Projection. En revanche, l'activation de la θ-correction dans le cadre du régime (iii) produit, au travers des ondes vraiment non linéaires et sur des maillages grossiers, des oscillations artificielles plus importantes pour le schéma proposé que pour le schéma Lagrange-Projection.

Chapitre 3 : Un schéma implicite-explicite adapté aux écoulements compressibles multi-régimes

Dans la lignée du chapitre précédent, le chapitre 3 ré-utilise le même splitting ainsi que les mêmes sous-systèmes $\mathcal{C}$ et $\mathcal{A}$ sous-jacents. Néanmoins, on s'intéresse ici au régime d'écoulement (ii) dont les ondes d'intérêt correspondent à l'onde de contact du système d'Euler. Pour des écoulements compressibles à faible nombre de Mach cette dernière se propage très lentement relativement aux ondes produites par l'opérateur acoustique. En effet, si l'on introduit de manière formelle

$$\mathscr{C}_{|u|} = \frac{\Delta t\,|\mathbf{u}|}{\Delta x}, \tag{1.27a}$$

$$\mathscr{C}_{|u|+c} = \frac{\Delta t\,(|\mathbf{u}|+c)}{\Delta x}, \tag{1.27b}$$

les nombres de Courant basés respectivement sur la valeur propre de l'onde de contact et les valeurs propres des ondes vraiment non-linéaires, on peut remarquer que :

$$\mathscr{C}_{|u|} = \frac{\mathrm{M}}{1+\mathrm{M}}\mathscr{C}_{|u|+c} \underset{\mathrm{M}\ll 1}{\ll} \mathscr{C}_{|u|+c}. \tag{1.28}$$

Si, comme au chapitre précédent, le sous-système acoustique est discrétisé à l'aide d'un solveur de Riemann approché d'ordre un, intégré explicitement en temps, alors la contrainte sur le pas de temps afin de garantir la stabilité du schéma numérique s'écrira $\mathscr{C}_{|u|+c} \approx 1$. Pour des temps de simulation basés sur la vitesse matérielle $|\mathbf{u}|$, la précision sur l'onde de contact sera, par conséquent, grandement détériorée de par l'application répétitive de l'opérateur de diffusion numérique sur un nombre important de pas de temps trop petits.

Le schéma numérique développé dans ce chapitre repose également sur une technique à pas fractionnaires. Comme au chapitre précédent, un schéma de relaxation explicite en temps est appliqué au sous-système $\mathcal{C}$. Néanmoins, afin de traiter la difficulté relative à la précision sur les

ondes de contact lentes, ce chapitre propose une intégration *implicite* en temps du sous-système acoustique $\mathcal{A}$. Pour ce faire, le même *modèle* de relaxation ayant servi à construire le solveur de Godunov approché du chapitre précédent est considéré. On cherche alors à construire une estimation implicite de $\left(\Pi^*_{\mathcal{A}}\right)_f$ et $\left(u^*_{\mathcal{A}}\right)_f$, la pression et la vitesse créées à la face f d'un maillage monodimensionnel par le problème de Riemann associé à ce système de relaxation acoustique. Ces variables interviennent notamment dans le flux acoustique donné par :

$$\left(\mathbf{F}^*_{\mathcal{A}}\right)_f = \left(1-\mathscr{E}_0^2\right)\begin{bmatrix} 0 \\ \left(\Pi^*_{\mathcal{A}}\right)_f \\ \left(\Pi^*_{\mathcal{A}}\right)_f \left(u^*_{\mathcal{A}}\right)_f \end{bmatrix}. \tag{1.29}$$

Les estimations requises sont obtenues en adaptant les idées développées dans [17, 22]. Ces dernières se basent sur une ré-écriture *équivalente* du système d'EDP de relaxation acoustique mettant en évidence les équations de transport relatives à deux invariants de Riemann *forts* notés :

$$\mathrm{W} = u - \frac{\Pi}{a_{\mathcal{A}}},\ \mathrm{R} = u + \frac{\Pi}{a_{\mathcal{A}}}, \tag{1.30}$$

avec $a_{\mathcal{A}}$ la constante de relaxation introduite dans ce modèle et Π la pression de relaxation. Par définition, W ne saute qu'au travers de la discontinuité de contact associée à la valeur propre de relaxation $\lambda^1_{\mathcal{A}} = -(1-\mathscr{E}_0^2)\, a_{\mathcal{A}}\, \tau$; τ étant le volume spécifique $1/\rho$. De manière symétrique, R ne saute qu'au travers de l'onde de contact associée à $\lambda^4_{\mathcal{A}} = +(1-\mathscr{E}_0^2)\, a_{\mathcal{A}}\, \tau$. La FIGURE 1.3 représente les régions d'invariance respectives de W et R dans le domaine espace-temps. L'axe spatial représente une cellule d'un maillage monodimensionnel délimitée par deux faces au niveau desquelles les ondes se propagent. Sur la base de ces propriétés, une intégration implicite en temps des équa-

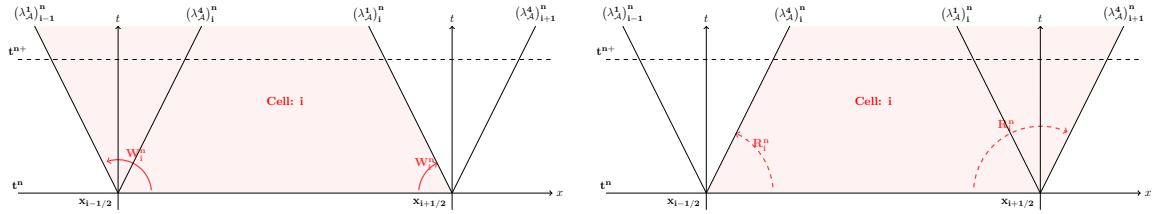

(a) Domaine d'invariance de W (b) Domaine d'invariance de R

FIGURE 1.3 – Comportement des invariants de Riemann forts

tions de transport associées à W et R est alors possible. Des relations (1.30), on peut alors déduire les estimations attendues sur les variables $\left(\Pi^*_{\mathcal{A}}\right)_f$ et $\left(u^*_{\mathcal{A}}\right)_f$.

Une fois le schéma numérique complètement défini, le chapitre se focalise sur deux types de scénarios d'écoulement. Le premier correspond au cas où le régime (ii) est établi. Le pas de temps discret est alors exprimé en fonction du nombre de Courant $\mathscr{C}_{|u|}$ introduit en (1.27a). Une étude heuristique basée sur la propagation d'une onde de contact isolée décrite en Section B de ce chapitre suggère que, pour tout nombre de Mach, l'approche semi-implicite développée est stable pour des valeurs de $\mathscr{C}_{|u|}$ de l'ordre de 0.5. Par ailleurs, les courbes de convergence et d'efficacité obtenues sur un problème de Riemann de type tube à choc révèlent que l'approche proposée est aussi précise et coûteuse en temps CPU qu'une version semi-implicite de la méthode Lagrange-Projection [17]. Le domaine de stabilité de cette dernière admet néanmoins des nombres de courant $\mathscr{C}_{|u|}$ plus élevés que le schéma numérique de ce chapitre.

Le deuxième type de scénarios étudiés correspond à la transition rapide entre le régime (ii) et le régime (iii) . Au cours du temps l'écoulement reste donc uniformément à faible nombre de Mach. Néanmoins, des ondes de choc associées à de fortes variations de pression apparaissent au cours de cette transition. Dans ce chapitre, deux nouveaux éléments viennent enrichir l'approche proposée afin de traiter au mieux cette configuration particulière.

Premièrement, on complète la définition du paramètre $\mathscr{E}_0 \in]0, 1]$ en y incluant un *détecteur de choc* dont le rôle est de faire tendre $\mathscr{E}_0$ vers 1 lorsqu'une variation de pression de grande amplitude traverse l'écoulement. Ce changement a un premier impact sur la discrétisation *spatiale*

de la méthode. En effet, lorsque $\mathscr{E}_0$ passe soudainement de 0^+ à 1, l'approche à pas fractionnaires dont l'intégration en temps est explicite sur $\mathcal{C}$ et implicite sur $\mathcal{A}$, se transforme en un solveur de relaxation explicite en temps, consistent avec le système d'Euler complet.

Un second impact porte également sur *l'ordre de grandeur* du pas de temps discret utilisé par le schéma. En effet ce dernier est construit en utilisant les valeurs propres $\lambda^{\mathcal{C}}_{1,3}$ (1.23) du sous-système $\mathcal{C}$. On peut l'écrire formellement comme :

$$\Delta t = \mathscr{C}_{\mathcal{C}} \frac{\Delta x}{|\mathbf{u}| + \mathscr{E}_0\, c_{\mathcal{C}}},\ \mathscr{C}_{\mathcal{C}} \approx 1/2. \tag{1.31}$$

Ainsi, tant que le régime (ii) est établi, $\mathscr{E}_0$ tend vers 0^+ et le pas de temps est similaire à celui basé sur $\mathscr{C}_{|u|}$ dans (1.27a). Puis, lors de la brusque transition vers le régime (iii) , $\mathscr{E}_0$ tend vers 1, $c_{\mathcal{C}}$ tend vers c de par la relation (1.22) et le pas de temps s'adapte *automatiquement* pour prendre des valeurs similaires à celui construit à partir des valeurs propres du système d'Euler complet (1.27b). Notons que dans ce chapitre, le détecteur de choc proposé s'appuie simplement sur la relation de Rankine-Hugoniot appliquée à l'équation de la masse du système d'Euler. Une autre piste, testée mais non présentée dans ce manuscrit, est basée sur une estimation de célérité grâce à la relation de Joukowski (1.17). L'idée sous-jacente est d'intégrer l'information relative à l'amplitude des sauts de pression issus du modèle asymptotique d' Allievi (1.16) ; modèle qui caractérise bien la propagation des coups de bélier hydrauliques.

La brusque transition entre le régime (ii) et le régime (iii) est illustrée à travers un cas test de vérification dans lequel le fluide est dense et doté d'une loi d'état de type gaz raide. La solution analytique, dont le nombre de Mach maximal reste inférieur à 10^{-2}, se construit comme la succession de deux problèmes de Riemann produisant des niveaux très différents de pression et de vitesse intermédiaires. Contrairement à la méthode semi-implicite de type Lagrange-Projection, l'approche proposée dans ce chapitre adapte son pas de temps ainsi que la discrétisation spatiale de son flux numérique afin de capturer avec un niveau de détail suffisant l'ensemble des états intermédiaires créés.

1.4.2 Partie II : Couplage convection-source pour un modèle bifluide à deux pressions et deux vitesses

La seconde partie des travaux de thèse se focalise sur les modèles diphasiques à deux pressions et deux vitesses en présence de termes sources. Plus particulièrement, son objectif est de s'intéresser à l'interaction entre l'opérateur de convection et l'opérateur algébrique de relaxation pour un système de type Baer-Nunziato isentropique soumis à des effets de relaxation en pression ainsi qu'en vitesse. Dans le cadre d'un écoulement diphasique monodimensionnel, un tel système, initialement proposé dans sa forme générale avec équations d'énergie, par Baer et Nunziato dans [5] peut s'écrire sous la forme :

$$\begin{array}{lcccccl}
\partial_t \alpha_k & + & u_{\mathrm{I}}\, \partial_x \alpha_k & & = & (-1)^k\, \mathrm{K_p}\,(\mathbf{U})\, \Delta p, \\
\partial_t m_k & + & \partial_x\, m_k u_k & & = & 0, \\
\partial_t m_k u_k & + & \partial_x \left(m_k u_k^2 + \alpha_k p_k\right) & - \quad p_{\mathrm{I}}\, \partial_x \alpha_k & = & (-1)^{k+1}\, \mathrm{K_u}\,(\mathbf{U})\, \Delta u.
\end{array} \tag{1.32}$$

Ici $k \in \{1, 2\}$ désigne l'indice de la phase correspondante. Les quantités α_k, m_k, u_k, ρ_k, p_k désignent respectivement le taux de présence statistique, la masse partielle, la vitesse, la densité ainsi que la pression de la phase k. La masse partielle est reliée à la densité par la relation : $m_k = \alpha_k \rho_k$. Dans ce modèle *isentropique*, la densité et la pression sont reliées par une loi d'état thermodynamique que l'on note :

$$\begin{aligned}
&p_k = p_k^{\mathrm{EOS}}\left(\rho_k\right),\ \left(p_k^{\mathrm{EOS}}\right)'(\rho_k) > 0, \\
&\lim_{\rho_k \to 0} p_k = 0,\ \lim_{\rho_k \to \infty} p_k = +\infty.
\end{aligned} \tag{1.33}$$

Des opérateurs différentiels dits *non-conservatifs* sont également présents dans ce modèle. Ils correspondent aux termes :

$$u_{\mathrm{I}}\, \partial_x \alpha_k,\ p_{\mathrm{I}}\, \partial_x \alpha_k, \tag{1.34}$$

où le couple (u_I, p_I) désigne une vitesse et une pression *interfaciales* que l'on prendra égal à (u_2, p_1). Enfin, dans le système (1.32), les termes à droite des égalités pilotent les effets de relaxation en pression et en vitesse et sont tels que :

$$\begin{aligned} \Delta p &= p_2 - p_1, \\ \Delta u &= u_2 - u_1. \end{aligned} \tag{1.35}$$

Les cofacteurs positifs $\mathrm{K}_\mathrm{p}(\mathbf{U})$ et $\mathrm{K}_\mathrm{u}(\mathbf{U})$, $\mathbf{U} = [\alpha_1, m_1, m_1 u_1, m_2, m_2 u_2]^\mathrm{T}$, caractérisent la forme ainsi que la vitesse des trajectoires de relaxation. Ils contiennent notamment des échelles de temps de relaxation en pression et en vitesse $\left(\tau_\mathrm{p}(\mathbf{U}), \tau_\mathrm{u}(\mathbf{U})\right)$ dont des estimations sont proposées dans [41, 56].

Contexte

La notion de système hyperbolique avec relaxation a été introduite par Liu dans [70]. Cette dernière désigne un système hyperbolique dont la partie convective peut-être ré-écrite sous la forme d'une *divergence de flux* complétée par des termes sources. L'expression de ces termes sources est telle qu'il existe un ensemble non-vide d'états pour lesquels ces derniers s'annulent. Par la suite cet ensemble est appelé *variété d'équilibre*. Dans ce formalisme, les travaux de Chen, Levermore et Liu [19] ont montré que, sous réserve d'existence d'une entropie mathématique pour le système hyperbolique avec relaxation, ce dernier converge vers un système *d'équilibre* de dimension inférieure. De plus cette convergence se traduit également à travers une condition dite "*sous-caractéristique*" [70, 92] qui insère les valeurs propres du système d'équilibre entre celles du système de relaxation. Le formalisme posé par les auteurs cités ci-dessus fournit un cadre théorique précieux auquel se raccrocher lors du développement de schémas numériques. Néanmoins trois types de difficultés apparaissent au cours de cet exercice :

(i) Apparition de solutions d'équilibre artificielles dues à des violations locales de la condition sous-caractéristique [14, 77], ou par manque de précision des schémas [68].

(ii) Perte de précision des schémas numériques d'ordre élevé dans des régimes de relaxation très raides [76, 78].

(iii) Non respect du principe de *préservation de l'asymptotique* associé au système d'équilibre étudié [57] et faible précision sur les variables dîtes de relaxation [8].

Dans la **Partie II**, nous ne traiterons *aucune* de ces difficultés. En effet, la présence des termes *non-conservatifs* dans le système (1.32) fait que ce dernier ne s'insère *pas* dans la théorie évoquée ci-dessus. Bien que des études formelles sur l'asymptotique d'équilibre de modèles bifluides de type Baer-Nunziato aient déjà été menées dans [4, 28, 69], d'importantes difficultés relevant de l'analyse théorique de ces systèmes d'EDP demeurent.

Aussi, le travail présenté ici se contente de s'approprier (chapitre 4) puis d'étendre (chapitre 5) certaines idées proposées par Bereux et Sainsaulieu dans [8] afin de proposer les premières esquisses d'un nouveau type de schémas numériques prenant en compte le couplage convection-source pour le système (1.32).

À ce titre, le chapitre 4 se veut pédagogique. Il synthétise certaines des idées développées dans [8] et présente des exemples simples d'application. Il écarte volontairement les difficultés relatives à la présence des termes non-conservatifs en "gelant" la matrice Jacobienne de convection du modèle (1.32). Les termes de relaxation en pression et en vitesse sont également remplacés afin de construire facilement des solutions analytiques au problème étudié. Le schéma numérique issu des travaux de Bereux et Sainsaulieu est généralisé afin de traîter des phénomènes de relaxation dont la non-linéarité et la non-monotonie sont plus importantes que les termes d'échange de quantité de mouvement présents dans le modèle bifluide de [8].

Le chapitre 5, quant à lui, reprend le même cadre de réflexion que celui posé au chapitre précédent et propose d'y introduire la présence des termes non-conservatifs du système Baer-Nunziato isentropique. Un nouveau schéma associé à (1.32) est alors mis en place. Outre une étude relative à

certaines propriétés discrètes telles que la conservativité ou le principe du maximum, ce schéma est comparé à des méthodes à pas fractionnaires sur des problèmes de Riemann homogènes et généralisés.

Chapitre 4 : Construction d'une méthode non-splittée pour les modèles bifluide avec effets de relaxation

Une fois le cadre d'étude relatif au système (1.32) introduit, le chapitre 4 s'attache à y détailler certaines propriétés mathématiques. Bien que certaines de ces propriétés aient déjà été prouvées par Embid et Baer [37] dans le contexte non-isentropique, d'autres, en revanche, sont moins connues et constituent le socle sur lequel s'appuie la stratégie de couplage convection-source proposée. Adaptant la preuve décrite dans [25], la Proposition 4.2.2 de ce chapitre montre notamment que le système (1.32) est *symétrisable*.

La stratégie proposée afin de prendre en compte le couplage entre la convection et les effets de relaxation est motivée par le constat suivant :

(i) Premièrement, une théorie unifiée visant à construire une ou des solutions associées à un problème de Riemann non-linéaire généralisé (*i.e* où des termes sources de relaxation sont actifs) n'a pas encore émergé.

(ii) Deuxièmement, même dans le cadre simplifié de problèmes de Riemann *linéaires* généralisés (matrice Jacobienne de convection constante, termes sources de relaxation linéaires) , il est difficile de construire une solution analytique si aucune hypothèse, reliant la matrice de relaxation à la matrice Jacobienne de convection, n'est faite.

Forts de ces observations, Bereux et Sainsaulieu mènent dans [8] une analyse basée sur l'existence et la régularité de solutions pour les problèmes de Riemann linéaires généralisés s'écrivant sous la forme :

$$\begin{aligned} &\partial_t \mathbf{U} + \underline{\underline{\mathbf{C}}}_0 \, \partial_x \mathbf{U} = \frac{1}{\tau} \underline{\underline{\mathbf{B}}}_0 \, \mathbf{U}, \\ &\mathbf{U}(., t=0) = \begin{cases} \mathbf{U}_{\mathrm{L}}^0 \text{ if } x < 0, \\ \mathbf{U}_{\mathrm{R}}^0 \text{ if } x > 0, \end{cases} \end{aligned} \tag{1.36}$$

avec $\mathbf{U} \in \mathbb{R}^p$, $\underline{\underline{\mathbf{C}}}_0 \in \mathbb{R}^p \times \mathbb{R}^p$ une matrice Jacobienne constante reliée à la partie convective, $\underline{\underline{\mathbf{B}}}_0 \in \mathbb{R}^p \times \mathbb{R}^p$ une matrice constante de relaxation, τ une échelle de temps de relaxation. Sous réserve d'hypothèses sur l'hyperbolicité et la *symétrisation* du système (1.36), ils mettent en évidence un système d'équations différentielles ordinaires (EDO) qui décrit la dynamique en temps de la *moyenne spatiale* $\mathbf{H}$ de la solution du problème (1.36). Ce système d'EDO, présenté dans ce chapitre à la Property 4.3.1 s'écrit :

$$\begin{cases} \dfrac{\mathrm{d}\mathbf{H}}{\mathrm{d}t} = \dfrac{1}{\tau} \underline{\underline{\mathbf{B}}}_0 \, \mathbf{H} - \dfrac{1}{\mathrm{L}} \underline{\underline{\mathbf{C}}}_0 \, (\mathbf{U}_{\mathrm{R}}(t) - \mathbf{U}_{\mathrm{L}}(t)), \; \mathbf{H}(0) = \dfrac{\mathbf{U}_{\mathrm{R}}^0 + \mathbf{U}_{\mathrm{L}}^0}{2}, \\ \forall k \in \{\mathrm{L}, \mathrm{R}\} : \\ \dfrac{\mathrm{d}\mathbf{U}_k}{\mathrm{d}t} = \dfrac{1}{\tau} \underline{\underline{\mathbf{B}}}_0 \, \mathbf{U}_k, \; \mathbf{U}_k(0) = \mathbf{U}_k^0, \end{cases} \tag{1.37}$$

avec L la longueur du domaine d'étude monodimensionnel.

Il est important d'insister sur le fait que, dans le chapitre 4, le système d'EDO (1.37) constitue la pierre d'angle permettant de construire un schéma numérique. Inspiré de [8], ce schéma numérique est en effet basé sur une intégration *implicite* en temps de (1.37). Cette dernière s'applique à chacune des cellules d'un maillage dual contenant les faces d'un maillage primal.

Sans pour autant donner tous les détails de la preuve proposée dans [8], ce chapitre synthétise les idées les plus importantes notamment à travers la Property 4.3.3. En effet, cette dernière traite du cas particulier où la matrice de relaxation $\underline{\underline{\mathbf{B}}}_0$ peut être diagonalisée dans la même base de vecteurs propres que la matrice $\underline{\underline{\mathbf{C}}}_0$. Par la suite, on qualifiera cette configuration de "processus de relaxation indépendants". En effet, considérons $\mathbf{a}_k$, $k \in [1, p]$, la k-ième composante de la solution projetée sur la base des vecteurs propres de $\underline{\underline{\mathbf{C}}}_0$. On peut alors remarquer que la contribution

du vecteur de termes sources à l'EDP vérifiée par $\mathbf{a}_k$ est indépendante de toutes les autres composantes $\mathbf{a}_j$, $j \neq k$. L'intérêt de ce cas particulier vient du fait qu'une solution analytique unique peut être trouvée.

Le point névralgique de la preuve de Bereux et Sainsaulieu consiste à appliquer une transformée de Fourier spatiale au système d'équations convection-source étudié. On peut alors remarquer que, dans le cas général, une unique solution appartenant à l'espace des fonctions à variations bornées existe. Cette solution peut être construite comme la somme de deux contributions. La première est solution d'un système convection-source avec processus de relaxation indépendants. L'expression de la seconde contribution n'est pas connue explicitement, en revanche les auteurs de [8] prouvent que cette dernière est *continue* en temps et en espace. Cette propriété de régularité est cruciale dans la mesure où elle permet par la suite d'intégrer la solution à travers l'éventail des ondes de contact associées à $\underline{\underline{\mathbf{C}}}_0$ sans se préoccuper des relations de saut à travers les fronts discontinus. On peut alors mettre en évidence le système d'EDO (1.37).

Le schéma à mailles décalées implicite en temps proposé dans ce chapitre est directement inspiré des travaux ménés par Bereux et Sainsaulieu. Néanmoins, une légère extension y est ajoutée afin de pouvoir traiter des phénomènes de relaxation plus fortement non-linéaires et moins monotones que les termes d'échange de moment présents dans le modèle bifluide de [8]. Cette extension se base sur une technique implicite d'intégration en temps d'ordre élevé appelée méthode de Rosenbrock [51]. Outre de bonnes propriétés de stabilité et de robustesse, cette approche s'appuie sur la linéarisation des termes sources. Le schéma numérique qui s'en dégage présente alors une certaine proximité avec le problème de Riemann linéaire généralisé (1.36).

Le schéma numérique développé dans ce chapitre est évalué sur un modèle bifluide simplifié à deux pressions et deux vitesses. Ce modèle a été construit en "gelant" la matrice Jacobienne de la partie convective du système (1.32). Ce faisant, la problématique liée à la présence des termes non-conservatifs n'est pas traitée dans ce chapitre. Les termes de relaxation en pression et en vitesse sont également remplacés par un terme source dont le comportement est arbitrairement assimilé à celui d'un ressort non-linéaire.

Par la suite, l'approche proposée est testée sur un problème de Riemann généralisé impliquant le modèle simplifié ci-dessus et dont les conditions initiales sont fortement hors-équilibre. Le temps de relaxation associé au ressort non-linéaire est, quant à lui, très petit devant les échelles de temps liées aux valeurs propres de la partie convective. Le problème est donc "raide" au sens de la relaxation. Les résultats obtenus sont comparés à ceux produits par une méthode à pas fractionnaires impliquant un flux de type Rusanov. Les courbes de convergence ainsi que les profils des variables $\left[\alpha_1, u_1, p_1, u_2, p_2\right]$ révèlent que le schéma développé est plus précis mais plus coûteux en temps de calcul que la méthode à pas fractionnaires.

Chapitre 5 : Extension de la méthode de couplage convection-source pour le modèle de Baer-Nunziato isentropique

La stratégie présentée dans ce chapitre consiste à adapter le formalisme du problème de Riemann linéaire généralisé (1.36) introduit précédemment pour y inclure de nouveaux termes modélisant les effets associés aux produits non-conservatifs du système (1.32). Pour ce faire, notre démarche s'appuie sur les travaux décrits dans [3, 24, 84]. En effet, les termes non-conservatifs y sont modélisés comme une *mesure de Dirac* portée par la demi-droite

$$t \in \mathbb{R}^+ \rightarrow \left(u_2^*(\mathbf{U}_\mathrm{R}^0, \mathbf{U}_\mathrm{L}^0)\, t,\, t\right), \tag{1.38}$$

où $u_2^*(\mathbf{U}_\mathrm{R}^0, \mathbf{U}_\mathrm{L}^0)$ est la vitesse exacte de l'onde de contact associée à la solution d'un problème de Riemann basé sur le système (1.32) et dont $\left(\mathbf{U}_\mathrm{R}^0, \mathbf{U}_\mathrm{L}^0\right)$ sont les données initiales. Plus précisément, l'application des relations de Rankine-Hugoniot au travers de cette onde de contact sur les équations du taux de présence statistique et de la quantité de mouvement phasique permet d'écrire

que, au sens faible :

$$\begin{bmatrix} u_2 \\ 0 \\ -p_1 \\ 0 \\ +p_1 \end{bmatrix} \partial_x \alpha_1 = \begin{bmatrix} [u_2\,\alpha_1]_{u_2^*(\mathbf{U}_\mathrm{R}^0,\mathbf{U}_\mathrm{L}^0)} \\ 0 \\ +[\alpha_2\,p_2]_{u_2^*(\mathbf{U}_\mathrm{R}^0,\mathbf{U}_\mathrm{L}^0)} \\ 0 \\ -[\alpha_2\,p_2]_{u_2^*(\mathbf{U}_\mathrm{R}^0,\mathbf{U}_\mathrm{L}^0)} \end{bmatrix} \delta_{\{x=u_2^*(\mathbf{U}_\mathrm{R}^0,\mathbf{U}_\mathrm{L}^0)\,t\}}, \tag{1.39}$$

la notation $[\phi]_{u_2^*(\mathbf{U}_\mathrm{R}^0,\mathbf{U}_\mathrm{L}^0)}$ représentant le saut de la variable ϕ à travers l'onde u_2^*.

Inspiré par l'expression (1.39), un nouveau type de problème de Riemann linéaire généralisé est alors introduit. Ce dernier s'écrit sous la forme :

$$\begin{aligned} &\partial_t \mathbf{U} + \underline{\underline{\mathbf{C}}}_0\,\partial_x \mathbf{U} = \frac{1}{\tau}\underline{\underline{\mathbf{B}}}_0\,\mathbf{U} + \mathbf{b}_0\,\delta_{\{x=u_\mathrm{I}^*\,t\}}, \\ &\mathbf{U}(.,\,t=0) = \begin{cases} \mathbf{U}_\mathrm{L}^0 \text{ if } x<0, \\ \mathbf{U}_\mathrm{R}^0 \text{ if } x>0, \end{cases} \end{aligned} \tag{1.40}$$

où $\mathbf{b}_0$ est une masse *constante* reliée à la mesure de Dirac portée par la demi-droite $t \in \mathbb{R}^+ \rightarrow \left(u_\mathrm{I}^*\,t,\,t\right)$ avec u_I^* une vitesse *constante* donnée. Il est important de noter que dans le problème (1.40), la vitesse u_I^* n'est égale à *aucune* des valeurs propres associées à la matrice Jacobienne convective $\underline{\underline{\mathbf{C}}}_0$. On s'intéresse alors à la dynamique temporelle des solutions moyennées en espace de ce problème. Dans ce chapitre on montre notamment que, dans le cas de processus de relaxation indépendants, une extension simple du système d'EDO (1.37) présenté au chapitre précédent peut être trouvée malgré la présence de la mesure de Dirac. Cette dernière s'écrit alors :

$$\begin{cases} \dfrac{\mathrm{d}\mathbf{H}}{\mathrm{d}t} = \dfrac{1}{\tau}\underline{\underline{\mathbf{B}}}_0\,\mathbf{H} - \dfrac{1}{\mathrm{L}}\underline{\underline{\mathbf{C}}}_0\,(\mathbf{U}_\mathrm{R}(t)-\mathbf{U}_\mathrm{L}(t)) + \dfrac{\mathbf{b}_0}{\mathrm{L}},\ \mathbf{H}(0) = \dfrac{\mathbf{U}_\mathrm{R}^0+\mathbf{U}_\mathrm{L}^0}{2}, \\ \forall k \in \{\mathrm{L},\mathrm{R}\}: \\ \dfrac{\mathrm{d}\mathbf{U}_k}{\mathrm{d}t} = \dfrac{1}{\tau}\underline{\underline{\mathbf{B}}}_0\,\mathbf{U}_k,\ \mathbf{U}_k(0) = \mathbf{U}_k^0. \end{cases} \tag{1.41}$$

Par la suite, le reste du chapitre s'attache à construire puis à étudier un schéma de couplage convection-source, basé sur la dynamique (1.41) pour le système de type Baer-Nunziato isentropique (1.32). Le schéma s'appuie sur une intégration *semi-implicite* en temps de cette dynamique. Comme au chapitre 4, c'est un schéma à mailles décalées. Il est à noter que, lors de la construction de ce schéma, la partie convective gelée

$$\underline{\underline{\mathbf{C}}}_0\,(\mathbf{U}_\mathrm{R}(t)-\mathbf{U}_\mathrm{L}(t)), \tag{1.42}$$

est remplacée par une divergence de flux conservatifs associée au système de type Baer-Nunziato isentropique :

$$\mathbf{F}(\mathbf{U}_\mathrm{R}(t)) - \mathbf{F}(\mathbf{U}_\mathrm{L}(t)), \tag{1.43}$$

avec $\mathbf{F}(\mathbf{U}) = \left[0,\,m_1\,u_1,\,m_1\,u_1^2+\alpha_1\,p_1,\,m_2\,u_2,\,m_2\,u_2^2+\alpha_2\,p_2\right]^\mathrm{T}$. Par ailleurs, la masse de Dirac $\mathbf{b}_0$ est remplacée par une formulation discrète des relations de saut décrites en (1.39). Ces relations de saut sont estimées à l'aide des invariants de Riemann simplifiés [72] associés à l'onde de contact u_2^* pour une configuration d'écoulement subsonique.

Par la suite, certaines propriétés discrètes du schéma numérique sont mises en évidence. Le traitement particulier des produits non-conservatifs sous la forme d'une mesure de Dirac garantit la conservativité des masses partielles ainsi que de la quantité de mouvement de mélange. La positivité des masses partielles discrètes s'obtient sous une contrainte de pas de temps basée *uniquement* sur les vitesses d'onde de la partie convective du système (1.32). Enfin, deux pistes sont proposées afin d'assurer la préservation du principe du maximum pour le taux de présence statistique α_1. La première, similaire à la stratégie menée au chapitre précédent, propose de linéariser l'opérateur de relaxation en pression puis de le projeter sur la variété d'équilibre

$\{\mathbf{U}$, tels que, $\Delta p = \Delta u = 0\}$. La nouvelle valeur de α_1 peut alors s'écrire comme une combinaison convexe des taux de présence statistiques des instants précédents. Le principe du maximum qui émerge de cette approche est donc plus fort que le principe d'invariance dans l'intervalle $]0, 1[$ dicté par l'équation continue de α_1. La seconde approche s'éloigne du cadre de travail de Bereux et Sainsaulieu pour reprendre une méthode utilisée dans [32, 81]. L'opérateur de relaxation en pression n'est pas linéarisé et un système *non-linéaire* doit être résolu afin de déterminer la nouvelle valeur de α_1. On montre que sous réserve de positivité des masses partielles, ce système non-linéaire admet une unique solution dans $]0, 1[$.

Le schéma numérique développé est comparé à deux approches à pas fractionnaires. La première utilise un flux de type Rusanov complété par une discrétisation de type "free-streaming" [82] pour les produits non-conservatifs. La seconde met en jeu une adaptation au cadre Baer-Nunziato isentropique du solveur de Riemann approché HLLAC proposé par Lochon *et al.* [72] et inspiré de [89]. Les produits non-conservatifs sont alors discrétisés en utilisant la "thin layer approximation" de Schwendeman *et al.* [84]. La discrétisation du système d'EDO relative aux termes sources est basée sur la stratégie proposée par Gallouët *et al.* [40].

Une étude comparative des profils de solutions obtenues avec les trois approches est alors menée sur des problèmes de Riemann généralisés et pour différentes échelles de temps de relaxation. Il s'avère que, à maillage donné, l'approche proposée est systématiquement plus proche des profils de solutions convergées en maillage que la méthode à pas fractionnaires de type Rusanov. En revanche, dans la région où se situe la discontinuité de contact u_2^*, elle demeure moins précise pour capturer les variations de la solution que l'approche basée sur le solveur HLLAC. Sur des problèmes de Riemann généralisés raides au sens des échelles de temps de relaxation, le schéma numérique proposé semble néanmoins mieux capturer le profil des variables de relaxation Δp et Δu que les deux autres approches.

1.4.3 Valorisation des travaux

Les travaux réalisés dans cette thèse ont fait l'objet des éléments de valorisation suivants :

- Les travaux du chapitre 2 ont été acceptés pour publication dans la revue *ESAIM: Mathematical Modelling and Numerical Analysis* sous la référence :

  D. Iampietro, F. Daude, P. Galon, and J. M. Hérard. A Mach-sensitive splitting approach for Euler-like systems. *ESAIM : Mathematical Modelling and Numerical Analysis*, 52 : 207–253, 2018.

  Ils ont été présentés lors du congrès international *FVCA VIII* (Lille, juin 2017) et apparaissent dans les proceedings associés sous la forme :

  D. Iampietro, F. Daude, P. Galon, and J. M. Hérard. A weighted splitting approach for low-Mach number flows. *Finite Volumes for Complex Applications VIII-Hyperbolic, Elliptic and Parabolic Problems : FVCA 8*, 200, 2017.

  Par ailleurs, l'extension de ces travaux à des cas multidimensionnels a été présentée lors du congrès international *CANUM 2018* (Cap d'Agde, mai 2018). Cette extension fait l'objet d'un article en cours de préparation.

- Les travaux réalisés dans le cadre du chapitre 3 ont été acceptés pour publication dans la revue *Journal of Computational and Applied Mathematics* sous la référence :

  D. Iampietro, F. Daude, P. Galon, and J. M. Hérard. A Mach-sensitive implicit-explicit scheme adapted to compressible multi-scale flows. *Journal of Computational and Applied Mathematics*, 340 : 122–150, 2018.

  Ils ont été présentés lors du Groupe de Travail "Schémas numériques pour les écoulements à faible nombre de Mach" (Toulouse, Novembre 2017).

- Les travaux associés au chapitre 4 ont été présentés lors d'une session poster du Groupe de Travail "Compressible Multiphase Flows : Derivation, closure laws, thermodynamics" (Strasbourg, Mai 2018).

Références

[1] R. Abgrall and R. Saurel. Discrete equations for physical and numerical compressible multiphase mixtures. *Journal of Computational Physics*, 186 :361–396, 2003. 5

[2] L. Allievi. *Teoria del colpo d'ariete*. Atti del Collegio degli Ingegneri ed Architetti Italiani, Milan, Italy (in Italian), 1913. 7

[3] A. Ambroso, C. Chalons, F. Coquel, and T. Galié. Relaxation and numerical approximation of a two-fluid two-pressure diphasic model. *ESAIM : Mathematical Modelling and Numerical Analysis*, 43 :1063–1097, 2009. 17

[4] A. Ambroso, C. Chalons, and P. A. Raviart. A Godunov-type method for the seven-equation model of compressible two-phase flow. *Computers and Fluids*, 54 :67–91, 2012. 15

[5] M. R. Baer and J. W. Nunziato. A two-phase mixture theory for the deflagration-to-detonation transition (DDT) in reactive granular materials. *International Journal of Multiphase Flow*, 12 : 861–889, 1986. 5, 14

[6] R. Baraille, G. Bourdin, F. Dubois, and A. Y. Le Roux. Une version à pas fractionnaires du schéma de Godunov pour l'hydrodynamique. *Compte Rendu de l'Académie des Sciences*, 314 : 147–152, 1992. 10

[7] T. Barberon and P. Helluy. Finite volume simulation of cavitating flows. *Computers and Fluids*, 34 :832–858, 2005. 4

[8] F. Bereux and L. Sainsaulieu. A Roe-type Riemann solver for hyperbolic systems with relaxation based on time-dependent wave decomposition. *Numerische Mathematik*, 2 :143–185, 1997. 15, 16, 17

[9] A. Bergant, A. R. Simpson, and A. S. Tijsseling. Water hammer with column separation : A historical review. *Journal of Fluids and Structures*, 22 :135–171, 2006. 2, 7

[10] R. A. Berry, L. Zou, H. Zhao, H. Zhang, J. W. Peterson, R. C. Martineau, and D. Andrs. *Relap-7 theory manual*. Idaho National Engineering Laboratory, Idaho Falls, United States, 2016. 6

[11] D. Bestion. The physical closure laws in the CATHARE code. *Nuclear Engineering and Design*, 124 :229–245, 1990. 6

[12] Z. Bilicki and J. Kestin. Physical aspects of the relaxation model in two-phase flow. *Proceedings of the Royal Society of London A : Mathematical, Physical and Engineering Sciences*, 428 : 379–397, 1990. 4

[13] F. Bouchut. *Nonlinear Stability of Finite Volume Methods for Hyperbolic Conservation Laws*. Birkäser, 2004. 11

[14] A. Bourlioux. *Analysis of numerical methods in a simplified detonation model*. PhD thesis, Princeton University, 1991. 15

[15] C. E. Brennen. *Fundamentals of Multiphase Flow*. Cambridge University Press, 2005. 2, 4

[16] H. B. Callen. *Thermodynamics and an Introduction to Thermostatistics*. John Wiley & sons, 1985. 4

[17] C. Chalons, M. Girardin, and S. Kokh. An all-regime Lagrange-Projection like scheme for the gas dynamics equations on unstructured meshes. *Communications in Computational Physics*, 20 :188–233, 2016. 9, 10, 12, 13

[18] C. Chalons, M. Girardin, and S. Kokh. An all-regime Lagrange-Projection like scheme for 2D homogeneous models for two-phase flows on unstructured meshes. *Journal of Computational Physics*, 335 :885–904, 2016. 12

[19] G. Q. Chen, C. D. Levermore, and T.-P. Liu. Hyperbolic conservation laws with stiff relaxation terms and entropy. *Communications on Pure and Applied Mathematics*, 47 :787–830, 1994. 15

[20] S. Clerc. Numerical simulation of the homogeneous equilibrium model for two-phase flows. *Journal of Computational Physics*, 161 :354–375, 2000. 4

[21] F. Coquel, T. Gallouët, J-M Hérard, and N. Seguin. Closure laws for a two-fluid two-pressure model. *Comptes Rendus de l'Académie des Sciences : Mathematique*, 334 :927–932, 2002. 5

[22] F. Coquel, Q. L. Nguyen, M. Postel, and Q. H. Tran. Entropy-satisfying relaxation method with large time-steps for Euler IBVPS. *Mathematics of Computation*, 79 :1493–1533, 2010. 12, 13

[23] F. Coquel, E. Godlewski, and N. Seguin. Relaxation of fluid systems. *Mathematical Models and Methods in Applied Science*, 22 :43–95, 2012. 11

[24] F. Coquel, J. M. Hérard, K. Saleh, and N. Seguin. A robust entropy-satisfying finite volume scheme for the isentropic Baer-Nunziato model. *ESAIM : Mathematical Modelling and Numerical Analysis*, 48 :165–206, 2014. 17

[25] F. Coquel, J. M. Hérard, K. Saleh, and N. Seguin. Two properties of two-velocity two-pressure models for two-phase flows. *Communications in Mathematical Sciences*, 12 :593–600, 2014. 16

[26] R. Courant and K. O. Friedrichs. *Supersonic Flow and Shock Waves (Vol. 21)*. Springer Science & Business Media, 1999. 9

[27] P. Degond and M. Tang. All speed scheme for the low Mach number limit of the isentropic Euler equation. *Communications in Computational Physics*, 10 :1–31, 2011. 6, 10

[28] S. Dellacherie. Relaxation schemes for the multicomponent Euler system. *ESAIM : Mathematical Modelling and Numerical Analysis*, 37 :909–936, 2003. 15

[29] S. Dellacherie. Analysis of Godunov type schemes applied to the compressible Euler system at low Mach number. *Journal of Computational Physics*, 229 :978–1016, 2009. 11

[30] S. Dellacherie, P. Omnes, and F. Rieper. The influence of cell geometry on the Godunov scheme applied to the linear wave equation. *Journal of Computational Physics*, 229 :5315–5338, 2010.

[31] S. Dellacherie, P. Omnes, J. Jung, and P.A. Raviart. Construction of modified Godunov type schemes accurate at any Mach number for the compressible Euler system. *Mathematical Models and Methods in Applied Science*, 26 :2525–2615, 2016. 11, 12

[32] C. Demay, C. Bourdarias, B. D. L. De Meux, S. Gerbi, and J. M. Hérard. A fractional step method adapted to the two-phase simulation of mixed flows in pipes with a compressible two-layer model. *ESAIM : Mathematical Modelling and Numerical Analysis*, Accepted for publication, 2018. 19

[33] G. Dimarco, R. Loubère, and M-H. Vignal. Study of a new asymptotic preserving scheme for the Euler system in the low Mach number limit. *SIAM : Journal of Scientific Computing*, 39 : 2099–2128, 2017. 6, 10

[34] P. Downar-Zapolski, Z. Bilicki, L. Bolle, and J. Franco. The non-equilibrium relaxation model for one-dimensional flashing liquid flow. *International journal of multiphase flow*, 22 :473–483, 1996. 4

[35] D. A. Drew. Mathematical modeling of two-phase flow. *Annual review of fluid mechanics*, 15 : 261–291, 1983. 4

[36] D. A. Drew and S. L. Passman. *Theory of Multicomponent Fluids*. Springer Science & Business Media, 2006. 3

[37] P. Embid and M. R. Baer. Mathematical analysis of a two-phase continuum mixture theory. *Continuum Mechanics and Thermodynamics*, 4 :279–312, 1992. 16

[38] I. Faille and E. Heintzé. A rough finite volume scheme for modeling two-phase flow in a pipeline. *Computers and Fluids*, 28 :213–241, 1999. 4

[39] P. Fillion, A. Chanoine, S. Dellacherie, and A. Kumbaro. FLICA-OVAP : A new platform for core thermal–hydraulic studies. *Nuclear Engineering and Design*, 241 :4348–4358, 2011. 12

[40] T. Gallouët, J-M Hérard, and N. Seguin. Numerical modeling of two-phase flows using the two-fluid two-pressure approach. *Mathematical Models and Methods in Applied Sciences*, 14 :663–700, 2004. 5, 19

[41] S. Gavrilyuk. The structure of pressure relaxation terms : one-velocity case. EDF internal report, H-I83-2014-00276-EN, 2014. 15

[42] S. Gavrilyuk and R. Saurel. Mathematical and numerical modeling of two-phase compressible flows with micro-inertia. *Journal of Computational Physics*, 175 :326–360, 2002. 5

[43] M. S. Ghidaoui, M. Zhao, D. A. McInnis, and D. H. Axworthy. A review of water hammer theory and practice. *Applied Mechanics Reviews*, 58 :49, 2005. 2, 7, 9

[44] J. Glimm, D. Saltz, and D. H. Sharp. Renormalization group solution of two-phase flow equations for Rayleigh-Taylor mixing. *Physics Letters*, 222 :171–176, 1996. 5

[45] J. Glimm, D. Saltz, and D. H. Sharp. Two-phase modelling of a fluid mixing layer. *Journal of Fluid Mechanics*, 378 :119–143, 1999. 5

[46] A. Guelfi, D. Bestion, M. Boucker, P. Boudier, P. Fillion, M. Grandotto, and P. Péturaud. NEPTUNE : a new software platform for advanced nuclear thermal hydraulics. *Nuclear Science and Engineering*, 156 :281–324, 2007. 6

[47] H. Guillard and F. Duval. A Darcy law for the drift velocity in a two-phase flow model. *Journal of Computational Physics*, 224 :288–313, 2007. 4

[48] H. Guillard and C. Viozat. On the behavior of upwind schemes in the low Mach number limit. *Computers and Fluids*, 28 :63–86, 1999. 6

[49] J. Haack, S. Jin, and J. G. Liu. An all-speed asymptotic-preserving method for the isentropic Euler and Navier-Stokes equations. *Communications in Computational Physics*, 12 :955–980, 2012. 6, 10

[50] L. Haar, J. S. Gallagher, and G. S. Kell. *NBS/NRC Steam Tables : Thermodynamic and Transport Properties and Computer Programs for Vapor and Liquid States of Water in SI Units*. Taylor & Francis, 1984. 4

[51] E. Hairer and G. Wanner. *Solving Ordinary Differential Equations II : Stiff and Differential-algebraic Problems*. Springer, 1991. 17

[52] J. M. Hérard and Y. Liu. Une approche bifluide statistique de modélisation des écoulements diphasiques à phases compressibles. EDF internal report, H-I81-2013-01162-FR, 2013. 5

[53] Electric Power Research Institute. *Water Hammer Handbook for Nuclear Plants Engineers and Operators*. EPRI, 1996. 2

[54] M. Ishii. *Thermo-Fluid Dynamic Theory of Two-Phase Flow*. Eyrolles, 1975. 2, 3, 4, 9

[55] M. Ishii and T. Hibiki. *Thermo-Fluid Dynamics of Two-Phase Flow*. Springer, 2006. 2, 3

[56] M. Ishii and N. Zuber. Drag coefficient and relative velocity in bubbly, droplet or particulate flows. *AIChE Journal*, 25 :843–855, 1979. 15

[57] S. Jin. Runge-Kutta methods for hyperbolic conservation laws with stiff relaxation terms. *Journal of Computational Physics*, 122 :51–67, 1995. 15

[58] S. Jin and Z.-P. Xin. The relaxation schemes for systems of conservation laws in arbitrary dimensions. *Communications on Pure and Applied Mathematics*, 48 :235–276, 1995. 11

[59] N. E. Joukowski. Memoirs of the Imperial Academy Society of St. Petersburg. *Proceedings of the American Water Works Association*, 24 :341–424, 1898. 8

[60] A. K. Kapila, S. F. Son, J. B. Bdzil, R. Menikoff, and D. S. Stewart. Two-phase modeling of DDT : Structure of the velocity-relaxation zone. *Physics of Fluids*, 9 :3885–3897, 1997. 5

[61] A. K. Kapila, R. Menikoff, J. B. Bdzil, S. F. Son, and D. S. Stewart. Two-phase modeling of deflagration-to-detonation transition in granular materials : Reduced equations. *Physics of Fluids*, 13 :3002–3024, 2001. 5

[62] L. Kelvin. Hydrokinetic solutions and observations. *Philosophical Magazine*, 42 :362–377, 1871. 2

[63] S. Klainerman and A. Majda. Singular limits of quasilinear hyperbolic systems with large parameters and the incompressible limit of compressible fluids. *Communications on Pure and Applied Mathematics*, 34 :481–524, 1981. 6

[64] S. Klainerman and A. Majda. Compressible and incompressible fluids. *Communications on Pure and Applied Mathematics*, 35 :629–651, 1981. 6

[65] R. Klein. Semi-implicit extension of a Godunov-type scheme based on low Mach number asymptotics I : One-dimensional flow. *Journal of Computational Physics*, 121 :213–237, 1995. 6, 10

[66] Idaho National Engineering Laboratory. *RELAP5/MOD3 code manual volume I*. Lockheed Idaho Technologies Company, 2001. 6

[67] G. Le Coq, S. Aubry, J. Cahouet, P. Lequesne, G. Nicolas, and S. Pastorini. Le logiciel THYC. modélisation en volume finis des écoulements tridimensionnels diphasiques dans les faisceaux de tubes. *Bulletin de la Direction des études et recherches-Electricité de France. Série A, nucléaire, hydraulique, thermique*, 1 :61–76, 1989. 4

[68] R. J. LeVeque and H. C. Yee. A study of numerical methods for hyperbolic conservation laws with stiff source terms. *Journal of Computational Physics*, 86 :187–210, 1987. 15

[69] G. Linga. A hierarchy of non-equilibrium two-fluid models. *SIAM Journal on Applied Mathematics*, 2015. Submitted. 15

[70] T.-P. Liu. Hyperbolic conservation laws with relaxation. *Communications in Mathematical Physics*, 108 :153–175, 1987. 15

[71] H. Lochon. *Modélisation et simulation d'écoulements transitoires eau-vapeur en approche bifluide*. PhD thesis, Université d'Aix-Marseille, 2016. URL https://tel.archives-ouvertes.fr/tel-01379453/. 5

[72] H. Lochon, F. Daude, P. Galon, and J. M. Hérard. HLLC-type Riemann solver with approximated two-phase contact for the computation of the Baer-Nunziato two-fluid model. *Journal of Computational Physics*, 326 :733–762, 2016. 18, 19

[73] G. Métivier and S. Schochet. The incompressible limit of the non-isentropic Euler equations. *Archive for Rational Mechanics and Analysis*, 158 :61–90, 2001. 6

[74] S. Noelle, G. Bispen, K. R. Arun, M. Lukáčová-Medvid'ová, and C. D. Munz. A weakly asymptotic preserving low Mach number scheme for the Euler equations of gas dynamics. *SIAM Journal on Scientific Computing*, 36 :B989–B1024, 2014. 6

[75] M. Papin and R. Abgrall. Fermetures entropiques pour les systèmes bifluides à sept équations. *Comptes Rendus de l'Académie des Sciences : Mécanique*, 333 :838–842, 2005. 5

[76] L. Pareschi and G. Russo. Implicit–explicit Runge–Kutta schemes and applications to hyperbolic systems with relaxation. *SIAM Journal of Scientific Computing*, 25 :129–155, 2005. 15

[77] R. B. Pember. Numerical methods for hyperbolic conservation laws with stiff relaxation I. Spurious solutions. *SIAM Journal on Applied Mathematics*, 53 :1293–1330, 1993. 15

[78] R. B. Pember. Numerical methods for hyperbolic conservation laws with stiff relaxation II. Higher-order Godunov methods. *SIAM Journal on Scientific Computing*, 14 :824–859, 1993. 15

[79] V. H. Ransom and D. L. Hicks. Hyperbolic two-pressure models for two-phase flow. *Journal of Computational Physics*, 53 :124–151, 1984. 5

[80] F. Rieper. A low-Mach number fix for Roe's approximate Riemann solver. *Journal of Computational Physics*, 230 :5263–5287, 2011. 12

[81] K. Saleh. *Analyse et simulation numérique par relaxation d'écoulements diphasiques compressibles. Contribution au traitement des phases evanescentes*. PhD thesis, Université Pierre et Marie Curie-Paris VI, 2012. URL https://tel.archives-ouvertes.fr/tel-00761099. 19

[82] R. Saurel and R. Abgrall. A multiphase Godunov method for compressible multifluid and multiphase flows. *Journal of Computational Physics*, 150 :425–467, 1999. 5, 19

[83] S. Schochet. The compressible Euler equations in a bounded domain : existence of solutions and the incompressible limit. *Communications in Mathematical Physics*, 104 :49–75, 1986. 6

[84] D. W. Schwendeman, C. W. Wahle, and A. K. Kapila. The Riemann problem and a high-resolution Godunov method for a model of compressible two-phase flow. *Journal of Computational Physics*, 212 :490–526, 2006. 17, 19

[85] A. R. Simpson. *Large water hammer pressures due to column separation in sloping pipes*. PhD thesis, Diss. University of Michigan, 1986. 8, 9

[86] G. A. Sod. *Numerical Methods in Fluid Dynamics, Initial and Initial-boundary Value Problems*. Cambridge University Press, 1985. (English translation by E. E. Halmos 1925, *The theory of waterhammer*, Trans. ASME). 12

[87] H. B. Stewart and B. Wendroff. Two-phase flow : models and methods. *Journal of Computational Physics*, 56 :363–409, 1984. 5

[88] I. Suliciu. On the thermodynamics of fluids with relaxation and phase transitions. *International Journal of Engineering Science*, 36 :921–947, 1998. 11

[89] S. Tokareva and E. F. Toro. HLLC-type Riemann solver for the Baer–Nunziato equations of compressible two-phase flow. *Journal of Computational Physics*, 229 :3573–3604, 2010. 19

[90] I. Toumi, A. Bergeron, D. Gallo, E. Royer, and D. Caruge. FLICA-4 : a three-dimensional two-phase flow computer code with advanced numerical methods for nuclear applications. *Nuclear Engineering and Design*, 1-2 :139–155, 2000. 4

[91] W. Wagner and H. J. Kretzschmar. IAPWS industrial formulation 1997 for the thermodynamic properties of water and steam. *International Steam Tables : Properties of Water and Steam Based on the Industrial Formulation IAPWS-IF97*, pages 7–150, 2008. 4

[92] J. B. Whitham. *Linear and Non Linear Waves*. John Wiley & Sons Inc, 1974. 11, 15

[93] N. Zuber and J. Findlay. Average volumetric concentration in two-phase flow systems. *Journal of Heat Transfer*, 87 :453–468, 1965. 4

Chapitre 2

Splitting d'opérateur dépendant du nombre de Mach pour le système d'Euler

Ce chapitre pose les bases d'une nouvelle méthode numérique afin d'aborder la problématique d'écoulements multi-régimes pour des modèles diphasiques homogènes. La stratégie repose sur un splitting du système d'Euler permettant d'identifier un sous-système dit convectif, noté $\mathcal{C}$, ainsi qu'un sous-système acoustique noté $\mathcal{A}$. Initialement proposé, dans une version statique, par les travaux de Baraille *et al.* [1], le splitting introduit ici a la capacité d'évoluer dans le temps par l'intermédiaire d'un paramètre $\mathscr{E}_0(t) \in]0, 1]$. Ce paramètre vient pondérer les contributions liées au gradient de pression au sein des flux de chacun des sous-systèmes. Dans ce chapitre $\mathscr{E}_0(t)$ est uniquement basé sur le nombre de Mach maximal instantané de l'écoulement :

$$\begin{aligned} &\mathscr{E}_0(t) \propto \max\left(\mathscr{E}_{inf}, \min\left(\mathrm{M}_{max}(t), 1\right)\right), \\ &\mathrm{M}_{max}(t) = \sup_{x\in\Omega}\left(\mathrm{M}(x,t) = \frac{|\mathbf{u}(x,t)|}{c(x,t)}\right),\ 0 < \mathscr{E}_{inf} \ll 1. \end{aligned} \tag{2.1}$$

Deux tendances asymptotiques peuvent alors être identifiées. Lorsque le nombre de Mach maximal à l'instant t est supérieur ou égal à un, $\mathscr{E}_0(t)$ tend vers un. Par construction le sous-système $\mathcal{C}$ converge formellement vers le système d'Euler complet pendant que le sous-système $\mathcal{A}$ dégénère en un système stationnaire. En revanche, si le nombre de Mach maximal de l'écoulement est très petit devant un, $\mathscr{E}_0(t)$ tend vers zéro et le splitting découple complètement les effets convectifs, traités dans $\mathcal{C}$, des effets acoustiques, traités dans $\mathcal{A}$.

Par la suite, ce chapitre s'attache à étudier, au niveau continu, les propriétés liées à l'hyperbolicité ainsi qu'à la positivité de la densité et de l'énergie interne des solutions des deux sous-systèmes. La méthode numérique issue de cette analyse est une approche à pas fractionnaires, dont l'intégration est explicite en temps, résolvant successivement le sous-système $\mathcal{C}$ et le sous-système $\mathcal{A}$. La technique de résolution employée pour ces derniers est un schéma de relaxation de type Suliciu [5, 42]. L'intégration explicite en temps des termes liés au gradient de pression impose de construire le pas de temps discret à partir des ondes non-linéaires les plus rapides du système d'Euler.

Une comparaison entre la méthode à pas fractionnaires proposée et une approche de type *Lagrange-Projection* [10, 14] est alors menée. Les éléments comparatifs sont les courbes de convergence, les profils de solutions calculées ainsi que les courbes d'efficacité obtenus sur une série de tubes à choc de type Sod [41]. Dans ces cas tests, le nombre de Mach maximal ainsi que la raideur de l'équation d'état du fluide étudié sont des paramètres d'entrée permettant de modéliser plusieurs types de régimes d'écoulement. Dans le cadre du régime particulier où l'écoulement compressible est à faible nombre de Mach mais développe des sauts de pression de grande amplitude, un terme correctif repris de certains travaux de la littérature [20, 22, 35] est introduit afin de pallier à une problématique de diffusion numérique sur ces sauts de pression.

Les travaux présentés dans ce chapitre ont été acceptés pour publication dans la revue *ESAIM: Mathematical Modelling and Numerical Analysis* sous la référence :

D. Iampietro, F. Daude, P. Galon, and J. M. Hérard. A Mach-sensitive splitting approach for Euler-like systems. *ESAIM : Mathematical Modelling and Numerical Analysis*, 52 : 207–253, 2018.

Sommaire

A Mach-Sensitive Splitting Approach for Euler-like Systems

D. Iampietro[a, b, e], F. Daude[a,b], P. Galon[b,c], J. M. Hérard[d,e]

[a]EDF R&D, Département ERMES, 7 Boulevard Gaspard Monge, 91120 Palaiseau, France
[b]IMSIA, UMR EDF/CNRS/CEA/ENSTA 9219, Université Paris-Saclay, 828 Boulevard des Maréchaux, 91762 Palaiseau Cedex, France
[c]CEA, DEN, DANS, DM2S, SEMT, DYN, F-91191 Gif-sur-Yvette, France
[d]EDF R&D, Département MFEE, 6 Quai Watier, F-78401 Chatou, France
[e]I2M, UMR CNRS 7373, Technopôle Château-Gombert, 39 rue F. Joliot Curie, F-13453 Marseille, France

Abstract

Herein, a Mach-sensitive fractional step approach is proposed for Euler-like systems. The key idea is to introduce a time-dependent splitting which dynamically decouples convection from acoustic phenomenon following the fluctuations of the flow Mach number. By doing so, one seeks to maintain the accuracy of the computed solution for all Mach number regimes. Indeed, when the Mach number takes high values, a time-explicit resolution of the overall Euler-like system is entirely performed in one of the present splitting step. On the contrary, in the low-Mach number case, convection is totally separated from the acoustic waves production. Then, by performing an appropriate correction on the acoustic step of the splitting, the numerical diffusion can be significantly reduced. A study made on both convective and acoustic subsystems of the present approach has revealed some key properties as hyperbolicity and positivity of the density and internal energy in the case of an ideal gas thermodynamics. The one-dimensional results made on a wide range of Mach numbers using an ideal and a stiffened gas thermodynamics show that the present approach is as accurate and CPU-consuming as a state of the art Lagrange-Projection-type method.

2.1 Introduction

Condensation Induced Water Hammer (CIWH) is a very specific two-phase fast transient phenomenon. It starts by the smooth deformation of a slow material interface between hot vapor and cooler liquid water. Then, as time goes on, shear instabilities and steep temperature gradients entail the trapping and then the sudden condensation of vapor pockets leading to the production of strong shock waves in the liquid phase.

In the above description, two time-scales can be identified: a material scale linked to the slow interface deformation and a fast acoustic scale related to the propagation of the shock front. As the Euler compressible system produces similar multi-scale waves, it constitutes the framework of the present paper. Indeed, the Mach number of the flow $\mathrm{M} = |\mathbf{u}|/c$, with $\mathbf{u}$ the velocity field and c the fluid speed of sound, measures the gap between the material and the acoustic time-scales. The particularity of a CIWH results from the fact that, initially, since the deformation of the slow material wave is the leading process, the fluid behaves as a low Mach number compressible flow: $0 < \mathrm{M} \ll 1$. Then, because of the stiffness of the liquid water thermodynamics, strong shock waves are triggered *even if* $0 < \mathrm{M} \ll 1$. In order to enforce this fact, one can find in [39] a water-hammer experiment in liquid water for which $|\mathbf{u}| \approx 0.2\, m.s^{-1}$, $c_{\text{liquid}} \approx 1.5 \times 10^3\, m.s^{-1}$ leading to pressure jumps of several bars. Besides, the analytical solution of a symmetric double shock Riemann problem obtained with the Euler compressible system endowed with a stiffened gas thermodynamics is derived later on in this work. It allows to better understand this peculiar aspect.

Thus, the long-term objective of the present work is to set out a method involving compressible Godunov-like solvers in order to fulfill a two-fold aim:

(I) Accurately follow the slow material waves when $0 < \mathrm{M} \ll 1$
in the absence of fast transient phenomena.

(II) Then, accurately follow the fast and strong acoustic waves even when $0 < \mathrm{M} \ll 1$.

In the sequel, the different issues inherent to point (I) and point (II) are described. However, the present study is *entirely* dedicated to point (II) and we leave point (I) for future works.

Godunov-like schemes perform poorly in the context of point (I) . A first issue is related to the first order time-discretization of such methods when $0 < M \ll 1$. Indeed, let us introduce Δx the cell size of a 1D mesh, Δt the time-step built using a time-explicit Godunov-like scheme, λ_{u+c} (respectively λ_u) the non-dimensional acoustic eigenvalue (respectively the slow convective eigenvalue). Besides, define $\mathscr{C}_{|u|+c} = \frac{1}{M}\frac{\Delta t \lambda_{u+c}}{\Delta x}$ (respectively $\mathscr{C}_{|u|} = \frac{\Delta t \lambda_u}{\Delta x}$) the acoustic Courant number (respectively the convective Courant number). The stability of the fast acoustic dynamics requires $\mathscr{C}_{|u|+c} = 1^-$ and then $\mathscr{C}_{|u|} \approx M\mathscr{C}_{|u|+c} \approx M \ll 1$. Hence, the slow material wave dynamics are largely depreciated because $\mathscr{C}_{|u|}$, associated with a first order time-discretization, is too small to compensate the numerical diffusion induced by the first-order space-discretization. In [32], the evolution of the stiffness of the profile of an isolated slow contact-discontinuity as function of $\mathscr{C}_{|u|+c}$ supports this point. A solution, described in [17, 29] for the Euler isentropic system and in [21, 34] for the whole Euler compressible system endowed with an ideal gas thermodynamics, consists in applying a time-implicit discretization on the stiff pressure gradient. By doing so, one can replace the constraining time-explicit acoustic CFL condition $\mathscr{C}_{|u|+c} = 1^-$ by a convective CFL one: $\mathscr{C}_{|u|} = 1^-$, the latter being adapted to accurately follow slow material waves. What is more, in the above references, additional time-implicit discretizations hold on the density convection term [17, 29] or on the total energy convection term [21]. The resulting implicit-explicit schemes are thus consistent, when $M \to 0$ and Δt, Δx fixed, with a discrete incompressible solver. Schemes that are stable under the CFL condition $\mathscr{C}_{|u|} = 1^-$ and have the above consistent behavior are said to be Asymptotic Preserving (AP) towards the Euler incompressible system.

A second issue, in the framework of point (I) is related to the spatial discretization of Godunov-like schemes. Indeed, in [27, 28] the authors show, using a 2D discrete asymptotic decomposition w.r.t M on a cartesian mesh, that Godunov-like schemes are not able to maintain an initial incompressible solution in the incompressible phase-space from one time-step to an other. In [18–20], the authors transpose the Schochet theory [36, 37] at the discrete level and highlight the same difficulty. Moreover, they point out that this issue only concerns 2D (respectively 3D) non-triangular (respectively non-tetrahedral) meshes for which the non-dimensional mesh size is bigger than M. Then, they concentrate on means to control the computed solution proximity towards the incompressible well-prepared space (see [20] for a definition) for non-dimensional time-scales lower than M. Without going into details, the key idea is that the discrete acoustic operator of Godunov-like schemes contains a non-centered diffusive part scaling as $O(\Delta x/M)$ notably in the discrete momentum equation. When applied to an initial well-prepared solution, the latter produces new acoustic pressure waves scaling as $O(M)$ instead of $O(M^2)$. In [22, 35] a low Mach number correction rescaling the momentum diffusive part as $O(\Delta x)$ is proposed. It has since been re-used in [10, 11, 20].

The background of point (II) is more simple since we "only" want to be accurate on fast acoustic waves neglecting the slow material wave diffusion induced by the time-discretization as well as the proximity towards the incompressible phase space. However, as mentioned in the above paragraph, Godunov-like schemes suffer from a numerical diffusion of order $O(\Delta x/M)$ due to the spatial discretization which can be observed even in 1D under the CFL condition $\mathscr{C}_{|u|+c} = (1/2)^-$.

In the light of the time-scale difficulties encountered in point (I) , it seems relevant to introduce a fractional step method allowing to solve the slow convection process and the fast acoustic waves production separately. It is based on a Weighted Splitting Approach (WSA). The "Weighted" notion stems from the fact that the proposed splitting relies on a decomposition of the pressure balanced by a time-dependent splitting parameter. Inspired from [1, 7], a first part of the pressure decomposition, seen as a "small" pressure fluctuation if $0 < M \ll 1$, is sent to a convective subsystem $\mathcal{C}$. The remaining part goes into an acoustic subsystem $\mathcal{A}$. In the context of point (I) , a time-implicit resolution of $\mathcal{A}$ combined with a time-explicit resolution of $\mathcal{C}$ moves the proposed approach towards the convective CFL condition $\mathscr{C}_{u_0} = 1^-$. The stability proof of the implicit-explicit version of the present method is examined a more recent companion paper [32]. As already men-

tioned, this paper focuses on the point (II) . Thus, a time-explicit Godunov-like scheme is applied for both subsystems $\mathcal{C}$ and $\mathcal{A}$. The spatial discretization comes from the relaxation schemes theory [2, 4, 12, 15, 33] and notably from the Suliciu-like relaxation solvers [4, 42]. It provides a simple approximate Riemann solver whose writing is independent of the equation of state. Besides, in order to reduce the numerical diffusion when $0 < M \ll 1$, an anti-diffusive term, directly taken from [10, 20, 35], but simply seen as a tool here, is added to the present acoustic pressure flux. In the sequel, the anti-diffusive term is referred to as θ-correction.

Let us end the present WSA description by saying that, in the more common case where the production of shock waves is associated with a local rise of the Mach number $M \approx 1$, the present splitting is canceled and the overall Euler system is retrieved in the $\mathcal{C}$ subsystem. Thus fast acoustic waves are accurately captured.

The paper is structured as follows: in section one, the dynamic splitting is firstly described at the continuous level. A study of each resulting conservative subsystem is done through hyperbolicity and positivity analyses involving ideal and stiffened gas equations of state. Section two deals with the approximate Riemann solvers derived for the subsystems spatial discretization. Discrete positivity properties in the case of ideal gas thermodynamics are also derived under a non-restrictive condition. Following the steps of [10], section three is devoted to different truncation error analyses. The dependence in terms of Mach number as well as the impact of the θ-correction on the numerical diffusive operator of the overall scheme is shown. Eventually, section four presents one-dimensional time-explicit results obtained for ideal and stiffened gas thermodynamics and for a wide panel of Mach numbers. It turns out that the presented method is as accurate and efficient as a Lagrange-Projection method presented in [10]. However in the case of a stiffened gas thermodynamics with $0 < M \ll 1$, the proposed method, although L^∞ stable, produces more oscillations than the Lagrange-Projection approach.

2.2 Convective and Acoustic Effects in Euler-like Systems

2.2.1 Homogeneous Equilibrium Model Equations

When the non-equilibrium effects are small, one way to model two-phase flows is to assume that the two phases have the same velocity, pressure, temperature and chemical potential. The conservation laws are then similar to the Euler compressible system. Define $\mathbf{U} = \left[\rho, \rho\mathbf{u}, \rho e\right]^T$ the conservative variables vector with ρ the fluid density, $\mathbf{u}$ its velocity vector and e its total specific energy. The mass, momentum and energy conservation then read:

$$\partial_t \rho + \underline{\nabla} \cdot (\rho \mathbf{u}) = 0, \tag{2.2a}$$

$$\partial_t (\rho \mathbf{u}) + \underline{\nabla} \cdot (\rho \mathbf{u} \otimes \mathbf{u} + p\,\mathbf{I}) = \mathbf{0}, \tag{2.2b}$$

$$\partial_t (\rho e) + \underline{\nabla} \cdot ((\rho e + p)\,\mathbf{u}) = 0, \tag{2.2c}$$

$$e = \frac{|\mathbf{u}|^2}{2} + \varepsilon,\ \varepsilon = \varepsilon^{\text{EOS}}\left(\rho, p\right). \tag{2.2d}$$

Equality in (2.2d) is the equation of state for a single phase fluid. It relates ε the specific internal energy with density and pressure. Its strong level of nonlinearity is known to produce rarefaction or shock waves inside the flow. Recall that the Euler system is strictly hyperbolic, its eigenvalues being in one-dimension: $\lambda_1^{\text{Euler}} = u - c < \lambda_2^{\text{Euler}} = u < \lambda_3^{\text{Euler}} = u + c$; with c the sound speed which strongly depends on the equation of state and can be defined as:

$$\rho c^2 = \left(\partial_p \varepsilon_{|\rho}\right)^{-1} \left(\frac{p}{\rho} - \rho\, \partial_\rho \varepsilon_{|p}\right). \tag{2.3}$$

What is more λ_1^{Euler} and λ_3^{Euler} are related to genuinely non-linear fields whereas λ_2^{Euler} is associated with a linearly degenerate one.

Eventually, let us write the second law of thermodynamics principle, introducing the specific entropy variable $s = s^{\mathrm{EOS}}(\rho, \varepsilon)$ related with ρ and ε by the differential equation:

$$\begin{aligned} &\mathrm{d}\varepsilon = \mathrm{T}\,\mathrm{d}s - p\,\mathrm{d}\left(\frac{1}{\rho}\right), \\ &\text{with: } \mathrm{T} = \mathrm{T}^{\mathrm{EOS}}(\rho, s) = \partial_s \varepsilon_{|\rho},\ p = p^{\mathrm{EOS}}(\rho, s) = \rho^2\, \partial_\rho \varepsilon_{|s}. \end{aligned} \tag{2.4}$$

Using equation (2.4), it can be easily verified that, for smooth EOS, s is also solution of the PDE:

$$\partial_\rho s_{|p} + c^2\, \partial_p s_{|\rho} = 0. \tag{2.5}$$

Such a physical entropy is used to characterise admissible weak solutions of Euler system (2.2). Indeed, as proved in [26], the mapping $(\rho, \rho\mathbf{u}, \rho e) \rightarrow -\rho s$ is a strictly convex function and $(-\rho s, -\rho\mathbf{u}\, s)$ constitutes a mathematical entropy pair. Thus, any admissible weak solution of the Euler system should verify the inequality:

$$\partial_t(\rho s) + \underline{\nabla} \cdot (\rho s \mathbf{u}) \geq 0. \tag{2.6}$$

Beyond conservativity and maximum principle, inequality (2.6) is a key theoretical property that one would like to obtain, at the discrete level, in a numerical scheme.

Let us end this subsection by defining the one-dimensional Riemann problem associated to system (2.2). Let $\mathbf{U}_{\mathrm{L}}$ and $\mathbf{U}_{\mathrm{R}}$ be two constant states of the one-dimensional Euler system (2.2). It reads:

$$\begin{aligned} &\partial_t \mathbf{U} + \partial_x \mathbf{F}(\mathbf{U}) = \mathbf{0}, \\ &\mathbf{U}(., t=0) = \begin{cases} \mathbf{U}_{\mathrm{L}}, \text{ if } x < 0 \\ \mathbf{U}_{\mathrm{R}}, \text{ if } x > 0, \end{cases} \quad \text{with: } \mathbf{F}(\mathbf{U}) = \begin{bmatrix} \rho u \\ \rho u^2 + p \\ (\rho e + p)\, u \end{bmatrix}. \end{aligned} \tag{2.7}$$

As proved in [40], in the case of ideal gas or in [26] under more general thermodynamical hypothesis, Riemann problem (2.7) admits a unique entropic solution made of contact waves, rarefaction waves and shock waves as long as $\mathbf{U}_{\mathrm{L}}$ and $\mathbf{U}_{\mathrm{R}}$ are close enough.

2.2.2 A Weighted Splitting Approach

As mentioned in the introduction in the context of point (I) , two different physics are at stake inside Euler-like systems. In 1D, the first convects conservative variables using velocity u, the second contains pressure effects responsible for shock and rarefaction waves propagating at speed $u \pm c$. Thus, in the case of low-Mach compressible flows, $|u| \ll c$ and the acoustic physics goes much faster than the convective one. Therefore, time-explicit schemes restricted by the acoustic CFL condition tend to diffuse material waves as time goes on.

Looking at the Euler compressible system (2.2), a first step to elaborate a cure consists in decoupling the convective from the acoustic physics and proceed to their resolution separately and successively. This can be done by splitting the conservation laws system into two new continuous subsystems:

$$\mathcal{C}: \begin{cases} \partial_t \rho + \underline{\nabla} \cdot (\rho \mathbf{u}) = 0, \\ \partial_t (\rho \mathbf{u}) + \underline{\nabla} \cdot \left(\rho \mathbf{u} \otimes \mathbf{u} + \mathscr{E}_0^2(t)\, p\, \mathbf{I}\right) = \mathbf{0}, \\ \partial_t (\rho e) + \underline{\nabla} \cdot \left((\rho e) + \mathscr{E}_0^2(t)\, p\right) \mathbf{u}\big) = 0, \end{cases} \tag{2.8}$$

$$\mathcal{A}: \begin{cases} \partial_t \rho = 0, \\ \partial_t (\rho \mathbf{u}) + \underline{\nabla} \cdot \left((1 - \mathscr{E}_0^2(t))\, p\, \mathbf{I}\right) = \mathbf{0}, \\ \partial_t (\rho e) + \underline{\nabla} \cdot \left((1 - \mathscr{E}_0^2(t))\, p\, \mathbf{u}\right) = 0. \end{cases} \tag{2.9}$$

Here, $\mathscr{E}_0(.)$ is a time-dependent weighting factor belonging to interval $]0, 1]$ and proportional to the maximal Mach number of the flow:

$$\begin{aligned} &\mathscr{E}_0(t) \propto \max\left(\mathscr{E}_{inf}, \min\left(\mathrm{M}_{max}(t), 1\right)\right), \\ &\mathrm{M}_{max}(t) = \sup_{x \in \Omega} \left(\mathrm{M}(x,t) = \frac{|\mathbf{u}(x,t)|}{c(x,t)}\right), \end{aligned} \tag{2.10}$$

Ω being the computational domain. It has to be mentioned that in [1], Baraille and co-authors introduce the same kind of splitting for the Euler barotropic system with $\mathscr{E}_0$ equal to zero. Since their resulting $\mathcal{C}$-subsystem is not hyperbolic, they re-introduce a similar pressure perturbation, with $\mathscr{E}_0$ seen as a fixed parameter. They solve the Riemann problem associated with the perturbed subsystem and make $\mathscr{E}_0$ tend towards zero in the obtained solution in order to derive their numerical scheme.

In the present splitting, $\mathscr{E}_0(t)$ is strictly positive because of the lower bound $\mathscr{E}_{inf}$ defined such that $0 < \mathscr{E}_{inf} \ll 1$. By doing so, the above loss of hyperbolicity on the jacobian of $\mathcal{C}$ is avoided. Besides, here $\mathscr{E}_0(t)$ has a physical interest since it measures the gap between the convective and the acoustic time-scales.

Indeed, assume that at instant t the flow is such that $\mathrm{M}_{max}(t)$ is close or superior to 1. Then, $\mathscr{E}_0(t)$ will be close to 1, the subsystem $\mathcal{C}$ formally converges towards the full Euler system while $\mathcal{A}$ is a degenerated stationary subsystem. Hence, if $\mathcal{C}$ is solved using a time-explicit Godunov-like scheme, Euler shocks related to a temporal rise of the Mach number would be correctly captured. On the contrary, In the case of a globally low-Mach number flow, $\mathrm{M}_{max}(t) \approx \mathscr{E}_0(t) \ll 1$, and pressure terms completely disappear from $\mathcal{C}$ which turns out to be a pure "convective" subsystem. Pressure terms are treated afterwards in $\mathcal{A}$ which becomes an "acoustic" subsystem. Particularly, a time-implicit scheme ([14, 21]) applied on it would remove the most constraining part of the CFL condition. Let us end the splitting description by saying that both subsystems $\mathcal{C}$ and $\mathcal{A}$ are conservative, and that their formal summation allows to recover the original Euler system (2.2).

In the sequel, $\mathcal{C}$ is referred as the convective subsystem and $\mathcal{A}$ the acoustic one. Before going further into the numerical resolution of $\mathcal{C}$ and $\mathcal{A}$, one has to study their basic mathematical properties: hyperbolicity and maximum principle. This is done in the next section.

Hyperbolicity of $\mathcal{C}$ and $\mathcal{A}$

Above all, the hyperbolicity of the two subsystems $\mathcal{C}$ and $\mathcal{A}$ is investigated. This ensures that solutions of $\mathcal{C}$ and $\mathcal{A}$ do not suffer from definition issues by producing waves with celerities evolving in the $\mathbb{C}$ space. This is the object of the following proposition written in one space dimension but easily extendable to the multi-dimensional case:

Proposition 2.2.1 (Hyperbolicity of convective and acoustic subsystems)
Let us introduce $c_{\mathcal{C}}(\rho, p)$ and $c_{\mathcal{A}}(\rho, p)$ two modified sound speeds such that:

$$\begin{aligned} \left(\rho\, c_{\mathcal{C}}(\rho, p)\right)^2 &= \left(\partial_p \varepsilon_{|\rho}\right)^{-1} \left(\mathscr{E}_0^2\, p - \rho^2\, \partial_\rho \varepsilon_{|p}\right), \\ \left(\rho\, c_{\mathcal{A}}(\rho, p)\right)^2 &= \left(\partial_p \varepsilon_{|\rho}\right)^{-1} p. \end{aligned} \tag{2.11}$$

In the case of a stiffened gas thermodynamics, $c_{\mathcal{C}}^2 \geq 0$. Besides, if pressure remains positive, $c_{\mathcal{A}}^2 \geq 0$. Under this condition, the subsystems $\mathcal{C}$ and $\mathcal{A}$ are hyperbolic. Their eigenvalues are:

$$\begin{aligned} \lambda_1^{\mathcal{C}} = u - \mathscr{E}_0\, c_{\mathcal{C}} \quad &\leq \lambda_2^{\mathcal{C}} = u \leq \lambda_3^{\mathcal{C}} = u + \mathscr{E}_0\, c_{\mathcal{C}}, \\ \lambda_1^{\mathcal{A}} = -\left(1 - \mathscr{E}_0^2\right) c_{\mathcal{A}} \quad &\leq \lambda_2^{\mathcal{A}} = 0 \leq \lambda_3^{\mathcal{A}} = \left(1 - \mathscr{E}_0^2\right) c_{\mathcal{A}}, \end{aligned} \tag{2.12}$$

the 1-wave and 3-wave of both subsystems are associated to genuinely non-linear fields whereas the 2-wave field are linearly degenerate. What is more, $c_{\mathcal{C}}$, $c_{\mathcal{A}}$ and c are related by:

$$(c_{\mathcal{C}})^2 + \left(1 - \mathscr{E}_0^2\right) (c_{\mathcal{A}})^2 = c^2. \tag{2.13}$$

The proof of this proposition is written in subsection B. Beside, using relation (2.13), it can be observed that, when $\mathscr{E}_0$ is close to one, $\mathcal{C}$ is approximately equivalent to the Euler system, and that is why: $\forall k$, $\lim_{\mathscr{E}_0 \to 1} \lambda_k^{\mathcal{C}} = \lambda_k^{\text{Euler}}$. Moreover, when $\mathscr{E}_0$ tends towards zero, $\lim_{\mathscr{E}_0 \to 0} \lambda_k^{\mathcal{C}} = \lambda_2^{\text{Euler}} = u$, because of the pressure terms disappearance. $\mathcal{C}$ then degenerates into a pure convective subsystem already exhibited in [1, 7]. However, thanks to equality (2.13), we have $\forall k \in \{1, 3\} : \left|\lambda_k^{\mathcal{A}}\right| \leq c$ even when $\mathscr{E}_0$ goes to zero. Thus, the weighted splitting approach always tends to underestimate acoustic wave

speeds whatever the thermodynamics is. In Section 2.3, the transcription, at the discrete level, of these non physical wave speeds will be seen. A numerical way to bridge the gap between $c_{\mathcal{A}}$ and c so that to follow the real physics will also be proposed. In order to make them less abstract, the expressions of $c_{\mathcal{C}}$ and $c_{\mathcal{A}}$ are provided below, in the case of ideal gas:

$$\begin{aligned} c_{\mathcal{C}} &= \sqrt{\frac{\gamma_{\mathscr{E}_0}\, p}{\rho}} < c,\ \gamma_{\mathscr{E}_0} = \mathscr{E}_0^2\left(\gamma-1\right)+1 < \gamma, \\ c_{\mathcal{A}} &= \sqrt{\frac{\left(\gamma-1\right)p}{\rho}} < c = \sqrt{\frac{\gamma\, p}{\rho}}. \end{aligned} \tag{2.14}$$

In the following, positivity of the relevant quantities got from the thermodynamical phase-space is analyzed in both continuous subsystems $\mathcal{C}$ and $\mathcal{A}$.

Positivity of Density and Internal Energy

Positivity requirements reflect the invariance of a given solution towards its thermodynamical phase space. In this study, one focuses on the ideal (IG) and the stiffened gas (SG) thermodynamics defined by the following sets:

$$\rho\varepsilon = \frac{p}{(\gamma-1)}, \tag{2.15a}$$

$$\Phi_{\mathrm{PG}} = \left\{\mathbf{U},\ \text{s. t. } e = \frac{|\mathbf{u}|^2}{2}+\varepsilon,\ \rho>0,\ \rho\varepsilon>0\right\}, \tag{2.15b}$$

$$= \left\{\mathbf{U},\ \text{s. t. } e = \frac{|\mathbf{u}|^2}{2}+\varepsilon,\ \rho>0,\ p>0\right\}, \tag{2.15c}$$

$$\rho\varepsilon = \frac{p+\gamma \mathrm{P}_\infty}{(\gamma-1)},\ \mathrm{P}_\infty>0, \tag{2.16a}$$

$$\Phi_{\mathrm{SG}} = \left\{\mathbf{U},\ \text{s. t. } e = \frac{|\mathbf{u}|^2}{2}+\varepsilon,\ \rho>0,\ \rho\varepsilon-\mathrm{P}_\infty>0\right\}, \tag{2.16b}$$

$$= \left\{\mathbf{U},\ \text{s. t. } e = \frac{|\mathbf{u}|^2}{2}+\varepsilon,\ \rho>0,\ p+\mathrm{P}_\infty>0\right\}. \tag{2.16c}$$

For both thermodynamics, the construction of the above phase-spaces allows to guarantee that the Euler speed of sound c is real and strictly positive since:

$$\begin{aligned} (\Phi)_{\mathrm{IG}}:\ c &= \sqrt{\frac{\gamma p}{\rho}} = \sqrt{\frac{\gamma(\gamma-1)(\rho\varepsilon)}{\rho}}, \\ (\Phi)_{\mathrm{SG}}:\ c &= \sqrt{\frac{\gamma(p+\mathrm{P}_\infty)}{\rho}} = \sqrt{\frac{\gamma(\gamma-1)(\rho\varepsilon-\mathrm{P}_\infty)}{\rho}}. \end{aligned} \tag{2.17}$$

Thus, in the case of an ideal gas thermodynamics (respectively in the case of a stiffened gas thermodynamics), the positivity of ρ and $\rho\varepsilon$ (respectively the positivity of ρ and $\rho\varepsilon-\mathrm{P}_\infty$) is studied. First of all, assume that $\forall\phi\in\left\{\rho,\rho\varepsilon,\rho\varepsilon-\mathrm{P}_\infty\right\}$ a positive inlet boundary condition as well as an admissible initial condition hold, namely:

$$\begin{aligned} &\phi_{|\partial\Omega}\geq 0 \text{ if } \mathbf{u}\cdot\mathbf{n}_{|\partial\Omega}\leq 0, \\ &\phi(.,t=0)\geq 0, \end{aligned} \tag{2.18}$$

with Ω the spatial domain of boundary $\partial\Omega$ and $\mathbf{n}$ the outward local normal vector of $\partial\Omega$.

Then, as recalled in [24] for sufficiently smooth solutions, positivity of density ρ is naturally obtained from mass equation in subsystem $\mathcal{C}$ for both thermodynamics. Density is also stationary in subsystem $\mathcal{A}$. So, after having successively solved $\mathcal{C}$ and $\mathcal{A}$, density remains positive.

In the case of an ideal gas thermodynamics, since ρ remains positive, the positivity of $\rho\varepsilon$ is equivalent to the positivity of ε. For smooth solutions, the specific internal energy in subsystems $\mathcal{C}$ and $\mathcal{A}$ verifies:

$$\begin{cases} \partial_t \varepsilon + \mathbf{u}\cdot\underline{\nabla}\varepsilon + \mathscr{C}_0^2(t)\,\dfrac{p}{\rho}\,\underline{\nabla}\cdot\mathbf{u} = 0, & (\mathcal{C}) \\ \partial_t \varepsilon + \left(1-\mathscr{C}_0^2(t)\right)\dfrac{p}{\rho}\,\underline{\nabla}\cdot\mathbf{u} = 0. & (\mathcal{A}) \end{cases} \tag{2.19}$$

By making the same kind of regularity hypothesis than in [24], one can prove that, in the case of an ideal gas thermodynamics, ε remains positive on Ω throughout time. See subsection C for more details.

In the case of a stiffened gas thermodynamics, let us introduce $\mathrm{P} = \rho\varepsilon - \mathrm{P}_\infty = \frac{p+\mathrm{P}_\infty}{(\gamma-1)}$ which is the variable concerned by the positivity requirement. In $\mathcal{C}$ and $\mathcal{A}$, it verifies the PDEs:

$$\begin{cases} \partial_t \mathrm{P} + \underline{\nabla}\cdot(\mathrm{P}\,\mathbf{u}) + \mathscr{C}_0^2(t)\,(\gamma-1)\,\mathrm{P}\,\underline{\nabla}\cdot(\mathbf{u}) + (1-\mathscr{C}_0^2(t))\,\mathrm{P}_\infty\,\underline{\nabla}\cdot\mathbf{u} = 0, & (\mathcal{C}) \\ \partial_t \mathrm{P} + (1-\mathscr{C}_0^2(t))\,(\gamma-1)\,\mathrm{P}\,\underline{\nabla}\cdot(\mathbf{u}) - (1-\mathscr{C}_0^2(t))\,\mathrm{P}_\infty\,\underline{\nabla}\cdot\mathbf{u} = 0. & (\mathcal{A}) \end{cases} \tag{2.20}$$

Let us first notice that $\frac{\mathrm{P}_\infty}{\mathrm{P}} = (\gamma-1)\frac{\mathrm{P}_\infty}{p+\mathrm{P}_\infty}$ is not *a priori* bounded since the stiffened gas phase-space allows p to tend towards $-\mathrm{P}_\infty$. Then, as shown in equation (2.104) of subsection C, this prevents from controlling the operator $(1-\mathscr{C}_0^2(t))\,\mathrm{P}_\infty\,\underline{\nabla}\cdot\mathbf{u}$, and the positivity of P cannot *a priori* be ensured unless $\mathrm{P}_\infty = 0$ which is the ideal gas case or $\mathscr{C}_0 = 1$ which corresponds to the resolution of Euler system with no splitting. More details are given in subsection C. Thus, in the case of a stiffened gas thermodynamics, computations involving the discrete resolution of subsystems $\mathcal{C}$ and $\mathcal{A}$ in which the discrete pressure field is close to $-\mathrm{P}_\infty$ could potentially produce complex numbers for c. Nevertheless, in most cases, pressure remains positive and this difficulty can be avoided.

The next section is dedicated to the design of a time-explicit scheme to solve the above Mach-sensitive fractional step.

2.3 Relaxation Scheme Applied to the Weighted Splitting Approach

For the sake of simplicity and with no loss of generality, the scheme description is done in one dimension. Literature dealing with relaxation schemes is vast. Without being exhaustive, we refer to [33] for the derivation of relaxation schemes applied to abstract hyperbolic systems in which the whole flux is relaxed. In [12], the authors question the existence of solutions for the relaxation systems as well as their convergence towards a local equilibrium. A detailed study of the entropy-satisfying relaxation method applied to the isentropic gas dynamics system and extended to the fully compressible Euler system is given in [5]. It uses a Suliciu-like relaxation technique [42] which is also applied in [2] on a Drift-Flux model. Besides, the acoustic part of the Lagrange-Projection splitting derived in [10, 25] is solved the same way too. Eventually in [15], an extension of the Suliciu approach to general fluid systems is done. Following the same approach, we proceed to a Suliciu-like relaxation method on both subsystems $\mathcal{C}$ and $\mathcal{A}$.

Let us recall that the Suliciu relaxation method applied on Euler-like systems consists in introducing a new pressure variable Π endowed with a "quasi-linear" dynamics converging towards the real pressure variable p. This convergence is ensured thanks to a source term whose timescale $\mu \ll 1$. The new system is still hyperbolic and has only linearly degenerate fields which makes the derivation of an exact Godunov solver easier. What is more, the high level of nonlinearity brought by the pressure variable *via* the equation of state (2.2d) is encapsulated in one single constant. As a consequence, the derivation of the numerical scheme can be done independently of the thermodynamics law. The cost to be paid is the increase of the system dimension through an additional equation for Π. What is more, one has to decide how to treat the equilibrium between Π and p numerically.

2.3.1 Suliciu Relaxation for the Weighted Splitting Approach

As previously mentioned, the Suliciu-like relaxation technique leans on a linearization of the pressure dynamics. Let us first derive the PDEs associated with p for both subsystems $\mathcal{C}$ and $\mathcal{A}$. Using the mass equations, internal energy equations (2.19), and the fact that

$$\forall \mathrm{D} \in \{\partial_t, \partial_x\},\ \mathrm{D}\, p = (\partial_\rho p)_{|\varepsilon}\, \mathrm{D}\rho + (\partial_\varepsilon p)_{|\rho}\, \mathrm{D}\varepsilon, \tag{2.21}$$

it yields:

$$\mathcal{C}:\ \partial_t p + u\partial_x p + \rho\, (c_{\mathcal{C}})^2\, \partial_x u = 0, \tag{2.22a}$$

$$\mathcal{A}:\ \partial_t p + (1-\mathscr{E}_0^2)\, \rho\, (c_{\mathcal{A}})^2\, \partial_x u = 0. \tag{2.22b}$$

Then, replace pressure $p(\rho, \varepsilon)$ by a new relaxation pressure variable Π which no longer depends of density and internal energy. One also expects Π to mimic the above physical pressure dynamics but with an additional linearization effect on the thermodynamics. This is done by introducing two constants $a_{\mathcal{C}} > 0$ and $a_{\mathcal{A}} > 0$ such that Π verifies:

$$\mathcal{C}:\ \partial_t \Pi + u\partial_x \Pi + \frac{a_{\mathcal{C}}^2}{\rho}\partial_x u = \frac{(p-\Pi)}{\mu}, \tag{2.23a}$$

$$\mathcal{A}:\ \partial_t \Pi + (1-\mathscr{E}_0^2)\,\frac{a_{\mathcal{A}}^2}{\rho}\partial_x u = \frac{(p-\Pi)}{\mu}. \tag{2.23b}$$

Here, $a_{\mathcal{C}}$ (respectively $a_{\mathcal{A}}$) is homogeneous to a density times a velocity and encapsulates the nonlinear effects brought by $\rho\, c_{\mathcal{C}}(\rho, \varepsilon)$ (respectively $\rho\, c_{\mathcal{A}}(\rho, \varepsilon)$). Besides, by using the mass equation and because $a_{\mathcal{C}}$ and $a_{\mathcal{A}}$ are constant, it is possible to rewrite equations (2.23a) and (2.23b) in a conservative way namely:

$$\mathcal{C}:\ \partial_t (\rho\Pi) + \partial_x \left((\rho\Pi + a_{\mathcal{C}}^2)\, u\right) = \frac{\rho\,(p-\Pi)}{\mu}, \tag{2.24a}$$

$$\mathcal{A}:\ \partial_t (\rho\Pi) + \partial_x \left((1-\mathscr{E}_0^2)\, a_{\mathcal{A}}^2\, u\right) = \frac{\rho\,(p-\Pi)}{\mu}. \tag{2.24b}$$

One can observe that, when $\mu \to 0$ in (2.23a) and (2.23b), the relaxation pressure Π tends formally towards p at zeroth order in μ. Hence $(p-\Pi)/\mu$ can be formally interpreted as a correction term of time scale μ forcing the relaxation pressure to converge towards the physical pressure instantaneously if μ tends to zero. Finally, the relaxation convective and acoustic systems read:

$$\mathcal{C}^\mu : \begin{cases} \partial_t \rho + \partial_x (\rho u) = 0, \\ \partial_t (\rho u) + \partial_x \left(\rho u^2 + \mathscr{E}_0^2(t)\, \Pi\right) = 0, \\ \partial_t (\rho e) + \partial_x \left((\rho e + \mathscr{E}_0^2(t)\, \Pi)\, u\right) = 0, \\ \partial_t (\rho\Pi) + \partial_x \left((\rho\Pi + a_{\mathcal{C}}^2)\, u\right) = \dfrac{\rho\,(p-\Pi)}{\mu}, \end{cases} \tag{2.25}$$

$$\mathcal{A}^\mu : \begin{cases} \partial_t \rho = 0, \\ \partial_t (\rho u) + \partial_x \left((1-\mathscr{E}_0^2(t))\, \Pi\right) = 0, \\ \partial_t (\rho e) + \partial_x \left((1-\mathscr{E}_0^2(t))\, \Pi\, u\right) = 0, \\ \partial_t (\rho\Pi) + \partial_x \left((1-\mathscr{E}_0^2(t))\, a_{\mathcal{A}}^2\, u\right) = \dfrac{\rho\,(p-\Pi)}{\mu}. \end{cases} \tag{2.26}$$

Remark 2.3.1
It is worth noting that, the relaxation schemes framework can be formulated differently. Indeed, one can rewrite the subsystems $\mathcal{C}^\mu$ and $\mathcal{A}^\mu$ without the relaxation term $\frac{\rho(p-\Pi)}{\mu}$. Hence, the relaxation

pressure Π *is free to move away from the real pressure* p*. However in that case, the resolution of the homogeneous relaxation subsystems is completed by a projection sub-step on the equilibrium manifold:*

$$\left\{ \left(\rho, \rho u, \rho e, \rho\Pi\right) \text{ such that, } \Pi = p(\rho, \varepsilon), \text{with } \varepsilon = e - \frac{\rho u^2}{2} \right\}. \tag{2.27}$$

As it will be seen in the sequel (see equation (2.47) *dealing with the overall algorithm of the fractional step), in practice both subsystems* $\mathcal{C}^\mu$ *and* $\mathcal{A}^\mu$ *are solved without* $\frac{\rho(p-\Pi)}{\mu}$*. Then, at the end of each subsystem resolution, the updated relaxation state is projected instantaneously on the equilibrium manifold.*

One way to calibrate the constant relaxation coefficient $a_\mathcal{C}$ (respectively $a_\mathcal{A}$) is to perform a Chapman-Enskog expansion by rewriting all the variables $\phi \in \{\rho, u, e, \Pi\}$ in power of μ:

$$\begin{aligned} \phi &= \phi_0 + \mu\phi_1 + \mu^2\phi_2 + .., \\ \Pi_0 &= p. \end{aligned}$$

By doing so, one can exhibit a subcharacteristic-like condition, also called Whitham-like condition [44]. It allows to prevent $\mathcal{C}^\mu$ (respectively $\mathcal{A}^\mu$) from triggering instabilities when $\mu \to 0$. What is more, it can be used as a sufficient condition to build an entropy pair and an extended entropy inequality for the relaxation system (see [5, 6, 12]). As detailed in subsection F, the subcharacteristic conditions obtained are:

$$\mathcal{C}^\mu : \ a_\mathcal{C} > \rho c_\mathcal{C}, \tag{2.28a}$$

$$\mathcal{A}^\mu : \ a_\mathcal{A} > \rho c_\mathcal{A}. \tag{2.28b}$$

Remark 2.3.2
By proceeding in the same manner, one could have obtained a Suliciu-like relaxation Euler system. The relaxation pressure PDE would have been:

$$\partial_t \Pi + u\partial_x \Pi + \frac{a_\mathrm{E}^2}{\rho}\partial_x u = \frac{(p-\Pi)}{\mu}, \tag{2.29}$$

with a_E *the constant relaxation coefficient constrained by the Euler subcharacteristic condition:*

$$a_\mathrm{E} > \rho c. \tag{2.30}$$

Recall that $\lim_{\mathscr{E}_0 \to 1} c_\mathcal{C} = c$*, and then* (2.28a) *becomes* (2.30) *in that case. More generally, the shape of such a Suliciu-like relaxation Euler system can be obtained by formally making* $\mathscr{E}_0$ *tend towards one in* $\mathcal{C}^\mu$*.*

Remark 2.3.3
In [13], [5], [9], [14] and [15], in order to solve the Euler system using relaxation techniques, the authors perform an inversion between the role played by total energy and entropy. The idea is to turn the total energy equation into a mathematical entropy constraint while injecting the pure transport entropy equation:

$$\partial_t s + u\partial_x s = 0. \tag{2.31}$$

By doing so, one can lean on good properties brought by relaxation methods applied on the barotropic Euler system and enforce the entropy inequality (2.6) *in the numerical resolution of the full Euler system. More details can be found in the above references. In our splitting approach, such a strategy is avoided. Indeed, let us consider* $\mathbf{U}^\mathcal{C}$ *(respectively* $\mathbf{U}^\mathcal{A}$*) the conservative state solution of the subsystem* $\mathcal{C}$ *(respectively* $\mathcal{A}$*). It can be shown that the physical entropy function* $s\left(\mathbf{U}^\mathcal{C}\right)$ *(respectively* $s\left(\mathbf{U}^\mathcal{A}\right)$*) defined in equation* (2.5) *does no longer verify equation* (2.31)*. For both subsystems, an additional non-conservative term appears and prevents from applying directly the barotropic-relaxation system results. That is why, in our case, a simple Suliciu-relaxation method is performed on the conservative system including total energy. Note that a similar relaxation treatment is done in [10] for the acoustic subsystem.*

Remark 2.3.4
As previously noted in Section 2.2.2, the lower bound in the acoustic subcharacteristic condition (2.28b) uses $c_{\mathcal{A}}$ an artificial celerity naturally provided by subsystem $\mathcal{A}$. In the case of an ideal or a stiffened gas thermodynamics, $c_{\mathcal{A}} < c$, so that one can provide, at the discrete level, a constant $a_{\mathcal{A}}$ fulfilling a discrete version of inequality (2.28b) while violating the natural acoustic subcharacteristic condition (2.30) based on the real sound speed which is found in [9], [14] and [25]. According to a formal Chapman-Enskog expansion, the subcharacteristic condition (2.28b) provides a sufficient condition guaranteeing the stability of the time-explicit scheme for the resolution of $\mathcal{A}^{\mu}$. However, no theoretical result has been found to prove that it was also a sufficient condition to obtain the stability of the overall weighted splitting approach. In particular, in the case of low Mach number compressible flows with $c_{\mathcal{A}} \ll c$, we think that it is relevant to numerically compare the effect of considering the more demanding condition (2.30) rather than (2.28b). This will be done in Section 2.5.2.

2.3.2 Derivation of the Relaxation Scheme

Let us define Δx (respectively Δt) the space step (respectively the time step) of the scheme. For $i \in [1, .., N_{cells}]$ let us set $x_i = i\,\Delta x$, the coordinate of the cell center i and $x_{i+1/2} = x_i + \Delta x/2$, the coordinate of face $i+1/2$. Let us consider $\mathbf{W} = \left[\rho, \rho\,u, \rho\,e, \rho\,\Pi\right]^{\mathrm{T}}$ the extended relaxation conservative vector. Following **Remark 1**, the Riemann problem related to the *homogeneous* versions of (2.25) or (2.26) writes:

$$\partial_t\,\mathbf{W} + \partial_x\,\mathbf{F}^{\mu}(\mathbf{W}) = \mathbf{0}, \qquad \mathbf{W}(t=0,.) = \begin{cases} \mathbf{W}_{\mathrm{L}} \text{ if } x < x_0, \\ \mathbf{W}_{\mathrm{R}} \text{ if } x > x_0, \end{cases} \tag{2.32}$$

with

$$\mathbf{F}^{\mu} \in \left\{ \mathbf{F}^{\mu}_{\mathcal{C}}(\mathbf{W}) = \begin{bmatrix} \rho\,u \\ \rho\,u^2 + \mathscr{E}_0^2\,\Pi \\ (\rho\,e + \mathscr{E}_0^2\,\Pi)\,u \\ (\rho\,\Pi + (a_{\mathcal{C}})^2)\,u \end{bmatrix}, \mathbf{F}^{\mu}_{\mathcal{A}}(\mathbf{W}) = (1-\mathscr{E}_0^2) \begin{bmatrix} 0 \\ \Pi \\ \Pi\,u \\ (a_{\mathcal{A}})^2\,u \end{bmatrix} \right\}. \tag{2.33}$$

Let us introduce $\mathbf{U}_i^n$ the discrete approximation of $\frac{1}{\Delta x}\int_{x_{i-1/2}}^{x_{i+1/2}} \mathrm{L}(\mathbf{W})(x, t^n)\,dx$, $\mathbf{W}$ verifying $\partial_t\,\mathbf{W} + \partial_x\,\mathbf{F}^{\mu}(\mathbf{W}) = \mathbf{0}\ \forall (x,t)$, and $\mathrm{L}: \mathbf{W} = [w_1, w_2, w_3, w_4]^{\mathrm{T}} \in \mathbb{R}^4 \to [w_1, w_2, w_3]$. Therefore $\mathbf{U}_i^n$ represents the discrete approximation of the solution of the relaxation system without the component $\rho\,\Pi$. Then, the Godunov solver can be derived easily and reads:

$$\begin{aligned} \mathbf{U}_i^{n+1} &= \mathbf{U}_i^n - \frac{\Delta t}{\Delta x}\left(\mathbf{H}_{i+1/2}^n - \mathbf{H}_{i-1/2}^n\right), \\ \mathbf{H}_{i+1/2}^n &= \mathrm{L}\left(\mathbf{F}^{\mu}\left(\mathbf{W}^{God}(0; \mathbf{W}_i^n, \mathbf{W}_{i+1}^n)\right)\right) = \mathbf{H}_{i+1/2}^n\left(\mathbf{U}_i^n, \mathbf{U}_{i+1}^n\right), \end{aligned} \tag{2.34}$$

and $(x,t) \to \mathbf{W}^{God}\left(\frac{x-x_{i+1/2}}{t}; \mathbf{W}_i^n, \mathbf{W}_{i+1}^n\right)$ the self similar solution of the Riemann problem (2.32) located at $x_0 = x_{i+1/2}$.

The study of $\mathcal{C}^{\mu}$ and $\mathcal{A}^{\mu}$ leading to the time-explicit expression of the Godunov flux has been done using the non-conservative variable $\mathbf{Z}^{\mathrm{T}} = [\rho, u, \Pi, e]^{\mathrm{T}}$. In the following, the structure of the fields, the eigenvalues and the Riemann invariants are described.

Convective Part

The relaxation system $\mathcal{C}^{\mu}$ is strictly hyperbolic, its eigenvalues being: $\lambda_1^{\mathcal{C},\mu} = u - \mathscr{E}_0\,a_{\mathcal{C}}\,\tau$, $\lambda_2^{\mathcal{C},\mu} = \lambda_3^{\mathcal{C},\mu} = u$, $\lambda_4^{\mathcal{C},\mu} = u + \mathscr{E}_0\,a_{\mathcal{C}}\,\tau$ with $\tau = 1/\rho$. Furthermore, each field is linearly degenerate and admits simple Riemann invariants:

$$\begin{aligned} \mathcal{I}^{\mathcal{C},\mu}_{\mathscr{E}_0,1} &= \left\{ u - \mathscr{E}_0\,a_{\mathcal{C}}\,\tau,\ \Pi + a_{\mathcal{C}}^2\,\tau,\ e + \frac{\mathscr{E}_0}{a_{\mathcal{C}}}\,\Pi\,u \right\}, \\ \mathcal{I}^{\mathcal{C},\mu}_{\mathscr{E}_0,2,3} &= \{u,\ \Pi\}, \\ \mathcal{I}^{\mathcal{C},\mu}_{\mathscr{E}_0,4} &= \left\{ u + \mathscr{E}_0\,a_{\mathcal{C}}\,\tau,\ \Pi + a_{\mathcal{C}}^2\,\tau,\ e - \frac{\mathscr{E}_0}{a_{\mathcal{C}}}\,\Pi\,u \right\}. \end{aligned} \tag{2.35}$$

Let us notice that, for smooth solutions, mass equation in subsystem $\mathcal{C}^\mu$ can be rewritten $\partial_t \tau + u\partial_x \tau - \tau \partial_x u = 0$. By multiplying this equation by $a_\mathcal{C}^2$ and summing it with the Π equation in (2.26), one obtains:

$$\partial_t \left(\Pi + a_\mathcal{C}^2 \tau\right) + u \partial_x \left(\Pi + a_\mathcal{C}^2 \tau\right) = 0. \tag{2.36}$$

Thus, $\Pi + a_\mathcal{C}^2 \tau$ remains constant along the characteristic curves of speed u. Besides, it is a 2,3-strong Riemann invariant meaning that it is invariant through the 1-wave and the 4-wave. Eventually one can notice that this quantity is solution of the following equation:

$$\partial_\rho (\psi)_{|\Pi} + \left(\frac{a_\mathcal{C}}{\rho}\right)^2 \partial_\Pi (\psi)_{|\rho} = 0, \tag{2.37}$$

which can be related to the entropy equation (2.5). The pressure term linearization induced by the relaxation method has logically implied a linearization of the equation originally verified by entropy and $\Pi + a_\mathcal{C}^2 \tau$ seems to play the same role.

Besides, the knowledge of the Riemann invariants allow to easily solve the one-dimensional Riemann problem at a given face f, with $\mathbf{Z}_\mathrm{L}$ and $\mathbf{Z}_\mathrm{R}$ taken as initial conditions. Figure 2.1a describes the different states and waves produced.

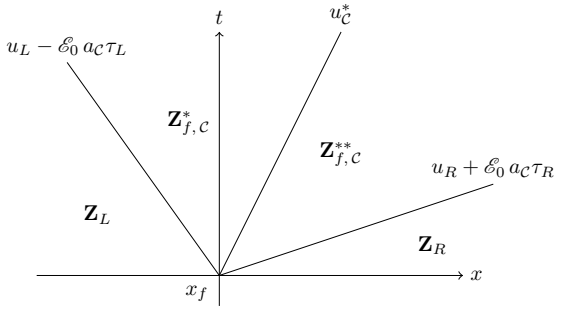

(a) Subsystem $\mathcal{C}^\mu$: waves and states

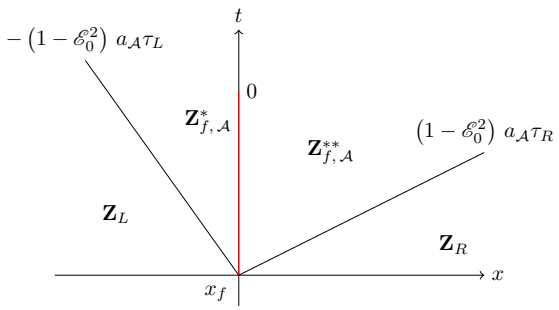

(b) Subsystem $\mathcal{A}^\mu$: waves and states

Figure 2.1 – Relaxation Riemann problems

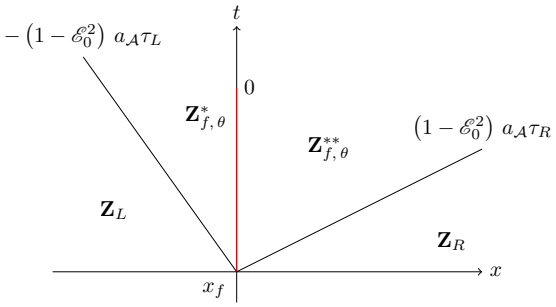

(a) Approximate Riemann Solver of Subsystem $\mathcal{A}^\mu$: waves and states

Figure 2.2 – Acoustic relaxation Riemann problems: θ-correction

The two intermediate states $\mathbf{Z}_{f,\mathcal{C}}^*$ and $\mathbf{Z}_{f,\mathcal{C}}^{**}$ are:

$$\mathbf{Z}_{f,\mathcal{C}}^* = \begin{bmatrix} \rho_{\mathrm{L},\mathcal{C}}^* \\ u_\mathcal{C}^* \\ \Pi_\mathcal{C}^* \\ e_{\mathrm{L},\mathcal{C}}^* \end{bmatrix}, \quad \mathbf{Z}_{f,\mathcal{C}}^{**} = \begin{bmatrix} \rho_{\mathrm{R},\mathcal{C}}^* \\ u_\mathcal{C}^* \\ \Pi_\mathcal{C}^* \\ e_{\mathrm{R},\mathcal{C}}^* \end{bmatrix}, \tag{2.38}$$

with,

$$\begin{cases} u_{\mathcal{C}}^{*} = \dfrac{u_{\mathrm{R}}+u_{\mathrm{L}}}{2} - \dfrac{\mathscr{E}_0}{2\,a_{\mathcal{C}}}\left(p_{\mathrm{R}}-p_{\mathrm{L}}\right), \\ \mathscr{E}_0^2\,\Pi_{\mathcal{C}}^{*} = \mathscr{E}_0^2\,\dfrac{p_{\mathrm{R}}+p_{\mathrm{L}}}{2} - \dfrac{\mathscr{E}_0\,a_{\mathcal{C}}}{2}\left(u_{\mathrm{R}}-u_{\mathrm{L}}\right), \\ \rho_{k,\mathcal{C}}^{*} = 1/\tau_{k,\mathcal{C}}^{*},\ \tau_{k,\mathcal{C}}^{*} = \tau_k + \dfrac{(-1)^{i_k+1}}{\mathscr{E}_0\,a_{\mathcal{C}}}\left(u_{\mathcal{C}}^{*}-u_k\right), \\ e_{k,\mathcal{C}}^{*} = e_k + \mathscr{E}_0\,\dfrac{(-1)^{i_k}}{a_{\mathcal{C}}}\left(\Pi_{\mathcal{C}}^{*}\,u_{\mathcal{C}}^{*} - p_k\,u_k\right), \\ k\in\{\mathrm{L},\mathrm{R}\},\ i_{\mathrm{L}}=1,\ i_{\mathrm{R}}=2. \end{cases} \tag{2.39}$$

Define $\mathbf{W}_{i+1/2}^{*,n}$ (respectively $\mathbf{W}_{i+1/2}^{**,n}$) using $\mathbf{Z}_{i+1/2,\mathcal{C}}^{*}$ (respectively $\mathbf{Z}_{i+1/2,\mathcal{C}}^{**}$) and introduce $\mathbf{U}_{i+1/2}^{*,n} = \mathrm{L}\left(\mathbf{W}_{i+1/2}^{*,n}\right)$, $\mathbf{U}_{i+1/2}^{**,n} = \mathrm{L}\left(\mathbf{W}_{i+1/2}^{**,n}\right)$. The convective numerical flux then reads:

$$\mathbf{H}_{\mathbf{c}}{}_{i+1/2}^{n} = \begin{cases} \mathrm{L}\left(\mathbf{F}_{\mathcal{C}}^{\mu}\right)\left(\mathbf{U}_i^n\right) & \text{if } u_i^n - \mathscr{E}_0^n\,(a_{\mathcal{C}}^n)_{i+1/2}\tau_i^n > 0, \\ \mathrm{L}\left(\mathbf{F}_{\mathcal{C}}^{\mu}\right)\left(\mathbf{U}_{i+1/2}^{*,n}\right) & \text{if } u_i^n - \mathscr{E}_0^n\,(a_{\mathcal{C}}^n)_{i+1/2}\tau_i^n \le 0 < (u_{\mathcal{C}}^{*})_{i+1/2}^{n}, \\ \mathrm{L}\left(\mathbf{F}_{\mathcal{C}}^{\mu}\right)\left(\mathbf{U}_{i+1/2}^{**,n}\right) & \text{if } (u_{\mathcal{C}}^{*})_{i+1/2}^{n} \le 0 < u_{i+1}^n + \mathscr{E}_0^n\,(a_{\mathcal{C}}^n)_{i+1/2}\tau_{i+1}^n, \\ \mathrm{L}\left(\mathbf{F}_{\mathcal{C}}^{\mu}\right)\left(\mathbf{U}_{i+1}^n\right) & \text{if } u_{i+1}^n + \mathscr{E}_0^n\,(a_{\mathcal{C}}^n)_{i+1/2}\tau_{i+1}^n \le 0, \\ (a_{\mathcal{C}}^n)_{i+1/2} = & \mathrm{K}\,max\left(\rho_i^n\,(c_{\mathcal{C}})_i^n,\,\rho_{i+1}^n\,(c_{\mathcal{C}})_{i+1}^n\right),\ \mathrm{K}>1. \end{cases} \tag{2.40}$$

Furthermore, using the exact Godunov structure and the fact that all the fields are linearly degenerate, one can rewrite the relaxation flux in a more compact way (see [2, 3]) as:

$$\mathbf{H}_{\mathbf{c}}{}_{i+1/2}^{n} = \begin{cases} \dfrac{1}{2}\left(\mathrm{L}\left(\mathbf{F}_{\mathcal{C}}^{\mu}\right)\left(\mathbf{U}_i^n\right) + \mathrm{L}\left(\mathbf{F}_{\mathcal{C}}^{\mu}\right)\left(\mathbf{U}_{i+1}^n\right)\right) \\ -\dfrac{1}{2}\left|u_i^n - \mathscr{E}_0^n\,(a_{\mathcal{C}}^n)_{i+1/2}\,\tau_i^n\right|\left(\mathbf{U}_{i+1/2}^{*,n} - \mathbf{U}_i^n\right) \\ -\dfrac{1}{2}\left|(u_{\mathcal{C}}^{*})_{i+1/2}^{n}\right|\left(\mathbf{U}_{i+1/2}^{**,n} - \mathbf{U}_{i+1/2}^{*,n}\right) \\ -\dfrac{1}{2}\left|u_{i+1}^n + \mathscr{E}_0^n\,(a_{\mathcal{C}}^n)_{i+1/2}\,\tau_{i+1}^n\right|\left(\mathbf{U}_{i+1}^n - \mathbf{U}_{i+1/2}^{**,n}\right). \end{cases} \tag{2.41}$$

Acoustic Part

The acoustic system $\mathcal{A}^{\mu}$ is also hyperbolic and its eigenvalues are: $\lambda_1^{\mathcal{A},\mu} = -(1-\mathscr{E}_0^2)\,a_{\mathcal{A}}\tau$, $\lambda_2^{\mathcal{A},\mu} = \lambda_3^{\mathcal{A},\mu} = 0$, $\lambda_4^{\mathcal{A},\mu} = (1-\mathscr{E}_0^2)\,a_{\mathcal{A}}\tau$. Once again the Riemann invariants can be easily found and read:

$$\begin{aligned} \mathcal{I}_{\mathscr{E}_0,1}^{\mathcal{A},\mu} &= \left\{\rho,\ u + \frac{\Pi}{a_{\mathcal{A}}},\ e + \frac{\Pi\,u}{a_{\mathcal{A}}}\right\}, \\ \mathcal{I}_{\mathscr{E}_0,2,3}^{\mathcal{A},\mu} &= \{u,\ \Pi\}, \\ \mathcal{I}_{\mathscr{E}_0,4}^{\mathcal{A},\mu} &= \left\{\rho,\ u - \frac{\Pi}{a_{\mathcal{A}}},\ e - \frac{\Pi\,u}{a_{\mathcal{A}}}\right\}. \end{aligned} \tag{2.42}$$

It can be noticed that:

$$\begin{aligned} \partial_t\left(u + \frac{\Pi}{a_{\mathcal{A}}}\right) + \lambda_4^{\mathcal{A},\mu}\,\partial_x\left(u + \frac{\Pi}{a_{\mathcal{A}}}\right) = 0, \\ \partial_t\left(u - \frac{\Pi}{a_{\mathcal{A}}}\right) + \lambda_1^{\mathcal{A},\mu}\,\partial_x\left(u - \frac{\Pi}{a_{\mathcal{A}}}\right) = 0. \end{aligned} \tag{2.43}$$

Thus, $\omega_{\mathcal{A}}^{+} = u + \frac{\Pi}{a_{\mathcal{A}}}$ (respectively $\omega_{\mathcal{A}}^{-} = u - \frac{\Pi}{a_{\mathcal{A}}}$) remains constant along the characteristic curves of speed $\lambda_4^{\mathcal{A},\mu}$ (respectively $\lambda_1^{\mathcal{A},\mu}$). Besides, $\omega_{\mathcal{A}}^{+}$ is a 4-strong Riemann invariant whereas $\omega_{\mathcal{A}}^{-}$ is a 1-strong Riemann invariant. Following the steps of [14] and [25], equations (2.43) associated with the strong Riemann invariants natural properties provides a simple way to derive a time-implicit relaxation scheme for the acoustic subsystem. More details are given in [31, 32].

The one-dimensional Riemann problem can be solved exactly without difficulty. The solution is described in Figure 2.1b.

$$\mathbf{Z}^*_{f,\mathcal{A}} = \begin{bmatrix} \rho_{\mathrm{L}} \\ u^*_{\mathcal{A}} \\ \Pi^*_{\mathcal{A}} \\ e^*_{\mathrm{L},\mathcal{A}} \end{bmatrix}, \quad \mathbf{Z}^{**}_{f,\mathcal{A}} = \begin{bmatrix} \rho_{\mathrm{R}} \\ u^*_{\mathcal{A}} \\ \Pi^*_{\mathcal{A}} \\ e^*_{\mathrm{R},\mathcal{A}} \end{bmatrix}, \tag{2.44}$$

with,

$$\begin{cases} u^*_{\mathcal{A}} = \dfrac{u_{\mathrm{R}} + u_{\mathrm{L}}}{2} - \dfrac{1}{2\,a_{\mathcal{A}}}\left(p_{\mathrm{R}} - p_{\mathrm{L}}\right), \\ \Pi^*_{\mathcal{A}} = \dfrac{p_{\mathrm{R}} + p_{\mathrm{L}}}{2} - \dfrac{a_{\mathcal{A}}}{2}\left(u_{\mathrm{R}} - u_{\mathrm{L}}\right), \\ e^*_{k,\mathcal{A}} = e_k + \dfrac{(-1)^{i_k}}{a_{\mathcal{A}}}\left(\Pi^*_{\mathcal{A}}\, u^*_{\mathcal{A}} - p_k\, u_k\right), \\ k \in \{\mathrm{L},\mathrm{R}\},\ i_{\mathrm{L}} = 1,\ i_{\mathrm{R}} = 2. \end{cases} \tag{2.45}$$

One can notice that the weighting parameter $\mathscr{E}_0$ does not appear in the different intermediate quantities. Besides, the intermediate velocity, pressure and energy formulas are similar to those obtained using the Lagrange-Projection method [10, 25]. The only difference is that, in the present approach, $a_{\mathcal{A}}$ is bounded by the modified acoustic subcharacteristic condition (2.28b) whereas in [10, 25] it is (2.30). The related numerical flux writes:

$$\begin{aligned} &\mathbf{H}_{\mathbf{ac}}{}^{n}_{i+1/2} = \left(1 - (\mathscr{E}_0^n)^2\right) \begin{bmatrix} 0 \\ (\Pi^*_{\mathcal{A}})^n_{i+1/2} \\ (\Pi^*_{\mathcal{A}})^n_{i+1/2}\,(u^*_{\mathcal{A}})^n_{i+1/2} \end{bmatrix}, \\ &(a^n_{\mathcal{A}})_{i+1/2} = \mathrm{K}\max\left(\rho^n_i\,(c_{\mathcal{A}})^n_i,\, \rho^n_{i+1}\,(c_{\mathcal{A}})^n_{i+1}\right),\ \mathrm{K} > 1. \end{aligned} \tag{2.46}$$

General Remarks on the Splitting Operator Algorithm:

The overall algorithm updating the discrete solution from t^n to $t^n + \Delta t$ is the following: starting from a given state $\mathbf{U}^n$, a given relaxation pressure $\Pi^n = p^{\mathrm{EOS}}(\mathbf{U}^n)$ and a given splitting parameter $\mathscr{E}_0^n$, the homogeneous versions of subsystems $\mathcal{C}^\mu$ and $\mathcal{A}^\mu$ are successively solved using the relaxation scheme fluxes presented in (2.40) and (2.46). At the end of each resolution, the new discrete states $\mathbf{W}_i^{n+}$ (after the convective sub-step) and $\mathbf{W}_i^{n+1}$ (after the acoustic sub-step) are projected on the equilibrium manifold (2.27). Such a projection procedure presented in [5] can be seen as an additional sub-step resolving $\partial_t \mathbf{W} = \mathbf{S}^\mu(\mathbf{W})$ with $\mathbf{S}^\mu(\mathbf{W}) = \left[0, 0, 0, (p - \Pi)/\mu\right]^{\mathrm{T}}$ and $\mu \to 0$. It allows to provide the appropriate physical pressure for the flux construction between two sub-steps. Afterwards, the weighting factor $\mathscr{E}_0$ is updated. One can notice that the overall operator splitting procedure is conservative since $\mathcal{C}$ and $\mathcal{A}$ are conservative subsystems and the resolution of $\mathcal{C}^\mu$ and $\mathcal{A}^\mu$ is performed using an exact conservative Godunov scheme. The global relaxation scheme including both steps writes:

$$\begin{cases} \mathbf{U}_i^{n+} = \mathbf{U}_i^n - \frac{\Delta t}{\Delta x}\left(\mathbf{H}_{\mathbf{c}\,i+1/2}\left(\mathbf{U}_i^n, \mathbf{U}_{i+1}^n\right) - \mathbf{H}_{\mathbf{c}\,i-1/2}\left(\mathbf{U}_{i-1}^n, \mathbf{U}_i^n\right)\right), \\ \Pi_i^{n+} = p^{\mathrm{EOS}}\left(\mathbf{U}_i^{n+}\right), \\ \mathbf{U}_i^{n+1} = \mathbf{U}_i^{n+} - \frac{\Delta t}{\Delta x}\left(\mathbf{H}_{\mathbf{ac}\,i+1/2}\left(\mathbf{U}_i^{n+}, \mathbf{U}_{i+1}^{n+}\right) - \mathbf{H}_{\mathbf{ac}\,i-1/2}\left(\mathbf{U}_{i-1}^{n+}, \mathbf{U}_i^{n+}\right)\right), \\ \Pi_i^{n+1} = p^{\mathrm{EOS}}\left(\mathbf{U}_i^{n+1}\right). \end{cases} \tag{2.47}$$

Written in one single conservative step, the scheme reads:

$$\begin{aligned} \mathbf{U}_i^{n+1} = \mathbf{U}_i^n &- \frac{\Delta t}{\Delta x}\left(\mathbf{H}_{\mathbf{c}\,i+1/2}\left(\mathbf{U}_i^n, \mathbf{U}_{i+1}^n\right) - \mathbf{H}_{\mathbf{c}\,i-1/2}\left(\mathbf{U}_{i-1}^n, \mathbf{U}_i^n\right)\right) \\ &- \frac{\Delta t}{\Delta x}\left(\mathbf{H}_{\mathbf{ac}\,i+1/2}\left(\mathbf{U}_i^{n+}, \mathbf{U}_{i+1}^{n+}\right) - \mathbf{H}_{\mathbf{ac}\,i-1/2}\left(\mathbf{U}_{i-1}^{n+}, \mathbf{U}_i^{n+}\right)\right). \end{aligned} \tag{2.48}$$

Following the continuous definition (2.10) of the parameter $\mathscr{E}_0$, one can introduce $\mathscr{E}_0^n$ as:

$$\begin{aligned} \mathscr{E}_0^n &= \max\left(\mathscr{E}_{inf}, \min\left(\mathrm{M}_{max}^n, 1\right)\right), \\ \text{with } \mathrm{M}_{max}^n &= \max_{i\in[1,\mathrm{N}_{cells}]}\left(\frac{|u_i^n|}{c_i^n}\right). \end{aligned} \tag{2.49}$$

Here, $c_i^n = c\left(\rho_i^n, p_i^n\right)$ where $c(.,.)$ is the sound speed function defined in equation (2.3). As already mentioned in Section 2.2.2, $0 < \mathscr{E}_{inf} \ll 1$ is only a lower bound preventing $\mathscr{E}_0^n$ from being exactly equal to zero if velocity is initially null everywhere.

2.3.3 CFL Condition Choice

Definition 2.3.1 (CFL condition based on the Euler system)
In order to adapt timesteps to the real waves produced by the Euler system, let us define the discrete time step at iteration n as:

$$\begin{aligned} &\Delta t_{\mathrm{E}}^n = \frac{\sigma}{2}\frac{\Delta x}{\max\limits_{i+1/2}\left(\max\left(|u_i^n| + c_i^n, |u_{i+1}^n| + c_{i+1}^n\right)\right)}, \\ &0 < \sigma < 1. \end{aligned} \tag{2.50}$$

CFL condition (2.50) is adapted to the resolution of the overall Euler system. However, because of the weighted splitting approach, one can exhibit two additional CFL conditions which would be sufficient to guarantee stability of both $\mathcal{C}$ and $\mathcal{A}$ subsystems if they were solved independently. These CFL conditions write:

$$\begin{aligned} \Delta t_{\mathcal{C}}^n &= \frac{\sigma}{2}\frac{\Delta x}{\max\limits_{i+1/2}\left(\max\left(\left|u_i^n - \mathscr{E}_0^n\,(a_{\mathcal{C}})_{i+1/2}^n\,\tau_i^n\right|, \left|u_{i+1}^n + \mathscr{E}_0^n\,(a_{\mathcal{C}})_{i+1/2}^n\,\tau_{i+1}^n\right|\right)\right)}, \\ \Delta t_{\mathcal{A}}^n &= \frac{\sigma}{2}\frac{\Delta x}{\left(1-(\mathscr{E}_0^n)^2\right)\max\limits_{i+1/2}\left((a_{\mathcal{A}})_{i+1/2}^n \max\left(\tau_i^n, \tau_{i+1}^n\right)\right)}, \\ &0 < \sigma < 1. \end{aligned} \tag{2.51}$$

One should keep in mind that it is absolutely not sufficient, in a fractional-step method, to constrain the time-step by only sub-steps CFL condition in order to guarantee the stability of the overall algorithm. A very simple hand-made but rather convincing example described in [16] shows that the CFL condition of the unsplit system has to be taken into account too. Hence, the final CFL condition reads:

$$\Delta t^n = \min\left(\Delta t_{\mathrm{E}}^n, \Delta t_{\mathcal{C}}^n, \Delta t_{\mathcal{A}}^n\right). \tag{2.52}$$

We now study the discrete properties of our weighted splitting approach. Special attention will be paid to the positivity of both density and internal energy.

2.3.4 Discrete Properties of the Overall Scheme

Discrete Density Positivity

Let us first notice that the acoustic resolution step of $\mathcal{A}^{\mu}$ does not modify density. Then, one has just to check that discrete density remains positive after the convective step. This is classically done in [2] by rewriting the convective relaxation scheme (2.34), (2.40) as:

$$\begin{aligned} \mathbf{U}_i^{n+1} &= \frac{\mathbf{U}^+\left(\mathbf{W}_i^n, \mathbf{W}_{i-1}^n\right) + \mathbf{U}^-\left(\mathbf{W}_{i+1}^n, \mathbf{W}_i^n\right)}{2}, \\ \text{with: } \mathbf{U}^+\left(\mathbf{W}_{\mathrm{L}}, \mathbf{W}_{\mathrm{R}}\right) &= \frac{2\Delta t}{\Delta x}\int_0^{\frac{\Delta x}{2\Delta t}} \mathrm{L}\left(\mathbf{W}^{God}\right)\left(\xi, \mathbf{W}_{\mathrm{L}}, \mathbf{W}_{\mathrm{R}}\right) d\xi, \\ \mathbf{U}^-\left(\mathbf{W}_{\mathrm{L}}, \mathbf{W}_{\mathrm{R}}\right) &= \frac{2\Delta t}{\Delta x}\int_{-\frac{\Delta x}{2\Delta t}}^0 \mathrm{L}\left(\mathbf{W}^{God}\right)\left(\xi, \mathbf{W}_{\mathrm{L}}, \mathbf{W}_{\mathrm{R}}\right) d\xi. \end{aligned} \tag{2.53}$$

Hence, positivity of the discrete density ρ_i^{n+1} is maintained if all the intermediate densities appearing in the Riemann problem described on Figure 2.1a and equalities (2.39) are positive. This can be done by adding an additional lower bound for constant $a_{\mathcal{C}}$ into the subcharacteristic condition (2.28a):

Lemma 2.3.1 (Positivity of intermediate density)
Consider a given mesh face and the related local Riemann problem related to subsystem $\mathcal{C}$, producing waves described on Figure 2.1a with $\mathbf{U}_{\mathrm{L}}$ and $\mathbf{U}_{\mathrm{R}}$ as initial data. Assume that the global CFL condition (2.52) holds so that waves produced by local Riemann problems do not interact. Consider the intermediate densities $\rho^*_{\mathrm{L},\mathcal{C}}$ and $\rho^*_{\mathrm{R},\mathcal{C}}$ defined in (2.39); then:

$$\begin{cases} \rho^*_{\mathrm{L},\mathcal{C}} \geq 0, \\ \rho^*_{\mathrm{R},\mathcal{C}} \geq 0, \end{cases} \Leftrightarrow \begin{cases} f_{\mathrm{L}}(a_{\mathcal{C}}) = a_{\mathcal{C}}^2 + \dfrac{\rho_{\mathrm{L}}\,(u_{\mathrm{R}}-u_{\mathrm{L}})}{2\mathscr{E}_0}\,a_{\mathcal{C}} - \dfrac{\rho_{\mathrm{L}}\,(p_{\mathrm{R}}-p_{\mathrm{L}})}{2} \geq 0, \\ f_{\mathrm{R}}(a_{\mathcal{C}}) = a_{\mathcal{C}}^2 + \dfrac{\rho_{\mathrm{R}}\,(u_{\mathrm{R}}-u_{\mathrm{L}})}{2\mathscr{E}_0}\,a_{\mathcal{C}} + \dfrac{\rho_{\mathrm{R}}\,(p_{\mathrm{R}}-p_{\mathrm{L}})}{2} \geq 0. \end{cases} \tag{2.54}$$

Define a_{L}^{ρ} (respectively a_{R}^{ρ}) the highest positive root related to the second order polynomial function $f_{\mathrm{L}}(a_{\mathcal{C}})$ (respectively $f_{\mathrm{R}}(a_{\mathcal{C}})$). Thus, under the modified subcharacteristic condition:

$$\mathcal{C}^{\mu}:\ a_{\mathcal{C}} \geq \max\left(\rho_{\mathrm{L}}\,(c_{\mathcal{C}})_{\mathrm{L}}, \rho_{\mathrm{R}}\,(c_{\mathcal{C}})_{\mathrm{R}}, a_{\mathrm{L}}^{\rho}, a_{\mathrm{R}}^{\rho}\right), \tag{2.55}$$

inequalities (2.54) hold. Furthermore, if $\mathbf{U}_{\mathrm{L}}$ and $\mathbf{U}_{\mathrm{R}}$ are such that a_{L}^{ρ} (respectively a_{R}^{ρ}) is complex or negative, $\rho^*_{\mathrm{L},\mathcal{C}} \geq 0$ (respectively $\rho^*_{\mathrm{R},\mathcal{C}} \geq 0$) is automatically fulfilled and a_{L}^{ρ} (respectively a_{R}^{ρ}) can be removed from (2.55). Eventually, it is equivalent to guarantee the intermediate density positivity and the ordering of the waves speeds: $u_{\mathrm{L}} - \mathscr{E}_0\,a_{\mathcal{C}}\,\tau_{\mathrm{L}} \leq u^*_{\mathcal{C}} \leq u_{\mathrm{R}} + \mathscr{E}_0\,a_{\mathcal{C}}\,\tau_{\mathrm{R}}$.

The proof of this lemma, including the expressions of a_{L}^{ρ} and a_{R}^{ρ}, is written in subsection D. The same kind of results can be found in [2] in order to enforce the mass fraction positivity. One has to mention that the non-dimensional expressions of a_{L}^{ρ} and a_{R}^{ρ} are of order $\mathrm{O}(1+\mathrm{M}/\mathscr{E}_0)$. Therefore considering the discrete splitting parameter $\mathscr{E}_0^n$ defined in (2.49), the non-dimensional roots a_{L}^{ρ} and a_{R}^{ρ} are of order one w.r.t the Mach number. Thus, their impact on the overall fractional step and notably on the numerical diffusion associated with the convective flux (2.41) is controlled in the sense that the modified subcharacteristic condition (2.55) does not imply that $\lim_{\mathrm{M}\to 0} a_{\mathcal{C}} = +\infty$.

Discrete Internal Energy Positivity for Ideal Gas Thermodynamics

As already presented in Section 2.2.2, in the case of an ideal gas thermodynamics, specific internal energy ε remains positive throughout space and time. Although ε is not a conservative variable, we can still consider equation (2.53) seen as a continuous convex combination of conservative states and notice that Φ_{PG} defined in (2.15) is a convex set in the conservative phase-space (see [5] for a proof). Thus, similarly to density, a sufficient condition to guarantee the positivity of ε^{n+1} is to make sure that for $k \in \{\mathrm{L},\mathrm{R}\}$, $\varepsilon^*_{k,\mathcal{C}} = e^*_{k,\mathcal{C}} - (u^*_{\mathcal{C}})^2/2$ as well as $\varepsilon^*_{k,\mathcal{A}} = e^*_{k,\mathcal{A}} - (u^*_{\mathcal{A}})^2/2$ are positive. Such a sufficient condition is presented in the next lemma:

Lemma 2.3.2 (Positivity of the intermediate internal energy)
Consider a given mesh face and the related local Riemann problem associated with subsystem $\mathcal{C}$ (respectively $\mathcal{A}$), producing waves described in Figure 2.1a (respectively Figure 2.1b) with $\mathbf{U}_{\mathrm{L}}$ and $\mathbf{U}_{\mathrm{R}}$ as initial data. Assume that the global CFL condition (2.52) holds so that waves produced by local Riemann problems do not interact. For $k \in \{\mathrm{L},\mathrm{R}\}$, consider the intermediate densities $\varepsilon^*_{k,\mathcal{C}}$ (respectively $\varepsilon^*_{k,\mathcal{A}}$) defined with quantities introduced in (2.39) (respectively (2.45));

for the acoustic subsystem:

$$\begin{cases} f_{\mathcal{A},\mathrm{L}}(a_{\mathcal{C}}) = a_{\mathcal{A}}^2 - \rho_{\mathrm{L}}^{\varepsilon}\dfrac{(u_{\mathrm{R}}-u_{\mathrm{L}})}{2}\,a_{\mathcal{A}} + \rho_{\mathrm{L}}^{\varepsilon}\dfrac{(p_{\mathrm{R}}-p_{\mathrm{L}})}{2} \geq 0, \\ f_{\mathcal{A},\mathrm{R}}(a_{\mathcal{A}}) = a_{\mathcal{A}}^2 - \rho_{\mathrm{R}}^{\varepsilon}\dfrac{(u_{\mathrm{R}}-u_{\mathrm{L}})}{2}\,a_{\mathcal{A}} - \rho_{\mathrm{L}}^{\varepsilon}\dfrac{(p_{\mathrm{R}}-p_{\mathrm{L}})}{2} \geq 0 \end{cases} \Rightarrow \begin{cases} \varepsilon^*_{\mathrm{L},\mathcal{A}} \geq 0, \\ \varepsilon^*_{\mathrm{R},\mathcal{A}} \geq 0, \end{cases} \tag{2.56}$$

with $\rho_k^\varepsilon = \frac{p_k}{\varepsilon_k}$.

for the convective subsystem:

$$\begin{cases} f_{\mathcal{C},\mathrm{L}}(a_\mathcal{C}) = a_\mathcal{C}^2 - \mathscr{E}_0\,\rho_\mathrm{L}^\varepsilon \dfrac{(u_\mathrm{R}-u_\mathrm{L})}{2}\,a_\mathcal{C} + \mathscr{E}_0^2\,\rho_\mathrm{L}^\varepsilon \dfrac{(p_\mathrm{R}-p_\mathrm{L})}{2} \geq 0, \\ f_{\mathcal{C},\mathrm{R}}(a_\mathcal{C}) = a_\mathcal{C}^2 - \mathscr{E}_0\,\rho_\mathrm{R}^\varepsilon \dfrac{(u_\mathrm{R}-u_\mathrm{L})}{2}\,a_\mathcal{C} - \mathscr{E}_0^2\,\rho_\mathrm{L}^\varepsilon \dfrac{(p_\mathrm{R}-p_\mathrm{L})}{2} \geq 0 \end{cases} \Rightarrow \begin{cases} \varepsilon_{\mathrm{L},\mathcal{C}}^* \geq 0, \\ \varepsilon_{\mathrm{R},\mathcal{C}}^* \geq 0, \end{cases} \tag{2.57}$$

Define $(a_{\mathcal{A},\mathrm{L}}^\varepsilon,\, a_{\mathcal{C},\mathrm{L}}^\varepsilon)$ *(respectively* $(a_{\mathcal{A},\mathrm{R}}^\varepsilon,\, a_{\mathcal{C},\mathrm{R}}^\varepsilon)$*) the highest positive roots related to the couple of second order polynomial functions* $(f_{\mathcal{A},\mathrm{L}}(a_\mathcal{A}),\, f_{\mathcal{C},\mathrm{L}}(a_\mathcal{C}))$ *(respectively* $(f_{\mathcal{A},\mathrm{R}}(a_\mathcal{A}),\, f_{\mathcal{C},\mathrm{R}}(a_\mathcal{C}))$*). Then one can show that:*

$$\begin{aligned} a_{\mathcal{C},\mathrm{L}}^\varepsilon &= \mathscr{E}_0\, a_{\mathcal{A},\mathrm{L}}^\varepsilon, \\ a_{\mathcal{C},\mathrm{R}}^\varepsilon &= \mathscr{E}_0\, a_{\mathcal{A},\mathrm{R}}^\varepsilon, \end{aligned} \tag{2.58}$$

so that under the modified subcharacteristic condition:

$$\begin{aligned} \mathcal{C}^\mu :\ & a_\mathcal{C} \geq \max\left(\rho_\mathrm{L}\,(c_\mathcal{C})_\mathrm{L},\, \rho_\mathrm{R}\,(c_\mathcal{C})_\mathrm{R},\, a_{\mathcal{A},\mathrm{L}}^\varepsilon,\, a_{\mathcal{A},\mathrm{R}}^\varepsilon\right), \\ \mathcal{A}^\mu :\ & a_\mathcal{A} \geq \max\left(\rho_\mathrm{L}\,(c_\mathcal{A})_\mathrm{L},\, \rho_\mathrm{R}\,(c_\mathcal{A})_\mathrm{R},\, a_{\mathcal{A},\mathrm{L}}^\varepsilon,\, a_{\mathcal{A},\mathrm{R}}^\varepsilon\right), \end{aligned} \tag{2.59}$$

inequalities (2.56) *and* (2.57) *hold. Eventually, if* $\mathbf{U}_\mathrm{L}$ *and* $\mathbf{U}_\mathrm{R}$ *are such that* $a_{\mathcal{A},\mathrm{L}}^\varepsilon$ *(respectively* $a_{\mathcal{A},\mathrm{R}}^\varepsilon$*) is complex or negative, the positivity of* $(\varepsilon_{\mathrm{L},\mathcal{C}}^*,\, \varepsilon_{\mathrm{L},\mathcal{A}}^*)$ *(respectively* $(\varepsilon_{\mathrm{R},\mathcal{C}}^*,\, \varepsilon_{\mathrm{R},\mathcal{A}}^*)$ *) is automatically fulfilled and* $a_{\mathcal{A},\mathrm{L}}^\varepsilon$ *(respectively* $a_{\mathcal{A},\mathrm{R}}^\varepsilon$*) can be removed from* (2.59).

The proof of this lemma and the formulas for the polynomial roots are provided in subsection E. Once again, it can be shown that the non-dimensional expressions of $a_{\mathcal{A},\mathrm{L}}^\varepsilon$ and $a_{\mathcal{A},\mathrm{R}}^\varepsilon$ are of order one w.r.t the Mach number.

In the following section, a truncation error analysis performed on smooth solutions is derived in order to assess the effect of the splitting parameter $\mathscr{E}_0$ in terms of numerical diffusion in the case of one-dimensional low Mach number compressible flows.

2.4 A Truncation Error Analysis

In [10, 25] a fractional step approach based on a Lagrange-Projection splitting [14] is proposed. The authors use a relaxation scheme, very similar to these introduced in (2.44), (2.45), (2.46), to discretize their corresponding acoustic flux. By performing a 1D non-dimensional truncation error analysis, they show that the dissipative part of the discrete acoustic momentum flux scales as $\mathrm{O}(\Delta x/\mathrm{M})$. This prohibitive dissipation does not vanish through their transport sub-step and the resulting diffusive operator for the overall scheme is of the same order.

A detailed study in [18–20] points out that this pathology actually holds for all Godunov-like schemes and hides far more intricate spatial discretization issues if one is interested in maintaining the solution of compressible Riemann solvers close to its incompressible initial part.

As explained in the introduction, the present work evolves within the point (II) framework. Then, we are simply interested in reducing the numerical diffusion which could occur on acoustic wave fronts in the case where $0 < \mathrm{M} \ll 1$. Hence, we only consider 1D non-dimensional truncation error analysis as a simple (although incomplete) tool to have a rough idea of the numerical diffusion produced by the spatial discretization of the present compressible solver when the Mach number is small compared with one. We notably want to measure the effect of the splitting parameter $\mathscr{E}_0^n$ on the amplitude of the overall scheme numerical diffusion. For that purpose, we start by performing a truncation error analysis for each subsystem as if they were solved independently. Then, the additional numerical diffusion due to the composition between the discrete convective state update and the acoustic flux is analyzed.

2.4.1 Truncation Error of the Weighted Splitting Subsystems

Each truncation error analysis is made on non-dimensional systems. Let us introduce

$$t_{\rm ref},\, l_{\rm ref},\, \rho_{\rm ref},\, u_{\rm ref},\, p_{\rm ref}, \tag{2.60}$$

the reference time-scale, space-scale, density, material velocity and pressure. Besides, define a reference acoustic celerity $c_{\rm r}$ such that $\rho_{\rm ref}\, c_{\rm r}^2 = p_{\rm ref}$. Finally, consider the Mach number $\mathrm{M} = u_{\rm ref}/c_{\rm r}$ and the Strouhal number $\mathrm{St_r} = l_{\rm ref}/(t_{\rm ref}\, u_{\rm ref})$. Then, the overall non-dimensional Euler compressible system reads:

$$\mathcal{E}: \begin{cases} \mathrm{St_r}\,\partial_t \rho + \partial_x(\rho\, u) = 0, \\ \mathrm{St_r}\,\partial_t(\rho\, u) + \partial_x\left(\rho\, u^2 + \dfrac{p}{\mathrm{M}^2}\right) = 0, \\ \mathrm{St_r}\,\partial_t(\rho\, e) + \partial_x\left((\rho\, e + p)\, u\right) = 0, \end{cases} \tag{2.61}$$

with $e = \varepsilon\left(\rho, \varepsilon\right) + \mathrm{M}^2\,\frac{u^2}{2}$. Note that in the context of point (II) , the reference time-scale is based on the fast acoustic waves: $t_{\rm ref} = l_{\rm ref}/c_{\rm r}$. Thus, $\mathrm{St_r} = 1/\mathrm{M}$. In the sequel, the Mach number is *fixed* to a given low value: $0 < \mathrm{M} \ll 1$. Then, by making the non-dimensional space-step Δx tend towards zero for smooth solutions, one seeks to find the amplitude of the diffusive operator induced by the spatial discretization of the overall fractional step. We notably want to identify the diffusion sources of order $\mathrm{O}(\Delta x/\mathrm{M})$.

Here is the truncation error analysis performed on the convective subsystem $\mathcal{C}$:

Proposition 2.4.1 (Truncation error analysis of the convective subsystem)
Consider the convective numerical scheme defined by equations (2.34), (2.40) *and* (2.41). *Under the CFL condition* (2.50), *This scheme is consistent with the non-dimensional convective subsystem:*

$$\mathcal{C}^{trunc}: \begin{cases} \mathrm{St_r}\,\partial_t \rho + \partial_x(\rho\, u) = \mathrm{O}(\mathrm{St_r}\,\Delta t) + \mathrm{O}\left((1 + \dfrac{\mathscr{E}_0}{\mathrm{M}} + \dfrac{\mathrm{M}}{\mathscr{E}_0})\Delta x\right), \\ \mathrm{St_r}\,\partial_t(\rho\, u) + \partial_x\left(\rho\, u^2 + \dfrac{\mathscr{E}_0^2(t)}{\mathrm{M}^2}\, p\right) = \mathrm{O}(\mathrm{St_r}\,\Delta t) + \mathrm{O}\left((1 + \dfrac{\mathscr{E}_0}{\mathrm{M}} + \dfrac{\mathrm{M}}{\mathscr{E}_0})\Delta x\right), \\ \mathrm{St_r}\,\partial_t(\rho\, e) + \partial_x\left((\rho\, e + \mathscr{E}_0^2(t)\, p)\, u\right) = \mathrm{O}(\mathrm{St_r}\,\Delta t) + \mathrm{O}\left((1 + \dfrac{\mathscr{E}_0}{\mathrm{M}} + \dfrac{\mathrm{M}}{\mathscr{E}_0})\Delta x\right). \end{cases} \tag{2.62}$$

The proof is given in subsection H. Let us start by mentioning that the first order time-discretization of the present approach produces a diffusion of order $\mathrm{O}(\mathrm{St_r}\,\Delta t) = \mathrm{O}(\Delta t/\mathrm{M})$ which can be important when $0 < \mathrm{M} \ll 1$. This difficulty is not treated in the present paper which focuses exclusively on simple means to reduce the numerical diffusion induced by the spatial discretization of Godunov-like schemes. In order to better understand the above orders of magnitude, consider the diffusive part of the convective flux written in (2.41). Then one can rewrite the difference of states as:

$$\mathbf{U}^*_{i+1/2} - \mathbf{U}_i = \begin{bmatrix} \rho^*_{i,\mathcal{C}} - \rho_i \\ (\rho^*_{i,\mathcal{C}} - \rho_i)\,(u^*_{\rm C})_{i+1/2} \\ (\rho^*_{i,\mathcal{C}} - \rho_i)\, e^*_{i,\mathcal{C}} \end{bmatrix} + \begin{bmatrix} 0 \\ \rho_i\,((u^*_{\rm C})_{i+1/2} - u_i) \\ \rho_i\,(e^*_{i,\mathcal{C}} - e_i) \end{bmatrix}, \tag{2.63}$$

$$\mathbf{U}^{**}_{i+1/2} - \mathbf{U}_{i+1} = \begin{bmatrix} \rho^*_{i+1,\mathcal{C}} - \rho_{i+1} \\ (\rho^*_{i+1,\mathcal{C}} - \rho_{i+1})\,(u^*_{\rm C})_{i+1/2} \\ (\rho^*_{i+1,\mathcal{C}} - \rho_{i+1})\, e^*_{i+1,\mathcal{C}} \end{bmatrix} + \begin{bmatrix} 0 \\ \rho_{i+1}\,((u^*_{\rm C})_{i+1/2} - u_{i+1}) \\ \rho_{i+1}\,(e^*_{i+1,\mathcal{C}} - e_{i+1}) \end{bmatrix}, \tag{2.64}$$

where the expressions of $(\rho^*_{i,\mathcal{C}}, e^*_{i,\mathcal{C}})$ respectively $(\rho^*_{i+1,\mathcal{C}}, e^*_{i+1,\mathcal{C}})$ are provided in (2.39) with $\mathrm{L} = i$, $\mathrm{R} = i+1$. The diffusion of order $\mathrm{O}\left(\frac{\mathrm{M}}{\mathscr{E}_0}\Delta x\right)$ has been produced by the density differences $\rho^*_{i,\mathcal{C}} - \rho_i$ and $\rho^*_{i+1,\mathcal{C}} - \rho_{i+1}$. It stems from the volume contraction operator $\rho\,\partial_x u$ which, contrary to [10], is present in our convective subsystem to provide a conservative mass flux when associated with the transport operator $u\,\partial_x \rho$. The diffusion of order $\mathrm{O}\left(\frac{\mathscr{E}_0}{\mathrm{M}}\Delta x\right)$ has been produced by the acoustic

part of the non-dimensional relaxation eigenvalues $u_i - \frac{\mathscr{E}_0}{\mathrm{M}}(a_{\mathcal{C}})_{i+1/2}\tau_i$ and $u_{i+1} + \frac{\mathscr{E}_0}{\mathrm{M}}(a_{\mathcal{C}})_{i+1/2}\tau_{i+1}$; as well as the non-centered part of the intermediate velocity $(u^*_{\mathcal{C}})_{i+1/2} = \frac{u_{i+1}+u_i}{2} - (\mathscr{E}_0/\mathrm{M})\frac{(p_{i+1}-p_i)}{2(a_{\mathcal{C}})_{i+1/2}}$. In both cases, the splitting parameter acts as a compensator of the strong diffusive effect of order $\mathrm{O}(1/\mathrm{M})$.

Therefore the numerical diffusion produced by the convective subsystem $\mathcal{C}$ is of order $\mathrm{O}(\Delta x)$ in every Mach regime. If the convective part of the present weighted splitting approach structurally avoids the numerical diffusion when $0 < \mathrm{M} \ll 1$, the acoustic one continues to suffer from it. Indeed:

Proposition 2.4.2 (Truncation error analysis of the acoustic subsystem)
Consider the acoustic numerical scheme defined by equations (2.34) and (2.46). Under the CFL condition (2.50), This scheme is consistent with the non-dimensional acoustic subsystem:

$$\mathcal{A}^{trunc}: \begin{cases} \mathrm{St_r}\,\partial_t \rho = \mathrm{O}(\mathrm{St_r}\,\Delta t), \\ \mathrm{St_r}\,\partial_t(\rho u) + \partial_x\left(\dfrac{(1-\mathscr{E}_0^2(t))}{\mathrm{M}^2}\,p\right) = \mathrm{O}(\mathrm{St_r}\,\Delta t) + \mathrm{O}\left(\dfrac{(1-\mathscr{E}_0^2)}{\mathrm{M}}\,\Delta x\right), \\ \mathrm{St_r}\,\partial_t(\rho e) + \partial_x\left((1-\mathscr{E}_0^2(t))\,p\,u\right) = \mathrm{O}(\mathrm{St_r}\,\Delta t) + \mathrm{O}\left((1-\mathscr{E}_0^2)(\mathrm{M}+\dfrac{1}{\mathrm{M}})\Delta x\right). \end{cases} \tag{2.65}$$

Here, the term of order $\mathrm{O}\left(\frac{(1-\mathscr{E}_0^2)}{\mathrm{M}}\Delta x\right)$ in the momentum equation truncation error is directly produced by the dissipative part of the intermediate acoustic pressure:

$$\frac{(\Pi^*_{\mathcal{A}})_{i+1/2}}{\mathrm{M}^2} = (1/\mathrm{M}^2)\,\frac{p_{i+1}+p_i}{2} - (1/\mathrm{M})\,\frac{(a_{\mathcal{A}})_{i+1/2}}{2}\,(u_{i+1}-u_i). \tag{2.66}$$

Besides, in the energy flux, the product between the centered part of $(\Pi^*_{\mathcal{A}})_{i+1/2}$ and the non-centered one of $(u^*_{\mathcal{A}})_{i+1/2} = \frac{u_{i+1}+u_i}{2} - (1/\mathrm{M})\frac{1}{2(a_{\mathcal{A}})_{i+1/2}}\left(p_{i+1}-p_i\right)$ provides the contribution $-(1/\mathrm{M})\frac{1}{4(a_{\mathcal{A}})_{i+1/2}}\left(p^2_{i+1}-p^2_i\right)$ also responsible for the $\mathrm{O}\left(\frac{(1-\mathscr{E}_0^2)}{\mathrm{M}}\Delta x\right)$ dissipative term. One can notice that the splitting parameter $\mathscr{E}_0$ does not allow to damp the above diffusive terms since it solely acts as a $(1-\mathscr{E}_0^2)$ factor.

What is more, the flux construction in the acoustic sub-step is fed by a modified conservative state $\mathbf{U}^{n+}$ which is solution of the discrete convective scheme (2.34), (2.40) and (2.41). Such a modified state can hold perturbations which, once injected in the non-dimensional acoustic pressure flux (2.66), can potentially bring additional numerical diffusion of order $\mathrm{O}\left(\frac{(1-\mathscr{E}_0^2)}{\mathrm{M}}\Delta x\right)$. This is studied in the following paragraph.

2.4.2 Effect of the Convective and Acoustic Operators Composition on the Truncation Error

Let us consider a smooth initial state $x_i \to \mathbf{U}(x_i)^{n+}$ solution of the non-dimensional discrete convective scheme. According to (2.62), under the CFL condition (2.50), $\mathbf{U}_i^{n+}$ is such that:

$$\begin{aligned} \mathbf{U}_i^{n+} &= \mathbf{U}_i^n + \mathbf{B}_i^n + \underline{\mathrm{O}}\left(\mathrm{M}(1+\frac{\mathscr{E}_0}{\mathrm{M}}+\frac{\mathrm{M}}{\mathscr{E}_0})\Delta x^2\right), \\ \text{with: } \mathbf{B}_i^n &= -\frac{\Delta t^n}{\mathrm{St_r}}\,\partial_x\,\mathrm{L}\left(\mathbf{F}^{\mu}_{\mathcal{C}}\right)\left(\mathbf{U}_i^n\right) = -\Delta t^n\,\mathrm{M}\,\partial_x\,\mathrm{L}\left(\mathbf{F}^{\mu}_{\mathcal{C}}\right)\left(\mathbf{U}_i^n\right), \\ \mathrm{L}\left(\mathbf{F}^{\mu}_{\mathcal{C}}\right)\left(\mathbf{U}_i^n\right) &= \left[\rho_i^n u_i^n,\, \rho_i^n\left(u_i^n\right)^2 + (\mathscr{E}_0^n/\mathrm{M})^2\,p_i^n,\, \left(\rho_i^n e_i^n + (\mathscr{E}_0^n)^2\,p_i^n\right)u_i^n\right]^{\mathrm{T}}, \\ \rho_i^n e_i^n &= \rho_i^n \varepsilon_i^n + \mathrm{M}^2\rho_i^n\frac{(u_i^n)^2}{2}, \\ \text{and } \Delta t^n &= \overline{\mathrm{A}}^n\,\Delta x = \frac{\sigma}{2}\,\frac{\Delta x}{\max\limits_{i+1/2}\left(\mathrm{M}\left|u_i^n\right| + c_i^n,\, \mathrm{M}\left|u_{i+1}^n\right| + c_{i+1}^n\right)},\ 0<\sigma<1. \end{aligned} \tag{2.67}$$

Neglecting the second order term $\underline{O}\left(M(1+\frac{\mathscr{E}_0}{M}+\frac{M}{\mathscr{E}_0})\Delta x^2\right)$, we want to study the influence of the perturbation $\mathbf{B}_i^n$ in terms of additional numerical diffusion when injected inside the non-dimensional pressure flux of the acoustic momentum equation (2.66). According to (2.67), $\mathbf{B}_i^n$ is of order $\underline{O}(M\Delta x)$ since, according to formula (2.49), $\mathscr{E}_0$ is proportional to the Mach number. Thus, it is only its contribution to the centered part of $(\Pi_{\mathcal{A}}^*)_{i+1/2}/M^2$ that can potentially create an additional numerical diffusion scaling as a $\underline{O}(\Delta x/M)$ term. Let us first rewrite $p\left(\mathbf{U}_i^{n+}\right)$ as:

$$\begin{aligned}
&p\left(\mathbf{U}_i^n\right) - \overline{A}^n M\Delta x\left[\nabla_{\mathbf{U}} p\left(\mathbf{U}_i^n\right)\cdot\partial_x \mathrm{L}\left(\mathbf{F}_{\mathcal{C}}^{\mu}\right)\left(\mathbf{U}_i^n\right)\right] + O\left((M\Delta x)^2\right),\\
&\text{with: } p\left(\mathbf{U}_i^n\right) = p(\rho_i^n, \underbrace{\rho_i^n e_i^n - M^2\frac{(\rho_i^n u_i^n)^2}{2\rho_i^n}}_{\rho_i^n\varepsilon_i^n}),\\
&\text{and } \nabla_{\mathbf{U}} p\left(\mathbf{U}_i^n\right) = \begin{bmatrix} \partial_\rho p_{|\rho\varepsilon}(\rho_i^n,\rho_i^n\varepsilon_i^n) + M^2\frac{(u_i^n)^2}{2}\partial_{\rho\varepsilon} p_{|\rho}(\rho_i^n,\rho_i^n\varepsilon_i^n)\\ -M^2\frac{u_i^n}{2}\partial_{\rho\varepsilon} p_{|\rho}(\rho_i^n,\rho_i^n\varepsilon_i^n)\\ \partial_{\rho\varepsilon} p_{|\rho}(\rho_i^n,\rho_i^n\varepsilon_i^n)\end{bmatrix}.
\end{aligned} \tag{2.68}$$

Then, the zeroth order terms w.r.t M of the product $\nabla_{\mathbf{U}} p\left(\mathbf{U}_i^n\right)\cdot\partial_x \mathrm{L}\left(\mathbf{F}_{\mathcal{C}}^{\mu}\right)\left(\mathbf{U}_i^n\right)$ are only:

$$\left[\partial_\rho p_{|\rho\varepsilon}(\rho_i^n,\rho_i^n\varepsilon_i^n)\right]\partial_x(\rho_i^n u_i^n) + \left[\partial_{\rho\varepsilon} p_{|\rho}(\rho_i^n,\rho_i^n\varepsilon_i^n)\right]\partial_x(\rho_i^n\varepsilon_i^n u_i^n). \tag{2.69}$$

In the case of a stiffened gas thermodynamics (2.16):

$$\begin{aligned}
&\partial_\rho p_{|\rho\varepsilon}(\rho_i^n,\rho_i^n\varepsilon_i^n) = 0,\\
&\left[\partial_{\rho\varepsilon} p_{|\rho}(\rho_i^n,\rho_i^n\varepsilon_i^n)\right]\partial_x(\rho_i^n\varepsilon_i^n u_i^n) = \partial_x(p_i^n u_i^n) = u_i^n\partial_x p_i^n + p_i^n\partial_x u_i^n.
\end{aligned} \tag{2.70}$$

Thus, if no supplementary hypothesis are made on the shape of p_i^n and u_i^n, the combination of both convective and acoustic sub-steps entails a spurious numerical diffusion because of the equation of state relating the pressure with the internal energy $\rho\varepsilon$. Such a difficulty can be circumvented if one assumes that at time t^n the discrete solution $\mathbf{U}_i^n$ lies into the discrete well-prepared space (see [18, 20, 38]):

$$\begin{aligned}
&u_i^n = u_0 + O(M),\\
&p_i^n = p_0 + O\left(M^2\right),\\
&\text{with: } u_0,\ p_0 \text{ constants of order one,}
\end{aligned} \tag{2.71}$$

since in that case $\partial_x(p_i^n u_i^n)$ becomes of order O(M). Recall that the present work concentrates on the point (II) described in the introduction. Hence, in the case where the stiffness of the thermodynamics allows to generate high amplitude pressure jumps even if $0 < M \ll 1$, the well-prepared conditions (2.71) do not hold. However we can still consider the above analysis as a basic way to identify the main sources of numerical diffusion, try to remove them when it is possible and observe the impact of the corrections on the numerical results. In the sequel, we restrict our truncation error analysis to stiffened gas thermodynamics and initial well-prepared conditions.

In any case, a last special treatment has to be implemented to remove the $O\left(\frac{(1-\mathscr{E}_0^2)\Delta x}{M}\right)$ diffusive terms brought by the acoustic non-centered part in the momentum flux.

2.4.3 Correction of the Acoustic Splitting Step

In [18, 25], facing at similar difficulties regarding the amplitude of the numerical diffusion brought by their acoustic sub-step, the authors apply a discrete correction to the non-centered part of the acoustic pressure. Such a correction, originally introduced in [22], has been also studied in [20, 35] as a way to control the accuracy of the computational solution towards its initial incompressible part when the Mach number is close to zero. Here, however, we only consider the correction as a tool which could potentially reduce the one-dimensional diffusion of our compressible solver and then provide a better accuracy towards the *compressible* solution of Riemann problems when the Mach number is small compared with one.

The correction consists in adding artificially a term of order O(M) in front of the non-centered part in the acoustic pressure. This new term can be built using the local velocity and sound speed. The modified acoustic flux reads:

$$\begin{aligned}
&\mathbf{H_{ac}}^n_{i+1/2} = \left(1-(\mathscr{C}_0^n)^2\right)\begin{bmatrix} 0 \\ (\Pi^*_{\mathcal{A},\theta})^n_{i+1/2} \\ (\Pi^*_{\mathcal{A},\theta}\, u^*_{\mathcal{A}})^n_{i+1/2}\end{bmatrix}, \\
&\text{with: } (\Pi^*_{\mathcal{A},\theta})^n_{i+1/2} = \frac{p^n_{i+1}+p^n_i}{2} - \frac{(a_{\mathcal{A}}\,\theta)^n_{i+1/2}}{2}\left(u^n_{i+1}-u^n_i\right), \\
&\text{and } \theta^n_{i+1/2} = \min\left(\frac{\left|(u^*_{\mathrm{A}})^n_{i+1/2}\right|}{\max\left(c^n_{i+1},\, c^n_i\right)},\, 1\right).
\end{aligned} \tag{2.72}$$

As noticed in [25], the introduction of this correction does not alter the consistency of the numerical scheme because it solely impacts the non-centered part in the momentum flux which is only responsible for the numerical diffusion. Furthermore, it is possible to build an approximate Riemann solver in the sense of Harten, Lax and Van Leer [30] with the same eigenvalues than those produced by the exact Riemann problem associated with the acoustic relaxation system $\mathcal{A}^\mu$. Details on this approximate Riemann solver are given in Figure 2.2a, and equations (2.73), (2.74). The insensitivity of the eigenvalues to the correction allows to maintain the same kind of CFL condition (2.52) for the modified acoustic scheme.

$$\mathbf{Z}^*_{f,\theta} = \begin{bmatrix} \rho_{\mathrm{L}} \\ u^*_{\mathrm{L},\theta} \\ \Pi^*_{\mathcal{A},\theta} \\ e^*_{\mathrm{L},\theta}\end{bmatrix}, \quad \mathbf{Z}^{**}_{f,\theta} = \begin{bmatrix} \rho_{\mathrm{R}} \\ u^*_{\mathrm{R},\theta} \\ \Pi^*_{\mathcal{A},\theta} \\ e^*_{\mathrm{R},\theta}\end{bmatrix}, \tag{2.73}$$

$$\text{with: } \begin{cases} u^*_{k,\theta} = u^*_{\mathcal{A}} + (-1)^{i_k}\,(1-\theta)\dfrac{(u_{\mathrm{R}}-u_{\mathrm{L}})}{2}, \\ e^*_{k,\theta} = e^*_{k,\mathcal{A}} + (-1)^{i_k}\,(1-\theta)\dfrac{(u_{\mathrm{R}}-u_{\mathrm{L}})\,u^*_{\mathcal{A}}}{2}, \\ \quad k\in\{\mathrm{L},\mathrm{R}\},\ i_{\mathrm{L}}=1,\ i_{\mathrm{R}}=2. \end{cases} \tag{2.74}$$

Thanks to this correction term, numerical diffusion of the subsystem $\mathcal{A}$ is modified, namely:

Proposition 2.4.3 (Truncation error analysis of the acoustic subsystem with correction)
Consider the acoustic numerical scheme defined by equations (2.34) with the corrected flux (2.72). Suppose that pressure follows the well-prepared initial condition written in (2.71). Then, under the CFL condition (2.50), This scheme is consistent with the non-dimensional acoustic subsystem:

$$\mathcal{A}^{trunc}: \begin{cases} \mathrm{St_r}\,\partial_t\,\rho = \mathrm{O}(\mathrm{St_r}\,\Delta t), \\ \mathrm{St_r}\,\partial_t\,(\rho\,u) + \partial_x\left(\dfrac{(1-\mathscr{C}_0^2(t))}{\mathrm{M}^2}\,p\right) = \mathrm{O}(\mathrm{St_r}\,\Delta t) + \mathrm{O}\left(\dfrac{(1-\mathscr{C}_0^2)\theta}{\mathrm{M}}\Delta x\right), \\ \mathrm{St_r}\,\partial_t\,(\rho\,e) + \partial_x\left((1-\mathscr{C}_0^2(t))\,p\,u\right) = \mathrm{O}(\mathrm{St_r}\,\Delta t) + \mathrm{O}\left((1-\mathscr{C}_0^2)(1+\theta)\mathrm{M}\Delta x\right). \end{cases} \tag{2.75}$$

Assume that there exists a smooth function $(x,t)\to\theta(x,t)$ such that $\forall(i,n)$, $\theta(x_{i+1/2},t^n) = \theta^n_{i+1/2}$. Then the numerical diffusion contained in the term of order $\mathrm{O}\left(\frac{(1-\mathscr{C}_0^2)\theta}{\mathrm{M}}\Delta x\right)$ is actually of order $\mathrm{O}\left((1-\mathscr{C}_0^2)\Delta x\right)$. Moreover, the global truncation error analysis writes:

Proposition 2.4.4 (Truncation error analysis of the overall scheme with correction)
Assume a fluid endowed with a stiffened gas thermodynamics (2.16). Consider the global relaxation scheme defined by equations (2.48) endowed with the corrected acoustic flux (2.72). Suppose that initial state $\mathbf{U}^n_i$ follows the well-prepared initial conditions written in (2.71). Then, under the CFL

condition (2.50)*, this scheme is consistent with the non-dimensional system:*

$$\mathcal{E}^{trunc}:\begin{cases} \mathrm{St_r}\,\partial_t \rho + \partial_x(\rho u) = \mathrm{O}(\mathrm{St_r}\,\Delta t) + \mathrm{O}\left((1+\dfrac{\mathscr{E}_0}{\mathrm{M}}+\dfrac{\mathrm{M}}{\mathscr{E}_0})\Delta x\right), \\ \mathrm{St_r}\,\partial_t(\rho u) + \partial_x\left(\rho u^2 + \dfrac{p}{\mathrm{M}^2}\right) = \mathrm{O}(\mathrm{St_r}\,\Delta t) + \mathrm{O}\left((1+\dfrac{\mathscr{E}_0}{\mathrm{M}}+\dfrac{\mathrm{M}}{\mathscr{E}_0})\Delta x\right) \\ \qquad\qquad + \mathrm{O}\left((1-\mathscr{E}_0^2)(1+\dfrac{\theta}{\mathrm{M}})\Delta x\right), \\ \mathrm{St_r}\,\partial_t(\rho e) + \partial_x\left((\rho e + p)u\right) = \mathrm{O}(\mathrm{St_r}\,\Delta t) + \mathrm{O}\left((1+\dfrac{\mathscr{E}_0}{\mathrm{M}}+\dfrac{\mathrm{M}}{\mathscr{E}_0})\Delta x\right) \\ \qquad\qquad + \mathrm{O}\left((1-\mathscr{E}_0^2)(1+\theta)\mathrm{M}\Delta x\right). \end{cases} \tag{2.76}$$

The proofs of the above propositions are written in subsection H. Since the local correction $\theta^n_{i+1/2}$ as well as the splitting parameter $\mathscr{E}_0^n$ are by construction of order M, the numerical diffusion for the overall fractional step becomes of order $\underline{\mathrm{O}}(\Delta x)$ even when the Mach number is small compared with one. In the sequel, the anti-diffusion introduced by the coefficient θ is refered as to "θ-correction".

In the next section, one-dimensional numerical results of the present weighted splitting approach are presented. They are only made of 1D compressible test cases including ideal and stiffened gas thermodynamics. The main objective here is to assess the accuracy w.r.t the compressible analytical solution of the present approach as well as its efficiency for a wide panel of Mach numbers. In order to do so, we systematically compare the present work with the Lagrange-Projection method described in [10, 25].

2.5 Numerical Results

2.5.1 Ideal Gas Thermodynamics

Let us first consider a one-dimensional configurable shock-tube test-case. The fluid has been firstly endowed with an ideal gas thermodynamics (2.15a) with the heat capacity ratio $\gamma = 7/5$. The simulation has been conducted on a domain of length 1 m, the initial discontinuity of the Riemann problem being located at $x = 0.5\,m$. The initial inputs of the Riemann problem are summed up on Table 2.1. Recall that the analytical solution is made of a left-going 1-rarefaction wave, a 2-contact

	Left state	Right state
$\rho\ (kg.m^{-3})$	$\rho_{0,\mathrm{L}} = 1.$	$\rho_{0,\mathrm{R}} = 0.125$
$u\ (m.s^{-1})$	$u_{0,\mathrm{L}} = 0.$	$u_{0,\mathrm{R}} = 0.$
$p\ (bar)$	$p_{0,\mathrm{L}} = p_{0,\mathrm{R}}\,(1+\Delta)$	$p_{0,\mathrm{R}} = 0.1$

Table 2.1 – Ideal gas shock tube initial conditions

discontinuity propagating to the right and a right-going 3-shock wave. The maximal Mach number is reached at the tail of the 1-rarefaction wave and can be controlled by increasing or diminishing the parameter Δ. When $\Delta = 9$, the classical Sod shock-tube described in [41] is retrieved, and the maximal Mach number M_{max} is about 0.92. We will refer to it as a Mach one case. When $\Delta = 2\times10^{-1}$, $\mathrm{M}_{max} \approx 9.5\times10^{-2}$. This will be considered as an intermediate regime. Finally, when $\Delta = 8\times10^{-3}$, $\mathrm{M}_{max} \approx 4.2\times10^{-3}$ and we call it low-Mach case. Let us mention that in the above three test cases, the Mach number across the left-going 3-rarefaction wave evolves from 0 to M_{max}. Then, low Mach number regions are present in every test case. However, the definition of the splitting parameter $\mathscr{E}_0(t)$, based on $\mathrm{M}_{max}(t)$, will provide a completely different behavior according to Δ. Indeed, in the first case, after several time-steps, $\mathscr{E}_0(t) \approx 1$ and the contribution of the acoustic subsystem $\mathcal{A}$ is almost negligible. This test case allows to assess the quality of the present approach in the classical configuration where large pressure variations are related to a sudden rise of the Mach number. In the third case $0 < \mathscr{E}_0(t) \ll 1$ and the Euler system is fully split. Besides, one can

notice that, in this case, the amplitude of the 1-rarefaction and the 3-shock waves is small due to the ideal gas thermodynamics. Indeed, initial conditions are such that:

$$\frac{\left|p_{0,\mathrm{R}} - p_{0,\mathrm{L}}\right|}{p_{0,\mathrm{R}}} = \mathrm{O}(\mathrm{M}_{max}). \tag{2.77}$$

For every test case, the computation ends when the right-going 3-shock wave reaches the position $x = 0.75\,m$. The corresponding final times are $\mathrm{T_{end}} = 4.51 \times 10^{-4}\,s$ for $\mathrm{M}_{max} = 0.92$, $\mathrm{T_{end}} = 7.31 \times 10^{-4}\,s$ for $\mathrm{M}_{max} = 9.5 \times 10^{-2}$ and $\mathrm{T_{end}} = 7.43 \times 10^{-4}\,s$ for $\mathrm{M}_{max} = 4.2 \times 10^{-3}$. Besides, transmissive boundary conditions have been considered. Finally, the CFL condition of our time-explicit scheme is the one written in (2.52) with $\sigma = 0.9$. In the sequel, M_{max} is rewritten M for the sake of simplicity.

As previously announced, three criteria have been involved in order to measure the quality of the present approach: mesh convergence in L^1 norm, profiles of the different computed solutions and efficiency.

Convergence Curves

Convergence curves have been built using a wide range of cells number:

$\mathrm{N}_{cells} \in \{10^2, 10^3, 10^4, 3\times10^4, 5\times10^4, 7\times10^4, 9\times10^4\}$. Convergence rates have been calculated using the error of the cases: $\mathrm{N}_{cells} = 7\times10^4$ and $\mathrm{N}_{cells} = 9\times10^4$. For each variable of interest, three convergence curves are plotted according to the three different maximal Mach numbers defined above. Besides, five different schemes have been tested: "no-Sp" corresponds to the case where $\mathscr{E}_0^n = 1$ is imposed along the simulation. Thus, the weighted splitting is not triggered. "Sp-($\sqrt{\mathrm{M}}$)" is the weighted splitting approach with $\mathscr{E}_0^n = \max\left(\sqrt{\mathscr{E}_{inf}}, \min\left(\sqrt{\mathrm{M}_{max}^n}, 1\right)\right)$ while "Sp-(M)" involves $\mathscr{E}_0^n$ defined in formula (2.49). Although the asymptotic behavior w.r.t the Mach number is the same for both above definitions of $\mathscr{E}_0^n$, the convective flux of the second should provide a lower numerical diffusion in smooth areas according to Proposition 2.4.1 and Proposition 2.4.4. Eventually, "LP" is the Lagrange-Projection splitting method, fully described in [10] and taken as a benchmark. The mention "-corr" means that the correction defined in (2.72) is triggered. Figure 2.3 corresponds to the velocity convergence curve while Figure 2.4 is associated with the pressure variable. Density convergence curve has intentionally not been plotted because results were extremely close.

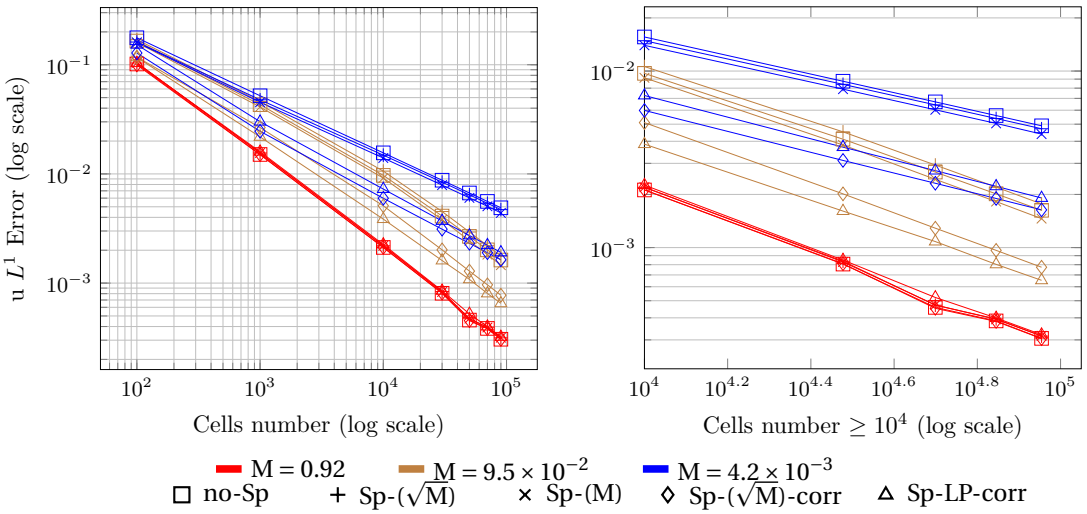

Figure 2.3 – Velocity Convergence Curves

Every numerical scheme converges towards the analytical compressible solution as the mesh is refined. In the Mach one regime, convergence curves overlap quasi perfectly. It is coherent with the fact that, in such a regime, subsystem $\mathcal{C}$ is almost similar to the full Euler system. By construction, the numerical contribution of the acoustic subsystem $\mathcal{A}$ is negligible. Still, the proximity

between the Lagrange-Projection scheme with correction and the weighted splitting schemes is less straightforward.

Furthermore, as M_{max} decreases one can observe that the schemes with the θ-correction Sp-($\sqrt{M}$)-corr and Sp-LP-corr are clearly more accurate than the other ones. For example in Figure 2.3, for $M = 9.5 \times 10^{-2}$, Sp-($\sqrt{M}$)-corr reaches the precision level of 2×10^{-3} with a 3×10^3 cells mesh whereas it requires more than 7×10^3 for No-Sp. This is in agreement with the acoustic truncation error result of Proposition 2.4.3 derived for a smooth and initially well-prepared solution. In 1D, the θ-correction has an anti-diffusion effect which improves the global accuracy of the proposed approach in smooth regions of the computational solution. Although this was already observed in [20] for a Godunov scheme (without splitting), it is satisfying to notice that the present splitting does not alter this anti-diffusion effect. Moreover, as it can be seen in Figure 2.4, for $M = 4.2 \times 10^{-3}$, switching the weighting parameter $\mathscr{E}_0^n$ from $\sqrt{M_{max}^n}$ to M_{max}^n has only a very slight positive effect on the scheme accuracy. This is due to the fact that, in case of low-Mach number compressible flow, most of the numerical diffusion is generated by the acoustic part of the weighted splitting approach. To complete this comparison, one could have wished to see the case Sp-(M)-corr which, according to Proposition 2.4.4, is supposed to reduce the convective and acoustic numerical diffusion for a smooth solution initially in the well-prepared space. Unfortunately this case suffers from strong non-physical oscillations located in the left rarefaction wave area. Plots of these oscillations for different cells numbers can be seen on subsection G.

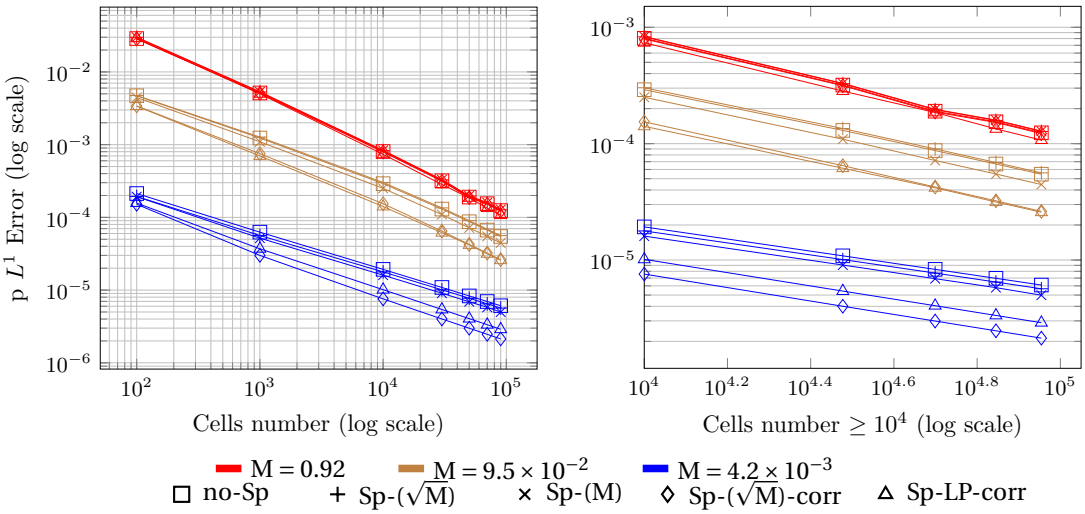

Figure 2.4 – Pressure Convergence Curves

They have already been observed for low-Mach corrected numerical schemes written in Eulerian coordinates (see [25], chapter 3, section 3.G). However, these spurious perturbations are damped in the sense of the L^∞ and L^1 norms as the mesh is refined. So far finding the optimal choice for the couple $(\mathscr{E}_0, \theta)$ in order to prevent the acoustic momentum flux from being completely centered and thus triggering such oscillations is still an open issue.

Let us do a last remark about the convergence rates of the different curves as the Mach number tends towards zero. In [23], the authors show that, for Riemann problems whose maximal Mach number M_{max} is close to 1, the rate of convergence of variables varying through genuinely non-linear waves is around 1. However, for variables jumping through a contact wave, typically the density ρ, the rate is around 0.5. This numerical observation holds independently of the approximate Riemann solver at stake and is also mentioned in [20]. Thus, since u and p do not jump through the right-going 2-contact discontinuity of the above shock tubes, the expected rate of convergence should be 1.

Table 2.2 presents these orders of convergence for pressure. One can see that for *every* schemes, the order of convergence is depreciated as the maximal Mach number decreases. Indeed for pressure, it passes from 0.87 at M = 0.92 (the expected order already obtained in [23]) to 0.82 at $M = 9.5 \times 10^{-2}$ and 0.56 in the low-Mach number case. Seeking to confirm this behavior, the same

	$M = 0.92$	$M = 9.5 \times 10^{-2}$	$M = 4.2 \times 10^{-3}$
No-Sp	0.870	0.803	0.530
Sp-($\sqrt{M}$)	0.868	0.814	0.531
Sp-M	0.860	0.829	0.597
Sp-($\sqrt{M}$)-corr	0.868	0.833	0.580
Sp-LP-corr	0.882	0.806	0.572
HLLC	0.879	0.802	0.528

Table 2.2 – Pressure Convergence Rate (L^1 norm)

test case has been computed using an HLLC-type scheme [43]; once again, at $M = 4.2 \times 10^{-3}$ the convergence rate is 0.528. This unusual behavior can be summed up as: the lowest the maximal Mach number is, the slowest Godunov-like schemes are to reach the analytical compressible solution as the mesh is refined. The same convergence rate order can be found in [21] (page 20, Table 6.2) for a 1D double rarefaction wave problem performed on the Euler barotropic system with $M \approx 3.1 \times 10^{-2}$. The implicit-explicit AP scheme used to obtain this order is based on a Rusanov spatial discretization. Further investigations have to be undertaken in order to understand this numerical phenomenon.

Beyond convergence curves and rates, one must also have a look on the solution profile obtained with the different numerical schemes at a fixed mesh size. This is done in the next subsection.

Solution Profiles

Figure 2.5 and Figure 2.6 show the velocity and pressure final profiles calculated with the different numerical solutions in the low-Mach regime. We only plot the left-going 1-rarefaction and the right-going 3-shock waves through which u and p change. Mesh is made of $N_{cells} = 10^3$ cells. Let us point out that the stiffness of the rarefaction wave exact profile is only due to the fact that the width of the fan at a given instant t writes: $\left|(u_{0,L} - c_{0,L}) - (u^* - c_L^*)\right| t = \left|c_L^* - c_{0,L} - u^*\right| t$; with u^* the intermediate analytical velocity and c_L^* the intermediate sound speed located at the left of the 2-contact discontinuity. Since the maximal Mach number is very low compared to one $|u^*| \ll \min(c_{0,L}, c_L^*)$, and since $c_{0,L} \approx c_L^*$, the width of the fan is approximately equal to $|u^*|\, t$. Thus, it is very small when acoustic time-scales such as $0 < t < 10^{-3}\, s$ are considered.

One can notice that No-Sp is always the most diffusive scheme. Besides, the positive effect of the $\mathscr{E}_0^n = \max(\mathscr{E}_{inf}, \min(M_{max}^n, 1))$ choice compared to $\mathscr{E}_0^n = \max\left(\mathscr{E}_{inf}, \min\left(\sqrt{M_{max}^n}, 1\right)\right)$ is exclusively located in the left rarefaction wave fan where the solution is continuous. In addition, No-Sp, Sp-($\sqrt{M}$) and Sp-(M) profiles overlap in the shock front region.

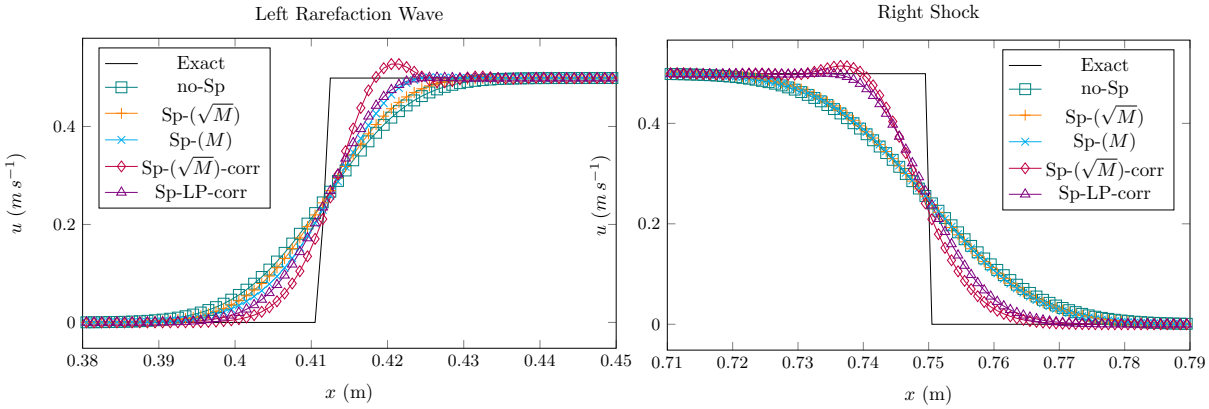

Figure 2.5 – Velocity profile at $M = 4.2 \times 10^{-3}$, with $N_{cells} = 10^3$

Eventually, the correction globally improves the computed solution accuracy. The Sp-($\sqrt{M}$)-

corr case produces profiles closer to the analytical solution than Sp-LP-corr at the cost of little overshoots in the tail of the left rarefaction wave and before the shock front.

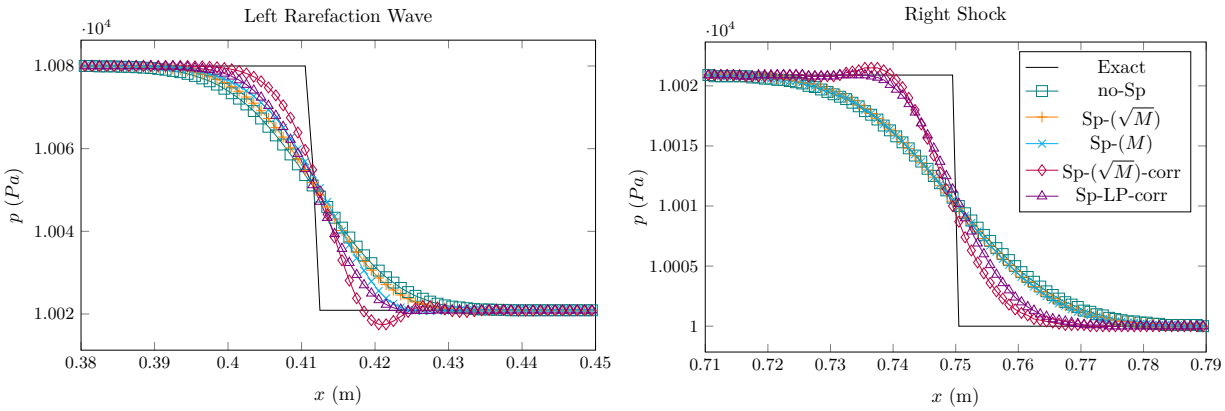

Figure 2.6 – Pressure profile at M = 4.2×10^{-3}, with $N_{cells} = 10^3$

Efficiency Curve

Computational cost at fixed accuracy level is now investigated. Figure 2.7 and Figure 2.8 describe the pressure efficiency curves of the different numerical schemes for the three Mach regimes. In the Mach one regime, every scheme seems to behave equivalently, the proposed weighted splitting approach requiring slightly more CPU time than No-Sp or Sp-LP-corr. When M = 9.5×10^{-2}, the weighted splitting approach is still slower than No-Sp, however the θ-corrected schemes are clearly less time consuming, at fixed error than the other ones. Indeed Sp-($\sqrt{M}$)-corr and Sp-LP-corr reach the precision of 7×10^{-5} in about one hour and a half whereas it requires six hours for No-Sp and more than seven hours for Sp-($\sqrt{M}$). Eventually, in the low-Mach case, Sp-($\sqrt{M}$)-corr seems to produce better results than Sp-LP-corr. For a fixed precision of 4×10^{-6} the weighted splitting method needs about one hour and forty minutes whereas the Lagrange-Projection method requires a little less than three hours.

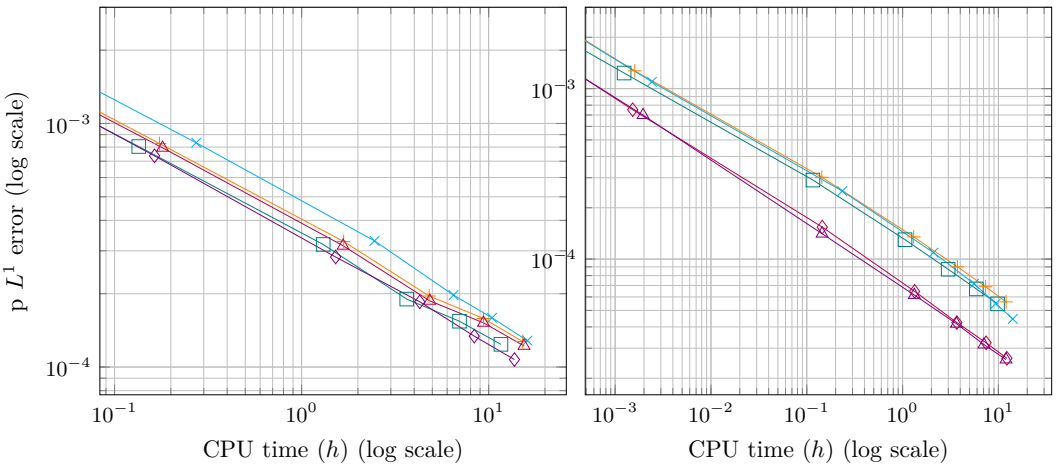

Figure 2.7 – Pressure Efficiency Curves: M = 0.92 (left), M = 9.5×10^{-2} (right)

2.5.2 Stiffened Gas Thermodynamics

In the above subsection, some elements seem to suggest that the weighted splitting approach produces satisfying results for a wide range of Mach number. The present method is notably

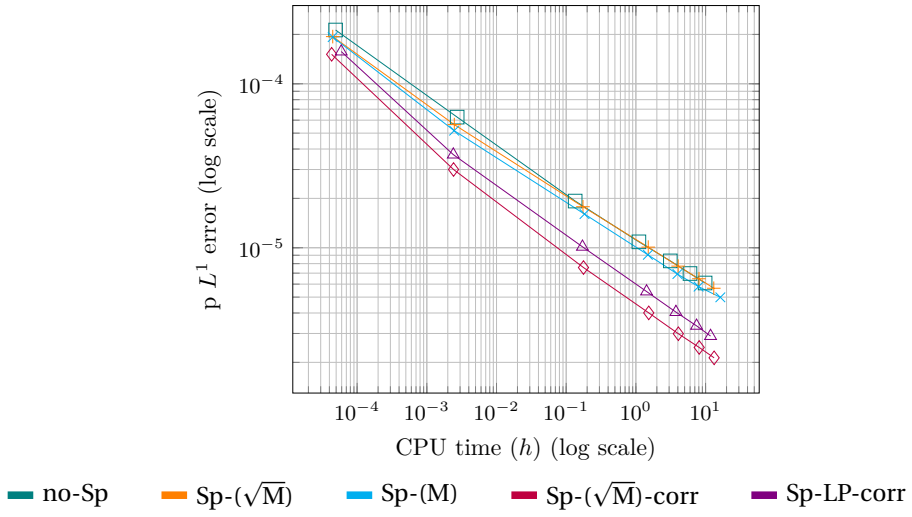

Figure 2.8 – Pressure Efficiency Curves: $\mathrm{M} = 4.2 \times 10^{-3}$

able to capture strong shock waves associated with a sudden rise of the maximal Mach number. Nevertheless, as mentioned in point (II) in the introduction, we are interested in configurations where strong shock waves appear even if $0 < \mathrm{M} \ll 1$. In subsection A, the analytical solution of a symmetric double shock Riemann problem involving the Euler compressible system endowed with a stiffened gas thermodynamics (2.16) is derived. Starting with initial states of density $\rho_0 = 10^3\, kg.m^{-3}$, velocity $|u_0| = 1\, m.s^{-1}$ and pressure $p_0 = 3 \times 10^5\, \mathrm{P}a$, one can analytically show that the non-dimensional pressure jump reads:

$$\begin{aligned} &\frac{|p^* - p_0|}{p_0} = \mathrm{M}_0\,(1+\alpha) \times \mathrm{O}(1) \text{ w.r.t } \mathrm{M}_0, \\ &\text{with: } \mathrm{M}_0 = \frac{|u_0|}{c_0},\ \alpha = \frac{\mathrm{P}_\infty}{p_0}, \\ &\text{and } p^* \text{ the intermediate pressure behind the shock fronts.} \end{aligned} \tag{2.78}$$

Then, one can notice that the stiffness of the non-dimensional thermodynamical coefficient α can compensate the amplitude reduction effect of M_0. By choosing $\gamma = 7.5$ and $\mathrm{P}_\infty = 3 \times 10^8\, \mathrm{P}a$, one can obtain $c_0 \approx 1.5 \times 10^3\, m.s^{-1}$ which is representative of liquid water at $\mathrm{T}_0 = 295\,\mathrm{K}$. A numerical application leads to:

$$\begin{aligned} &\mathrm{M}_0 \approx 7 \times 10^{-4}, \\ &\alpha = 10^3, \\ &\frac{|p^* - p_0|}{p_0} \approx 5.2. \end{aligned} \tag{2.79}$$

Hence, 15-bar amplitude shock waves are created while the Mach number is of order 10^{-3}.

In the following, a shock tube Riemann problem using the above stiffened gas thermodynamics is tested. The initial conditions have been defined in Table 2.3, and we still have $\gamma = 7.5$, $\mathrm{P}_\infty = 3 \times 10^8\, \mathrm{P}a$. In this case, the maximal Mach number is about $\mathrm{M}_{max} \approx 4.6 \times 10^{-5}$. Thus, we are still in a very low-Mach regime. The final time of the simulation is $\mathrm{T}_{\mathrm{end}} = 1.58 \times 10^{-4}\, s$.

	Left state	Right state
$\rho\ (kg.m^{-3})$	$\rho_{0,\mathrm{L}} = 10^3$	$\rho_{0,\mathrm{R}} = 9 \times 10^2$
$u\ (m.s^{-1})$	$u_{0,\mathrm{L}} = 0.$	$u_{0,\mathrm{R}} = 0.$
$p\ (bar)$	$p_{0,\mathrm{L}} = 3$	$p_{0,\mathrm{R}} = 1$

Table 2.3 – Stiffened gas shock tube initial conditions

Acoustic Relaxation Coefficient Calibration

Let us go back to Remark 2.3.4. Testing a stiffened gas thermodynamics allows to compare the acoustic subcharacteristic condition (2.28b) derived from the weighted splitting approach and (2.30) obtained directly from the relaxation of the full Euler system and found in [25]. Let us recall that the inferior bound of (2.28b) uses an artificial acoustic sound speed $c_{\mathcal{A}}$ whereas (2.30) is based on the physical sound speed c. In the previous ideal gas thermodynamics case $c_{\mathcal{A}} = \sqrt{(\gamma-1)p/\rho} = \sqrt{(\gamma-1)/\gamma}\,c$ and $\sqrt{(\gamma-1)/\gamma} \approx 0.53$ such that this non-physical acoustic celerity was of the same order that the real sound speed. However, with a stiffened gas thermodynamics, $c_{\mathcal{A}}$ does not change while c becomes $\sqrt{\gamma(p+P_\infty)/\rho} \approx \sqrt{\gamma P_\infty/\rho}$. Thus $c_{\mathcal{A}}/c \approx \sqrt{(\gamma-1)/\gamma}\sqrt{p/P_\infty} \ll 1$. One could wonder if considering the subcharacteristic condition (2.28b) based on a non-physical celerity rather than the one based on the real sound speed (2.30) has an effect on the overall scheme accuracy? So far, numerical arguments seem to go in favor of an acoustic relaxation coefficient based on the real sound speed. Indeed, Figure 2.9 shows two weighted splitting simulations of type Sp-($\sqrt{M}$). The first one, noted Sp-($\sqrt{M}$)-$a_{\mathcal{A}}$, takes the subcharacteristic condition (2.28b) into account whereas the second one, Sp-($\sqrt{M}$)-a_E, involves (2.30). The mesh was composed of 10^3 cells.

It turns out that Sp-($\sqrt{M}$)-$a_{\mathcal{A}}$ produces non-physical oscillations inside the rarefaction fan and before the shock front. Things are even worse when Sp-(M)-$a_{\mathcal{A}}$ and Sp-(M)-a_E are compared. Indeed, even if the non-physical subcharacteristic condition (2.28b) is fulfilled, the amplitude of the spurious oscillations is such that pressure becomes negative after several timesteps. Simulation crashes because $c_{\mathcal{A}}$ becomes a complex number. On the contrary, Sp-(M)-a_E does not suffer from any oscillations or stability issues. Recall that the relaxation coefficient $a_{\mathcal{A}}$ multiplies the non-centered part of the acoustic momentum flux responsible for most of the numerical diffusion of the scheme. Hence, by considering subcharacteristic condition (2.30) rather than (2.28b) this coefficient has been considerably increased as well as the numerical diffusion coefficient. Non-physical oscillations are then removed.

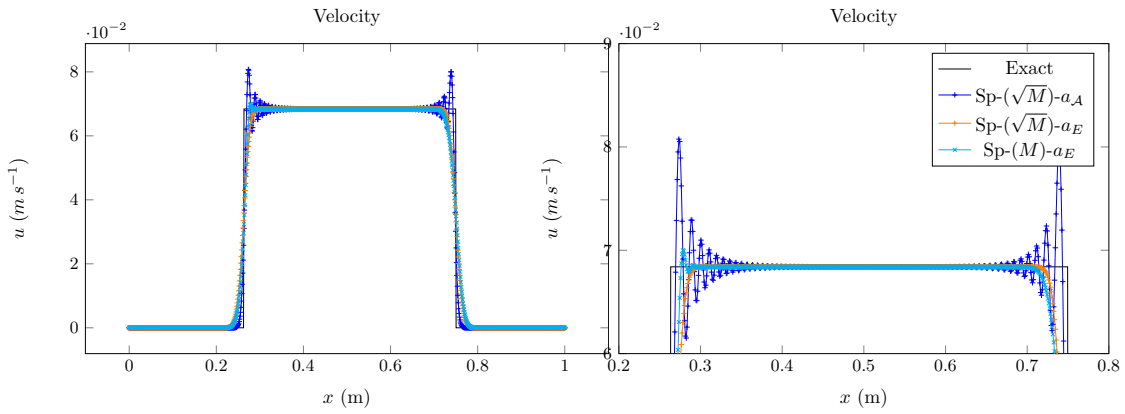

Figure 2.9 – Effect of the Estimation of the Relaxation Coefficient

In the sequel, the acoustic relaxation coefficient $a_{\mathcal{A}}$ has been calculated using the physical sound speed: $a_{\mathcal{A}} > \rho c$. The global CFL condition (2.52) is modified in consequence.

Convergence Curves and Computed Solutions Profiles

Similarly to the ideal gas thermodynamics configuration, pressure convergence curve plotted in Figure 2.10 shows that the θ-corrected schemes are the most accurate as the mesh is refined. However, one can notice that the Sp-($\sqrt{M}$)-corr curve remains at the same level of accuracy than the non-corrected schemes until $N_{cells} > 10^3$. This can be explained by observing the solutions profiles drawn in Figure 2.11. The correction centers the pressure flux since the Mach number is very small in every computational region. Hence, it triggers oscillations in areas where the solution is sharp. Such oscillations are present even in the case of Sp-LP-corr but their amplitude is smaller. In any case, the domain on which these oscillations are located as well as their relative height w.r.t

the analytical solution are reduced as the mesh is refined. The present method is thus L^∞ stable. For $N_{cells} \geq 3 \times 10^4$ the Sp-($\sqrt{M}$)-corr becomes as accurate as the Sp-LP-corr one.

Once again let us point out an amazing numerical result already observed in the above ideal gas thermodynamics shock tube with $M = 4.2 \times 10^{-3}$. For every scheme (expect Sp-($\sqrt{M}$)-corr but additional points should be added to catch the asymptotic trend of its convergence curve), the observed pressure convergence rate written in Table 2.4 is close to 0.5, the expected order for variables jumping through contact discontinuities; which was not the expected.

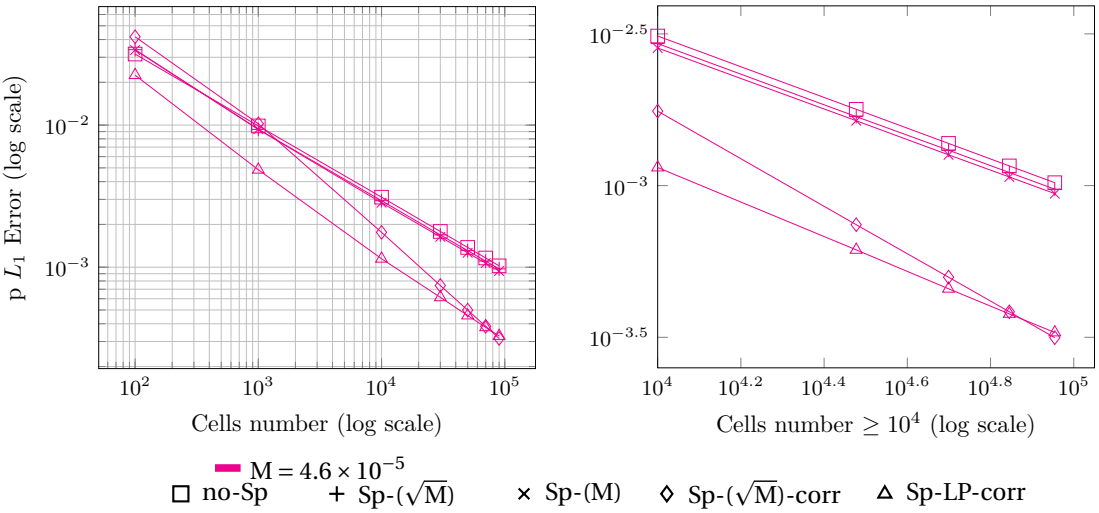

Figure 2.10 – Pressure Convergence Curve

	$M = 4.6 \times 10^{-5}$
No-Sp	0.506
Sp-($\sqrt{M}$)	0.502
Sp-M	0.503
Sp-($\sqrt{M}$)-corr	0.783
Sp-LP-corr	0.561

Table 2.4 – Pressure Convergence Rate (L^1 norm)

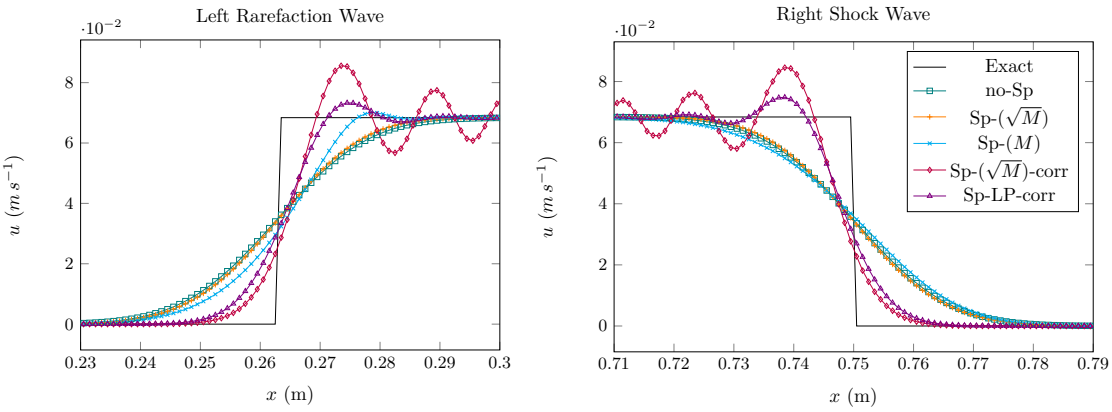

Figure 2.11 – Velocity Profile at $M = 4.6 \times 10^{-5}$ with $N_{cells} = 10^3$

2.6 Conclusions

In this work, a conservative fractional step approach based on a time-weighted splitting has been proposed for Euler-like models. The weighting parameter is proportional to the instantaneous maximal flow Mach number M. When the latter takes high values the splitting allows to directly solve the overall Euler-like system in one step with an explicit time integration. Thus, shock waves are correctly captured without any diffusion or dispersion induced by the acoustic time-implicit discretization. On the contrary, if M is close to zero, convection is completely decoupled from acoustic. In that case, the acoustic discrete flux is modified by an anti-diffusive correction. If the fluid is endowed with a stiffened gas thermodynamics and if the solution is smooth as well as initially well-prepared, it results in a uniform truncation error with respect to M.

What is more, the Suliciu-like relaxation method used to discretize both convective and acoustic subsystems provides the density and internal energy positivity, in the case of an ideal gas thermodynamics, up to the introduction of new non-restrictive lower bounds for the relaxation constants. Besides, such relaxation constants encapsulate the thermodynamic nonlinearity and offer an easy way to deal with general equations of state.

The one-dimensional results performed with an ideal and a stiffened gas thermodynamics show that the time-explicit weighted splitting approach is as accurate and efficient as the time-explicit Lagrange-Projection method [10] for a wide range of Mach numbers. It can notably capture strong shock and rarefaction waves linked to a sudden rise of the Mach number of the flow. In the specific case where high amplitude shock waves appear even if $0 < M \ll 1$, the present method, completed with the anti-diffusive correction, remains L^∞ stable but suffer from stronger oscillations than the Lagrange-Projection method.

Besides, if one is interested in following the slow material waves of low-Mach number compressible flows when no fast transient phenomenon is present, the implicit-explicit version of the present approach can be relevant. Additional developments whose results are presented in [31, 32] deal with the adaptation of a time-implicit discretization technique proposed in [10, 14] to the present acoustic subsystem.

Among many areas of improvement, one would concern the definition of the discrete weighting parameter $\mathscr{E}_0^n$: in the same manner as for the relaxation constants, it could be transformed into a local weighting factor which would be only uniform for the Riemann problem solved at the interface. By doing so, the present weighted splitting approach could react to the spatial fluctuations of the flow Mach number and could improve even further the global accuracy of the method. Eventually, a reflection about the relevance of an extension of the present weighted splitting approach to homogeneous relaxed models will be undertaken.

Acknowledgement
The first author received a financial support through the EDF-CIFRE contract 0561-2015. Computational facilities were provided by EDF.

The authors would also like to thank the reviewers who have spent time reading this paper. Indeed, the remarks and questions they have pointed out have considerably allowed the present work to be improved.

2.7 Appendices

A A Symmetric Double Shock Rieman Problem with a Stiffened Gas Equation of State

Let us consider a fluid endowed with a stiffened gas equation of state described in (2.16). Let us define the 1D Riemann problem: The analytical solution is made of a left-going 1-shock, a

	Left state	Right state
$\rho\ (kg.m^{-3})$	$\rho_{0,\mathrm{L}} = \rho_0 = 10^3$	$\rho_{0,\mathrm{R}} = \rho_0$
$u\ (m.s^{-1})$	$u_{0,\mathrm{L}} = u_0 = 1.$	$u_{0,\mathrm{R}} = -u_0$
$p\ (bar)$	$p_{0,\mathrm{L}} = p_0 = 3$	$p_{0,\mathrm{R}} = p_0$

Table 2.5 – Stiffened gas symmetric double shock initial conditions

steady 2-contact discontinuity and a right-going 3-shock. The symmetry of the problem forces the intermediate velocity u^* related to the contact discontinuity speed to be equal to zero. This considerably simplifies the Rankine-Hugoniot relations. The intermediate pressure p^* and density ρ^* can be found analytically. Since $u^* = 0$, there is only one remaining Mach number that one can control through the initial conditions: $\mathrm{M}_0 = (|u_0|/c_0)$. In the sequel, the analytical formula for the pressure jump $|p^* - p_0| = p^* - p_0$ is derived.

Let us focus on the 3-shock Rankine-Hugoniot relations. Using the mass and the momentum equations, one obtains:

$$\begin{aligned}
&-\sigma\left[\rho_0 - \rho^*\right] + \left[-\rho_0 u_0 - \rho^* \overbrace{u^*}^{=0}\right] = 0 \Rightarrow \sigma = \frac{u_0}{\left(\frac{\tau_0}{\tau^*} - 1\right)},\\
&\rho_0 u_0 \sigma + \left(\rho_0 u_0^2 + p_0 - p^*\right) = 0 \Rightarrow \rho_0 u_0^2 \left(1 + \frac{1}{\left(\frac{\tau_0}{\tau^*} - 1\right)}\right) + (p_0 - p^*) = 0,\\
&\text{with: } \tau = 1/\rho.
\end{aligned} \tag{2.80}$$

Recall that the energy equation reads: $[\varepsilon] + \overline{p}\,[\tau] = 0$; with $\overline{p} = (p^* + p_0)/2$ and $\varepsilon = \frac{(p+\gamma \mathrm{P}_\infty)\tau}{\gamma - 1}$. Let us introduce $\mathrm{P} = p + \mathrm{P}_\infty$ and $\mathrm{P}_0 = p_0 + \mathrm{P}_\infty$. As explained in subsection 2.2.2, P is the relevant variable in the case of a stiffened gas thermodynamics. It results that:

$$\begin{aligned}
&\tau^*(\mathrm{P}^*) = \tau_0 \frac{\left((\mathrm{P}_0/\beta) + \mathrm{P}^*\right)}{\left((\mathrm{P}^*/\beta) + \mathrm{P}_0\right)},\\
&\text{with: } \beta = \frac{\gamma - 1}{\gamma + 1}.
\end{aligned} \tag{2.81}$$

After calculation,

$$1 + \frac{1}{\left(\frac{\tau_0}{\tau^*} - 1\right)} = 1 + \frac{\beta}{1-\beta} \frac{\left((\mathrm{P}_0/\beta) + \mathrm{P}^*\right)}{(\mathrm{P}^* - \mathrm{P}_0)}. \tag{2.82}$$

When (2.82) is injected in (2.80) and after having multiplied by $(\mathrm{P}^* - \mathrm{P}_0)$, one obtains a second-order polynomial function equation, namely:

$$\begin{aligned}
&\mathrm{X}^2 - \frac{\gamma}{1-\beta}\mathrm{M}_0^2 \mathrm{X} - \gamma \frac{1+\beta}{1-\beta}\mathrm{M}_0^2 = 0,\\
\Leftrightarrow &\mathrm{X}^2 - \frac{\gamma(\gamma+1)}{2}\mathrm{M}_0^2 \mathrm{X} - \gamma^2 \mathrm{M}_0^2 = 0, \qquad \text{with: } \mathrm{X} = \frac{\mathrm{P}^* - \mathrm{P}_0}{\mathrm{P}_0}.
\end{aligned} \tag{2.83}$$

As $\mathrm{P}^* > \mathrm{P}_0$, we are looking for a strictly positive root , the solution writes:

$$\frac{\mathrm{P}^* - \mathrm{P}_0}{\mathrm{P}_0} = \mathrm{M}_0 \gamma \left(\frac{\gamma+1}{4}\mathrm{M}_0 + \sqrt{1 + \frac{(\gamma+1)^2}{16}\mathrm{M}_0^2}\right). \tag{2.84}$$

One can notice that if $P_\infty = 0$ then, $P^* = p^*$, $P_0 = p_0$, and equality (2.84) becomes similar to these obtained in [8] (page 845) for an isolated shock endowed with an ideal gas thermodynamics. Thus, in the case of an ideal gas thermodynamics:

$$\frac{p^* - p_0}{p_0} = M_0 \times O(1) \text{ w.r.t } M_0 \Rightarrow \lim_{M_0 \to 0} \frac{p^* - p_0}{p_0} = 0. \tag{2.85}$$

However, in the case of a stiffened gas thermodynamics, since $P_0 = p_0(1+\alpha)$ with $\alpha = (P_\infty / p_0)$:

$$\begin{aligned} \frac{p^* - p_0}{p_0} &= M_0 (1+\alpha)\gamma \left(\frac{\gamma+1}{4} M_0 + \sqrt{1 + \frac{(\gamma+1)^2}{16} M_0^2} \right), \\ &= M_0 (1+\alpha) \times O(1) \text{ w.r.t } M_0. \end{aligned} \tag{2.86}$$

Here we can clearly see that, provided that the non-dimensional thermodynamical coefficient α behaves as $M_0^{-\delta}$ with $\delta > 1$, the stiffened gas thermodynamics is "stiff enough" to compensate the damping effect of M_0 when $M_0 \to 0$. For example, if one considers $\gamma = 7.5$ and $P_\infty = 3 \times 10^8$ so that to obtain a speed of sound $c_0 \approx 1.5 \times 10^3\, m.s^{-1}$ and a temperature of $T_0 = 295\,K$, a numerical calculation gives:

$$\begin{aligned} &M_0 \approx 7 \times 10^{-4}, \\ &\alpha = 10^3, \\ &\frac{p^* - p_0}{p_0} \approx 5.26. \end{aligned} \tag{2.87}$$

Hence, on this analytical solution got from the Euler compressible system endowed with a stiffened gas thermodynamics, a pressure jump of approximately 15 bars is created whereas the flow Mach number is of order 10^{-3}.

B Subsystems Hyperbolicity

For the sake of simplicity, we prove Proposition 2.2.1 in 1D. Let us consider the set of non conservative variables $\mathbf{V} = [\rho, u, p]^T$. If the solutions of subsystems $\mathcal{C}$ and $\mathcal{A}$ are smooth, one can rewrite them equivalently as:

$$\mathcal{C}^{NC} : \begin{cases} \partial_t \rho + u \partial_x \rho + \rho \partial_x u = 0, \\ \partial_t u + u \partial_x u + \dfrac{1}{\rho} \partial_x \left(\mathscr{E}_0^2(t)\, p \right) = 0, \\ \partial_t p + u \partial_x p + \rho c_{\mathcal{C}}^2 \partial_x u = 0, \end{cases} \tag{2.88}$$

$$\mathcal{A}^{NC} : \begin{cases} \partial_t \rho = 0, \\ \partial_t u + \dfrac{1}{\rho} \partial_x \left((1 - \mathscr{E}_0^2(t))\, p \right) = \underline{0}, \\ \partial_t p + (1 - \mathscr{E}_0^2(t)) \rho c_{\mathcal{A}}^2 \partial_x u = 0. \end{cases} \tag{2.89}$$

In variables $\mathbf{V}$ the Jacobian matrices of subsystems $\mathcal{C}^{NC}$ and $\mathcal{A}^{NC}$ are:

$$\mathcal{C}^{NC} : \begin{bmatrix} u & \rho & 0 \\ 0 & u & \mathscr{E}_0^2/\rho \\ 0 & \rho c_{\mathcal{C}}^2 & u \end{bmatrix}, \tag{2.90}$$

$$\mathcal{A}^{NC} : \begin{bmatrix} 0 & 0 & 0 \\ 0 & 0 & (1 - \mathscr{E}_0^2)/\rho \\ 0 & (1 - \mathscr{E}_0^2)\rho c_{\mathcal{A}}^2 & 0 \end{bmatrix}. \tag{2.91}$$

Supposing that $c_{\mathcal{C}}^2 \geq 0$ and $c_{\mathcal{A}}^2 \geq 0$, the eigenvalues and eigenvectors can be easily obtained and read:

$$\mathcal{C}^{\mathrm{NC}} : \begin{array}{l} \lambda_1^{\mathcal{C}} = u - \mathscr{E}_0\, c_{\mathcal{C}}, \\ \lambda_2^{\mathcal{C}} = u, \\ \lambda_3^{\mathcal{C}} = u + \mathscr{E}_0\, c_{\mathcal{C}}, \end{array} \quad \mathbf{r}_1^{\mathcal{C}} = \begin{bmatrix} \rho \\ -\mathscr{E}_0\, c_{\mathcal{C}} \\ \rho\, c_{\mathcal{C}}^2 \end{bmatrix}, \ \mathbf{r}_2^{\mathcal{C}} = \begin{bmatrix} 1 \\ 0 \\ 0 \end{bmatrix}, \ \mathbf{r}_3^{\mathcal{C}} = \begin{bmatrix} \rho \\ +\mathscr{E}_0\, c_{\mathcal{C}} \\ \rho\, c_{\mathcal{C}}^2 \end{bmatrix}, \tag{2.92}$$

$$\mathcal{A}^{\mathrm{NC}} : \begin{array}{l} \lambda_1^{\mathcal{A}} = -\left(1 - \mathscr{E}_0^2\right) c_{\mathcal{A}}, \\ \lambda_2^{\mathcal{A}} = 0, \\ \lambda_3^{\mathcal{A}} = \left(1 - \mathscr{E}_0^2\right) c_{\mathcal{A}}, \end{array} \quad \mathbf{r}_1^{\mathcal{A}} = \begin{bmatrix} 0 \\ 1 \\ -\rho\, c_{\mathcal{A}} \end{bmatrix}, \ \mathbf{r}_2^{\mathcal{A}} = \begin{bmatrix} 1 \\ 0 \\ 0 \end{bmatrix}, \ \mathbf{r}_3^{\mathcal{A}} = \begin{bmatrix} 0 \\ 1 \\ \rho\, c_{\mathcal{A}} \end{bmatrix}. \tag{2.93}$$

Then, one can notice that, for the two subsystems, the 1-field and 3-field are genuinely non linear whereas the 2-field is linearly degenerate. Let us now study the sufficient conditions for which $c_{\mathcal{C}}^2 \geq 0$ and $c_{\mathcal{A}}^2 \geq 0$. Consider the ideal gas thermodynamics presented in equation (2.15). Then:

$$\begin{aligned} c_{\mathcal{C}}^2 &= \left(1 + \mathscr{E}_0^2(\gamma - 1)\right) \frac{p}{\rho} = \gamma_{\mathscr{E}_0} \frac{p}{\rho}, \\ c_{\mathcal{A}}^2 &= (\gamma - 1) \frac{p}{\rho}. \end{aligned} \tag{2.94}$$

Since $\mathscr{E}_0^2 \in [0, 1]$, $\gamma_{\mathscr{E}_0} \in \left[1, \gamma\right]$. What is more, by definition of the ideal gas phase-space (2.15), the pressure variable p is positive. Thus, in case of an ideal gas thermodynamics, $c_{\mathcal{C}}^2$ and $c_{\mathcal{A}}^2$ are naturally positive. On the contrary, when the stiffened gas thermodynamics is at stake one obtains:

$$\begin{aligned} c_{\mathcal{C}}^2 &= \frac{\gamma_{\mathscr{E}_0}\, p + \gamma \mathrm{P}_\infty}{\rho}, \\ c_{\mathcal{A}}^2 &= (\gamma - 1) \frac{p}{\rho}. \end{aligned} \tag{2.95}$$

The stiffened gas phase-space (2.16) ensures that $p > -\mathrm{P}_\infty \Rightarrow \gamma_{\mathscr{E}_0}\, p + \gamma\, \mathrm{P}_\infty > (\gamma - \gamma_{\mathscr{E}_0})\, \mathrm{P}_\infty$. And $\gamma - \gamma_{\mathscr{E}_0}$ is positive. Once again, $c_{\mathcal{C}}^2$ is positive without any condition. However $c_{\mathcal{A}}^2 \geq 0 \Leftrightarrow p \geq 0$ which is not guaranteed in the stiffened gas phase space since $p + \mathrm{P}_\infty > 0$.

C Phase Space Invariance of the Continuous Subsystems

Consider Ω a bounded spatial domain of $\mathbb{R}^d$, $d \in \{1, 2, 3\}$ which boundary is $\partial\Omega$. The objective here is to study the positivity of ε (respectively $\mathrm{P} = \rho\varepsilon - \mathrm{P}_\infty$) in the case of an ideal gas thermodynamics (respectively a stiffened gas thermodynamics). According to (2.15), (2.16), it corresponds to the phase-space invariance for both ideal and stiffened gas thermodynamics.

Ideal Gas Thermodynamics

The specific internal energy of both subsystems verifies the following PDEs:

$$\begin{cases} \partial_t \varepsilon + \mathbf{u} \cdot \underline{\nabla} \varepsilon + \mathscr{E}_0^2(t) \dfrac{p}{\rho} \underline{\nabla} \cdot \mathbf{u} = 0, & (\mathcal{C}) \\ \partial_t \varepsilon + \left(1 - \mathscr{E}_0^2(t)\right) \dfrac{p}{\rho} \underline{\nabla} \cdot \mathbf{u} = 0, & (\mathcal{A}) \end{cases} \tag{2.96}$$

which can also be rewritten:

$$\begin{cases} \partial_t \varepsilon + \mathbf{u} \cdot \underline{\nabla} \varepsilon + \mathscr{E}_0^2(t)\, (\gamma - 1) \varepsilon \underline{\nabla} \cdot \mathbf{u} = 0, & (\mathcal{C}) \\ \partial_t \varepsilon + \left(1 - \mathscr{E}_0^2(t)\right) (\gamma - 1) \varepsilon \underline{\nabla} \cdot \mathbf{u} = 0, & (\mathcal{A}) \end{cases} \tag{2.97}$$

because $p/\rho = (\gamma - 1)\varepsilon$.

Define $\varepsilon^- = \frac{\varepsilon - |\varepsilon|}{2}$ the negative part of the specific internal energy. Consider the following hypothesis about the solution's smoothness and the initial and boundary conditions:

$$\forall t \geq 0,\ \mathbf{u}(t,.) \in \mathrm{L}^\infty(\Omega),\ \underline{\nabla} \cdot \mathbf{u}(t,.) \in \mathrm{L}^\infty(\Omega), \tag{2.98a}$$

$$\forall t \geq 0,\ \varepsilon(t,.) \in \mathrm{L}^\infty(\Omega),\ \underline{\nabla}\varepsilon(t,.) \in \mathrm{L}^\infty(\Omega)^d, \tag{2.98b}$$

$$\forall \mathbf{x} \in \Omega,\ \varepsilon(t=0,\mathbf{x}) > 0 \Leftrightarrow \varepsilon^-(0,\mathbf{x}) = 0, \tag{2.98c}$$

$$\varepsilon_{|\partial\Omega} \geq 0 \text{ if } \mathbf{u}\cdot\mathbf{n}_{|\partial\Omega} \leq 0. \tag{2.98d}$$

By multiplying equation (2.96) by ε^- and integrating over Ω one obtains:

$$\begin{cases} \dfrac{d}{dt}\displaystyle\int_\Omega \frac{(\varepsilon^-)^2}{2}\,d\Omega + \int_\Omega \mathbf{u}\cdot\underline{\nabla}\frac{(\varepsilon^-)^2}{2}\,d\Omega + \int_\Omega (\gamma-1)\mathscr{E}_0^2(t)\,(\varepsilon^-)^2\underline{\nabla}\cdot\mathbf{u}\,d\Omega = 0 & (\mathcal{C}), \\ \dfrac{d}{dt}\displaystyle\int_\Omega \frac{(\varepsilon^-)^2}{2}\,d\Omega + \int_\Omega (\gamma-1)\left(1-\mathscr{E}_0^2(t)\right)(\varepsilon^-)^2\underline{\nabla}\cdot\mathbf{u}\,d\Omega = 0 & (\mathcal{A}). \end{cases} \tag{2.99}$$

By using Green's formula, the above equations can be transformed into:

$$\begin{cases} \dfrac{d}{dt}\dfrac{||\varepsilon^-||^2_{\mathrm{L}^2}}{2} = \displaystyle\int_\Omega \underline{\nabla}\cdot\mathbf{u}\left(\frac{1}{2}-(\gamma-1)\mathscr{E}_0^2(t)\right)(\varepsilon^-)^2\,d\Omega - \int_{\partial\Omega}\frac{(\varepsilon^-)^2}{2}\mathbf{u}\cdot\mathbf{n}\,d\Gamma & (\mathcal{C}), \\ \dfrac{d}{dt}\dfrac{||\varepsilon^-||^2_{\mathrm{L}^2}}{2} = -\displaystyle\int_\Omega \underline{\nabla}\cdot\mathbf{u}(\gamma-1)\left(1-\mathscr{E}_0^2(t)\right)(\varepsilon^-)^2\,d\Omega & (\mathcal{A}). \end{cases} \tag{2.100}$$

Because of the admissible inlet boundary condition (2.98d), $-\int_{\partial\Omega}\frac{(\varepsilon^-)^2}{2}\mathbf{u}\cdot\mathbf{n}\,d\Gamma$ is always negative so that we can derive the following inequalities:

$$\begin{cases} \dfrac{d}{dt}||\varepsilon^-||^2_{\mathrm{L}^2} \leq \overbrace{\sup_\Omega\left|\underline{\nabla}\cdot\mathbf{u}\left(1-2\,\mathscr{E}_0^2(t)\,(\gamma-1)\right)\right|}^{\mathrm{L}_{\mathcal{C}}(t)}||\varepsilon^-||^2_{\mathrm{L}^2} & (\mathcal{C}), \\ \dfrac{d}{dt}||\varepsilon^-||^2_{\mathrm{L}^2} \leq \underbrace{\sup_\Omega\left|2\underline{\nabla}\cdot\mathbf{u}\left(1-\mathscr{E}_0^2(t)\right)(\gamma-1)\right|}_{\mathrm{L}_{\mathcal{A}}(t)}||\varepsilon^-||^2_{\mathrm{L}^2} & (\mathcal{A}). \end{cases} \tag{2.101}$$

Thus, because of Grönwall's lemma:

$$\begin{cases} ||\varepsilon^-||^2_{\mathrm{L}^2}(t) \leq ||\varepsilon^-||^2_{\mathrm{L}^2}(0)\,e^{\int_0^t \mathrm{L}_{\mathcal{C}}(s)\,ds} = 0 \Rightarrow ||\varepsilon^-||^2_{\mathrm{L}^2}(t) = 0 & (\mathcal{C}), \\ ||\varepsilon^-||^2_{\mathrm{L}^2}(t) \leq ||\varepsilon^-||^2_{\mathrm{L}^2}(0)\,e^{\int_0^t \mathrm{L}_{\mathcal{A}}(s)\,ds} = 0 \Rightarrow ||\varepsilon^-||^2_{\mathrm{L}^2}(t) = 0 & (\mathcal{A}). \end{cases} \tag{2.102}$$

One can notice that, beyond hypothesis presented in (2.98), a sufficient condition to derive inequalities (2.101) is $\frac{p}{\rho} = \mathrm{K}\varepsilon$ with K a bounded function on Ω. Indeed, as previously seen, it allows to control the term $\int_\Omega \varepsilon^- \frac{p}{\rho}\underline{\nabla}\cdot\mathbf{u}\,d\Omega$ by $\sup_\Omega\left|\mathrm{K}\underline{\nabla}\cdot\mathbf{u}\right|||\varepsilon^-||^2_{\mathrm{L}^2}$.

Stiffened Gas Thermodynamics

When a stiffened gas thermodynamics defined by (2.16a) and (2.16b) is at stake, one is interested in the positivity of $\mathrm{P} = \rho\varepsilon - \mathrm{P}_\infty$. Such a variable follows the PDEs:

$$\begin{cases} \partial_t \mathrm{P} + \underline{\nabla}\cdot(\mathrm{P}\,\mathbf{u}) + \mathscr{E}_0^2(t)\,(\gamma-1)\,\mathrm{P}\,\underline{\nabla}\cdot\mathbf{u} + \mathrm{P}_\infty(1-\mathscr{E}_0^2(t))\,\underline{\nabla}\cdot\mathbf{u} = 0, & (\mathcal{C}) \\ \partial_t \mathrm{P} + (1-\mathscr{E}_0^2(t))\,(\gamma-1)\,\mathrm{P}\,\underline{\nabla}\cdot\mathbf{u} - \mathrm{P}_\infty(1-\mathscr{E}_0^2(t))\,\underline{\nabla}\cdot\mathbf{u} = 0. & (\mathcal{A}) \end{cases} \tag{2.103}$$

By doing exactly the same kind of hypothesis (but replacing ε by P) and calculations than for the ideal case, one can obtain:

$$\begin{cases} \dfrac{d}{dt}||\mathrm{P}^-||^2_{\mathrm{L}^2} \leq (2\mathscr{E}_0^2(\gamma-1)+1)\sup_\Omega\left|\underline{\nabla}\cdot\mathbf{u}\right|||\mathrm{P}^-||^2_{\mathrm{L}^2} - (1-\mathscr{E}_0^2(t))\,\mathrm{P}_\infty\displaystyle\int_\Omega \mathrm{P}^-\underline{\nabla}\cdot\mathbf{u}\,d\Omega, & (\mathcal{C}) \\ \dfrac{d}{dt}||\mathrm{P}^-||^2_{\mathrm{L}^2} \leq 2(1-\mathscr{E}_0^2)(\gamma-1)\sup_\Omega\left|\underline{\nabla}\cdot\mathbf{u}\right|||\mathrm{P}^-||^2_{\mathrm{L}^2} + (1-\mathscr{E}_0^2(t))\,\mathrm{P}_\infty\displaystyle\int_\Omega \mathrm{P}^-\underline{\nabla}\cdot\mathbf{u}\,d\Omega. & (\mathcal{A}) \end{cases} \tag{2.104}$$

Assume that there exists a function $K \in L^\infty(\Omega)$ such that:

$$P^\infty = K P. \tag{2.105}$$

Then, it is possible to control the term $P_\infty \int_\Omega P^- \underline{\nabla} \cdot \mathbf{u}\, d\Omega$ with $||P^-||^2_{L^2}$. Inequalities (2.104) turn into:

$$\begin{aligned} \frac{d}{dt}||P^-||^2_{L^2} &\leq \sup_\Omega \left|\left((2\mathscr{E}_0^2(\gamma-1)+1) - K(1-\mathscr{E}_0^2)\right)\underline{\nabla}\cdot\mathbf{u}\right| ||P^-||^2_{L^2}, \qquad (\mathcal{C}) \\ \frac{d}{dt}||P^-||^2_{L^2} &\leq \sup_\Omega \left|(1-\mathscr{E}_0^2)\left(2(\gamma-1)+K\right)\underline{\nabla}\cdot\mathbf{u}\right| ||P^-||^2_{L^2}, \qquad (\mathcal{A}) \end{aligned} \tag{2.106}$$

and the Grönwall's lemma can be applied so that to obtain $||P^-||^2_{L^2}(t) = 0$. However, in the case of a stiffened gas thermodynamics $P_\infty/P = \frac{(\gamma-1)P_\infty}{(p+P_\infty)}$ and p is allowed to tend towards $-P_\infty$. Thus, hypothesis (2.105) does not hold *a priori* and we cannot ensure the positivity of P unless $P_\infty = 0$ (ideal gas thermodynamics) or $\mathscr{E}_0 = 1$ (splitting not triggered).

D Positivity of the Discrete Intermediate Density

Consider the Riemann problem presented in Figure 2.1a related to the convective subsystem. It produces intermediate states described in relations (2.38) and (2.39). Let us find a sufficient condition on the subcaracteristic coefficient $a_\mathcal{C}$ so that the intermediate densities $\rho^*_{k,\mathcal{C}}$, $k \in \{L, R\}$ are positive.

$$\begin{aligned} \rho^*_{k,\mathcal{C}} \geq 0 &\Leftrightarrow \tau^*_{k,\mathcal{C}} \geq 0, \\ &\Leftrightarrow \tau_k + \frac{(-1)^{i_k+1}}{\mathscr{E}_0\, a_\mathcal{C}}\left(u^*_\mathcal{C} - u_k\right) \geq 0, \\ &\Leftrightarrow a^2_\mathcal{C} + \frac{\rho_k\,(u_R - u_L)}{2\mathscr{E}_0}\, a_\mathcal{C} + \frac{(-1)^{i_k}\rho_k\left(p_R - p_L\right)}{2} \geq 0. \end{aligned} \tag{2.107}$$

The second order polynomial function admits real roots if and only if

$$\Delta^\rho_k \equiv \frac{\rho_k\,(u_R - u_L)^2}{8\,\mathscr{E}_0^2} + (-1)^{i_k+1}\left(p_R - p_L\right) \geq 0. \tag{2.108}$$

Let us notice that $\Delta^\rho_L < 0 \Rightarrow \Delta^\rho_R > 0$ and conversely. In that case the polynomial constraint (2.107) related to Δ^ρ_L is automatically verified. Thus, consider the most demanding case where $\Delta^\rho_L \geq 0$ and $\Delta^\rho_R \geq 0$, namely:

$$-\frac{\rho_L\,(u_R - u_L)^2}{8} \leq \mathscr{E}_0^2\left(p_R - p_L\right) \leq \frac{\rho_R\,(u_R - u_L)^2}{8}. \tag{2.109}$$

If $u_L \neq u_R$, inequality (2.109) holds easily with low-Mach flows when $\mathscr{E}_0$ tends toward zero.

Let us define a^ρ_k, $k \in \{L, R\}$ the highest roots related to the above polynomial functions:

$$\begin{aligned} a^\rho_L &\equiv \frac{1}{2}\left(-\frac{\rho_L\,(u_R - u_L)}{2\,\mathscr{E}_0} + \sqrt{\frac{\rho_L^2\,(u_R - u_L)^2}{4\,\mathscr{E}_0^2} + 2\rho_L\,(p_R - p_L)}\right), \\ a^\rho_R &\equiv \frac{1}{2}\left(-\frac{\rho_R\,(u_R - u_L)}{2\,\mathscr{E}_0} + \sqrt{\frac{\rho_R^2\,(u_R - u_L)^2}{4\,\mathscr{E}_0^2} - 2\rho_R\,(p_R - p_L)}\right). \end{aligned} \tag{2.110}$$

By noticing that $\forall A \geq 0, -A + \sqrt{A^2 + B} > 0 \Leftrightarrow B > 0$, one can build the following table which gives the sign of a^ρ_L and a^ρ_R: In practice, when either a^ρ_L or a^ρ_R are positive, we add it as an additional constraint into the subcaracteristic condition (2.28a) leading to the modified subcaracteristic condition (2.55).

	$u_R > u_L$	$u_R < u_L$
$p_R > p_L$	$a_L^\rho > 0,\ a_R^\rho < 0$	$a_L^\rho > 0,\ a_R^\rho > 0$
$p_R < p_L$	$a_L^\rho < 0,\ a_R^\rho > 0$	$a_L^\rho > 0,\ a_R^\rho > 0$

Table 2.6 – Positivity Domain of a_L^ρ and a_R^ρ

The non-dimensional expressions of a_L^ρ and a_R^ρ are:

$$\begin{aligned} a_L^\rho &\equiv \frac{1}{2}\left(-\frac{M}{\mathscr{E}_0}\frac{\rho_L\,(u_R-u_L)}{2}+\sqrt{\left(\frac{M}{\mathscr{E}_0}\right)^2\frac{\rho_L^2\,(u_R-u_L)^2}{4}+2\,\rho_L\,(p_R-p_L)}\right),\\ a_R^\rho &\equiv \frac{1}{2}\left(-\frac{M}{\mathscr{E}_0}\frac{\rho_R\,(u_R-u_L)}{2}+\sqrt{\left(\frac{M}{\mathscr{E}_0}\right)^2\frac{\rho_R^2\,(u_R-u_L)^2}{4}-2\,\rho_R\,(p_R-p_L)}\right). \end{aligned} \tag{2.111}$$

Thus, if $\mathscr{E}_0$ is proportional to the Mach number as defined in (2.49), the above non-dimensional roots are of order one.

Concerning the equivalence between the intermediate density positivity and the ordering of the eigenvalues of subsystem $\mathcal{C}^\mu$, one can notice that:

$$\begin{aligned} &u_L-\mathscr{E}_0\,a_{\mathcal{C}}\,\tau_L\le u_{\mathcal{C}}^*,\\ &\Leftrightarrow 0\le \mathscr{E}_0\,a_{\mathcal{C}}\left(\tau_L+\frac{1}{\mathscr{E}_0\,a_{\mathcal{C}}}\left(u_{\mathcal{C}}^*-u_L\right)\right),\\ &\Leftrightarrow 0\le \tau_{L,\mathcal{C}}^*. \end{aligned} \tag{2.112}$$

By doing the same calculation, one can see that $u_{\mathcal{C}}^*\le u_R+\mathscr{E}_0\,a_{\mathcal{C}}\,\tau_R \Leftrightarrow \tau_{R,\mathcal{C}}^*\ge 0$.

Finally, let us recall that, in the acoustic Riemann problem presented in Figure 2.1b, $\rho_{L,\mathcal{A}}^*=\rho_L$ and $\rho_{R,\mathcal{A}}^*=\rho_R$. The intermediate densities are then already positive. No additional constraint on $a_{\mathcal{A}}$ needs to be provided in order to preserve the density positivity.

E Positivity of the Discrete Intermediate Internal Energy

For an ideal gas thermodynamics, the specific internal energy is supposed to remain positive throughout space and time under admissible boundary conditions. Here a sufficient condition under the relaxation constants $a_{\mathcal{C}}$ and $a_{\mathcal{A}}$ is looked for in order to obtain the positivity of the intermediate internal energies produced by the Riemann problems described in Figure 2.1a and Figure 2.1b.

Relaxed Convective Subsystem

Once again, for the Riemann problem related to the convective relaxed subsystem $\mathcal{C}$, the specific internal energy reads:

$$\begin{aligned} \varepsilon_{k,\mathcal{C}}^* &= e_{k,\mathcal{C}}^*-\frac{(u_{\mathcal{C}}^*)^2}{2},\\ &= e_k-\frac{(u_{\mathcal{C}}^*)^2}{2}+\mathscr{E}_0\,\frac{(-1)^{i_k}}{a_{\mathcal{C}}}\left(\Pi_{\mathcal{C}}^*\,u_{\mathcal{C}}^*-\Pi_k\,u_k\right),\\ &= \varepsilon_k+\frac{u_k^2-(u_{\mathcal{C}}^*)^2}{2}+\mathscr{E}_0\,\frac{(-1)^{i_k}}{a_{\mathcal{C}}}\left(\Pi_{\mathcal{C}}^*\,u_{\mathcal{C}}^*-\Pi_k\,u_k\right),\\ &= \varepsilon_k+\frac{u_k^2+(u_{\mathcal{C}}^*)^2}{2}+\mathscr{E}_0\,\frac{(-1)^{i_k}}{a_{\mathcal{C}}}\,u_{\mathcal{C}}^*\left(\Pi_{\mathcal{C}}^*+\frac{(-1)^{i_k+1}\,a_{\mathcal{C}}}{\mathscr{E}_0}\,u_{\mathcal{C}}^*\right)-\mathscr{E}_0\,\frac{(-1)^{i_k}}{a_{\mathcal{C}}}\,\Pi_k\,u_k. \end{aligned} \tag{2.113}$$

By combining, $u+(-1)^{i_k}\,\mathscr{E}_0\,a_{\mathcal{C}}\,\tau$ and $\Pi+(a_{\mathcal{C}})^2\,\tau$ which both are 1-Riemann invariants of subsystem $\mathcal{C}^\mu$, one can build a new one: $\Pi+\frac{(-1)^{i_k+1}\,a_{\mathcal{C}}}{\mathscr{E}_0}\,u$. Then, one can simplify the above expression of $\varepsilon_{k,\mathcal{C}}^*$,

namely:

$$\begin{aligned}\varepsilon^*_{k,\mathcal{C}} &= \varepsilon_k + \frac{u_k^2 + (u^*_{\mathrm{C}})^2}{2} + \mathscr{E}_0 \frac{(-1)^{i_k}}{a_{\mathcal{C}}} u^*_{\mathcal{C}} \left(\Pi_k + \frac{(-1)^{i_k+1} a_{\mathcal{C}}}{\mathscr{E}_0} u_k \right) - \mathscr{E}_0 \frac{(-1)^{i_k}}{a_{\mathcal{C}}} \Pi_k u_k, \\ &= \varepsilon_k + \mathscr{E}_0 \frac{(-1)^{i_k}}{a_{\mathcal{C}}} \Pi_k \left(u^*_{\mathcal{C}} - u_k \right) + \frac{\left(u^*_{\mathcal{C}} - u_k \right)^2}{2}.\end{aligned} \tag{2.114}$$

Thus, a sufficient condition which would guarantee that $\forall k \in \{\mathrm{L}, \mathrm{R}\}$, $\varepsilon^*_{k,\mathcal{C}} \geq 0$ is:

$$\varepsilon_k + \mathscr{E}_0 \frac{(-1)^{i_k}}{a_{\mathcal{C}}} p_k \left(u^*_{\mathcal{C}} - u_k \right) \geq 0 \Leftrightarrow a^2_{\mathcal{C}} - \mathscr{E}_0 \rho^{\varepsilon}_k \frac{(u_{\mathrm{R}} - u_{\mathrm{L}})}{2} a_{\mathcal{C}} + (-1)^{i_k+1} \mathscr{E}_0^2 \rho^{\varepsilon}_k \frac{(p_{\mathrm{R}} - p_{\mathrm{L}})}{2} \geq 0, \tag{2.115}$$

with $\rho^{\varepsilon}_k = \frac{p_k}{\varepsilon_k}$, and considering that $p_k = \Pi_k$. Inequality (2.115) is very similar to the one obtained for the intermediate density positivity. The most demanding case is the one where $\forall k \in \{\mathrm{L}, \mathrm{R}\}$, $\Delta^{\varepsilon}_k \equiv \rho^{\varepsilon}_k \frac{(u_{\mathrm{R}} - u_{\mathrm{L}})^2}{8} + (-1)^{i_k} \left(p_{\mathrm{R}} - p_{\mathrm{L}} \right) \geq 0$:

$$-\frac{\rho^{\varepsilon}_{\mathrm{R}} (u_{\mathrm{R}} - u_{\mathrm{L}})^2}{8} \leq p_{\mathrm{R}} - p_{\mathrm{L}} \leq \frac{\rho^{\varepsilon}_{\mathrm{L}} (u_{\mathrm{R}} - u_{\mathrm{L}})^2}{8}. \tag{2.116}$$

Once again the highest roots related to the polynomial functions written in (2.115) are:

$$\begin{aligned} a^{\varepsilon}_{\mathcal{C},\mathrm{L}} &\equiv \frac{\mathscr{E}_0}{2} \left(\frac{\rho^{\varepsilon}_{\mathrm{L}} (u_{\mathrm{R}} - u_{\mathrm{L}})}{2} + \sqrt{\frac{(\rho^{\varepsilon}_{\mathrm{L}})^2 (u_{\mathrm{R}} - u_{\mathrm{L}})^2}{4} - 2 \rho^{\varepsilon}_{\mathrm{L}} (p_{\mathrm{R}} - p_{\mathrm{L}})} \right), \\ a^{\varepsilon}_{\mathcal{C},\mathrm{R}} &\equiv \frac{\mathscr{E}_0}{2} \left(\frac{\rho^{\varepsilon}_{\mathrm{R}} (u_{\mathrm{R}} - u_{\mathrm{L}})}{2} + \sqrt{\frac{(\rho^{\varepsilon}_{\mathrm{R}})^2 (u_{\mathrm{R}} - u_{\mathrm{L}})^2}{4} + 2 \rho^{\varepsilon}_{\mathrm{R}} (p_{\mathrm{R}} - p_{\mathrm{L}})} \right). \end{aligned} \tag{2.117}$$

The sign of $a^{\varepsilon}_{\mathrm{L}}$ and $a^{\varepsilon}_{\mathrm{R}}$ is given by the following table: The non-dimensional version of these roots

	$u_{\mathrm{R}} > u_{\mathrm{L}}$	$u_{\mathrm{R}} < u_{\mathrm{L}}$
$p_{\mathrm{R}} > p_{\mathrm{L}}$	$a^{\varepsilon}_{\mathcal{C},\mathrm{L}} > 0$, $a^{\varepsilon}_{\mathcal{C},\mathrm{R}} > 0$	$a^{\varepsilon}_{\mathcal{C},\mathrm{L}} < 0$, $a^{\varepsilon}_{\mathcal{C},\mathrm{R}} > 0$
$p_{\mathrm{R}} < p_{\mathrm{L}}$	$a^{\varepsilon}_{\mathcal{C},\mathrm{L}} > 0$, $a^{\varepsilon}_{\mathcal{C},\mathrm{R}} > 0$	$a^{\varepsilon}_{\mathcal{C},\mathrm{L}} > 0$, $a^{\varepsilon}_{\mathcal{C},\mathrm{R}} < 0$

Table 2.7 – Positivity Domain of $a^{\varepsilon}_{\mathcal{C},\mathrm{L}}$ and $a^{\varepsilon}_{\mathcal{C},\mathrm{R}}$

reads:

$$\begin{aligned} a^{\varepsilon}_{\mathcal{C},\mathrm{L}} &\equiv \frac{\mathscr{E}_0}{2} \left(\frac{\mathrm{M} \rho^{\varepsilon}_{\mathrm{L}} (u_{\mathrm{R}} - u_{\mathrm{L}})}{2} + \sqrt{\frac{\mathrm{M}^2 (\rho^{\varepsilon}_{\mathrm{L}})^2 (u_{\mathrm{R}} - u_{\mathrm{L}})^2}{4} - 2 \rho^{\varepsilon}_{\mathrm{L}} (p_{\mathrm{R}} - p_{\mathrm{L}})} \right), \\ a^{\varepsilon}_{\mathcal{C},\mathrm{R}} &\equiv \frac{\mathscr{E}_0}{2} \left(\frac{\mathrm{M} \rho^{\varepsilon}_{\mathrm{R}} (u_{\mathrm{R}} - u_{\mathrm{L}})}{2} + \sqrt{\frac{\mathrm{M}^2 (\rho^{\varepsilon}_{\mathrm{R}})^2 (u_{\mathrm{R}} - u_{\mathrm{L}})^2}{4} + 2 \rho^{\varepsilon}_{\mathrm{R}} (p_{\mathrm{R}} - p_{\mathrm{L}})} \right). \end{aligned} \tag{2.118}$$

Then, contrary to the non-dimensional roots involved in the intermediate density positivity they are of order $\mathrm{O}(\mathscr{E}_0)$. When either $a^{\varepsilon}_{\mathrm{L}}$ or $a^{\varepsilon}_{\mathrm{R}}$ are positive, they are injected in the subcaracteristic condition (2.28a).

Relaxed Acoustic Subsystem

The acoustic relaxed subsystem $\mathcal{A}^{\mu}$ also produces intermediate specific internal energies $\varepsilon^*_{k,\mathcal{A}} = e^*_{k,\mathcal{A}} - \frac{(u^*_{\mathcal{A}})^2}{2} = \varepsilon_k + \frac{(-1)^{i_k}}{a_{\mathcal{A}}} \Pi_k \left(u^*_{\mathcal{A}} - u_k \right) + \frac{\left(u^*_{\mathcal{A}} - u_k \right)^2}{2}$. The proof is similar to the one done for the con-

vective relaxed subsystem. Indeed:

$$\begin{aligned}
\varepsilon^*_{k,\mathcal{A}} &= e^*_{k,\mathcal{A}} - \frac{(u^*_{\mathcal{A}})^2}{2}, \\
&= e_k - \frac{(u^*_{\mathcal{A}})^2}{2} + \frac{(-1)^{i_k}}{a_{\mathcal{A}}}\left(\Pi^*_{\mathcal{A}}\, u^*_{\mathcal{A}} - \Pi_k\, u_k\right), \\
&= \varepsilon_k + \frac{u_k^2 - (u^*_{\mathcal{A}})^2}{2} + \frac{(-1)^{i_k}}{a_{\mathcal{A}}}\left(\Pi^*_{\mathcal{A}}\, u^*_{\mathcal{A}} - \Pi_k\, u_k\right), \\
&= \varepsilon_k + \frac{u_k^2 + (u^*_{\mathcal{A}})^2}{2} + \frac{(-1)^{i_k}}{a_{\mathcal{A}}}\, u^*_{\mathcal{A}}\left(\Pi^*_{\mathcal{A}} + (-1)^{i_k+1}\, a_{\mathcal{A}}\, u^*_{\mathcal{A}}\right) - \frac{(-1)^{i_k}}{a_{\mathcal{A}}}\,\Pi_k\, u_k.
\end{aligned} \tag{2.119}$$

Recall that $\omega^-_{\mathcal{A}} = u - \frac{\Pi}{a_{\mathcal{A}}}$ (respectively $\omega^+_{\mathcal{A}} = u + \frac{\Pi}{a_{\mathcal{A}}}$) introduced in Section 2.3.2 is 1-Riemann invariant (respectively a 4-Riemann invariant). Then, one can replace $\Pi^*_{\mathcal{A}} + (-1)^{i_k+1}\, a_{\mathcal{A}}\, u^*_{\mathcal{A}}$ by $\Pi_k + (-1)^{i_k+1}\, a_{\mathcal{A}}\, u_k$. Hence, equality (2.119) is equivalent to:

$$\varepsilon^*_{k,\mathcal{A}} = \varepsilon_k + \frac{(-1)^{i_k}}{a_{\mathcal{A}}}\Pi_k\left(u^*_{\mathcal{A}} - u_k\right) + \frac{\left(u^*_{\mathcal{A}} - u_k\right)^2}{2}. \tag{2.120}$$

Thus, a sufficient condition which would guarantee that $\forall\, k \in \{\mathrm{L},\mathrm{R}\}$, $\varepsilon^*_{k,\mathcal{A}} \geq 0$ is:

$$\varepsilon_k + \frac{(-1)^{i_k}}{a_{\mathcal{A}}}\, p_k\left(u^*_{\mathcal{A}} - u_k\right) \geq 0 \Leftrightarrow a^2_{\mathcal{A}} - \rho^{\varepsilon}_k \frac{(u_{\mathrm{R}} - u_{\mathrm{L}})}{2}\, a_{\mathcal{A}} + (-1)^{i_k+1}\rho^{\varepsilon}_k \frac{\left(p_{\mathrm{R}} - p_{\mathrm{L}}\right)}{2} \geq 0. \tag{2.121}$$

Sufficient conditions allowing to guarantee the intermediate specific energy positivity turns into the positivity of two polynomial functions of order two in $a_{\mathcal{A}}$. The most demanding case corresponds exactly to inequalities (2.116). Finally the roots above which the relaxation coefficient has to be are:

$$a^{\varepsilon}_{\mathcal{A},\mathrm{L}} \equiv \frac{a^{\varepsilon}_{\mathcal{C},\mathrm{L}}}{\mathscr{E}_0};\ a^{\varepsilon}_{\mathcal{A},\mathrm{R}} \equiv \frac{a^{\varepsilon}_{\mathcal{C},\mathrm{R}}}{\mathscr{E}_0}. \tag{2.122}$$

Since for $k \in \{\mathrm{L},\mathrm{R}\}$, $a^{\varepsilon}_{\mathcal{C},k} = \mathrm{O}(\mathscr{E}_0)$, the non-dimensional expressions of $a^{\varepsilon}_{\mathcal{A},k}$ are of order one. One can notice that, in case of low-Mach flows, the constraint imposed by the relaxation convective subsystem on the specific internal energy positivity is negligible compared to the one of the relaxed acoustic subsystem.

F Subcharacteristic Conditions for the Subsystems

The proof written below is only formal. It aims at exhibiting subcaracteristic conditions under which the relaxation subsystems contain diffusive operators. The latter would avoid instabilities which could prevent the convergence of the relaxation subsystems $\mathcal{C}^{\mu}$ and $\mathcal{A}^{\mu}$ towards $\mathcal{C}$ and $\mathcal{A}$.

Relaxed Convective Subsystem

Consider the relaxed convective subsystem $\mathcal{C}^{\mu}$:

$$\mathcal{C}^{\mu}: \begin{cases}
\partial_t \rho + \partial_x(\rho\, u) = 0, \\
\partial_t \rho\, u + \partial_x(\rho\, u^2) + \partial_x\left(\mathscr{E}_0^2(t)\,\Pi\right) = 0, \\
\partial_t \rho\, e + \partial_x\left((\rho\, e + \mathscr{E}_0^2(t)\,\Pi)\, u\right) = 0, \\
\partial_t \Pi + u\,\partial_x \Pi + \dfrac{a^2_{\mathcal{C}}}{\rho}\,\partial_x u = \dfrac{1}{\mu}\left(p - \Pi\right).
\end{cases} \tag{2.123}$$

Define $\mathbf{W} = \left[\rho, \rho\, u, \rho\, e, \rho\,\Pi\right]^{\mathrm{T}}$ and $\mathbf{U} = \left[\rho, \rho\, u, \rho\, e\right]^{\mathrm{T}}$. Assume that one can perform a Chapman-Enskog expansion on $\mathbf{U}$ and Π and write them in powers of μ, namely:

$$\begin{aligned}
\mathbf{U} &= \mathbf{U}_0 + \mu\,\mathbf{U}_1 + \mathrm{O}(\mu^2), \\
\Pi &= p\,(\mathbf{U}_0) + \mu\,\Pi_1 + \mathrm{O}(\mu^2),
\end{aligned} \tag{2.124}$$

with $\mathbf{U}_0$ and $p(\mathbf{U}_0)$ solutions of subsystem $\mathcal{C}$ and $\mathbf{U}_1$, Π_1 of order one. Making μ tend formally toward zero, the relaxed pressure equation becomes at order zero:

$$\partial_t p(\mathbf{U}_0) + u_0 \partial_x p(\mathbf{U}_0) + \frac{a_{\mathcal{C}}^2}{\rho_0} \partial_x u_0 = -\Pi_1 \Leftrightarrow \left(\frac{a_{\mathcal{C}}^2}{\rho_0} - \rho_0 c_{\mathcal{C}}(\mathbf{U}_0)^2 \right) \partial_x u_0 = -\Pi_1. \tag{2.125}$$

In order to make $\mathcal{C}^\mu$ converge towards $\mathcal{C}$, a basic step is to make sure that $\mathbf{U}_1$ remains of order one throughout time. Its evolution is influenced by non linear convective effects which mix order zero and order one terms as well as pressure effects related to $\mathscr{E}_0^2 \partial_x \Pi_1$ for the momentum equation and $\mathscr{E}_0^2 \partial_x (\Pi_1 u_0 + p_0 u_1)$ for the energy equation. Using equation (2.125), one can notice that:

$$-\mathscr{E}_0^2 \partial_x \Pi_1 = \mathscr{E}_0^2 \partial_x \left(\left(\frac{a_{\mathcal{C}}^2}{\rho_0} - \rho_0 c_{\mathcal{C}}(\mathbf{U}_0)^2 \right) \partial_x u_0 \right). \tag{2.126}$$

Thus, under the convective subcaracteristic condition $a_{\mathcal{C}} > \rho_0 c_{\mathcal{C}}(\mathbf{U}_0)$, order zero terms results in a *diffusive* effect on the order one momentum equation. One can believe that this diffusion will be sufficient to prevent $\mathbf{U}_1$ from exploding when μ tends toward zero.

Relaxed Acoustic Subsystem

The same argumentation can be done on the relaxed acoustic subsystem $\mathcal{A}^\mu$. It gives the expected subcaracteristic condition (2.28b).

G Bounded Oscillations of Sp-(M)-corr

According to the truncation error analyses derived in Section 2.4, the scheme Sp-(M)-corr allows to reduce the spatial numerical diffusion in the convective as well as in the acoustic subsystem in the case of low-Mach number compressible flows. In Figure 2.12 velocity profiles are plotted for different meshes. The diffusion reduction results in non-physical oscillations in the tail of the left rarefaction wave. However, the L^∞ and the L^1 norms of the induced error decay as the cells number increases. Hence, the scheme is stable and converges to the analytical solution.

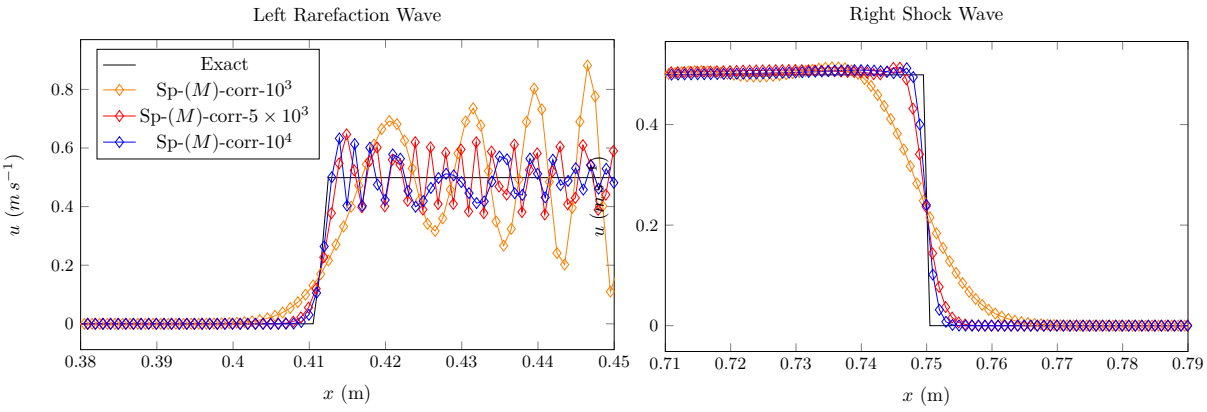

Figure 2.12 – Velocity profile at $M = 4.2 \times 10^{-3}$, Sp-(M)-corr

H Truncation Error Analysis

Truncation Error of the Convective Subsystem

Let us consider the convective numerical flux located at face indexed by $i+1/2$. For the sake of notations simplicity and in order to adopt an unstructured formalism, let us rewrite the index $i+1/2$ as f for "face". Finally let us call L (respectively R) the index of the left (respectively the right) neighbor cell of the face f. Typically, in 1D L $= i$ and R $= i+1$. As mentioned in Section 2.3.2 the relaxation scheme for the convective subsystem can be written:

$$\begin{aligned}\mathbf{H_c}_f^n = \mathbf{H_c}^n(\mathbf{U}_\mathrm{L},\mathbf{U}_\mathrm{R}) = \frac{1}{2}\left(\mathrm{L}(\mathbf{F}_\mathcal{C}^\mu)(\mathbf{U}_\mathrm{L}) + \mathrm{L}(\mathbf{F}_\mathcal{C}^\mu)(\mathbf{U}_\mathrm{R})\right) &- \frac{1}{2}\left|u_\mathrm{L} - \mathscr{E}_0\, a_\mathcal{C}\,\tau_\mathrm{L}\right|\left(\mathbf{U}_f^* - \mathbf{U}_\mathrm{L}\right)\\ &- \frac{1}{2}\left|u_\mathrm{C}^*\right|\left(\mathbf{U}_f^{**} - \mathbf{U}_f^*\right)\\ &- \frac{1}{2}\left|u_\mathrm{R} + \mathscr{E}_0\, a_\mathcal{C}\,\tau_\mathrm{R}\right|\left(\mathbf{U}_\mathrm{R} - \mathbf{U}_f^{**}\right),\\ \mathrm{L}(\mathbf{F}_\mathcal{C}^\mu)(\mathbf{U}) = \left[\rho\, u,\, \rho\, u^2 + \mathscr{E}_0^2\, p,\, (\rho\, e + \mathscr{E}_0^2\, p)\, u\right]^\mathrm{T}&.\end{aligned} \tag{2.127}$$

Using the classical rescaling described in [10], the non-dimensional version of this numerical flux writes:

$$\begin{aligned}\mathbf{H_c}_f^n = \mathbf{H}^n(\mathbf{U}_\mathrm{L},\mathbf{U}_\mathrm{R}) = \frac{1}{2}\left(\mathrm{L}(\mathbf{F}_\mathcal{C}^\mu)(\mathbf{U}_\mathrm{L}) + \mathrm{L}(\mathbf{F}_\mathcal{C}^\mu)(\mathbf{U}_\mathrm{R})\right) &- \frac{1}{2}\left|u_\mathrm{L} - \frac{\mathscr{E}_0}{\mathrm{M}}\, a_\mathcal{C}\,\tau_\mathrm{L}\right|\left(\mathbf{U}_f^* - \mathbf{U}_\mathrm{L}\right)\\ &- \frac{1}{2}\left|u_\mathrm{C}^*\right|\left(\mathbf{U}_f^{**} - \mathbf{U}_f^*\right)\\ &- \frac{1}{2}\left|u_\mathrm{R} + \frac{\mathscr{E}_0}{\mathrm{M}}\, a_\mathcal{C}\,\tau_\mathrm{R}\right|\left(\mathbf{U}_\mathrm{R} - \mathbf{U}_f^{**}\right),\\ \mathrm{L}(\mathbf{F}_\mathcal{C}^\mu)(\mathbf{U}) = \left[\rho\, u,\, \rho\, u^2 + (\mathscr{E}_0/\mathrm{M})^2\, p,\, (\rho\, e + \mathscr{E}_0^2\, p)\, u\right]^\mathrm{T}&,\ \rho\, e = \rho\varepsilon + \frac{\mathrm{M}^2}{2}\rho\, u^2.\end{aligned} \tag{2.128}$$

For the sake of notations, let us rewrite $\mathbf{U}_f^*$ as $\mathbf{U}_\mathrm{L}^*$ and $\mathbf{U}_f^{**}$ as $\mathbf{U}_\mathrm{R}^*$. The non-dimensional intermediate states $\mathbf{U}_k^*,\ k \in \{\mathrm{L},\mathrm{R}\}$ can be expressed as:

$$\mathbf{U}_k^* = \begin{bmatrix}\rho_{k,\mathcal{C}}^*\\ \rho_{k,\mathcal{C}}^*\, u_\mathrm{C}^*\\ \rho_{k,\mathcal{C}}^*\, e_{k,\mathcal{C}}^*\end{bmatrix}, \tag{2.129}$$

with:

$$\begin{cases} u_\mathrm{C}^* = \dfrac{u_\mathrm{R}+u_\mathrm{L}}{2} - \dfrac{\mathscr{E}_0}{\mathrm{M}}\dfrac{(p_\mathrm{R}-p_\mathrm{L})}{2\,a_\mathcal{C}},\\ p^* = \dfrac{p_\mathrm{R}+p_\mathrm{L}}{2} - \dfrac{\mathrm{M}}{\mathscr{E}_0}\dfrac{a_\mathcal{C}\,(u_\mathrm{R}-u_\mathrm{L})}{2},\\ \rho_{k,\mathcal{C}}^* = 1/\tau_k^*,\ \tau_k^* = \tau_k + \dfrac{\mathrm{M}}{\mathscr{E}_0}\dfrac{(-1)^{i_k+1}}{a_\mathcal{C}}\left(u_\mathrm{C}^* - u_k\right),\\ e_{k,\mathcal{C}}^* = e_k + \mathscr{E}_0\,\mathrm{M}\dfrac{(-1)^{i_k}}{a_\mathcal{C}}\left(p^*\,u_\mathrm{C}^* - p_k\,u_k\right),\\ a_\mathcal{C} = \mathrm{K}\cdot\max\left(\rho_\mathrm{L}\,c_\mathcal{C}(\rho_\mathrm{L},p_\mathrm{L}),\,\rho_\mathrm{R}\,c_\mathcal{C}(\rho_\mathrm{R},p_\mathrm{R})\right),\ \mathrm{K}>1,\\ k\in\{\mathrm{L},\mathrm{R}\},\ i_\mathrm{L}\equiv 1,\ i_\mathrm{R}\equiv 2.\end{cases} \tag{2.130}$$

Let us define x_f, x_L and x_R the positions of the face, left cell and right cell barycenters. In 1D: $x_\mathrm{L} = x_i$, $x_\mathrm{R} = x_{i+1}$ and $x_f = x_\mathrm{L} + \Delta x/2 = x_\mathrm{R} - \Delta x/2$. At a given time t, for a smooth function $\phi(.,t)$ let us write ϕ_f for $\phi(x_f,t)$ and ϕ_L for $\phi(x_\mathrm{L},t)$. Particularly, we will consider $x \to a(x,t)$ a smooth function such that $a_\mathcal{C}(x_{i+1/2},t^n) = (a_\mathcal{C})_{i+1/2}^n$.

Let us consider a non-dimensional smooth state $(x,t) \to \mathbf{U}(x,t)$ verifying:

$$\mathrm{St_r}\,\frac{\mathbf{U}(x_i,\,t^n+\Delta t) - \mathbf{U}(x_i,\,t^n)}{\Delta t} + \frac{\mathbf{H_c}\left(\mathbf{U}(x_i,\,t^n),\,\mathbf{U}(x_{i+1},\,t^n)\right) - \mathbf{H_c}\left(\mathbf{U}(x_{i-1},\,t^n),\,\mathbf{U}(x_i,\,t^n)\right)}{\Delta x} = 0, \tag{2.131}$$

One wonders which partial differential equation does such a smooth solution verify?

It can be first noticed that $\frac{\mathbf{U}(x_i,t^n+\Delta t)-\mathbf{U}(x_i,t^n)}{\Delta t}$ is consistent with $\partial_t \mathbf{U}_i + \underline{\mathrm{O}}(\Delta t)$. Let us now focus on $\mathbf{H_c}^n(\mathbf{U}_\mathrm{L},\mathbf{U}_\mathrm{R})$: first, $\forall k \in \{\mathrm{L},\mathrm{R}\}$:

$$\mathbf{U}_k^* - \mathbf{U}_k = \begin{bmatrix} \rho_{k,\mathcal{C}}^* - \rho_k \\ (\rho_{k,\mathcal{C}}^* - \rho_k)\, u_\mathrm{C}^* + \rho_k\,(u_\mathrm{C}^* - u_k) \\ (\rho_{k,\mathcal{C}}^* - \rho_k)\, e_{k,\mathcal{C}}^* + \rho_k\,(e_{k,\mathcal{C}}^* - e_k) \end{bmatrix}. \tag{2.132}$$

Furthermore, performing a Taylor expansion around x_f, and setting $i_\mathrm{L}=1$, $i_\mathrm{R}=2$, one obtains:

$$\begin{cases} \rho_{k,\mathcal{C}}^* - \rho_k = \left[-\dfrac{\rho_f^2}{a_f}\left(\dfrac{\mathrm{M}}{\mathscr{E}_0}\right)\partial_x u_{|f} + (-1)^{i_k+1}\left(\dfrac{\rho_f}{a_f}\right)^2 \partial_x p_{|f}\right]\dfrac{\Delta x}{2} + \mathrm{O}\left((1+\dfrac{\mathrm{M}}{\mathscr{E}_0})\Delta x^2\right), \\ u_\mathrm{C}^* - u_k = \left[(-1)^{i_k+1}\partial_x u_{|f} - \left(\dfrac{\mathscr{E}_0}{\mathrm{M}}\right)\dfrac{1}{a_f}\partial_x p_{|f}\right]\dfrac{\Delta x}{2} + \mathrm{O}\left((1+\dfrac{\mathscr{E}_0}{\mathrm{M}})\Delta x^2\right), \\ e_{k,\mathcal{C}}^* - e_k = \mathrm{M}\mathscr{E}_0\left[-\dfrac{1}{a_f}\partial_x p\, u_{|f} + (-1)^{i_k+1}\left(\left(\dfrac{\mathscr{E}_0}{\mathrm{M}}\right)\dfrac{p_f}{a_f^2}\partial_x p_{|f} + \left(\dfrac{\mathrm{M}}{\mathscr{E}_0}\right)u_f\partial_x u_{|f}\right)\right]\dfrac{\Delta x}{2} \\ \qquad\qquad + \mathrm{O}\left(\mathrm{M}\mathscr{E}_0(1+\dfrac{\mathscr{E}_0}{\mathrm{M}}+\dfrac{\mathrm{M}}{\mathscr{E}_0})\Delta x^2\right), \\ u_\mathrm{C}^* = u_f - \left(\dfrac{\mathscr{E}_0}{\mathrm{M}}\right)\dfrac{1}{a_f}\partial_x p_{|f}\dfrac{\Delta x}{2} + \mathrm{O}\left((1+\dfrac{\mathscr{E}_0}{\mathrm{M}})\Delta x^2\right), \\ e_{k,\mathcal{C}}^* = e_f + (-1)^{i_k}\partial_x e_{|f}\dfrac{\Delta x}{2} + e_{k,\mathcal{C}}^* - e_k. \end{cases} \tag{2.133}$$

Then:

$$\mathbf{U}_k^* - \mathbf{U}_k = \frac{\Delta x}{2}\begin{bmatrix} -\frac{\rho_f^2}{a_f}\left(\frac{\mathrm{M}}{\mathscr{E}_0}\right)\partial_x u_{|f} + (-1)^{i_k+1}\left(\frac{\rho_f}{a_f}\right)^2\partial_x p_{|f} \\ \rho_f\left((-1)^{i_k+1} - \frac{\rho_f u_f}{a_f}\frac{\mathrm{M}}{\mathscr{E}_0}\right)\partial_x u_{|f} + \frac{\rho_f}{a_f}\left((-1)^{i_k+1}\frac{\rho_f uf}{a_f} - \frac{\mathscr{E}_0}{\mathrm{M}}\right)\partial_x p_{|f} \\ \rho_f e_f\left(\left(\frac{\rho_f}{a_f}\frac{\mathrm{M}}{\mathscr{E}_0} + (-1)^{i_k+1}\frac{u_f}{e_f}\mathscr{E}_0\frac{\mathrm{M}}{\mathscr{E}_0}\right)\partial_x u_{|f} + (-1)^{i_k+1}\left(\frac{\rho_f}{a_f^2} + \mathscr{E}_0\frac{\mathscr{E}_0}{\mathrm{M}}\frac{p_f}{a_f^2 e_f}\right)\partial_x p_{|f}\right) \\ +\mathscr{E}_0\frac{\mathscr{E}_0}{\mathrm{M}}\frac{p_f}{a_f^2 e_f}\partial_x p\, u_{|f} \end{bmatrix} \\ +\underline{\mathrm{O}}\left((1+\frac{\mathscr{E}_0}{\mathrm{M}}+\frac{\mathrm{M}}{\mathscr{E}_0})\Delta x^2\right). \tag{2.134}$$

One can finally observe that, for the terms in order one in space, the Mach number is always compensated with the weighting parameter $\mathscr{E}_0$. Thus $\forall k \in \{\mathrm{L},\mathrm{R}\}$:

$$\mathbf{U}_k^* - \mathbf{U}_k = \underline{\mathrm{O}}\left((1+\frac{\mathscr{E}_0}{\mathrm{M}}+\frac{\mathrm{M}}{\mathscr{E}_0})\Delta x\right)_f. \tag{2.135}$$

Similarly:

$$\begin{aligned} \mathbf{U}_\mathrm{R}^* - \mathbf{U}_\mathrm{L}^* &= \left(\mathbf{U}_\mathrm{R}^* - \mathbf{U}_\mathrm{R}\right) + \left(\mathbf{U}_\mathrm{R} - \mathbf{U}_\mathrm{L}\right) + \left(\mathbf{U}_\mathrm{L} - \mathbf{U}_\mathrm{L}^*\right), \\ &= \underline{\mathrm{O}}\left((1+\frac{\mathscr{E}_0}{\mathrm{M}}+\frac{\mathrm{M}}{\mathscr{E}_0})\Delta x\right)_f. \end{aligned} \tag{2.136}$$

Furthermore, one can easily see that $\forall k \in \{\mathrm{L},\mathrm{R}\}$:

$$\begin{aligned} \left|u_k + (-1)^{i_k}\frac{\mathscr{E}_0}{\mathrm{M}}a_\mathcal{C}\,\tau_k\right| &= \left|u_f + (-1)^{i_k}\frac{\mathscr{E}_0}{\mathrm{M}}a_f\,\tau_f\right| + \mathrm{O}\left((1+\frac{\mathscr{E}_0}{\mathrm{M}})\Delta x\right), \\ \left|u_\mathrm{C}^*\right| &= \left|u_f\right| + \mathrm{O}\left((1+\frac{\mathscr{E}_0}{\mathrm{M}})\Delta x\right). \end{aligned} \tag{2.137}$$

Thus, at a given face f we have:

$$\mathbf{H_c}_f^n = \mathbf{H_c}^n(\mathbf{U}_\mathrm{L},\mathbf{U}_\mathrm{R}) = \frac{1}{2}\left(\mathrm{L}(\mathbf{F}_\mathcal{C}^\mu)(\mathbf{U}_\mathrm{L}) + \mathrm{L}(\mathbf{F}_\mathcal{C}^\mu)(\mathbf{U}_\mathrm{R})\right) + \underline{\mathrm{O}}\left((1+\frac{\mathscr{E}_0}{\mathrm{M}}+\frac{\mathrm{M}}{\mathscr{E}_0})\Delta x\right)_f. \tag{2.138}$$

Besides, $\frac{1}{2}\left(\mathrm{L}(\mathbf{F}_{\mathcal{C}}^{\mu})(\mathbf{U}_{\mathrm{L}})+\mathrm{L}(\mathbf{F}_{\mathcal{C}}^{\mu})(\mathbf{U}_{\mathrm{R}})\right)$ is consistent with $\mathrm{L}(\mathbf{F}_{\mathcal{C}}^{\mu})\left(\mathbf{U}_f\right)+\underline{\mathrm{O}}\left(\Delta x^2\right)$.

Finally $\frac{\mathbf{H}_{i+1/2}^n-\mathbf{H}_{i-1/2}^n}{\Delta x}$ is consistent with $\partial_x\,\mathrm{L}(\mathbf{F}_{\mathcal{C}}^{\mu})(\mathbf{U}_i)+\underline{\mathrm{O}}\left((1+\frac{\mathscr{E}_0}{\mathrm{M}}+\frac{\mathrm{M}}{\mathscr{E}_0})\Delta x\right)$. Thus we have found that the smooth solution $\mathbf{U}(x,\,t)$ verified the PDE $\forall x_i,\,t^n$:

$$\mathrm{St_r}\,\partial_t\,\mathbf{U}_i^n+\partial_x\,\mathrm{L}(\mathbf{F}_{\mathcal{C}}^{\mu})\left(\mathbf{U}_i^n\right)=\underline{\mathrm{O}}\left(\mathrm{St_r}\,\Delta t\right)+\underline{\mathrm{O}}\left((1+\frac{\mathscr{E}_0}{\mathrm{M}}+\frac{\mathrm{M}}{\mathscr{E}_0})\Delta x\right). \tag{2.139}$$

Truncation Error of the Acoustic Subsystem

Keeping the same notations than previously, the non-dimensional relaxation flux for the acoustic subsystem writes:

$$\begin{aligned}\mathbf{H_{ac}}_f^n&=\left(1-\mathscr{E}_0^2\right)\begin{bmatrix}0\\ \Pi_{\mathcal{A}}^*\\ \Pi_{\mathcal{A}}^*\,u_{\mathcal{A}}^*\end{bmatrix}\\&=\left(1-\mathscr{E}_0^2\right)\left(\begin{bmatrix}0\\ \frac{1}{\mathrm{M}^2}\frac{p_{\mathrm{R}}+p_{\mathrm{L}}}{2}\\ \frac{p_{\mathrm{R}}\,u_{\mathrm{R}}+p_{\mathrm{L}}\,u_{\mathrm{L}}}{2}\end{bmatrix}-\begin{bmatrix}0\\ \frac{1}{\mathrm{M}}\frac{a_{\mathcal{A}}}{2}\left(u_{\mathrm{R}}-u_{\mathrm{L}}\right)\\ \frac{\mathrm{M}\,a_{\mathcal{A}}}{4}\left(u_{\mathrm{R}}^2-u_{\mathrm{L}}^2\right)+\frac{1}{4}\frac{1}{\mathrm{M}\,a_{\mathcal{A}}}\left(p_{\mathrm{R}}^2-p_{\mathrm{L}}^2\right)\end{bmatrix}\right),\\&\text{with: }a_{\mathcal{A}}=\mathrm{K}\cdot\max\left(\rho_{\mathrm{L}}\,c_{\mathcal{A}}(\rho_{\mathrm{L}},\,p_{\mathrm{L}}),\,\rho_{\mathrm{R}}\,c_{\mathcal{A}}(\rho_{\mathrm{R}},\,p_{\mathrm{R}})\right),\ \mathrm{K}>1.\end{aligned} \tag{2.140}$$

It is easy to check that

$$\left(1-\mathscr{E}_0^2\right)\begin{bmatrix}0\\ \frac{1}{\mathrm{M}^2}\frac{p_{\mathrm{R}}+p_{\mathrm{L}}}{2}\\ \frac{p_{\mathrm{R}}\,u_{\mathrm{R}}+p_{\mathrm{L}}\,u_{\mathrm{L}}}{2}\end{bmatrix}, \tag{2.141}$$

is consistent with

$$\left(1-\mathscr{E}_0^2\right)\begin{bmatrix}0\\ \frac{p_f}{\mathrm{M}^2}\\ p_f\,u_f\end{bmatrix}+\begin{bmatrix}0\\ \mathrm{O}\left((1-\mathscr{E}_0^2)(\Delta x/\mathrm{M})^2\right)\\ \mathrm{O}\left((1-\mathscr{E}_0^2)\Delta x^2\right)\end{bmatrix}. \tag{2.142}$$

Besides,

$$-\left(1-\mathscr{E}_0^2\right)\begin{bmatrix}0\\ \frac{1}{\mathrm{M}}\frac{a_{\mathcal{A}}}{2}\left(u_{\mathrm{R}}-u_{\mathrm{L}}\right)\\ \frac{\mathrm{M}\,a_{\mathcal{A}}}{4}\left(u_{\mathrm{R}}^2-u_{\mathrm{L}}^2\right)+\frac{1}{4}\frac{1}{\mathrm{M}\,a_{\mathcal{A}}}\left(p_{\mathrm{R}}^2-p_{\mathrm{L}}^2\right)\end{bmatrix}, \tag{2.143}$$

is consistent with

$$-\left(1-\mathscr{E}_0^2\right)\frac{\Delta x}{2}\begin{bmatrix}0\\ \frac{1}{\mathrm{M}}a_f\partial_x\,u_{|f}\\ \mathrm{M}\,a_f\,u_f\partial_x\,u_{|_f}+\frac{1}{\mathrm{M}\,a_f}\,p_f\partial_x\,p_{|f}\end{bmatrix}+\begin{bmatrix}0\\ \mathrm{O}\left(\frac{(1-\mathscr{E}_0^2)}{\mathrm{M}}\Delta x^2\right)\\ \mathrm{O}\left((1-\mathscr{E}_0^2)(\mathrm{M}+\frac{1}{\mathrm{M}})\Delta x^2\right)\end{bmatrix}_f. \tag{2.144}$$

Finally, one obtains at order one in space:

$$\mathbf{H_{ac}}_f^n=\left(1-\mathscr{E}_0^2\right)\begin{bmatrix}0\\ \frac{p_f}{\mathrm{M}^2}\\ p_f\,u_f\end{bmatrix}+\begin{bmatrix}0\\ \mathrm{O}\left(\frac{(1-\mathscr{E}_0^2)}{\mathrm{M}}\Delta x\right)\\ \mathrm{O}\left((1-\mathscr{E}_0^2)(\mathrm{M}+\frac{1}{\mathrm{M}})\Delta x\right)\end{bmatrix}_f. \tag{2.145}$$

Thus we have found that the smooth solution $\underline{\mathrm{U}}(x,\,t)$ verified the PDE $\forall x_i,\,t^n$:

$$\begin{aligned}&\mathrm{St_r}\,\partial_t\,\rho=\mathrm{O}(\mathrm{St_r}\,\Delta t),\\&\mathrm{St_r}\,\partial_t\left(\rho\,u\right)+\partial_x\left((1-\mathscr{E}_0^2(t))\,p\right)=\mathrm{O}(\mathrm{St_r}\,\Delta t)+\mathrm{O}\left(\frac{(1-\mathscr{E}_0^2)}{\mathrm{M}})\Delta x\right),\\&\mathrm{St_r}\,\partial_t\left(\rho\,e\right)+\partial_x\left((1-\mathscr{E}_0^2(t))\,p\,u\right)=\mathrm{O}(\mathrm{St_r}\,\Delta t)+\mathrm{O}\left((1-\mathscr{E}_0^2)(\mathrm{M}+\frac{1}{\mathrm{M}})\Delta x\right).\end{aligned} \tag{2.146}$$

Truncation Error of the Acoustic Subsystem with low-Mach Correction

Endowed with the low-Mach correction described in equation (2.72), the acoustic flux at face x_f reads:

$$\begin{aligned}\mathbf{H_{ac}}_f^n &= \left(1-\mathscr{C}_0^2\right)\begin{bmatrix}0\\ \Pi^*\\ \Pi^*\,u^*\end{bmatrix}\\ &= \left(1-\mathscr{C}_0^2\right)\left(\begin{bmatrix}0\\ \frac{1}{\mathrm{M}^2}\frac{\Pi_\mathrm{R}+\Pi_\mathrm{L}}{2}\\ \frac{\Pi_\mathrm{R}\,u_\mathrm{R}+\Pi_\mathrm{L}\,u_\mathrm{L}}{2}\end{bmatrix}-\begin{bmatrix}0\\ \frac{\theta}{\mathrm{M}}\frac{a_\mathcal{A}}{2}\left(u_\mathrm{R}-u_\mathrm{L}\right)\\ \frac{\mathrm{M}\theta\,a_\mathcal{A}}{4}\left(u_\mathrm{R}^2-u_\mathrm{L}^2\right)+\frac{1}{4}\frac{1}{\mathrm{M}\,a_\mathcal{A}}\left(\Pi_\mathrm{R}^2-\Pi_\mathrm{L}^2\right)\end{bmatrix}\right).\end{aligned} \tag{2.147}$$

The correction part is now consistent with:

$$-(1-\mathscr{C}_0^2)\frac{\Delta x}{2}\begin{bmatrix}0\\ \frac{\theta_f}{\mathrm{M}}a_f\partial_x u_{|f}\\ \mathrm{M}\theta_f\,a_f\,u_f\partial_x u_{|_f}+\frac{1}{\mathrm{M}\,a_f}\,p_f\partial_x p_{|f}\end{bmatrix}+\begin{bmatrix}0\\ \mathrm{O}\left(\frac{(1-\mathscr{C}_0^2)\theta}{\mathrm{M}}\Delta x^2\right)\\ \mathrm{O}\left((1-\mathscr{C}_0^2)(\mathrm{M}\theta+\frac{1}{\mathrm{M}})\Delta x^2\right)\end{bmatrix}_f.$$

At first order w.r.t Δx:

$$\mathbf{H_{ac}}_f^n = \left(1-\mathscr{C}_0^2\right)\begin{bmatrix}0\\ \frac{p_f}{\mathrm{M}^2}\\ p_f\,u_f\end{bmatrix}+\begin{bmatrix}0\\ \mathrm{O}\left(\frac{(1-\mathscr{C}_0^2)\theta}{\mathrm{M}}\Delta x\right)\\ \mathrm{O}\left((1-\mathscr{C}_0^2)(\mathrm{M}\theta+\frac{1}{\mathrm{M}})\Delta x\right)\end{bmatrix}_f. \tag{2.148}$$

For a smooth solution $\underline{\mathrm{U}}(x,t)$, the truncation error analysis made on the acoustic scheme with low-Mach correction gives $\forall x_i,\, t^n$:

$$\begin{aligned}&\mathrm{St_r}\,\partial_t\rho = \mathrm{O}(\mathrm{St_r}\,\Delta t),\\ &\mathrm{St_r}\,\partial_t(\rho\,u)+\partial_x\left((1-\mathscr{C}_0^2(t))\,p\right) = \mathrm{O}(\mathrm{St_r}\,\Delta t)+\mathrm{O}\left(\frac{(1-\mathscr{C}_0^2)\theta}{\mathrm{M}})\Delta x\right),\\ &\mathrm{St_r}\,\partial_t(\rho\,e)+\partial_x\left((1-\mathscr{C}_0^2(t))\,p\,u\right) = \mathrm{O}(\mathrm{St_r}\,\Delta t)+\mathrm{O}\left((1-\mathscr{C}_0^2)(\mathrm{M}\theta+\frac{1}{\mathrm{M}})\Delta x\right).\end{aligned} \tag{2.149}$$

2.8 References

[1] R. Baraille, G. Bourdin, F. Dubois, and A. Y. Le Roux. Une version à pas fractionnaires du schéma de Godunov pour l'hydrodynamique. *Compte Rendu de l'Académie des Sciences*, 314: 147–152, 1992. 27, 30, 33

[2] M. Baudin, C. Berthon, F. Coquel, R. Masson, and Q. H. Tran. A relaxation method for two-phase flow models with hydrodynamic closure laws. *Numerische Mathematik*, 99:411–440, 2005. 31, 35, 40, 42, 43

[3] M. Baudin, F. Coquel, and Q. H. Tran. A semi-implicit relaxation scheme for modelling two-phase flow in a pipeline. *SIAM Journal of Scientific Computing*, 27:914–936, 2005. 40

[4] F. Bouchut. Entropy satisfying flux vector splittings and kinetic BGK models. *Numerische Mathematik*, 94:623–672, 2003. 31

[5] F. Bouchut. *Nonlinear Stability of Finite Volume Methods for Hyperbolic Conservation Laws*. Birkäser, 2004. 27, 35, 37, 41, 43

[6] F. Bouchut. A reduced stability condition for nonlinear relaxation to conservation laws. *Journal of Hyperbolic Differential Equations*, 1:149–170, 2004. 37

[7] T. Buffard and J-M. Hérard. A conservative fractional step method to solve non-isentropic Euler equations. *Computer Methods in Applied Mechanics and Engineering*, 144:199–225, 1996. 30, 33

[8] T. Buffard, T. Gallouët, and J-M. Hérard. A sequel to a rough Godunov scheme: application to real gases. *Computer & Fluids*, 29:813–847, 2000. 59

[9] C. Chalons and J.F. Coulombel. Relaxations approximation of the Euler equations. *Journal of Mathematical Analysis and Applications*, 348:872–893, 2008. 37, 38

[10] C. Chalons, M. Girardin, and S. Kokh. An all-regime Lagrange-Projection like scheme for the gas dynamics equations on unstructured meshes. *Communications in Computational Physics*, 20:188–233, 2016. 27, 30, 31, 35, 37, 41, 44, 45, 49, 50, 57, 67

[11] C. Chalons, M. Girardin, and S. Kokh. An all-regime Lagrange-Projection like scheme for 2D homogeneous models for two-phase flows on unstructured meshes. *Journal of Computational Physics*, 335:885–904, 2016. 30

[12] G. Q. Chen, C. D. Levermore, and T.-P. Liu. Hyperbolic conservation laws with stiff relaxation terms and entropy. *Communications on Pure and Applied Mathematics*, 47:787–830, 1994. 31, 35, 37

[13] F. Coquel, E. Godlewski, B. Perthame, A. In, and P. Rascle. Some new Godunov and relaxation methods for two-phase flow problems. *Kluwer Academic/Plenum Publishers (New York)*, pages 179–188, 2001. 37

[14] F. Coquel, Q. L. Nguyen, M. Postel, and Q. H. Tran. Entropy-satisfying relaxation method with large time-steps for Euler IBVPS. *Mathematics of Computation*, 79:1493–1533, 2010. 27, 33, 37, 38, 40, 44, 57

[15] F. Coquel, E. Godlewski, and N. Seguin. Relaxation of fluid systems. *Mathematical Models and Methods in Applied Science*, 22:43–95, 2012. 31, 35, 37

[16] S. Dallet. *Simulation numérique d'écoulements diphasiques en régime compressible ou à faible nombre de Mach*. PhD thesis, Aix-Marseille Université, 2017. 42

[17] P. Degond and M. Tang. All speed scheme for the low Mach number limit of the isentropic Euler equation. *Communications in Computational Physics*, 10:1–31, 2011. 30

[18] S. Dellacherie. Analysis of Godunov type schemes applied to the compressible Euler system at low Mach number. *Journal of Computational Physics*, 229:978–1016, 2009. 30, 44, 47

[19] S. Dellacherie, P. Omnes, and F. Rieper. The influence of cell geometry on the Godunov scheme applied to the linear wave equation. *Journal of Computational Physics*, 229:5315–5338, 2010.

[20] S. Dellacherie, P. Omnes, J. Jung, and P.A. Raviart. Construction of modified Godunov type schemes accurate at any Mach number for the compressible Euler system. *Mathematical Models and Methods in Applied Science*, 26:2525–2615, 2016. 27, 30, 31, 44, 47, 51

[21] G. Dimarco, R. Loubère, and M-H. Vignal. Study of a new asymptotic preserving scheme for the Euler system in the low Mach number limit. *SIAM: Journal of Scientific Computing*, 39: 2099–2128, 2017. 30, 33, 52

[22] P. Fillion, A. Chanoine, S. Dellacherie, and A. Kumbaro. FLICA-OVAP: A new platform for core thermal–hydraulic studies. *Nuclear Engineering and Design*, 241:4348–4358, 2011. 27, 30, 47

[23] T. Gallouët, J-M Hérard, and N. Seguin. Some recent finite volume schemes to compute Euler equations using real gas EOS. *International Journal for Numerical Methods in Fluids*, 39: 1073–1138, 2002. 51

[24] T. Gallouët, J-M Hérard, and N. Seguin. Numerical modeling of two-phase flows using the two-fluid two-pressure approach. *Mathematical Models and Methods in Applied Sciences*, 14: 663–700, 2004. 34, 35

[25] M. Girardin. *Asymptotic preserving and all-regime Lagrange-Projection like numerical schemes: application to two-phase flows in low Mach regime*. PhD thesis, Université Pierre et Marie Curie, https://tel.archives-ouvertes.fr/tel-01127428, 2015. 35, 38, 40, 41, 44, 47, 48, 49, 51, 55

[26] E. Godlewski and P.A. Raviart. *Numerical Approximation of Hyperbolic Systems of Conservation Laws*. Springer, 1996. 32

[27] H. Guillard and A. Murrone. On the behavior of upwind schemes in the low Mach number limit: II Godunov type schemes. *Computers and Fluids*, 33:655–675, 2004. 30

[28] H. Guillard and C. Viozat. On the behavior of upwind schemes in the low Mach number limit. *Computers and Fluids*, 28:63–86, 1999. 30

[29] J. Haack, S. Jin, and J. G. Liu. An all-speed asymptotic-preserving method for the isentropic Euler and Navier-Stokes equations. *Communications in Computational Physics*, 12:955–980, 2012. 30

[30] A. Harten, P. D. Lax, and B. Van Leer. On upstream differencing and Godunov-type schemes for hyperbolic conservation laws. *SIAM Review*, 25:35–61, 1983. 48

[31] D. Iampietro, F. Daude, P. Galon, and J. M. Hérard. A weighted splitting approach for low-Mach number flows. *Finite Volumes for Complex Applications VIII-Hyperbolic, Elliptic and Parabolic Problems: FVCA 8*, 200, 2017. 40, 57

[32] D. Iampietro, F. Daude, P. Galon, and J. M. Hérard. A Mach-sensitive implicit-explicit scheme adapted to compressible multi-scale flows. *Journal of Computational and Applied Mathematics*, 340:122–150, 2018. 30, 40, 57

[33] S. Jin and Z.-P. Xin. The relaxation schemes for systems of conservation laws in arbitrary dimensions. *Communications on Pure and Applied Mathematics*, 48:235–276, 1995. 31, 35

[34] S. Noelle, G. Bispen, K. R. Arun, M. Lukáčová-Medvid'ová, and C. D. Munz. A weakly asymptotic preserving low Mach number scheme for the Euler equations of gas dynamics. *SIAM Journal on Scientific Computing*, 36:B989–B1024, 2014. 30

[35] F. Rieper. A low-Mach number fix for Roe's approximate Riemann solver. *Journal of Computational Physics*, 230:5263–5287, 2011. 27, 30, 31, 47

[36] S. Schochet and G. Metivier. Fast singular limits of hyperbolic PDEs. *Journal of Differential Equations*, 114:476–512, 1994. 30

[37] S. Schochet and G. Metivier. Limite incompressible des équations d' Euler non-isentropiques. *Preprint, https://www.math.u-bordeaux.fr/ gmetivie/Preprints.html*, 2000. 30

[38] S. Schochet and G. Metivier. The incompressible limit of Euler non-isentropic equations. *Archive for Rational Mechanics and Analysis*, 158:61–90, 2001. 47

[39] A. R. Simpson. *Large water hammer pressures due to column separation in sloping pipes*. PhD thesis, Diss. University of Michigan, 1986. 29

[40] J. Smoller. *Shock Waves and Reaction-Diffusion Equations*. Springer-Verlag, 1994. 32

[41] G. A. Sod. *Numerical Methods in Fluid Dynamics, Initial and Initial-boundary Value Problems*. Cambridge University Press, 1985. 27, 49

[42] I. Suliciu. On the thermodynamics of fluids with relaxation and phase transitions. *International Journal of Engineering Science*, 36:921–947, 1998. 27, 31, 35

[43] E.F. Toro. *Riemann Solvers and Numerical Methods for Fluid Dynamics*. Springer, 1999. 52

[44] J. B. Whitham. *Linear and Non Linear Waves*. John Wiley & Sons Inc, 1974. 37

Chapitre 3

Un schéma implicite-explicite adapté aux écoulements compressibles multi-régimes

Sur la base de l'approche à pas fractionnaires développée précédemment, ce chapitre est dédié à la construction d'un schéma implicite-explicite adapté à la transition entre différents régimes d'écoulement pour un modèle diphasique homogène. On souhaite notamment que le schéma numérique proposé puisse suivre précisément, au cours du même scénario d'écoulement basse vitesse, des ondes matérielles lentes puis des ondes de choc très rapides associées à des sauts de pression de grande amplitude.

Pour ce faire, un schéma de relaxation explicite en temps est appliqué au sous-système convectif $\mathcal{C}$ tandis qu'une technique d'intégration implicite est développée pour le sous système acoustique $\mathcal{A}$. Cette technique d'intégration est construite en adaptant les idées développées dans [8, 11]. Ces idées sont basées sur les équations de transport relatives à deux invariants de Riemann *forts* obtenues à partir du sous-système $\mathcal{A}$ par une technique de relaxation de type Suliciu [36].

Une fois le schéma implicite-explicite complètement défini, une étude heuristique, basée sur la propagation d'ondes de contact isolées, propose d'évaluer les contraintes de stabilité de l'approche. Cette étude suggère que, pour tout nombre de Mach, la méthode développée est stable pour des valeurs de nombre de Courant basé sur les vitesses d'ondes matérielles de l'ordre de 0.5.

Afin de traiter l'apparition soudaine de sauts de pression de grande amplitude au sein d'un écoulement compressible étant uniformément à basse vitesse, la définition du paramètre $\mathscr{E}_0 \in]0, 1]$ est enrichie afin d'y inclure un détecteur de choc. Le rôle d'un tel détecteur est de faire tendre $\mathscr{E}_0$ vers 1 lorsqu'une variation de pression de grande amplitude traverse l'écoulement. Une telle évolution des valeurs prises par $\mathscr{E}_0$ engendre alors simultanément deux changements au sein de l'approche proposée. Premièrement, l'intégration implicite en temps des contributions liées au gradient de pression du sous-système $\mathcal{A}$ disparait au profit d'un solveur de relaxation complètement explicite en temps, consistant avec le système d'Euler complet. Le deuxième changement vient du fait que le pas de temps discret utilisé pour ce type de scénario de transition est construit sur la base des valeurs propres du sous-système convectif $\mathcal{C}$:

$$\begin{aligned} &\Delta t = \mathscr{C}_{\mathcal{C}} \frac{\Delta x}{|\mathbf{u}| + \mathscr{E}_0 \, c_{\mathcal{C}}}, \ \mathscr{C}_{\mathcal{C}} \approx 1/2, \\ &\lim_{\mathscr{E}_0 \to 1} c_{\mathcal{C}} = c. \end{aligned} \tag{3.1}$$

Ainsi, lors de l'activation du détecteur de choc, le pas de temps initialement basé sur la vitesse matérielle $|\mathbf{u}|$ (car $\mathscr{E}_0 \ll 1$), s'adapte automatiquement pour prendre des valeurs similaires à celui construit à partir des valeurs propres du système d'Euler complet.

La capacité de la méthode proposée à saisir la transition entre un régime d'écoulement privilégiant les ondes matérielles lentes et un régime où des sauts de pression de grande amplitude se

propagent très rapidement est alors testée pour un fluide dense doté d'une loi d'état de type gaz raide. Un des cas tests est construit comme la succession de deux problèmes de Riemann produisant des échelles très différentes de pression et de vitesse intermédiaires au sein d'un écoulement à faible nombre de Mach. Contrairement à la méthode semi-implicite de type Lagrange-Projection [8, 11], l'approche proposée dans ce chapitre parvient à capturer avec un niveau de détail suffisant l'ensemble des états intermédiaires créés.

Les travaux présentés dans ce chapitre ont été acceptés pour publication dans la revue *Journal of Computational and Applied Mathematics* sous la référence :

D. Iampietro, F. Daude, P. Galon, and J. M. Hérard. A Mach-sensitive implicit-explicit scheme adapted to compressible multi-scale flows. *Journal of Computational and Applied Mathematics*, 340 : 122–150, 2018.

Sommaire

A Mach-sensitive implicit-explicit scheme adapted to compressible multi-scale flows

D. Iampietro[a, b, e], F. Daude[a,b], P. Galon[b,c], J. M. Hérard[d,e]

[a]EDF R&D, Département ERMES, 7 Boulevard Gaspard Monge, 91120 Palaiseau, France
[b]IMSIA, UMR EDF/CNRS/CEA/ENSTA 9219, Université Paris-Saclay, 828 Boulevard des Maréchaux, 91762 Palaiseau Cedex, France
[c]CEA, DEN, DANS, DM2S, SEMT, DYN, F-91191 Gif-sur-Yvette, France
[d]EDF R&D, Département MFEE, 6 Quai Watier, F-78401 Chatou, France
[e]I2M, UMR CNRS 7373, Technopôle Château-Gombert, 39 rue F. Joliot Curie, F-13453 Marseille, France

Abstract

The method presented below focuses on the numerical approximation of the Euler compressible system. It pursues a two-fold objective: being able to accurately follow slow material waves as well as strong shock waves in the context of low Mach number flows. The resulting implicit-explicit fractional step approach leans on a dynamic splitting designed to react to the time fluctuations of the maximal flow Mach number. When the latter rises suddenly, the IMEX scheme, so far driven by a material-wave Courant number, turn into a time-explicit approximate Riemann solver constrained by an acoustic-wave Courant number. It is also possible to enrich the dynamic splitting in order to capture high pressure jumps even when the flow Mach number is low. One-dimensional low Mach number test cases involving single or multiple waves confirm that the present approach is as accurate and efficient as an IMEX Lagrange-Projection method. Besides, numerical results suggest that the stability of the present method holds for *any Mach number* if the Courant number related to the *convective* subsystem arising from the splitting is of order unity.

3.1 Introduction

The present work deals with the construction of a time implicit-explicit scheme providing a sketch of answer to cope with multi-scale wave scenarios and more specifically with what is called a *condensation induced water hammer* (CIWH).
Indeed, in the very first instants of this phenomenon, one is interested in following a slow interface between hot vapor and cooler liquid water. Since the speed of such a material wave is of the order of 1 $m.s^{-1}$, which is considerably smaller than the acoustic wave speeds in both phases, the interface dynamics is typical of low Mach number flows. Nonetheless, as time goes on, shear instabilities and steep temperature gradients entail the trapping and then the sudden condensation of vapor pockets. This leads finally to the production of strong shock waves in the liquid phase.
The objective is thus to design a numerical scheme accurate for material waves in a low Mach number flow while being able to capture high pressure gradients.
On one hand, fulfilling both aims might seem contradictory if one considers the Euler or Navier-Stokes incompressible systems since their divergence-free constraint prohibits any compressible effects and hence the occurrence of compressive shock waves. On the other hand, the pioneering works of Joukowski [27] and Allievi [1] state that, at constant temperature, pressure jumps in a low Mach number compressible flow are given by: $\Delta p = \rho^0 c^0 \Delta u$; with ρ^0 (respectively c^0) the constant density (respectively the constant speed of sound) of the fluid. See also [18] for a review of the water hammer theory. Thus, in the case of liquid water, at 295 K, $\rho^0 \approx 10^3\ kg.m^{-3}$, $c^0 \approx 1.5 \times 10^3\ m.s^{-1}$. If one assumes that $\Delta u \approx 1\ m.s^{-1}$, pressure jumps amplitude is of 15 bar which is the order of magnitude observed experimentally in [35].

From a numerical point of view, different strategies have been adopted in order to be accurate on slow material waves in the case of low Mach number flows. Preconditioning methods stemming from [37] and improved in [20, 21, 32] aim at modifying the Jacobian eigenvalues of hyperbolic systems in order to get rid of their constraining acoustic part. Asymptotic preserving schemes (AP

schemes), introduced by Jin in [26], are based on the identification of a non-stiff and a stiff part of hyperbolic systems. The latter is then discretized using a time-implicit method which allows the scheme to be consistent, for fixed time and space-steps, with a targeted asymptotic discrete solver as a scale parameter tends towards zero. Recently in [14, 16, 22, 33], different kinds of AP schemes have been derived to seize the incompressible limit of the Euler or the Navier-Stokes system as the flow Mach number tends towards zero. It results in an implicit-explicit (IMEX) algorithm providing a time-implicit discretization for the hydrodynamic pressure gradient, and a time-explicit discretization for the convective terms. Besides, if one considers the Courant number $\mathscr{C}$ based on the slowest material waves of the flow, a key property for the above AP schemes is also to remain stable for $\mathscr{C} \approx 1$ at any Mach number. This typical issue has been explored using the "modified equation" tools as well as the spectral theory by Noelle an his collaborators in [34, 40]. See also [39] in which the AP property as well as the Mach-uniform stability property has been proved for a Lagrange-Projection method described in [8].
If the Mach number flow is small, the above strategies produce satisfying results when one seeks to seize the slow material waves dynamics as well as the pressure incompressible profile. However, no satisfying solution has been yet found in order to dynamically capture strong shock waves if they suddenly appear in such a configuration.

Continuing ideas suggested in [11, 24, 25], the present work derives an IMEX scheme based on a Mach-sensitive splitting of the Euler system. Such a splitting stems from the pioneering work of Baraille *et al.* [4] extended by Buffard *et al.* [7]. Contrary to [4, 7, 8, 16], the splitting evolves dynamically in time thanks to a parameter measuring *a priori* the instantaneous maximal Mach number of the flow. It results in a dynamically Weighted Fractional Step Approach (WFSA) enabling to cope with a wide panel of situations. Indeed, in the context of a low Mach number flow, starting from a completely decoupled IMEX formulation with $\mathscr{C} \approx 1$, it offers the possibility to retrieve a time-explicit Godunov-like solver for the overall Euler system if a sudden rise of the Mach number is detected. The CFL condition adapts itself and is re-based on the fastest physically relevant wave speed, *i.e.* the acoustic one. Thus, if this rise of the Mach number is associated with the production of shock waves, they will be optimally captured. What is more, the temporal splitting parameter can be enriched by a simple "shock detector" ensuring that a time-explicit solver is recovered when high amplitude shock waves arise *even if* the material velocity is low. Then, strong water hammer pressure jumps occurring in low Mach number flows can also be handled.

The second section of this article is a condensed presentation of the Mach-sensitive splitting fully described in [24, 25]. The readers are notably referred to this work for the construction of a time-explicit scheme for both convective and acoustic parts of the Mach-sensitive splitting. Hence, the third and the fourth section of the present manuscript are entirely dedicated to the study and then the derivation of a time-implicit scheme related to the acoustic part of the splitting. It leans on the relaxation schemes theory and particularly on a Suliciu-like relaxation procedure detailed in [6, 11, 12, 36]. The fifth section aggregates four types of one-dimensional numerical results. A first part briefly describes the effect of the Courant number when an IMEX scheme is triggered on isolated shock or contact waves in the context of a low Mach number flow. Secondly, the accuracy and the efficiency of the present approach are compared with the Lagrange-Projection fractional step method described in [8]. This comparative study is based on a low-Mach shock tube test case in which pressure fluctuations remain small. Thirdly a double Riemann problem involving a stiffened gas equation of state is examined. It aims at modeling the occurrence of water hammers in a low-Mach number flow. Finally, in the last part of the numerical results, the ability of the proposed IMEX scheme to deal with very specific low-velocity flow regimes is assessed. It focuses on the capture of constant states initially perturbed by small amplitude acoustic waves as well as the capacity to compute weakly compressible approximate solutions.

3.2 A Mach-Sensitive Fractional Step Approach

The present work focuses on the Euler compressible system. However its extension to the two-phase Homogeneous Equilibrium Model (HEM, [10]) in which both phases have the same velocity $\mathbf{u}$, pressure p, temperature T and chemical potential is straightforward since it results in the same conservation law structure, namely:

$$\partial_t \rho + \underline{\nabla} \cdot (\rho \mathbf{u}) = 0, \tag{3.2a}$$
$$\partial_t (\rho \mathbf{u}) + \underline{\nabla} \cdot (\rho \mathbf{u} \otimes \mathbf{u} + p \mathbf{I}) = \mathbf{0}, \tag{3.2b}$$
$$\partial_t (\rho e) + \underline{\nabla} \cdot ((\rho e + p) \mathbf{u}) = 0, \tag{3.2c}$$
$$e = \frac{|\mathbf{u}|^2}{2} + \varepsilon, \ \varepsilon = \varepsilon^{\mathrm{EOS}}(\rho, p), \tag{3.2d}$$
$$(\rho c)^2 = (\partial_p \varepsilon_{|\rho})^{-1} (p - \rho^2 \partial_\rho \varepsilon_{|p}), \tag{3.2e}$$

with ρ the density of the mixture and ε its specific internal energy. The function $\varepsilon^{\mathrm{EOS}}(.,.)$ defines the equation of state between the thermodynamic variables while c is the sound speed involved in the nonlinear wave propagation.
As described in [24, 25], it is possible to derive a scheme able to deal with highly compressible flows as well as low Mach number flows by splitting the system (3.2) into a convective ($\mathcal{C}$) and an acoustic ($\mathcal{A}$) subsystem:

$$\mathcal{C} : \begin{cases} \partial_t \rho + \underline{\nabla} \cdot (\rho \mathbf{u}) = 0, \\ \partial_t (\rho \mathbf{u}) + \underline{\nabla} \cdot \left(\rho \mathbf{u} \otimes \mathbf{u} + \mathscr{E}_0^2(t)\, p \mathbf{I}\right) = \mathbf{0}, \\ \partial_t (\rho e) + \underline{\nabla} \cdot \left((\rho e) + \mathscr{E}_0^2(t)\, p\right) \mathbf{u}\right) = 0, \end{cases} \tag{3.3}$$

$$\mathcal{A} : \begin{cases} \partial_t \rho = 0, \\ \partial_t (\rho \mathbf{u}) + \underline{\nabla} \cdot \left((1 - \mathscr{E}_0^2(t))\, p \mathbf{I}\right) = \mathbf{0}, \\ \partial_t (\rho e) + \underline{\nabla} \cdot \left((1 - \mathscr{E}_0^2(t))\, p \mathbf{u}\right) = 0. \end{cases} \tag{3.4}$$

Here, $\mathscr{E}_0(t) \in]0, 1]$ is a dynamic splitting parameter designed to be equal to one in the case of sonic or supersonic flows or equal to the maximal flow Mach number in the case of subsonic flows:

$$\begin{aligned} \mathscr{E}_0(t) &= \max\left(\mathrm{M}_{inf}, \min\left(\mathrm{M}_{max}(t), 1\right)\right), \\ \mathrm{M}_{max}(t) &= \sup_{x \in \Omega} \left(\mathrm{M}(x,t) = \frac{|u(x,t)|}{c(x,t)}\right), \end{aligned} \tag{3.5}$$

with M_{inf} a given lower bound preventing $\mathscr{E}_0(t)$ from being exactly equal to zero. As shown in [24, 25], both subsystems are hyperbolic for a stiffened gas EOS provided that the pressure remains positive throughout space and time. In one dimension, their eigenvalues are:

$$\begin{aligned} \lambda_1^{\mathcal{C}} &= u - \mathscr{E}_0\, c_{\mathcal{C}} && \leq \lambda_2^{\mathcal{C}} = u \leq \lambda_3^{\mathcal{C}} = u + \mathscr{E}_0\, c_{\mathcal{C}}, \\ \lambda_1^{\mathcal{A}} &= -\left(1 - \mathscr{E}_0^2\right) c_{\mathcal{A}} && \leq \lambda_2^{\mathcal{A}} = 0 \leq \lambda_3^{\mathcal{A}} = \left(1 - \mathscr{E}_0^2\right) c_{\mathcal{A}}, \end{aligned} \tag{3.6}$$

with $c_{\mathcal{C}}$ (respectively $c_{\mathcal{A}}$) the convective (respectively the acoustic) celerity defined by:

$$\begin{aligned} \left(\rho\, c_{\mathcal{C}}(\rho, p)\right)^2 &= (\partial_p \varepsilon_{|\rho})^{-1} \left(\mathscr{E}_0^2\, p - \rho^2 \partial_\rho \varepsilon_{|p}\right), \\ \left(\rho\, c_{\mathcal{A}}(\rho, p)\right)^2 &= (\partial_p \varepsilon_{|\rho})^{-1}\, p, \end{aligned} \tag{3.7}$$

and:

$$(c_{\mathcal{C}})^2 + \left(1 - \mathscr{E}_0^2\right) (c_{\mathcal{A}})^2 = c^2. \tag{3.8}$$

What is more, for both subsystems, the 1-wave and 3-wave are associated to genuinely non-linear fields whereas the 2-wave field is linearly degenerate.
It can be noticed that, when the Mach number is small so that $\mathscr{E}_0(t)$ is close to zero, pressure terms completely disappear from the subsystem $\mathcal{C}$ which only conserves the convective spatial operator

$\underline{\nabla} \cdot (\mathbf{u} *)$. Pressure terms are retrieved in the subsystem $\mathcal{A}$ which turns out to hold most of the acoustic effects. That is why, in the case of low Mach number flows, if the physics of interest is essentially related to material waves propagating at speed $|u| \ll c$, a time-implicit discretization will be provided for subsystem $\mathcal{A}$ while $\mathcal{C}$ will be solved with a time-explicit scheme.
Indeed, define Δx the space-step of the computational domain. If Δt is the time-step guaranteeing the stability of the numerical scheme, one can formally introduce several Courant numbers related to the above wave speeds, namely:

$$\begin{aligned}
\mathscr{C}_{\mathrm{E}} &= \frac{\Delta t}{\Delta x}(|u|+c) && \text{Euler Courant number,}\\
\mathscr{C}_{|u|} &= \frac{\Delta t}{\Delta x}|u| && \text{Convective Courant number,}\\
\mathscr{C}_{\mathcal{C}} &= \frac{\Delta t}{\Delta x}(|u|+\mathscr{E}_0\, c_{\mathcal{C}}) && \text{Courant number related to } \mathcal{C},\\
\mathscr{C}_{\mathcal{A}} &= \frac{\Delta t}{\Delta x}((1-\mathscr{E}_0^2)\, c_{\mathcal{A}}) && \text{Courant number related to } \mathcal{A}.
\end{aligned} \tag{3.9}$$

By using a time-implicit scheme for the resolution of the subsystem $\mathcal{A}$, one seeks to be relieved from most of the time-explicit stability condition: $\mathscr{C}_{\mathrm{E}} < 1$. Particularly, if the scheme allows to fulfill $\mathscr{C}_{\mathcal{C}} \approx 1$ when $\mathscr{E}_0 \ll 1$, one expects a substantial drop of the numerical diffusion holding on the material waves propagating at speed $|u|$. We refer the readers to [24, 25] for the complete study of both continuous subsystems $\mathcal{C}$ and $\mathcal{A}$ as well as the derivation of *a full time-explicit* fractional step involving relaxation schemes. A short description of the time-explicit convective flux related to the subsystem $\mathcal{C}$ is written in subsection A.
In the following, the derivation of the $\mathcal{A}$-time-implicit $\mathcal{C}$-time-explicit fractional step approach is presented. As the $\mathcal{C}$-time-explicit scheme described in [24, 25] is given in subsection A, focus is only given on the $\mathcal{A}$-time-implicit integration.

3.3 A Sulicu-like Relaxation Scheme for the Acoustic Subsystem

Let us introduce a new Suliciu-like *relaxation* subsystem $\mathcal{A}^{\mu}$ as:

$$\mathcal{A}^{\mu}: \begin{cases}
\partial_t \rho = 0,\\
\partial_t (\rho u) + \partial_x \left((1-\mathscr{E}_0^2(t))\,\Pi\right) = 0,\\
\partial_t (\rho \Pi) + \partial_x \left((1-\mathscr{E}_0^2(t))\, a_{\mathcal{A}}^2\, u\right) = \dfrac{\rho\,(p-\Pi)}{\mu},\\
\partial_t (\rho e) + \partial_x \left((1-\mathscr{E}_0^2(t))\,\Pi\, u\right) = 0,
\end{cases} \tag{3.10}$$

$$(\mathcal{A}^{\mu})^{\mathrm{NC}}: \begin{cases}
\partial_t \tau = 0,\\
\partial_t u + (1-\mathscr{E}_0^2(t))\tau\, \partial_x \Pi = 0,\\
\partial_t \Pi + (1-\mathscr{E}_0^2(t))\, a_{\mathcal{A}}^2\, \tau\, \partial_x u = \dfrac{(p-\Pi)}{\mu},\\
\partial_t e + (1-\mathscr{E}_0^2(t))\tau\, \partial_x (\Pi u) = 0.
\end{cases} \tag{3.11}$$

More details on relaxation schemes can be found in [5, 12, 36]. Moreover, the derivation of the above relaxation subsystem can be found in [24, 25]. Recall that Π is the relaxation pressure forced to converge towards the real pressure p thanks to a source term of timescale $\mu \ll 1$. Besides, $a_{\mathcal{A}}$ is a relaxation constant encapsulating the thermodynamic nonlinearity. In order to provide sufficient diffusion to the relaxation subsystem, one can exhibit (see [8, 24, 25, 38]) the following subcharacteristic condition:

$$a_{\mathcal{A}} > \rho\, c_{\mathcal{A}}. \tag{3.12}$$

Let us define $\tau = 1/\rho$ the specific volume. Using the fact that the density is independent of time, the relaxation subsystem $\mathcal{A}^\mu$ is equivalent to its non-conservative version $(\mathcal{A}^\mu)^{\mathrm{NC}}$. Then, one can easily prove that the relaxation subsystem is hyperbolic, and that its eigenvalues are:

$$\lambda_1^{\mathcal{A},\mu} = -(1-\mathscr{E}_0^2)\, a_{\mathcal{A}}\tau < \lambda_2^{\mathcal{A},\mu} = \lambda_3^{\mathcal{A},\mu} = 0 < \lambda_4^{\mathcal{A},\mu} = (1-\mathscr{E}_0^2)\, a_{\mathcal{A}}\tau. \tag{3.13}$$

Besides all its characteristic fields are linearly degenerate. Let us now introduce W and R as:

$$\begin{aligned} \mathrm{W} &= u - \Pi/a_{\mathcal{A}}, \\ \mathrm{R} &= u + \Pi/a_{\mathcal{A}}. \end{aligned} \tag{3.14}$$

It is worth noticing that the non-conservative subsystem $(\mathcal{A}^\mu)^{\mathrm{NC}}$ is equivalent to:

$$\begin{cases} \partial_t \tau = 0, \\ \partial_t \mathrm{W} + \lambda_1^{\mathcal{A},\mu}\, \partial_x \mathrm{W} = -\dfrac{(p-\Pi)}{a_{\mathcal{A}}\,\mu}, \\ \partial_t \mathrm{R} + \lambda_4^{\mathcal{A},\mu}\, \partial_x \mathrm{R} = \dfrac{(p-\Pi)}{a_{\mathcal{A}}\,\mu}, \\ \partial_t e + (1-\mathscr{E}_0^2(t))\tau\, \partial_x (\Pi\, u) = 0. \end{cases} \tag{3.15}$$

with $u(\mathrm{W},\mathrm{R}) = (\mathrm{R}+\mathrm{W})/2$ and $\Pi(\mathrm{W},\mathrm{R}) = a_{\mathcal{A}}\,(\mathrm{R}-\mathrm{W})/2$. Thus, W (respectively R) is constant along the 1-characteristic curves (respectively the 4-characteristic curves). What is more, it is a 1-strong Riemann invariant (respectively a 4-strong Riemann invariant) meaning that it is constant through the 2,3 and 4 waves (respectively the 1 and 2,3 waves). In Figure 3.1 the domains of invariance of R and W are drawn.

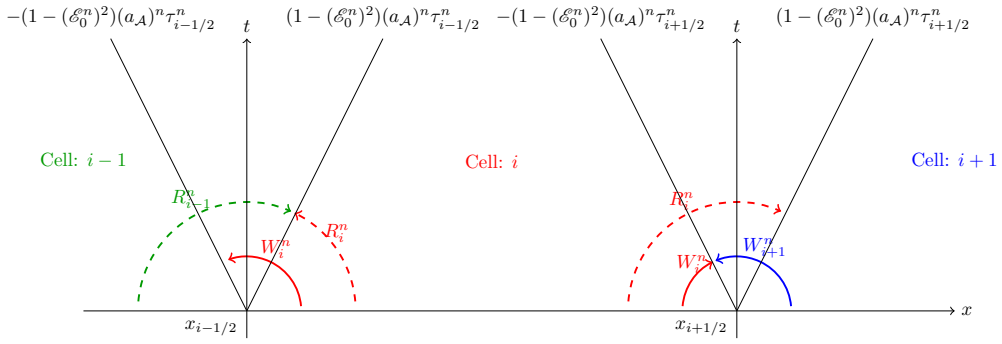

Figure 3.1 – Strong Riemann Invariants Behaviors

As already noticed in [11, 19], if one formally removes the relaxation terms $\pm(p-\Pi)/(a_{\mathcal{A}}\,\mu)$ from the PDEs (3.15), the dynamics of W and R become totally uncoupled. Besides the energy flux depends only on these two quantities since according to equation (3.14):

$$\Pi\, u = \frac{a_{\mathcal{A}}}{4}\left(\mathrm{R}^2 - \mathrm{W}^2\right). \tag{3.16}$$

In the next subsection, the time-implicit scheme for the subsystem $\mathcal{A}$ is derived. It is based on the discretization of the simple transport dynamics of the quantities W and R.

3.4 The Acoustic Time-Implicit Scheme

This section focuses on the space and time discretization of the acoustic subsystem $\mathcal{A}$. It is split in three parts. Section 3.4.1 and Section 3.4.2 provide the way to derive the time-implicit acoustic flux. Section 3.4.3 points out some properties of the overall IMEX scheme while Section 3.4.4 concentrates of the discrete time-step construction.

3.4.1 A One-dimensional Implicit-Solver for the Evolution Step

The numerical resolution of the acoustic relaxation subsystem $\mathcal{A}^{\mu}$ is split into two steps: the first one, sometimes called *the evolution step* corresponds to the resolution of the *homogeneous* subsystem where the term $(p-\Pi)/\mu$ has been removed. It becomes active afterwards in an additional step which consists in solving:

$$\partial_t \Pi = \left(p-\Pi\right)/\mu. \tag{3.17}$$

However, in the present approach, the relaxation pressure Π is relaxed instantaneously. Then, $\mu = 0$ and the resolution of Eq (3.17) is replaced by the *projection onto the equilibrium manifold*:

$$\left\{\mathbf{W} = \left[\rho, \rho u, \rho\Pi, \rho e\right]^{\mathrm{T}},\ \varepsilon = e - u^2/2,\ \text{s.t. } p(\rho,\varepsilon) = \Pi\right\}. \tag{3.18}$$

For the sake of simplicity, this second step is called the *projection step*.
Suppose that the computational domain $\Omega = [0, \mathrm{L}]$ is made of N_{cells} cells. Let us define $\Delta x = \mathrm{L}/\mathrm{N}_{cells}$ (respectively Δt) the space-step (respectively the time-step) of the scheme.
For $i \in [1,..,\mathrm{N}_{cells}]$ let us set $x_i = (i-1/2)\Delta x$, the coordinate of the cell center i and $x_{i+1/2} = x_i + \Delta x/2$, the coordinate of face $i+1/2$. Finally define $\Omega_i =]x_{i-1/2}, x_{i+1/2}[$. Suppose that at time t^{n+}, the set of states $\mathbf{U}_i^{n+} = \left[\rho_i^{n+}, (\rho u)_i^{n+}, (\rho e)_i^{n+}\right]^{\mathrm{T}}$, $i \in [1,..,\mathrm{N}_{cells}]$ produced after the resolution of the *convective* subsystem $\mathcal{C}$ is provided to $\mathcal{A}^{\mu}$ as an initial piece-wise constant datum on $\sqcup_{i=1}^{\mathrm{N}_{cells}} \Omega_i$. Then, by averaging the W-equation and the R-equation in (3.15) over $\Omega_i \times]t^{n+}, t^{\tilde{n}} > t^{n+}[$ one obtains:

$$\begin{aligned}
&\frac{\mathrm{W}_i^{\tilde{n}} - \mathrm{W}_i^{n+}}{\Delta t} - \frac{\left(1-(\mathscr{E}_0^n)^2\right)(a_{\mathcal{A}})^{n+}\tau_i^{n+}}{\Delta x}\left(\mathrm{W}_{i+1/2}(t^n, t^{n+}) - \mathrm{W}_{i-1/2}(t^n, t^{n+})\right) = 0,\\
&\frac{\mathrm{R}_i^{\tilde{n}} - \mathrm{R}_i^{n+}}{\Delta t} + \frac{\left(1-(\mathscr{E}_0^n)^2\right)(a_{\mathcal{A}})^{n+}\tau_i^{n+}}{\Delta x}\left(\mathrm{R}_{i+1/2}(t^n, t^{n+}) - \mathrm{R}_{i-1/2}(t^n, t^{n+})\right) = 0,
\end{aligned} \tag{3.19}$$

with W_i^{n+} the spatial average over Ω_i at time t^{n+},

$$\mathrm{W}_{i+1/2}(t^n, t^{n+}) = \left(1/(t^{\tilde{n}} - t^{n+})\right) \times \int_{t^{n+}}^{t^{\tilde{n}}} \mathrm{W}(x_{i+1/2}/t)\, dt, \tag{3.20}$$

and $(a_{\mathcal{A}})^{n+} = \mathrm{K} \max\limits_{i\in[1,\mathrm{N}_{cells}]}\left(\rho_i^{n+}(c_{\mathcal{A}})_i^{n+}\right)$, $\mathrm{K} > 1$, the discrete acoustic relaxation constant fulfilling inequality (3.12) throughout the whole computational domain. Eventually the Mach-sensitive discrete parameter, built using the initial states $\mathbf{U}_i^n$, $i \in [1,..,\mathrm{N}_{cells}]$ before the convective subsystem resolution, is given by:

$$\begin{aligned}
&\mathscr{E}_0^n = \max\left(\mathrm{M}_{inf}, \min\left(\mathrm{M}_{max}^n, 1\right)\right),\\
&\text{with: } \mathrm{M}_{max}^n = \max_{i\in[1,\mathrm{N}_{cells}]}\left(\frac{|u_i^n|}{c_i^n}\right).
\end{aligned} \tag{3.21}$$

Remark 3.4.1 (Averaging over a non-conservative term)
One can notice that, even if the R and W PDEs are non-conservative because of the $\tau\partial_x(.)$ operator, the fact that $\partial_t \tau = 0$ in the acoustic subsystem of the current splitting and the piecewise continuous structure of the computed solution at time t^n allow to derive exactly relations (3.19). This, is a key point to make sure that the discrete acoustic relaxation subsystem is conservative which, for the present IMEX scheme, is a necessary condition to ensure that the overall fractional step approach is conservative (see Proposition 3.4.1 below). Finally, it has to be mentioned that, up to the Mach-sensitive parameter, similar equations have already been obtained in the framework of the Lagrange-Projection methods where a mass variable m such as $\partial_m = \tau\partial_x$ is at stake. See [8, 11] for more details.

The end of the scheme derivation follows naturally by remembering that W (respectively R) is constant over the 2,3 and 4-waves (respectively the 1 and 2,3-waves). Indeed, the signs of the different eigenvalues drawn in Figure 3.1 suggest that $\mathrm{W}_{i+1/2}(t^n, t^{n+})$ (respectively $\mathrm{R}_{i+1/2}(t^n, t^{n+})$) can be approximated by $\mathrm{W}_{i+1}^{\tilde{n}}$ (respectively by $\mathrm{R}_{i-1}^{\tilde{n}}$). Finally the two discrete dynamics write:

$$\begin{aligned}
&\frac{\mathrm{W}_i^{\tilde{n}} - \mathrm{W}_i^{n+}}{\Delta t} - \frac{\left(1-(\mathscr{E}_0^n)^2\right)(a_{\mathcal{A}})^{n+}\tau_i^{n+}}{\Delta x}\left(\mathrm{W}_{i+1}^{\tilde{n}} - \mathrm{W}_i^{\tilde{n}}\right) = 0,\\
&\frac{\mathrm{R}_i^{\tilde{n}} - \mathrm{R}_i^{n+}}{\Delta t} + \frac{\left(1-(\mathscr{E}_0^n)^2\right)(a_{\mathcal{A}})^{n+}\tau_i^{n+}}{\Delta x}\left(\mathrm{R}_i^{\tilde{n}} - \mathrm{R}_{i-1}^{\tilde{n}}\right) = 0.
\end{aligned} \tag{3.22}$$

Thus, $\left(\mathrm{W}_i^{\tilde{n}}\right)_{i\in[1,\mathrm{N}_{cells}]}$ (respectively $\left(\mathrm{R}_i^{\tilde{n}}\right)_{i\in[1,\mathrm{N}_{cells}]}$) is solution of an uncoupled linear system involving an upper-bidiagonal matrix (respectively a lower-bidiagonal matrix). If transmissive boundary conditions are used by introducing fictitious states $\underline{\mathbf{U}}_0^{\tilde{n}} = \underline{\mathbf{U}}_1^{\tilde{n}}$ and $\underline{\mathbf{U}}_{\mathrm{N}_{cells}+1}^{\tilde{n}} = \underline{\mathbf{U}}_{\mathrm{N}_{cells}}^{\tilde{n}}$, then $\mathrm{W}_{\mathrm{N}_{cells}+1}^{\tilde{n}} = \mathrm{W}_{\mathrm{N}_{cells}}^{\tilde{n}}$ and $\mathrm{W}_0^{\tilde{n}} = \mathrm{W}_1^{\tilde{n}}$. The matrices involved in (3.22) are then non singular since all their diagonal terms are strictly positive. What is more their bidiagonal structure, inherited from the transport dynamics of the strong relaxation Riemann invariants W and R, allows to invert them without using any particular linear solver.

3.4.2 Projection Step and Time-Implicit Acoustic Flux

Once the two uncoupled linear systems (3.22) have been solved, the time-implicit acoustic flux related to the subsystem $\mathcal{A}^{\mu}$ can be deduced immediately. It reads:

$$\begin{aligned}
&\mathbf{H}_{\mathcal{A}^{\mu}\,i+1/2}^{\tilde{n}} = \left(1-(\mathscr{E}_0^n)^2\right)\begin{bmatrix} 0 \\ (\Pi_{\mathcal{A}}^*)_{i+1/2}^{\tilde{n}} \\ (a_{\mathcal{A}}^{n+})^2 (u_{\mathcal{A}}^*)_{i+1/2}^{\tilde{n}} \\ (\Pi_{\mathcal{A}}^*)_{i+1/2}^{\tilde{n}} (u_{\mathcal{A}}^*)_{i+1/2}^{\tilde{n}} \end{bmatrix},\\
&(u_{\mathcal{A}}^*)_{i+1/2}^{\tilde{n}} = \frac{\mathrm{R}_i^{\tilde{n}} + \mathrm{W}_{i+1}^{\tilde{n}}}{2},\\
&(\Pi_{\mathcal{A}}^*)_{i+1/2}^{\tilde{n}} = \frac{(a_{\mathcal{A}})^{n+}\left(\mathrm{R}_i^{\tilde{n}} - \mathrm{W}_{i+1}^{\tilde{n}}\right)}{2}.
\end{aligned} \tag{3.23}$$

In the present work, the projection step is performed instantaneously. Indeed, μ is forced to tend fictively towards zero such that $p = \Pi$. Particularly, the time-implicit acoustic pressure at face $i+1/2$ can be defined as: $(p_{\mathcal{A}}^*)_{i+1/2}^{n+1} = (\Pi_{\mathcal{A}}^*)_{i+1/2}^{\tilde{n}}$. The other flux quantities remain invariant through the projection step and one can rewrite $(u_{\mathcal{A}}^*)_{i+1/2}^{\tilde{n}}$ as $(u_{\mathcal{A}}^*)_{i+1/2}^{n+1}$. Finally the time-implicit scheme for the acoustic subsystem $\mathcal{A}$ writes:

$$\begin{aligned}
&\mathbf{U}_i^{n+1} = \mathbf{U}_i^{n+} - \frac{\Delta t}{\Delta x}\left(\mathbf{H}_{\mathcal{A}\,i+1/2}^{n+1} - \mathbf{H}_{\mathcal{A}\,i-1/2}^{n+1}\right),\\
&\text{with } \mathbf{H}_{\mathcal{A}\,i+1/2}^{n+1} = \left(1-(\mathscr{E}_0^n)^2\right)\begin{bmatrix} 0 \\ (p_{\mathcal{A}}^*)_{i+1/2}^{n+1} \\ (p_{\mathcal{A}}^*)_{i+1/2}^{n+1}(u_{\mathcal{A}}^*)_{i+1/2}^{n+1} \end{bmatrix}.
\end{aligned} \tag{3.24}$$

One can notice that, up to the factor $(1-(\mathscr{E}_0^n)^2)$, the obtained time-implicit acoustic flux is identical to the one derived in [8, 19]. Furthermore, the relaxation constant $a_{\mathcal{A}}$ makes it independent of the fluid EOS. As already stated, it requires no particular linear solver since the two uncoupled systems (3.22) can be inverted by hand. Besides, as proved in subsection A, solving the discrete momentum equation of (3.24) is equivalent to setting:

$$u_i^{n+1} = \frac{\mathrm{R}_i^{n+1} + \mathrm{W}_i^{n+1}}{2}, \tag{3.25}$$

provided that $u_i^{n+} = \frac{\mathrm{R}_i^{n+} + \mathrm{W}_i^{n+}}{2}$.
In the sequel, some additional properties of the overall IMEX fractional step are presented.

3.4.3 The IMEX Scheme Properties

Three properties are underlined below. The two first deal with the conservativity and the maximum principle whereas the last one concerns the discrete preservation of the Riemann Invariants of single contact discontinuities.

Proposition 3.4.1 (Conservativity and maximum principle of the overall IMEX scheme)
• *Conservativity:*

Let us formally introduce $\mathbf{H}_{\mathcal{C}}{}^{n}_{i+1/2}\left(\mathbf{U}_i^n, \mathbf{U}_{i+1}^n\right)$ *the time-explicit numerical flux associated to the subsystem* $\mathcal{C}$ *(see [24, 25] or (3.51) in subsection A for a definition). Then, the overall IMEX scheme is conservative and writes:*

$$\mathbf{U}_i^{n+1} = \mathbf{U}_i^n - \frac{\Delta t}{\Delta x}\left(\mathbf{H}_{\mathcal{C}}{}^{n}_{i+1/2}\left(\mathbf{U}_i^n, \mathbf{U}_{i+1}^n\right) + \mathbf{H}_{\mathcal{A}}{}^{n+1}_{i+1/2} - \mathbf{H}_{\mathcal{C}}{}^{n}_{i-1/2}\left(\mathbf{U}_{i-1}^n, \mathbf{U}_i^n\right) - \mathbf{H}_{\mathcal{A}}{}^{n+1}_{i-1/2}\right). \tag{3.26}$$

• *Maximum principle:*

Consider $\rho\phi$ *a given conservative variable such as* $\forall\,(x,t):\ \partial_t(\rho\phi) + \partial_x\left(\rho\phi\, u\right) = 0$. *Assume that* $(\rho\phi)_i^n \in [(\rho\phi)_{Min}, (\rho\phi)_{Max}]$. *Then, the maximum principle preservation* $(\rho\phi)_i^{n+1} \in [(\rho\phi)_{Min}, (\rho\phi)_{Max}]$ *depends only on the convective sub-step discretization. It naturally holds under a non-restrictive sufficient condition written in [24]: p.17,* ***Lemma 1 (Positivity of intermediate density)****, (see Lemma 2.3.1 in the former chapter).*

It is well known that the above global conservativity result, which in this case is directly obtained because the acoustic sub-step discretization is conservative by construction, is a necessary step in order to capture the Euler physical shock fronts (see [23]). As for the maximum principle preservation for purely convected quantities, it can be considered as a first step towards the L^∞ stability of the overall scheme.

Proposition 3.4.2 (Discrete preservation of the contact discontinuity Riemann invariants)
Assume that the equation of state is such that $\left(\rho\varepsilon\right)^{\text{EOS}}\left(\rho, p\right) = C(p)\rho + B(p)$, *with* $p \to C(p)$ *and* $p \to B(p)$ *smooth functions such as* $\left(\rho\varepsilon\right)^{EOS}_{|\rho}: p \to C(p)\rho + B(p)$ *is injective on the domain of definition of* p *(see [17] or subsection A for an explanation of such hypothesis); then, the overall IMEX scheme exactly preserves the constant velocity and the constant pressure of an isolated contact discontinuity from one time-step to another.*

According to [17], the above general expression of $\left(\rho\varepsilon\right)^{\text{EOS}}\left(\rho, p\right)$ belongs to the category of the "T1" equation of state. One can notably notice that the stiffened gas EOS: $\rho\varepsilon = p + \gamma\Pi$, is included in it. However the Van der Waals EOS: $\rho\varepsilon = \frac{(p+a\rho^2)(1-b\rho)}{\gamma-1} - a\rho^2$ is out of it. The above proposition will be useful in the sequel to detect the appearance of instabilities related to high convective Courant number $\mathscr{C}_{|u|}$. Proofs, including a brief description of the time-explicit convective flux related to subsystem $\mathcal{C}$, can be found in subsection A. The next subsection is devoted to the discrete time-step specification.

3.4.4 Construction of the numerical time-step

The time-step of the IMEX scheme is built using the convective eigenvalues $\lambda_1^{\mathcal{C}}$ and $\lambda_3^{\mathcal{C}}$ written in equation (3.6). As described in [24, 25], the convective subsystem $\mathcal{C}$ is discretized using the same relaxation techniques as the one described in Section 3.3. The eigenvalues of the resulting relaxation system $\mathcal{C}^\mu$ then write: $\lambda_1^{\mathcal{C},\mu} = u - \mathscr{E}_0\, a_{\mathcal{C}}\,\tau$, $\lambda_{2,3}^{\mathcal{C},\mu} = u$ and $\lambda_4^{\mathcal{C},\mu} = u + \mathscr{E}_0\, a_{\mathcal{C}}\,\tau$. They are related to the subcharacteristic condition $a_{\mathcal{C}} > \rho\, c_{\mathcal{C}}$.

For a given convective Courant number $\mathscr{C}_{\mathcal{C}}$, the time-step at the n-th iteration of the numerical scheme is:

$$\begin{aligned}
&\Delta t_{\mathcal{C}}^n = \mathscr{C}_{\mathcal{C}}\frac{\Delta x}{\max\limits_{i+1/2}\left(\max\left(\left|u_i^n - \mathscr{E}_0^n\,(a_{\mathcal{C}})_{i+1/2}^n\,\tau_i^n\right|, \left|u_{i+1}^n + \mathscr{E}_0^n\,(a_{\mathcal{C}})_{i+1/2}^n\,\tau_{i+1}^n\right|\right)\right)},\\
&(a_{\mathcal{C}}^n)_{i+1/2} = K\max\left(\rho_i^n\,(c_{\mathcal{C}})_i^n, \rho_{i+1}^n\,(c_{\mathcal{C}})_{i+1}^n\right),\ K > 1.
\end{aligned} \tag{3.27}$$

Let us assume that the stiffness of the discrete pressure gradient in the acoustic subsystem $\mathcal{A}$ has been completely removed thanks to the time-implicit integration. In that case one should expect that the present IMEX scheme is stable under the convective CFL condition: $\mathscr{C}_{\mathcal{C}} \approx 1$.

From a numerical stability point of view, the time-step definition (3.27) is thus the only admissible one regarding the waves produced by the convective subsystem. However, these waves never exist in the overall Euler system. For low Mach number flows under convective time-scales, the acoustic waves have vanished and the leading phenomenon is driven by the material velocity u. For that reason, one can introduce another time-step as:

$$\Delta t^n = \mathscr{C}_{|u|} \frac{\Delta x}{\max_i \left(|u_i^n| \right)}. \tag{3.28}$$

Once again, let us stress that the time-step definition (3.28) is essentially motivated by physical considerations. In the context of IMEX schemes based on convective-acoustic splittings, its formulation has also the advantage of being completely independent of the way to split as well as the way to discretize the associated subsystems. That is why, in the following numerical results section, the cases appealing to a fine accuracy or stability comparison between IMEX schemes are performed using the physical and universal time-step formula (3.28). On the contrary, more complicated configurations requiring the proposed approach to be stable in order to capture some specific asymptotic regimes at low Mach number are tested with the convective-like time-step (3.27).

3.5 Numerical Results

The following section is devoted to one-dimensional numerical results produced by the present IMEX approach. Section 3.5.1 focuses on the sensitivity w.r.t $\mathscr{C}_{|u|}$ of the acoustic and material waves propagation. Section 3.5.2 mainly concentrates on grid-convergence studies completed by efficiency comparisons between time-explicit and time-implicit solvers. For the reasons given in the above paragraph, IMEX schemes involved in Section 3.5.1 and Section 3.5.2 use the discrete time-step (3.28). Nevertheless for each value of $\mathscr{C}_{|u|}$ an estimation of $\mathscr{C}_{\mathcal{C}}$ is systematically provided. Section 3.5.3 deals with the appearance, in a fluid endowed with a stiff equation of state, of strong pressure jumps in an uniformly low-Mach number flow. Finally, Section 3.5.4 aims at testing the ability of the present approach to treat a larger application spectrum like weakly compressible flows. In the last two subsections, the proposed method is systematically combined with the convective-like time-step (3.27).

3.5.1 Low Mach Isolated Waves

The first part of the numerical results is dedicated to the influence of the Courant number on quantities varying through the acoustic or material waves. Indeed, it is well known (see [2, 3, 13, 29–31]) that full time-implicit schemes, even with the use of high-order accurate discretizations in space, are only accurate on σ-like waves when the time-steps Δt are such that $\mathscr{C}_{\sigma} = (|\sigma|\,\Delta t)/\Delta x \approx 1$. In the following, one seeks to investigate the accuracy of the above IMEX fractional step with respect to $\mathscr{C}_{|u|}$ and compare it with an other IMEX Lagrange-Projection (LP) fractional step described in [8, 9] in the context of low Mach number flows. Two low Mach number cases are thus evaluated. The first one details the propagation of a single 3-shock wave while the second one corresponds to the evolution of a single contact wave. In both cases, a particular attention will be paid to the diffusive or stiffening effects associated with the increase of $\mathscr{C}_{|u|}$. Transmissive conditions are used at the inlet and the outlet of the computational domain.

Isolated Shock Wave

For this test case, the fluid is endowed with an ideal gas EOS:

$$\varepsilon = \frac{p}{(\gamma-1)\rho}, \text{ and } c = \sqrt{\frac{\gamma p}{\rho}}, \tag{3.29}$$

with $\gamma = 7/5$, the heat capacity ratio. The left state of the considered 3-isolated shock wave is completely defined by:

$$\rho_L^0 = 1\ (kg.m^{-3}),\ p_L^0 = 10^4\ (Pa),\ \text{and}\ u_L^0 = M_0 \times c_L^0, \tag{3.30}$$

with $M_0 = 10^{-2}$ the maximal Mach number of the flow. What is more, the shock wave speed σ is fixed equal to $c_L^0 \approx 118.32\ (m.s^{-1})$. The three remaining unknowns ρ_R^0, u_R^0 and p_R^0 are the solutions of the corresponding Rankine-Hugoniot problem and can then be found analytically. Besides, the resulting right state abides by the Lax entropy criterion: $u_R^0 + c_R^0 < \sigma < u_L^0 + c_L^0$. The analytical solution is then composed of a single 3-shock wave.
In Figure 3.2, the isolated 3-shock wave pressure profile is shown. The physical time of the simulation is such that the initial discontinuity located at $x_0 = 0.5\ m$ stops at $x = 0.75\ m$. The mesh is made of 10^3 cells.
Different curves are plotted; Sp-(M) stands for the current splitting presented in Eqs (3.3) and (3.4) whereas Sp-LP refers to a Lagrange-Projection splitting method fully described in [8] and taken as a benchmark in this work. Besides the abbreviation "Exp" indicates that the acoustic part of the Sp-(M) splitting (respectively the Sp-LP splitting) has been discretized using a time-explicit scheme detailed in [24, 25] (respectively [8]). In this case, the CFL condition is such that $\mathscr{C}_E = 1$. On the contrary "Imp" refers to the above time-implicit approach.

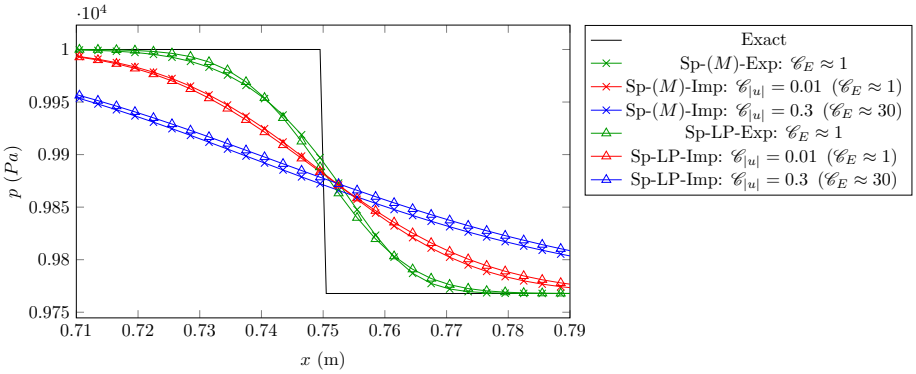

Figure 3.2 – Pressure profile, Ideal Gas, $M = 10^{-2}$, with $N_{cells} = 10^3$

Two different convective Courant numbers values have been tested in the implicit-explicit approaches: the first one $\mathscr{C}_{|u|} = 0.01$ ($\mathscr{C}_C \approx 2.37 \times 10^{-2}$) has been deliberately chosen to provide time-steps close to those based on the constraint $\mathscr{C}_E \approx 1$ since formally $\mathscr{C}_{|u|} = M/(1+M)\mathscr{C}_E$ and $M = 10^{-2}$. The other value $\mathscr{C}_{|u|} = 0.3$ ($\mathscr{C}_C \approx 7.11 \times 10^{-1}$) corresponds to $\mathscr{C}_E \approx 30$ and is thus expected to be too high for the IMEX scheme to accurately follow the shock wave front.
In this low Mach number case, it turns out that the sharper pressure profiles are those provided by the time-explicit schemes complying with the constraint: $\mathscr{C}_E \approx 1$. On the contrary the higher is $\mathscr{C}_E$, the more diffused the shock profile is. Besides, for a fixed Euler Courant number $\mathscr{C}_E \approx 1$, the averaging effect of the time-implicit schemes relatively to the time-explicit ones can be observed as the profile of "Sp-(M)-Imp: $\mathscr{C}_{|u|} = 0.01$" is largely more diffused than "Sp-(M)-Exp: $\mathscr{C}_E = 1$".
Finally, one can notice that, for all the Courant number values involved here, the Sp-(M) splitting is as accurate as the Sp-LP method. These results, obtained in the context of the Euler system, seem to be close to the predictions given by the linear stability analysis in [13].
The above simple test case, involving a fast acoustic wave related to a genuinely non-linear field, has allowed to test the robustness with respect to $\mathscr{C}_{|u|}$ of the present approach compared with the

LP method. In the sequel the same study is performed on a slow material wave associated with a linearly degenerate field.

Isolated Contact Discontinuity

For the same thermodynamical law, a single contact discontinuity is created by imposing:

$$\begin{aligned} &\rho_L^0 = 1\ (kg.m^{-3}),\ \rho_R^0 = 0.125\ (kg.m^{-3}),\\ &p_L^0 = p_R^0 = p^0 = 10^4\ (Pa),\\ &u_L^0 = u_R^0 = M_0 \times c_R^0 = u^0, \end{aligned} \tag{3.31}$$

with $M_0 = 10^{-2}$. This wave linked to a linearly degenerate field propagates at speed $u_0 \approx 3.35\ (m.s^{-1})$. In Figure 3.3, one can observe the density profiles. As it was expected, the isolated contact discontinuity sharpens as the convective Courant number $\mathscr{C}_{|u|}$ reaches 1. Once again, for the same Courant number, the profiles between the present IMEX scheme and the IMEX-LP scheme overlap quasi-perfectly.

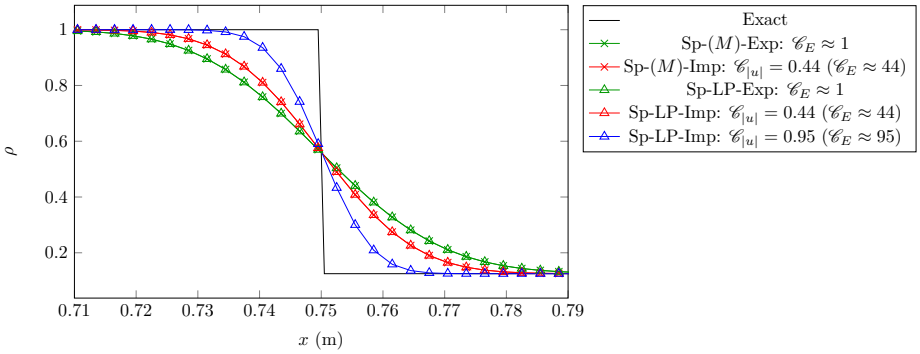

Figure 3.3 – Density profile, Ideal Gas, $M_{min} = 10^{-2}$, with $N_{cells} = 10^3$

However, one can notice that the ideal target associated to $\mathscr{C}_{|u|} = 0.95 \approx 1$ has only been achieved for the LP method. Indeed, for this test case, the present splitting and the resulting IMEX approach triggers instabilities for $\mathscr{C}_{|u|}$ above 0.44. Trying to connect this threshold with a reconstructed value of the convective Courant number $\mathscr{C}_{\mathcal{C}}$, one can define:

$$(\mathscr{C}_{\mathcal{C}})_{i+1/2}^n = \frac{\max\left(\left|u_i^n - \mathscr{E}_0^n\,(a_{\mathcal{C}})_{i+1/2}^n\,\tau_i^n\right|, \left|u_{i+1}^n + \mathscr{E}_0^n\,(a_{\mathcal{C}})_{i+1/2}^n\,\tau_{i+1}^n\right|\right)\Delta t^n}{\Delta x}, \tag{3.32}$$

with Δt^n the discrete time-step defined in equation (3.28) and used in this test case. In Figure 3.4 the value of $(\mathscr{C}_{\mathcal{C}})_{i+1/2}^n$ is displayed at the final simulation time and overall the computational domain. One can observe that the reconstructed convective Courant number is strictly higher than one in the region where the Mach number is minimal. Let us recall that, as the term $\mathscr{E}_0$ decreases, the proportion of the pressure gradient that is discretized using a time-implicit integration increases as $\left(1-\mathscr{E}_0^2\right)$ according to the definition of the time-implicit acoustic flux (3.24). Then, when $\mathscr{E}_0$ is small enough, the amount of numerical diffusion produced by the time-implicit part of the scheme is sufficient to balance the anti-diffusive effect brought by the time-explicit discretization if $\mathscr{C}_{\mathcal{C}} > 1$. Such a phenomenon is analyzed in [34, 40] using the *modified equation* tool.
Conversely, when M_0 is high enough, the splitting parameter $\mathscr{E}_0$ tends towards one so that the time-implicit numerical diffusion is canceled out. The classical time-explicit CFL condition $\mathscr{C}_{\mathcal{C}} \approx 1$ is then retrieved.
Details dealing with the stability of the proposed IMEX scheme when applied to this test case with varying Mach number M_0 are provided in subsection B. The residual term $\mathscr{E}_0\,c_{\mathcal{C}}$ prevents from reaching the material CFL condition $\mathscr{C}_{|u|} = 1$ proved by Zakerzadeh in [39] for the IMEX LP scheme. This is the price to be paid after having introduced $\mathscr{E}_0^2\,p$ into the convective subsystem $\mathcal{C}$. Nevertheless, in this test case, the stability of the proposed IMEX scheme holds under $\mathscr{C}_{\mathcal{C}} \approx 1$

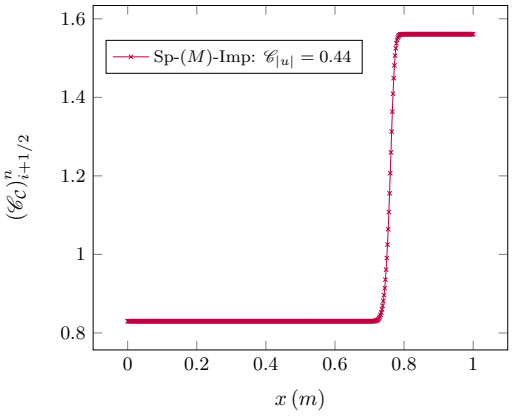

Figure 3.4 – Reconstructed local convective Courant number

for *any value of the flow Mach number*. These numerical observations support a "Mach-uniform" $\mathscr{C}_{\mathcal{C}}$-stability property of the present method.
In the sequel, accuracy and efficiency of the above IMEX schemes are compared with their full time-explicit versions in the context of low Mach number flows.

3.5.2 A Low Mach Sod Shock Tube

By imposing a common Courant number relying on the material velocity u, the above isolated wave test cases have pointed out some stability differences between the proposed IMEX scheme and the LP-IMEX method. In the sequel, one wishes to refine the comparison by adding some grid-convergence and efficiency results obtained from a multiple wave test case.
Herein, a low Mach number shock tube is computed. The fluid is endowed with the same previous ideal gas EOS. The initial conditions are made of a density discontinuity, a constant velocity, and a slightly discontinuous pressure:

$$\begin{aligned} &\rho_{\mathrm{L}}^0 = 1\ kg\,m^{-3},\ \rho_{\mathrm{L}}^0 = 0.125\ kg\,m^{-3} \\ &u_{\mathrm{L}}^0 = u_{\mathrm{R}}^0 = u^0 = 1\ m\,s^{-1} \\ &p_{\mathrm{L}}^0 = 10080\ \mathrm{P}a,\ p_{\mathrm{R}}^0 = 10000\ \mathrm{P}a. \end{aligned} \tag{3.33}$$

It results in a left-going 1-rarefaction wave, a 2-contact discontinuity propagating to the right and a right-going 3-shock wave. The maximal Mach number of the flow, reached in the head of the rarefaction wave, is equal to 1.26×10^{-2}.
Various time-explicit schemes have been tested: "no-Sp" corresponds to the case where $\mathscr{E}_0^n = 1$ is imposed along the simulation. Thus, the splitting is not triggered. "Sp-($\sqrt{\mathrm{M}}$)" is the weighted splitting approach with $\mathscr{E}_0^n = \max\left(\sqrt{\mathrm{M}_{inf}}, \min\left(\sqrt{\mathrm{M}_{max}^n}, 1\right)\right)$ while "Sp-(M)" involves $\mathscr{E}_0^n$ defined in formula (3.21) which is *a priori* optimal for a time-explicit scheme, because, as shown in [24, 25], it minimizes the numerical diffusion of the subsystem $\mathcal{C}$ in the low-Mach number case. Lastly, "Sp-LP" is again the Lagrange Projection splitting method, described in [8]. Besides, the mention "-corr" means that a low-Mach correction inspired from [15] and written in [24, 25] is triggered. As observed in [8, 9, 24, 25], it aims at considerably reducing the numerical diffusion in the case of low Mach number flows.
Regarding the time-implicit schemes, two values for $\mathscr{C}_{|u|}$ have been tested. As shown in subsection E, the ratio between $\mathscr{C}_{|u|}$ the convective Courant number based on u^0 and $\mathscr{C}_{\mathrm{E}}^{0,*}$ the most constraining Euler Courant number is:

$$\mathscr{C}_{|u|}^{u^0} \approx 1.5 \times 10^{-3}\,\mathscr{C}_{\mathrm{E}}^{0,*}. \tag{3.34}$$

Then, the selected convective Courant numbers are $\mathscr{C}_{|u|} = 1.5 \times 10^{-2}$ ($\mathscr{C}_{\mathrm{E}}^{0,*} \approx 10$, $\mathscr{C}_{\mathcal{C}} \approx 6.34 \times 10^{-2}$) and $\mathscr{C}_{|u|} = 4.5 \times 10^{-2}$ ($\mathscr{C}_{\mathrm{E}}^{0,*} \approx 30$, $\mathscr{C}_{\mathcal{C}} \approx 1.9 \times 10^{-1}$).

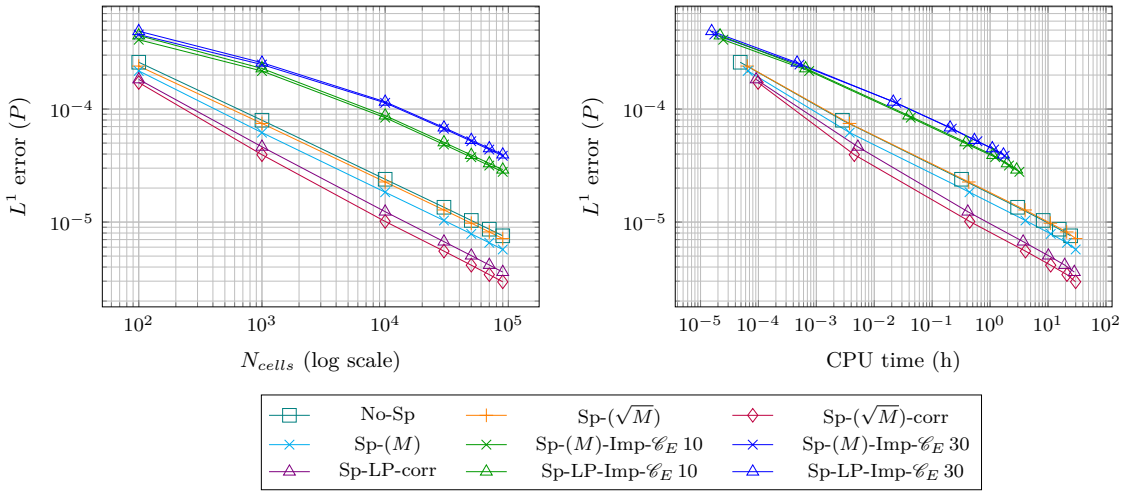

Figure 3.5 – Convergence curve (left), Efficiency curve (right) for the pressure variable p: M = 1.26×10^{-2}

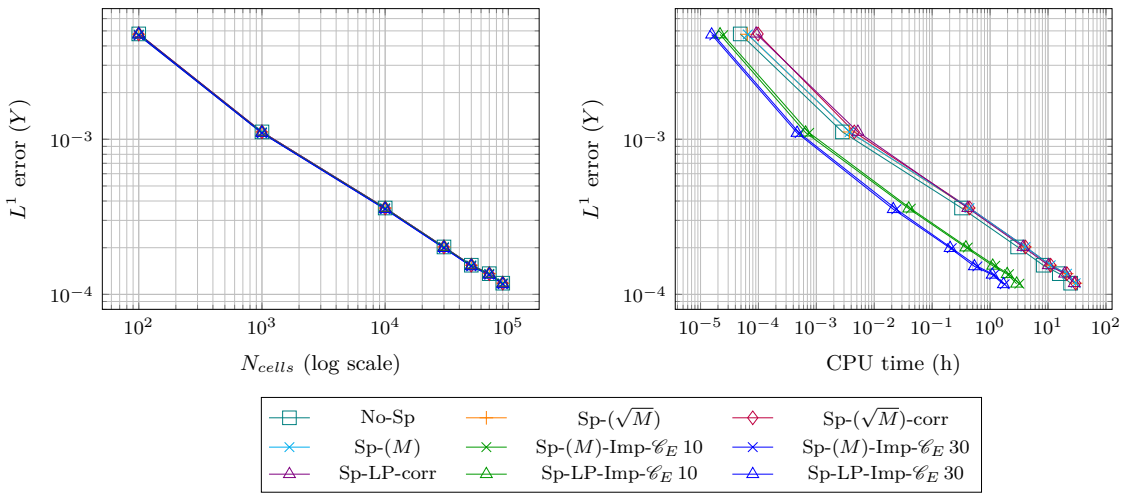

Figure 3.6 – Convergence curve (left), Efficiency curve (right) for the passive tracer variable Y: M = 1.26×10^{-2}

In this test case, in order to isolate the effect of the IMEX scheme on the contact discontinuity, a passive tracer Y has been added to the Euler system. Its PDE writes:

$$\partial_t(\rho Y) + \partial_x(\rho Y u) = 0. \tag{3.35}$$

Starting from $Y_L^0 = 1$ and $Y_R^0 = 0.5$, the exact solution jumps only through the contact discontinuity. Figure 3.5 (respectively Figure 3.6) presents the convergence curve and the efficiency curve for the pressure (respectively Y) variable. As already pointed out in [24, 25], for such a low Mach number, and focusing on the pressure (or any variable jumping through the genuinely non-linear fields), the time-explicit schemes with the low Mach number correction Sp-($\sqrt{M}$)-corr and Sp-LP-corr, are the most accurate as well as the most efficient. As already observed in the isolated 3-shock wave test case, time-implicit schemes such that $\mathscr{C}_E > 1$ are less accurate than any of the time-explicit schemes. Besides, according to the pressure efficiency curve, this lack of accuracy is not compensated by a substantial gain in CPU time. Indeed, for a given pressure L^1-error level, time-implicit schemes are still more CPU-consuming than the time-explicit ones.
In the case of the passive tracer Y, no specific difference on the convergence curve can be noticed between the time-explicit and the time-implicit schemes. Indeed, the convective Courant number $\mathscr{C}_{|u|} \leq 4.5\times10^{-2}$ is still very far from one. Thus for every scheme, numerical diffusion has uniformly smoothed the variables only jumping through the slow material wave. Nevertheless, as shown in Table 3.1, time-implicit schemes are clearly more efficient, for the Y variable, than the time-explicit ones, the latter being 7 (respectively 13) times more CPU-consuming than time-implicit schemes when setting $\mathscr{C}_E^{0,*} = 10$ (respectively $\mathscr{C}_E^{0,*} = 30$).

$Ncells$	$\mathscr{C}_E = 10$	$\mathscr{C}_E = 30$
10^2	1.97	2.80
10^3	3.75	5.51
10^4	7.52	13.36
3×10^4	7.26	13.71
5×10^4	6.74	13.66
7×10^4	7.39	13.34
9×10^4	7.67	13.78

Table 3.1 – $T^{CPU}_{\text{No-Sp}}/T^{CPU}_{\text{Sp-(M)-Imp}}$

As announced in the introduction, one of the objective of the present approach is to capture high amplitude pressure jumps in low velocity areas as it is noticed in water-hammer events. This is the purpose of the next numerical example.

3.5.3 A Double Riemann Problem With Stiff Thermodynamics

In the following test case, two Riemann problems are triggered at $x_0 = 0.55\,m$ and $x_1 = 1.23\,m$ in a domain of length $L = 2\,m$. The three initial condition areas are written in Table 3.2.

	Left state ($x < x_0$)	Middle state ($x_0 < x < x_1$)	Right state ($x_1 < x$)
$\rho\ (kg.m^{-3})$	$\rho_L^0 = 10^3$	$\rho_m^0 = 9.98\times10^2$	$\rho_R^0 = 9.97\times10^2$
$u\ (m.s^{-1})$	$u_L^0 = 1$	$u_m^0 = 1$	$u_R^0 = 1$
$p\ (bar)$	$p_L^0 = 10^3$	$p_m^0 = 10$	$p_R^0 = 1$
Y	$Y_L^0 = 0.7$	$Y_m^0 = 0.2$	$Y_R^0 = 0.1$

Table 3.2 – Double Riemann Problem: initial conditions

The fluid is endowed with a stiffened gas EOS, *i.e.*:

$$\varepsilon = \frac{p + P_\infty}{(\gamma-1)\rho}, \text{ and } c = \sqrt{\frac{\gamma(p+P_\infty)}{\rho}}, \tag{3.36}$$

with $\gamma = 7.5$ and $P_\infty = 3 \times 10^3$ bar. These constants have been chosen such that, at a given temperature $T = 295$ K, the value of the speed of sound is approximately $c \approx 1.5 \times 10^3\, m.s^{-1}$. It is representative of the liquid water behavior.
The analytical solution of the present test case is composed of two successive shock tubes whose waves are similar to these presented in Section 3.5.2. The maximal Mach number of the Riemann problem initially located at x_0 (respectively x_1) is $M^{x_0}_{max} \approx 2 \times 10^{-2}$ (respectively $M^{x_1}_{max} \approx 8.6 \times 10^{-4}$). Thus, the flow Mach number is uniformly low. Besides the important variations of the Mach number are associated with strong velocity fluctuations. It passes from $u \approx 32\, m.s^{-1}$ in the contact wave related to the Riemann problem located at x_0 to $u \approx 1.3\, m.s^{-1}$ in the contact wave of the one located at x_1. That is why in the sequel, the Riemann problem initially located at x_0 is referred as "high-velocity" shock tube, whereas the one initially located at x_1 is called "low-velocity" shock tube.
In any case, the stiffened gas EOS combined with high initial pressure discontinuities produce strong shock waves in both Riemann problems. The pressure jump amplitude associated with the high-velocity shock tube (respectively the low-velocity shock tube) is approximately 480 bar (respectively 4.5 bar). The above test case represents the sudden occurrence of high amplitude shock waves in a uniformly low Mach number flow as it can be observed in water-hammer scenarios.
In the sequel, a comparison between the IMEX fractional steps Sp-(M)-Imp and Sp-LP-Imp is done. For each numerical scheme, the time-step is only provided by the waves produced by the convective subsystem: Δt^n_C written in formula (3.27) for the present splitting and

$$\begin{aligned}
&\Delta t^n_{\mathrm{LP}} = \mathscr{C}_C \frac{\Delta x}{\max\limits_{i+1/2}\left(\left((u^*_{\mathcal{A}})^n_{i-1/2}\right)^+ - \left((u^*_{\mathcal{A}})^n_{i+1/2}\right)^-\right)},\\
&(u^*_{\mathcal{A}})^n_{i+1/2} = \frac{u^n_{i+1}+u^n_i}{2} - \frac{1}{2\,a^n_{i+1/2}}\left(p^n_{i+1}-p^n_i\right),\\
&a^n_{i+1/2} = \mathrm{K}\max\left(\rho^n_i\, c^n_i, \rho^n_{i+1}\, c^n_{i+1}\right),\ \mathrm{K} > 1,
\end{aligned} \tag{3.37}$$

for the Lagrange-Projection splitting (see [8]). For both time-steps, the convective Courant number $\mathscr{C}_C$ is set to 0.9. What is more, the discrete splitting parameter $\mathscr{E}^n_0$ defined in Eqs (3.21) is here enriched for the present test case with a simple hand-made shock detector:

$$\begin{aligned}
&\mathscr{E}^n_0 = \max\left(\mathrm{M}_{inf}, \min\left(\max\left(\mathrm{M}^n_{max}, \mathrm{M}^n_{\mathrm{S},max}\right) 1\right)\right),\\
&\text{with}\quad \mathrm{M}^n_{max} = \max_{i\in[1,\mathrm{N}_{cells}]}\left(\frac{|u^n_i|}{c^n_i}\right)\quad,\quad \mathrm{M}^n_{\mathrm{S},max} = \max_{i\in[1,\mathrm{N}_{cells}]}\left(\frac{|(\sigma_{\mathrm{S}})^n_{i+1/2}|}{\max\left(c^n_{i+1}, c^n_i\right)}\right),
\end{aligned} \tag{3.38}$$

and

$$(\sigma_{\mathrm{S}})^n_{i+1/2} = \begin{cases} \dfrac{(\rho\,u)^n_{i+1} - (\rho\,u)^n_i}{\rho^n_{i+1} - \rho^n_i} & \text{if } \left|\rho^n_{i+1} - \rho^n_i\right| > \epsilon^{\mathrm{thres}} \max\left(\rho^n_{i+1}, \rho^n_i\right) \\ 0 & \text{otherwise,} \end{cases} \tag{3.39}$$

where $\epsilon^{\mathrm{thres}} = 10^{-8}$. One can notice that in Eqs (3.38), $(\sigma_{\mathrm{S}})^n_{i+1/2}$ corresponds to the exact shock front speed formula in the case of an isolated shock wave separating the states $\mathbf{U}^n_i$ and $\mathbf{U}^n_{i+1}$. If one considers the waves related to the genuinely non-linear fields, *i.e.* $u \pm c$, the Lax entropy conditions related to admissible shock waves then give:

$$u^n_i \pm c^n_i > (\sigma_{\mathrm{S}})^n_{i+1/2} > u^n_{i+1} \pm c^n_{i+1}. \tag{3.40}$$

Hence, in the case of a low Mach number flow, for which $\left|u^n_{i+1}\right|/c^n_{i+1} \ll 1$ and $\left|u^n_i\right|/c^n_i \ll 1$, the term $\left|(\sigma_{\mathrm{S}})^n_{i+1/2}\right|$ should approximately belong to $\left]\min(c^n_{i+1}, c^n_i), \max(c^n_{i+1}, c^n_i)\right[$. Besides, the low compressibility of a fluid endowed with the above stiffened gas EOS involves very small variations of ρ if $p \ll P_\infty$. Then, c should remain constant at least in the low-velocity shock tube area. Thus, in the case of shock waves, $\mathrm{M}^n_{\mathrm{S},max}$ should be of order one and the present IMEX approach should turn into a fully time-explicit Godunov-like solver.

The number of cells is 2×10^3 and the simulation time $T_{end} = 1.95 \times 10^{-4}\ s$ is set in order to avoid interactions between the 3-right-going shock wave of the high-velocity shock tube and the 1-left-going rarefaction wave of the low-velocity shock tube. Transmissive boundary conditions have been used.
Figure 3.7 and Figure 3.8 show the pressure and the velocity profiles for both successive shock tubes. Figure 3.9 displays the passive tracer profile Y which only jumps through the contact waves.

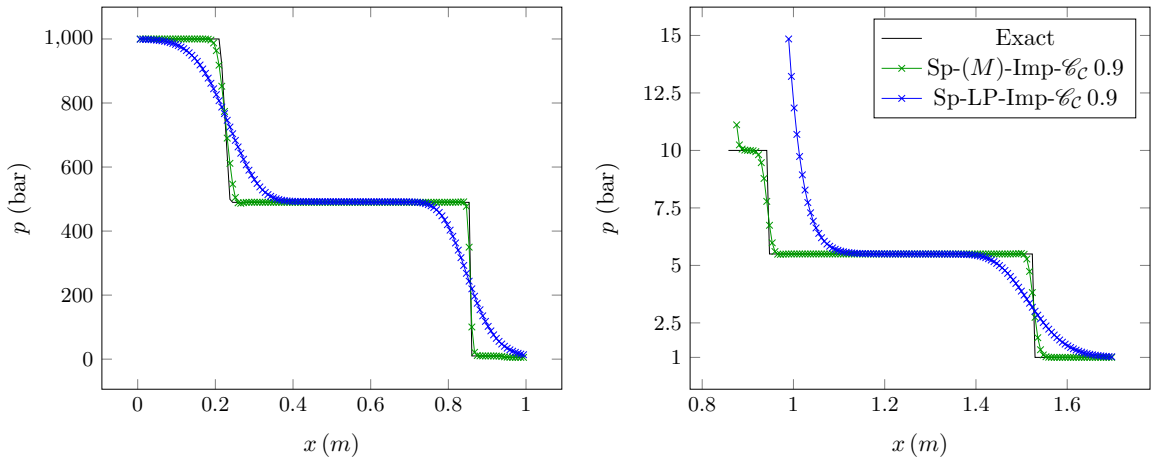

(a) Pressure profile: high velocity area (b) Pressure profile: low velocity area

Figure 3.7 – Pressure profile, stiffened gas EOS, $N_{cells} = 2 \times 10^3$

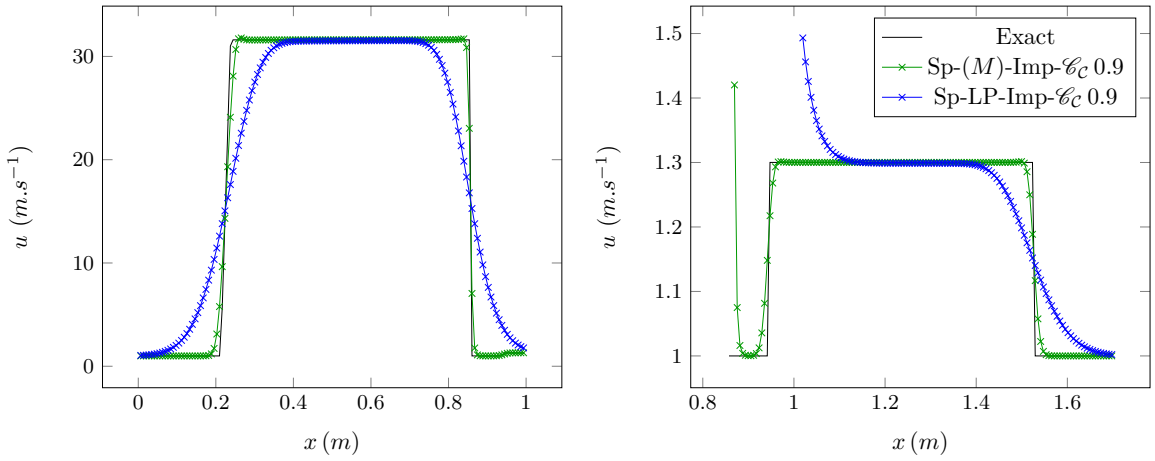

(a) Velocity profile: high velocity area (b) Velocity profile: low velocity area

Figure 3.8 – Velocity profile, stiffened gas EOS, $N_{cells} = 2 \times 10^3$

In the case of Sp-(M)-Imp, once the different waves have appeared, the measured shock detector $M^n_{S,max}$ is of order one through the rarefaction and the shock waves. Then after several time-steps $\mathscr{E}^n_0 = 1$, and a full time-explicit Riemann solver associated with an Euler-like time-steps,

$$\begin{aligned} \Delta t^n_C &\approx \mathscr{C}_C \frac{\Delta x}{\max\limits_{i+1/2}\left(\max\left(\left|u^n_i - c^n_i\right|, \left|u^n_{i+1} + c^n_{i+1}\right|\right)\right)}, \\ \mathscr{C}_C &= 0.9, \end{aligned} \tag{3.41}$$

is recovered. Thanks to the degree of freedom offered by $\mathscr{E}^n_0$, the present fractional step is therefore able to select the appropriate time-discretization for the acoustic flux *and in the same time* the right time-step adapted to the physics of interest. On the contrary, the acoustic part of the Lagrange-Projection fractional step is still discretized using a time-implicit scheme linked to a CFL

condition based on a very low material velocity such as $u \ll c$. Then, it is far less accurate at capturing stiff rarefaction and shock waves in both "high-" and "low-velocity" shock tubes. One can notably observe in Figure 3.7b and Figure 3.8b that, on this mesh, Sp-LP-Imp fails to capture the initial state (u_m^0, p_m^0) between the 1-right-going shock wave of the high-velocity shock tube and the 3-left-going rarefaction wave of the low-velocity one. This is due to an excessive numerical dissipation through the associated waves.

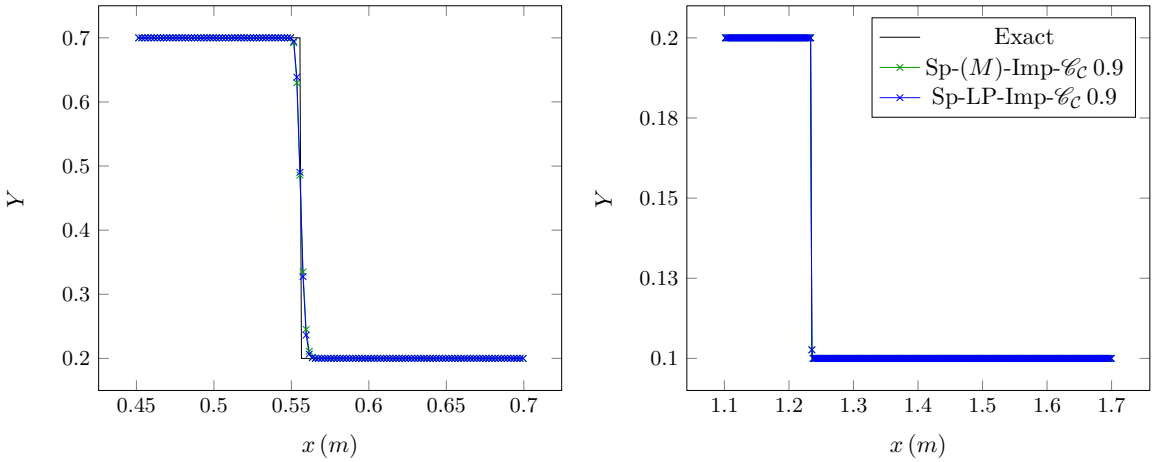

(a) Y profile: high velocity area

(b) Y profile: low velocity area

Figure 3.9 – Y profile, stiffened gas EOS, $N_{cells} = 2 \times 10^3$

Eventually, as seen in Figure 3.9, both IMEX schemes produce similar results regarding the accuracy of the Y profile. It can be explained because the simulation time T_{end} is based on the fast acoustic waves, the exact contact discontinuities only move a few space-steps. One can assume that, on a larger time of simulation, the Sp-LP-Imp should be more accurate on Y than Sp-(M)-Imp. Indeed, the LP time-step is directly based on slow material velocities.
Therefore, this test case has shown that the degree of freedom offered by the splitting parameter $\mathscr{C}_0^n$ allows to automatically switch from a scheme designed to follow slow material dynamics to a scheme able to capture fast acoustic waves even when the flow Mach number is low.
The next section proposes to widen the application fields of the present IMEX scheme. Indeed, it aims at assessing the scheme ability to seize some simple constant states as well as weakly compressible flows.

3.5.4 Applications to some other asymptotic regimes

Constant state perturbed by small amplitude acoustic waves

The first configuration is a "dimensionalized" version of a Riemann problem taken from [16]. The fluid at stake is endowed with an ideal gas EOS with $\gamma = 1.4$. Its density and pressure are initially constant: $\rho^0 = 1\, kg.m^{-3}$, $p^0 = 1$ bar. Let us also introduce $u^0 = 1\, m.s^{-1}$ and a reference Mach number $M^0 = u^0/c^0$ with $c^0 \equiv= \sqrt{p^0/\rho^0}$. For these values, one obtains $M^0 \approx 3.2 \times 10^{-3}$.
As detailed in Table 3.3, the computational domain of length $L^0 = 1\, m$ is split in three areas in which the constant velocity u^0 is perturbed by a term scaling as $O(M^0)$. The initial conditions are thus "well-prepared" according to the definition written in [15, 32].
As time goes on, the four discontinuities of the initial velocity field will produce interacting nonlinear waves of small amplitude. For long convective time-scales one expects that these waves fade away and leave a constant velocity field. Here, the ability of the present IMEX approach to seize this almost incompressible state is analyzed.
Once again the proposed IMEX method is compared with the LP-IMEX scheme. The time-steps are given by formulas (3.27) and (3.37) and the computational domain is made of a 10^3 cells mesh.

	(zone 1): $x < 0.2$ or $x > 0.8$	(zone 2): $x \in [0.2, 0.25]$ or $x \in [0.75, 0.8]$	(zone 3): $x \in [0.25, 0.75]$
$\rho\ (kg.m^{-3})$	ρ^0	ρ^0	ρ^0
$u\ (m.s^{-1})$	$u^0_{\mathrm{L}} = u^0 \times \left(1 - \mathrm{M}^0/2\right)$	$u^0_{\mathrm{R}} = u^0 \times \left(1 + \mathrm{M}^0/2\right)$	$u^0_{\mathrm{m}} = u^0$
$p\ (bar)$	p^0	p^0	p^0

Table 3.3 – Dimarco *et al* Riemann Problem: initial conditions

The physical time of the simulation is $\mathrm{T}_{\mathrm{end}} = 0.05 \times t^0$ with $t^0 = \mathrm{L}^0/u^0$ the convective time-scale of reference. Finally periodic boundary conditions are imposed so that the acoustic waves are constantly re-introduced in the computational domain. Let us end the setting description by mentioning that the shock detector presented in equations (3.38), (3.39) has been unplugged in this test case.

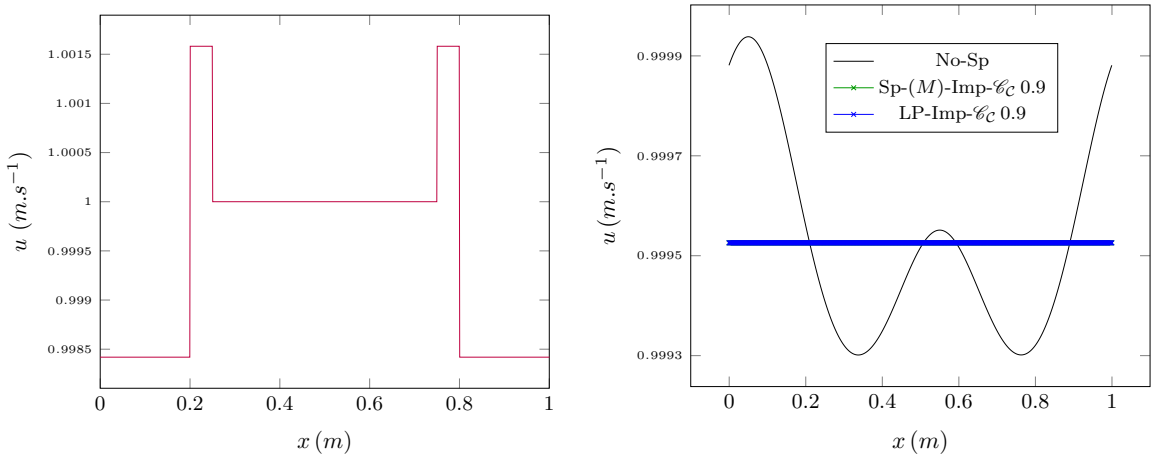

(a) Velocity profile: initial conditions

(b) Velocity profile: $\mathrm{T}_{\mathrm{end}} = 0.05\,s$

Figure 3.10 – Dimarco's *et al* Riemann problem: initial conditions and comparison with a full time-explicit scheme

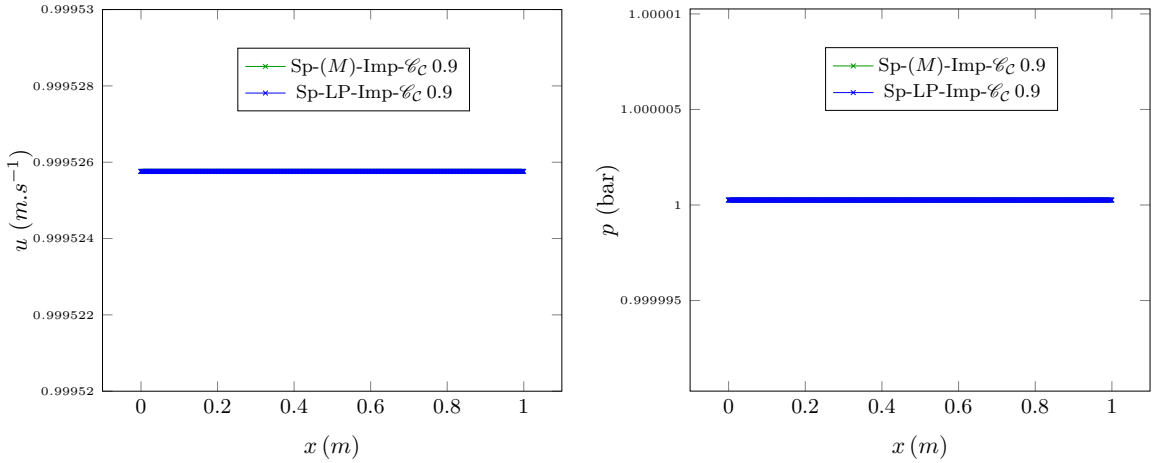

(a) Velocity profile: $\mathrm{T}_{\mathrm{end}} = 0.05\,s$, (zoom)

(b) Pressure profile: $\mathrm{T}_{\mathrm{end}} = 0.05\,s$, (zoom)

Figure 3.11 – Dimarco's *et al* Riemann problem: zoom on the constant incompressible state

At the final simulation time, Figure 3.10a shows the velocity initial distribution while Figure 3.10b displays the profiles, of the present approach, the LP-IMEX method and a full time-explicit Riemann solver No-Sp. The latter has already been used in Section 3.5.2 and is obtained by imposing $\mathscr{C}^n_0 = 1$ at every time-step during the simulation. One can notice that both IMEX schemes manage to reach a plateau by the end of the simulation. On the contrary, No-Sp continues to solve all the

details produced by the acoustic waves interaction. A closer look at Figure 3.11a reveals that both time-implicit methods reach the constant value $u^* \approx 0.999526\, m.s^{-1}$. Such a velocity is consistent with the total momentum conservation since periodic boundary conditions are at stake:

$$\begin{aligned} &\int_\Omega \rho^0\, u^*\, d\Omega = \int_\Omega \rho^0\, u(x,\, t=0)\, d\Omega, \\ \Leftrightarrow\, &\rho^0\, u^* = \rho^0\, u^0 \left[0.4\,(1 - M^0/2) + 0.5 + 0.1\,(1 + M^0/2)\right], \\ \Leftrightarrow\, &u^* \approx 0.9995256. \end{aligned} \tag{3.42}$$

Finally, a look at Figure 3.11b confirms that the pressure obtained from the IMEX methods also remains constant at the end of the simulation.

3.5.5 Weakly Compressible Colliding Pulses

The last test considered has been taken from [28] and is also treated in [16, 33]. It deals with weakly compressible flows whose solutions are made of long wave acoustic pressure and density pulses. Here, the ability of the present IMEX scheme to follow smooth but fast acoustic waves associated with an intermediate value of the Mach number is assessed. The fluid is endowed with an ideal gas EOS with $\gamma = 1.4$. The non-dimensional initial conditions presented in [28] read:

$$\begin{aligned} \overline{\rho}(x,0) &= \overline{\rho}_0 + \left(\frac{M^0_{ref}}{2}\right)\overline{\rho}_1\left(1 - \cos\left(\frac{2\pi x}{L}\right)\right),\ \overline{\rho}_0 = 0.955,\ \overline{\rho}_1 = 2, \\ \overline{u}(x,0) &= -\frac{\overline{u}_0}{2}\,\mathrm{sign}(x)\left(1 - \cos\left(\frac{2\pi x}{L}\right)\right),\ \overline{u}_0 = 2\sqrt{\gamma}, \\ \overline{p}(x,0) &= \overline{p}_0 + \left(\frac{M^0_{ref}}{2}\right)\overline{p}_1\left(1 - \cos\left(\frac{2\pi x}{L}\right)\right),\ \overline{p}_0 = 1,\ \overline{p}_1 = 2\gamma. \end{aligned} \tag{3.43}$$

The Mach number of reference M^0_{ref} has been taken equal to $1/11 \approx 9.1 \times 10^{-2}$. The computational domain Ω is $[-L, L]$ with $L = 2/M^0_{ref}$. Thus, the first-order pulses w.r.t M^0_{ref} evolve with a large space-scale variable $\xi = M^0_{ref}\, x$. Let us introduce p^0_{ref} (respectively ρ^0_{ref}, u^0_{ref}) a reference pressure (respectively a reference density, a reference velocity) such that:

$$\begin{aligned} &\rho^0_{ref} = 1\ kg.m^{-3},\ u^0_{ref} = 1\ m.s^{-1}, \\ &p^0_{ref} = \frac{\rho^0_{ref}\overline{\rho}_0}{\gamma}\left(\frac{u^0_{ref}\overline{u}_0}{M^0_{ref}}\right)^2. \end{aligned} \tag{3.44}$$

The reference pressure p^0_{ref} has been set such that the exact maximal value of the initial Mach number is of the order of M^0_{ref}. The dimensional initial conditions then write: $\rho(x,0) = \rho^0_{ref}\overline{\rho}(x,0)$, $u(x,0) = u^0_{ref}\,\overline{u}(x,0)$ and $p(x,0) = p^0_{ref}\,\overline{p}(x,0)$.
Figure 3.12 and Figure 3.13 display the pressure and velocity profiles at two physical times. The first one captures the time when the two pulses collide producing an over-pressure peak at the center of the computational domain. The second one corresponds to the instant where the two pressure pulses have separated again.
The present IMEX approach with no shock detector, is compared with the LP-IMEX and No-Sp schemes. The non-dimensional initial conditions have been added as a dashed line in order to observe the diffusion and dispersion introduced w.r.t the initial pulses.
In Figure 3.12a, one can notice that both IMEX methods manage to catch the over-pressure peak although they are slightly more diffusive than the full time-explicit scheme. However, in Figure 3.12b, the full time-implicit discretization of the pressure gradient in the LP-Imp approach combined with a CFL condition based on u completely diffuses the re-appearing pressure pulses. On the contrary, in the case of the present IMEX method, one can notice that $\mathscr{E}_0^n$ remains of order M^0_{ref} during most of the simulation. For example, at time $t = 8.41 \times 10^{-1}\ s$, $M^n_{max} = 7.4 \times 10^{-2} = \mathscr{E}_0^n$. The intermediate value of $\mathscr{E}_0$ is enough to produce considerably lower time-steps which are more

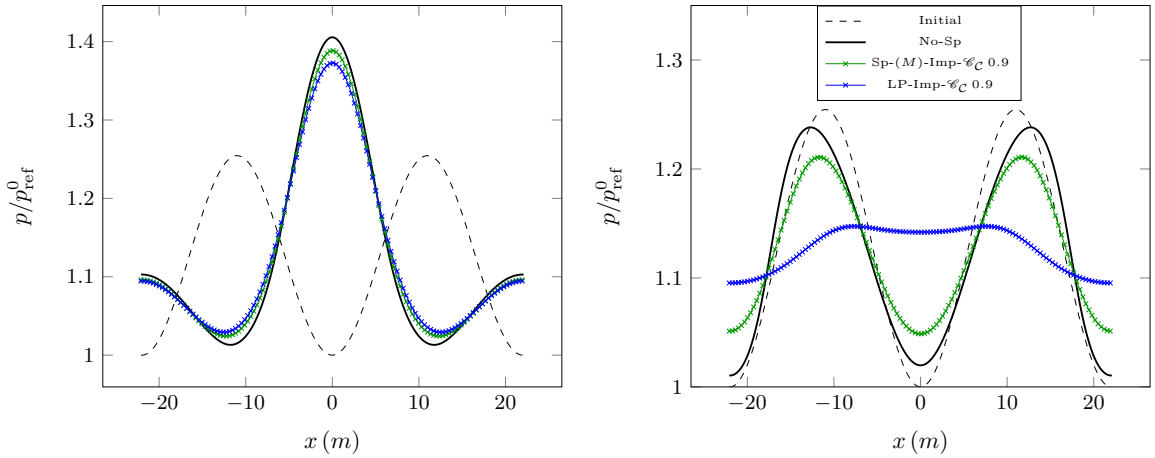

(a) Pressure profile: $t = 3.78 \times 10^{-1}\ s$ (b) Pressure profile: $t = 8.41 \times 10^{-1}\ s$

Figure 3.12 – Pressure: just after the pulses super-position (a), once the pulses have separated again (b)

appropriate to follow the long acoustic waves. As a result, even if it is more diffused compared with the full-time explicit scheme, the global shape of the pressure pulses is retrieved. However, the present approach suffers from the same drawback as the one noticed in [28]: in the vicinity of the locations $x \approx \pm 18.5\,m$, the pressure gradient stiffens such that the long-length scale acoustic wave hypothesis no longer holds, and the time-implicit discretization of the acoustic subsystem considerably smears the appearing discontinuities. In any case, a specific additional work should be undertaken if one is interested in capturing the fast acoustic dynamics related to first-order pressure terms w.r.t $\mathrm{M}^0_{\text{ref}}$.

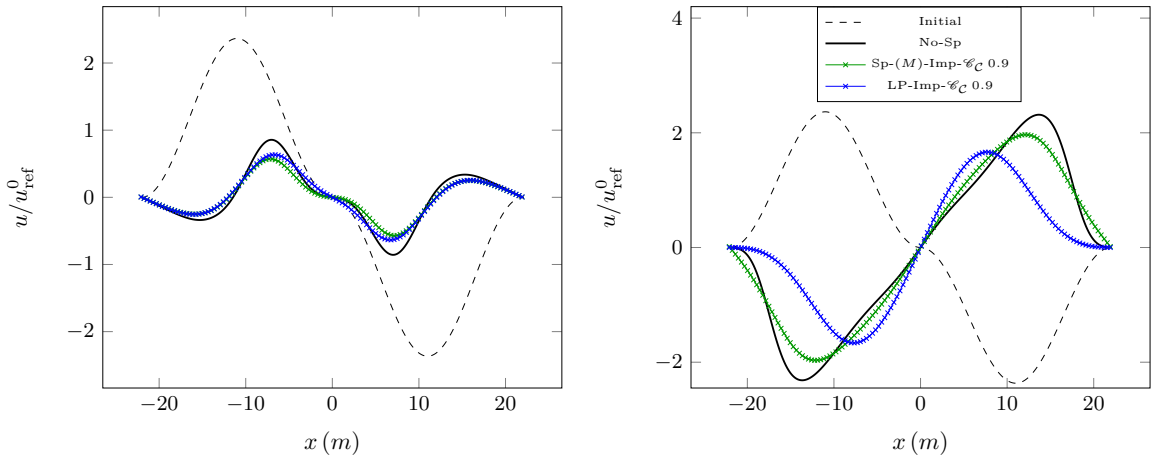

(a) Velocity profile: $t = 3.78 \times 10^{-1}\ s$ (b) Velocity profile: $t = 8.41 \times 10^{-1}\ s$

Figure 3.13 – Velocity: just after the pulses super-position (a), once the pulses have separated again (b)

3.6 Conclusions

The present work focuses on the derivation of an IMEX version of the Mach-sensitive fractional step introduced in [24, 25]. The time-implicit scheme derived for the acoustic subsystem is based on the non-conservative dynamics of strong Riemann invariants provided by the relaxation schemes framework. Although such a technique stems from the Lagrange-Projection theory [11, 19], it can be extended to the present splitting because of density time invariance in the acoustic sub-step and the piece-wise constant structure of the computed solution. The resulting IMEX scheme is simple, the implicit part being inverted by hand, and conservative by construction. What is more, the maximum principle preservation for purely convected quantities holds under a non-restrictive condition for the time-explicit *convective flux*.

A low Mach number shock tube involving an ideal gas thermodynamics and small pressure jumps has highlighted a trade-off in the use of IMEX schemes. Indeed, if one is interested by pressure jumps through shock waves, then using an IMEX scheme with $\mathscr{C}_{\mathrm{E}} \gg 1$ might be inappropriate in terms of accuracy. Besides, the gain in CPU time is not sufficient to compensate the implicit diffusion and dispersion errors: for the pressure variable, IMEX schemes are still less efficient than full time-explicit ones. However, any quantities varying only through material waves should be depicted more efficiently and with a sufficient accuracy.

When the thermodynamics becomes stiffer, high amplitude pressure jumps can occur in low-Mach number flows. This is for example the case during water-hammer events. Then, one can complete the splitting parameter $\mathscr{E}_0^n$ with a basic "shock detector" which enforces the initial IMEX scheme associated with a convective-like CFL condition to turn into a fully time-explicit approximate Riemann solver related to an acoustic-like CFL condition. Hence, the splitting parameter allows to select the acoustic-flux time-discretization *and in the same time* the time-step adapted to the physical-scale looked at. The application of such a strategy to a double Riemann problem endowed with a stiffened gas EOS has shown that, contrary to the IMEX version of the Lagrange-Projection fractional step, the present IMEX approach is able to accurately follow stiff rarefaction and shock waves even in low velocity regions.

Besides, when the fluid is at rest, the proposed IMEX scheme is able to filter out small amplitude acoustic waves of no interest in order to retrieve the underlying constant state. The present IMEX approach has also been tried on intermediate configurations in which smooth and large-scale acoustic waves associated with first order terms w.r.t the flow Mach number propagate and need to be followed. The proposed method provides lower time-steps than the one produced by the LP-IMEX scheme. It is thus able to capture the global shape of the pressure colliding or re-appearing pulses but considerably smears the solution in regions where the pressure gradient stiffens.

Finally, the different test cases presented in this study show that the present IMEX scheme is stable, whatever the Mach number, under $\mathscr{C}_{\mathcal{C}} \approx 1$; with $\mathscr{C}_{\mathcal{C}}$ the Courant number based on the eigenvalues of the *convective* subsystem $\mathcal{C}$. Even if it is not yet rigorously proved, the *Mach-uniform-*$\mathscr{C}_{\mathcal{C}}$ stability property seems to hold.

The fact is that, at a given instant, the computational domain can feature subsonic areas as well as sonic or supersonic ones. Thus, the spatial dependence of the splitting parameter could also been examined. Indeed, provided that the consistency of the overall fractional step is not deteriorated, such a spatial dependence would allow to capture local fluctuations of the Mach number, and the present approach to react more finely. In addition, some improvements regarding the construction of the "shock detector" could also be proposed.

Acknowledgement

The first author received a financial support through the EDF-CIFRE contract 0561-2015. Computational facilities were provided by EDF.

The authors would also like to thank the reviewers who have spent time reading this paper. Indeed, the remarks and questions they have pointed out have considerably allowed the present work to

be improved.

3.7 Appendices

A Discrete Preservation of the Contact Discontinuity Riemann Invariants

Before focusing on the preservation of the contact discontinuity Riemann invariants property, let us have a look on the discrete momentum equation related to the flux (3.24).

$$
\begin{aligned}
&\text{Assume that: } u_i^{n+} = \frac{\mathrm{R}_i^{n+} + \mathrm{W}_i^{n+}}{2} \text{ ,then:} \\
&u_i^{n+1} = \frac{\mathrm{R}_i^{n+1} + \mathrm{W}_i^{n+1}}{2} \\
&\Leftrightarrow \frac{u_i^{n+1} - u_i^{n+}}{\Delta t} = \frac{1}{2}\left[\frac{\mathrm{R}_i^{n+1} - \mathrm{R}_i^{n+}}{\Delta t} + \frac{\mathrm{W}_i^{n+1} - \mathrm{W}_i^{n+}}{\Delta t}\right] \\
&\Leftrightarrow \frac{u_i^{n+1} - u_i^{n+}}{\Delta t} = -\frac{(1-(\mathscr{E}_0^n)^2)(a_{\mathcal{A}})^{n+}\,\tau_i^{n+}}{2}\left[\frac{\mathrm{R}_i^{n+1} - \mathrm{R}_{i-1}^{n+1}}{\Delta x} - \frac{\mathrm{W}_{i+1}^{n+1} - \mathrm{W}_i^{n+1}}{\Delta x}\right] \\
&\underbrace{\Leftrightarrow}_{\rho_i^{n+1}=\rho_i^{n+}} \frac{\rho_i^{n+1}\,u_i^{n+1} - \rho_i^{n+}\,u_i^{n+}}{\Delta t} + \frac{(1-(\mathscr{E}_0^n)^2)\,(a_{\mathcal{A}})^{n+}}{\Delta x}\left[\frac{\mathrm{R}_i^{n+1} - \mathrm{W}_{i+1}^{n+1}}{2} - \frac{\mathrm{R}_{i-1}^{n+1} - \mathrm{W}_i^{n+1}}{2}\right] = 0 \\
&\Leftrightarrow \frac{\rho_i^{n+1}\,u_i^{n+1} - \rho_i^{n+}\,u_i^{n+}}{\Delta t} + (1-(\mathscr{E}_0^n)^2)\frac{(p^*_{\mathcal{A}})_{i+1/2}^{n+1} - (p^*_{\mathcal{A}})_{i-1/2}^{n+1}}{\Delta x} = 0, \\
&\text{with: } (p^*_{\mathcal{A}})_{i+1/2}^{n+1} = (a_{\mathcal{A}})^{n+}\,\frac{\mathrm{R}_i^{n+1} - \mathrm{W}_{i+1}^{n+1}}{2}.
\end{aligned}
\tag{3.45}
$$

Thus:

$$
\begin{aligned}
&u_i^{n+} = \frac{\mathrm{R}_i^{n+} + \mathrm{W}_i^{n+}}{2}, \text{ and } u_i^{n+1} = \frac{\mathrm{R}_i^{n+1} + \mathrm{W}_i^{n+1}}{2} \Leftrightarrow \\
&u_i^{n+} = \frac{\mathrm{R}_i^{n+} + \mathrm{W}_i^{n+}}{2}, \text{ and } \frac{(\rho\,u)_i^{n+1} - (\rho\,u)_i^{n+}}{\Delta t} + (1-(\mathscr{E}_0^n)^2))\frac{(p^*_{\mathcal{A}})_{i+1/2}^{n+1} - (p^*_{\mathcal{A}})_{i-1/2}^{n+1}}{\Delta x} = 0.
\end{aligned}
\tag{3.46}
$$

Then, if $u_i^{n+} = \left(\mathrm{R}_i^{n+} + \mathrm{W}_i^{n+}\right)/2$, solving the momentum equation is strictly equivalent to directly setting $u_i^{n+1} = \left(\mathrm{R}_i^{n+1} + \mathrm{W}_i^{n+1}\right)/2$.

Discrete Preservation of the Riemann Invariants of a Contact Discontinuity

Consider an equation of state such that:

$$
\left(\rho\,\varepsilon\right)^{\mathrm{EOS}}\left(\rho,\,p\right) = \mathrm{C}(p)\,\rho + \mathrm{B}(p), \tag{3.47}
$$

with $p \to \mathrm{C}(p)$ and $p \to \mathrm{B}(p)$ smooth functions such as $\left(\rho\,\varepsilon\right)^{\mathrm{EOS}}_{|\rho} : p \to \mathrm{C}(p)\,\rho + \mathrm{B}(p)$ is injective on the domain of definition of p. Formula (3.47) belongs to the "T1-class" of EOS introduced in [17]. One can notice that the stiffened gas EOS is included in this category. In the sequel, the exact invariance of velocity and pressure in the case of an isolated contact wave described in Section 3.5.1 is checked.

Acoustic Sub-step

Assume that at the end of the convective sub-step, the isolated contact discontinuity has been preserved:

$$
\begin{aligned}
&\forall\, i:\ u_i^{n+} = u^0,\ p_i^{n+} = p^0, \\
\Rightarrow &\forall\, i:\ \mathrm{W}_i^{n+} = u^0 - \frac{p^0}{a_{\mathcal{A}}^{n+}} = \mathrm{W}^{0,n+},\ \mathrm{R}_i^{n+} = u^0 + \frac{p^0}{a_{\mathcal{A}}^{n+}} = \mathrm{R}^{0,n+}.
\end{aligned}
\tag{3.48}
$$

Considering the discrete dynamics of W and R written in (3.22) coupled with the transparent boundary conditions $\mathrm{W}^{n+}_{\mathrm{N}_{cells}+1} = \mathrm{W}^{n+}_{\mathrm{N}_{cells}}$ and $\mathrm{W}^{n+}_{0} = \mathrm{W}^{n+}_{1}$, one can easily see that:

$$\forall\, i:\ \mathrm{W}_i^{n+1} = \mathrm{W}^{0,n+},\ \mathrm{R}_i^{n+1} = \mathrm{R}^{0,n+}. \tag{3.49}$$

Please note that the constant relaxation hypothesis $(a_{\mathcal{A}})^n = \mathrm{K} \max\limits_{i\in[1,\mathrm{N}_{cells}]} \left(\rho_i^n (c_{\mathcal{A}})_i^n\right)$, $\mathrm{K} > 1$, plays an important role here since a local value of $a_{\mathcal{A}}$ would have been sensible to the density discontinuity preventing W and R to remain constant. Thus, property (3.49) cannot be guaranteed in this case. Then, $(p^*_{\mathcal{A}})^{n+1}_{i+1/2} = (p^*_{\mathcal{A}})^{n+1}_{i-1/2} = a^{n+}_{\mathcal{A}} \left(\mathrm{R}^{0,n+} - \mathrm{W}^{0,n+}\right)/2$ and $(u^*_{\mathcal{A}})^{n+1}_{i+1/2} = (u^*_{\mathcal{A}})^{n+1}_{i-1/2} = \left(\mathrm{R}^{0,n+} + \mathrm{W}^{0,n+}\right)/2$ such that the discrete fluctuation of the time-implicit acoustic flux is null. The mass, momentum and the energy equations thus become:

$$\begin{aligned}
&\frac{\rho_i^{n+1} - \rho_i^{n+}}{\Delta t} = 0,\\
&\rho_i^{n+} \frac{u_i^{n+1} - u_i^{n+}}{\Delta t} = 0,\\
&\rho_i^{n+} \frac{\left(\varepsilon_i^{n+1} - \varepsilon_i^{n+}\right) + \left((u_i^{n+1})^2/2 - (u_i^{n+})^2/2\right)}{\Delta t} = 0.
\end{aligned}
\quad \Rightarrow \quad
\begin{aligned}
&\rho_i^{n+1} = \rho_i^{n+},\\
&u_i^{n+1} = u_i^{n+} = u^0,\\
&(\rho\varepsilon)^{\mathrm{EOS}}\left(\rho_i^{n+}, p_i^{n+1}\right) = (\rho\varepsilon)^{\mathrm{EOS}}\left(\rho_i^{n+}, p_i^{n+}\right).
\end{aligned} \tag{3.50}$$

Since $\left(\rho\varepsilon\right)^{\mathrm{EOS}}_{|\rho} : p \to \mathrm{C}(p)\rho + \mathrm{B}(p)$ is injective, $p_i^{n+1} = p_i^{n+} = p^0$ and the acoustic sub-step exactly preserves the velocity and pressure uniform profiles.

Convective Sub-step

The convective flux associated to subsystem $\mathcal{C}$ is obtained using the same kind of relaxation method. Details are given in [24, 25]. The convective flux formula at face $i+1/2$ reads:

$$\mathbf{H}_{\mathcal{C}}{}^{n}_{i+1/2} = \begin{cases}
\left(\mathbf{F}_{\mathcal{C}}\right)^n_i & \text{if } u_i^n - \mathscr{E}_0^n (a_{\mathcal{C}}^n)_{i+1/2}\tau_i^n > 0\\
\left(\mathbf{F}_{\mathcal{C}}\right)^{*,n}_{i+1/2} & \text{if } u_i^n - \mathscr{E}_0^n (a_{\mathcal{C}}^n)_{i+1/2}\tau_i^n \le 0 < (u^*_{\mathcal{C}})^n_{i+1/2}\\
\left(\mathbf{F}_{\mathcal{C}}\right)^{**,n}_{i+1/2} & \text{if } (u^*_{\mathcal{C}})^n_{i+1/2} \le 0 < u_{i+1}^n + \mathscr{E}_0^n (a_{\mathcal{C}}^n)_{i+1/2}\tau_{i+1}^n\\
\left(\mathbf{F}_{\mathcal{C}}\right)^n_{i+1} & \text{if } u_{i+1}^n + \mathscr{E}_0^n (a_{\mathcal{C}}^n)_{i+1/2}\tau_{i+1}^n \le 0\\
(a_{\mathcal{C}}^n)_{i+1/2} = & \mathrm{K}\max\left(\rho_i^n (c_{\mathcal{C}})_i^n, \rho_{i+1}^n (c_{\mathcal{C}})_{i+1}^n\right),\ \mathrm{K} > 1\\
\mathbf{F}_{\mathcal{C}}\left(\mathbf{U}\right) = & \left[\rho u, \rho u^2 + \mathscr{E}_0^2 p, (\rho e + \mathscr{E}_0^2 p) u\right]^{\mathrm{T}},
\end{cases} \tag{3.51}$$

where $(a_{\mathcal{C}}^n)_{i+1/2} = \mathrm{K}\max\left(\rho_i^n (c_{\mathcal{C}})_i^n, \rho_{i+1}^n (c_{\mathcal{C}})_{i+1}^n\right)$, $\mathrm{K} > 1$, the discrete convective relaxation constant fulfilling the convective subcharacteristic condition, *i.e.* $a_{\mathcal{C}} > \rho\, c_{\mathcal{C}}$, throughout the whole computational domain and with:

$$\begin{aligned}
\left(\mathbf{F}_{\mathcal{C}}\right)^{*,n}_{i+1/2} &= \begin{bmatrix} (\rho^*_{\mathcal{C}})^n_i\, (u^*_{\mathcal{C}})^n_{i+1/2} \\ (\rho^*_{\mathcal{C}})^n_i \left((u^*_{\mathcal{C}})^n_{i+1/2}\right)^2 + (\mathscr{E}_0^n)^2 (\Pi^*_{\mathcal{C}})^n_{i+1/2} \\ \left((\rho^*_{\mathcal{C}}\, e^*_{\mathcal{C}})^n_i + (\mathscr{E}_0^n)^2 (\Pi^*_{\mathcal{C}})^n_{i+1/2}\right)(u^*_{\mathcal{C}})^n_{i+1/2} \end{bmatrix},\\
\left(\mathbf{F}_{\mathcal{C}}\right)^{**,n}_{i+1/2} &= \begin{bmatrix} (\rho^*_{\mathcal{C}})^n_{i+1}\, (u^*_{\mathcal{C}})^n_{i+1/2} \\ (\rho^*_{\mathcal{C}})^n_{i+1} \left((u^*_{\mathcal{C}})^n_{i+1/2}\right)^2 + (\mathscr{E}_0^n)^2 (\Pi^*_{\mathcal{C}})^n_{i+1/2} \\ \left((\rho^*_{\mathcal{C}}\, e^*_{\mathcal{C}})^n_{i+1} + (\mathscr{E}_0^n)^2 (\Pi^*_{\mathcal{C}})^n_{i+1/2}\right)(u^*_{\mathcal{C}})^n_{i+1/2} \end{bmatrix},\\
(u^*_{\mathcal{C}})^n_{i+1/2} &= \frac{u_{i+1}^n + u_i^n}{2} - \frac{\mathscr{E}_0^n}{2\,(a_{\mathcal{C}})^n_{i+1/2}} \left(p_{i+1}^n - p_i^n\right),\\
(\mathscr{E}_0^n)^2\, (\Pi^*_{\mathcal{C}})^n_{i+1/2} &= (\mathscr{E}_0^n)^2\, \frac{p_{i+1}^n + p_i^n}{2} - \frac{\mathscr{E}_0^n\, (a_{\mathcal{C}})^n_{i+1/2}}{2} \left(u_{i+1}^n - u_i^n\right),\\
(\rho^*_{\mathcal{C}})^n_k &= 1/(\tau^*_{k,\mathcal{C}})^n,\ (\tau^*_{k,\mathcal{C}})^n = \tau_k^n + \frac{(-1)^{\mathrm{J}_k+1}}{\mathscr{E}_0^n\, (a_{\mathcal{C}})^n_{i+1/2}} \left((u^*_{\mathcal{C}})^n_{i+1/2} - u_k^n\right),\\
(e^*_{\mathcal{C}})^n_k &= e_k^n + \mathscr{E}_0^n\, \frac{(-1)^{\mathrm{J}_k}}{(a_{\mathcal{C}})^n_{i+1/2}} \left((\Pi^*_{\mathcal{C}}\, u^*_{\mathcal{C}})^n_{i+1/2} - p_k^n\, u_k^n\right),\\
k &\in \{i,\, i+1\},\ \mathrm{J}_i = 1,\ \mathrm{J}_{i+1} = 2.
\end{aligned} \tag{3.52}$$

The time-explicit scheme solving the convective subsystem then reads:

$$\mathbf{U}_i^{n+} = \mathbf{U}_i^n - \frac{\Delta t}{\Delta x}\left(\mathbf{H_C}_{i+1/2}^{\,n} - \mathbf{H_C}_{i-1/2}^{\,n}\right). \tag{3.53}$$

In the case of an isolated contact discontinuity with $\underline{u^0 > 0}$, the convective flux writes:

$$\mathbf{H_C}_{i+1/2}^{\,n,\text{Contact}} = \begin{bmatrix} \rho_i^n\, u^0 \\ \rho_i^n\,(u^0)^2 + (\mathscr{E}_0^n)^2\, p^0 \\ (\rho\varepsilon)^{\text{EOS}}\left(\rho_i^n, p^0\right) u^0 + \rho_i^n \frac{(u^0)^3}{2} + (\mathscr{E}_0^n)^2\, p^0\, u^0 \end{bmatrix}. \tag{3.54}$$

The mass, momentum and energy dynamics then read:

$$\begin{aligned} &\frac{\rho_i^{n+} - \rho_i^n}{\Delta t} + u^0 \frac{\rho_i^n - \rho_{i-1}^n}{\Delta x} = 0, \\ &\frac{\rho_i^{n+} u_i^{n+} - \rho_i^n u^0}{\Delta t} + (u^0)^2 \frac{\rho_i^n - \rho_{i-1}^n}{\Delta x} = 0, \\ &\frac{(\rho\varepsilon)^{\text{EOS}}\left(\rho_i^{n+}, p_i^{n+}\right) - (\rho\varepsilon)^{\text{EOS}}\left(\rho_i^n, p^0\right)}{\Delta t} + \frac{1}{2}\frac{\rho_i^{n+}(u_i^{n+})^2 - \rho_i^n (u^0)^2}{\Delta t} \\ &+ u^0 \frac{(\rho\varepsilon)^{\text{EOS}}\left(\rho_i^n, p^0\right) - (\rho\varepsilon)^{\text{EOS}}\left(\rho_{i-1}^n, p^0\right)}{\Delta x} + \frac{(u^0)^3}{2}\frac{\rho_i^n - \rho_{i-1}^n}{\Delta x} = 0. \end{aligned} \tag{3.55}$$

By rewriting $\rho_i^{n+} u_i^{n+} - \rho_i^n u^0$ as $\rho_i^{n+}\left(u_i^{n+} - u^0\right) + \left(\rho_i^{n+} - \rho_i^n\right) u^0$ and using the discrete mass equation, the momentum equation can be simplified:

$$\rho_i^{n+} \frac{u_i^{n+} - u^0}{\Delta t} = 0 \Rightarrow u_i^{n+} = u^0. \tag{3.56}$$

The kinetic part in the discrete energy equation then vanishes by factorizing by $(u^0)^2/2$ and using, once again, the discrete mass equation. Injecting formula (3.47), one obtains:

$$\frac{\mathrm{C}(p_i^{n+})\rho_i^{n+} + \mathrm{B}(p_i^{n+}) - \left(\mathrm{C}(p^0)\rho_i^n + \mathrm{B}(p^0)\right)}{\Delta t} + u^0 \frac{\mathrm{C}(p^0)\left(\rho_i^n - \rho_{i-1}^n\right)}{\Delta x} = 0. \tag{3.57}$$

The linear behavior of $\left(\rho\varepsilon\right)_{|p}^{\text{EOS}} : \rho \to \mathrm{C}(p)\,\rho + \mathrm{B}(p)$ as well as the fact that $\mathrm{C}(p) = \mathrm{C}(p^0)$ is a constant in this configuration, play an important role. Indeed, it allows to retrieve the discrete mass equation by factorizing by $\mathrm{C}(p^0)$. Finally, one obtains:

$$\begin{aligned} &\frac{\mathrm{C}(p_i^{n+})\rho_i^{n+} + \mathrm{B}(p_i^{n+}) - \left(\mathrm{C}(p^0)\rho_i^{n+} + \mathrm{B}(p^0)\right)}{\Delta t} = 0 \\ \Leftrightarrow\ &\frac{(\rho\varepsilon)^{\text{EOS}}\left(\rho_i^{n+}, p_i^{n+}\right) - (\rho\varepsilon)^{\text{EOS}}\left(\rho_i^{n+}, p^0\right)}{\Delta t} = 0. \end{aligned} \tag{3.58}$$

Using the fact that $\left(\rho\varepsilon\right)_{|\rho_i^{n+}}^{\text{EOS}} : p \to \mathrm{C}(p)\,\rho_i^{n+} + \mathrm{B}(p)$ is injective, it results in $p_i^{n+} = p^0$.

B Stability Analysis

This appendix deals with the definition of a stability criterion for the proposed IMEX scheme. It focuses on the isolated contact discontinuity test case discussed in Section 3.5.1. As shown in Figure 3.15 and Figure 3.16 in subsection D, the present splitting seems to suffer from instabilities when the convective Courant number $\mathscr{C}_{|u|}$ goes over a certain threshold. In the following, the dependence to the Mach number M of such a threshold is examined. One can notably wonder whether the time-explicit CFL condition $\mathscr{C}_{|u|} = \mathrm{M}/(1+\mathrm{M})\mathscr{C}_{\mathrm{E}}$ is retrieved as M tends toward zero. In the sequel, the first subsection describes a pragmatic way to measure stable Courant numbers while the second one endeavors to derive a von Neumann stability analysis predicting stable Courant numbers analytically.

Empirical Stable Courant Numbers

As stated in Proposition 3.4.2 for a sufficiently simple shape of the equation of state, velocity and pressure are supposed to be left constant by the overall scheme from one time-step to another. Nonetheless, truncation errors on double-precision floating-point numbers can be amplified by the scheme's instability and lead to the crash of the simulation. Thus, the selected criterion to detect the instability appearance is: $\max_i \left(\left| p_i^n - p^0 \right| \right) / p^0 > \eta$ with $\eta = 10^{-7}$ which is nearly the single-precision for floating-point numbers. Besides at the beginning of each calculation a ramp of CFL is enforced so that the targeted Courant number is reached after 200 time-steps, which corresponds to a propagation of 0.1 m of the exact contact discontinuity. If the calculation ends without triggering the above pressure stability criterion then the same calculation is launched again on a five times finer mesh of 5×10^3 cells in order to make sure that the numerical diffusion has not damped the instability appearance.

In Figure 3.14, the curve labeled Sp-(M) gathers the different points resulting from the above stable convective Courant number research. Recall that in this test case the velocity is given by $u^0 = \mathrm{M}_{min}\, c_{\mathrm{R}}^0$, with $c^{0,\mathrm{R}} = \sqrt{(\gamma\, p^0)/\rho_{\mathrm{R}}^0}$ the maximal sound speed and M_{min} the minimal Mach number of the flow used as an input parameter here. Hence the stable Courant number upper bound is displayed as a function of M_{min}. The latter starts from $\mathrm{M}_{min} = 1$, $u^0 = 335\,(m.s^{-1})$ and decreases until $\mathrm{M}_{min} = 10^{-4}$, $u^0 = 0.0335\,(m.s^{-1})$.

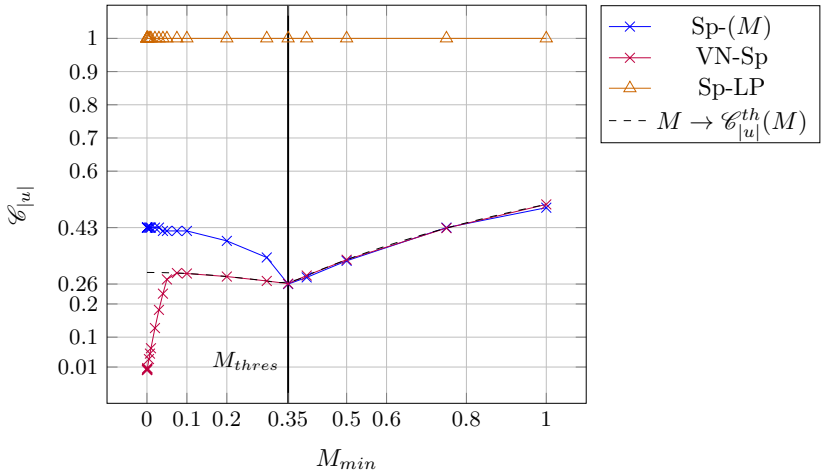

(a) Global view

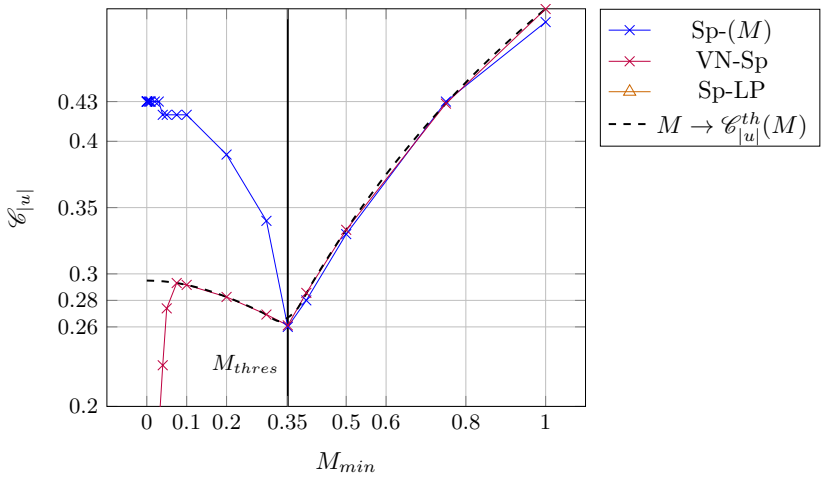

(b) Zoom: $\mathscr{C}_{|u|} \in [0.2, 0.5]$

Figure 3.14 – Evaluation of an upper bound for the stable convective Courant number $\mathscr{C}_{|u|}$ as function of the Mach number M_{min}: global view (a) and zoom in the region $\mathscr{C}_{|u|} \in [0.2, 0.5]$ (b)

One can observe that for $\mathrm{M}_{min} \approx 1$, $\mathscr{E}_0^n \approx 1$ so that the full Euler system is brought back into the time-explicit convective subsystem. The latter is thus bound by the classical CFL condition $\mathscr{C}_\mathrm{E} \approx 1$. As $\mathscr{C}_{|u|} = \mathrm{M}/(1+\mathrm{M})\mathscr{C}_\mathrm{E}$, this leads to $\mathscr{C}_{|u|} \approx 0.5$ for $\mathrm{M}_{min} \approx 1$ which is observed here. Then, as the Mach number decreases, the contribution of the time-implicit part of the acoustic subsystem becomes more and more active. It results in a drop of the Euler time-explicit CFL condition until $\mathrm{M}_{min} \approx 0.35$ where $\mathscr{C}_{|u|} = 0.26$.
An attempt at explaining this decline is given in the following. First, as it will be shown, this behavior might be related to the gap between the definition of $\mathscr{C}_{|u|}$ and the Courant number involving the largest eigenvalues of the convective subsystem as given in Section 3.4.4:

$$\begin{aligned} &\mathscr{C}_\mathcal{C} = \frac{\Delta t}{\Delta x}\left(\left|u^0\right| + \mathscr{E}_0^n\, c_\mathcal{C}^{0,\mathrm{R}}\right) \\ &\text{with: } c_\mathcal{C}^{0,\mathrm{R}} = c_\mathcal{C}\left(\rho_\mathrm{R}^0,\, p^0\right). \end{aligned} \tag{3.59}$$

One can notice that:

$$\begin{aligned} &\mathscr{C}_{|u|} = \left(1 + \mathscr{E}_0^n \frac{c_\mathcal{C}^{0,\mathrm{R}}}{\left|u^0\right|}\right)^{-1} \mathscr{C}_\mathcal{C} = \left(1 + \frac{\mathscr{E}_0^n}{\mathrm{M}_{min}} \frac{c_\mathcal{C}^{0,\mathrm{R}}}{c^{0,\mathrm{R}}}\right)^{-1} \mathscr{C}_\mathcal{C}, \\ &\text{since: } \left|u^0\right| = \mathrm{M}_{min}\, c^{0,\mathrm{R}}, \\ &\text{and: } \frac{c_\mathcal{C}^{0,\mathrm{R}}}{c^{0,\mathrm{R}}} = \sqrt{(\mathscr{E}_0^n)^2 \frac{\gamma-1}{\gamma} + \frac{1}{\gamma}} \in \left[1/\gamma,\, 1\right]. \end{aligned} \tag{3.60}$$

Besides, according to formula (3.21):

$$\begin{aligned} \mathscr{E}_0^n &= \min\left(\mathrm{M}_{max}^n,\, 1\right) = \min\left(\left|u^0\right| / c^{0,\mathrm{L}},\, 1\right) \\ &= \min\left(\mathrm{M}_{min}\sqrt{\frac{\rho_\mathrm{L}^0}{\rho_\mathrm{R}^0}},\, 1\right), \\ \text{then for } \mathrm{M}_{min} \geq \mathrm{M}_{thres} &= \sqrt{\frac{\rho_\mathrm{R}^0}{\rho_\mathrm{L}^0}} :\ \mathscr{E}_0^n = 1, \\ \text{and for } \mathrm{M}_{min} < \mathrm{M}_{thres} &= \sqrt{\frac{\rho_\mathrm{R}^0}{\rho_\mathrm{L}^0}} :\ \mathscr{E}_0^n = \mathrm{M}_{min}/\mathrm{M}_{thres}. \end{aligned} \tag{3.61}$$

It results that:

$$\mathscr{C}_{|u|} = \begin{cases} \left(1 + \dfrac{1}{\mathrm{M}_{min}}\right)^{-1} \mathscr{C}_\mathcal{C}, & \text{if } \mathrm{M}_{min} \geq \mathrm{M}_{thres}, \\ \left(1 + \dfrac{1}{\mathrm{M}_{thres}}\sqrt{\left(\dfrac{\mathrm{M}_{min}}{\mathrm{M}_{thres}}\right)^2 \dfrac{\gamma-1}{\gamma} + \dfrac{1}{\gamma}}\right)^{-1} \mathscr{C}_\mathcal{C}, & \text{otherwise.} \end{cases} \tag{3.62}$$

Define $\mathrm{M}_{min} \rightarrow \mathscr{C}_{|u|}^{th}(\mathrm{M}_{min})$, the continuous function described by formula (3.62). This function has been plotted as a dashed black line in Figure 3.14.

For every M_{min} between M_{thres} and 1 the comparison between $\mathscr{C}_{|u|}^{th}$ and the measured stable convective Courant number is fair: the cut-off $\mathrm{M}_{min} = \mathrm{M}_{thres} \approx 0.35$, the $\mathscr{C}_{|u|}^{th}(\mathrm{M}_{thres}) \approx 0.26$ value as well as the global shape of $\mathscr{C}_{|u|}^{th}(.)$ are retrieved. Yet, as M_{min} falls below M_{thres}, the measured stable convective Courant number increases to reach the plateau value $\mathscr{C}_{|u|} = 0.43$ which is bigger than the one predicted by the above analysis.

In any case, for this specific test case, $\mathscr{C}_{|u|} \approx 0.26$ or equivalently $\mathscr{C}_\mathcal{C} \approx 1$ is sufficient to ensure the scheme stability for *every Mach number*. Thus, the "Mach-uniform" stability property, $\mathscr{C}_{|u|} \approx 1$, $\forall \mathrm{M}_{min}$, obtained by Zakerzadeh in [39] for the IMEX LP scheme and which can be observed in Figure 3.14, is not retrieved for the present method. At a given Mach number, the presence of $\pm\mathscr{E}_0\, c_\mathcal{C}$ in the eigenvalues of the convective subsystem prevents from reaching the stability

condition $\mathscr{C}_{|u|} \approx 1$. However, in the above simple test case, the stable convective Courant number $\mathscr{C}_{\mathcal{C}}$ no longer behaves as $\mathrm{O}(\mathrm{M}_{min})$ as $\mathrm{M}_{min} \to 0$.

This latter result is absolutely not guaranteed by the time-implicit integration of the stiff part of the IMEX approach and strongly depends on the splitting at stake. Indeed, in [34, 40] several IMEX fractional steps on Euler-like systems are studied. It turns out that the "modified" equation obtained from the order two Taylor expansion of a smooth solution of an IMEX fractional step approach exhibits a diffusive operator which can be written as $\mathbf{D}_0\,\partial_{xx}\,\mathbf{U}$; with $\mathbf{D}_0 = \beta\,\mathscr{C}_{|u|}\,\mathbf{I} - (\mathbf{A}_0^{\mathcal{C}})^2 + (\mathbf{A}_0^{\mathcal{A}})^2 + \left[\mathbf{A}_0^{\mathcal{C}}, \mathbf{A}_0^{\mathcal{A}}\right]$, β being a coefficient related to the scheme numerical diffusion of the convective sub-step, $\mathbf{A}_0^{\mathcal{C}}$ (respectively $\mathbf{A}_0^{\mathcal{A}}$) the linearized jacobian matrix related to the convective (respectively the acoustic) subsystem, and $\left[\mathbf{A}_0^{\mathcal{C}}, \mathbf{A}_0^{\mathcal{A}}\right] = \mathbf{A}_0^{\mathcal{C}}\mathbf{A}_0^{\mathcal{A}} - \mathbf{A}_0^{\mathcal{A}}\mathbf{A}_0^{\mathcal{C}}$ being the commutator linked to the splitting. The latter can be viewed as a mathematical operator which couples the two subsystems of the fractional step approach. Hence, even if it is discretized using a time-implicit scheme, the acoustic subsystem can still have an influence on the overall fractional step stability through the commutator which can impact the diffusion (or the anti-diffusion) effect of the modified equation. In Figure 3.14, the orange-triangle line labeled "Sp-LP" represents the stable convective Courant number obtained with the Lagrange-Projection IMEX approach. As already proven in [39], this scheme is Mach-uniformly stable for $\mathscr{C}_{|u|} = 1$.

The next subsection provides an analytical stability analysis in order to compare with the above measured stable Courant numbers.

A Von Neumann Stability Analysis

In order to better understand the shape of the stable Courant number, a von Neumann-like stability analysis based on a linearized version of the IMEX approach has been performed. This strategy is motivated by the fact that, as shown in Figure 3.15 of subsection D, the instability seems to appear in a region where ρ, u and p are constant. The linearization required by the von Neumann analysis is thus justified. However, one should keep in mind that such a method relies on periodic boundary conditions which is not the case here because of the density discontinuity.

Starting at time-step t^n with a perturbed constant flow:

$$\begin{aligned} \rho_i^n &= \rho^0 + \epsilon\,\rho_i^{1,n},\ \rho^0 = \rho_{\mathrm{R}}^0, \\ u_i^n &= u^0 + \epsilon\,u_i^{1,n}, \\ p_i^n &= p^0 + \epsilon\,p_i^{1,n}, \end{aligned} \tag{3.63}$$

the discrete dynamics of the perturbation is derived when a Rusanov scheme is used to solve the first convective subsystem (3.3). The numerical flux at face $i+1/2$ associated to this scheme reads:

$$\begin{aligned} &\mathbf{H_{rus}}_{i+1/2}^n = \frac{\mathbf{F}^{\mathcal{C}}\left(\mathbf{U}_{i+1}^n\right) + \mathbf{F}^{\mathcal{C}}\left(\mathbf{U}_i^n\right)}{2} - \frac{\left|\lambda_{i+1/2}^n\right|}{2}\left(\mathbf{U}_{i+1}^n - \mathbf{U}_i^n\right), \\ &\text{with: } \mathbf{F}^{\mathcal{C}}(\mathbf{U}) = \left[\rho\,u,\ \rho\,u^2 + \mathscr{E}_0^2\,p,\ (\rho\,e + \mathscr{E}_0^2\,p)\,u\right]^{\mathrm{T}}, \\ &\text{and: } \left|\lambda_{i+1/2}^n\right| = \max\left(\left|u_{i+1}^n\right| + (\mathscr{E}_0)^n\,(c_{\mathcal{C}})_{i+1}^n,\ \left|u_i^n\right| + (\mathscr{E}_0)^n\,(c_{\mathcal{C}})_i^n\right). \end{aligned} \tag{3.64}$$

Let us define $\rho_i^{n+} = \rho_i^{0,n+} + \epsilon\,\rho_i^{1,n+}$, $u_i^{n+} = u_i^{0,n+} + \epsilon\,u_i^{1,n+}$, and $p_i^{n+} = p_i^{0,n+} + \epsilon\,p_i^{1,n+}$ the solution produced by the Rusanov scheme applied to the convective subsystem. Then, zeroth order and

first order dynamics can be decoupled and one obtains:

$$
\begin{aligned}
&\rho_i^{0,n+} = \rho^0,\\
&u_i^{0,n+} = u^0,\\
&p_i^{0,n+} = p^0,\\
&\frac{\rho_i^{1,n+}-\rho_i^{1,n}}{\Delta t} + u^0\,\frac{\rho_{i+1}^{1,n}-\rho_{i-1}^{1,n}}{2\Delta x} + \rho^0\,\frac{u_{i+1}^{1,n}-u_{i-1}^{1,n}}{2\Delta x} - \left|\lambda^0\right|\frac{\rho_{i+1}^{1,n}-2\rho_i^{1,n}+\rho_{i-1}^{1,n}}{2\Delta x} = 0,\\
&\frac{u_i^{1,n+}-u_i^{1,n}}{\Delta t} + u^0\,\frac{u_{i+1}^{1,n}-u_{i-1}^{1,n}}{2\Delta x} + \left((\mathscr{E}_0^n)^2/\rho^0\right)\frac{p_{i+1}^{1,n}-p_{i-1}^{1,n}}{2\Delta x} - \left|\lambda^0\right|\frac{u_{i+1}^{1,n}-2\,u_i^{1,n}+u_{i-1}^{1,n}}{2\Delta x} = 0,\\
&\frac{p_i^{1,n+}-p_i^{1,n}}{\Delta t} + u^0\,\frac{p_{i+1}^{1,n}-p_{i-1}^{1,n}}{2\Delta x} + \rho^0\,(c_{\mathcal{C}}^0)^2\,\frac{u_{i+1}^{1,n}-u_{i-1}^{1,n}}{2\Delta x} - \left|\lambda^0\right|\frac{p_{i+1}^{1,n}-2\,p_i^{1,n}+p_{i-1}^{1,n}}{2\Delta x} = 0,\\
&\text{with: } \left|\lambda^0\right| = \left|u^0\right| + (\mathscr{E}_0)^n\,(c_{\mathcal{C}}^0).
\end{aligned}
\tag{3.65}
$$

If $\forall\phi \in \{\rho,\, u,\, p\}$ the following sinus spatial pulse is conjectured $\phi_i^t = \hat{\phi}^t\, e^{j\,k\,x_i},\ t \in \{n,\, n+\}$; one can derive the von Neumann gain matrix related to the convective subsystem:

$$
\begin{bmatrix}\hat{\rho}^{n+}\\ \hat{u}^{n+}\\ \hat{p}^{n+}\end{bmatrix} = \begin{bmatrix} \mathrm{G} & -\frac{\rho^0\mathscr{C}_{|u|}}{|u^0|}\,j\,\sin(k\Delta x) & 0\\ 0 & \mathrm{G} & -\frac{(\mathscr{E}_0^n)^2\mathscr{C}_{|u|}}{\rho^0\,|u^0|}\,j\,\sin(k\Delta x)\\ 0 & -\frac{\rho^0\,(c_{\mathcal{C}}^0)^2\mathscr{C}_{|u|}}{|u^0|}\,j\,\sin(k\Delta x) & \mathrm{G}\end{bmatrix}\begin{bmatrix}\hat{\rho}^{n}\\ \hat{u}^{n}\\ \hat{p}^{n}\end{bmatrix},
\tag{3.66}
$$

$$
\text{with: } \mathrm{G} = 1 - 2\frac{\left|\lambda^0\right|}{\left|u^0\right|}\mathscr{C}_{|u|}\,\sin^2(k\Delta x/2) - j\,\frac{u^0}{\left|u^0\right|}\mathscr{C}_{|u|}\,\sin(k\Delta x).
$$

The spectral radius $|\mathrm{G}|_{\mathcal{C}}$ related to this gain matrix can be found easily and one can state that (See subsection C for a proof):

$$
\mathscr{C}_{|u|} < \mathscr{C}_{|u|}^{\mathrm{crit}} = \left|u^0\right| / \left|\lambda^0\right| \Rightarrow |\mathrm{G}|_{\mathcal{C}} < 1. \tag{3.67}
$$

In particular, when M_{min} tends towards one, $(\mathscr{E}_0)^n$ tends towards one and $c_{\mathcal{C}}^0$ tends towards c^0 such that $|\mathrm{G}|_{\mathcal{C}} < 1 \Leftrightarrow \mathscr{C}_{|u|} < \mathrm{M}_{min}/\,(1+\mathrm{M}_{min})$. Thus, the classical CFL condition is retrieved.

The same kind of analysis is performed on the acoustic subsystem. However, the time-implicit flux (3.24) raises new issues in the sense that its energy contribution strongly couples zeroth-order and first-order terms:

$$
\begin{aligned}
(p_{\mathcal{A}}^*)_{i+1/2}^{n+1}\,(u_{\mathcal{A}}^*)_{i+1/2}^{n+1} = {}& (p_{\mathcal{A}}^{0,*})_{i+1/2}^{n+1}\,(u_{\mathcal{A}}^{0,*})_{i+1/2}^{n+1}\\
&+ \epsilon\left((p_{\mathcal{A}}^{0,*})_{i+1/2}^{n+1}\,(u_{\mathcal{A}}^{1,*})_{i+1/2}^{n+1} + (p_{\mathcal{A}}^{1,*})_{i+1/2}^{n+1}\,(u_{\mathcal{A}}^{0,*})_{i+1/2}^{n+1}\right).
\end{aligned}
\tag{3.68}
$$

What is more, this coupling is strongly non-linear and prevents from deriving a simple von Neumann analysis. That is why, it has been additionally assumed that zeroth-order terms including these taken at time t^{n+1} were constant namely:

$$
\begin{aligned}
&\rho_i^{0,n+1} = \rho^0,\\
&u_i^{0,n+1} = u^0,\\
&p_i^{0,n+1} = p^0;
\end{aligned}
\tag{3.69}
$$

then, as proved in subsection C the dynamics of the perturbation reads:

$$
\begin{aligned}
&\frac{\rho_i^{1,n+1}-\rho_i^{1,n+}}{\Delta t} = 0,\\
&\frac{u_i^{1,n+1}-u_i^{1,n+}}{\Delta t} + \left(1-(\mathscr{E}_0^n)^2\right)\left[\frac{1}{\rho^0}\,\frac{p_{i+1}^{1,n+1}-p_{i-1}^{1,n+1}}{2\Delta x} - \frac{a_{\mathcal{A}}^0}{\rho^0}\,\frac{u_{i+1}^{1,n+1}-2\,u_i^{1,n+1}+u_{i-1}^{1,n+1}}{2\Delta x}\right] = 0,\\
&\frac{p_i^{1,n+1}-p_i^{1,n+}}{\Delta t} + \left(1-(\mathscr{E}_0^n)^2\right)\rho^0\,(c_{\mathcal{A}}^0)^2\left[\frac{u_{i+1}^{1,n+1}-u_{i-1}^{1,n+1}}{2\Delta x} - \frac{1}{a_{\mathcal{A}}^0}\,\frac{p_{i+1}^{1,n+1}-2\,p_i^{1,n+1}+p_{i-1}^{1,n+1}}{2\Delta x}\right] = 0.
\end{aligned}
\tag{3.70}
$$

The von Neumann gain matrix writes:

$$\begin{bmatrix} 1 & 0 & 0 \\ 0 & 1+2\alpha^n \sin^2(k\Delta x/2) & \frac{\alpha^n}{a^0_{\mathcal{A}}} j \sin(k\Delta x) \\ 0 & \alpha^n (\omega^0_{\mathcal{A}})^2 a^0_{\mathcal{A}} j \sin(k\Delta x) & 1+2\alpha^n (\omega^0_{\mathcal{A}})^2 \sin^2(k\Delta x/2) \end{bmatrix} \begin{bmatrix} \hat{\rho}^{n+1} \\ \hat{u}^{n+1} \\ \hat{p}^{n+1} \end{bmatrix} = \begin{bmatrix} \hat{\rho}^{n+} \\ \hat{u}^{n+} \\ \hat{p}^{n+} \end{bmatrix},$$
$$\text{with: } \alpha^n = \left(1-(\mathscr{E}_0^n)^2\right) \frac{a^0_{\mathcal{A}} \mathscr{C}_{|u|}}{\rho^0 |u^0|}, \tag{3.71}$$
$$\text{and: } \omega^0_{\mathcal{A}} = \frac{\rho^0 c^0_{\mathcal{A}}}{a^0_{\mathcal{A}}}.$$

Finally the von Neumann gain matrix related to the fractional step approach reads:

$$\begin{bmatrix} \mathrm{G} & 0 \\ 0 & \mathbf{G}_{\mathcal{A}}^{-1}\mathbf{G}_{\mathcal{C}} \end{bmatrix},$$
with:
$$\mathbf{G}_{\mathcal{C}} = \begin{bmatrix} \mathrm{G} & -\frac{(\mathscr{E}_0^n)^2 \mathscr{C}_{|u|}}{\rho^0 |u^0|} j \sin(k\Delta x) \\ -\frac{\rho^0 (c^0_{\mathcal{C}})^2 \mathscr{C}_{|u|}}{|u^0|} j \sin(k\Delta x) & \mathrm{G} \end{bmatrix}, \tag{3.72}$$
$$\mathbf{G}_{\mathcal{A}} = \begin{bmatrix} 1+2\alpha^n \sin^2(k\Delta x/2) & \frac{\alpha^n}{a^0_{\mathcal{A}}} j \sin(k\Delta x) \\ \alpha^n (\omega^0_{\mathcal{A}})^2 a^0_{\mathcal{A}} j \sin(k\Delta x) & 1+2\alpha^n (\omega^0_{\mathcal{A}})^2 \sin^2(k\Delta x/2) \end{bmatrix},$$
$$\mathbf{G}_{\mathcal{A}}^{-1} = \frac{1}{\Delta} \begin{bmatrix} 1+2\alpha^n (\omega^0_{\mathcal{A}})^2 \sin^2(k\Delta x/2) & -\frac{\alpha^n}{a^0_{\mathcal{A}}} j \sin(k\Delta x) \\ -\alpha^n (\omega^0_{\mathcal{A}})^2 a^0_{\mathcal{A}} j \sin(k\Delta x) & 1+2\alpha^n \sin^2(k\Delta x/2) \end{bmatrix}, \ \Delta = \det \mathbf{G}_{\mathcal{A}}.$$

G is a first eigenvalue related to the mass equation. As written in C, $|\mathrm{G}| < 1$ if $\mathscr{C}_{|u|} < \mathscr{C}^{\mathrm{crit}}_{|u|}$. The two remaining eigenvalues are linked to the matrix $\mathbf{G}_{\mathcal{A}}^{-1}\mathbf{G}_{\mathcal{C}}$ which couples the momentum and the energy equations and can not be easily found analytically. Starting from $\mathscr{C}^{\mathrm{crit}}_{|u|}$, a loop on all the k modes $\in [0, 4\pi/\Delta x]$ is performed and the spectral radius $|\mathrm{G}|^k_{\mathcal{AC}}$ associated to $\left(\mathbf{G}_{\mathcal{A}}^{-1}\mathbf{G}_{\mathcal{C}}\right)(k)$ is calculated. If, during the loop, $|\mathrm{G}|^k_{\mathcal{AC}} > 1$, then $\mathscr{C}^{\mathrm{crit}}_{|u|}$ is slightly decreased and the loop is restarted. Otherwise the current Courant number is stored and considered as the stable Courant number of the above von Neumann analysis.

In Figure 3.14, the curve labeled "VN-Sp" (red line) displays the different stable convective Courant numbers obtained thanks to the above von Neumann method. Recall that the analytical curve $\mathrm{M} \rightarrow \mathscr{C}^{th}_{|u|}(\mathrm{M})$ is equivalent to $\mathscr{C}_{\mathcal{C}} = 1$ for this test case. For $\mathrm{M}_{min} \in \left[7.5\times10^{-2}, 1\right]$, "VN-Sp" and $\mathrm{M} \rightarrow \mathscr{C}^{th}_{|u|}(\mathrm{M})$ overlap quasi-perfectly. Unfortunately, for very low Mach numbers, $\mathscr{C}_{|u|}$ plunges down. For example, it predicts $\mathscr{C}_{|u|} = 10^{-2}$ when $\mathrm{M}_{min} = 10^{-4}$.

This difference could stem from the assumptions made on the time-implicit acoustic scheme in order to linearize it. Indeed the zeroth order terms of the updated solution have been assumed to be constant:

$$\begin{aligned} \rho_i^{0,n+1} &= \rho^0, \\ u_i^{0,n+1} &= u^0, \\ p_i^{0,n+1} &= p^0. \end{aligned} \tag{3.73}$$

The resulting dynamics then binds only first-order pressure terms with first-order velocity terms. Yet, in that case the small perturbation parameter ϵ is not related to the flow Mach number. As formally shown in [24, 25] on the continuous subsystem $\mathcal{A}$, one could make the discrete acoustic scheme (3.24) non-dimensional and consider a constant base flow perturbed by modes written in powers of the Mach number. Then, one would observe that the zeroth-order momentum term is fed by the second-order pressure gradient. Thus, one could assume that if the amplitude of this second-order pressure gradient explodes because of an instability, the zeroth-order momentum term would rise too. It would result in an increase of the Mach number associated with a decrease

of the discrete numerical time-step built on the zeroth-order velocity terms. This might damp the instability. In any case, further investigations should be done in order to better understand this sudden drop.

C Study of the von Neumann Gain Matrices

This appendix is dedicated to the study of the von Neumann gain matrices written in (3.66) and (3.72). The derivation of the convective gain matrix being relatively straightforward, special attention is paid to the expression of its eigenvalues as well as a sufficient condition ensuring that their modulus is strictly lower than one. Besides, the derivation of the acoustic gain matrix is completely done.

Analysis of the Convective Gain Matrix Eigenvalues

Let us consider the von Neumann gain matrix associated with the convective sub-step:

$$\begin{bmatrix} \mathrm{G} & -\frac{\rho^0 \mathscr{C}_{|u|}}{|u^0|} j \sin(k\Delta x) & 0 \\ 0 & \mathrm{G} & -\frac{(\mathscr{E}_0^n)^2 \mathscr{C}_{|u|}}{\rho^0 |u^0|} j \sin(k\Delta x) \\ 0 & -\frac{\rho^0 (c_{\mathcal{C}}^0)^2 \mathscr{C}_{|u|}}{|u^0|} j \sin(k\Delta x) & \mathrm{G} \end{bmatrix},$$
$$\text{and: } \mathrm{G} = 1 - 2\frac{\mathscr{C}_{|u|}}{\mathscr{C}_{|u|}^{\mathrm{crit}}} \sin^2(k\Delta x/2) - j\frac{u^0}{|u^0|}\mathscr{C}_{|u|} \sin(k\Delta x), \tag{3.74}$$
$$\text{with: } \mathscr{C}_{|u|}^{\mathrm{crit}} = |u^0| / |\lambda^0| \in]0, 1[.$$

G is the first eigenvalue of this matrix. Define $\mathrm{X} = \sin^2(k\Delta x/2) \in [0, 1]$, then $\sin^2(k\Delta x) = 4\mathrm{X}(1-\mathrm{X})$. Thus:

$$|\mathrm{G}|^2 = \left(1 - 2\frac{\mathscr{C}_{|u|}}{\mathscr{C}_{|u|}^{\mathrm{crit}}}\mathrm{X}\right)^2 + 4\mathscr{C}_{|u|}^2 \mathrm{X}(1-\mathrm{X}),$$
$$|\mathrm{G}|^2 < 1 \Leftrightarrow \mathscr{C}_{|u|} < \frac{\mathscr{C}_{|u|}^{\mathrm{crit}}}{\left((1 - (\mathscr{C}_{|u|}^{\mathrm{crit}})^2)\mathrm{X} + (\mathscr{C}_{|u|}^{\mathrm{crit}})^2\right)}. \tag{3.75}$$

Since $\mathrm{X} \in [0, 1]$ the most constraining CFL condition is $\mathscr{C}_{|u|} < \mathscr{C}_{|u|}^{\mathrm{crit}}$.

The two other eigenvalues of the above gain matrix are the roots of the characteristic polynomial function:

$$(\mathrm{G} - \lambda)^2 + (\mathscr{E}_0^n)^2 (\mathscr{C}_{|u|})^2 \left(\frac{c_{\mathcal{C}}^0}{u^0}\right)^2 \sin^2(k\Delta x). \tag{3.76}$$

They write:

$$\lambda^{\pm} = \mathrm{G} \mp j\mathscr{E}_0^n \mathscr{C}_{|u|} \left|\frac{c_{\mathcal{C}}^0}{u^0}\right| |\sin(k\Delta x)|,$$
$$|\lambda^{\pm}|^2 = \left(1 - 2\frac{\mathscr{C}_{|u|}}{\mathscr{C}_{|u|}^{\mathrm{crit}}}\mathrm{X}\right)^2 + \mathscr{C}_{|u|}^2 \left([1 + (\mathscr{E}_0^n)^2 \left|\frac{c_{\mathcal{C}}^0}{u^0}\right|^2] 4\mathrm{X}(1-\mathrm{X}) \pm 2\mathscr{E}_0^n \frac{u^0}{|u^0|}\left|\frac{c_{\mathcal{C}}^0}{u^0}\right| \sin(k\Delta x)\,|\sin(k\Delta x)|\right) \tag{3.77}$$
$$\Rightarrow |\lambda^{\pm}|^2 \leq \left(1 - 2\frac{\mathscr{C}_{|u|}}{\mathscr{C}_{|u|}^{\mathrm{crit}}}\mathrm{X}\right)^2 + 4\left(1 + \mathscr{E}_0^n \left|\frac{c_{\mathcal{C}}^0}{u^0}\right|\right)^2 \mathscr{C}_{|u|}^2 \mathrm{X}(1-\mathrm{X}) = \left(1 - 2\frac{\mathscr{C}_{|u|}}{\mathscr{C}_{|u|}^{\mathrm{crit}}}\mathrm{X}\right)^2 + 4\left(\frac{\mathscr{C}_{|u|}}{\mathscr{C}_{|u|}^{\mathrm{crit}}}\right)^2 \mathrm{X}(1-\mathrm{X}).$$

A sufficient condition ensuring that $|\lambda^{\pm}| < 1$ is once again $\mathscr{C}_{|u|} < \mathscr{C}_{|u|}^{\mathrm{crit}}$.

Derivation of the Linearized Acoustic Dynamics

The von Neumann analysis has to be made on the relaxation system (3.10). Define at time t^{n+}:

$$\begin{aligned} \mathrm{W}_i^{n+} &= u_i^{n+} - \frac{p_i^{n+}}{a_{\mathcal{A}}^{n+}} = u_i^{n+} - \frac{\Pi_i^{n+}}{a_{\mathcal{A}}^{n+}}, \\ \mathrm{R}_i^{n+} &= u_i^{n+} + \frac{p_i^{n+}}{a_{\mathcal{A}}^{n+}} = u_i^{n+} + \frac{\Pi_i^{n+}}{a_{\mathcal{A}}^{n+}}. \end{aligned} \tag{3.78}$$

Then,

$$\begin{aligned} &\begin{cases} \frac{\rho_i^{n+1}-\rho_i^{n+}}{\Delta t} = 0, \\ \frac{(\rho u)_i^{n+1}-(\rho u)_i^{n+}}{\Delta t} + \left(1-(\mathscr{E}_0^n)^2\right)\frac{(p_{\mathcal{A}}^*)_{i+1/2}^{n+1}-(p_{\mathcal{A}}^*)_{i-1/2}^{n+1}}{\Delta x} = 0, \\ \frac{(\rho \Pi)_i^{n+1}-(\rho \Pi)_i^{n+}}{\Delta t} + \left(1-(\mathscr{E}_0^n)^2\right)(a_{\mathcal{A}}^{n+})^2\frac{(u_{\mathcal{A}}^*)_{i+1/2}^{n+1}-(u_{\mathcal{A}}^*)_{i-1/2}^{n+1}}{\Delta x} = 0, \\ \frac{(\rho e)_i^{n+1}-(\rho e)_i^{n+}}{\Delta t} + \left(1-(\mathscr{E}_0^n)^2\right)\frac{(p_{\mathcal{A}}^* u_{\mathcal{A}}^*)_{i+1/2}^{n+1}-(p_{\mathcal{A}}^* u_{\mathcal{A}}^*)_{i-1/2}^{n+1}}{\Delta x} = 0, \end{cases} \\ \Leftrightarrow \\ &\begin{cases} \frac{\rho_i^{n+1}-\rho_i^{n+}}{\Delta t} & = 0, \\ \frac{(\rho u)_i^{n+1}-(\rho u)_i^{n+}}{\Delta t} & + \left(1-(\mathscr{E}_0^n)^2\right)\left[\frac{\Pi_{i+1}^{n+1}-\Pi_{i-1}^{n+1}}{2\Delta x} - \frac{a_{\mathcal{A}}^{n+}}{2}\frac{u_{i+1}^{n+1}-2u_i^{n+1}+u_{i-1}^{n+1}}{\Delta x}\right] = 0, \\ \frac{(\rho \Pi)_i^{n+1}-(\rho \Pi)_i^{n+}}{\Delta t} & + \left(1-(\mathscr{E}_0^n)^2\right)\left[(a_{\mathcal{A}}^{n+})^2\frac{u_{i+1}^{n+1}-u_{i-1}^{n+1}}{2\Delta x} - \frac{a_{\mathcal{A}}^{n+}}{2}\frac{\Pi_{i+1}^{n+1}-2\Pi_i^{n+1}+\Pi_{i-1}^{n+1}}{\Delta x}\right] = 0, \\ \frac{(\rho e)_i^{n+1}-(\rho e)_i^{n+}}{\Delta t} & + \left(1-(\mathscr{E}_0^n)^2\right)[\frac{(\Pi u)_{i+1}^{n+1}-(\Pi u)_{i-1}^{n+1}}{2\Delta x} - \frac{1}{4a_{\mathcal{A}}^{n+}}\frac{(\Pi^2)_{i+1}^{n+1}-2(\Pi^2)_i^{n+1}+(\Pi^2)_{i-1}^{n+1}}{\Delta x} \\ & - \frac{a_{\mathcal{A}}^{n+}}{4}\frac{(u^2)_{i+1}^{n+1}-2(u^2)_i^{n+1}+(u^2)_{i-1}^{n+1}}{\Delta x}] = 0. \end{cases} \end{aligned} \tag{3.79}$$

Supposing that $\forall \phi \in \{\rho, u, \Pi, e\}$, $\phi_i^{0,n+1} = \phi^0$ a constant, one can extract the linearized dynamics related to (3.79):

$$\begin{aligned} &\frac{\rho_i^{1,n+1}-\rho_i^{1,n+}}{\Delta t} = 0, \\ &\rho^0\frac{u_i^{1,n+1}-u_i^{1,n+}}{\Delta t} + \left(1-(\mathscr{E}_0^n)^2\right)\left[\frac{\Pi_i^{1,n+1}-\Pi_i^{1,n+1}}{2\Delta x} - \frac{a_{\mathcal{A}}^0}{2}\frac{u_{i+1}^{1,n+1}-2u_i^{1,n+1}+u_{i-1}^{1,n+1}}{\Delta x}\right] = 0, \\ &\rho^0\frac{\Pi_i^{1,n+1}-\Pi_i^{1,n+}}{\Delta t} + \left(1-(\mathscr{E}_0^n)^2\right)\left[(a_{\mathcal{A}}^0)^2\frac{u_i^{1,n+1}-u_i^{1,n+1}}{2\Delta x} - \frac{a_{\mathcal{A}}^0}{2}\frac{\Pi_{i+1}^{1,n+1}-2\Pi_i^{1,n+1}+\Pi_{i-1}^{1,n+1}}{\Delta x}\right] = 0, \\ &\rho^0\frac{e_i^{1,n+1}-e_i^{1,n+}}{\Delta t} + \left(1-(\mathscr{E}_0^n)^2\right)\left[p^0\frac{u_i^{1,n+1}-u_i^{1,n+1}}{2\Delta x} + u^0\frac{\Pi_i^{1,n+1}-\Pi_i^{1,n+1}}{2\Delta x}\right] \\ &\qquad - \left(1-(\mathscr{E}_0^n)^2\right)\left[\frac{p^0}{a_{\mathcal{A}}^0}\frac{\Pi_{i+1}^{1,n+1}-2\Pi_i^{1,n+1}+\Pi_{i-1}^{1,n+1}}{2\Delta x} + u^0 a_{\mathcal{A}}^0\frac{u_{i+1}^{1,n+1}-2u_i^{1,n+1}+u_{i-1}^{1,n+1}}{2\Delta x}\right] = 0. \end{aligned} \tag{3.80}$$

During the projection step, $\Pi_i^{n+1} = p_i^{n+1} = p^{\mathrm{EOS}}\left(\rho_i^{n+1}, \varepsilon_i^{n+1}\right)$ is imposed with $\varepsilon_i^{n+1} = e_i^{n+1} - (u_i^{n+1})^2/2$. If one assumes that this projection holds separately for zeroth order and first order terms then $\forall \sharp \in \{n+, n+1\}$:

$$\Pi_i^{1,\sharp} = p_i^{1,\sharp} = (\partial_\rho p_{|\varepsilon})^0 \rho_i^{1,\sharp} + (\partial_\varepsilon p_{|\rho})^0\left(e_i^{1,\sharp} - u^0 u_i^{1,\sharp}\right). \tag{3.81}$$

Using the momentum equation, the perturbed pressure dynamics is then:

$$\frac{p_i^{1,n+1}-p_i^{1,n+}}{\Delta t} + \left(1-(\mathscr{E}_0^n)^2\right)(\partial_\varepsilon p_{|\rho})^0\frac{p^0}{\rho^0}\left[\frac{u_{i+1}^{1,n+1}-u_{i-1}^{1,n+1}}{2\Delta x} - \frac{1}{a_{\mathcal{A}}^0}\frac{p_{i+1}^{1,n+1}-2p_i^{1,n+1}+p_{i-1}^{1,n+1}}{2\Delta x}\right] = 0. \tag{3.82}$$

According to definition (3.7), $\left(\partial_\varepsilon p_{|\rho}\right)^0\frac{p^0}{\rho^0}$ is exactly equal to $\rho^0(c_{\mathcal{A}}^0)^2$. The linearized dynamics of

the non conservative variables related to the acoustic scheme is then:

$$
\begin{aligned}
&\frac{\rho_i^{1,n+1}-\rho_i^{1,n+}}{\Delta t}=0,\\
&\frac{u_i^{1,n+1}-u_i^{1,n+}}{\Delta t}+\left(1-(\mathscr{C}_0^n)^2\right)\left[\frac{1}{\rho^0}\frac{p_{i+1}^{1,n+1}-p_{i-1}^{1,n+1}}{2\Delta x}-\frac{a_{\mathcal{A}}^0}{\rho^0}\frac{u_{i+1}^{1,n+1}-2\,u_i^{1,n+1}+u_{i-1}^{1,n+1}}{2\Delta x}\right]=0,\\
&\frac{p_i^{1,n+1}-p_i^{1,n+}}{\Delta t}+\left(1-(\mathscr{C}_0^n)^2\right)\rho^0\,(c_{\mathcal{A}}^0)^2\left[\frac{u_{i+1}^{1,n+1}-u_{i-1}^{1,n+1}}{2\Delta x}-\frac{1}{a_{\mathcal{A}}^0}\frac{p_{i+1}^{1,n+1}-2\,p_i^{1,n+1}+p_{i-1}^{1,n+1}}{2\Delta x}\right]=0.
\end{aligned}
\tag{3.83}
$$

D Location of the IMEX Instability

Figure 3.15 and Figure 3.16 show the growth of the numerical instability observed in the case presented in Section 3.5.1. The picture is taken at time $t = 2.496\times10^{-2}\,s$ but for a mesh of 10^3 cells (Figure 3.15) and for a finer one of 5×10^3 cells (Figure 3.16).

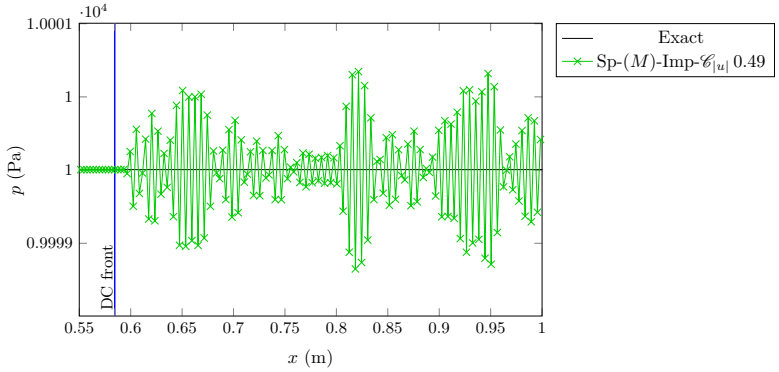

Figure 3.15 – p, Ideal Gas, $\mathrm{M}_{min}=10^{-2}$, with $\mathbf{N_{cells}}=\mathbf{10^3}$, $\mathscr{C}_{|u|}=0.49$, iteration 270, ($t=2.496\times10^{-2}\ s$)

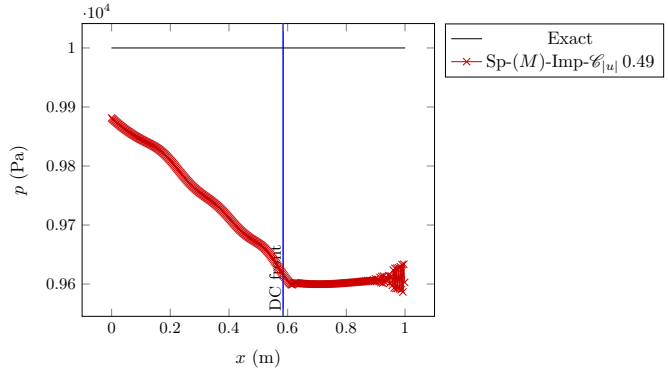

Figure 3.16 – p, Ideal Gas, $\mathrm{M}_{min}=10^{-2}$, with $\mathbf{N_{cells}}=\mathbf{5\times10^3}$, $\mathscr{C}_{|u|}=0.49$, iteration 1399, ($t=2.497\times10^{-2}\ s$)

One can observe than the instability originates from the region located after the contact discontinuity front where the Mach number takes its lowest value. As the mesh is refined, the amplitude of the instability surges considerably since the numerical diffusion is largely diminished.

E The Most Constraining Euler Courant Number

Let us consider the shock tube test case presented in Section 3.5.2. The fastest Euler eigenvalue is $u^* + c_{\mathrm{R}}^{0,*}$ with $c_{\mathrm{R}}^{0,*} = c\left(\rho_{\mathrm{R}}^*, p^*\right)$. It corresponds to the characteristic colliding with the 3-shock wave front speed. Here u^* and p^* are the intermediate velocity and pressure whose values can be approximatively calculated: $u^* \approx 1.49886\ m\,s^{-1}$, $p^* \approx 10020.9\ \mathrm{P}a$. What is more, the conservation of entropy through the 3-shock brings: $\rho_{\mathrm{R}}^* = \rho_{\mathrm{R}}^0 \left(p^*/p_{\mathrm{R}}^0\right)^{1/\gamma}$, and $c\left(\rho_{\mathrm{R}}^*, p^*\right) = c_{\mathrm{R}}^0 \left(p^*/p_{\mathrm{R}}^0\right)^{(\gamma-1)/\gamma} \approx 336.36256\ m\,s^{-1}$.

The most constraining time-step got from the above wave speed writes:

$$\Delta t_{\mathrm{E}}^{0,*} = \frac{\mathscr{C}_{\mathrm{E}}^{0,*}}{2} \frac{\Delta x}{u^* + c_{\mathrm{R}}^{0,*}}. \tag{3.84}$$

Besides the time-step related to u^0 writes simply $\Delta t_{\mathcal{C}}^{u^0} = \mathscr{C}_{|u|}^{u^0} \Delta x / u^0$. Then:

$$\Delta t_{\mathcal{C}}^{u^0} = \Delta t_{\mathrm{E}}^{0,*} \Leftrightarrow \mathscr{C}_{|u|}^{u^0} = \frac{u^0}{2\left(u^* + c_{\mathrm{R}}^{0,*}\right)} \mathscr{C}_{\mathrm{E}}^{0,*} \approx 1.48649 \times 10^{-3}\, \mathscr{C}_{\mathrm{E}}^{0,*}. \tag{3.85}$$

3.8 References

[1] L. Allievi. *Teoria del colpo d'ariete*. Atti del Collegio degli Ingegneri ed Architetti Italiani, Milan, Italy (in Italian), 1913. 77

[2] W. F. Ballhaus and P. M. Goorjian. Implicit finite-difference computations of unsteady transonic flows about airfoils. *AIAA Journal*, 15:1728–1735, 1977. 85

[3] W. F. Ballhaus and P. M. Goorjian. Implicit methods of second-order accuracy for the Euler equations. *AIAA Journal*, 23:33–40, 1985. 85

[4] R. Baraille, G. Bourdin, F. Dubois, and A. Y. Le Roux. Une version à pas fractionnaires du schéma de Godunov pour l'hydrodynamique. *Compte Rendu de l'Académie des Sciences*, 314: 147–152, 1992. 78

[5] F. Bouchut. Entropy satisfying flux vector splittings and kinetic BGK models. *Numerische Mathematik*, 94:623–672, 2003. 80

[6] F. Bouchut. *Nonlinear Stability of Finite Volume Methods for Hyperbolic Conservation Laws*. Birkäser, 2004. 78

[7] T. Buffard and J-M. Hérard. A conservative fractional step method to solve non-isentropic Euler equations. *Computer Methods in Applied Mechanics and Engineering*, 144:199–225, 1996. 78

[8] C. Chalons, M. Girardin, and S. Kokh. An all-regime Lagrange-Projection like scheme for the gas dynamics equations on unstructured meshes. *Communications in Computational Physics*, 20:188–233, 2016. 75, 76, 78, 80, 82, 83, 85, 86, 88, 91

[9] C. Chalons, M. Girardin, and S. Kokh. An all-regime Lagrange-Projection like scheme for 2D homogeneous models for two-phase flows on unstructured meshes. *Journal of Computational Physics*, 335:885–904, 2016. 85, 88

[10] S. Clerc. Numerical simulation of the homogeneous equilibrium model for two-phase flows. *Journal of Computational Physics*, 161:354–375, 2000. 79

[11] F. Coquel, Q. L. Nguyen, M. Postel, and Q. H. Tran. Entropy-satisfying relaxation method with large time-steps for Euler IBVPS. *Mathematics of Computation*, 79:1493–1533, 2010. 75, 76, 78, 81, 82, 97

[12] F. Coquel, E. Godlewski, and N. Seguin. Relaxation of fluid systems. *Mathematical Models and Methods in Applied Science*, 22:43–95, 2012. 78, 80

[13] F. Daude, I. Mary, and P. Comte. Self-adaptative Newton-based iteration strategy for the LES of turbulent multi-scale flows. *Computers and Fluids*, 100:278–290, 2014. 85, 86

[14] P. Degond and M. Tang. All speed scheme for the low Mach number limit of the isentropic Euler equation. *Communications in Computational Physics*, 10:1–31, 2011. 78

[15] S. Dellacherie, P. Omnes, J. Jung, and P.A. Raviart. Construction of modified Godunov type schemes accurate at any Mach number for the compressible Euler system. *Mathematical Models and Methods in Applied Science*, 26:2525–2615, 2016. 88, 93

[16] G. Dimarco, R. Loubère, and M-H. Vignal. Study of a new asymptotic preserving scheme for the Euler system in the low Mach number limit. *SIAM: Journal of Scientific Computing*, 39: 2099–2128, 2017. 78, 93, 95

[17] T. Gallouët, J-M Hérard, and N. Seguin. A hybrid scheme to compute contact discontinuities in one-dimensional Euler systems. *ESAIM: Mathematical Modelling and Numerical Analysis*, 36:1133–1159, 2002. 84, 99

[18] M. S. Ghidaoui, M. Zhao, D. A. McInnis, and D. H. Axworthy. A review of water hammer theory and practice. *Applied Mechanics Reviews*, 58:49, 2005. 77

[19] M. Girardin. *Asymptotic preserving and all-regime Lagrange-Projection like numerical schemes: application to two-phase flows in low Mach regime*. PhD thesis, Université Pierre et Marie Curie, 2015. URL https://tel.archives-ouvertes.fr/tel-01127428. 81, 83, 97

[20] H. Guillard and A. Murrone. On the behavior of upwind schemes in the low Mach number limit: II Godunov type schemes. *Computers and Fluids*, 33:655–675, 2004. 77

[21] H. Guillard and C. Viozat. On the behavior of upwind schemes in the low Mach number limit. *Computers and Fluids*, 28:63–86, 1999. 77

[22] J. Haack, S. Jin, and J. G. Liu. An all-speed asymptotic-preserving method for the isentropic Euler and Navier-Stokes equations. *Communications in Computational Physics*, 12:955–980, 2012. 78

[23] T. Y. Hou and P. G. LeFloch. Why nonconservative schemes converge to wrong solutions: error analysis. *Mathematics of Computation*, 62:497–530, 1994. 84

[24] D. Iampietro, F. Daude, P. Galon, and J. M. Hérard. A Mach-sensitive splitting approach for Euler-like systems. https://hal.archives-ouvertes.fr/hal-01466827, 2017. 78, 79, 80, 84, 86, 88, 90, 97, 100, 106

[25] D. Iampietro, F. Daude, P. Galon, and J. M. Hérard. A Mach-sensitive splitting approach for Euler-like systems. *ESAIM: Mathematical Modelling and Numerical Analysis*, 52:207–253, 2018. 78, 79, 80, 84, 86, 88, 90, 97, 100, 106

[26] S. Jin. Efficient asymptotic-preserving (AP) schemes for some multiscale kinetic equations. *SIAM Journal on Scientific Computing*, 21:441–454, 1999. 78

[27] N. E. Joukowski. Memoirs of the Imperial Academy Society of St. Petersburg. *Proceedings of the American Water Works Association*, 24:341–424, 1898. 77

[28] R. Klein. Semi-implicit extension of a Godunov-type scheme based on low Mach number asymptotics I: One-dimensional flow. *Journal of Computational Physics*, 121:213–237, 1995. 95, 96

[29] M. P. Martín and G. V. Candler. A parallel implicit method for the direct numerical simulation of wall-bounded compressible turbulence. *Journal of Computational Physics*, 215:153–171, 2006. 85

[30] G. R. McGuire and J. L. Morris. A class of implicit, second-order accurate, dissipative schemes for solving systems of conservation laws. *Journal of Computational Physics*, 14:126–147, 1974.

[31] G. R. McGuire and J. L. Morris. Explicit-implicit schemes for the numerical solution of non-linear hyperbolic systems. *Mathematics of Computation*, 29:407–424, 1975. 85

[32] A. Murrone and H. Guillard. Behavior of upwind scheme in the low Mach number limit: III. Preconditioned dissipation for a five equation two phase model. *Computers and Fluids*, 37(10):1209–1224, 2008. 77, 93

[33] S. Noelle, G. Bispen, K. R. Arun, M. Lukáčová-Medvid'ová, and C. D. Munz. A weakly asymptotic preserving low Mach number scheme for the Euler equations of gas dynamics. *SIAM Journal on Scientific Computing*, 36:B989–B1024, 2014. 78, 95

[34] J. Schütz and S. Noelle. Flux splitting for stiff equations: a notion on stability. *Journal of Scientific Computing*, 64:522–540, 2015. 78, 87, 104

[35] A. R. Simpson and E. B. Wylie. Large water-hammer pressures for column separation in pipelines. *Journal of Hydraulic Engineering*, 117:1310–1316, 1991. 77

[36] I. Suliciu. On the thermodynamics of fluids with relaxation and phase transitions. *International Journal of Engineering Science*, 36:921–947, 1998. 75, 78, 80

[37] E. Turkel. Preconditioned methods for solving the incompressible and low speed compressible equations. *Journal of Computational Physics*, 72:277–298, 1987. 77

[38] J. B. Whitham. *Linear and Non Linear Waves*. John Wiley & Sons Inc, 1974. 80

[39] H. Zakerzadeh. On the Mach-uniformity of the Lagrange-Projection scheme. *ESAIM: Mathematical Modelling and Numerical Analysis*, 51:1343–1366, 2017. 78, 87, 103, 104

[40] H. Zakerzadeh and S. Noelle. A note on the stability of implicit-explicit flux splittings for stiff hyperbolic systems. Preprint, 2016. URL https://www.igpm.rwth-aachen.de/forschung/preprints/449. 78, 87, 104

Chapitre 4

Construction d'une méthode non-splittée pour les modèles bifluide avec effets de relaxation

Le contexte physique en filigrane des deux chapitres précédents se basait sur un écoulement monophasique liquide à faible vitesse. La transition entre un régime d'écoulement nominal et la production de coups de bélier hydrauliques était alors initiée par une fermeture soudaine d'une vanne d'arrêt présente sur le circuit.

Les développements proposés dans ce chapitre s'insèrent dans le cadre de la transition d'un écoulement stratifié eau-vapeur vers un régime de type "slug" où des poches de vapeur se retrouvent piégées au sein de l'eau liquide [32]. L'origine de la transition provenant des effets de cisaillement dus à l'écart de vitesse entre les phases au niveau de l'interface eau-vapeur, la modélisation diphasique homogène utilisée précédemment est remplacée par une modélisation par approche bifluide. Plus précisément le système d'équations mis en jeu correspond à une version isentropique d'un modèle de type Baer-Nunziato [5] avec effets de relaxation en pression ainsi qu'en vitesse.

Dans ce type de modèle, la présence simultanée de termes sources et de produits non-conservatifs fait que ces derniers ne relève pas de la théorie des systèmes hyperboliques avec effets de relaxation développée par Liu [38]. Dans la littérature, ce niveau de complexité se traduit fréquemment par le recours à des approches à pas fractionnaires où la résolution des effets de relaxation est séparée de la discrétisation de l'opérateur de convection [22, 40, 47].

Ce chapitre se place volontairement à contre-courant de ces stratégies et présente les premières esquisses d'un nouveau type de schéma numérique prenant en compte le couplage convection-source pour le modèle Baer-Nunziato isentropique. Certaines propriétés inhérentes à l'opérateur de convection sont dans un premier temps introduites et démontrées. Ces propriétés sont notamment nécessaires pour appliquer certains résultats issus des travaux de Bereux et Sainsaulieu [6] portant sur l'analyse de la solution de problèmes de Riemann linéaires généralisés (*i. e.* avec présence de termes sources linéaires).

Ces travaux sont succinctement décrits puis illustrés de manière pédagogique à travers des exemples simples d'application. Par la suite le schéma numérique à maillage décalé proposé est une simple adaptation de celui développé dans [6]. Une légère extension y est ajoutée afin que ce dernier puisse traiter des phénomènes de relaxation plus fortement non-linéaires et moins monotones que la relaxation en vitesse.

Dans ce chapitre, on écarte volontairement les difficultés relatives à la présence des termes non-conservatifs en "gelant" la matrice Jacobienne de convection du modèle de Baer-Nunziato. Les termes de relaxation en pression et en vitesse sont également remplacés par un vecteur source dont le comportement de chacune des composantes correspond à un ressort non-linéaire indépendant. On peut alors exhiber des solutions analytiques associées au problème de Riemann généralisé de ce nouveau modèle bifluide simplifié.

Par la suite, l'approche proposée est testée sur un problème de Riemann généralisé impliquant des conditions initiales fortement hors-équilibre ainsi que des échelles de temps de relaxation très raides. Les résultats obtenus sont comparés à ceux produits par une méthode à pas fractionnaires impliquant un flux de type Rusanov.

Sommaire

4.1 Introduction

The present work is devoted to the computation of two-phase flows in presence of non-equilibrium relaxation terms.

In the literature, this problem has been extensively studied for models abiding by the Liu's general definition of hyperbolic systems of conservation laws with relaxation [38]. In such a definition, the convection part of the hyperbolic system is *conservative* and endowed with an additional entropy pair. Besides, the set of variables can be split between *equilibrium variables*, for which relaxation source terms are null, and *relaxation variables*, whose formal time-relaxation dynamics projects them into an *equilibrium manifold*. In [10], the authors prove that, when the relaxation time-scale tends to zero, solutions of the above system tend towards solutions of a well-posed homogeneous hyperbolic *equilibrium system*. Such a system derives from the set of conservation laws associated with the equilibrium variables in which every relaxation variable has been projected into the equilibrium manifold. What is more, a *subcharacteristic condition* interlacing the eigenvalues of the original hyperbolic system with those of the equilibrium hyperbolic system holds. As proved in [38, 50], the above subcharacteristic condition ensures that the resulting equilibrium system is stable under small perturbations.

In the present approach, the two-fluid two-pressure Baer-Nunziato model [5, 18] is considered. Contrary to Liu's equations setting, non-conservative terms appear in its formulation. The presence of the latter is mandatory to enforce a binding between both phases through the appearance of a coupling wave. As a consequence, the convergence result proved in [10] cannot be applied to this model. However, in [1, 16], formal Chapman-Enskog expansions have been performed for similar two-fluid two-pressure models in the vanishing relaxation time-scale limit. They underline strong relations between the obtained asymptotic two-fluid two-pressure models and some other class of models of lower dimension such as the drift-flux models [19, 51]. Starting from a two-pressure one-velocity six-equation model, a hierarchy of two-phase relaxation models can also be found in [20, 41]. A similar hierarchy is established in [37] whose root model is the non-equilibrium Baer-Nunziato system with pressure, temperature, chemical potential and velocity relaxation.

Even in the convenient framework of Liu, the simulation of hyperbolic systems with relaxation raises different issues, the origins of which do not find consensus in the community. Before going further, let us mention that every numerical method that will be considered in the sequel *under-resolves* the stiff relaxation time-scales of the source terms. This means that discrete time-steps are only based on the eigenvalues of the Jacobian matrix related to the convective part of the system. By definition, stiff problems are those where at least one time-scale of the relaxation source terms is very small with respect to the convective time-scales.

The first difficulty deals with the appearance of *spurious solutions*. Indeed, in [44], Pember studies the evolution of discrete solutions computed with a first-order fractional-step method that solves separately the relaxation source terms and the convective part of the system. He points out that, when the subcharacteristic condition is locally violated, one can construct and observe non-physical *one-cell per time-step* discrete discontinuities fulfilling the Rankine-Hugoniot conditions of the equilibrium hyperbolic system. In [8], Bourlioux shows simulations based on split or unsplit methods that exhibit the same kind of spurious solutions.

A second issue focuses on the accuracy of the numerical methods when relaxation source terms become stiff. In [45], by performing truncation error analysis, Pember proves that second-order Strang-splitting techniques involving Godunov schemes degenerate into first-order methods with respect to the equilibrium system when the relaxation source terms tend to zero. He suggests the use of appropriate unsplit methods to cure this drawback. He ends up by stating that the approximate Riemann solver involved in the unsplit method should be asymptotically consistent, when the relaxation time-scales tend to zero, with an approximate Riemann solver related to the equilibrium system. In contrast to the conclusions of Pember, Jin in [34] emphasizes that the above asymptotic-preserving condition is a key property, whether the numerical method is split or unsplit, to provide accurate solutions at equilibrium.

Bridging the gap between both parts, the work of Bereux and Sainsaulieu [6] proves that, when the relaxation time-scales tend to zero, second-order Strang-splitting techniques *do* preserve the second-order accuracy of the equilibrium variables. However, they underline that nothing is told about the accuracy of the relaxation variables in this asymptotic regime. Then, focusing on the need to compute accurate relaxation-variable solutions in stiff and non-stiff configurations, they derive an unsplit time-implicit staggered scheme that is asymptotically consistent with the equilibrium system. Subsequently, other high-order unsplit asymptotically-preserving schemes have been proposed [43].

When it comes to the simulation of two-fluid models with relaxation, the complexity of the wave pattern, the presence of non-conservative products, as well as the strong non-linear coupling introduced by relaxation source terms are such that, in many works, fractional-step approaches are preferred. Without being exhaustive, let us mention the works of Saurel and Abgrall [47] and Andrianov et *al.* [4] in which Strang-splitting techniques are applied to two-fluid two-pressure models. First-order fractional-step methods ensuring a discrete maximum principle of the statistical fraction and the positivity of pressures during the relaxation sub-step are also proposed by Gallouët et *al.* in [22]. In line with [22], the fractional-step method is extended in [15, 40] in order to include mass transfer and temperature relaxation.

To our knowledge, the only attempt to use partially unsplit methods for two-fluid two-pressure models has been proposed by Ambroso et *al.* in [3]. In this work, the convection part is discretized using an approximate Riemann solver that is consistent, in the integral sense, with a seven-equation model endowed with velocity-relaxation source terms.

In this context, the present work proposes some building blocks for the derivation of fully unsplit numerical methods in order to compute two-fluid two-pressure models with relaxation. The starting point of the study leans on the work of Bereux and Sainsaulieu [6] in which an analytical result is proved about the shape of the exact solution of a generalized linear Riemann problem when linear relaxation source terms are active. The proposed time-implicit staggered scheme lies on a formal extension of this analytical result. The first section of this work introduces the two-fluid two-pressure model considered here. It is the isentropic Baer-Nunziato model with pressure and velocity relaxations [2, 13]. In the second section, the analytical result stated by Bereux and Sainsaulieu is presented. The third section concentrates on the derivation of the proposed numerical scheme. Finally, the last part is dedicated to numerical test cases. They are based on a simplified frozen version of the isentropic Baer-Nunziato model allowing to derive analytical solutions. Accuracy and efficiency comparisons between the present approach and more classical fractional-step methods are performed.

4.2 The isentropic Baer-Nunziato system with pressure and velocity relaxation

This section is dedicated to the presentation of the framework in which the study of two-phase flows with relaxation effects will be carried out. One focuses on the two-fluid two-pressure Baer-Nunziato model. For the sake of simplicity, energy equations of both phases are omitted, and the analysis is restricted to the five-equation isentropic Baer-Nunziato model. Thereafter, one starts by describing the main differential blocks composing the set of equations at stake. Key mathematical properties that will be useful to derive a convection-relaxation coupling scheme are introduced. Lastly, the section ends with a hand-made example pointing out some drawbacks related to the use of standard fractional-step methods in the resolution of hyperbolic systems with relaxation source terms.

4.2.1 Presentation of the two-fluid two-pressure model

The Baer-Nunziato system is a two-velocity two-pressure model originally formulated by Baer and Nunziato [5] in the context of granular materials embedded in gaseous combustion products.

Its mathematical properties have been analysed by Embid and Baer in [18]. Then, this model has been extensively studied in deflagration-to-detonation transition scenarios [36] and more generally in two-phase flows modelling [24, 25, 46–48]. Contrary to the category of homogeneous models [11], both phases have their own dynamics in the system. In the specific context of isentropic Baer-Nunziato system (in which both energy equations are dropped off) each phase indexed $k \in \{1, 2\}$ has its own mass equation and momentum equation. A last transport equation involves a volume fraction variable $\alpha_1 \in [0, 1]$. The latter can be seen as a measure of the presence of phase 1 in a given bounded domain. Consider the vector,

$$\mathbf{U} = [\alpha_1, m_1, m_1 u_1, m_2, m_2 u_2]^{\mathrm{T}}. \tag{4.1}$$

The 5-equation two-velocity two-pressure model finally reads $\forall k \in \{1, 2\}$:

$$\begin{array}{lcccccl} \partial_t \alpha_k & + & u_{\mathrm{I}} \partial_x \alpha_k & & & = & (-1)^k \, \mathrm{K_p}(\mathbf{U}) \, \Delta p, \\ \partial_t m_k & + & \partial_x m_k u_k & & & = & 0, \\ \partial_t m_k u_k & + & \partial_x \left(m_k u_k^2 + \alpha_k p_k \right) & - & p_{\mathrm{I}} \partial_x \alpha_k & = & (-1)^{k+1} \, \mathrm{K_u}(\mathbf{U}) \, \Delta u, \end{array} \tag{4.2}$$

with ρ_k, u_k and p_k respectively the density, velocity and pressure of phase k. As for the partial mass m_k, it reads: $m_k = \alpha_k \rho_k$. Let us also define,

$$\begin{aligned} \Delta p &= p_2 - p_1, \\ \Delta u &= u_2 - u_1, \end{aligned} \tag{4.3}$$

the relative pressure and velocity. Eventually, $\mathrm{K_p}(\mathbf{U})$ and $\mathrm{K_u}(\mathbf{U})$ are positive cofactors whose definition will be discussed below. For both phases, pressure is a smooth function of density defined by the EOS:

$$\begin{aligned} & p_k = p_k^{\mathrm{EOS}}(\rho_k), \ \left(p_k^{\mathrm{EOS}}\right)'(\rho_k) > 0, \\ & \lim_{\rho_k \to 0} p_k = 0, \ \lim_{\rho_k \to \infty} p_k = +\infty. \end{aligned} \tag{4.4}$$

In the following, for ease of notation, each thermodynamical function $\rho_k \to \phi^{\mathrm{EOS}}(\rho_k)$ is directly referred to as ϕ_k. Let us also introduce the specific internal energy $\varepsilon_k(\rho_k)$, the specific internal enthalpy $h_k(\rho_k)$ as well as the speed of sound $c_k(\rho_k)$:

$$(\varepsilon_k)'(\rho_k) = \frac{p_k}{\rho_k^2}, \ h_k(\rho_k) = \varepsilon_k(\rho_k) + \frac{p_k(\rho_k)}{\rho_k}, \ c_k^2(\rho_k) = p_k'(\rho_k). \tag{4.5}$$

Finally, let us define the positive quantity C_k as:

$$\mathrm{C}_k = \rho_k c_k^2. \tag{4.6}$$

Note that $(h_k)'(\rho_k) = \mathrm{C}_k / \rho_k^2$. Since phases 1 and 2 are not miscible, volume fractions are constrained by the condition :

$$\alpha_1 + \alpha_2 = 1. \tag{4.7}$$

The equation of α_2 is thus redundant with the one of α_1. In (4.2), the couple of interfacial velocity and interfacial pressure $\left(u_{\mathrm{I}}, p_{\mathrm{I}}\right)$ needs to be specified with closure laws. Subsequently, this couple is set to

$$\left(u_{\mathrm{I}}, p_{\mathrm{I}}\right) = \left(u_2, p_1\right), \tag{4.8}$$

which is a choice already done in [5, 12, 24]. Different alternatives have been explored in the literature, see for instance [47]. In [22], the authors point at different categories of closure laws providing two main properties for system (4.2). The first property deals with the linearly-degenerate aspect of the field related to the transport of α_1. The second property focuses on the existence of a mixture entropy pair $\left(\eta, \mathrm{F}_\eta\right)(\mathbf{U})$ such that

$$\partial_t \eta + \partial_x \mathrm{F}_\eta \leq 0. \tag{4.9}$$

In [39], a comparison is performed between seven-equation models (that is five equations plus two equations involving total energy for both phases) corresponding to different closure laws proposed in [12, 22]. It concludes that, when relaxation terms are active in fast transient scenarios, only a few differences hold between the several choices of closure laws.

System (4.2) admits pressure and velocity relaxation processes. Pressure relaxation acts on the transport equation of α_1 through the term:

$$-\mathrm{K_p}(\mathbf{U})\,\Delta p = -\mathrm{K_p}(\mathbf{U})\left(p_2 - p_1\right). \tag{4.10}$$

In a region where the spatial gradient of the volume fraction is null, the time-variation of α_1 is driven by the local pressure difference between both phases. Such a relaxation phenomenon cancels out when both phases have the same pressure $\Delta p = 0$ or when the transport of α_1 is sufficiently strong to balance the pressure difference $u_I \partial_x \alpha_1 = -\mathrm{K_p}(\mathbf{U})\,\Delta p$. The strength of the pressure relaxation process is characterized by the non-linear positive cofactor $\mathrm{K_p}(\mathbf{U})$. One can rewrite it formally by introducing a pressure relaxation time-scale $\tau_\mathrm{p}(\mathbf{U})$, a pressure of reference p_ref and a positive *non-dimensional* cofactor $\widetilde{\mathrm{K}}_\mathrm{p}(\mathbf{U})$:

$$-\mathrm{K_p}(\mathbf{U})\,\Delta p = -\frac{\widetilde{\mathrm{K}}_\mathrm{p}(\mathbf{U})}{\tau_\mathrm{p}(\mathbf{U})}\frac{\Delta p}{p_\mathrm{ref}},\ \widetilde{\mathrm{K}}_\mathrm{p}(\mathbf{U}) \geq 0, \tag{4.11a}$$

$$\lim_{\alpha_1 \to 0} \widetilde{\mathrm{K}}_\mathrm{p}(\mathbf{U}) = \lim_{\alpha_1 \to 1} \widetilde{\mathrm{K}}_\mathrm{p}(\mathbf{U}) = 0. \tag{4.11b}$$

In single-phase regions, pressure relaxation process does not take place and the non-dimensional cofactor has to vanish. This is imposed by equation (4.11b). It is crucial to have a good estimation of the pressure relaxation time-scale $\tau_\mathrm{p}(\mathbf{U})$. The latter strongly depends on the kind of two-phase flow configurations. On that topic, we refer to the work [23] in which an analytical expression for $\tau_\mathrm{p}(\mathbf{U})$ is proposed. It is based on the analysis of a bubble dynamics in an infinite domain and includes surface tension, viscous effects, thermal diffusion as well as radiation effects. The same kind of correlation between the Rayleigh-Plesset dynamics and pressure relaxation time-scale has been conducted in [17]. The pressure relaxation time-scale is related to a *micro-inertia* coefficient modeling the microscopic pulsations of the interface between a bubble and the surrounding liquid phase. The obtained pressure relaxation time-scales are then similar to those derived by Gavrilyuk and Saurel in [24].

The second relaxation phenomenon acts on the momentum equation of both phases. It reads:

$$(-1)^{k+1}\,\mathrm{K_u}(\mathbf{U})\,\Delta u = (-1)^{k+1}\,\mathrm{K_u}(\mathbf{U})\,(u_2 - u_1), \tag{4.12}$$

and models the relative drag forces that one phase applies to the other. Such a relaxation term vanishes when both phases have the same velocity or when a pressure gradient is at equilibrium with the drag effects. Similarly, one can rewrite the momentum source term using a velocity relaxation time-scale $\tau_\mathrm{u}(\mathbf{U})$ and a reference density ρ_ref:

$$\mathrm{K_u}(\mathbf{U})\,\Delta u = \frac{\widetilde{\mathrm{K}}_\mathrm{u}(\mathbf{U})}{\tau_\mathrm{u}(\mathbf{U})}\rho_\mathrm{ref}\,\Delta u, \tag{4.13a}$$

$$\lim_{\alpha_1 \to 0} \widetilde{\mathrm{K}}_\mathrm{u}(\mathbf{U}) = \lim_{\alpha_1 \to 1} \widetilde{\mathrm{K}}_\mathrm{u}(\mathbf{U}) = 0. \tag{4.13b}$$

Once again, the relaxation time-scale modeling depends on the flow settings. We refer to [33] in which constitutive relations between relative-velocity relaxation terms and drag forces are derived in the context of bubbly, droplet or particulate flows.

In the following, the isentropic Baer-Nunziato system will be written in a contracted form:

$$\begin{gathered}\partial_t \mathbf{U} + \partial_x \mathbf{F}(\mathbf{U}) + \underline{\underline{\mathbf{E}}}(\mathbf{U})\, \partial_x \mathbf{U} = \mathbf{S}(\mathbf{U}), \\ \mathbf{F}(\mathbf{U}) = \begin{bmatrix} 0 \\ m_1 u_1 \\ m_1 u_1^2 + \alpha_1 p_1 \\ m_2 u_2 \\ m_2 u_2^2 + \alpha_2 p_2 \end{bmatrix}, \underline{\underline{\mathbf{E}}}(\mathbf{U}) = \left[\mathbf{b}(\mathbf{U}), \mathbf{0}, \mathbf{0}, \mathbf{0}, \mathbf{0}\right], \mathbf{b}(\mathbf{U}) = \begin{bmatrix} u_I \\ 0 \\ -p_I \\ 0 \\ +p_I \end{bmatrix}, \\ \mathbf{S}(\mathbf{U}) = \begin{bmatrix} -\mathrm{K_p}(\mathbf{U})\, \Delta p \\ 0 \\ \mathrm{K_u}(\mathbf{U})\, \Delta u \\ 0 \\ -\mathrm{K_u}(\mathbf{U})\, \Delta u \end{bmatrix}.\end{gathered} \tag{4.14}$$

In the next subsection, special attention is paid to the mathematical properties of the isentropic Baer-Nunziato system.

4.2.2 Mathematical properties of the isentropic Baer-Nunziato system

A substantial advantage of two-fluid two-pressure models (like the Baer-Nunziato model) with respect to the two-fluid single pressure models is that, up to specific resonant configurations (see [26, 31] for a general definition of resonance), they do not suffer from any lack of hyperbolicity. Thus, the Cauchy problem associated with the two-fluid two-pressure models is not "ill-posed" *a priori*. A second important property is directly related to the definition of the non-conservative product $\mathbf{b}(\mathbf{U})\, \partial_x \alpha_1$ through shock and contact discontinuities. Property 4.2.1 and Property 4.2.2 summarize these issues.

Property 4.2.1 (Hyperbolicity of the isentropic Baer-Nunziato system)
The convective part of system (4.14) is weakly hyperbolic in the sense that the Jacobian matrix

$$\underline{\underline{\mathbf{C}}}(\mathbf{U}) = \partial_{\mathbf{U}} \mathbf{F}(\mathbf{U}) + \underline{\underline{\mathbf{E}}}(\mathbf{U}) = \begin{bmatrix} u_I & 0 & 0 & 0 & 0 \\ 0 & 0 & 1 & 0 & 0 \\ \left[(p_1 - p_I - C_1)\right] & (c_1)^2 - (u_1)^2 & 2u_1 & 0 & 0 \\ 0 & 0 & 0 & 0 & 1 \\ -\left[(p_2 - p_I - C_2)\right] & 0 & 0 & (c_2)^2 - (u_2)^2 & 2u_2 \end{bmatrix} \tag{4.15}$$

admits five real eigenvalues associated with five right eigenvectors that span $\mathbb{R}^5$ if the non-resonant sufficient condition

$$\forall k \in \{1, 2\}, \ |u_I - u_k| \neq c_k, \tag{4.16}$$

is fulfilled. The eigenvalues read:

$$\lambda_1 = u_I, \ \lambda_2 = u_1 + c_1, \ \lambda_3 = u_1 - c_1, \ \lambda_4 = u_2 + c_2, \ \lambda_5 = u_2 - c_2. \tag{4.17}$$

The corresponding right eigenvectors are:

$$\begin{aligned}\underline{\underline{\mathbf{R}}} &= \left[\mathbf{r}_1, \mathbf{r}_2, \mathbf{r}_3, \mathbf{r}_4, \mathbf{r}_5\right] \\ &= \begin{bmatrix} 1 & 0 & 0 & 0 & 0 \\ -\frac{[p_1 - p_I - C_1]}{(c_1)^2 - (u_1 - u_I)^2} & \rho^0_{\mathrm{ref}} & \rho^0_{\mathrm{ref}} & 0 & 0 \\ -\frac{[p_1 - p_I - C_1]\, u_I}{(c_1)^2 - (u_1 - u_I)^2} & \rho^0_{\mathrm{ref}}(u_1 + c_1) & \rho^0_{\mathrm{ref}}(u_1 - c_1) & 0 & 0 \\ \frac{[p_2 - p_I - C_2]}{(c_2)^2 - (u_2 - u_I)^2} & 0 & 0 & \rho^0_{\mathrm{ref}} & \rho^0_{\mathrm{ref}} \\ \frac{[p_2 - p_I - C_2]\, u_I}{(c_2)^2 - (u_2 - u_I)^2} & 0 & 0 & \rho^0_{\mathrm{ref}}(u_2 + c_2) & \rho^0_{\mathrm{ref}}(u_2 - c_2) \end{bmatrix},\end{aligned} \tag{4.18}$$

with ρ^0_{ref} an arbitrary constant density introduced to make the eigenvectors homogeneous to the dimensions of the state $\mathbf{U}$.

Property 4.2.2 (Isentropic Baer-Nunziato system: fields structure and non-conservative products definition)
Consider the closure laws given in (4.8) where $u_I = u_2$. Then, λ_1 is related to a linearly-degenerate field whereas $\{\lambda_2,\dots,\lambda_5\}$ correspond to genuinely non-linear fields. The volume fraction α_1 is a Riemann invariant for the 2-5-fields meaning that it only jumps through the 1-wave. Besides, one can identify four 1-Riemann invariants which provide a parametrization for the crossing of the 1-contact-wave. They write:

$$\begin{cases} \mathcal{I}_1 = u_2, \\ \mathcal{I}_2 = m_1\,(u_1-u_2), \\ \mathcal{I}_3 = m_1\,(u_1-u_2)^2 + \alpha_1\,p_1 + \alpha_2\,p_2, \\ \mathcal{I}_4 = \dfrac{(u_1-u_2)^2}{2} + h_1. \end{cases} \tag{4.19}$$

Then, the non-conservative products $\mathbf{b}(\mathbf{U})\,\partial_x\alpha_1$ are only active through the 1-wave and are fully defined, in the weak-sense, using this parametrization.

The proof of Property 4.2.1 can be found in [2, 13, 42] for the barotropic case. For the general Baer-Nunziato system, detailed proofs of Property 4.2.1 and Property 4.2.2 can be found in [12, 22]. The non-resonant condition (4.16) prevents the superposition of the material wave u_I and the non-linear acoustic waves $u_k \pm c_k$. In most applications of nuclear industry, material velocities u_k are assumed to be small with respect to the acoustic-wave speeds of both vapor and liquid phases. Then, condition (4.16) is generally replaced by the more constraining *subsonic flows* hypothesis:

$$\forall k \in \{1,2\},\ |u_I - u_k| < c_k. \tag{4.20}$$

As shown in [22], $u_I = u_2$ is sufficient to bring the linearly-degenerate property to the 1-field. The other closure law $p_I = p_1$ contributes to establish an additional entropy PDE for system (4.14) as stated in Proposition 4.2.1.

Proposition 4.2.1 (A mathematical entropy pair for the isentropic Baer-Nunziato system)
Define the specific total energy of the mixture and the total energy flux as:

$$\begin{aligned} \mathrm{E} &= m_1\left(u_1^2/2+\varepsilon_1\right) + m_2\left(u_2^2/2+\varepsilon_2\right), \\ \mathcal{F}(\mathbf{U}) &= m_1\left(u_1^2/2+\varepsilon_1\right)u_1 + m_2\left(u_2^2/2+\varepsilon_2\right)u_2 + \alpha_1\,p_1\,u_1 + \alpha_2\,p_2\,u_2. \end{aligned} \tag{4.21}$$

For smooth solutions of the isentropic Baer-Nunziato system, the PDE verified by E *reads:*

$$\partial_t \mathrm{E} + \partial_x \mathcal{F}(\mathbf{U}) + \mathrm{A}(\mathbf{U})\,\partial_x\alpha_1 = -\mathrm{K_p}(\mathbf{U})\left(\Delta p\right)^2 - \mathrm{K_u}(\mathbf{U})\,(\Delta u)^2, \tag{4.22}$$

with,

$$\mathrm{A}(\mathbf{U}) = p_I\,(u_2-u_1) + p_1\,(u_1-u_I) + p_2\,(u_I-u_2). \tag{4.23}$$

Assume that u_I is closed by the relation $u_I = \beta(\mathbf{U})\,u_1 + (1-\beta(\mathbf{U}))\,u_2$ with $\beta(\mathbf{U}) \in [0,1]$. Then, provided that $p_I = (1-\beta(\mathbf{U}))\,p_1 + \beta(\mathbf{U})\,p_2$,

$$\mathrm{A}(\mathbf{U}) = 0. \tag{4.24}$$

Thus, the couple $(\mathrm{E}, \mathcal{F}(\mathbf{U}))$ is an entropy-pair of system (4.14) in the sense that $\mathbf{U} \to \mathrm{E}(\mathbf{U})$ is convex (not strictly convex) and, equality (4.22) can be signed:

$$\partial_t \mathrm{E} + \partial_x \mathcal{F}(\mathbf{U}) \le 0. \tag{4.25}$$

Proof 1
The convexity proof of the function $\mathbf{U} \to \mathrm{E}(\mathbf{U})$ is similar to the one presented in [14] in the case of the Baer-Nunziato system with energy equations. It consists in re-writting $\mathrm{E}(\mathbf{U})$ *as:*

$$\begin{aligned} \mathrm{E}(\mathbf{U}) &= \alpha_1\,(\rho e)_1(\mathbf{u}_1) + (1-\alpha_1)\,(\rho e)_2(\mathbf{u}_2), \\ &= \alpha_1\,(\rho e)_1\left(\frac{\alpha_1\mathbf{u}_1}{\alpha_1}\right) + (1-\alpha_1)\,(\rho e)_2\left(\frac{(1-\alpha_1)\mathbf{u}_2}{1-\alpha_1}\right), \end{aligned} \tag{4.26}$$

with $\forall k \in \{1,2\}$, $\mathbf{u}_k = \left[\rho_k, \rho_k u_k\right]^{\mathrm{T}}$, $\mathbf{U} = [\alpha_1, \alpha_1\mathbf{u}_1, (1-\alpha_1)\mathbf{u}_2]$ *and* $(\rho e)_k = \rho_k\left(u_k^2/2 + \varepsilon_k\right)$. *Thus, differentiating twice equation* (4.26)*, one can obtain the Hessian matrix:*

$$\mathrm{E}''(\mathbf{U}) = \begin{bmatrix} a & \mathbf{c}^{\mathrm{T}} & \mathbf{d}^{\mathrm{T}} \\ \mathbf{c} & (\rho e)_1''(\mathbf{u}_1)/\alpha_1 & \underline{\underline{\mathbf{0}}} \\ \mathbf{d} & \underline{\underline{\mathbf{0}}} & (\rho e)_2''(\mathbf{u}_2)/(1-\alpha_1) \end{bmatrix}, \tag{4.27}$$

with,

$$\begin{aligned} a &= \frac{1}{\alpha_1}\mathbf{u}_1^{\mathrm{T}}(\rho e)_1''(\mathbf{u}_1)\mathbf{u}_1 + \frac{1}{1-\alpha_1}\mathbf{u}_2^{\mathrm{T}}(\rho e)_2''(\mathbf{u}_2)\mathbf{u}_2, \\ \mathbf{c} &= -\frac{1}{\alpha_1}(\rho e)_1''(\mathbf{u}_1)\mathbf{u}_1, \\ \mathbf{d} &= \frac{1}{1-\alpha_1}(\rho e)_2''(\mathbf{u}_2)\mathbf{u}_2. \end{aligned} \tag{4.28}$$

Let us define $\mathbf{X} = \left[x, \mathbf{y}, \mathbf{z}\right] \in \mathbb{R}^5$. *Then, one can notice that:*

$$\mathbf{X}^{\mathrm{T}}\mathrm{E}''(\mathbf{U})\mathbf{X} = \left(\mathbf{y} - x\mathbf{u}_1\right)\frac{1}{\alpha_1}(\rho e)_1''(\mathbf{u}_1)\left(\mathbf{y} - x\mathbf{u}_1\right) + (\mathbf{z} + x\mathbf{u}_2)\frac{1}{1-\alpha_1}(\rho e)_2''(\mathbf{u}_2)(\mathbf{z} + x\mathbf{u}_2). \tag{4.29}$$

Recalling [7] that $\forall k \in \{1,2\}$, $\mathbf{u}_k \to (\rho e)_k(\mathbf{u}_k)$ *is strictly convex, the quantity* $\mathbf{X}^{\mathrm{T}}\mathrm{E}''(\mathbf{U})\mathbf{X}$ *is non-negative.*

Equation (4.25) *results from classical manipulations of system* (4.14)*. The idea is to derive the kinetic energy PDE of phase* k *and to combine it with the one associated with* ε_k*. Thus, one can derive the dynamics of the specific total energy of both phases. Summing them allows to exhibit the proposed closure law for* p_{I} *as a sufficient condition to obtain the negative right hand side in equation* (4.25)*. Additional details can be found in [12, 22] for the Baer-Nunziato system with energy equations.*

Let us end this section by focusing on the symmetrization of system (4.14). This property will be crucial, in section 4.3, in order to state an important theoretical result related to the integration of the relaxation source terms into a general linearized Riemann problem.

Proposition 4.2.2 (Symmetrization of the isentropic Baer-Nunziato system)
Consider the C^1*-diffeomorphism* $\mathbf{U} \to \mathbf{W}(\mathbf{U}) = \left[\alpha_1, u_1, p_1, u_2, p_2\right]$. *There exists a symmetric positive definite matrix* $\underline{\underline{\mathbf{P}}}(\mathbf{W})$ *and a symmetric matrix* $\underline{\underline{\mathbf{Q}}}(\mathbf{W})$ *such that, out of the resonant condition* (4.16)*, smooth solutions* $\mathbf{U}(\mathbf{W})$ *of system* (4.14) *verify equivalently:*

$$\underline{\underline{\mathbf{P}}}(\mathbf{W})\,\partial_t\mathbf{W} + \underline{\underline{\mathbf{Q}}}(\mathbf{W})\,\partial_x\mathbf{W} = \mathbf{0}. \tag{4.30}$$

In that sense, system (4.14) *is said to be symmetrizable.*

Proof 2
The proof is similar to the one derived for the Baer-Nunziato system with energy equations in [14]. Considering smooth solutions of system (4.14)*, one can rewrite it equivalently in a non-conservative form using variable* $\mathbf{W}$*. It reads:*

$$\begin{aligned} &\partial_t\mathbf{W} + \underline{\underline{\mathbf{M}}}(\mathbf{W})\,\partial_x\mathbf{W} = \mathbf{0}, \\ &\underline{\underline{\mathbf{M}}}(\mathbf{W}) = \begin{bmatrix} u_{\mathrm{I}} & \mathbf{0}^{\mathrm{T}} & \mathbf{0}^{\mathrm{T}} \\ \mathbf{M}_{\alpha,1} & \underline{\underline{\mathbf{M}}}_1 & \underline{\underline{\mathbf{0}}} \\ \mathbf{M}_{\alpha,2} & \underline{\underline{\mathbf{0}}} & \underline{\underline{\mathbf{M}}}_2 \end{bmatrix}, \\ &\underline{\underline{\mathbf{M}}}_k = \begin{bmatrix} u_k & \tau_k \\ \mathrm{C}_k & u_k \end{bmatrix},\ \mathbf{M}_{\alpha,k} = (-1)^{k+1}\begin{bmatrix} (p_k - p_{\mathrm{I}})/m_k \\ \mathrm{C}_k(u_k - u_{\mathrm{I}})/\alpha_k \end{bmatrix}. \end{aligned} \tag{4.31}$$

Let us define a symmetric matrix $\underline{\underline{\mathbf{P}}}$ *as:*

$$\underline{\underline{\mathbf{P}}} = \begin{bmatrix} \mathrm{P}_\alpha & \mathbf{P}_1^{\mathrm{T}} & \mathbf{P}_2^{\mathrm{T}} \\ \mathbf{P}_1 & \underline{\underline{\mathbf{D}}}_1 & \underline{\underline{\mathbf{0}}} \\ \mathbf{P}_2 & \underline{\underline{\mathbf{0}}} & \underline{\underline{\mathbf{D}}}_2 \end{bmatrix}, \ \underline{\underline{\mathbf{D}}}_k = \begin{bmatrix} (\rho_k c_k)^2 & 0 \\ 0 & 1 \end{bmatrix}, \ \mathbf{P}_k = \left[p_{1,k}, p_{2,k} \right]^{\mathrm{T}}. \tag{4.32}$$

Then, one can observe that the matrix

$$\begin{aligned} \underline{\underline{\mathbf{Q}}}(\mathbf{W}) &= \underline{\underline{\mathbf{P}}}\,\underline{\underline{\mathbf{M}}}(\mathbf{W}) \\ &= \begin{bmatrix} \mathrm{P}_\alpha u_\mathrm{I} + \mathbf{P}_1^{\mathrm{T}} \mathbf{M}_{\alpha,1} + \mathbf{P}_2^{\mathrm{T}} \mathbf{M}_{\alpha,2} & \mathbf{P}_1^{\mathrm{T}} \underline{\underline{\mathbf{M}}}_1 & \mathbf{P}_2^{\mathrm{T}} \underline{\underline{\mathbf{M}}}_2 \\ u_\mathrm{I} \mathbf{P}_1 + \underline{\underline{\mathbf{D}}}_1 \mathbf{M}_{\alpha,1} & \underline{\underline{\mathbf{D}}}_1 \underline{\underline{\mathbf{M}}}_1 & \underline{\underline{\mathbf{0}}} \\ u_\mathrm{I} \mathbf{P}_2 + \underline{\underline{\mathbf{D}}}_2 \mathbf{M}_{\alpha,2} & \underline{\underline{\mathbf{0}}} & \underline{\underline{\mathbf{D}}}_2 \underline{\underline{\mathbf{M}}}_2 \end{bmatrix}, \end{aligned} \tag{4.33}$$

is symmetric if $\forall\, k \in \{1,2\}$*:*

$$\begin{aligned} &\underline{\underline{\mathbf{D}}}_k \underline{\underline{\mathbf{M}}}_k \text{ is symmetric,} \\ &\left(\underline{\underline{\mathbf{M}}}_k^{\mathrm{T}} - u_\mathrm{I} \mathbf{I} \right) \mathbf{P}_k = \underline{\underline{\mathbf{D}}}_k \mathbf{M}_{\alpha,k}. \end{aligned} \tag{4.34}$$

By construction of $\underline{\underline{\mathbf{D}}}_k$*, the matrix* $\underline{\underline{\mathbf{D}}}_k \underline{\underline{\mathbf{M}}}_k = \begin{bmatrix} (\rho_k c_k)^2 u_k & \mathrm{C}_k \\ \mathrm{C}_k & u_k \end{bmatrix}$ *is symmetric. Besides, in* (4.34) *the linear system can be solved if* $\det\left(\underline{\underline{\mathbf{M}}}_k^{\mathrm{T}} - u_\mathrm{I} \mathbf{I} \right) = (u_k - u_\mathrm{I})^2 - c_k^2 \neq 0$*. This condition is exactly the non-resonant condition* (4.16)*. Both vectors* $\mathbf{P}_k$ *being completely defined, let us now concentrate on the positive-definite property of matrix* $\underline{\underline{\mathbf{P}}}$*. Recall [30] that a symmetric matrix is positive-definite if and only if all its principal minors are strictly positive. In the case of matrix* $\underline{\underline{\mathbf{P}}}$*, positivity of the five principal minors reads:*

$$\begin{aligned} &\delta_1 = \mathrm{P}_\alpha > 0, \\ &\delta_2 = \delta_1 (\rho_1 c_1)^2 - p_{1,1}^2 > 0, \\ &\delta_3 = \delta_2 - (\rho_1 c_1)^2 p_{2,1}^2 > 0, \\ &\delta_4 = (\rho_2 c_2)^2 \delta_3 - (\rho_1 c_1)^2 p_{1,2}^2 > 0, \\ &\delta_5 = \delta_4 - (\rho_1 c_1)^2 (\rho_2 c_2)^2 p_{2,2}^2 > 0. \end{aligned} \tag{4.35}$$

One can observe that $\delta_5 > 0 \Rightarrow \forall\, k \in \{1,..,4\}$, $\delta_k > 0$*. This condition can be rewritten:*

$$(\rho_1 c_1)^2 (\rho_2 c_2)^2 \mathrm{P}_\alpha > (\rho_2 c_2)^2 p_{1,1}^2 + (\rho_1 c_1)^2 p_{1,2}^2 + (\rho_1 c_1)^2 (\rho_2 c_2)^2 \left(p_{2,1}^2 + p_{2,2}^2 \right). \tag{4.36}$$

Then, if P_α *is taken sufficiently large so that inequality* (4.36) *holds, matrix* $\underline{\underline{\mathbf{P}}}$ *is positive-definite.*

The above properties provide a convenient framework to study the weak solutions of the isentropic Baer-Nunziato model. Non-conservative terms in the convection part vanish through rarefaction and shock waves and are completely defined across the u_I-contact wave using the corresponding Riemann invariants. The closure laws are compatible with the relaxation source terms so that an entropy inequality can be derived for smooth solutions.

However, the presence of the source terms triggers two main difficulties that one needs to tackle.

The first one arises in the more general Baer-Nunziato model endowed with energy equations or in the isentropic Baer-Nunziato model with mass transfer. Indeed, even in the very specific case where two-phase variables do not depend on space, the remaining system of ODEs is strongly coupled.

In [28], Guillemaud analyses the behavior of the time trajectories of the ODE system associated with a seven-equation model with pressure, temperature and velocity relaxation. Under mild thermodynamical assumptions and using entropy considerations he shows that any bounded time trajectory converges towards the unique point where both phases have the same pressure, temperature and velocity. Such a point is also compatible with the mixture mass, momentum and energy constraints.

Nevertheless, the analytical derivation of the time-relaxation trajectories is still out of reach for such a complex system.

As a result, successive operator splitting strategies separating the relaxation effects according to the stiffness of their time-scale are needed to provide an exact time-integration. For example, details about the two-steps splitting approach for the Baer-Nunziato model with velocity-pressure relaxations can be found in [22].

The second difficulty is related to the stiffness of the pressure and velocity relaxation time-scales $\tau_p(\mathbf{U})$, $\tau_u(\mathbf{U})$ with respect to the time-step based on the eigenvalues $u_k \pm c_k$ of the Baer-Nunziato convective Jacobian matrix. Avoiding computations with prohibitive CFL constraints requires to apply robust time-implicit integrations on the source terms.

The above issues related to the coupling and the stiffness of the relaxation processes entail that, in the literature, the time-integration of the source terms is generally treated separately with respect to the convection discretization [4, 17, 22, 40, 47]. Yet, this additional operator splitting procedure can lead to a substantial depreciation of the accuracy of the numerical scheme. The following subsection provides a simple analytical model underlining the main issues met in such a context.

4.2.3 Inaccuracy of fractional step methods applied to hyperbolic systems with relaxation

Consider a Riemann problem involving the Burgers' equation,

$$\begin{aligned} &\partial_t u + \partial_x \frac{u^2}{2} = 0, \\ &u(.,\, t=0) = \begin{cases} u_L^0 \text{ if } x<0, \\ u_R^0 \text{ if } x>0. \end{cases} \end{aligned} \tag{4.37}$$

Assume that the initial datum is such that $0 < u_R^0 < u_L^0$. As proved in [27], the entropic solution associated with (4.37) is a shock wave propagating at speed $\sigma = \left(u_R^0 + u_L^0\right)/2$:

$$u^{\text{shock}}(x/t) = \begin{cases} u_L^0 \text{ if } x/t < \sigma, \\ u_R^0 \text{ if } x/t > \sigma. \end{cases} \tag{4.38}$$

In this example, system (4.37) and solution (4.38) are considered as the formal asymptotic limit of a relaxation system of higher dimension including relaxation source terms. The formalism to derive the Riemann problem associated with such a relaxation system has been introduced by Jin and Xin in [35]. It reads:

$$\begin{aligned} &\partial_t u + \partial_x v = 0, \\ &\partial_t v + \partial_x \left(a^2 u\right) = -\frac{1}{\tau}\left(v - u^2/2\right), \end{aligned} \tag{4.39}$$

$$u(.,\, t=0) = \begin{cases} u_L^0 \text{ if } x<0, \\ u_R^0 \text{ if } x>0, \end{cases} \qquad v(.,\, t=0) = \begin{cases} v_L^0 \text{ if } x<0, \\ v_R^0 \text{ if } x>0. \end{cases} \tag{4.40}$$

Here, τ is a stiff relaxation time-scale formally forcing v to converge towards $u^2/2$. One can notice that injecting $v = u^2/2$ in the equation of u allows to retrieve the Burgers' equation. In system (4.39), a is a relaxation coefficient constant in the computational domain Ω. Decomposing v as $u^2/2 + \tau\, v^1 + O\left(\tau^2\right)$, a Chapman-Enskog expansion allows to exhibit a sufficient condition in order to enforce the diffusivity of the first-order convection-diffusion system related to (4.39). Such a condition writes:

$$a > \sup_{\Omega} |u|. \tag{4.41}$$

Inequality (4.41) is often referred to as the subcharacteristic condition or the Whitam's condition (see [10, 35, 50] for more details on the relaxation scheme theory). In the above example, a is defined as:

$$a = \max\left(u_L^0,\, u_R^0\right) = u_L^0. \tag{4.42}$$

Once more, let us stress that Riemann problem (4.37) has to be seen as the resulting equilibrium system that couples the convection part,

$$\partial_x \begin{bmatrix} v \\ a^2\, u \end{bmatrix}, \tag{4.43}$$

with the relaxation source terms

$$-\frac{1}{\tau}\left(v - u^2/2\right), \tag{4.44}$$

in the limit $\tau \to 0$. Solution (4.38) then represents the physical solution that one expects to find out when performing the fractional-step resolution of (4.39) using a splitting between convection and source terms.

In the following, one time-step of such a procedure is solved analytically. The shape of the obtained solution is then compared with the shock wave profile (4.38). Starting from a piece-wise constant initial solution (4.40), the first step of fractional-step methods consists in solving in the half-planes $x<0$ and $x>0$ (labeled "L" and "R" in the sequel) the relaxation ODEs:

$$\begin{aligned} &k \in \{\mathrm{L},\mathrm{R}\}, \\ &\mathrm{d}_t\, u_k = 0, \\ &\mathrm{d}_t\, v_k = -\frac{1}{\tau}\left(v_k - u_k^2/2\right), \\ &u_k\,(t=0) = u_k^0,\ v_k\,(t=0) = v_k^0. \end{aligned} \tag{4.45}$$

After one time-step Δt, the exact solution of (4.45) reads $\forall k \in \{\mathrm{L},\mathrm{R}\}$:

$$\begin{aligned} u_k^{0,\mathrm{rel}}(\Delta t) &= u_k^0, \\ v_k^{0,\mathrm{rel}}(\Delta t) &= \frac{\left(u_k^0\right)^2}{2}\left(1 - e^{-\Delta t/\tau}\right) + e^{-\Delta t/\tau}\, v_k^0. \end{aligned} \tag{4.46}$$

The second step of the convection-source operator splitting technique has to solve:

$$\begin{aligned} &\partial_t\, u + \partial_x\, v = 0, \\ &\partial_t\, v + \partial_x\left(a^2\, u\right) = 0, \\ &u(.,\, t=0) = \begin{cases} u_{\mathrm{L}}^{0,\mathrm{rel}}(\Delta t) \text{ if } x<0, \\ u_{\mathrm{R}}^{0,\mathrm{rel}}(\Delta t) \text{ if } x>0, \end{cases} \qquad v(.,\, t=0) = \begin{cases} v_{\mathrm{L}}^{0,\mathrm{rel}}(\Delta t) \text{ if } x<0, \\ v_{\mathrm{R}}^{0,\mathrm{rel}}(\Delta t) \text{ if } x>0. \end{cases} \end{aligned} \tag{4.47}$$

System (4.47) is strictly hyperbolic, its eigenvalues, $\lambda^{\pm} = \pm a$, are associated with linearly degenerate fields whose Riemann invariants write $\mathcal{I}^{\pm} = u \mp v/a$. The Godunov solution can be derived exactly and reads:

$$\begin{bmatrix} u^{\mathrm{fs}} \\ v^{\mathrm{fs}} \end{bmatrix}(x/t) = \begin{cases} \left[u_{\mathrm{L}}^{0,\mathrm{rel}}(\Delta t),\ v_{\mathrm{L}}^{0,\mathrm{rel}}(\Delta t)\right]^{\mathrm{T}} & \text{if } x/t < -a, \\ \left[u^*,\ v^*\right]^{\mathrm{T}} & \text{if } -a < x/t < a, \\ \left[u_{\mathrm{R}}^{0,\mathrm{rel}}(\Delta t),\ v_{\mathrm{R}}^{0,\mathrm{rel}}(\Delta t)\right]^{\mathrm{T}} & \text{if } x/t > a, \end{cases} \tag{4.48}$$

with,

$$\begin{aligned} u^* &= \frac{u_{\mathrm{R}}^{0,\mathrm{rel}}(\Delta t) + u_{\mathrm{L}}^{0,\mathrm{rel}}(\Delta t)}{2} - \frac{1}{2a}\left(v_{\mathrm{R}}^{0,\mathrm{rel}}(\Delta t) - v_{\mathrm{L}}^{0,\mathrm{rel}}(\Delta t)\right), \\ v^* &= \frac{v_{\mathrm{R}}^{0,\mathrm{rel}}(\Delta t) + v_{\mathrm{L}}^{0,\mathrm{rel}}(\Delta t)}{2} - \frac{a}{2}\left(u_{\mathrm{R}}^{0,\mathrm{rel}}(\Delta t) - u_{\mathrm{L}}^{0,\mathrm{rel}}(\Delta t)\right). \end{aligned} \tag{4.49}$$

Focusing on the first component u^{fs}, one can simplify its expression by using relations (4.46). It yields:

$$u^{\mathrm{fs}}(x/t) = \begin{cases} u_{\mathrm{L}}^0 & \text{if } x/t < -a, \\ u^* = \frac{u_{\mathrm{R}}^0 + u_{\mathrm{L}}^0}{2} - \frac{(1-e^{-\Delta t/\tau})}{2a}\left(\frac{(u_{\mathrm{R}}^0)^2}{2} - \frac{(u_{\mathrm{L}}^0)^2}{2}\right) - \frac{e^{-\Delta t/\tau}}{2a}\left(v_{\mathrm{R}}^0 - v_{\mathrm{L}}^0\right) & \text{if } -a < x/t < a, \\ u_{\mathrm{R}}^0 & \text{if } x/t > a. \end{cases} \tag{4.50}$$

Solution (4.50) then has to be compared with the Burgers' shock wave (4.38). First of all, suppose an instantaneous time-relaxation, $e^{-\Delta t/\tau} = 0$. The intermediate state u^* then becomes:

$$u^* = \frac{u_L^0}{2}\left[1 + \frac{u_L^0}{2a}\right] + \frac{u_R^0}{2}\left[1 - \frac{u_R^0}{2a}\right]. \tag{4.51}$$

Then, assume that initial conditions are such that:

$$0 < u_L^0,\ 0 < u_R^0,\ u_L^0 \gg u_R^0. \tag{4.52}$$

Hence, $\sigma = \left(u_R^0 + u_L^0\right)/2 \approx u_L^0/2 < a = u_L^0$. The fractional step method produces waves that systematically propagate faster than the physical shock speed. What is more, injecting (4.42) into (4.51), one can notice that,

$$\begin{aligned} u^* &= \frac{3}{4}u_L^0 + \frac{u_R^0}{2}\left[1 - \frac{1}{2}\frac{u_R^0}{u_L^0}\right] \\ &\approx \frac{3}{4}u_L^0 < u_L^0. \end{aligned} \tag{4.53}$$

Thus, after one time-step, whatever the stiffness of the relaxation sub-step (4.45), the fractional-step approach will never reach the right physical state u_L^0 in the intermediate region created by the relaxation Riemann problem. Conversely, one can observe that:

$$u^* = u_L^0 \Leftrightarrow a = \frac{u_R^0 + u_L^0}{2}. \tag{4.54}$$

The appropriate shock speed is thus retrieved but it strongly violates the subcharacteristic condition (4.41) that ensures the stability of the relaxation system (4.39).

The above hand-made example points out the fact that, injecting the effect of time-relaxation only through the initial conditions of the *homogeneous* relaxation Riemann problem (4.39) does not provide enough "information" to catch up the right Rankine-Hugoniot jump relations related to the relaxed equilibrium system (4.37). It also highlights that straightly imposing the right equilibrium shock speed, $a = \left(u_R^0 + u_L^0\right)/2$, may trigger instabilities during the resolution of the homogeneous relaxation Riemann problem.

Of course the highlighted drawbacks have to be balanced by the fact that the intermediate velocity expression (4.53) has been obtained after one time-step Δt. As shown in [9], fractional-step methods applied to hyperbolic systems with sufficiently stiff relaxation converge in practice towards the equilibrium solution. Nevertheless our assumption is that convection-relaxation splitting techniques entail additional accuracy issues that one needs to tackle.

As a consequence the following section is devoted to the conception of a scheme able to *couple* convection with relaxation source terms into one single step for the isentropic Baer-Nunziato model with pressure-velocity relaxation. On that topic, one can mention the works of Ambroso and co-authors [3] which integrate velocity-relaxation effects into the flux-discretization by using the notion of *consistency in the integral sense* for hyperbolic systems with source terms. In the end, their approach associates the velocity-relaxation term with a Dirac function following the material wave u_I. Readers are referred to [3] for additional details about the resulting HLL-like scheme.

Let us also underline the work of Pareschi and Russo [43] based on high order finite-volume Implicit-Explicit (IMEX) schemes applied to general hyperbolic systems with relaxation. Their approach simultaneously includes the contributions of both convective fluxes and stiff source terms. However, contrary to [3], the presence of the latter has no influence on the convective-flux discretization. Besides, their strategy is only applied to hyperbolic systems with relaxation fulfilling the Liu's definition [38] in which non-conservative products are absent. Attention has been actually drawn to this work because it describes how to increase the scheme's accuracy order by combining WENO techniques for the convective time-explicit flux discretization and Diagonally Implicit Runge-Kutta methods (DIRK) [29] for the stiff source terms time-integration.

The present approach relies on a result proved by Bereux and Saintsaulieu in [6]. Starting from the analysis of a generalized Riemann problem with a linearized Jacobian matrix and linearized

source terms, it has the advantage to show exactly how source terms interact with waves produced by the convection-operator. Then, contrary to [3], source terms effects are not artificially projected on a particular wave. Hereafter, details about the Bereux-Sainsaulieu results are provided.

4.3 Solution of a generalized linear convection-relaxation hyperbolic system

In the first part of this section, the Bereux-Sainsaulieu lemma is set out. Some elements of proof are subsequently added in order to help the reader to understand the stated result. The second part proposes to illustrate the Bereux-Sainsaulieu lemma with a simple hand-made example. The exact solution of a simple generalized Riemann problem with linear coupling relaxation terms is derived. Then, the properties proved by the authors of [6] can be easily retrieved.

4.3.1 The Bereux-Sainsaulieu lemma

Let us introduce the generalized Riemann problem presented below:

$$\begin{aligned} &\partial_t \mathbf{U} + \partial_x \mathbf{F}(\mathbf{U}) = \frac{1}{\tau}\mathbf{S}(\mathbf{U}), \\ &\mathbf{U}(., t=0) = \begin{cases} \mathbf{U}_\mathrm{L}^0 \text{ if } x < 0, \\ \mathbf{U}_\mathrm{R}^0 \text{ if } x > 0. \end{cases} \end{aligned} \tag{4.55}$$

$\mathbf{S}(.)$ is a source term forcing the conservative variable vector $\mathbf{U} \in \mathbb{R}^p$ to relax towards a given equilibrium $\mathbf{U}^{\mathrm{eq}}$ such as $\mathbf{S}\left(\mathbf{U}^{\mathrm{eq}}\right) = \mathbf{0}$. The relaxation time-scale is provided by the parameter τ.

Remark 4.3.1 (About the structure of system (4.55))
It can be noted that the structure of system (4.55) abides by the Liu's definition of hyperbolic systems with relaxation: no non-conservative flux are present in such systems. This is the framework in which the strategy presented in [6] has been developed and tested. Nevertheless extensions of the Bereux-Sainsaulieu method to the Baer-Nunziato model will be presented in the next chapter.

Although solutions of problem (4.55) are still out of reach, Bereux and Sainsaulieu in [6, lemma 3.1, p. 152] bring a substantial breakthrough by stating the following lemma:

Property 4.3.1 (Bereux-Sainsaulieu lemma [6])
Define a time-space domain $\Omega = [0, \mathrm{T}] \times [-\mathrm{L}/2, \mathrm{L}/2]$, L *being a given length and* T *a given final time. Consider the generalized linear Riemann problem:*

$$\begin{aligned} &\partial_t \mathbf{U} + \underline{\underline{\mathbf{C}}}_0 \, \partial_x \mathbf{U} = \frac{1}{\tau} \underline{\underline{\mathbf{B}}}_0 \, \mathbf{U}, \\ &\mathbf{U}(., t=0) = \begin{cases} \mathbf{U}_\mathrm{L}^0 \textit{ if } x < 0, \\ \mathbf{U}_\mathrm{R}^0 \textit{ if } x > 0, \end{cases} \end{aligned} \tag{4.56}$$

with $\underline{\underline{\mathbf{C}}}_0$ *a constant convection matrix and* $\underline{\underline{\mathbf{B}}}_0$ *a constant source term matrix. Assume that there exists an eigenvector basis for* $\underline{\underline{\mathbf{C}}}_0$ *related to a set of ordered eigenvalues* $\{\lambda_0^1 < \ldots < \lambda_0^p\}$. *Additionally, assume that system (4.56) is symmetrizable in the sense that there exists a positive definite symmetric matrix* $\underline{\underline{\mathbf{S}}}_0$ *such that* $\underline{\underline{\mathbf{S}}}_0 \underline{\underline{\mathbf{C}}}_0$ *is symmetric. Consider the space-averaged variable* $\mathbf{H}$*:*

$$\mathbf{H} = \frac{1}{\mathrm{L}} \int_{-\mathrm{L}/2}^{\mathrm{L}/2} \mathbf{U} \, \mathrm{d}x. \tag{4.57}$$

Then, problem (4.56) admits a unique solution $\mathbf{U} \in \mathrm{C}^1([0, \mathrm{T}], \mathrm{BV}([-\mathrm{L}/2, \mathrm{L}/2]))$; $\mathrm{BV}([-\mathrm{L}/2, \mathrm{L}/2])$ *being the set of bounded-variation functions in* $[-\mathrm{L}/2, \mathrm{L}/2]$. *What is more, if* T *is such that,*

$$\mathrm{T} < \frac{\mathrm{L}}{2 \max\limits_{k \in [1,p]} \left|\lambda_0^k\right|}, \tag{4.58}$$

H *is solution of the following ODE system:*

$$\begin{cases} \dfrac{\mathrm{d}\mathbf{H}}{\mathrm{d}t} = \dfrac{1}{\tau}\underline{\underline{\mathbf{B}}}_0\,\mathbf{H} - \dfrac{1}{\mathrm{L}}\underline{\underline{\mathbf{C}}}_0\,\left(\mathbf{U}_{\mathrm{R}}(t) - \mathbf{U}_{\mathrm{L}}(t)\right),\ \mathbf{H}(0) = \dfrac{\mathbf{U}_{\mathrm{R}}^0 + \mathbf{U}_{\mathrm{L}}^0}{2}, \\ \forall\, k \in \{\mathrm{L},\,\mathrm{R}\}: \\ \dfrac{\mathrm{d}\mathbf{U}_k}{\mathrm{d}t} = \dfrac{1}{\tau}\underline{\underline{\mathbf{B}}}_0\,\mathbf{U}_k,\ \mathbf{U}_k(0) = \mathbf{U}_k^0. \end{cases} \tag{4.59}$$

Without detailing the entire proof of Property 4.3.1, one can catch the main idea by setting two additional results. Let us first define some notations which will remain unchanged subsequently. First of all, consider

$$\underline{\underline{\mathbf{R}}}_0 = \begin{bmatrix} \mathbf{r}_1^0 & \dots & \mathbf{r}_k^0 & \dots & \mathbf{r}_p^0 \end{bmatrix},\ \underline{\underline{\mathbf{R}}}_0^{-1} = \begin{bmatrix} \mathbf{l}_1^0 \\ \dots \\ \mathbf{l}_k^0 \\ \dots \\ \mathbf{l}_p^0 \end{bmatrix}, \tag{4.60}$$

the matrices of the right and left eigenvectors related to the frozen Jacobian matrix $\underline{\underline{\mathbf{C}}}_0$. Recall that $\forall\ (i,\,j) \in [1,\,p]^2$:

$$\mathbf{l}_i^0 \cdot \mathbf{r}_j^0 = \begin{cases} 0 & \text{if } i \neq j, \\ 1 & \text{if } i = j. \end{cases} \tag{4.61}$$

The Jacobian matrix can be rewritten:

$$\begin{aligned} \underline{\underline{\mathbf{C}}}_0 &= \underline{\underline{\mathbf{R}}}_0\,\underline{\underline{\Lambda}}_0\,\underline{\underline{\mathbf{R}}}_0^{-1}, \\ \underline{\underline{\Lambda}}_0 &= \underline{\underline{\mathrm{diag}}}\left(\left[\lambda_1^0, \dots, \lambda_p^0\right]^{\mathrm{T}}\right). \end{aligned} \tag{4.62}$$

For a given vector $\mathbf{v} \in \mathbb{R}^p$, $\underline{\underline{\mathrm{diag}}}(\mathbf{v})$ is a $p \times p$ diagonal matrix filled with the components of $\mathbf{v}$. For a given state $\mathbf{U} \in \mathbb{R}^p$, consider $\mathbf{a} \in \mathbb{R}^p$ the vector of coordinates of $\mathbf{U}$ projected into the right eigenvector basis:

$$\mathbf{a} = \begin{bmatrix} \mathbf{a}_1 \\ \vdots \\ \mathbf{a}_k \\ \vdots \\ \mathbf{a}_p \end{bmatrix} = \underline{\underline{\mathbf{R}}}_0^{-1}\,\mathbf{U} \Leftrightarrow \mathbf{U} = \underline{\underline{\mathbf{R}}}_0\,\mathbf{a}. \tag{4.63}$$

Eventually, define:

$$\mathbf{a}^0 = \underline{\underline{\mathbf{R}}}_0^{-1}\left(\mathbf{U}_{\mathrm{R}}^0 - \mathbf{U}_{\mathrm{L}}^0\right). \tag{4.64}$$

Some notations also need to be defined for the linear relaxation source terms. First, the matrix $\underline{\underline{\mathbf{B}}}_0$ can be expressed using the right eigenvector basis $\underline{\underline{\mathbf{R}}}_0$. It reads:

$$\underline{\underline{\mathbf{B}}}_0^{\mathbf{r}} = \underline{\underline{\mathbf{R}}}_0^{-1}\,\underline{\underline{\mathbf{B}}}_0\,\underline{\underline{\mathbf{R}}}_0. \tag{4.65}$$

Then, one can isolate $\underline{\underline{\mathbf{B}}}_0^{\mathbf{d}}$, the diagonal of the matrix $\underline{\underline{\mathbf{B}}}_0^{\mathbf{r}}$:

$$\begin{aligned} \underline{\underline{\mathbf{B}}}_0^{\mathbf{r}} &= \underline{\underline{\mathbf{B}}}_0^{\mathbf{d}} + \delta\underline{\underline{\mathbf{B}}}_0, \\ \underline{\underline{\mathbf{B}}}_0^{\mathbf{d}} &= \underline{\underline{\mathrm{diag}}}\left(\left[(\mathbf{l}_1^0)^{\mathrm{T}}\,\underline{\underline{\mathbf{B}}}_0\,\mathbf{r}_1^0, \dots, (\mathbf{l}_p^0)^{\mathrm{T}}\,\underline{\underline{\mathbf{B}}}_0\,\mathbf{r}_p^0\right]^{\mathrm{T}}\right). \end{aligned} \tag{4.66}$$

We can now state a first known result (see [27] for a proof) dealing with *homogeneous* linear hyperbolic systems:

Property 4.3.2 (Solution of a linear homogeneous Riemann problem)
Consider problem (4.56) in the case $\underline{\underline{\mathbf{B}}}_0 = \underline{\underline{\mathbf{0}}}$. *Then, the solution is made of* $p+1$ *constant states,*

$$\left\{\mathbf{U}_0^0 = \mathbf{U}_\mathrm{L}^0, \dots \mathbf{U}_k^0, \mathbf{U}_{k+1}^0, \dots, \mathbf{U}_p^0 = \mathbf{U}_\mathrm{R}^0\right\}, \tag{4.67}$$

such that

$$\mathbf{U}_k^0 = \mathbf{U}_{k-1}^0 + (\mathbf{a}^0)_k \mathbf{r}_k^0, \tag{4.68}$$

separated by p *contact discontinuities propagating at speed* λ_k^0, $k \in [1, p]$. *Hence, the solution is* ***self-similar*** *and simply writes:*

$$\mathbf{U}(x/t) = \mathbf{U}_\mathrm{L}^0 + \sum_{k=1}^{p} \left(\mathbf{a}^0\right)_k \mathrm{H}\left(x - \lambda_k^0 t\right) \mathbf{r}_k^0, \tag{4.69}$$

with $\mathrm{H}(x)$, *the Heaviside function.*

The next property aims at presenting the structure of the solution of (4.56) when linear relaxation terms are active.

Property 4.3.3 (Influence of the linear relaxation terms on the solution's structure)
Consider problem (4.56) with a full relaxation matrix $\underline{\underline{\mathbf{B}}}_0$. *The solution is made of two contributions:*

$$\mathbf{U}(x,\, t) = \tilde{\mathbf{U}}(x,\, t) + \delta\mathbf{U}(x,\, t). \tag{4.70}$$

$\tilde{\mathbf{U}}$ *can be determined explicitly as:*

$$\tilde{\mathbf{U}}(x,\, t) = \underline{\underline{\mathbf{R}}}_0\, \tilde{\mathbf{a}}(x,\, t), \tag{4.71}$$

with $\tilde{\mathbf{a}}$, *the solution of,*

$$\begin{aligned} &\partial_t \tilde{\mathbf{a}} + \underline{\underline{\Lambda}}_0\, \partial_x \tilde{\mathbf{a}} = \frac{1}{\tau} \underline{\underline{\mathbf{B}^\mathbf{d}}}_0 \tilde{\mathbf{a}}, \\ &\tilde{\mathbf{a}}(.,\, t=0) = \begin{cases} \mathbf{a}_\mathrm{L}^0 \ \textit{if}\ x < 0, \\ \mathbf{a}_\mathrm{R}^0 \ \textit{if}\ x > 0. \end{cases} \end{aligned} \tag{4.72}$$

Assume that solutions of problem (4.56) belong to the tempered distribution space and apply Fourier transform on this system. Then, one can prove that, $\delta\mathbf{U}(x,\, t)$ *is continuous on* Ω. *Besides, under the condition (4.58):*

$$\begin{aligned} &\tilde{\mathbf{U}}(x,\, t) + \delta\mathbf{U}(x,\, t) = e^{\underline{\underline{\mathbf{B}}}_0\, t/\tau} \mathbf{U}_\mathrm{L}^0 \ \ \textit{if}\ x < \lambda_1^0\, t, \\ &\tilde{\mathbf{U}}(x,\, t) + \delta\mathbf{U}(x,\, t) = e^{\underline{\underline{\mathbf{B}}}_0\, t/\tau} \mathbf{U}_\mathrm{R}^0 \ \ \textit{if}\ x > \lambda_p^0\, t. \end{aligned} \tag{4.73}$$

For a detailed proof of Property 4.3.3, the reader is referred to [6]. Let us underline that the structure of the solution $\tilde{\mathbf{U}}$ is similar to the one presented in Property 4.3.2. Indeed, the diagonal shape of $\underline{\underline{\mathbf{B}^\mathbf{d}}}_0$ ensures that relaxation effects are decoupled component by component. Following the characteristic line $\dfrac{\mathrm{d}x}{\mathrm{d}t} = \lambda_k^0$, the dynamics of each k-th component $(\tilde{\mathbf{a}})_k$ of $\tilde{\mathbf{a}}$ reads:

$$\frac{\mathrm{d}(\tilde{\mathbf{a}})_k}{\mathrm{d}t} = \frac{(\mathbf{l}_k^0)^\mathrm{T}\, \underline{\underline{\mathbf{B}}}_0\, \mathbf{r}_k^0}{\tau} (\tilde{\mathbf{a}})_k. \tag{4.74}$$

The integration is thus straightforward and gives:

$$(\tilde{\mathbf{a}})_k(x,\, t) = e^{\left\{(\mathbf{l}_k^0)^\mathrm{T}\, \underline{\underline{\mathbf{B}}}_0\, \mathbf{r}_k^0\right\} t/\tau} \left((\mathbf{a}_\mathrm{L}^0)_k + \underbrace{[(\mathbf{a}_\mathrm{R}^0)_k - (\mathbf{a}_\mathrm{L}^0)_k]}_{(\mathbf{a}^0)_k} \mathrm{H}(x - \lambda_k^0\, t) \right). \tag{4.75}$$

Finally, $\tilde{\mathbf{U}}$ simply writes:

$$\tilde{\mathbf{U}}(x,\,t) = \underline{\underline{\mathbf{R}}}_0\,\tilde{\mathbf{a}}(x,\,t) = \sum_{k=1}^{p} (\tilde{\mathbf{a}})_k(x,\,t)\,\mathbf{r}_k^0. \tag{4.76}$$

Across the wave fronts, the produced states are constant in space but evolve exponentially in time due to the contribution of the diagonal source term. Similarly to equality (4.68), the jump relations between the $p+1$ states read:

$$\begin{aligned} \tilde{\mathbf{U}}_k^0(t) &= \tilde{\mathbf{U}}_{k-1}^0(t) + (\tilde{\mathbf{a}}^0)_k(t)\,\mathbf{r}_k^0, \\ (\tilde{\mathbf{a}}^0)_k(t) &= e^{\left\{(\mathbf{l}_k^0)^{\mathrm{T}}\,\underline{\underline{\mathbf{B}}}_0\,\mathbf{r}_k^0\right\} t/\tau}\,(\mathbf{a}^0)_k. \end{aligned} \tag{4.77}$$

Let us also point out that the second contribution $\delta\mathbf{U}$ somehow aggregates the effect of the off-diagonal relaxation terms $\delta\underline{\underline{\mathbf{B}}}_0$ on the convective part of the system. Contrary to $\tilde{\mathbf{U}}$, it cannot be determined explicitly for such a general system.

Figure 4.1a and Figure 4.1b summarize the ideas developed through the above properties. The

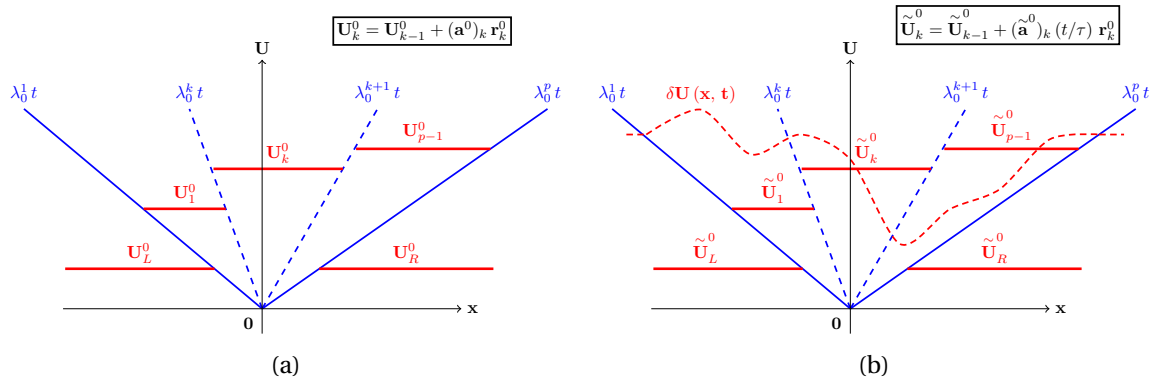

Figure 4.1 – Solution of the generalized linear Riemann problem: (a) without source terms, (b) with source terms.

red-dotted curve displayed in Figure 4.1b illustrates the *continuous behavior* of $\delta\mathbf{U}$ across the wave fronts associated with $\tilde{\mathbf{U}}$.

Coming back to the proof of Property 4.3.1, one can decompose the variable $\mathbf{H}$ as a sum of integrals throughout the fan of waves. Under condition (4.58), the time derivative then gives:

$$\begin{aligned} \mathrm{L}\frac{\mathrm{d}\mathbf{H}}{\mathrm{d}t} &= \int_{-\mathrm{L}/2}^{\lambda_1^0 t} \partial_t\mathbf{U}\,\mathrm{d}x + \lambda_1^0\mathbf{U}\left((\lambda_1^0 t)^-,\,t\right) \\ &\quad + \sum_{k=1}^{p-1}\left\{\int_{\lambda_k^0 t}^{\lambda_{k+1}^0 t} \partial_t\mathbf{U}\,\mathrm{d}x + \lambda_{k+1}^0\mathbf{U}\left((\lambda_{k+1}^0 t)^-,\,t\right) - \lambda_k^0\mathbf{U}\left((\lambda_k^0 t)^+,\,t\right)\right\} \\ &\quad + \int_{\lambda_p^0 t}^{\mathrm{L}/2} \partial_t\mathbf{U}\,\mathrm{d}x - \lambda_p^0\mathbf{U}\left((\lambda_p^0 t)^+,\,t\right). \end{aligned} \tag{4.78}$$

After having replaced $\partial_t\mathbf{U}$ by $-\underline{\underline{\mathbf{C}}}_0\,\partial_x\mathbf{U} + \frac{1}{\tau}\underline{\underline{\mathbf{B}}}_0\,\mathbf{U}$ inside the integrals, one obtains:

$$\begin{aligned} \mathrm{L}\frac{\mathrm{d}\mathbf{H}}{\mathrm{d}t} &= \mathrm{L}\frac{1}{\tau}\underline{\underline{\mathbf{B}}}_0\,\mathbf{H} - \underline{\underline{\mathbf{C}}}_0\left(\mathbf{U}(\mathrm{L}/2,\,t) - \mathbf{U}(-\mathrm{L}/2,\,t)\right) \\ &\quad + \sum_{k=1}^{p}\left\{\left[-\underline{\underline{\mathbf{C}}}_0 + \lambda_k^0\mathbf{I}\right]\left(\mathbf{U}\left((\lambda_k^0 t)^-,\,t\right) - \mathbf{U}\left((\lambda_k^0 t)^+,\,t\right)\right)\right\}. \end{aligned} \tag{4.79}$$

Using relations (4.70), (4.77) and the continuity of $\delta\mathbf{U}$ one can deduce that:

$$\begin{aligned} \left[-\underline{\underline{\mathbf{C}}}_0 + \lambda_k^0\mathbf{I}\right]\left(\mathbf{U}\left((\lambda_k^0 t)^-,\,t\right) - \mathbf{U}\left((\lambda_k^0 t)^+,\,t\right)\right) &= \left[-\underline{\underline{\mathbf{C}}}_0 + \lambda_k^0\mathbf{I}\right]\left(\tilde{\mathbf{U}}\left((\lambda_k^0 t)^-,\,t\right) - \tilde{\mathbf{U}}\left((\lambda_k^0 t)^+,\,t\right)\right) \\ &= \left[-\underline{\underline{\mathbf{C}}}_0 + \lambda_k^0\mathbf{I}\right](\tilde{\mathbf{a}}^0)_k(t)\,\mathbf{r}_k^0 \\ &= \mathbf{0}. \end{aligned} \tag{4.80}$$

ODEs (4.59) immediately follow from equations (4.73) and the fact that

$$\forall\, t \in [0,\mathrm{T}],\ |\mathrm{L}/2| > \max\left(\left|\lambda_1^0\right| t,\ \left|\lambda_p^0\right| t\right). \tag{4.81}$$

In the above sketch of proof, the *continuity* of $\delta\mathbf{U}$ is the key property allowing to derive the $\mathbf{H}$-dynamics. In the sequel, the exact solution of a hand-made linear convection-source system is provided. The expression of $\delta\mathbf{U}$ as well as its continuous behavior are shown. Once again, the reader is referred to [6] for a rigorous proof of Property 4.3.1.

4.3.2 Application to a hand-made linear system with coupling relaxation processes

The following example is made of two transport equations. In each of them a "diagonal" relaxation term is active. Furthermore, the first equation also contains a linear relaxation term involving the variable related to the second transport equation.

Example 4.3.1 (Exact solution of a hand-made convection-source system)
Consider $\mathbf{U} = [u,\, v]^{\mathrm{T}}$ *such that:*

$$\begin{array}{rcrcl} \partial_t u & + & \lambda_u^0\, \partial_x u & = & -\frac{1}{\tau_u}\, u \quad -\frac{1}{\tau}\, v, \\ \partial_t v & + & \lambda_v^0\, \partial_x v & = & -\frac{1}{\tau_v}\, v, \end{array} \tag{4.82}$$

$$\begin{bmatrix} u \\ v \end{bmatrix}(.,\, t=0) = \begin{cases} \left[u_{\mathrm{L}}^0,\, v_{\mathrm{L}}^0\right]^{\mathrm{T}} \ \textit{if}\ x<0, \\ \left[u_{\mathrm{R}}^0,\, v_{\mathrm{R}}^0\right]^{\mathrm{T}} \ \textit{if}\ x>0, \end{cases} \tag{4.83}$$

with $0 < \lambda_u^0 < \lambda_v^0$ *two constant eigenvalues,* τ_u, τ *and* τ_v *three positive time-relaxation constants. If* $\tau_u \neq \tau_v$ *the solution of system* (4.82) (4.83) *reads:*

$$\begin{aligned} u(x,\, t) &= e^{-\,t/\tau_u}\left[u_{\mathrm{L}}^0 + \Delta u^0\, \mathrm{H}(x - \lambda_u^0\, t)\right] - \frac{1}{\tau}\frac{\tau_u\,\tau_v}{\tau_v - \tau_u}\,\delta u(x,\, t), \\ v(x,\, t) &= e^{-\,t/\tau_v}\left[v_{\mathrm{L}}^0 + \Delta v^0\, \mathrm{H}(x - \lambda_v^0\, t)\right], \end{aligned} \tag{4.84}$$

with $\Delta u^0 = u_{\mathrm{R}}^0 - u_{\mathrm{L}}^0$, $\Delta v^0 = v_{\mathrm{R}}^0 - v_{\mathrm{L}}^0$, *and*

$$\delta u(x,\, t) = \begin{cases} v_{\mathrm{L}}^0\left(e^{-t/\tau_v} - e^{-t/\tau_u}\right) & \textit{if} \quad x < \lambda_u^0\, t, \\ v_{\mathrm{R}}^0\left(e^{(1/\tau_u - 1/\tau_v)\,\frac{x-\lambda_u^0 t}{\lambda_v^0 - \lambda_u^0} - \frac{t}{\tau_u}} - e^{-t/\tau_u}\right) + v_{\mathrm{L}}^0\left(e^{-t/\tau_v} - e^{(1/\tau_u - 1/\tau_v)\,\frac{x-\lambda_u^0 t}{\lambda_v^0 - \lambda_u^0} - \frac{t}{\tau_u}}\right) & \textit{if} \quad x \in]\lambda_u^0\, t, \lambda_v^0\, t[, \\ v_{\mathrm{R}}^0\left(e^{-t/\tau_v} - e^{-t/\tau_u}\right) & \textit{if} \quad x > \lambda_v^0\, t. \end{cases} \tag{4.85}$$

Thus, one can notice that,

$$\delta\mathbf{U}(x,\, t) = \begin{bmatrix} -\frac{1}{\tau}\frac{\tau_u\,\tau_v}{\tau_v - \tau_u}\,\delta u(x,\, t) \\ 0 \end{bmatrix}, \tag{4.86}$$

is continuous on $\mathbb{R}\times\mathbb{R}^+$. *Besides, if one defines the matrix* $\underline{\underline{\mathbf{B}}}_0$ *as:*

$$\underline{\underline{\mathbf{B}}}_0 = \begin{bmatrix} -1/\tau_u & -1/\tau \\ 0 & -1/\tau_v \end{bmatrix}, \tag{4.87}$$

one recovers the result shown by Bereux and Sainsaulieu,

$$\begin{bmatrix} u \\ v \end{bmatrix}(x,\, t) = \begin{cases} e^{\underline{\underline{\mathbf{B}}}_0\, t}\begin{bmatrix} u_{\mathrm{L}}^0 \\ v_{\mathrm{L}}^0 \end{bmatrix} & \textit{if} \quad x < \lambda_u^0\, t, \\ \\ e^{\underline{\underline{\mathbf{B}}}_0\, t}\begin{bmatrix} u_{\mathrm{R}}^0 \\ v_{\mathrm{R}}^0 \end{bmatrix} & \textit{if} \quad x > \lambda_v^0\, t. \end{cases} \tag{4.88}$$

Proof 3
The dynamics of variable v being completely independent of the one of variable u, it can be solved easily by following the characteristic curve $\frac{\mathrm{d}x}{\mathrm{d}t} = \lambda_v^0$. It yields directly:

$$v(x,\,t) = e^{-\,t/\tau_v}\left[v_{\mathrm{L}}^0 + \Delta v^0\,\mathrm{H}(x-\lambda_v^0\,t)\right]. \tag{4.89}$$

Injecting solution (4.89) into (4.82) and introducing $u'(x,\,t) = u(x+\lambda_u^0\,t,\,t)$, one looks for a function u' such that:

$$\begin{aligned} \partial_t\,u'(x,\,t) &= -\frac{1}{\tau_u}\,u'(x,\,t) - \frac{1}{\tau}\,e^{-\,t/\tau_v}\left[v_{\mathrm{L}}^0 + \Delta v^0\,\mathrm{H}\left(x+(\lambda_u^0-\lambda_v^0)\,t\right)\right],\\ u'(x,\,0) &= \left[u_{\mathrm{L}}^0 + \Delta u^0\,\mathrm{H}(x)\right]. \end{aligned} \tag{4.90}$$

Applying the variation of constants method, let us introduce $\tilde{u}$ such that $u'(x,\,t) = \tilde{u}(x,\,t)\,e^{-t/\tau_u}$. The time-integration of $\tilde{u}$ gives:

$$\tilde{u}(x,\,t) = \tilde{u}(x,\,0) - \frac{1}{\tau}\int_0^t e^{(1/\tau_u-1/\tau_v)\,t'}\left[v_{\mathrm{L}}^0 + \Delta v^0\,\mathrm{H}\left(x+(\lambda_u^0-\lambda_v^0)\,t'\right)\right]\mathrm{d}t'. \tag{4.91}$$

In order to derive the analytical expression of the above time integral, one needs to specify three different spatial areas for x. Indeed, if $x<0$, then for any $t'\in[0,\,t]$, $\mathrm{H}\left(x+(\lambda_u^0-\lambda_v^0)\,t'\right)=0$ since $\lambda_u^0<\lambda_v^0$. If $x>(\lambda_v^0-\lambda_u^0)\,t$, then $\forall\,t'\in[0,\,t]$, $\mathrm{H}\left(x+(\lambda_u^0-\lambda_v^0)\,t'\right)=1$. Otherwise, the time integral can be split in two contributions:

$$\int_0^{x/(\lambda_v^0-\lambda_u^0)} v_{\mathrm{R}}^0\,e^{(1/\tau_u-1/\tau_v)\,t'}\,\mathrm{d}t' + \int_{x/(\lambda_v^0-\lambda_u^0)}^t v_{\mathrm{L}}^0\,e^{(1/\tau_u-1/\tau_v)\,t'}\,\mathrm{d}t'. \tag{4.92}$$

In the end, one can write:

$$\tilde{u}(x,\,t) = \tilde{u}(x,\,0) - \frac{1}{\tau}\,\delta\tilde{u}(x,\,t), \tag{4.93}$$

with,

$$\delta\tilde{u}(x,\,t) = \begin{cases} \int_0^t v_{\mathrm{L}}^0\,e^{(1/\tau_u-1/\tau_v)\,t'}\,\mathrm{d}t' & \text{if}\quad x<0,\\ \int_0^{x/(\lambda_v^0-\lambda_u^0)} v_{\mathrm{R}}^0\,e^{(1/\tau_u-1/\tau_v)\,t'}\,\mathrm{d}t' + \int_{x/(\lambda_v^0-\lambda_u^0)}^t v_{\mathrm{L}}^0\,e^{(1/\tau_u-1/\tau_v)\,t'}\,\mathrm{d}t' & \text{if}\quad x\in]0,\,(\lambda_v^0-\lambda_u^0)\,t[,\\ \int_0^t v_{\mathrm{R}}^0\,e^{(1/\tau_u-1/\tau_v)\,t'}\,\mathrm{d}t' & \text{if}\quad x>(\lambda_v^0-\lambda_u^0)\,t. \end{cases} \tag{4.94}$$

With formula (4.94), one can notice that $\tilde{u}$ is continuous at points $x=0$ and $x=(\lambda_v^0-\lambda_u^0)\,t$. After calculations, one obtains:

$$\delta\tilde{u}(x,\,t) = \frac{\tau_u\,\tau_v}{\tau_v-\tau_u}\begin{cases} v_{\mathrm{L}}^0\left(e^{(1/\tau_u-1/\tau_v)\,t}-1\right) & \text{if}\quad x<0,\\ v_{\mathrm{R}}^0\left(e^{\frac{(1/\tau_u-1/\tau_v)}{(\lambda_v^0-\lambda_u^0)}\,x}-1\right) + v_{\mathrm{L}}^0\left(e^{(1/\tau_u-1/\tau_v)\,t} - e^{\frac{(1/\tau_u-1/\tau_v)}{(\lambda_v^0-\lambda_u^0)}\,x}\right) & \text{if}\quad x\in]0,\,(\lambda_v^0-\lambda_u^0)\,t[,\\ v_{\mathrm{R}}^0\left(e^{(1/\tau_u-1/\tau_v)\,t}-1\right) & \text{if}\quad x>(\lambda_v^0-\lambda_u^0)\,t. \end{cases} \tag{4.95}$$

In formulas (4.93), (4.95), replacing x by $x-\lambda_u^0\,t$ and multiplying by e^{-t/τ_u}, allows to finally recover the expression of $u(x,\,t)$ provided in (4.84) and (4.85).

The next subsection describes how to apply the theoretical Property 4.3.1 in order to derive a numerical scheme for hyperbolic systems with relaxation whose structure is similar to the one presented in (4.55). This will provide a first step towards the construction of a convection-relaxation coupling scheme for the isentropic Baer-Nunziato system.

4.4 A time-implicit staggered scheme

As proved in Section 4.2, under the non-resonant condition (4.16), the isentropic Baer-Nunziato system is hyperbolic and symmetrizable. Hence, after having linearized its Jacobian matrix and its relaxation source terms, the Bereux-Sainsaulieu lemma holds for this system.

The numerical scheme that is proposed is based on the hypothesis that the Bereux-Sainsaulieu lemma can be extended to the non-linear case. Consider the generalized Riemann problem (4.55) and the following computational domain: $\Omega = [-\Delta x/2, \Delta x/2]$. Assume that the dynamics of the space-averaged variable

$$\mathbf{H} = \frac{1}{\Delta x}\int_{-\Delta x/2}^{\Delta x/2} \mathbf{U}\,\mathrm{d}x, \tag{4.96}$$

reads:

$$\begin{cases} \dfrac{\mathrm{d}\mathbf{H}}{\mathrm{d}t} = \dfrac{1}{\tau}\mathbf{S}(\mathbf{H}) - \dfrac{1}{\Delta x}\left[\mathbf{F}(\mathbf{U}_\mathrm{R}(t)) - \mathbf{F}(\mathbf{U}_\mathrm{L}(t))\right],\ \mathbf{H}(0) = \dfrac{\mathbf{U}_\mathrm{R}^0 + \mathbf{U}_\mathrm{L}^0}{2}, \\ \forall k \in \{\mathrm{L},\mathrm{R}\}: \\ \dfrac{\mathrm{d}\mathbf{U}_k}{\mathrm{d}t} = \dfrac{1}{\tau}\mathbf{S}(\mathbf{U}_k),\ \mathbf{U}_k(0) = \mathbf{U}_k^0. \end{cases} \tag{4.97}$$

Then, similarly to [6], a two-step staggered scheme is derived. In the following, the overall derivation of the numerical approach is first described. Then, special attention is paid to the time-integration of the relaxation source terms. Subsequently, the resulting numerical scheme is completely written in the linear case. Its numerical diffusion as well as its stability properties are compared to other existing schemes of the literature. Finally, a short discussion about the computational cost of the approach with respect to fractional-step methods is carried out.

4.4.1 Derivation of the scheme

Consider a one-dimensional computational domain $\Omega = [0, \mathrm{L}]$ made of N_{cells} cells. Let us define $\Delta x = \mathrm{L}/\mathrm{N}_{cells}$ (respectively Δt) the space-step (respectively the time-step) of the scheme. For $i \in [1,..,\mathrm{N}_{cells}]$ let us set $x_i = (i-1/2)\,\Delta x$, the coordinate of the cell center i and $x_{i+1/2} = x_i + \Delta x/2$, the coordinate of face $i+1/2$. Finally define $\Omega_i =]x_{i-1/2}, x_{i+1/2}[$ the cell of a primal mesh centered around x_i and $\Omega_{i+1/2} =]x_i, x_{i+1}[$ the cell of a dual mesh centered around $x_{i+1/2}$.

Assume that at time t^n, the solution of (4.55) is approximated by a set of piece-wise constant datum:

$$\left\{\mathbf{U}_j^n,\ j \in \sqcup_{i=1}^{\mathrm{N}_{cells}} \Omega_i\right\}. \tag{4.98}$$

Let us also introduce an abstract function $\Phi_\tau(\mathbf{U}, \Delta t)$ such that, for a smooth function $\mathbf{U}(t)$,

$$\frac{\mathbf{U}(t^n + \Delta t) - \mathbf{U}(t^n)}{\Delta t} = \Phi_\tau\left(\mathbf{U}(t^n), \Delta t\right), \tag{4.99}$$

is consistent to a certain order with

$$\frac{\mathrm{d}\mathbf{U}(t^n)}{\mathrm{d}t} = \frac{1}{\tau}\mathbf{S}\left(\mathbf{U}(t^n)\right), \tag{4.100}$$

when $\Delta t \to 0$. As shown in the left picture in Figure 4.2, the first step of the staggered scheme focuses on the dual mesh $\sqcup_{i+1/2}\Omega_{i+1/2}$ endowed with a reconstructed piece-wise constant set of states $\mathbf{H}_{i+1/2}^n = \left(\mathbf{U}_{i+1}^n + \mathbf{U}_i^n\right)/2$. The update $\mathbf{H}_{i+1/2}^{n+1/2}$ is obtained thanks to a consistent time-

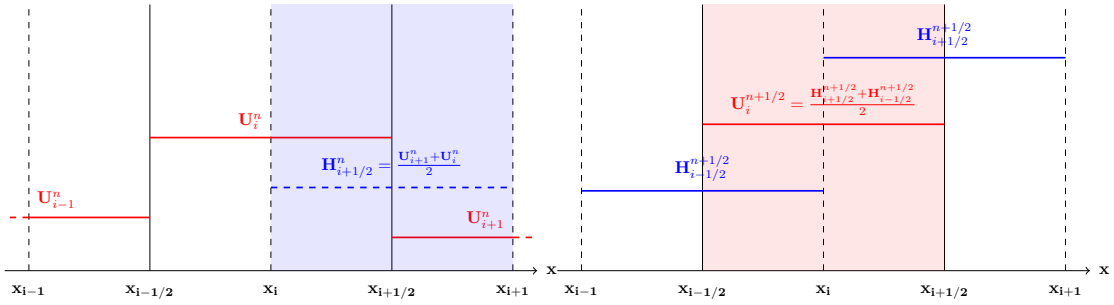

Figure 4.2 – Staggered scheme: (left) dual grid, (right) primal grid

integration of the extended dynamics (4.97):

$$\begin{cases} \mathbf{H}_{i+1/2}^{n+1/2} = \mathbf{H}_{i+1/2}^{n} + (\Delta t/2)\,\Phi_\tau\left(\mathbf{H}_{i+1/2}^{n}, \Delta t/2\right) \\ \qquad -\dfrac{\Delta t}{2\Delta x}\left(\mathbf{F}\left(\mathbf{U}_{i+1}^{n+1/2}\right) - \mathbf{F}\left(\mathbf{U}_{i}^{n+1/2}\right)\right), \\ \quad \forall\, j \in \{i, i+1\}: \\ \mathbf{U}_{j}^{n+1/2} = \mathbf{U}_{j}^{n} + (\Delta t/2)\,\Phi_\tau\left(\mathbf{U}_{j}^{n}, \Delta t/2\right). \end{cases} \tag{4.101}$$

Then, one reconstructs the intermediate update on the primal mesh as $\mathbf{U}_i^{n+1/2} = \left(\mathbf{H}_{i+1/2}^{n+1/2} + \mathbf{H}_{i-1/2}^{n+1/2}\right)/2$ (see the right picture in Figure 4.2). In the end, the final update $\mathbf{U}_i^{n+1}$ is obtained by a similar time-integration:

$$\begin{cases} \mathbf{U}_{i}^{n+1} = \mathbf{U}_{i}^{n+1/2} + (\Delta t/2)\,\Phi_\tau\left(\mathbf{U}_{i}^{n+1/2}, \Delta t/2\right) \\ \qquad -\dfrac{\Delta t}{2\Delta x}\left(\mathbf{F}\left(\mathbf{H}_{i+1/2}^{n+1}\right) - \mathbf{F}\left(\mathbf{H}_{i-1/2}^{n+1}\right)\right), \\ \quad \forall\, j \in \{i-1/2, i+1/2\}: \\ \mathbf{H}_{j}^{n+1} = \mathbf{H}_{j}^{n+1/2} + (\Delta t/2)\,\Phi_\tau\left(\mathbf{H}_{j}^{n+1/2}, \Delta t/2\right). \end{cases} \tag{4.102}$$

Introducing the operator $\Psi_\tau^{\Delta x}(\mathbf{U}_\mathrm{R}, \mathbf{U}_\mathrm{L}, \delta t)$ such that,

$$\begin{aligned} \Psi_\tau^{\Delta x}(\mathbf{U}_\mathrm{R}, \mathbf{U}_\mathrm{L}, \delta t) = &\frac{\mathbf{U}_\mathrm{R} + \mathbf{U}_\mathrm{L}}{2} + \delta t\,\Phi_\tau\left(\frac{\mathbf{U}_\mathrm{R} + \mathbf{U}_\mathrm{L}}{2}, \delta t\right) \\ &-\frac{\delta t}{\Delta x}\left(\mathbf{F}\left(\mathbf{U}_\mathrm{R} + \delta t\,\Phi_\tau(\mathbf{U}_\mathrm{R}, \delta t)\right) - \mathbf{F}\left(\mathbf{U}_\mathrm{L} + \delta t\,\Phi_\tau(\mathbf{U}_\mathrm{L}, \delta t)\right)\right), \end{aligned} \tag{4.103}$$

the above staggered scheme can be rewritten more compactly as:

$$\mathbf{U}_i^{n+1} = \Psi_\tau^{\Delta x}\left[\Psi_\tau^{\Delta x}\left(\mathbf{U}_{i+1}^{n}, \mathbf{U}_i^{n}, \Delta t/2\right), \Psi_\tau^{\Delta x}\left(\mathbf{U}_i^{n}, \mathbf{U}_{i-1}^{n}, \Delta t/2\right), \Delta t/2\right]. \tag{4.104}$$

4.4.2 Choice of the discrete source terms operator

This section synthetically describes how the system of ODEs (4.100) is discretized. Consider a discrete time-step Δt defined using $\left|\lambda\right|^n$, the spectral radius related to the convective part of the system (4.55) at time t^n:

$$\begin{aligned} &\Delta t = \mathscr{C}\,\frac{\Delta x}{\max\limits_{i+1/2}\left(\max\left(\left|\lambda\right|_i^n, \left|\lambda\right|_{i+1}^n\right)\right)}, \\ &\mathscr{C} \in]0, 1[. \end{aligned} \tag{4.105}$$

When the relaxation time-scale τ is such that $\tau \ll \Delta t$, problem (4.55) is said to be stiff. After a very thin time-boundary layer of order $\mathrm{O}(\tau)$, the solution is formally projected on the equilibrium manifold $\{\mathbf{U},\, \mathbf{S}(\mathbf{U}) = \mathbf{0}\}$. From a numerical point of view, one wishes to accurately capture the steep transition towards the equilibrium while guaranteeing the stability of the discretization. High-order time-explicit Runge-Kutta methods [29] are thus automatically put aside since their stability domain would require to adapt the Courant number such that $\Delta t \leq \tau$. In a stiff regime, such a CFL constraint is extremely expensive computationally. Besides, in the context of conservation laws with stiff relaxation terms, large numerical diffusion would smear the waves profile related to the j-components of $\mathbf{U}$ that do not "feel" the relaxation process ($\mathbf{S}_j(\mathbf{U}) = 0$).

As a result the discrete source term operator $\Phi_\tau(\mathbf{U}, \Delta t)$ is obtained thanks to a fourth-order *linearly-implicit* Runge-Kutta method called: the Rosenbrock method [29]. Details presenting the main lines of the approach are provided below.

Let us consider a state $\mathbf{U}^n$ at time t^n and introduce

$$\underline{\underline{\mathbf{J}}}^n = \partial_{\mathbf{U}}\mathbf{S}\left(\mathbf{U}^n\right), \tag{4.106}$$

the Jacobian matrix of the relaxation source term involved in equation (4.100).

A s-stage Rosenbrock method is given by the formulas:

$$\mathbf{U}^{n+1} = \mathbf{U}^n + \sum_{j=1}^{s} b_j \mathbf{k}_j, \tag{4.107a}$$

$$\forall i \in [1,\, s],\ \left[\mathbf{I} - \gamma \frac{\Delta t}{\tau} \underline{\underline{\mathbf{J}}}^n\right] \mathbf{k}_i = \frac{\Delta t}{\tau} \mathbf{S}\left(\mathbf{U}^n + \sum_{j=1}^{i-1} \alpha_{ij} \mathbf{k}_j\right) + \frac{\Delta t}{\tau} \underline{\underline{\mathbf{J}}}^n \sum_{j=1}^{i-1} \gamma_{ij} \mathbf{k}_j. \tag{4.107b}$$

Assume that $\mathbf{U}^{\mathrm{ex}}(t^n)$ is a solution of (4.100). For a fourth-order Rosenbrock method, the coefficients $(\alpha_{ij})_{j<i}$, $(\gamma_{ij})_{j<i}$, $(b_j)_j$, γ are chosen so that, for any smooth solution $\mathbf{U}$ verifying (4.107), equality

$$\mathbf{U}\left(t^n\right) = \mathbf{U}^{\mathrm{ex}}\left(t^n\right) + \mathrm{O}\left(\Delta t^5\right), \tag{4.108}$$

holds.

Among the large class of high-order implicit or semi-implicit techniques, the Rosenbrock method has been chosen for its capacity to avoid the resolution of non-linear systems (as soon as implicit time-integration is applied to $\mathbf{S}(\mathbf{U})$) by replacing them with a sequence of linear systems. Indeed, if one imposes $\gamma = 1$ and $\forall (i,\, j),\ \gamma_{ij} = 0$, equality (4.107b) formally corresponds to the application of *one* Newton iteration to each stage $i \in [1\ s]$.

What is more, such a linear strategy is compatible with Property 4.3.1. As a matter of fact, in the linear configuration

$$\mathbf{F}(\mathbf{U}) = \underline{\underline{\mathbf{C}}}_0 \mathbf{U},\ \mathbf{S}(\mathbf{U}) = \frac{\underline{\underline{\mathbf{B}}}_0}{\tau} \mathbf{U}, \tag{4.109}$$

the application of the scheme (4.107) with $s = 1$ and $b_1 = \gamma = 1$ corresponds exactly to an implicit Euler time integration of the exact dynamics (4.59).

Finally, as proved in [29], the method is A-stable and can be L-stable for a convenient choice of γ. Besides, it is relatively cheap computationally. Indeed, all the $\mathbf{k}_j$'s can be obtained with the computation and the inversion of one single matrix: $\mathbf{I} - \gamma \frac{\Delta t}{\tau} \underline{\underline{\mathbf{J}}}^n$. Additional details dealing with the analysis of the Rosenbrock methods can be found in [29].

4.4.3 Properties of the scheme in the linear case

Here, one is interested in deriving the expression of the overall numerical scheme (4.104) in the simplified linear case (4.109). Let us first start by the homogeneous case: $\underline{\underline{\mathbf{B}}}_0 = \underline{\underline{\mathbf{0}}}$. After calculations, the scheme (4.104) reads:

$$\mathbf{U}_i^{n+1} = \mathbf{U}_i^n - \Delta t \underline{\underline{\mathbf{C}}}_0 \frac{\mathbf{U}_{i+1}^n - \mathbf{U}_{i-1}^n}{2\Delta x} + \frac{\Delta t}{2}\left[\frac{\Delta x}{\Delta t}\mathbf{I} + \frac{\Delta t}{\Delta x}\left(\underline{\underline{\mathbf{C}}}_0\right)^2\right] \frac{\mathbf{U}_{i+1}^n - 2\mathbf{U}_i^n + \mathbf{U}_{i-1}^n}{2\Delta x}. \tag{4.110}$$

The linear flux $\mathbf{F}^{\mathrm{BS}}$ ("BS" stands for Bereux-Sainsaulieu) at face $i + 1/2$ writes:

$$\mathbf{F}^{\mathrm{BS}}\left(\mathbf{U}_{i+1}^n, \mathbf{U}_i^n\right) = \underline{\underline{\mathbf{C}}}_0 \frac{\mathbf{U}_{i+1}^n + \mathbf{U}_i^n}{2} - \frac{1}{4}\left[\frac{\Delta x}{\Delta t}\mathbf{I} + \frac{\Delta t}{\Delta x}\left(\underline{\underline{\mathbf{C}}}_0\right)^2\right]\left(\mathbf{U}_{i+1}^n - \mathbf{U}_i^n\right). \tag{4.111}$$

Introducing the Lax-Friedrichs flux $\mathbf{F}^{\mathrm{LF}}$ and the Rusanov flux $\mathbf{F}^{\mathrm{Rus}}$ as,

$$\begin{cases} \mathbf{F}^{\mathrm{LF}}\left(\mathbf{U}_{i+1}^n, \mathbf{U}_i^n\right) &= \underline{\underline{\mathbf{C}}}_0 \frac{\mathbf{U}_{i+1}^n + \mathbf{U}_i^n}{2} &- \frac{\Delta x}{2\Delta t}\left(\mathbf{U}_{i+1}^n - \mathbf{U}_i^n\right), \\ \mathbf{F}^{\mathrm{Rus}}\left(\mathbf{U}_{i+1}^n, \mathbf{U}_i^n\right) &= \underline{\underline{\mathbf{C}}}_0 \frac{\mathbf{U}_{i+1}^n + \mathbf{U}_i^n}{2} &- \frac{|r_0|}{2}\left(\mathbf{U}_{i+1}^n - \mathbf{U}_i^n\right), \end{cases} \tag{4.112}$$

with $|r_0|$ the spectral radius related to the Jacobian matrix $\underline{\underline{\mathbf{C}}}_0$, one can express $\mathbf{F}^{\mathrm{BS}}$ using the expression of $\mathbf{F}^{\mathrm{LF}}$ or $\mathbf{F}^{\mathrm{Rus}}$. It yields:

$$\begin{cases} \mathbf{F}^{\mathrm{BS}}\left(\mathbf{U}_{i+1}^n, \mathbf{U}_i^n\right) &= \mathbf{F}^{\mathrm{LF}}\left(\mathbf{U}_{i+1}^n, \mathbf{U}_i^n\right) &- \frac{1}{4}\left[\frac{\Delta t}{\Delta x}\left(\underline{\underline{\mathbf{C}}}_0\right)^2 - \frac{\Delta x}{\Delta t}\mathbf{I}\right]\left(\mathbf{U}_{i+1}^n - \mathbf{U}_i^n\right), \\ \mathbf{F}^{\mathrm{BS}}\left(\mathbf{U}_{i+1}^n, \mathbf{U}_i^n\right) &= \mathbf{F}^{\mathrm{Rus}}\left(\mathbf{U}_{i+1}^n, \mathbf{U}_i^n\right) &- \frac{1}{4}\left[\frac{\Delta t}{\Delta x}\left(\underline{\underline{\mathbf{C}}}_0\right)^2 + \left(\frac{\Delta x}{\Delta t} - 2\,|r_0|\right)\mathbf{I}\right]\left(\mathbf{U}_{i+1}^n - \mathbf{U}_i^n\right). \end{cases} \tag{4.113}$$

Let us introduce the matrices:

$$\begin{aligned}\underline{\underline{\mathbf{D}}}_0^{\text{BS-LF}} &= \left[\frac{\Delta t}{\Delta x}\left(\underline{\underline{\mathbf{C}}}_0\right)^2 - \frac{\Delta x}{\Delta t}\mathbf{I}\right],\\ \underline{\underline{\mathbf{D}}}_0^{\text{BS-Rus}} &= \left[\frac{\Delta t}{\Delta x}\left(\underline{\underline{\mathbf{C}}}_0\right)^2 + \left(\frac{\Delta x}{\Delta t} - 2\,|r_0|\right)\mathbf{I}\right].\end{aligned} \tag{4.114}$$

Consider that the time-step is defined according to formula (4.105). Thus, in the case of a frozen Jacobian matrix $\underline{\underline{\mathbf{C}}}_0$, $\Delta t = \mathscr{C}\,\Delta x/|r_0|$, and the eigenvalues $\lambda_k^{\text{BS-LF},0}$, $\lambda_k^{\text{BS-Rus},0}$ of matrices (4.114) write:

$$\begin{aligned}\lambda_k^{\text{BS-LF},0} &= \frac{1}{\mathscr{C}\,|r_0|}\left(\mathscr{C}^2\,(\lambda_k^0)^2 - |r_0|^2\right),\\ \lambda_k^{\text{BS-Rus},0} &= \frac{\mathscr{C}\,(\lambda_k^0)^2}{|r_0|} + 2\,|r_0|\,(\frac{1}{2\mathscr{C}} - 1).\end{aligned} \tag{4.115}$$

It can be seen that under the classical CFL condition $\mathscr{C} < 1/2$: $\lambda_k^{\text{BS-LF},0} < 0$ and $\lambda_k^{\text{BS-Rus},0} > 0$. Hence, in the homogeneous linear case, the present scheme is less diffusive that the Lax-Friedrichs scheme but more diffusive than the Rusanov one.

Besides, one can project equation (4.110) on the eigenvector basis $\underline{\underline{\mathbf{R}}}_0$ related to the frozen Jacobian matrix $\underline{\underline{\mathbf{C}}}_0$. For a given cell i at time t^n, consider $\mathbf{a}_i^n = \underline{\underline{\mathbf{R}}}_0^{-1}\,\mathbf{U}_i^n$. Each component $(\mathbf{a}_k)_i^n$ of $\mathbf{a}_i^n$ verifies:

$$\begin{aligned}(\mathbf{a}_k)_i^{n+1} &= (\mathbf{a}_k)_i^n - \Delta t\,\lambda_k^0\,\frac{(\mathbf{a}_k)_{i+1}^n - (\mathbf{a}_k)_{i-1}^n}{2\,\Delta x} + \Delta t\,\mathrm{D}_k^0\,\frac{(\mathbf{a}_k)_{i+1}^n - 2\,(\mathbf{a}_k)_i^n + (\mathbf{a}_k)_{i-1}^n}{2\,\Delta x},\\ \mathrm{D}_k^0 &= \frac{1}{2}\left[\frac{\Delta x}{\Delta t} + \frac{\Delta t}{\Delta x}\,(\lambda_k^0)^2\right] = \frac{1}{2}\left[\frac{|r_0|}{\mathscr{C}} + \frac{\mathscr{C}}{|r_0|}\,(\lambda_k^0)^2\right].\end{aligned} \tag{4.116}$$

The right hand side of equality (4.116) can be rewritten as a convex combination of $(\mathbf{a}_k)_i^n$, $(\mathbf{a}_k)_{i+1}^n$ and $(\mathbf{a}_k)_{i-1}^n$:

$$(\mathbf{a}_k)_i^{n+1} = \frac{\Delta t}{2\,\Delta x}\left[\mathrm{D}_k^0 - \lambda_k^0\right](\mathbf{a}_k)_{i+1}^n + \frac{\Delta t}{2\,\Delta x}\left[\mathrm{D}_k^0 + \lambda_k^0\right](\mathbf{a}_k)_{i-1}^n + \left[1 - \frac{\Delta t}{\Delta x}\,\mathrm{D}_k^0\right](\mathbf{a}_k)_i^n. \tag{4.117}$$

One can notice that, under the CFL condition $\mathscr{C} < 1/2$: $\mathrm{D}_k^0 \pm \lambda_k^0 > 0$, $\mathrm{D}_k^0 < \Delta x/\Delta t$. As a consequence, in the linear homogeneous case, a discrete maximum principle holds for every component $\mathbf{a}_k$ and the scheme is L^∞-stable.

Linear source terms are now present. Let us consider the case where the first-order implicit Euler scheme $\Phi_\tau^{\text{Ieu-1}}$ is used to discretize $(\underline{\underline{\mathbf{B}}}_0/\tau)\,\mathbf{U}$:

$$\Phi_\tau^{\text{Ieu-1}}(\mathbf{U},\delta t) = \left[\mathbf{I} - (\delta t/\tau)\,\underline{\underline{\mathbf{B}}}_0\right]^{-1}(\underline{\underline{\mathbf{B}}}_0/\tau)\,\mathbf{U} = \underline{\underline{\Phi}}_\tau^{\text{Ieu-1}}(\delta t)\,\mathbf{U}. \tag{4.118}$$

Consider $\underline{\underline{\Psi}}_\tau = \mathbf{I} + (\Delta t/2)\,\underline{\underline{\Phi}}_\tau^{\text{Ieu-1}}(\Delta t/2)$. The proposed time-implicit staggered scheme can be written:

$$\begin{aligned}\mathbf{U}_i^{n+1} = (\underline{\underline{\Psi}}_\tau)^2\,\mathbf{U}_i^n &- \frac{\Delta t}{2}\left[\underline{\underline{\Psi}}_\tau\,\underline{\underline{\mathbf{C}}}_0\,\underline{\underline{\Psi}}_\tau + \underline{\underline{\mathbf{C}}}_0\,(\underline{\underline{\Psi}}_\tau)^2\right]\frac{\mathbf{U}_{i+1}^n - \mathbf{U}_{i-1}^n}{2\,\Delta x}\\ &+ \frac{\Delta t}{2}\left[\frac{\Delta x}{\Delta t}\,(\underline{\underline{\Psi}}_\tau)^2 + \frac{\Delta t}{\Delta x}\,(\underline{\underline{\Psi}}_\tau\,\underline{\underline{\mathbf{C}}}_0)^2\right]\frac{\mathbf{U}_{i+1}^n - 2\,\mathbf{U}_i^n + \mathbf{U}_{i-1}^n}{2\,\Delta x}.\end{aligned} \tag{4.119}$$

Let us stress that when $\tau \to +\infty$ with Δt fixed, $\underline{\underline{\Psi}}_\tau \to \mathbf{I}$ and the homogeneous scheme (4.110) is retrieved. Even in the linear case, the general study of the scheme (4.119) is complex. Let us assume that $\underline{\underline{\mathbf{B}}}_0$ can be diagonalized using the eigenvector basis $\underline{\underline{\mathbf{R}}}_0$. Such a strong hypothesis is not true for the frozen isentropic Baer-nunziato system with linear relaxations. However it allows to study the discrete evolution of the eigenvector coordinates when relaxation source terms are discretized with the Bereux-Sainsaulieu strategy.

Assume that there exists a diagonal matrix $\underline{\underline{\Lambda}}_0^S$ of positive coefficients $\lambda_k^{0,s}$ such that:

$$\underline{\underline{\mathbf{B}}}_0 = -\underline{\underline{\mathbf{R}}}_0 \underline{\underline{\Lambda}}_0^S \underline{\underline{\mathbf{R}}}_0^{-1}. \tag{4.120}$$

In that case, the dynamics of the discrete components $(\mathbf{a}_k)$ reads:

$$\begin{aligned} (\mathbf{a}_k)_i^{n+1} &= \omega_k^{0,s} \left\{ \frac{\Delta t}{2\Delta x} \left[\mathrm{D}_k^0 - \lambda_k^0 \right] (\mathbf{a}_k)_{i+1}^n + \frac{\Delta t}{2\Delta x} \left[\mathrm{D}_k^0 + \lambda_k^0 \right] (\mathbf{a}_k)_{i-1}^n + \left[1 - \frac{\Delta t}{\Delta x} \mathrm{D}_k^0 \right] (\mathbf{a}_k)_i^n \right\}, \\ \omega_k^{0,s} &= \frac{1}{\left(1 + (\Delta t/2\tau)\, \lambda_k^{0,s} \right)^2}. \end{aligned} \tag{4.121}$$

Consider the vector $\mathbf{a}^{\mathrm{eq}}$, an equilibrium state projected on the eigenvector basis $\underline{\underline{\mathbf{R}}}_0$. Up to the translation $\mathbf{a} \to \mathbf{a} - \mathbf{a}^{\mathrm{eq}}$ applied to the continuous linear Riemann problem with linear relaxations, one can replace every $\mathbf{a}_k$ by $\mathbf{a}_k - \mathbf{a}_k^{\mathrm{eq}}$ into the discrete dynamics (4.121). Consider the CFL condition $\Delta t = \mathscr{C}\, \Delta x / |r_0|$ with $\mathscr{C} < 1/2$. Thus, using the fact that $\omega_k^{0,s} \in [0, 1]$, one can notice that a discrete maximum principle still holds. Besides,

$$\sup_{i \in [1,\mathrm{N}]} \left| (\mathbf{a}_k)_i^{n+1} \right| \leq \omega_k^{0,s} \sup_{i \in [1,\mathrm{N}]} \left| (\mathbf{a}_k)_i^n \right| \leq \sup_{i \in [1,\mathrm{N}]} \left| (\mathbf{a}_k)_i^n \right|. \tag{4.122}$$

The scheme is therefore L^∞-stable and convergences towards $\mathbf{a}^{\mathrm{eq}}$ in L^∞-norm.

4.4.4 Comparison with a time-implicit fractional-step approach

The quality of the above staggered scheme approach is assessed with respect to a fractional-step strategy. The latter is built using a Rusanov scheme for the flux discretization. The overall fractional-step method can be written:

$$\begin{cases} \mathbf{U}_i^{n+} = \mathbf{U}_i^n + \Delta t\, \Phi_\tau \left(\mathbf{U}_i^n, \Delta t \right), \\ \mathbf{U}_i^{n+1} = \mathbf{U}_i^{n+} - \dfrac{\Delta t}{\Delta x} \left(\mathbf{F}^{\mathrm{Rus}} \left(\mathbf{U}_{i+1}^{n+}, \mathbf{U}_i^{n+} \right) - \mathbf{F}^{\mathrm{Rus}} \left(\mathbf{U}_i^{n+}, \mathbf{U}_{i-1}^{n+} \right) \right), \end{cases} \tag{4.123}$$

with,

$$\mathbf{F}^{\mathrm{Rus}} \left(\mathbf{U}_\mathrm{R}, \mathbf{U}_\mathrm{L} \right) = \frac{\mathbf{F}(\mathbf{U}_\mathrm{R}) + \mathbf{F}(\mathbf{U}_\mathrm{L})}{2} - \frac{\left| r_{\mathrm{L,R}} \right|}{2} \left(\mathbf{U}_\mathrm{R} - \mathbf{U}_\mathrm{L} \right), \tag{4.124}$$

and $\left| r_{\mathrm{L,R}} \right|$ the maximum spectral radius between the Jacobian matrix $\partial_{\mathbf{U}} \mathbf{F}(\mathbf{U})$ evaluated at $\mathbf{U}_\mathrm{L}$ and $\mathbf{U}_\mathrm{R}$. Recall that in (4.123), the function $(\mathbf{U}, \delta t) \to \Phi_\tau (\mathbf{U}, \delta t)$ corresponds to an *implicit* time integration of the relaxation ODEs system (4.100) using a first order implicit Euler scheme or a fourth order Rosenbrock method.

In the sequel, one wishes to compare the fractional step method (4.123), (4.124) with respect to the extended Bereux-Sainsaulieu approach (4.104). The quality criteria are based on convergence and efficiency curves. Without going into too much details, it can be argued that the computational cost of the proposed time-implicit staggered scheme is higher than the fractional-step approach. Let us first stress that the implementation of both methods involve the same number of loops through the computational domain: a loop on the cell-list plus a loop on the face-list for the fractional-step scheme, a loop on the primal-face-list plus a loop on the dual-face-list for the present approach. However, the CPU time spent for the discretization of the relaxation source terms is considerably larger in the case of the time-implicit staggered scheme. Indeed, for each primal or dual face, three calls to build the function Φ_τ are necessary: one for the update of the average state, and two for the update of the left and right fluxes. In contrast, the fractional-step method builds only once Φ_τ for each cell during the relaxation step.

Thereafter, the present approach is tested against a hand-made two-fluid two-pressure system with a frozen Jacobian matrix. Three configurations are studied: absence of relaxation source terms, presence of linear relaxation source terms and finally presence of non-linear relaxation source terms. In the last case, the Bereux-Sainsaulieu Property 4.3.1 does not hold and the relevance of the extended Bereux-Sainsaulieu ODEs system (4.97) is assessed.

4.5 Application to hand-made two-fluid two pressure systems

The objective of this section is twofold. First, recall that the time-implicit staggered scheme provided in (4.104) lies on the hypothesis that the Bereux-Sainsaulieu **Property 4.3.1**, holding for linear Riemann problems with linear source terms, can be extended to the non-linear case. Thus, one is interested in evaluating the limits of such an assumption. The accuracy of the approach when non-linear and non-monotonous relaxation source terms are active has to be checked. Secondly, we wish to compare the accuracy and the efficiency of the staggered scheme with respect to the more classical fractional step approach presented in (4.123), (4.124).

Both methods are tested in the context of the isentropic Baer-Nunziato model (4.14). However, one can notice that the proposed staggered scheme is based on a general *conservative* system with relaxation source terms. For the sake of clarity, the extension of the Bereux-Sainsaulieu lemma for non-linear hyperbolic systems with *non-conservative products* will be treated in the next chapter. As a consequence, in this section, the isentropic Baer-Nunziation system written in (4.14) is replaced by,

$$
\begin{aligned}
&\partial_t \mathbf{U} + \underline{\underline{\mathbf{C}}}_0 \, \partial_x \mathbf{U} = \mathbf{S}(\mathbf{U}), \\
&\underline{\underline{\mathbf{C}}}_0 = \partial_{\mathbf{U}} \mathbf{F}(\mathbf{U}_0) + \underline{\underline{\mathbf{E}}}(\mathbf{U}_0), \\
&\mathbf{F}(\mathbf{U}) = \begin{bmatrix} 0, \\ m_1 u_1 \\ m_1 u_1^2 + \alpha_1 p_1 \\ m_2 u_2 \\ m_2 u_2^2 + \alpha_2 p_2 \end{bmatrix}, \underline{\underline{\mathbf{E}}}(\mathbf{U}) = \left[\mathbf{b}(\mathbf{U}), \mathbf{0}, \mathbf{0}, \mathbf{0}, \mathbf{0} \right], \mathbf{b}(\mathbf{U}) = \begin{bmatrix} u_I \\ 0 \\ -p_I \\ 0 \\ +p_I \end{bmatrix}, \\
&\mathbf{S}(\mathbf{U}) = \begin{bmatrix} -\mathrm{K_p}(\mathbf{U}) \, \Delta p \\ 0 \\ \mathrm{K_u}(\mathbf{U}) \, \Delta u \\ 0 \\ -\mathrm{K_u}(\mathbf{U}) \, \Delta u \end{bmatrix}.
\end{aligned}
\tag{4.125}
$$

Here, $\mathbf{U}_0$ is a constant state and $\underline{\underline{\mathbf{C}}}_0$ is the *frozen* convective Jacobian matrix for the isentropic Baer-Nunziato system. In the following subsections, in order to provide simple analytical solutions for system (4.125), the relaxation source terms $\mathbf{S}(\mathbf{U})$ are artificially replaced by a more convenient form which acts only on the coordinates associated with the eigenvector basis $\underline{\underline{\mathbf{R}}}_0$ of $\underline{\underline{\mathbf{C}}}_0$. Let us write,

$$
\underline{\underline{\mathbf{C}}}_0 = \underline{\underline{\mathbf{R}}}_0 \, \underline{\underline{\Lambda}}_0 \, \underline{\underline{\mathbf{R}}}_0^{-1}, \tag{4.126}
$$

the expression of the frozen eigenvector basis $\underline{\underline{\mathbf{R}}}_0$ being given in (4.18) and,

$$
\begin{aligned}
&\underline{\underline{\Lambda}}_0 = \underline{\underline{\mathrm{diag}}}\left(\underline{\Lambda}_0\right), \\
&\underline{\Lambda}_0 = \left[u_I = u_2, \, u_1 + c_1, \, u_1 - c_1, \, u_2 + c_2, \, u_2 - c_2 \right]_0^{\mathrm{T}}.
\end{aligned}
\tag{4.127}
$$

Then, consider $\mathbf{a}$, the coordinates of state $\mathbf{U}$ projected on the eigenvector basis $\underline{\underline{\mathbf{R}}}_0$:

$$
\mathbf{a} = \underline{\underline{\mathbf{R}}}_0^{-1} \mathbf{U} = \begin{bmatrix} \mathbf{a}_1 \\ \vdots \\ \mathbf{a}_k \\ \vdots \\ \mathbf{a}_5 \end{bmatrix}. \tag{4.128}
$$

In the sequel, $\mathbf{S}(\mathbf{U})$ is replaced by,

$$
\underline{\underline{\mathbf{R}}}_0 \, \widetilde{\mathbf{S}}(\mathbf{a}(\mathbf{U})), \tag{4.129}
$$

such that system (4.125) is equivalent to,

$$\partial_t \mathbf{a} + \underline{\underline{\Lambda}}_0 \, \partial_x \mathbf{a} = \widetilde{\mathbf{S}}(\mathbf{a}). \tag{4.130}$$

The present time-implicit staggered scheme is applied to Riemann problems of increasing difficulty. First, the convergence of the method is assessed in the very simple homogeneous case ($\widetilde{\mathbf{S}}(\mathbf{a}) = \mathbf{0}$). Then, the approach is tested in presence of linear relaxation source terms. Finally, accuracy and efficiency comparisons between the present scheme and fractional-step methods are performed in the case where the relaxation source terms are stiff and act as a non-linear spring.

4.5.1 Linearized homogeneous isentropic Baer-Nunziato system

Consider the computational domain $\Omega =]0, \mathrm{L}[$, $\mathrm{L} = 1\,m$, and the homogeneous Riemann problem,

$$\begin{aligned} &\partial_t \mathbf{U} + \underline{\underline{\mathbf{C}}}_0 \, \partial_x \mathbf{U} = \mathbf{0}, \\ &\mathbf{U}(., t=0) = \begin{cases} \mathbf{U}_\mathrm{L}^0 \text{ if } x < 0.5, \\ \mathbf{U}_\mathrm{R}^0 \text{ if } x > 0.5. \end{cases} \end{aligned} \tag{4.131}$$

Define $\mathbf{a}_{\Delta\mathbf{U}} = \underline{\underline{\mathbf{R}}}_0^{-1} \left(\mathbf{U}_\mathrm{R}^0 - \mathbf{U}_\mathrm{L}^0\right)$. As shown in [49], the analytical solution of problem (4.131) reads:

$$\mathbf{U}(x/t) = \mathbf{U}_\mathrm{L} + \sum_{k=1}^{5} (\mathbf{a}_{\Delta\mathbf{U}})_k \, \mathrm{H}\left(x - \lambda_k^0 t\right) \mathbf{r}_k^0, \tag{4.132}$$

with $\left(\lambda_k^0\right)_{k\in[1,5]}$, the eigenvalues given in (4.17). Consider the non-conservative vector

$$\mathbf{W} = \left[\alpha_1, \, u_1, \, p_1, \, u_2, \, p_2\right]^\mathrm{T}. \tag{4.133}$$

The initial states $\mathbf{W}_\mathrm{L}^0$ and $\mathbf{W}_\mathrm{R}^0$ are summarized in Table 4.1.

	α_1	u_1 $(m.s^{-1})$	p_1 (bar)	u_2 $(m.s^{-1})$	p_2 (bar)
$\mathbf{W}_\mathrm{L}^0$	0.2	3	4	10	10
$\mathbf{W}_\mathrm{R}^0$	0.8	2	1	5	20

Table 4.1 – Homogeneous Riemann problem: initial conditions

The Jacobian matrix of the system is frozen using the averaged constant state

$$\mathbf{U}_0 = \mathbf{U}\left((\mathbf{W}_\mathrm{R}^0 + \mathbf{W}_\mathrm{L}^0)/2\right). \tag{4.134}$$

For both phases, the isentropic EOS reads:

$$\begin{aligned} &\forall k \in \{1,2\}, \; p_k = \kappa_k \left(\rho_k\right)^{\gamma_k}, \\ &\kappa_1 = 1.86 \times 10^3 \, \mathrm{J}\,(kg)^{-1}\,\mathrm{K}^{-1}, \; \gamma_1 = 2.26, \\ &\kappa_2 = 4.15 \times 10^3 \, \mathrm{J}\,(kg)^{-1}\,\mathrm{K}^{-1}, \; \gamma_2 = 1.03. \end{aligned} \tag{4.135}$$

The coefficients have been chosen such that $\rho_2 \approx 10^3\, kg.m^{-3}$ for $p_2 = 50$ bar and $\rho_1 \approx 10\, kg.m^{-3}$ for $p_1 = 3.4$ bar. The simulation time is $\mathrm{T_{end}} = 8.5 \times 10^{-4}\, s$. Finally the time-step is determined using the fastest wave speeds at instant t^n:

$$\begin{aligned} \Delta t^n &= \mathscr{C} \, \frac{\Delta x}{\max\limits_{i+1/2} \left(\max\left(\left|u_1^n + c_1^n\right|, \left|u_1^n - c_1^n\right|, \left|u_2^n + c_2^n\right|, \left|u_2^n - c_2^n\right|\right)\right)}, \\ \mathscr{C} &= 0.45. \end{aligned} \tag{4.136}$$

As presented in (4.69), the analytical solution of problem (4.131) is made of five contact discontinuities whose speed corresponds to one component of $\underline{\Lambda}_0$ in (4.127). The convergence of the

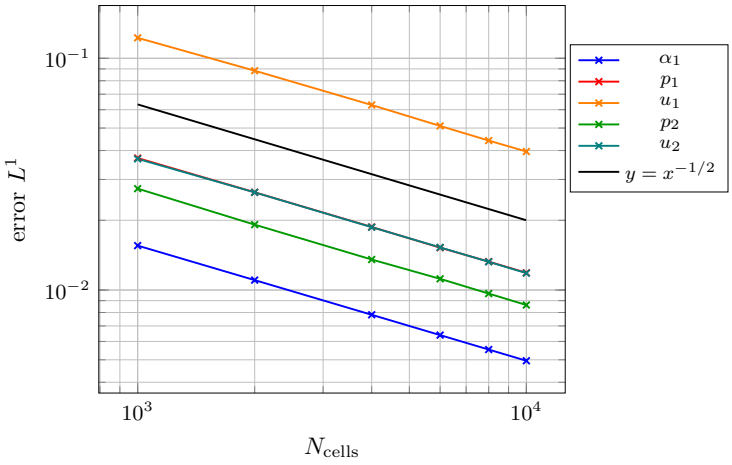

Figure 4.3 – Convergence curve: homogeneous Riemann problem

method is verified by plotting the error in L^1 norm for each component of $\mathbf{W}$ as a function of the mesh size. The number of cells is taken in the set:

$$\left\{10^3, 2\times10^3, 4\times10^3, 6\times10^3, 8\times10^3, 10^4\right\}.$$

The convergence curve is displayed in Figure 4.3. As mentioned in subsection 4.4.3, in the homogeneous case, the method is close to the Lax-Friedrich or the Rusanov schemes and has no difficulty to converge towards the analytical solution. As already noticed in [21], the presence of contact discontinuities deteriorates the convergence rate of first-order schemes. It is depreciated to 0.5.

In the next subsection, linear relaxation source terms are present.

4.5.2 Linearized isentropic Baer-Nunziato system with linear relaxations

Here, the general linearized Riemann problem writes:

$$\begin{aligned}
&\partial_t \mathbf{U} + \underline{\underline{\mathbf{C}}}_0\, \partial_x \mathbf{U} = -\underline{\underline{\mathbf{R}}}_0\, \underline{\underline{\tau}}^{-1}\, \underline{\underline{\mathbf{R}}}_0^{-1} \left(\mathbf{U} - \mathbf{U}^{\text{eq}}\right),\\
&\mathbf{U}(.,\, t=0) = \begin{cases} \mathbf{U}_{\text{L}}^0 \text{ if } x < 0.5,\\ \mathbf{U}_{\text{R}}^0 \text{ if } x > 0.5. \end{cases}
\end{aligned} \tag{4.137}$$

The matrix $\underline{\underline{\tau}}^{-1}$ governs the relaxation time-scales,

$$\underline{\underline{\tau}}^{-1} = \frac{1}{\tau}\, \underline{\underline{\text{diag}}}\left(\left[\mu_1, \ldots, \mu_5\right]^{\text{T}}\right). \tag{4.138}$$

Besides, $\mathbf{U}^{\text{eq}}$ is an equilibrium state towards which the solution of (4.137) converges. The above general linear Riemann problem can be projected on the eigenvector basis. It reads:

$$\begin{aligned}
&\partial_t \mathbf{a} + \underline{\underline{\Lambda}}_0\, \partial_x \mathbf{a} = -\underline{\underline{\tau}}^{-1} \left(\mathbf{a} - \mathbf{a}^{\text{eq}}\right),\\
&\mathbf{a}(.,\, t=0) = \begin{cases} \mathbf{a}_{\text{L}}^0 \text{ if } x < 0.5,\\ \mathbf{a}_{\text{R}}^0 \text{ if } x > 0.5. \end{cases}
\end{aligned} \tag{4.139}$$

with $\mathbf{a}^{\text{eq}} = \underline{\underline{\mathbf{R}}}_0^{-1}\, \mathbf{U}^{\text{eq}}$, $\mathbf{a}_{\text{L}}^0 = \underline{\underline{\mathbf{R}}}_0^{-1}\, \mathbf{U}_{\text{L}}^0$, $\mathbf{a}_{\text{R}}^0 = \underline{\underline{\mathbf{R}}}_0^{-1}\, \mathbf{U}_{\text{R}}^0$. The analytical solution of each component $\mathbf{a}_k$, $k \in [1, 5]$ of the vector $\mathbf{a}$ can be found since, along the characteristics $\dfrac{\mathrm{d}x}{\mathrm{d}t} = \lambda_k^0$, it verifies:

$$\begin{aligned}
&\frac{\mathrm{d}\mathbf{a}_k}{\mathrm{d}t} = -\frac{\mu_k}{\tau}\left(\mathbf{a}_k - \mathbf{a}_k^{\text{eq}}\right),\\
&\Leftrightarrow \mathbf{a}_k(x,\, t) = \mathbf{a}_k(x,\, t=0)\, e^{-\mu_k\, t/\tau} + \mathbf{a}_k^{\text{eq}}\left(1 - e^{-\mu_k\, t/\tau}\right),\\
&\Leftrightarrow \mathbf{a}_k(x,\, t) = \left[(\mathbf{a}_{\text{L}}^0)_k + \text{H}\,(x)\, (\mathbf{a}_{\text{R}}^0 - \mathbf{a}_{\text{L}}^0)_k\right] e^{-\mu_k\, t/\tau} + \mathbf{a}_k^{\text{eq}}\left(1 - e^{-\mu_k\, t/\tau}\right).
\end{aligned} \tag{4.140}$$

The analytical solution finally writes:

$$\begin{aligned}\mathbf{U}(x,t) = &\sum_{k=1}^{5} \left[(\mathbf{a}_{\mathrm{L}}^0)_k + \mathrm{H}\left(x-\lambda_k^0 t\right)(\mathbf{a}_{\mathrm{R}}^0 - \mathbf{a}_{\mathrm{L}}^0)_k\right] e^{-\mu_k t/\tau}\mathbf{r}_k^0 \\ &+ \sum_{k=1}^{5} \mathbf{a}_k^{\mathrm{eq}}\left(1-e^{-\mu_k t/\tau}\right)\mathbf{r}_k^0.\end{aligned} \tag{4.141}$$

It can be observed that the Bereux-Sainsaulieu Property 4.3.1 holds for the above general linearized Riemann problem. Thus, if $\mathbf{U}$ is solution of (4.137), the ODEs system (4.97), with $\mathbf{F}(\mathbf{U}) = \underline{\underline{\mathbf{C}}}_0\,\mathbf{U}$ and $\mathbf{S}(\mathbf{U}) = -\underline{\underline{\mathbf{R}}}_0\,\underline{\underline{\tau}}^{-1}\,\underline{\underline{\mathbf{R}}}_0^{-1}\left(\mathbf{U}-\mathbf{U}^{\mathrm{eq}}\right)$ is exactly verified.

The linearity of the relaxation source terms entails that no high order time-integration method is required to catch the trajectories towards the equilibrium state. As a consequence, the proposed time-implicit staggered scheme (4.104) is tested with $\Phi_\tau = \Phi_\tau^{\text{Ieu-1}}$, the relaxation operator related to the first-order implicit-Euler time-integration.

CFL condition is the same that the one derived in (4.136). The EOS and the initial conditions are similar to these presented in (4.135) and Table 4.1. The physical time of the simulation is $\mathrm{T_{end}} = 8.5\times10^{-4}\,s$. The relaxation time-scales are initially the same for every component of $\mathbf{a}$:

$$\forall k \in [1,5],\ \mu_k = 1,\ \tau = 10^{-3}\,s. \tag{4.142}$$

By using pressure values given as initial conditions, one can observe that the order of the maximal speed of sound is $c \approx 300\,m.s^{-1}$. Then, for a mesh made of 5×10^2 cells, the order of the discrete time-step (4.136) is $\Delta t \approx 3\times10^{-6}\,s \ll \tau$. In that sense, the linear Riemann problem (4.137) is not stiff. The idea here is only to check that the proposed staggered scheme has no difficulty to capture the analytical solution of a generalized linear Riemann problem for which the Bereux-Sainsaulieu lemma holds. Besides, the exponential operator appearing in (4.141) prevents from taking $\tau \ll \Delta t$ if one wishes to observe the propagation of the contact-wave profiles.

The equilibrium state writes $\mathbf{U}^{\mathrm{eq}} = \mathbf{U}\left(\mathbf{W}^{\mathrm{eq}}\right)$, with $\mathbf{W}^{\mathrm{eq}}$ an input state given in Table 4.2. In Figure 4.4, the convergence curves of the non-conservative variables are displayed. All of them converge towards their analytical solution as the mesh is refined. Figure 4.5, 4.6 and 4.7 show the pro-

	α_1	$u_1\ (m.s^{-1})$	p_1 (bar)	$u_2\ (m.s^{-1})$	p_2 (bar)
$\mathbf{W}^{\mathrm{eq}}$	0.5	1	15	1	15

Table 4.2 – Linear Riemann problem: equilibrium state

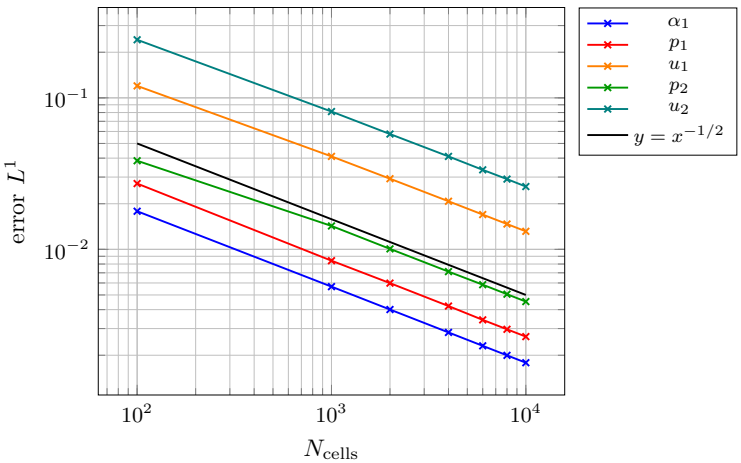

Figure 4.4 – Convergence curve: linear Riemann problem

file of the non-conservative variables through the computational domain at the end of the simulation. The couple (u_1, p_1) (respectively (u_2, p_2)) does not jump through the waves $(u_2 \pm c_2)_0$ (respec-

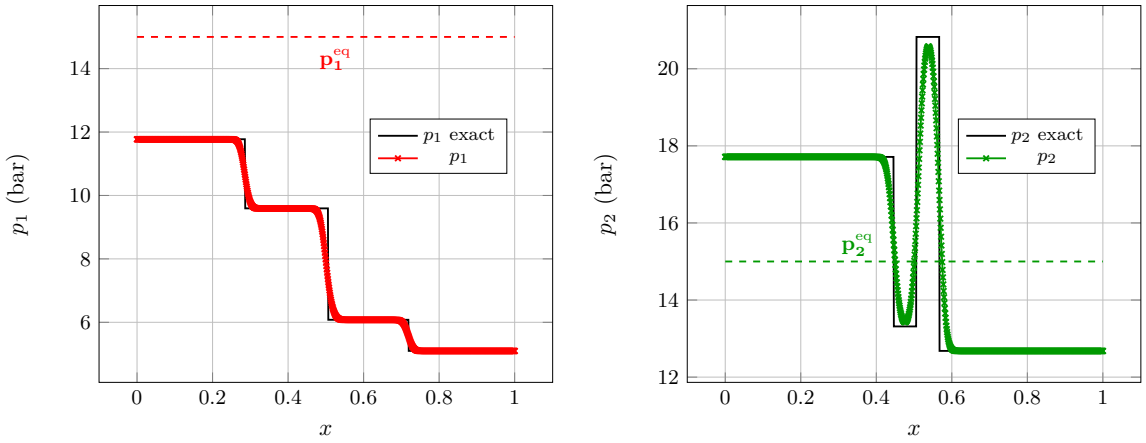

(a) p_1 (b) p_2

Figure 4.5 – Pressure profiles, linear Riemann problem: $N_{cells} = 10^3$

tively $(u_1 \pm c_1)_0$). This is simply due to the fact that, in matrix (4.18), the eigenvectors $\{\mathbf{r}_2^0, \mathbf{r}_3^0\}$ are linearly independent from $\{\mathbf{r}_4^0, \mathbf{r}_5^0\}$. Up to some numerical diffusion, the proposed time-implicit

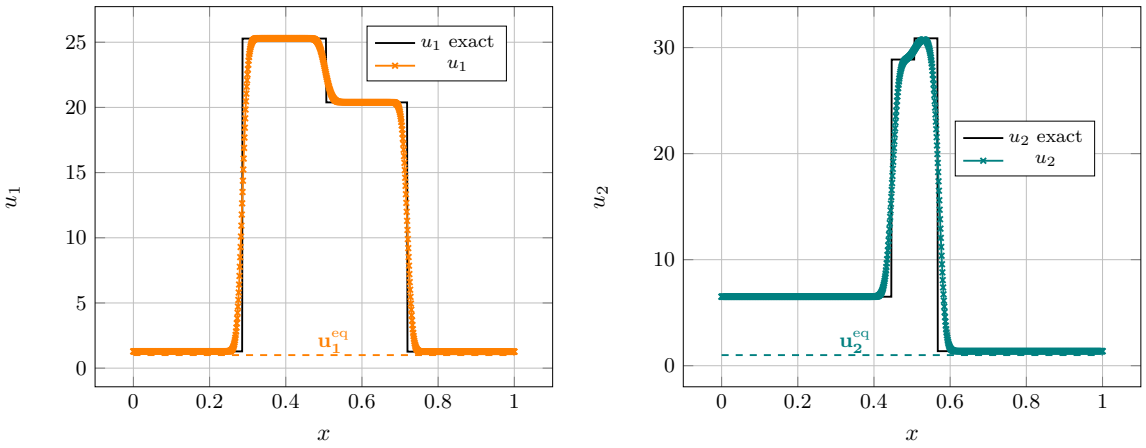

(a) u_1 (b) u_2

Figure 4.6 – Velocity profiles, linear Riemann problem: $N_{cells} = 10^3$

staggered scheme manages to capture the right speed of contact waves and also the right states undergoing the exponential time-relaxation. Away from the contact waves, the time-implicit Euler scheme has no difficulty to capture the time-relaxation of system (4.137).

In Figure 4.8, the profile of p_2 is compared according to the value of the relaxation time-scale τ. The green curve is for $\tau = 10^{-3}\,s$ whereas the red one stands for $\tau = 5 \times 10^{-4}\,s$. As expected, in the stiffest relaxation-regime, the computed solution is considerably closer to the pressure equilibrium value. Eventually, in Figure 4.9, the shape of p_2 is plotted when the relaxation time-scale related to the first component of $\mathbf{a}$, $\mathbf{a}_1 = \alpha_1$, is a hundred times lower than those of the other components: $\mu_1 = 10^2$, $\forall k \in [2,5]$, $\mu_k = 1$. In that case, the relaxation of the variable α_1 is expected to be quasi-instantaneous with respect to the other components. As a consequence, the pressure jump through the $(u_2)_0$-contact wave vanishes. One can notice that the non-linearity of the reconstruction function $\mathbf{a} \to p_2\left(\underline{\underline{\mathbf{C}}}_0, \mathbf{a}\right)$ is such that the instantaneous relaxation of $\mathbf{a}_1 = \alpha_1$ considerably slows down the relaxation of process of pressure p_2. Indeed, away from the contact waves in the left part of the computational domain, $p_2 \approx 22\,\text{bar}$ when $\mu_1 = 10^2$ while $p_2 \approx 18\,\text{bar}$ in the non-instantaneous relaxation configuration.

The above test case has shown that the proposed approach works perfectly when both the Jacobian matrix and the relaxation source terms are linear. In the sequel, non-linearity is injected

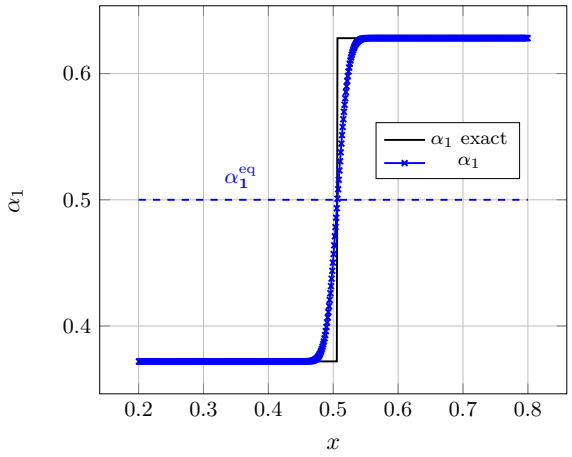

(a) α_1

Figure 4.7 – α_1 profile, linear Riemann problem: $N_{cells} = 10^3$

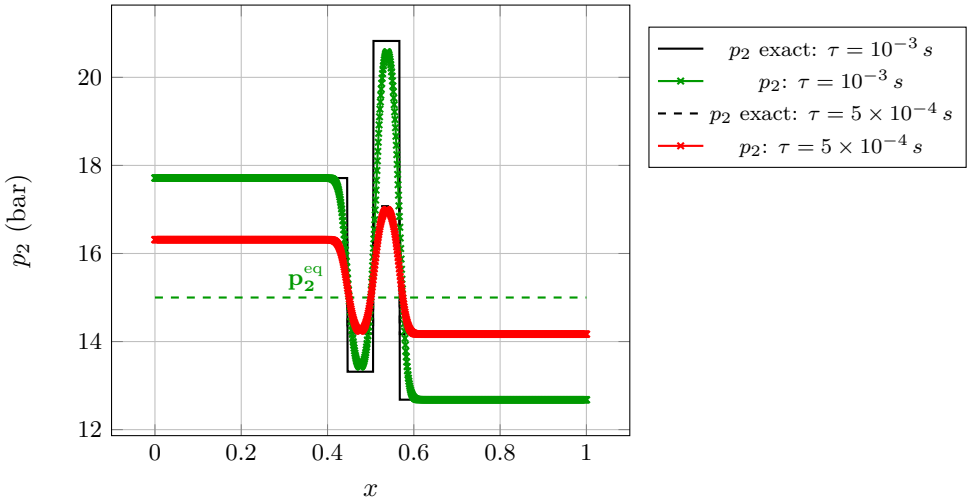

Figure 4.8 – p_2 profile: (green) $\tau = 10^{-3}\ s$, (red) $\tau = 5 \times 10^{-4}\ s$.

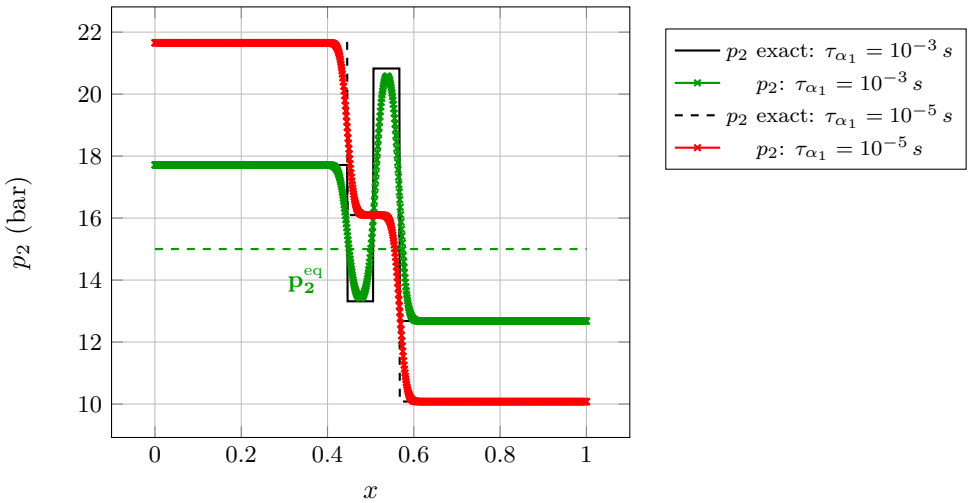

Figure 4.9 – p_2 profile, $\tau = 10^{-3}\ s$: (green) $\mu_1 = 1$, (red) $\mu_1 = 10^2$.

into the relaxation process. Besides, relaxation time-scales are such that, for coarse meshes, the Riemann problem is stiff.

4.5.3 Linear isentropic Baer-Nunziato system with non-linear non-monotone time-relaxation

In order to easily derive analytical solutions, the relaxation non-linearity takes the form of a cubic spring. The generalized Riemann problem writes:

$$\begin{aligned} &\partial_t \mathbf{U} + \underline{\underline{\mathbf{C}}}_0 \partial_x \mathbf{U} = -\underline{\underline{\mathbf{R}}}_0 \underline{\underline{\tau}}^{-1} \underline{\underline{\mathrm{diag}}}\left(\left\{ \underline{\underline{\mathbf{R}}}_0^{-1} \left(\mathbf{U} - \mathbf{U}^{\mathrm{eq}} \right) \right\}^3 \right), \\ &\mathbf{U}(., t=0) = \begin{cases} \mathbf{U}_{\mathrm{L}}^0 \text{ if } x < 0.5, \\ \mathbf{U}_{\mathrm{R}}^0 \text{ if } x > 0.5, \end{cases} \end{aligned} \tag{4.143}$$

with $\forall \mathbf{a} \in \mathbb{R}^5$, $\underline{\underline{\mathrm{diag}}}\left(\mathbf{a}^3\right) = \underline{\underline{\mathrm{diag}}}\left(\left[\mathbf{a}_1^3, \cdots, \mathbf{a}_5^3 \right]^{\mathrm{T}} \right)$. Matrix $\underline{\underline{\tau}}^{-1}$ is now a function of a reference state $\mathbf{U}^{\mathrm{ref}}$ in order to correctly scale the relaxation source term:

$$\underline{\underline{\tau}}^{-1} = \frac{1}{\tau} \underline{\underline{\mathrm{diag}}}\left(\left[\mu_1, \ldots, \mu_5 \right]^{\mathrm{T}} \right) \cdot \underline{\underline{\mathrm{diag}}}\left(\left\{ \mathbf{U}^{\mathrm{ref}} \right\}^{-2} \right). \tag{4.144}$$

Once again, the above generalized Riemann problem can be projected on the eigenvector basis. Along the λ_k^0-characteristics , each component $\mathbf{a}_k$, $k \in [1, 5]$ of $\mathbf{a} = \underline{\underline{\mathbf{R}}}_0^{-1} \mathbf{U}$ is solution of:

$$\frac{\mathrm{d}\mathbf{a}_k}{\mathrm{d}t} = -\frac{\mu_k}{\tau} \frac{\left(\mathbf{a}_k - \mathbf{a}_k^{\mathrm{eq}} \right)^3}{(\mathbf{U}_k^{\mathrm{ref}})^2}. \tag{4.145}$$

ODE (4.145) can be integrated easily and provides solutions which do not blow up for finite or infinite time. The analytical solution related to (4.143) reads:

$$\mathbf{a}_k(x, t) = \begin{cases} \mathbf{a}_k^{\mathrm{eq}} + \dfrac{1}{\sqrt{\left(\mathbf{a}_k(x, t=0) - \mathbf{a}_k^{\mathrm{eq}} \right)^{-2} + 2\mu_k (t/\tau) (\mathbf{U}_k^{\mathrm{ref}})^{-2}}} & \text{if} \quad \mathbf{a}_k(x, t=0) > \mathbf{a}_k^{\mathrm{eq}}, \\ \mathbf{a}_k^{\mathrm{eq}} - \dfrac{1}{\sqrt{\left(\mathbf{a}_k(x, t=0) - \mathbf{a}_k^{\mathrm{eq}} \right)^{-2} + 2\mu_k (t/\tau) (\mathbf{U}_k^{\mathrm{ref}})^{-2}}} & \text{if} \quad \mathbf{a}_k(x, t=0) < \mathbf{a}_k^{\mathrm{eq}}, \end{cases} \tag{4.146}$$

with $\mathbf{a}_k(x, t=0) = (\mathbf{a}_{\mathrm{L}}^0)_k + \mathrm{H}(x) \, (\mathbf{a}_{\mathrm{R}}^0 - \mathbf{a}_{\mathrm{L}}^0)_k$. The analytical solution (4.146) contains two asymptotic relaxation behaviors depending on how far from the equilibrium are the initial conditions. Consider a reference time-scale t_{ref} based on the waves produced by the Jacobian matrix $\underline{\underline{\mathbf{C}}}_0$. Assume that the initial states are far from equilibrium,

$$\left| \frac{\mathbf{U}_k^{\mathrm{ref}}}{\mathbf{a}_k(x, t=0) - \mathbf{a}_k^{\mathrm{eq}}} \right| \ll \mathrm{O}(1). \tag{4.147}$$

In that case, for $t = \delta t = \mathrm{O}(\tau)$, the time-relaxation slope between $\mathbf{a}_k(x, \delta t)$ and $\mathbf{a}^{\mathrm{eq}}$ writes:

$$\left| \frac{\mathbf{a}_k(x, \delta t) - \mathbf{a}_k^{\mathrm{eq}}}{\delta t} \right| \approx \frac{\left| \mathbf{U}^{\mathrm{ref}} \right|}{\delta t \sqrt{2\mu_k (\delta t/\tau)}} \approx \mathrm{O}\left(\frac{\left| \mathbf{U}^{\mathrm{ref}} \right|}{\tau} \right). \tag{4.148}$$

For stiff relaxation source terms, $\tau \ll t_{\mathrm{ref}}$, and the time-relaxation slope (4.148) is very steep with respect to the time-scale t_{ref}. However, if initial conditions are sufficiently close from equilibrium:

$$\left| \frac{\mathbf{U}_k^{\mathrm{ref}}}{\mathbf{a}_k(x, t=0) - \mathbf{a}_k^{\mathrm{eq}}} \right| = \mathrm{O}\left(\frac{t_{\mathrm{ref}}}{\tau} \right), \tag{4.149}$$

using once again $\delta t = \mathrm{O}(\tau)$ allows to find,

$$\left| \frac{\mathbf{a}_k(x, \delta t) - \mathbf{a}_k^{\mathrm{eq}}}{\delta t} \right| \approx \frac{\left| \mathbf{U}^{\mathrm{ref}} \right|}{\delta t \sqrt{(t_{\mathrm{ref}}/\tau)^2 + 2\mu_k (\delta t/\tau)}} \approx \mathrm{O}\left(\frac{\left| \mathbf{U}^{\mathrm{ref}} \right|}{t_{\mathrm{ref}}} \right). \tag{4.150}$$

And the convergence towards the equilibrium state is relatively slow on the time-scale related to τ.

In the context of two-phase flows involving subcooled water and overheated vapor, the EOS parameters of both phases have been defined using saturated pressure, densities and heat capacity ratios. The values of these quantities are summarized in Table 4.3.

	p (bar)	$\rho\ (kg.m^{-3})$	γ	$\kappa\ (J.kg^{-1}.K^{-1})$
Liquid	$p^{sat} = 150$	$\rho_{liq}^{sat} = 603.52$	$\gamma_{liq}^{sat} = 2.76$	$\kappa_{liq}^{sat} = 0.32$
Vapor	$p^{sat} = 150$	$\rho_{vap}^{sat} = 97.73$	$\gamma_{vap}^{sat} = 3.62$	$\kappa_{vap}^{sat} = 0.94$

Table 4.3 – Saturation parameters

with $\kappa_{liq}^{sat} = p^{sat}\left(\rho_{liq}^{sat}\right)^{-\gamma_{liq}^{sat}}$, $\kappa_{vap}^{sat} = p^{sat}\left(\rho_{vap}^{sat}\right)^{-\gamma_{vap}^{sat}}$. The EOS write

$$\begin{cases} p_1 = \kappa_{vap}^{sat}\left(\rho_1\right)^{\gamma_{vap}^{sat}}, \\ p_2 = \kappa_{liq}^{sat}\left(\rho_2\right)^{\gamma_{liq}^{sat}}. \end{cases} \tag{4.151}$$

As shown in Table 4.4, the equilibrium pressure is p^{sat} for both phases. The initial conditions, presented in Table 4.5 are taken out of equilibrium for both phases. Besides, initial pressure jumps for both p_1 and p_2 are sufficiently important to produce high amplitude contact discontinuities notably for phase 1 which is the most compressible phase. In the sequel, the relaxation time-scale τ is equal to $10^{-9}\ s$.

	α_1	$u_1\ (m.s^{-1})$	p_1 (bar)	$u_2\ (m.s^{-1})$	p_2 (bar)
$\mathbf{W}^{eq}$	0.6	1	p^{sat}	1	p^{sat}

Table 4.4 – Riemann problem, non-linear spring relaxation: equilibrium state

	α_1	$u_1\ (m.s^{-1})$	p_1 (bar)	$u_2\ (m.s^{-1})$	p_2 (bar)
$\mathbf{W}_L^0$	0.8	1.5	110	-2	170
$\mathbf{W}_R^0$	0.2	2	158	-1.5	120

Table 4.5 – Riemann problem, non-linear spring relaxation: initial conditions

In Figure 4.10 and Figure 4.11a are displayed the time evolution of the components of vector $\mathbf{W}$ built using the analytical solutions written in (4.146). In that case, the initial condition is $\mathbf{W}(t=0) = \mathbf{W}_L^0$. The time-trajectories are in agreement with formulas (4.148) and (4.150): at the beginning, when initial conditions are far from equilibrium, the slope of the time-relaxation is steep with respect to the convective time-scale. However, as times goes on, the solution comes closer to the equilibrium and the time evolution is smoothed. What is more, one can underline that the convergence towards equilibrium is non-monotonous for every variable except α_1.

In the following, three schemes are compared. The first one called "BS-Ros-4" stands for the proposed time-implicit staggered scheme (4.104) (BS refers to "Bereux-Sainsaulieu"). The fourth-order Rosenbrock method is used for the time-integration of the source terms. The second, "FS-Ros-4" corresponds to the fractional-step approach (4.123), (4.124) combining the fourth-order Rosenbrock method with a first-order time-explicit Rusanov scheme. Finally, "FS-Ieu-1" stands for the same fractional-step strategy but with a first-order Rosenbrock method that is equivalent to the first-order implicit Euler time-integration in the linear case.

As mentioned previously many authors in the literature [4, 22, 40, 47] apply Strang-splitting techniques to successively treat the hyperbolic part and the relaxation part of the system at stake. As highlighted in [43], even for high order splitting methods, the order of accuracy in time is depreciated, in the case of stiff problems, to one. Thus, "FS-Ieu-1" might be regarded as a representative

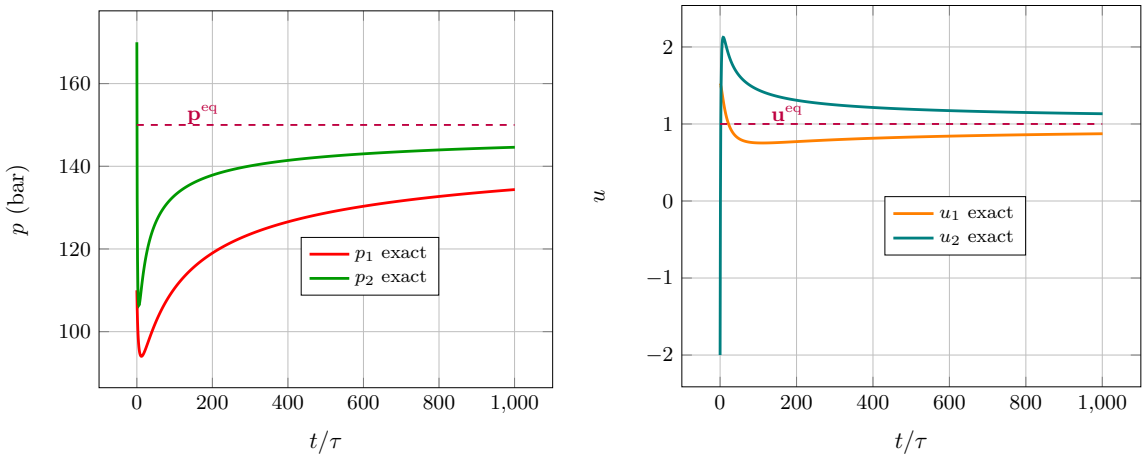

(a) (p_1, p_2) (b) (u_1, u_2)

Figure 4.10 – Pressure-velocity time relaxation: non-linear spring

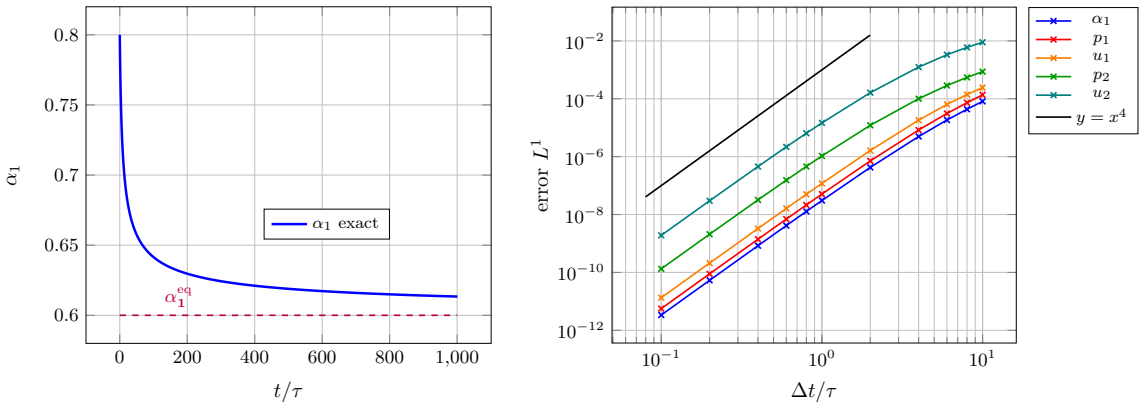

(a) α_1 (b) Convergence curve: $\Phi_\tau = \Phi_\tau^{\text{Ros-4}}$

Figure 4.11 – (left) α_1 time relaxation: non-linear spring, (right) Convergence curve: fourth-order Rosenbrock

of these splitting methods in the above simplified setting where convection is frozen and relaxation is stiff.

Let us end the setting of the test case by showing, in Figure 4.11b, the convergence curves of the non-conservative variables associated with the resolution of the relaxation system of ODEs (4.145) using the fourth-order Rosenbrock method. As expected, when $\Delta t/\tau \to 0$, the curves are aligned with $y = x^4$. Besides the method is stable even for $\Delta t/\tau \gg 1$.

Discrete solutions of the generalized Riemann problem (4.143) are now considered. In Figure 4.12, 4.13 and 4.14, the profiles of the non-conservative variables at final time $T_{end} = 2 \times 10^{-4}\, s$ are presented. The pictures are zoomed around the u_2^0-contact-discontinuity. The mesh is made of 10^3 cells. Let us point out that the speeds of sound at equilibrium are $c_1(p^{sat}) \approx 7.46 \times 10^2\, m.s^{-1}$ and $c_2(p^{sat}) \approx 2.62 \times 10^2\, m.s^{-1}$. Thus, the most constraining CFL condition is given by phase 1. For a mesh of 10^3 cells, the scale of the convective time-step produced is $\Delta t \approx 6.7 \times 10^{-7}\, s$. Recall that the relaxation time-scale is $\tau = 10^{-9}\, s$. Hence, the generalized Riemann problem is stiff since $\Delta t/\tau \approx 6.7 \times 10^2$.

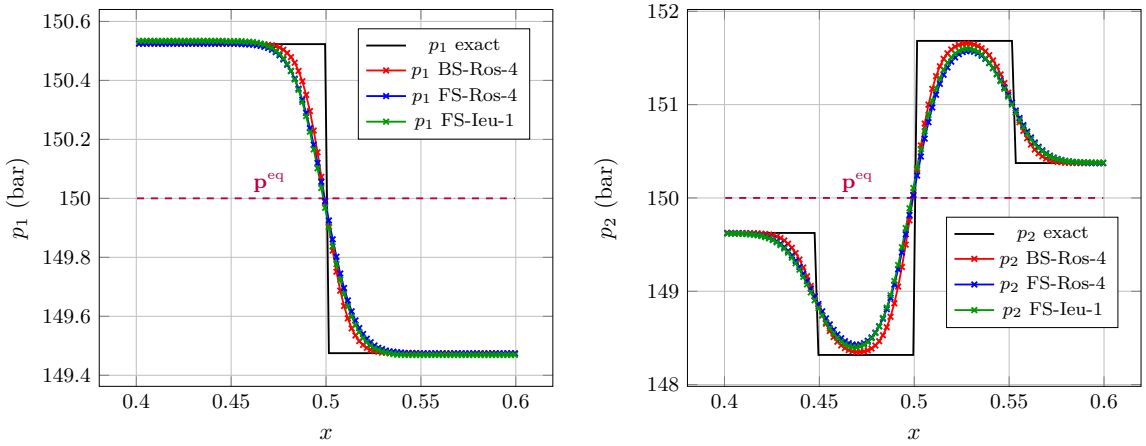

(a) p_1 (b) p_2

Figure 4.12 – Pressure profiles, linear Riemann problem, non-linear spring relaxation: $N_{cells} = 10^3$

It turns out that for every variable, the proposed time-implicit staggered-scheme is slightly more accurate than both fractional-step methods. Differences between fourth and first order time-integration of the relaxation source terms can be observed in the u_1 profile. Indeed, the scheme FS-Ieu-1 localizes the right plateau of the contact-discontinuity around $-3.46\, m.s^{-1}$ whereas BS-Ros-4 and FS-Ros-4 manage to catch the exact value around $-3.405\, m.s^{-1}$.

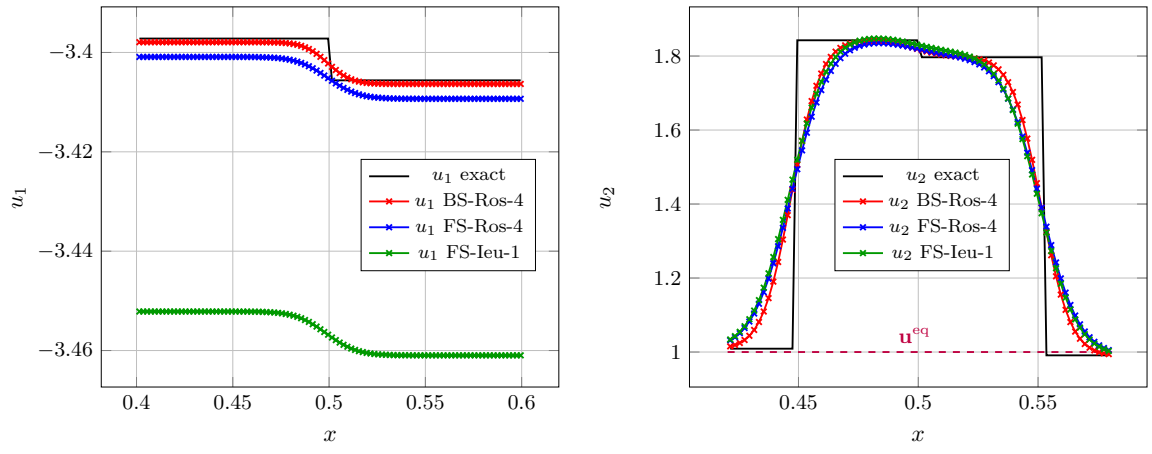

(a) u_1 (b) u_2

Figure 4.13 – Velocity profiles, linear Riemann problem, non-linear spring relaxation: $N_{cells} = 10^3$

Nevertheless, a close look to the u_2-profile reveals that, up to a translation along the ordinate axis, the shape of the u_2^0-contact discontinuity front is not necessarily better captured with FS-Ros-4 than with FS-Ieu-1. However, a substantial sharpening effect can be observed between FS-Ieu-1 and BS-Ros-4.

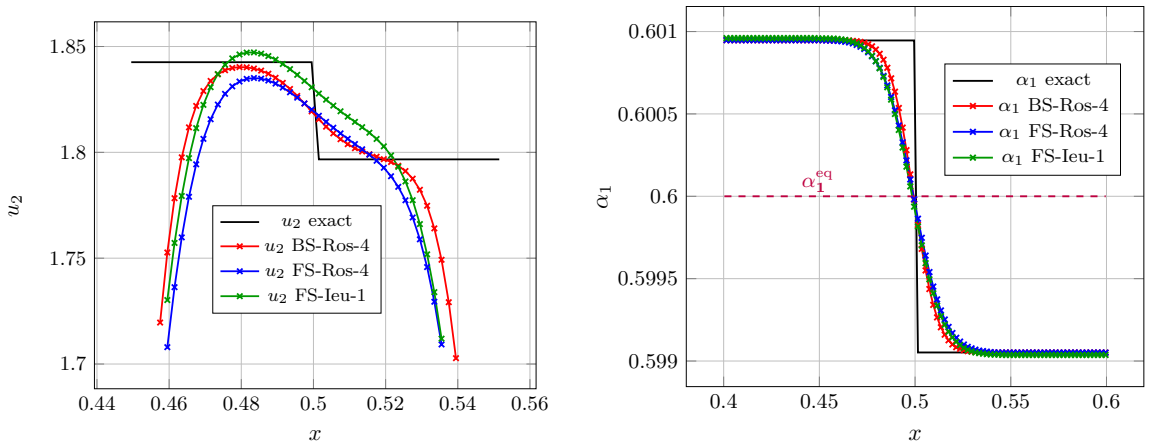

(a) u_2 (zoom) (b) α_1

Figure 4.14 – u_2 profile zoomed (left), α_1 profile (right), linear Riemann problem, non-linear spring relaxation: $N_{cells} = 10^3$

Figure 4.15, Figure 4.16 and Figure 4.17 display the convergence curves for the three numerical methods. Each of them converges towards the analytical solution as the mesh is refined. Besides, they confirm the trend already observed on the profile of the u_2^0-contact discontinuity: the proposed method is more accurate that the fractional-step approaches.

More precisely, differences between the convergence curves of (u_1, p_1), (u_2, p_2) and α_1 have to be underlined. Recall that the couple (u_1, p_1) jumps through the fastest waves whose speed magnitude is approximately c_1^0. For these variables, one can notice that the gap of errors between the schemes FS-Ieu-1 and BS-Ros-4 is larger on coarse meshes. Consider $e_r^{X,N}$, the error in L^1-norm of the scheme X related to a mesh made of N-cells. Then, for the variable u_1: $e_r^{\text{BS-Ros-4},10^2}/e_r^{\text{FS-Ieu-1},10^2} \approx 7.8 \times 10^{-2}$, whereas $e_r^{\text{BS-Ros-4},10^4}/e_r^{\text{FS-Ieu-1},10^4} \approx 8.3 \times 10^{-1}$.

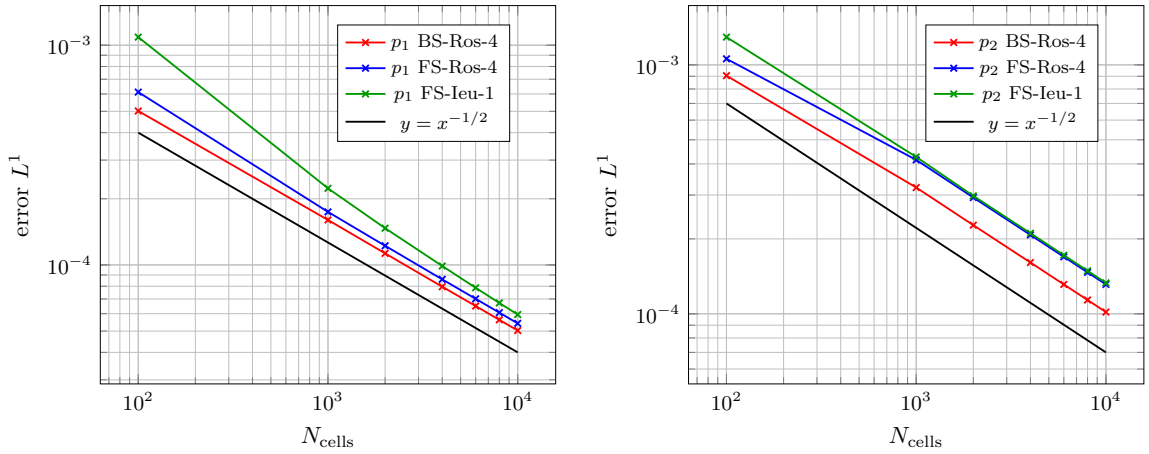

(a) p_1 (b) p_2

Figure 4.15 – Pressure convergence curves, linear Riemann problem, non-linear spring relaxation

Besides, for the variables u_1 and p_1, only small differences can be seen between the convergence curves of the BS-Ros-4 and FS-Ros-4 schemes. That is why, the gap of errors reduction observed between the BS-Ros-4 and FS-Ieu-1 methods might be due to the fact that the rate $\Delta t/\tau$ decreases as the mesh is refined. Indeed, for finer meshes, the discrete resolution becomes less

stiff and the relative accuracy advantage held by fourth-order time-integration methods with respect to first-order ones is lost.

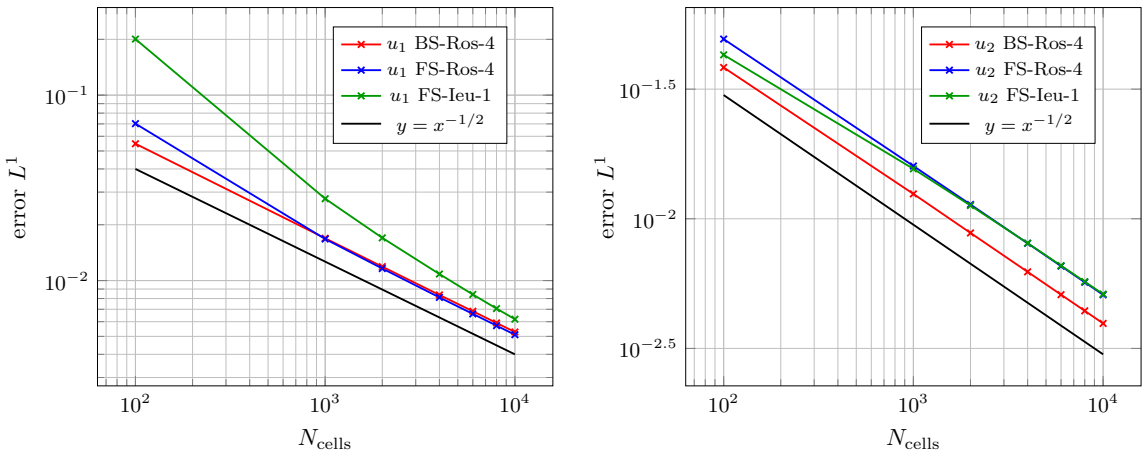

(a) u_1 (b) u_2

Figure 4.16 – Velocity convergence curves, linear Riemann problem, non-linear spring relaxation

The second behavior concerns the couple of variables (u_2, p_2) which jumps through the slowest acoustic waves whose celerity magnitude is approximately c_2^0. Here, the additional accuracy brought by high-order time-integration methods applied to the source terms seems to vanish. Indeed, the curves related to the fractional-step approaches FS-Ros-4 and FS-Ieu-1 overlap. Nevertheless, the curve of the proposed scheme remains systematically below the ones of the fractional-step methods. The gap between the curves appears to be approximately the same for any mesh size.

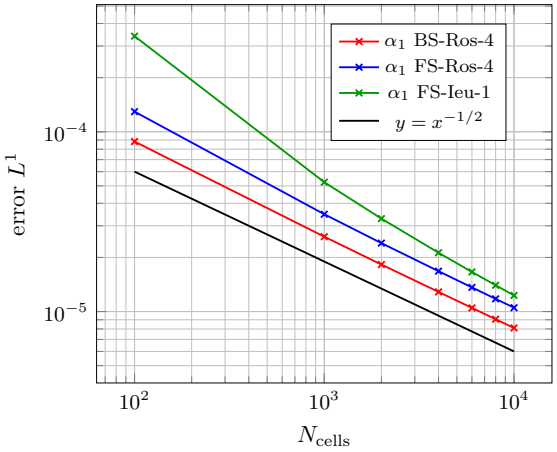

(a) α_1

Figure 4.17 – α_1 convergence curve, linear Riemann problem, non-linear spring relaxation

Finally, for the variable α_1 jumping through the slowest u_2^0-contact wave, convergence curves seem to aggregate the trends observed for (u_1, p_1) and (u_2, p_2): the gap of errors between fourth and first order time-integration schemes is reduced as the mesh is refined, a constant gap is maintained between the present time-implicit staggered scheme and the fractional-step methods.

Unfortunately, accuracy that seems to be gained by the present coupling method is paid in terms of efficiency. Indeed, Figure 4.18 displays the efficiency curve related to the variable p_1 for the three above schemes. As expected, the resolution of two additional Rosenbrock methods that directly take into account the relaxation effect into the fluxes, makes the present approach less efficient, for every mesh size, than the fractional step methods. This trend is also observed for all the other variables.

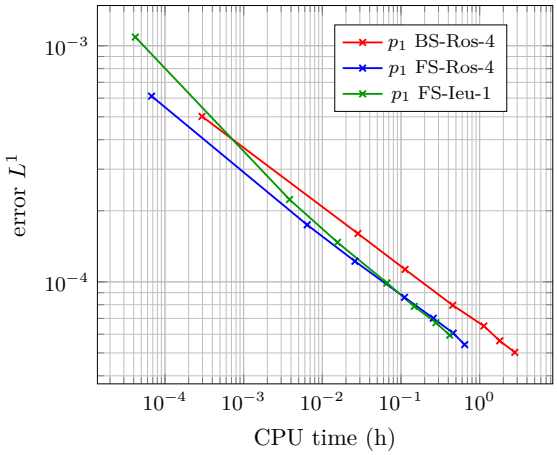

(a) p_1

Figure 4.18 – p_1 efficiency curve, linear Riemann problem, non-linear spring relaxation

However, one can nuance this result by noting that the present non-linear spring relaxation vector is artificially acting on the *five* equations of the hand-made two-fluid two-pressure model. Hence, the discrete time integration techniques are applied to vectors and matrices of dimension five. However, the isentropic Baer-Nunziato system (4.14) with pressure and velocity relaxations can be rewritten as a set of three PDEs involving three conserved quantities for which relaxation source terms are *null* completed by two convection-relaxation PDEs related to the variables Δp and Δu. Hence, the measured loss of efficiency might be substantially decreased if the Bereux-Sainsaulieu strategy was only applied to the *reduced* relaxation variables system of dimension two.

4.6 Conclusions

In the present work, the two-fluid two-pressure isentropic Baer-Nunziato model has been introduced. Pressure and velocity relaxations are also added in this hyperbolic system. It has been shown that such a model is endowed with the appropriate symmetrization property needed to apply a lemma proved by Bereux and Sainsaulieu. This important result sets the ODEs system verified by the space-averaged solution of a generalized Riemann problem obtained after the linearization of an hyperbolic system with relaxation abiding by the Liu's definition.

From this general result, assuming that the Bereux-Sainsaulieu ODEs system can be formally generalized to the non-linear case, one can derive a time-implicit staggered scheme. Such a scheme couples convection and relaxation into one single step. A brief analysis made in the context of linear hyperbolic systems has shown that, when relaxation source terms are omitted, the resulting numerical flux is slightly more diffusive than a Rusanov one. Besides, when stiff linear relaxation is active and acts independently on each component of the solution projected into the eigenvector basis, the scheme is stable under a CFL condition only based on the eigenvalues of the convective Jacobian matrix.

The present approach has been compared with a classical fractional-step method involving a Rusanov numerical flux. The generalized Riemann problem on which the comparison has been conducted is based on a hand-made two-fluid two-pressure system in which the convective part of the Baer-Nunziato system has been substituted for its frozen Jacobian matrix. As for the Baer-Nunziato relaxation source terms, they have been replaced by a stiff non-linear spring vector. Hence, analytical solutions can be derived and convergence as well as efficiency curves can be drawn. It appears that, for very stiff configurations, the proposed method is more accurate than the fractional step strategy. Nevertheless, the gain of accuracy is balanced by a loss of efficiency. This is caused by the injection of relaxation effects into the convective numerical flux which requires two additional calls to the high-order discrete time-relaxation operator.

Beyond its computational cost, one of the main drawbacks of the proposed method is that it relies on the Bereux-Sainsaulieu lemma which was originally formulated for *conservative* hyperbolic systems with relaxation. For such models, the frozen Jacobian matrix $\underline{\underline{\mathbf{C}}}_0$ related to the space-averaged dynamics (4.59) can be replaced by a Roe matrix in order to retrieve conservativity in the numerical method. In the case of the isentropic Baer-Nunziato model with pressure and velocity relaxations, non-conservative products are present in the convective part and the Bereux-Sainsaulieu approach needs to be extended. This is the objective of the next chapter.

4.7 References

[1] A. Ambroso, C. Chalons, F. Coquel, T. Galié, E. Godlewski, P. A. Raviart, and N. Seguin. The drift-flux asymptotic limit of barotropic two-phase two-pressure models. *Communications in Mathematical Sciences*, 6:521–529, 2008. 117

[2] A. Ambroso, C. Chalons, F. Coquel, and T. Galié. Relaxation and numerical approximation of a two-fluid two-pressure diphasic model. *ESAIM: Mathematical Modelling and Numerical Analysis*, 43:1063–1097, 2009. 118, 122

[3] A. Ambroso, C. Chalons, and P. A. Raviart. A Godunov-type method for the seven-equation model of compressible two-phase flow. *Computers and Fluids*, 54:67–91, 2012. 118, 127, 128

[4] N. Andrianov, R. Saurel, and G. Warnecke. A simple method for compressible multiphase mixtures and interfaces. *International Journal for Numerical Methods in Fluids*, 41:109–131, 2003. 118, 125, 146

[5] M. R. Baer and J. W. Nunziato. A two-phase mixture theory for the deflagration-to-detonation transition (DDT) in reactive granular materials. *International Journal of Multiphase Flow*, 12: 861–889, 1986. 115, 117, 118, 119

[6] F. Bereux and L. Sainsaulieu. A Roe-type Riemann solver for hyperbolic systems with relaxation based on time-dependent wave decomposition. *Numerische Mathematik*, 2:143–185, 1997. 115, 118, 127, 128, 130, 132, 134

[7] F. Bouchut. *Nonlinear Stability of Finite Volume Methods for Hyperbolic Conservation Laws*. Birkäser, 2004. 123

[8] A. Bourlioux. *Analysis of numerical methods in a simplified detonation model*. PhD thesis, Princeton University, 1991. 117

[9] C. Chalons and J. F. O. Coulombel. Relaxation approximation of the Euler equations. *Journal of Mathematical Analysis and Applications*, 348:872–893, 2008. 127

[10] G. Q. Chen, C. D. Levermore, and T.-P. Liu. Hyperbolic conservation laws with stiff relaxation terms and entropy. *Communications on Pure and Applied Mathematics*, 47:787–830, 1994. 117, 125

[11] S. Clerc. Numerical simulation of the homogeneous equilibrium model for two-phase flows. *Journal of Computational Physics*, 161:354–375, 2000. 119

[12] F. Coquel, T. Gallouët, J-M Hérard, and N. Seguin. Closure laws for a two-fluid two-pressure model. *Comptes Rendus de l'Académie des Sciences: Mathematique*, 334:927–932, 2002. 119, 120, 122, 123

[13] F. Coquel, J. M. Hérard, K. Saleh, and N. Seguin. A robust entropy-satisfying finite volume scheme for the isentropic Baer-Nunziato model. *ESAIM: Mathematical Modelling and Numerical Analysis*, 48:165–206, 2014. 118, 122

[14] F. Coquel, J. M. Hérard, K. Saleh, and N. Seguin. Two properties of two-velocity two-pressure models for two-phase flows. *Communications in Mathematical Sciences*, 12:593–600, 2014. 122, 123

[15] F. Crouzet, F. Daude, P. Galon, J. M. Hérard, O. Hurisse, and Y. Liu. Validation of a two-fluid model on unsteady liquid–vapor water flows. *Computers and Fluids*, 119:131–142, 2015. 118

[16] S. Dellacherie. Relaxation schemes for the multicomponent Euler system. *ESAIM: Mathematical Modelling and Numerical Analysis*, 37:909–936, 2003. 117

[17] F. Drui. *Modélisation et simulation Eulériennes des écoulements diphasiques à phases séparées et dispersées: développement d'une modélisation unifiée et de méthodes numériques adaptées au calcul massivement parallèle*. PhD thesis, Université Paris-Saclay, 2017. URL https://tel.archives-ouvertes.fr/tel-01618320. 120, 125

[18] P. Embid and M. R. Baer. Mathematical analysis of a two-phase continuum mixture theory. *Continuum Mechanics and Thermodynamics*, 4:279–312, 1992. 117, 119

[19] I. Faille and E. Heintzé. A rough finite volume scheme for modeling two-phase flow in a pipeline. *Computers and Fluids*, 28:213–241, 1999. 117

[20] T. Fåtten and H. Lund. Relaxation two-phase flow models and the subcharacteristic condition. *Mathematical Models and Methods in Applied Sciences*, 21:2379–2407, 2011. 117

[21] T. Gallouët, J-M Hérard, and N. Seguin. Some recent finite volume schemes to compute Euler equations using real gas EOS. *International Journal for Numerical Methods in Fluids*, 39: 1073–1138, 2002. 141

[22] T. Gallouët, J-M Hérard, and N. Seguin. Numerical modeling of two-phase flows using the two-fluid two-pressure approach. *Mathematical Models and Methods in Applied Sciences*, 14: 663–700, 2004. 115, 118, 119, 120, 122, 123, 125, 146

[23] S. Gavrilyuk. The structure of pressure relaxation terms: one-velocity case. EDF internal report, H-I83-2014-00276-EN, 2014. 120

[24] S. Gavrilyuk and R. Saurel. Mathematical and numerical modeling of two-phase compressible flows with micro-inertia. *Journal of Computational Physics*, 175:326–360, 2002. 119, 120

[25] J. Glimm, D. Saltz, and D. H. Sharp. Two-phase modelling of a fluid mixing layer. *Journal of Fluid Mechanics*, 378:119–143, 1999. 119

[26] P. Goatin and P. G. LeFloch. The Riemann problem for a class of resonant hyperbolic systems of balance laws. *Annales de l'Institut Henri Poincaré (C) Non Linear Analysis*, 21:881–902, 2004. 121

[27] E. Godlewski and P.A. Raviart. *Numerical Approximation of Hyperbolic Systems of Conservation Laws*. Springer, 1996. 125, 129

[28] V. Guillemaud. *Modélisation et simulation numérique des écoulements diphasiques par une approche bifluide à deux pressions*. PhD thesis, Université de Provence-Aix-Marseille I, https://tel.archives-ouvertes.fr/tel-00169178/, 2007. 124

[29] E. Hairer and G. Wanner. *Solving Ordinary Differential Equations II: Stiff and Differential-algebraic Problems*. Springer, 1991. 127, 135, 136

[30] R. A. Horn and C. R. Johnson. *Matrix Analysis*. Cambridge university press, 1990. 124

[31] E. Isaacson and B. Temple. Nonlinear resonance in systems of conservation laws. *SIAM Journal on Applied Mathematics*, 52:1260–1278, 1992. 121

[32] M. Ishii. *Thermo-Fluid Dynamic Theory of Two-Phase Flow*. Eyrolles, 1975. 115

[33] M. Ishii and N. Zuber. Drag coefficient and relative velocity in bubbly, droplet or particulate flows. *AIChE Journal*, 25:843–855, 1979. 120

[34] S. Jin. Runge-Kutta methods for hyperbolic conservation laws with stiff relaxation terms. *Journal of Computational Physics*, 122:51–67, 1995. 117

[35] S. Jin and Z.-P. Xin. The relaxation schemes for systems of conservation laws in arbitrary dimensions. *Communications on Pure and Applied Mathematics*, 48:235–276, 1995. 125

[36] A. K. Kapila, S. F. Son, J. B. Bdzil, R. Menikoff, and D. S. Stewart. Two-phase modeling of DDT: Structure of the velocity-relaxation zone. *Physics of Fluids*, 9:3885–3897, 1997. 119

[37] G. Linga. A hierarchy of non-equilibrium two-fluid models. *SIAM Journal on Applied Mathematics*, 2015. Submitted. 117

[38] T.-P. Liu. Hyperbolic conservation laws with relaxation. *Communications in Mathematical Physics*, 108:153–175, 1987. 115, 117, 127

[39] H. Lochon, F. Daude, P. Galon, and J. M. Hérard. Comparison of two-fluid models on steam-water transients. *ESAIM: Mathematical Modelling and Numerical Analysis*, 50:1631–1657, 2016. 120

[40] H. Lochon, F. Daude, P. Galon, and J. M. Hérard. Computation of fast depressurization of water using a two-fluid model: revisiting Bilicki modelling of mass transfer. *Computers & Fluids*, 156:162–174, 2017. 115, 118, 125, 146

[41] H. Lund. A hierarchy of relaxation models for two-phase flow. *SIAM Journal on Applied Mathematics*, 72:1713–1741, 2012. 117

[42] S. T. Munkejord. Comparison of Roe-type methods for solving the two-fluid model with and without pressure relaxation. *Computers and Fluids*, 36:1061–1080, 2007. 122

[43] L. Pareschi and G. Russo. Implicit–explicit Runge–Kutta schemes and applications to hyperbolic systems with relaxation. *SIAM Journal of Scientific Computing*, 25:129–155, 2005. 118, 127, 146

[44] R. B. Pember. Numerical methods for hyperbolic conservation laws with stiff relaxation I. Spurious solutions. *SIAM Journal on Applied Mathematics*, 53:1293–1330, 1993. 117

[45] R. B. Pember. Numerical methods for hyperbolic conservation laws with stiff relaxation II. Higher-order Godunov methods. *SIAM Journal on Scientific Computing*, 14:824–859, 1993. 117

[46] V. H. Ransom and D. L. Hicks. Hyperbolic two-pressure models for two-phase flow. *Journal of Computational Physics*, 53:124–151, 1984. 119

[47] R. Saurel and R. Abgrall. A multiphase Godunov method for compressible multifluid and multiphase flows. *Journal of Computational Physics*, 150:425–467, 1999. 115, 118, 119, 125, 146

[48] H. B. Stewart and B. Wendroff. Two-phase flow: models and methods. *Journal of Computational Physics*, 56:363–409, 1984. 119

[49] E.F. Toro. *Riemann Solvers and Numerical Methods for Fluid Dynamics*. Springer, 1999. 140

[50] J. B. Whitham. *Linear and Non Linear Waves*. John Wiley & Sons Inc, 1974. 117, 125

[51] N. Zuber and J. Findlay. Average volumetric concentration in two-phase flow systems. *Journal of Heat Transfer*, 87:453–468, 1965. 117

Chapitre 5

Extension de la méthode de couplage convection-source pour le modèle de Baer-Nunziato isentropique

Dans la lignée des pistes de réflexion décrites précédemment, ce chapitre propose de construire un schéma numérique couplant opérateur de convection et termes sources pour le système Baer-Nunziato isentropique avec relaxation pression-vitesse. Contrairement au chapitre précédent, un traitement particulier lié à la présence des produits non-conservatifs du modèle est proposé. La démarche s'appuie sur les travaux décrits dans [1, 3, 10] dans lesquels les termes non-conservatifs sont modélisés comme une mesure de Dirac portée par une demi-droite du plan espace-temps. Par la suite, un nouveau type de problème de Riemann linéaire généralisé est étudié. Ce dernier contient notamment une mesure de Dirac de masse constante. Dans la configuration particulière où les effets de relaxation linéaires sont indépendants les uns des autres, une solution analytique peut être construite.

Suivant une démarche similaire à celle proposée par Bereux et Sainsaulieu dans [2], la pierre d'angle de la méthode numérique développée dans ce chapitre repose sur un système d'EDO représentant la dynamique temporelle de la moyenne spatiale de la solution analytique mentionnée ci-dessus. Deux contributions peuvent alors être identifiées dans ce système. La première est une divergence de flux de bord basée sur des états relaxés. La seconde est un terme de dérive associé à la masse de la mesure de Dirac. L'intégration en temps du schéma à maille décalée proposé est implicite pour les termes en divergence de flux et explicite pour le terme de dérive. De plus la discrétisation de la masse de la mesure de Dirac est basée sur l'égalité d'invariants de Riemann approchés au travers l'onde de couplage du modèle Baer-Nunziato isentropique.

Le schéma numérique proposé est alors conservatif pour les masses partielles ainsi que pour la quantité de mouvement de mélange. La positivité des masses partielles est également garantie sous-réserve d'une condition CFL seulement basée sur les valeurs propres de la partie convective du système étudié. Enfin, un traitement des effets de relaxation en pression similaire à celui présenté dans [5, 8] permet au schéma de préserver le principe du maximum sur le taux de présence statistique.

Le schéma numérique développé est comparé à deux approches à pas fractionnaires. La première utilise un flux de type Rusanov complété par une discrétisation de type "free-streaming" [9] pour les produits non-conservatifs. La seconde met en jeu une adaptation du solveur de Riemann approché HLLAC proposé dans [7] et inspiré de [11]. Les produits non-conservatifs sont alors discrétisés sur la base des travaux présentés dans [10]. La discrétisation du système d'EDO relative aux termes sources est inspirée d'une stratégie proposée par Gallouët *et al.* [6].

Les éléments de comparaison sont construits à partir du profil des solutions de problèmes de Riemann généralisés associés au système Baer-Nunziato isentropique avec relaxation en pression-vitesse. Les échelles de temps de relaxation sont alternativement très petites puis très grandes devant celles liées aux valeurs propres de l'opérateur convectif. La qualité des profils obtenus est

alors mise en regard de ceux issus de solutions convergées en maillage.

Sommaire

5.1 Introduction

The objective of this chapter is to extent the previous strategy to the complete isentropic Baer-Nunziato system (4.14). As pointed out in the introduction of Chapter 4, the formalism of such a system differs from Liu's definition of hyperbolic systems with relaxation in the sense that non-conservative products are now present. In order to tackle this new difficulty the analysis conducted by Bereux and Sainsaulieu in [2] has to be revisited. It notably requires to redefine the shape of the generalized linear Riemann problem which is the cornerstone of their strategy in order to isolate the role played by the non-conservative products.

In order to do so, the present work leans on the non-conservative products formulation proposed in [1, 3, 10]. In such a formulation, these terms are assimilated to a Dirac measure binded to the u_I-contact-wave trajectory accross the time-and-space half plane. Besides, the "mass" of such a measure is determined by applying the Rankine-Hugoniot relations through the u_I-contact-wave to the momentum and energy equations of both phases.

The first section of the present work is dedicated to the analysis of a generalized Riemann problem involving a linear convective Jacobian matrix, linear relaxation source terms as well as a frozen-mass Dirac measure. An analytical solution is notably derived in the specific case where the relaxation matrix can be diagonalized using the right eigenvector basis of the convective Jacobian matrix. Taking profit of such an analytical solution, the Bereux-Sainsaulieu ODEs system involving a space-averaged state and already presented in (4.59) can be simply extended.

The second section relies on this new time-dynamics to provide a time-implicit staggered scheme for the isentropic Baer-Nunziato system with pressure and velocity relaxations. Special attention is paid to the non-conservative products discretization as well as the ability, of the proposed method, to be conservative for the mass and momentum mixture variables. One can also prove that the resulting approach preserves the volume fraction maximum principle under a classical CFL condition.

The last section is devoted to numerical results. The first two verification test cases focus on the proposed scheme suitability to converge towards the analytical solution of a hand-made linear model similar to the one studied in the first section. The third verification test case is a Riemann problem related to the *homogeneous* isentropic Baer-Nunziato system. The time-implicit staggered scheme is compared with the Rusanov scheme and an isentropic adaptation of the HLLAC approximate Riemann solver developed in [7]. Finally, the last test cases are generalized Baer-Nunziato Riemann problems in which pressure and velocity relaxations are no longer omitted. The present scheme is compared with fractional step approaches composed of Rusanov or HLLAC convective schemes and time relaxations based on the work of Gallouët *et al.* in [6] combined with more recent approaches proposed in [5, 8].

5.2 Analysis of a generalized linear Riemann problem endowed with a Dirac measure

The extension of the former coupling scheme is based on the study of a new generalized linear Riemann problem involving a frozen mass Dirac measure. Let us introduce a given *constant* mass vector $\mathbf{b}_0$ and a given *constant* interfacial velocity u_I^*. In this subsection, these quantities are simply considered as given *inputs*. In the following, one is interested in studying the solutions $\mathbf{U} \in \mathbb{R}^p$ of:

$$\begin{aligned} &\partial_t \mathbf{U} + \underline{\underline{\mathbf{C}}}_0 \partial_x \mathbf{U} = \frac{1}{\tau} \underline{\underline{\mathbf{B}}}_0 \mathbf{U} + \mathbf{b}_0 \delta_{\{x=u_I^* t\}}, \\ &\mathbf{U}(., t=0) = \begin{cases} \mathbf{U}_L^0 \text{ if } x < 0, \\ \mathbf{U}_R^0 \text{ if } x > 0. \end{cases} \end{aligned} \tag{5.1}$$

Here, $\underline{\underline{\mathbf{C}}}_0$ is a frozen convective Jacobian matrix which can be diagonalized in $\mathbb{R}$. In the sequel we note,

$$\lambda_1^0 < \ldots < \lambda_k^0 < \ldots < \lambda_p^0, \tag{5.2}$$

the sequence of its ordered eigenvalues. Besides, $\underline{\underline{\mathbf{B}}}_0/\tau$ is a constant relaxation matrix. Eventually, $\delta_{\{x=u_I^*\,t\}}$ is a Dirac measure binded to the half straight line $t\in\mathbb{R}^+\to\left(u_I^*\,t,\,t\right)$. Introducing,

$$\mathbf{C}_0^\infty\left(\mathbb{R}\times[0,+\infty[\right)^p, \tag{5.3}$$

the space of $\mathbf{C}^\infty$ functions with compact support in $\mathbb{R}\times[0,+\infty[$, $\delta_{\{x=u_I^*\,t\}}$ can be defined in the sense of distributions as:

$$\forall\boldsymbol{\phi}\in\mathbf{C}_0^\infty\left(\mathbb{R}\times[0,+\infty[\right)^p,\ \langle\mathbf{b}_0\,\delta_{\{x=u_I^*\,t\}},\boldsymbol{\phi}\rangle=\mathbf{b}_0\int_0^{+\infty}\boldsymbol{\phi}\left(u_I^*\,t,\,t\right)dt, \tag{5.4}$$

with $\langle .,.\rangle$ standing for the integration over $\mathbb{R}\times[0,+\infty[$. Let us stress that equation (5.1) has to be considered in a weak sense. We look for piece-wise $\mathbf{C}^1\left(\mathbb{R}\times[0,+\infty[\right)^p$ solutions verifying,

$$\partial_t\mathbf{U}+\underline{\underline{\mathbf{C}}}_0\,\partial_x\mathbf{U}=\frac{1}{\tau}\underline{\underline{\mathbf{B}}}_0\,\mathbf{U}, \tag{5.5}$$

in smooth regions, and abiding by appropriate Rankine-Hugoniot relations across discontinuities. The convective Jacobian matrix being frozen, two categories of Rankine-Hugoniot relations can be pointed out. These categories are described in the following property:

Property 5.2.1 (Two kinds of Rankine-Hugoniot relations)
Assume that $\forall k\in[1,\,p],\ \lambda_k^0\neq u_I^*$. *Then, across the discontinuity front line* $t\to\left(\lambda_k^0\,t,\,t\right)$, *weak solutions of problem* (5.1) *verify,*

$$\begin{aligned}\left(-\lambda_k^0\,\mathbf{I}+\underline{\underline{\mathbf{C}}}_0\right)[\mathbf{U}]_{\lambda_k^0}&=\mathbf{0},\\ [\mathbf{U}]_{\lambda_k^0}&=\mathbf{U}\left((\lambda_k^0\,t)^+,\,t\right)-\mathbf{U}\left((\lambda_k^0\,t)^-,\,t\right),\end{aligned} \tag{5.6}$$

with,

$$\forall X\in\mathbb{R},\ (X)^+=\lim_{x\to X,\ x>X}x,\ \ (X)^-=\lim_{x\to X,\ x<X}x. \tag{5.7}$$

Besides, across the discontinuity front line $t\to\left(u_I^*\,t,\,t\right)$, *the Rankine-Hugoniot relations read:*

$$\begin{aligned}\left(-u_I^*\,\mathbf{I}+\underline{\underline{\mathbf{C}}}_0\right)[\mathbf{U}]_{u_I^*}&=\mathbf{b}_0,\\ [\mathbf{U}]_{u_I^*}&=\mathbf{U}\left((u_I^*\,t)^+,\,t\right)-\mathbf{U}\left((u_I^*\,t)^-,\,t\right).\end{aligned} \tag{5.8}$$

In the sequel, the analytical solution of problem (5.1) is derived in the case where the relaxation matrix $\underline{\underline{\mathbf{B}}}_0$ can be diagonalized using the right eigenvector basis $\underline{\underline{\mathbf{R}}}_0$ of $\underline{\underline{\mathbf{C}}}_0$.

5.2.1 Analytical solution in the case of independent linear relaxation processes

The relaxation matrix $\frac{1}{\tau}\underline{\underline{\mathbf{B}}}_0$ is now replaced by $-\underline{\underline{\mathbf{R}}}_0\,\underline{\underline{\tau}}^{-1}\,\underline{\underline{\mathbf{R}}}_0^{-1}$. Recall that $\underline{\underline{\mathbf{R}}}_0$ (respectively $\underline{\underline{\mathbf{R}}}_0^{-1}$) is the matrix of the right eigenvectors (respectively of the left eigenvectors) of the frozen Jacobian matrix $\underline{\underline{\mathbf{C}}}_0$ already defined in (4.60). Furthermore, $\underline{\underline{\tau}}^{-1}$ is a diagonal time-relaxation matrix introduced in (4.138). Finally, $\mathbf{U}^{\text{eq}}$ is a given *constant* equilibrium state. Hence, the generalized linear Riemann problem writes:

$$\begin{aligned}&\partial_t\mathbf{U}+\underline{\underline{\mathbf{C}}}_0\,\partial_x\mathbf{U}=-\underline{\underline{\mathbf{R}}}_0\,\underline{\underline{\tau}}^{-1}\,\underline{\underline{\mathbf{R}}}_0^{-1}\left(\mathbf{U}-\mathbf{U}^{\text{eq}}\right)+\mathbf{b}_0\,\delta_{\{x=u_I^*\,t\}},\\ &\mathbf{U}(.,\,t=0)=\begin{cases}\mathbf{U}_L^0\text{ if }x<0,\\ \mathbf{U}_R^0\text{ if }x>0.\end{cases}\end{aligned} \tag{5.9}$$

As previously, problem (5.9) can be projected into the right eigenvector basis $\underline{\underline{\mathbf{R}}}_0$. Using the same notations than in (4.128), if $\mathbf{U}$ is solution of (5.9), then the k-th component $\mathbf{a}_k$ of $\underline{\underline{\mathbf{R}}}_0^{-1}\,\mathbf{U}$ verifies equivalently:

$$\begin{aligned}&\partial_t\mathbf{a}_k+\lambda_k^0\,\partial_x\mathbf{a}_k=-\frac{\mu_k}{\tau}\left(\mathbf{a}_k-\mathbf{a}_k^{\text{eq}}\right)+\mathbf{l}_k^0\cdot\mathbf{b}_0\,\delta_{\{x=u_I^*\,t\}},\\ &\mathbf{a}_k(.,\,t=0)=\begin{cases}\mathbf{a}_L^0\text{ if }x<0,\\ \mathbf{a}_R^0\text{ if }x>0.\end{cases}\end{aligned} \tag{5.10}$$

The exact solution of problem (5.10) can be found by looking at Figure 5.1 which displays the two discontinuities related to λ_k^0 (thick blue line) and u_{I}^* (thick red line) in the x-t plane in the case where $\lambda_k^0 < u_{\mathrm{I}}^*$.

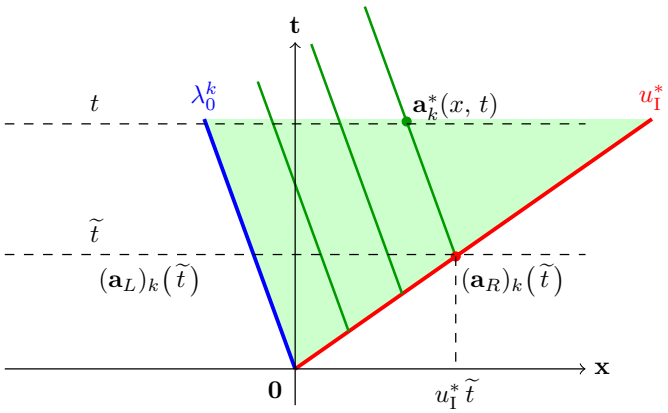

Figure 5.1 – Generalized linear Riemann problem with Dirac mass: characteristic lines

For a given time $\widetilde{t}$ three different regions can be defined:

$$\begin{aligned}
\mathcal{A}_{\mathrm{L}} &= \left\{x \in \mathbb{R},\ \text{s. t.},\ x < \lambda_k^0\,\widetilde{t}\right\},\\
\mathcal{A}^* &= \left\{x \in \mathbb{R},\ \text{s. t.},\ \lambda_k^0\,\widetilde{t} < x < u_{\mathrm{I}}^*\,\widetilde{t}\right\},\\
\mathcal{A}_{\mathrm{R}} &= \left\{x \in \mathbb{R},\ \text{s. t.},\ x > u_{\mathrm{I}}^*\,\widetilde{t}\right\}.
\end{aligned} \tag{5.11}$$

In each of these regions, $\mathbf{a}_k$ verifies,

$$\partial_t\,\mathbf{a}_k + \lambda_k^0\,\partial_x\,\mathbf{a}_k = -\frac{\mu_k}{\tau}\left(\mathbf{a}_k - \mathbf{a}_k^{\mathrm{eq}}\right). \tag{5.12}$$

Then, for a given point in $\mathcal{A}_{\mathrm{L}} \sqcup \mathcal{A}_{\mathrm{R}}$, one can follow the characteristic line $\dfrac{\mathrm{d}x}{\mathrm{d}t} = \lambda_k^0$ downwards and reach the initial conditions: $\mathbf{a}_{\mathrm{L}}^0$ for a point in $\mathcal{A}_{\mathrm{L}}$, $\mathbf{a}_{\mathrm{R}}^0$ for a point belonging to $\mathcal{A}_{\mathrm{R}}$. The time integration of equation (5.12) is thus straightforward and gives:

$$\begin{cases}
(\mathbf{a}_{\mathrm{L}})_k(\widetilde{t}) = (\mathbf{a}_{\mathrm{L}}^0)_k\,e^{-\mu_k\,\widetilde{t}/\tau} + \mathbf{a}_k^{\mathrm{eq}}\left(1 - e^{-\mu_k\,\widetilde{t}/\tau}\right) & \text{if} \quad x \in \mathcal{A}_{\mathrm{L}},\\
(\mathbf{a}_{\mathrm{R}})_k(\widetilde{t}) = (\mathbf{a}_{\mathrm{R}}^0)_k\,e^{-\mu_k\,\widetilde{t}/\tau} + \mathbf{a}_k^{\mathrm{eq}}\left(1 - e^{-\mu_k\,\widetilde{t}/\tau}\right) & \text{if} \quad x \in \mathcal{A}_{\mathrm{R}}.
\end{cases} \tag{5.13}$$

Consider the u_{I}^*-discontinuity front at time $\widetilde{t}$ and define $\mathbf{a}_k^*(\widetilde{t})$ the value of the component $\mathbf{a}_k$ at the point $\left((u_{\mathrm{I}}^*\,\widetilde{t})^-,\,\widetilde{t}\right)$ in the $\mathcal{A}^*$ region. Then, thanks to the Rankine-Hugoniot relations (5.8), one can completely determine the value of $\mathbf{a}_k^*(\widetilde{t})$ as:

$$\mathbf{a}_k^*(\widetilde{t}) = (\mathbf{a}_{\mathrm{R}})_k(\widetilde{t}) - \frac{\mathbf{l}_k^0 \cdot \mathbf{b}_0}{\lambda_k^0 - u_{\mathrm{I}}^*}. \tag{5.14}$$

Hence, for a given point $(x,\,t) \in \mathcal{A}^*$, one can once again follow the λ_k^0-characteristic line. Nevertheless, the root of such characteristic line will never reach initial conditions since, at a given instant $\widetilde{t} < t$ it is crossed by the u_{I}^*-characteristic line. As a consequence the problem to be solved writes:

$$\begin{aligned}
\frac{\mathrm{d}\mathbf{a}_k}{\mathrm{d}t}_{|\lambda_k^0} &= -\frac{\mu_k}{\tau}\left(\mathbf{a}_k - \mathbf{a}_k^{\mathrm{eq}}\right),\\
\mathbf{a}_k\left(t = \widetilde{t}\right) &= \mathbf{a}_k^*(\widetilde{t}),
\end{aligned} \tag{5.15}$$

where $\dfrac{\mathrm{d}}{\mathrm{d}t}_{|\lambda_k^0}$ stands for the time derivative along the λ_k^0-characteristic line. After calculations, one obtains $\forall (x,\,t) \in \mathcal{A}^*$:

$$\mathbf{a}_k(x,\,t) = (\mathbf{a}_{\mathrm{R}})_k(t) - e^{-(\mu_k/\tau)\left(\frac{u_{\mathrm{I}}^*\,t - x}{u_{\mathrm{I}}^* - \lambda_k^0}\right)}\,\frac{\mathbf{l}_k^0 \cdot \mathbf{b}_0}{\lambda_k^0 - u_{\mathrm{I}}^*}. \tag{5.16}$$

The expression obtained in (5.16) requires a few comments that are summarized below.

Remark 5.2.1 (On the structure of the solution in the $\mathcal{A}^*$ region)
Recall that, as shown in equation (4.140) in the previous chapter, when the Dirac measure is omitted, the solution in the $\mathcal{A}^* \sqcup \mathcal{A}_R$ region simply reads:

$$\mathbf{a}_k(x,\, t) = (\mathbf{a}_R)_k(t). \tag{5.17}$$

The self-similarity is lost because of the time-relaxation effect, but at a given instant t, the solution is spatially constant in this region.

Here, the presence of the Dirac measure brings the second term in the right hand side of equation (5.16) which is exponentially decreasing in space. Then, at $x = (u_I^*\, t)^-$,

$$e^{-(\mu_k/\tau)\left(\frac{u_I^*\, t - x}{u_I^* - \lambda_k^0}\right)} \frac{\mathbf{l}_k^0 \cdot \mathbf{b}_0}{\lambda_k^0 - u_I^*} \to \frac{\mathbf{l}_k^0 \cdot \mathbf{b}_0}{\lambda_k^0 - u_I^*}, \tag{5.18}$$

and the jump relation (5.14) is retrieved. In that case, the mass of the Dirac measure is totally "transmitted" to the solution through the discontinuity line. However, at $x = (\lambda_k\, t)^+$,

$$e^{-(\mu_k/\tau)\left(\frac{u_I^*\, t - x}{u_I^* - \lambda_k^0}\right)} \frac{\mathbf{l}_k^0 \cdot \mathbf{b}_0}{\lambda_k^0 - u_I^*} \to e^{-(\mu_k\, t/\tau)} \frac{\mathbf{l}_k^0 \cdot \mathbf{b}_0}{\lambda_k^0 - u_I^*}, \tag{5.19}$$

and the mass brought by the Dirac measure decreases due to relaxation effects.

Let us stress that for the converse configuration in which $u_I^* < \lambda_k^0$, the solution is similar to the one obtained in (5.16):

$$\mathbf{a}_k(x,\, t) = (\mathbf{a}_L)_k(t) + e^{-(\mu_k/\tau)\left(\frac{u_I^*\, t - x}{u_I^* - \lambda_k^0}\right)} \frac{\mathbf{l}_k^0 \cdot \mathbf{b}_0}{\lambda_k^0 - u_I^*}. \tag{5.20}$$

Finally, the solution of problem (5.9) can be completely written.

Property 5.2.2 (Solution of a linear Riemann problem with independent linear relaxation effects and a frozen mass Dirac measure)
For the ease of notations, let us introduce,

$$\begin{aligned} [\mathbf{a}_k]_{u_I^*} &= \frac{\mathbf{l}_k^0 \cdot \mathbf{b}_0}{\lambda_k^0 - u_I^*}, \\ \mathbf{a}_k^0(x,\, t) &= \left[(\mathbf{a}_L^0)_k + (\mathbf{a}_R^0 - \mathbf{a}_L^0)_k\, \mathrm{H}\left(x - \lambda_k^0\, t\right)\right] e^{-\mu_k\, t/\tau} + \mathbf{a}_k^{\mathrm{eq}}\left(1 - e^{-\mu_k\, t/\tau}\right). \end{aligned} \tag{5.21}$$

The solution of problem (5.9) can be written in a compact form as:

$$\mathbf{U}(x,\, t) = \sum_{k=1}^{p} \left\{ \mathbf{a}_k^0(x,\, t) - e^{-(\mu_k/\tau)\left(\frac{u_I^*\, t - x}{u_I^* - \lambda_k^0}\right)} [\mathbf{a}_k]_{u_I^*} \left(\mathrm{H}\left(x - \lambda_k^0\, t\right) - \mathrm{H}\left(x - u_I^*\, t\right)\right) \right\} \mathbf{r}_k^0. \tag{5.22}$$

If one wishes to isolate the contribution brought by the crossing of the u_I^*-discontinuous line, one can rewrite the solution as:

$$\begin{aligned} \mathbf{U}(x,\, t) = &\sum_{k=1}^{p} \left\{ \mathbf{a}_k^0(x,\, t) - e^{-(\mu_k/\tau)\left(\frac{u_I^*\, t - x}{u_I^* - \lambda_k^0}\right)} [\mathbf{a}_k]_{u_I^*}\, \mathrm{H}\left(x - \lambda_k^0\, t\right) \right\} \mathbf{r}_k^0 \\ &+ \left\{ \sum_{k=1}^{p} e^{-(\mu_k/\tau)\left(\frac{u_I^*\, t - x}{u_I^* - \lambda_k^0}\right)} [\mathbf{a}_k]_{u_I^*}\, \mathbf{r}_k^0 \right\} \mathrm{H}\left(x - u_I^*\, t\right). \end{aligned} \tag{5.23}$$

Proof 4
The proof of Property 5.2.2 results from equalities (5.11), (5.13) and (5.16) combined with the fact that $\mathbf{U}(x,\, t) = \underline{\underline{\mathbf{R}}}_0\, \mathbf{a}(x,\, t)$.

Using the analytical solution derived in (5.23), the next subsection proposes to show how the Bereux-Sainsaulieu lemma written in Property 4.3.1 of the previous chapter is impacted by the presence of a frozen mass Dirac measure.

5.2.2 Extension of the Bereux-Sainsaulieu lemma

Using the same formalism than the one introduced in **Property 4.3.1**, one can state the following proposition:

Proposition 5.2.1 (Extension of the Bereux-Sainsaulieu lemma: independent relaxation processes and frozen mass Dirac measure)
Define a time-space domain $\Omega = [0, \mathrm{T}] \times [-\mathrm{L}/2, \mathrm{L}/2]$, L *being a given length and* T *a given final time. Consider the solution* (5.23) *of problem* (5.9). *Up to the change of variable* $\widetilde{\mathbf{U}} = \mathbf{U} - \mathbf{U}^{\mathrm{eq}}$, *one can rewrite it in the non-restrictive case* $\mathbf{U}^{\mathrm{eq}} = \mathbf{0}$. *Consider the space-averaged variable* $\mathbf{H}$,

$$\mathbf{H} = \frac{1}{\mathrm{L}} \int_{-\mathrm{L}/2}^{\mathrm{L}/2} \mathbf{U} \, \mathrm{d}x. \tag{5.24}$$

Then, if T *is such that,*

$$\mathrm{T} < \frac{\mathrm{L}}{2 \max\limits_{k \in [1,p]} \left| \lambda_k^0 \right|}, \tag{5.25}$$

$\mathbf{H}$ *is solution of the following ODE system:*

$$\begin{cases} \dfrac{\mathrm{d}\mathbf{H}}{\mathrm{d}t} = \dfrac{1}{\tau} \underline{\underline{\mathbf{B}}}_0 \, \mathbf{H} - \dfrac{1}{\mathrm{L}} \underline{\underline{\mathbf{C}}}_0 \, (\mathbf{U}_{\mathrm{R}}(t) - \mathbf{U}_{\mathrm{L}}(t)) + \dfrac{\mathbf{b}_0}{\mathrm{L}}, \; \mathbf{H}(0) = \dfrac{\mathbf{U}_{\mathrm{R}}^0 + \mathbf{U}_{\mathrm{L}}^0}{2}, \\ \forall k \in \{\mathrm{L}, \mathrm{R}\} : \\ \dfrac{\mathrm{d}\mathbf{U}_k}{\mathrm{d}t} = \dfrac{1}{\tau} \underline{\underline{\mathbf{B}}}_0 \, \mathbf{U}_k, \; \mathbf{U}_k(0) = \mathbf{U}_k^0, \end{cases} \tag{5.26}$$

with $\frac{1}{\tau} \underline{\underline{\mathbf{B}}}_0 = -\underline{\underline{\mathbf{R}}}_0 \, \underline{\underline{\tau}} \, \underline{\underline{\mathbf{R}}}_0^{-1}$.

Hence, in the specific case where the relaxation matrix $\underline{\underline{\mathbf{B}}}_0$ can be diagonalized using the same right eigenvector basis than $\underline{\underline{\mathbf{C}}}_0$, the presence of a frozen mass Dirac measure only entails the appearance of a drifting constant term $\mathbf{b}_0/\mathrm{L}$ in the $\mathbf{H}$ dynamics.

Proof 5
The proof is similar to the one briefly presented in equation (4.78) *in the previous chapter. Assume that there exists an index* $\mathrm{J} \in [1, p]$ *such that:*

$$\lambda_{\mathrm{J}}^0 < u_{\mathrm{I}}^* < \lambda_{\mathrm{J}+1}^0. \tag{5.27}$$

At a given instant t, *the variable* $\mathbf{H}$ *is decomposed as a sum of integrals across the smooth regions of the solution* (5.23),

$$]-\frac{\mathrm{L}}{2}, \lambda_1^0 \, t[\, \ldots \,] \lambda_{\mathrm{J}}^0 \, t, \, u_{\mathrm{I}}^* \, t[\sqcup] u_{\mathrm{I}}^* \, t, \lambda_{\mathrm{J}+1}^0 \, t[\, \ldots \,] \lambda_p^0 \, t, \, \frac{\mathrm{L}}{2}[. \tag{5.28}$$

Applying the Leibniz rule, the time derivative of $\mathbf{H}$ *reads:*

$$\begin{aligned} \mathrm{L} \frac{\mathrm{d}\mathbf{H}}{\mathrm{d}t} = & \int_{-\mathrm{L}/2}^{\lambda_1^0 \, t} \partial_t \mathbf{U} \, \mathrm{d}x + \lambda_1^0 \mathbf{U}\left((\lambda_1^0 \, t)^-, \, t \right) \\ & + \sum_{l=1}^{\mathrm{J}-1} \left\{ \int_{\lambda_l^0 \, t}^{\lambda_{l+1}^0 \, t} \partial_t \mathbf{U} \, \mathrm{d}x + \lambda_{l+1}^0 \mathbf{U}\left((\lambda_{l+1}^0 \, t)^-, \, t \right) - \lambda_l^0 \mathbf{U}\left((\lambda_l^0 \, t)^+, \, t \right) \right\} \\ & + \int_{\lambda_{\mathrm{J}}^0 \, t}^{u_{\mathrm{I}}^* \, t} \partial_t \mathbf{U} \, \mathrm{d}x + u_{\mathrm{I}}^* \mathbf{U}\left((u_{\mathrm{I}}^* \, t)^-, \, t \right) - \lambda_{\mathrm{J}}^0 \mathbf{U}\left((\lambda_{\mathrm{J}}^0 \, t)^+, \, t \right) \\ & + \int_{u_{\mathrm{I}}^* \, t}^{\lambda_{\mathrm{J}+1}^0 \, t} \partial_t \mathbf{U} \, \mathrm{d}x + \lambda_{\mathrm{J}+1}^0 \mathbf{U}\left((\lambda_{\mathrm{J}+1}^0 \, t)^-, \, t \right) - u_{\mathrm{I}}^* \mathbf{U}\left(u_{\mathrm{I}}^* \, t)^+, \, t \right) \\ & + \sum_{l=\mathrm{J}+1}^{p-1} \left\{ \int_{\lambda_l^0 \, t}^{\lambda_{l+1}^0 \, t} \partial_t \mathbf{U} \, \mathrm{d}x + \lambda_{l+1}^0 \mathbf{U}\left((\lambda_{l+1}^0 \, t)^-, \, t \right) - \lambda_l^0 \mathbf{U}\left((\lambda_l^0 \, t)^+, \, t \right) \right\} \\ & + \int_{\lambda_p^0 \, t}^{\mathrm{L}/2} \partial_t \mathbf{U} \, \mathrm{d}x - \lambda_p^0 \mathbf{U}\left((\lambda_p^0 \, t)^+, \, t \right). \end{aligned} \tag{5.29}$$

After having replaced $\partial_t \mathbf{U}$ *by* $-\underline{\underline{\mathbf{C}}}_0 \partial_x \mathbf{U} + \frac{1}{\tau}\underline{\underline{\mathbf{B}}}_0 \mathbf{U}$ *inside the integrals, one obtains:*

$$\begin{aligned} \mathrm{L}\frac{\mathrm{d}\mathbf{H}}{\mathrm{d}t} = \mathrm{L}\frac{1}{\tau}\underline{\underline{\mathbf{B}}}_0 \mathbf{H} - \underline{\underline{\mathbf{C}}}_0 \left(\mathbf{U}(\mathrm{L}/2,\, t) - \mathbf{U}(-\mathrm{L}/2,\, t)\right) \\ + \sum_{l=1}^{p} \left\{ \left[-\underline{\underline{\mathbf{C}}}_0 + \lambda_l^0 \mathbf{I} \right] \left(\mathbf{U}\left((\lambda_l^0\, t)^-,\, t\right) - \mathbf{U}\left((\lambda_l^0\, t)^+,\, t\right) \right) \right\} \\ + \left[-\underline{\underline{\mathbf{C}}}_0 + u_{\mathrm{I}}^* \mathbf{I} \right] \left(\mathbf{U}\left((u_{\mathrm{I}}^*\, t)^-,\, t\right) - \mathbf{U}\left((u_{\mathrm{I}}^*\, t)^+,\, t\right) \right). \end{aligned} \tag{5.30}$$

Looking at the solution (5.23)*, the contribution gained through the crossing of a given* λ_l^0*-contact wave is:*

$$\mathbf{U}\left((\lambda_l^0\, t)^+,\, t\right) - \mathbf{U}\left((\lambda_l^0\, t)^-,\, t\right) = \left\{ \mathbf{a}_l^0(x,\, t) - e^{-(\mu_l/\tau)\left(\frac{u_{\mathrm{I}}^*\, t - x}{u_{\mathrm{I}}^* - \lambda_l^0}\right)} [\mathbf{a}_k]_{u_{\mathrm{I}}^*} \mathrm{H}\left(x - \lambda_l^0\, t\right) \right\} \mathbf{r}_l^0. \tag{5.31}$$

Since it is colinear with $\mathbf{r}_l^0$*, the third term in the right hand side of equality* (5.30) *is null. Furthermore, looking at the contribution related to* $\mathrm{H}\left(x - u_{\mathrm{I}}^*\, t\right)$ *in* (5.23)*, one can deduce that:*

$$\begin{aligned} \left[-\underline{\underline{\mathbf{C}}}_0 + u_{\mathrm{I}}^* \mathbf{I} \right] \left(\mathbf{U}\left((u_{\mathrm{I}}^*\, t)^-,\, t\right) - \mathbf{U}\left((u_{\mathrm{I}}^*\, t)^+,\, t\right) \right) &= -\sum_{k=1}^{p} [\mathbf{a}_k]_{u_{\mathrm{I}}^*} \left[-\underline{\underline{\mathbf{C}}}_0 + u_{\mathrm{I}}^* \mathbf{I} \right] \mathbf{r}_k^0 \\ &= \sum_{k=1}^{p} [\mathbf{a}_k]_{u_{\mathrm{I}}^*} \left(\lambda_k^0 - u_{\mathrm{I}}^* \right) \mathbf{r}_k^0 \\ &= \sum_{k=1}^{p} (\mathbf{l}_k^0 \cdot \mathbf{b}_0)\, \mathbf{r}_k^0. \end{aligned} \tag{5.32}$$

Using relations (4.61)*, one can deduce that the last sum in* (5.32) *corresponds to the vector* $\mathbf{b}_0$ *decomposed on the right eigenvector basis. This completes the proof.*

The extension of the space-averaged state dynamics has been performed using the analytical solution derived in the specific case where source terms act independently on each right eigenvector component. Of course, in order to completely extend the Bereux-Sainsaulieu approach, one should be able to prove that the ODEs system (5.26) holds for any relaxation matrix $\underline{\underline{\mathbf{B}}}_0$. Recall that in their paper [2] the authors manage to prove this result in the general case by using continuity arguments based on a Fourier transform analysis. A similar approach has been conducted in the present configuration. Unfortunately, the presence of the frozen mass Dirac measure adds complexity to the Fourier transform analysis. So far, the proof remains incomplete.

Still, we conjecture that the time-dynamics (5.26) is an incentive to construct a new staggered scheme adapted to the isentropic Baer-Nunziato system. In the following section, the derivation of such scheme is presented. Particular attention will be paid to the non-conservative products discretization. Numerical properties dealing with conservativity and volume fraction maximum principle are also proved.

5.3 A time-implicit staggered scheme for the isentropic Baer-Nunziato system

For the sake of clarity, the isentropic Baer-Nunziato system with pressure and velocity relaxations is recalled. The state vector is,

$$\mathbf{U} = [\alpha_1,\, m_1,\, m_1 u_1,\, m_2,\, m_2 u_2]^{\mathrm{T}}. \tag{5.33}$$

Closure laws defined in (4.8) are directly injected in the two-fluid two-pressure system. Besides, constant pressure and velocity relaxation time-scales are considered. Eventually, the non-dimensional

cofactors $\widetilde{\mathrm{K}}_{\mathrm{p}}(\mathbf{U})$, $\widetilde{\mathrm{K}}_{\mathrm{u}}(\mathbf{U})$ introduced in (4.11b), (4.13b) are set equal to the product $\alpha_1\alpha_2$. As a result, the system reads:

$$\begin{gathered}
\partial_t \mathbf{U} + \partial_x \mathbf{F}(\mathbf{U}) + \underline{\underline{\mathbf{E}}}(\mathbf{U})\,\partial_x \mathbf{U} = \mathbf{S}(\mathbf{U}), \\
\mathbf{F}(\mathbf{U}) = \begin{bmatrix} 0 \\ m_1 u_1 \\ m_1 u_1^2 + \alpha_1 p_1 \\ m_2 u_2 \\ m_2 u_2^2 + \alpha_2 p_2 \end{bmatrix}, \quad \underline{\underline{\mathbf{E}}}(\mathbf{U}) = \big[\mathbf{b}(\mathbf{U}),\, \mathbf{0},\, \mathbf{0},\, \mathbf{0},\, \mathbf{0}\big], \quad \mathbf{b}(\mathbf{U}) = \begin{bmatrix} u_2 \\ 0 \\ -p_1 \\ 0 \\ +p_1 \end{bmatrix}, \\
\mathbf{S}(\mathbf{U}) = \begin{bmatrix} -\frac{\alpha_1\alpha_2}{\tau_{\mathrm{p}}}\frac{\Delta p}{p_1+p_2} \\ 0 \\ \frac{1}{\tau_{\mathrm{u}}}\frac{m_1 m_2}{m_1+m_2}\Delta u \\ 0 \\ -\frac{1}{\tau_{\mathrm{u}}}\frac{m_1 m_2}{m_1+m_2}\Delta u \end{bmatrix}.
\end{gathered} \tag{5.34}$$

Recall that, in the expression of $\mathbf{S}(\mathbf{U})$, $\Delta p = p_2 - p_1$ and $\Delta u = u_2 - u_1$. The derivation of a numerical scheme based on the Bereux-Sainsaulieu approach will require the computation of the gradient of the relaxation source terms with respect to the state $\mathbf{U}$. It is given by,

$$\partial_{\mathbf{U}}\mathbf{S}(\mathbf{U}) = \begin{bmatrix} -\frac{(1-2\alpha_1)}{\tau_{\mathrm{p}}}\frac{\Delta p}{p_2+p_1} - \frac{\alpha_1\alpha_2}{\tau_{\mathrm{p}}}\frac{\mathcal{P}}{p_2+p_1} & \frac{1}{\tau_{\mathrm{p}}}\frac{2\alpha_2 p_2 c_1^2}{(p_2+p_1)^2} & 0 & -\frac{1}{\tau_{\mathrm{p}}}\frac{2\alpha_1 p_1 c_2^2}{(p_2+p_1)^2} & 0 \\ 0 & 0 & 0 & 0 & 0 \\ 0 & \frac{1}{\tau_{\mathrm{u}}}\mathrm{Y}_2\,\mathrm{U} & -\frac{1}{\tau_{\mathrm{u}}}\mathrm{Y}_2 & -\frac{1}{\tau_{\mathrm{u}}}\mathrm{Y}_1\,\mathrm{U} & \frac{1}{\tau_{\mathrm{u}}}\mathrm{Y}_1 \\ 0 & 0 & 0 & 0 & 0 \\ 0 & -\frac{1}{\tau_{\mathrm{u}}}\mathrm{Y}_2\,\mathrm{U} & \frac{1}{\tau_{\mathrm{u}}}\mathrm{Y}_2 & \frac{1}{\tau_{\mathrm{u}}}\mathrm{Y}_1\,\mathrm{U} & -\frac{1}{\tau_{\mathrm{u}}}\mathrm{Y}_1 \end{bmatrix}, \tag{5.35}$$

with,

$$\begin{aligned}
&\mathcal{P} = \left(\frac{\mathrm{C}_2}{\alpha_2} + \frac{\mathrm{C}_1}{\alpha_1}\right) - \left(\frac{\mathrm{C}_2}{\alpha_2} - \frac{\mathrm{C}_1}{\alpha_1}\right)\frac{\Delta p}{p_2+p_1}, \\
&\mathrm{Y}_k = m_k/m,\ m = m_1 + m_2, \\
&\mathrm{U} = \mathrm{Y}_1\,u_1 + \mathrm{Y}_2\,u_2.
\end{aligned} \tag{5.36}$$

After having set these preliminary notations, one can present the numerical scheme inspired from Proposition 5.2.1.

5.3.1 Derivation of the scheme

The same discrete notations that these presented in subsection 4.4.1 are adopted. Recall that the function $(\mathbf{U}, \Delta t) \to \Phi_\tau(\mathbf{U}, \Delta t)$ is related to the consistent discretization of the ODEs system:

$$\frac{\mathrm{d}\mathbf{U}}{\mathrm{d}t} = \mathbf{S}(\mathbf{U}), \tag{5.37}$$

the expression of $\mathbf{S}(\mathbf{U})$ being provided in (5.34). Consider a given face indexed $i+1/2$; at a given instant t^n

$$\mathbf{H}_{i+1/2}^n = \frac{\mathbf{U}_{i+1}^n + \mathbf{U}_i^n}{2}, \tag{5.38}$$

is the space-averaged variable associated with the dual mesh cell centered around the face $i+1/2$. Then, the first step of the numerical method reads:

$$\begin{cases}
\mathbf{H}_{i+1/2}^{n+1/2} = \mathbf{H}_{i+1/2}^n + (\Delta t/2)\,\Phi_\tau\left(\mathbf{H}_{i+1/2}^n, \Delta t/2\right) \\
\qquad -\dfrac{\Delta t}{2\Delta x}\left(\mathbf{F}\left(\mathbf{U}_{i+1}^{n+1/2}\right) - \mathbf{F}\left(\mathbf{U}_i^{n+1/2}\right)\right) + \dfrac{\Delta t}{2\Delta x}\widetilde{\mathbf{b}}_{i+1/2}^n, \\
\qquad \forall\, j \in \{i,\, i+1\}: \\
\mathbf{U}_j^{n+1/2} = \mathbf{U}_j^n + (\Delta t/2)\,\Phi_\tau\left(\mathbf{U}_j^n, \Delta t/2\right).
\end{cases} \tag{5.39}$$

After having reconstructed the intermediate update on the primal mesh as

$$\mathbf{U}_i^{n+1/2} = \left(\mathbf{H}_{i+1/2}^{n+1/2} + \mathbf{H}_{i-1/2}^{n+1/2}\right)/2, \tag{5.40}$$

the second step writes equivalently:

$$\begin{cases} \mathbf{U}_i^{n+1} = \mathbf{U}_i^{n+1/2} + (\Delta t/2)\,\Phi_\tau\left(\mathbf{U}_i^{n+1/2}, \Delta t/2\right) \\ \qquad -\dfrac{\Delta t}{2\Delta x}\left(\mathbf{F}\left(\mathbf{H}_{i+1/2}^{n+1}\right) - \mathbf{F}\left(\mathbf{H}_{i-1/2}^{n+1}\right)\right) + \dfrac{\Delta t}{2\Delta x}\widetilde{\mathbf{b}}_i^{n+1/2}, \\ \quad \forall\, j \in \{i-1/2,\, i+1/2\}: \\ \mathbf{H}_j^{n+1} = \mathbf{H}_j^{n+1/2} + (\Delta t/2)\,\Phi_\tau\left(\mathbf{H}_j^{n+1/2}, \Delta t/2\right). \end{cases} \tag{5.41}$$

Up to the additional terms $\widetilde{\mathbf{b}}_{i+1/2}^{n}$, $\widetilde{\mathbf{b}}_i^{n+1/2}$ which will be specified in the next subsection, the proposed numerical scheme is completely defined. Besides, it is very similar to the one already derived in (4.101), (4.102). Nevertheless, let us underline that, in the numerical applications presented in the previous chapter, $\mathbf{F}(\mathbf{U})$ was systematically replaced by $\underline{\underline{\mathbf{C}}}(\mathbf{U}_0)\,\mathbf{U}$; with

$$\underline{\underline{\mathbf{C}}}(\mathbf{U}) = \partial_{\mathbf{U}}\mathbf{F}(\mathbf{U}) + \underline{\underline{\mathbf{E}}}(\mathbf{U}), \tag{5.42}$$

the convective Jacobian matrix of the isentropic Baer-Nunziato system including the *non-conservative products* contributions. Here, $\mathbf{F}(\mathbf{U})$ corresponds to the true conservative flux written in (5.34). As for the non-conservative products, they are put aside and treated separately *via* the "$\widetilde{\mathbf{b}}$" terms. It will be seen later that such a distinction will play an important role for the conservativity of the numerical method.

Let us make a final remark about the time integration of the above approach:

Remark 5.3.1 (An implicit-explicit time integration in order to tackle the stiff relaxation effects)
In each step (5.39), (5.41) of the present staggered scheme, the abstract functional

$$(\mathbf{U}, \delta t) \rightarrow \mathbf{U} + \delta t\,\Phi_\tau(\mathbf{U}, \delta t), \tag{5.43}$$

*systematically stands for a **implicit** time integration of ODEs system (5.37). By doing so, one expects that the stability issues associated with the stiffness of the relaxation source terms is handled. Nevertheless, such a time-implicit integration of the relaxation process is injected afterwards into an **explicit** time integration of the discrete flux divergence as well as the non-conservative products discretization. Hence, one could say that the proposed scheme stems from an implicit-explicit time integration.*

In the sequel, attention is paid to the discretization of the "$\widetilde{\mathbf{b}}$" terms.

5.3.2 Non-conservative products discretization

Formerly in Chapter 4, it has been seen in Property 4.2.2 that the closure law $u_I = u_2$ ensures that non-conservative products are only active accross the u_I-wave. What is more, the u_I-field is linearly degenerate. Hence, as proved in [6] and used in [1, 3], the non-conservative products can be completely defined by using the four Riemann invariants (4.19) or equivalently the Rankine-Hugoniot jump relations involving the partial mass, the momentum and the total energy mixtures. In any case, in the weak sense, one can write:

$$\mathbf{b}(\mathbf{U})\,\partial_x\alpha_1 = \begin{bmatrix} u_2 \\ 0 \\ -p_1 \\ 0 \\ +p_1 \end{bmatrix} \partial_x\alpha_1 = \begin{bmatrix} [u_2\,\alpha_1]_{u_2^*(\mathbf{U})} \\ 0 \\ +\left[\alpha_2\,p_2\right]_{u_2^*(\mathbf{U})} \\ 0 \\ -\left[\alpha_2\,p_2\right]_{u_2^*(\mathbf{U})} \end{bmatrix} \delta_{\{x=u_2^*(\mathbf{U})\,t\}}, \tag{5.44}$$

where the expression $[\phi]_{u_2^*(\mathbf{U})}$ stands for the jump of the variable ϕ across the $u_2^*(\mathbf{U})$-contact wave. Besides, $\delta_{\{x=u_2^*(\mathbf{U})\,t\}}$ is the Dirac measure centered around the point $x = u_2^*(\mathbf{U})\,t$.

In the sequel, the expressions of the "$\widetilde{\mathbf{b}}$" terms in (5.39) and (5.41) are based on a consistent estimation of the mass vector

$$\begin{bmatrix} [u_2\,\alpha_1]_{u_2^*(\mathbf{U})} \\ 0 \\ +[\alpha_2\,p_2]_{u_2^*(\mathbf{U})} \\ 0 \\ -[\alpha_2\,p_2]_{u_2^*(\mathbf{U})} \end{bmatrix}. \tag{5.45}$$

Following the strategy presented in [7], let us start by simplifying the Riemann invariants (4.19) associated with the u_1-contact wave in the context of subsonic flows.

Property 5.3.1 (Estimation of $[u_2\,\alpha_1]_{u_2^*(\mathbf{U})}$ and $[\alpha_2\,p_2]_{u_2^*(\mathbf{U})}$ thanks to Riemann-invariant simplifications)
For both phase $k \in \{1,2\}$ define the thermodynamical coefficient:

$$\hat{\gamma}_k = \frac{C_k}{p_k} \Leftrightarrow \frac{p_k}{\rho_k} = \frac{c_k^2}{\hat{\gamma}_k}. \tag{5.46}$$

Assume that the two-phase flow is such that:

$$(u_1 - u_2)^2 \ll \frac{c_1^2}{\hat{\gamma}_1}. \tag{5.47}$$

Then, one can provide four simplified Riemann invariants related to the u_1-contact wave:

$$\begin{cases} \widetilde{\mathcal{I}}_1 = u_2, \\ \widetilde{\mathcal{I}}_2 = \alpha_1\,(u_1 - u_2), \\ \widetilde{\mathcal{I}}_3 = \alpha_1\,p_1 + \alpha_2\,p_2, \\ \widetilde{\mathcal{I}}_4 = p_1. \end{cases} \tag{5.48}$$

For a given instant t, define ϕ^+ (respectively ϕ^-) the value of the variable ϕ in the half plane $\{x > u_2^*(\mathbf{U})\,t\}$ (respectively in the half plane $\{x < u_2^*(\mathbf{U})\,t\}$). Then, equalities

$$\begin{aligned} \widetilde{\mathcal{I}}_1^- &= \widetilde{\mathcal{I}}_1^+, \\ \widetilde{\mathcal{I}}_3^- &= \widetilde{\mathcal{I}}_3^+, \\ \widetilde{\mathcal{I}}_4^- &= \widetilde{\mathcal{I}}_4^+, \end{aligned} \tag{5.49}$$

allow to find an estimation of $[u_2\,\alpha_1]_{u_2^*(\mathbf{U})}$ and $[\alpha_2\,p_2]_{u_2^*(\mathbf{U})}$:

$$[u_2\,\alpha_1]_{u_2^*(\mathbf{U})} = (u_2\,\alpha_1)^+ - (u_2\,\alpha_1)^- = +\left(\alpha_1^+ - \alpha_1^-\right)\frac{u_2^+ + u_2^-}{2}, \tag{5.50a}$$

$$[\alpha_2\,p_2]_{u_2^*(\mathbf{U})} = \left(\alpha_2\,p_2\right)^+ - \left(\alpha_2\,p_2\right)^- = -\left(\alpha_1^+ - \alpha_1^-\right)\frac{p_1^+ + p_1^-}{2}. \tag{5.50b}$$

Before detailing the proof of the above property, let us make a remark about the link between the obtained estimations (5.50a), (5.50b) and the non-conservative products path theory introduced by Dal Maso Le Floch and Murat in [4]:

Remark 5.3.2 (The choice of a path for the non-conservative products definition)
Consider

$$\begin{bmatrix} u_2 \\ 0 \\ -p_1 \\ 0 \\ +p_1 \end{bmatrix} \partial_x \alpha_1, \tag{5.51}$$

the non-conservative products differential term related to the isentropic Baer-Nunziato system. For the variable $\phi \in \{\alpha_1, u_2, p_1\}$*, let us introduce the linear path:*

$$s \in [0,1] \rightarrow \phi(s) = (1-s)\,\phi^- + s\,\phi^+. \tag{5.52}$$

Then, one can notice that:

$$\int_0^1 \begin{bmatrix} u_2(s) \\ 0 \\ -p_1(s) \\ 0 \\ +p_1(s) \end{bmatrix} \partial_s \alpha_1(s)\,\mathrm{d}s = \begin{bmatrix} +\left(\alpha_1^+ - \alpha_1^-\right)\frac{u_2^+ + u_2^-}{2} \\ 0 \\ -\left(\alpha_1^+ - \alpha_1^-\right)\frac{p_1^+ + p_1^-}{2} \\ 0 \\ +\left(\alpha_1^+ - \alpha_1^-\right)\frac{p_1^+ + p_1^-}{2} \end{bmatrix}. \tag{5.53}$$

Hence, provided the choice of the linear path (5.52), the non-conservative products path theory results in the same estimations than the approximated Riemann invariants equality (5.49).

Proof 6 (Property 5.3.1)
The proof is straightforward. It relies on the fact that one can rewrite $\mathcal{I}_3$ *as:*

$$\begin{aligned} \mathcal{I}_3 &= \alpha_1 \rho_1 (u_1 - u_2)^2 + \alpha_1 p_1 + \alpha_2 p_2 \\ &= \alpha_1 \rho_1 \left((u_1 - u_2)^2 + \frac{c_1^2}{\hat{\gamma}_1} \right) + \alpha_2 p_2. \end{aligned} \tag{5.54}$$

Using assumption (5.47), one can deduce that,

$$\mathcal{I}_3 \approx \alpha_1 \rho_1 \frac{c_1^2}{\hat{\gamma}_1} + \alpha_2 p_2 = \alpha_1 p_1 + \alpha_2 p_2 = \widetilde{\mathcal{I}}_3. \tag{5.55}$$

Thus, one can approximate equality $\mathcal{I}_3^- = \mathcal{I}_3^+$ *by,*

$$\begin{aligned} &\left(\alpha_1 p_1\right)^- + \left(\alpha_2 p_2\right)^- = \left(\alpha_1 p_1\right)^+ + \left(\alpha_2 p_2\right)^+, \\ &\qquad\qquad \Leftrightarrow \\ &\left(\alpha_2 p_2\right)^+ - \left(\alpha_2 p_2\right)^- = \left(\alpha_1 p_1\right)^- - \left(\alpha_1 p_1\right)^+. \end{aligned} \tag{5.56}$$

Besides, one can rewrite $\mathcal{I}_4$ *as:*

$$\begin{aligned} \mathcal{I}_4 &= \frac{(u_1 - u_2)^2}{2} + h_1 \\ &= \frac{(u_1 - u_2)^2}{2} + \frac{c_1^2}{\hat{\gamma}_1} + \varepsilon_1 \\ &\approx h_1. \end{aligned} \tag{5.57}$$

As a consequence if h_1 *is considered as an approximated Riemann invariants, it is also the case for* p_1 *and* ρ_1*. Thus, one can replace* $\mathcal{I}_2$ *by* $\widetilde{\mathcal{I}}_2$ *since:*

$$\mathcal{I}_2 = m_1 (u_1 - u_2) \quad = \rho_1 \alpha_1 (u_1 - u_2). \tag{5.58}$$

Finally, $\mathcal{I}_4^- = \mathcal{I}_4^+$ *can be approximated by* $p_1^- = p_1^+ \Leftrightarrow \widetilde{\mathcal{I}}_4^- = \widetilde{\mathcal{I}}_4^+$ *and the last equality in (5.56) becomes:*

$$\left(\alpha_2 p_2\right)^+ - \left(\alpha_2 p_2\right)^- = \left(\alpha_1^- - \alpha_1^+\right)\frac{p_1^+ + p_1^-}{2}, \tag{5.59}$$

which is the relation stated in (5.50b).

One can notice that in the case of an isentropic equation of state,

$$p_k = \kappa_k \rho_k^{\gamma_k}, \tag{5.60}$$

the parameter $\hat{\gamma}_k$ is equal to γ_k which is bigger than one but remains bounded. It is thus a O(1) term and inequality (5.47) is only slightly more restrictive than the classical subsonic flow condition:

$$(u_1 - u_2)^2 \ll c_1^2. \tag{5.61}$$

Let us come back to the numerical scheme (5.39), (5.41). Following equality (5.50b), one can set:

$$\begin{aligned}
\widetilde{\mathbf{b}}_{i+1/2}^n &= \begin{bmatrix} -\frac{(u_2)_{i+1}^n + (u_2)_i^n}{2} \\ 0 \\ \frac{(p_1)_{i+1}^n + (p_1)_i^n}{2} \\ 0 \\ -\frac{(p_1)_{i+1}^n + (p_1)_i^n}{2} \end{bmatrix} \left((\alpha_1)_{i+1}^n - (\alpha_1)_i^n \right), \\
\widetilde{\mathbf{b}}_i^{n+1/2} &= \begin{bmatrix} -\frac{(u_2)_{i+1/2}^{n+1/2} + (u_2)_{i-1/2}^{n+1/2}}{2} \\ 0 \\ \frac{(p_1)_{i+1/2}^{n+1/2} + (p_1)_{i-1/2}^{n+1/2}}{2} \\ 0 \\ -\frac{(p_1)_{i+1/2}^{n+1/2} + (p_1)_{i-1/2}^{n+1/2}}{2} \end{bmatrix} \left((\alpha_1)_{i+1/2}^{n+1/2} - (\alpha_1)_{i-1/2}^{n+1/2} \right).
\end{aligned} \tag{5.62}$$

The numerical method is thus completely defined. One can observe that $\widetilde{\mathbf{b}}_{i+1/2}^n / \Delta x$ (respectively $\widetilde{\mathbf{b}}_i^{n+1/2} / \Delta x$) is consistent with $-\mathbf{b}(\mathbf{U}(x_{i+1/2}, t^n))\, \partial_x \alpha_1(x_{i+1/2}, t^n)$
(respectively $-\mathbf{b}(\mathbf{U}(x_i, t^n))\, \partial_x \alpha_1(x_i, t^n)$).

In the sequel, the main properties of the numerical scheme are given.

5.3.3 Numerical scheme properties

So as to facilitate the understanding of the discrete notations, in the following any spatial index "i" refers to a quantity associated with the i-cell of the primal mesh. On the contrary, "j" stands for an j-cell located on the dual mesh.

What is more, in order to derive the discrete properties verified by the present numerical scheme one needs to specify the choice of the discrete relaxation function $(\mathbf{U}, \delta t) \to \Phi_\tau(\mathbf{U}, \delta t)$. Here, the source-term time integration is fulfilled using an *implicit* Euler method. In that case,

$$\Phi_\tau(\mathbf{U}, \delta t) = \left[\mathbf{I} - \delta t\, \partial_{\mathbf{U}} \mathbf{S}(\mathbf{U}) \right]^{-1} \delta t\, \mathbf{S}(\mathbf{U}). \tag{5.63}$$

After calculations, one obtains:

$$\Phi_\tau(\mathbf{U}, \delta t) = \begin{bmatrix} \frac{-\alpha_1 \alpha_2 (\delta t/\tau_p) \frac{\Delta p}{p_2 + p_1}}{1 + (\delta t/\tau_p) \left[(1 - 2\alpha_1) \frac{\Delta p}{p_2 + p_1} + \alpha_1 \alpha_2 \frac{\mathcal{P}}{p_2 + p_1} \right]} \\ 0 \\ \frac{\delta t/\tau_u}{1 + \delta t/\tau_u} \frac{m_1 m_2}{m_1 + m_2} \Delta u \\ 0 \\ -\frac{\delta t/\tau_u}{1 + \delta t/\tau_u} \frac{m_1 m_2}{m_1 + m_2} \Delta u \end{bmatrix}, \tag{5.64}$$

the expression of $\mathcal{P}$ being given in (5.36) and $\Delta p = p_2 - p_1$ while $\Delta u = u_2 - u_1$. Hence, one can completely write the discrete dynamics of both steps (5.39), (5.41). As a consequence, one can state the following propositions.

Proposition 5.3.1 (Conservativity and positivity of the discrete partial masses)

(i) *The discrete equation verified by* $(m_k)_i^n$, $k \in \{1,2\}$ *is conservative.*

(ii) *The discrete equation verified by* $(m_1 u_1)_i^n + (m_2 u_2)_i^n$ *is conservative.*

(iii) *Suppose that at time* t^n, *the discrete time-step is defined as:*

$$\Delta t^n = \mathscr{C} \frac{\Delta x}{\max\limits_i \left(\left| (u_1)_i^n \pm (c_1)_i^n \right|, \left| (u_2)_i^n \pm (c_2)_i^n \right| \right)}, \; 0 < \mathscr{C} < 1. \tag{5.65}$$

For $j \in \{i-1/2, i+1/2\}$ *and* $k \in \{1,2\}$ *consider* $(m_k)_j^{n+1/2}$ *the discrete partial masses solutions of* (5.39). *Then,*

$$\forall i, \; (m_k)_i^n > 0 \Rightarrow (m_k)_j^{n+1/2} > 0. \tag{5.66}$$

Consider

$$(u_k)_j^{n+1/2} = \frac{(m_k u_k)_j^{n+1/2}}{(m_k)_j^{n+1/2}}, \tag{5.67}$$

with, $(m_k u_k)_j^{n+1/2}$ *the discrete momentum solution of* (5.39). *Assume that,*

$$\left| (u_k)_j^{n+1/2} \right| \leq \max_i \left(\left| (u_1)_i^n \pm (c_1)_i^n \right|, \left| (u_2)_i^n \pm (c_2)_i^n \right| \right). \tag{5.68}$$

Then,

$$\forall j, \; (m_k)_j^{n+1/2} > 0 \Rightarrow (m_k)_i^{n+1} > 0. \tag{5.69}$$

Proof 7

(i) *In the discrete partial mass equations of both steps* (5.39), (5.41), *the discrete source terms* $\Phi_\tau\left(\mathbf{H}_{i+1/2}^n, \Delta t/2\right)$, $\Phi_\tau\left(\mathbf{U}_i^{n+1/2}, \Delta t/2\right)$ *as well as the Dirac masses* $\widetilde{\mathbf{b}}_{i+1/2}^n$, $\widetilde{\mathbf{b}}_i^{n+1/2}$ *are null. Thus, for both steps, the partial mass update is only based on a flux difference which makes the final scheme conservative.*

(ii) *Looking at the momentum discrete source term formulas in* (5.64) *as well as the discrete momentum contributions of the Dirac masses in* (5.62), *one can notice that, for both steps* (5.39), (5.41),

$$\begin{cases} \left\{\Phi_\tau\left(\mathbf{H}_{i+1/2}^n, \Delta t/2\right)\right\}_{(m_1u_1)} + \left\{\Phi_\tau\left(\mathbf{H}_{i+1/2}^n, \Delta t/2\right)\right\}_{(m_2u_2)} = 0, \\ \left\{\widetilde{\mathbf{b}}_{i+1/2}^n\right\}_{(m_1u_1)} + \left\{\widetilde{\mathbf{b}}_{i+1/2}^n\right\}_{(m_2u_2)} = 0, \\ \\ \left\{\Phi_\tau\left(\mathbf{U}_i^{n+1/2}, \Delta t/2\right)\right\}_{(m_1u_1)} + \left\{\Phi_\tau\left(\mathbf{U}_i^{n+1/2}, \Delta t/2\right)\right\}_{(m_2u_2)} = 0, \\ \left\{\widetilde{\mathbf{b}}_i^{n+1/2}\right\}_{(m_1u_1)} + \left\{\widetilde{\mathbf{b}}_i^{n+1/2}\right\}_{(m_2u_2)} = 0. \end{cases} \tag{5.70}$$

Thus, for both steps, the momentum mixture update is only based on a flux difference which makes the final scheme conservative for this quantity.

(iii) *Let us start by focusing on implication* (5.66). *In the first step* (5.39), *in absence of mass transfer, one knows that* $\forall l \in \{i+1, i\}$,

$$(m_1)_l^{n+1/2} = (m_1)_l^n. \tag{5.71}$$

Thus, introducing

$$(u_1)_l^{n+1/2} = (m_1 u_1)_l^{n+1/2} / (m_1)_l^{n+1/2}, \tag{5.72}$$

the discrete equation related to the partial mass m_1 *can be written:*

$$\begin{aligned} &(m_1)_{i+1/2}^{n+1/2} = \frac{1}{2}\left(1 - \frac{\Delta t}{\Delta x}(u_1)_{i+1}^{n+1/2}\right)(m_1)_{i+1}^n + \frac{1}{2}\left(1 + \frac{\Delta t}{\Delta x}(u_1)_i^{n+1/2}\right)(m_1)_i^n, \\ &\forall l \in \{i+1, i\}: \\ &(u_1)_l^{n+1/2} = \left(1 - \frac{\frac{\Delta t}{2\tau_u}}{1 + \frac{\Delta t}{2\tau_u}} \frac{(m_2)_l^n}{(m_1)_l^n + (m_2)_l^n}\right)(u_1)_l^n + \left(\frac{\frac{\Delta t}{2\tau_u}}{1 + \frac{\Delta t}{2\tau_u}} \frac{(m_2)_l^n}{(m_1)_l^n + (m_2)_l^n}\right)(u_2)_l^n. \end{aligned} \tag{5.73}$$

Hence, $\forall\, l \in \{i+1,\, i\}$,

$$(u_1)_l^{n+1/2} \in \left[\min_{k\in\{1,2\},\ l'\in\{i+1,\,i\}} (u_k)_{l'}^n,\ \max_{k\in\{1,2\},\ l'\in\{i+1,\,i\}} (u_k)_{l'}^n \right]. \tag{5.74}$$

Thus, under the CFL condition (5.65) $(m_1)_{i+1/2}^{n+1/2}$ *is positive. The same result holds for* $(m_2)_{i+1/2}^{n+1/2}$. *During the second step* (5.41), *the same equalities that in* (5.73) *hold after having replaced the spatial indexes* $\{i+1,\, i\}$ *by* $\{i+1/2,\, i-1/2\}$ *and the time indexes* $\{n+1/2,\, n\}$ *by* $\{n+1,\, n+1/2\}$. *Then, assumption* (5.68), *which is non-trivial a priori, ensures that* $\forall\, j \in \{i+1/2,\, i-1/2\}$,

$$1 \pm \frac{\Delta t}{\Delta x} (u_1)_j^{n+1} > 0, \tag{5.75}$$

which implies that $(m_1)_i^{n+1}$ *is positive.*

The next proposition deals with the ability of the scheme to maintain the volume fraction α_1 in the interval $]0,\, 1[$ from one time-step to another. As it will be seen later on, such a property is obtained after having modified the discrete pressure relaxation source term. The remark below introduces such a new time integration operator.

Remark 5.3.3 (Another choice for the discrete pressure relaxation time integration)
Consider the implicit Euler discrete relaxation operator written in (5.63) *and* (5.64). *One can observe that if the matrix* $[\mathbf{I} - \delta t\, \partial_{\mathbf{U}} \mathbf{S}(\mathbf{U})]^{-1}$ *is approximated by* $[\mathbf{I} - \delta t\, \partial_{\mathbf{U}} \mathbf{S}(\mathbf{U})]_{\boldsymbol{eq}}^{-1}$, *which stands for its value on the equilibrium manifold*

$$\left\{ \mathbf{U},\ s.\ t.\ \Delta p = 0,\ \Delta u = 0 \right\}, \tag{5.76}$$

then, the implicit Euler time-integration operator simplifies into:

$$[\mathbf{I} - \delta t\, \partial_{\mathbf{U}} \mathbf{S}(\mathbf{U})]_{\boldsymbol{eq}}^{-1}\, \delta t\, \mathbf{S}(\mathbf{U}) = \begin{bmatrix} \dfrac{-\alpha_1\alpha_2\,(\delta t/\tau_p)\,\frac{\Delta p}{p_2+p_1}}{1+(\delta t/\tau_p)\,\frac{\alpha_1 C_2+\alpha_2 C_1}{p_2+p_1}} \\ 0 \\ \dfrac{\delta t/\tau_u}{1+\delta t/\tau_u}\,\dfrac{m_1 m_2}{m_1+m_2}\,\Delta u \\ 0 \\ -\dfrac{\delta t/\tau_u}{1+\delta t/\tau_u}\,\dfrac{m_1 m_2}{m_1+m_2}\,\Delta u \end{bmatrix}. \tag{5.77}$$

Proposition 5.3.2 (Maximum principle on the volume fraction)
Consider the approximated pressure relaxation operator written in (5.77). *The discrete equation of the volume fraction during the first step* (5.39) *writes:*

$$\begin{aligned} (\alpha_1)_{i+1/2}^{n+1/2} = (\alpha_1)_{i+1/2}^n - \frac{\Delta t}{2\Delta x} (u_2)_{i+1/2}^n \left((\alpha_1)_{i+1}^n - (\alpha_1)_i^n \right) \\ - (\alpha_1)_{i+1/2}^n (\alpha_2)_{i+1/2}^n \frac{\left(\Delta t/2\tau_p\right) \left(\frac{\Delta p}{p_2+p_1}\right)_{i+1/2}^n}{1 + \left(\Delta t/2\tau_p\right) \left(\frac{\alpha_1 C_2+\alpha_2 C_1}{p_2+p_1}\right)_{i+1/2}^n}, \end{aligned} \tag{5.78}$$

with

$$\begin{cases} (\alpha_1)_{i+1/2}^n = \dfrac{(\alpha_1)_{i+1}^n + (\alpha_1)_i^n}{2}, \\ (u_2)_{i+1/2}^n = \dfrac{(u_2)_{i+1}^n + (u_2)_i^n}{2}, \\ \left(\dfrac{\Delta p}{p_2+p_1}\right)_{i+1/2}^n = \left(\dfrac{\Delta p}{p_2+p_1}\right)^{func} \left(\dfrac{\mathbf{U}_{i+1}^n + \mathbf{U}_i^n}{2}\right), \\ \left(\dfrac{\alpha_1 C_2+\alpha_2 C_1}{p_2+p_1}\right)_{i+1/2}^n = \left(\dfrac{\alpha_1 C_2+\alpha_2 C_1}{p_2+p_1}\right)^{func} \left(\dfrac{\mathbf{U}_{i+1}^n + \mathbf{U}_i^n}{2}\right), \end{cases} \tag{5.79}$$

noting $\mathbf{U} \rightarrow \phi^{func}(\mathbf{U})$, *the variable* ϕ *expressed as a function of* $\mathbf{U}$. *Assume that each phase* k *is endowed with an EOS sucht that*

$$\hat{\gamma}_k = \frac{C_k}{p_k} > 1, \text{ with } C_k = \rho_k c_k^2. \tag{5.80}$$

Then, under the modified CFL condition

$$\Delta t^n = \mathscr{C} \frac{\Delta x \, (1-\Phi^n)}{\max\limits_i \left(\left| (u_1)_i^n \pm (c_1)_i^n \right|, \left| (u_2)_i^n \pm (c_2)_i^n \right| \right)}, \; 0 < \mathscr{C} < 1, \tag{5.81}$$

with,

$$\Phi^n = \max_{i+1/2} \left(\left| \Phi_{i+1/2}^n \right| \right), \tag{5.82}$$

and

$$\left| \Phi_{i+1/2}^n \right| = \begin{cases} \dfrac{\left| (\Delta p)_{i+1/2}^n \right|}{\left(\frac{\alpha_1}{\alpha_2} \right)_{i+1/2}^n (C_2)_{i+1/2}^n + (C_1)_{i+1/2}^n} & \text{if } \left(\dfrac{\alpha_1}{\alpha_2} \right)_{i+1/2}^n > 1, \\ \dfrac{\left| (\Delta p)_{i+1/2}^n \right|}{(C_2)_{i+1/2}^n + \left(\frac{\alpha_2}{\alpha_1} \right)_{i+1/2}^n (C_1)_{i+1/2}^n} & \text{otherwise,} \end{cases} \tag{5.83}$$

the discrete maximum principle holds for $(\alpha_1)_{i+1/2}^{n+1/2}$, *that is:*

$$\forall i, \; (\alpha_1)_i^n \in]0,1[\quad \Rightarrow \quad (\alpha_1)_{i+1/2}^{n+1/2} \in]0,1[. \tag{5.84}$$

Proof 8
Let us consider the non-restrictive case where $\left(\dfrac{\alpha_1}{\alpha_2} \right)_{i+1/2}^n > 1$. *Define*

$$\Psi_{i+1/2}^n = (\alpha_2)_{i+1/2}^n \frac{\left(\Delta t / 2\tau_p \right) \left(\dfrac{\Delta p}{p_2 + p_1} \right)_{i+1/2}^n}{1 + \left(\Delta t / 2\tau_p \right) \left(\dfrac{\alpha_1 C_2 + \alpha_2 C_1}{p_2 + p_1} \right)_{i+1/2}^n}. \tag{5.85}$$

Using inequality (5.80), *one can deduce that,*

$$\left| \Psi_{i+1/2}^n \right| = \left| \frac{\left(\Delta t / 2\tau_p \right) \left(\dfrac{\Delta p}{p_2 + p_1} \right)_{i+1/2}^n}{\dfrac{1}{(\alpha_2)_{i+1/2}^n} + \left(\Delta t / 2\tau_p \right) \left(\dfrac{\left(\frac{\alpha_1}{\alpha_2} \right) \hat{\gamma}_2 p_2 + \hat{\gamma}_1 p_1}{p_2 + p_1} \right)_{i+1/2}^n} \right| < \left| \Phi_{i+1/2}^n \right| < 1, \tag{5.86}$$

with $\left| \Phi_{i+1/2}^n \right|$ *given in* (5.83). *Injecting the expression of* $\Psi_{i+1/2}^n$ *in* (5.78), *the discrete dynamics of* α_1 *can be rewritten:*

$$(\alpha_1)_{i+1/2}^{n+1/2} = \frac{1}{2} \left[1 - \Psi_{i+1/2}^n + \frac{\Delta t}{\Delta x} (u_2)_{i+1/2}^n \right] (\alpha_1)_{i+1}^n + \frac{1}{2} \left[1 - \Psi_{i+1/2}^n - \frac{\Delta t}{\Delta x} (u_2)_{i+1/2}^n \right] (\alpha_1)_i^n. \tag{5.87}$$

One can notice that equality (5.81) *is a sufficient condition guaranteeing*

$$\frac{1}{2} \left[1 - \Phi_{i+1/2}^n \pm \frac{\Delta t}{\Delta x} (u_2)_{i+1/2}^n \right] \in]0,1[. \tag{5.88}$$

Looking at the modified CFL condition (5.81), one can observe that in regions where one of the phases vanishes we have $\left(\dfrac{\alpha_2}{\alpha_1} \right)_{i+1/2}^n \rightarrow +\infty$ or $\left(\dfrac{\alpha_1}{\alpha_2} \right)_{i+1/2}^n \rightarrow +\infty$; implying that $\left| \Phi_{i+1/2}^n \right| \rightarrow 0$. Thus, the local time-step built using $\left| \Phi_{i+1/2}^n \right|$ becomes identical to the classical CFL condition for the isentropic Baer-Nunziato system (5.65). On the contrary, the highest depreciation of the local time-step is observed in mixing regions where $\left(\dfrac{\alpha_2}{\alpha_1} \right)_{i+1/2}^n \approx 1$. Such a depreciation actually results from the choice of the implicit time-integration technique which is based on a *linearization* of the

pressure source term. This choice has been initially made to remain as close as possible to the Bereux-Sainsaulieu generalized linear Riemann problem formalism (5.1). It is also to circumvent the computational cost involved in the resolution of a non-linear system.

However, beyond the more constraining CFL condition, Proposition 5.3.2 has the disadvantage to potentially impose non-physical bounds to the volume fraction values. Indeed, looking at equality (5.87), one can observe that, whatever is the pressure difference $(\Delta p)^n_{i+1/2}$, the averaged volume fraction $(\alpha_1)^{n+1/2}_{i+1/2}$ cannot leave the interval between the minimum and the maximum values of the couple $\{(\alpha_1)^n_i, (\alpha_1)^n_{i+1}\}$. As a result, the present scheme might have difficulties to reach the right volume fraction equilibrium value.

In order to cure this drawback, another alternative is proposed for the discretization of the volume fraction equation. The idea stems from [8] and has been used in [5]. It is summarized in the property below.

Property 5.3.2 (Another discretization for the volume fraction equation)
Define

$$\left\{\Phi_\tau\left(\mathbf{H}^n_{i+1/2}, \Delta t/2\right)\right\}_{\alpha_1}, \ \left\{\widetilde{\mathbf{b}}^n_{i+1/2}\right\}_{\alpha_1}, \tag{5.89}$$

the discrete relaxation source term and the non-conservative product components related to the volume fraction equation. Consider the first step (5.39) of the proposed time-implicit staggered scheme after having removed those terms.

If, at the end of such a step, the volume fraction update is given by the resolution of the non-linear system:

$$\begin{aligned}\frac{(\alpha_1)^{n+1/2}_{i+1/2} - (\alpha_1)^n_{i+1/2}}{\Delta t/2} &= \frac{\left\{\widetilde{\mathbf{b}}^n_{i+1/2}\right\}_{\alpha_1}}{\Delta x} \\ &\quad - \frac{1}{\tau_p}\left(\frac{\alpha_1\alpha_2}{p_2+p_1}\right)^n_{i+1/2}\left[p_2\left(\frac{(m_2)^{n+1/2}_{i+1/2}}{1-(\alpha_1)^{n+1/2}_{i+1/2}}\right) - p_1\left(\frac{(m_1)^{n+1/2}_{i+1/2}}{(\alpha_1)^{n+1/2}_{i+1/2}}\right)\right],\end{aligned} \tag{5.90}$$

with $(m_1)^{n+1/2}_{i+1/2}$, $(m_2)^{n+1/2}_{i+1/2}$ the partial masses obtained in (5.39); then provided that these partial masses are positive,

$$(\alpha_1)^{n+1/2}_{i+1/2} \in]0,1[, \tag{5.91}$$

without any additional constraint on the time-step.

Proof 9
Let us introduce the function

$$\mathcal{G}(\alpha_1, m_1, m_2, r) = \alpha_1 + r\left[p_2\left(\frac{m_2}{1-\alpha_1}\right) - p_1\left(\frac{m_1}{\alpha_1}\right)\right], \tag{5.92}$$

with $r>0$, $m_2>0$, $m_1>0$. Under the EOS assumptions (4.4) made in the previous chapter one can notice that:

$$\begin{aligned}&\partial_{\alpha_1}\mathcal{G}(\alpha_1, m_1, m_2, r) = 1 + r\left[\frac{m_2}{(1-\alpha_1)^2}c_2^2\left(\frac{m_2}{1-\alpha_1}\right) + \frac{m_1}{(\alpha_1)^2}c_1^2\left(\frac{m_1}{\alpha_1}\right)\right] > 0, \\ &\lim_{\alpha_1\to 0^+}\mathcal{G}(\alpha_1, m_1, m_2, r) = -\infty, \ \lim_{\alpha_1\to 1^-}\mathcal{G}(\alpha_1, m_1, m_2, r) = +\infty.\end{aligned} \tag{5.93}$$

Hence, after having fixed the parameters r, m_1 and m_2, one can deduce that $\alpha_1 \to \mathcal{G}(\alpha_1, m_1, m_2, r)$ is bijective from $]0,1[$ to $\mathbb{R}$. The proof ends by observing that equality (5.90) can be recast as

$$\mathcal{G}\left((\alpha_1)^{n+1/2}_{i+1/2}, (m_1)^{n+1/2}_{i+1/2}, (m_2)^{n+1/2}_{i+1/2}, \frac{\Delta t}{2\tau_p}\left(\frac{\alpha_1\alpha_2}{p_2+p_1}\right)^n_{i+1/2}\right) = (\alpha_1)^n_{i+1/2} + \frac{\Delta t}{2\Delta x}\left\{\widetilde{\mathbf{b}}^n_{i+1/2}\right\}_{\alpha_1}. \tag{5.94}$$

As a consequence, there exists a unique $(\alpha_1)^{n+1/2}_{i+1/2} \in]0,1[$ solution of (5.94).

In the above proposition, one has to highlight that the partial mass positivity assumptions hold thanks to Proposition 5.3.1 under the classical CFL condition (5.65). In the sequel, the proposed time-implicit staggered scheme solves equation (5.90) using a dichotomy method in order to obtain the volume fraction update.

The above discrete properties take part of the most essential requirements for the computation of two-phase flows using the isentropic Baer-Nunziato system. Other alternatives like fractional step methods fulfill these requirements and thus constitute a benchmark for the proposed scheme. These numerical approaches are presented below.

5.3.4 Fractional step methods

As it will be seen in the numerical result section below, the present numerical scheme is compared with fractional step methods. That is why in this subsection, we recall the two main steps of these approaches. The time integration procedure of the relaxation source terms is notably completely written. In a compact form, the overall fractional step strategy reads:

$$\left\{\begin{array}{l} \mathbf{U}_i^{n+} = \Phi_\tau^{\mathrm{FS}}\left(\mathbf{U}_i^n, \Delta t\right), \\ \mathbf{U}_i^{n+1} = \mathbf{U}_i^{n+} - \dfrac{\Delta t}{\Delta x}\left(\mathbf{F}_{\mathrm{L}}\left(\mathbf{U}_{i+1}^{n+}, \mathbf{U}_i^{n+}\right) - \mathbf{F}_{\mathrm{R}}\left(\mathbf{U}_i^{n+}, \mathbf{U}_{i-1}^{n+}\right)\right). \end{array}\right. \tag{5.95}$$

First equation in (5.95) corresponds to the discrete time-integration of the ODEs system:

$$\begin{array}{l} \dfrac{\mathrm{d}\alpha_1}{\mathrm{d}t} = -\dfrac{\alpha_1\alpha_2}{\tau_{\mathrm{p}}}\dfrac{\Delta p}{p_2+p_1}, \\ \forall k \in \{1,2\}: \\ \dfrac{\mathrm{d}m_k}{\mathrm{d}t} = 0, \ \dfrac{\mathrm{d}m_k u_k}{\mathrm{d}t} = (-1)^{k+1}\dfrac{m_1 m_2}{m_1+m_2}\dfrac{\Delta u}{\tau_{\mathrm{u}}}. \end{array} \tag{5.96}$$

Following the velocity-pressure splitting strategy proposed in [6], the velocity relaxation is based on a *time-implicit* scheme associated with the system:

$$\begin{array}{l} \dfrac{\mathrm{d}\alpha_1}{\mathrm{d}t} = 0, \\ \forall k \in \{1,2\}: \\ \dfrac{\mathrm{d}m_k}{\mathrm{d}t} = 0, \ \dfrac{\mathrm{d}u_k}{\mathrm{d}t} = (-1)^{k+1}\dfrac{m_{3-k}}{m_1+m_2}\dfrac{\Delta u}{\tau_{\mathrm{u}}}. \end{array} \tag{5.97}$$

It leads to the velocity updates:

$$\begin{array}{rcl} (u_1)_i^{n+} & = & \frac{1+(\mathrm{Y}_1)_i^n(\Delta t/\tau_{\mathrm{u}})}{1+(\Delta t/\tau_{\mathrm{u}})}(u_1)_i^n + \frac{(\mathrm{Y}_2)_i^n(\Delta t/\tau_{\mathrm{u}})}{1+(\Delta t/\tau_{\mathrm{u}})}(u_2)_i^n, \\ (u_2)_i^{n+} & = & \frac{(\mathrm{Y}_1)_i^n(\Delta t/\tau_{\mathrm{u}})}{1+(\Delta t/\tau_{\mathrm{u}})}(u_1)_i^n + \frac{1+(\mathrm{Y}_2)_i^n(\Delta t/\tau_{\mathrm{u}})}{1+(\Delta t/\tau_{\mathrm{u}})}(u_2)_i^n. \end{array} \tag{5.98}$$

One can note that the transfer matrix allowing to obtain $\left[(u_1)_i^{n+}, (u_2)_i^{n+}\right]^{\mathrm{T}}$ from $\left[(u_1)_i^n, (u_2)_i^n\right]^{\mathrm{T}}$ is identical to the one associated with the implicit Euler time integration method proposed in (5.64). As for the pressure relaxation, it is taken into account by focusing on the system

$$\begin{array}{l} \dfrac{\mathrm{d}\alpha_1}{\mathrm{d}t} = -\dfrac{\alpha_1\alpha_2}{\tau_{\mathrm{p}}}\dfrac{\Delta p}{p_2+p_1}, \\ \forall k \in \{1,2\}: \\ \dfrac{\mathrm{d}m_k}{\mathrm{d}t} = 0, \ \dfrac{\mathrm{d}m_k u_k}{\mathrm{d}t} = 0. \end{array} \tag{5.99}$$

Following, the same technique than the one presented in Property 5.3.2, the volume fraction update is given by

$$\frac{(\alpha_1)_i^{n+} - (\alpha_1)_i^n}{\Delta t/2} = -\frac{1}{\tau_p}\left(\frac{\alpha_1\alpha_2}{p_2+p_1}\right)_i^n \left[p_2\left(\frac{(m_2)_i^{n+}}{1-(\alpha_1)_i^{n+}}\right) - p_1\left(\frac{(m_1)_i^{n+}}{(\alpha_1)_i^{n+}}\right)\right], \tag{5.100}$$
$$\forall k \in \{1,2\},\ (m_k)_i^{n+} = (m_k)_i^n.$$

It guarantees existence and uniqueness of $(\alpha_1)_i^{n+}$ in the interval $]0,1[$ provided that $(m_k)_i^n > 0$.

The second equality in (5.95) is linked to the resolution of local *homogeneous* Riemann problems for the isentropic Baer-Nunziato system. For a given face noted f separating two constant states $\mathbf{U}_L$ and $\mathbf{U}_R$, $\mathbf{F}_L(\mathbf{U}_L, \mathbf{U}_R)$ (respectively $\mathbf{F}_R(\mathbf{U}_L, \mathbf{U}_R)$) stands for the combined contribution of a conservative flux and a non-conservative term acting on the left cell (respectively on the right cell) with respect to face f.

In the numerical results section, two kinds of discretization for $\mathbf{F}_L(\mathbf{U}_L, \mathbf{U}_R)$ and $\mathbf{F}_R(\mathbf{U}_L, \mathbf{U}_R)$ are involved. The first one corresponds to the Rusanov scheme whose numerical flux is given in equation (4.124) of the previous chapter. This scheme is very simple to implement. However it does not belong to the category of approximate Riemann solvers and the non-centered part of its flux is known to be diffusive. As for the non-conservative part of such a method, it is discretized using the *free-streaming* physical condition proposed in [9].

The second numerical method is based on the HLLAC scheme proposed by Lochon *et al.* in [7] inspired from the work of Tokareva and Toro [11]. It has been adapted to the isentropic Baer-Nunziato system in subsonic configurations. We briefly recall that such a scheme is an approximate Riemann solver. The genuinely non-linear waves related to $u_k \pm c_k,\ k \in \{1,2\}$ are taken into account through HLLC-like jump conditions (see [12] for additional details). Besides, the presence of the u_2-contact wave is also considered in the numerical flux construction. Indeed, the resolution of the Riemann solver intermediate states ends up with the equality of the approximated Riemann invariants (5.48) obtained in subsonic configurations. Eventually the discretization of the non-conservative part of the system is performed using the *thin layer approximation* proposed by Schwendeman *et al.* in [10]. The reader is referred to [7] or to subsection A for additional details on this approach. Before going further on, let us make some comments about the position of the proposed approach with respect to the Rusanov and the HLLAC schemes.

Remark 5.3.4 (On the position of the proposed method between the Rusanov and the HLLAC schemes)
Recall that the proposed scheme is based on the time evolution of space-averaged state vectors centered around primal or dual-mesh faces. As a consequence, all the wealth of information contained in the local-face convective fluxes of approximate Riemann solvers is, in the present case, diluted into the space-averaging process. According to our understanding, this is the price to be paid for not knowing the shape of the exact solution of generalized non-linear Riemann problems.

Hence, when source terms are omitted, we may expect that the proposed numerical scheme is closer to the Rusanov scheme than to the HLLAC one.

After having briefly presented the numerical methods which will constitute the benchmark for the present approach, one can switch to the next section dedicated to numerical results.

5.4 Numerical results

The scheme (5.39), (5.41) resulting from the extension of the Bereux-Sainsaulieu approach is now applied to a series of numerical applications. The first two ones are verification test cases related to the analytical solution exhibited in (5.23). They aim at checking that, when applied to a hand-made linear frozen model, the scheme stemming from the ODEs system derived in (5.26) converges towards the expected solution.

A third test case is a Riemann problem based on the *homogeneous* isentropic Baer-Nunziato system for which an analytical solution can be found. Finally, pressure and velocity relaxation source terms are added and a generalized non-linear Riemann problem is performed. In that case no analytical solution is available. The present scheme is compared with a fractional step methods involving the Rusanov scheme and an HLLAC approximate Riemann solver.

5.4.1 Verification test cases of a hand-made linear frozen model

In this subsection, one concentrates on a generalized linear Riemann problem with linear independent time-relaxation processes and a frozen mass Dirac measure. Consider a computational domain of length $\mathrm{L} = 1\,m$. The problem reads:

$$\begin{aligned} &\partial_t \mathbf{U} + \underline{\underline{\mathbf{C}}}_0\, \partial_x \mathbf{U} = -\underline{\underline{\mathbf{R}}}_0\, \underline{\underline{\tau}}^{-1}\, \underline{\underline{\mathbf{R}}}_0^{-1} \left(\mathbf{U} - \mathbf{U}^{\mathrm{eq}}\right) + \mathbf{b}_0\, \delta_{\{x=u_{\mathrm{I}}^*\, t\}}, \\ &\mathbf{U}(.,\, t=0) = \begin{cases} \mathbf{U}_{\mathrm{L}}^0 \text{ if } x < 0.5, \\ \mathbf{U}_{\mathrm{R}}^0 \text{ if } x > 0.5. \end{cases} \end{aligned} \tag{5.101}$$

Consider $\mathbf{W}_{\mathrm{L}}^0$ and $\mathbf{W}_{\mathrm{R}}^0$ two state vectors whose values are given in Table 5.1. Then, define

	α_1	$u_1\ (m.s^{-1})$	p_1 (bar)	$u_2\ (m.s^{-1})$	p_2 (bar)
$\mathbf{W}_{\mathrm{L}}^0$	0.8	5	4	2	2
$\mathbf{W}_{\mathrm{R}}^0$	0.2	3	5	4.5	3.5

Table 5.1 – Linear Riemann problem with dirac mass: initial conditions

$$\mathbf{U}_{\mathrm{L}}^0 = \mathbf{U}\left(\mathbf{W}_{\mathrm{L}}^0\right),\, \mathbf{U}_{\mathrm{R}}^0 = \mathbf{U}\left(\mathbf{W}_{\mathrm{R}}^0\right),\, \mathbf{U}_0 = \mathbf{U}\left(\frac{\mathbf{W}_{\mathrm{R}}^0 + \mathbf{W}_{\mathrm{L}}^0}{2}\right). \tag{5.102}$$

In this hand-made model, $\underline{\underline{\mathbf{C}}}_0 = \underline{\underline{\mathbf{C}}}(\mathbf{U}_0)$ with $\mathbf{U} \to \underline{\underline{\mathbf{C}}}(\mathbf{U})$ the Jacobian matrix of the isentropic Baer-Nunziato system written in (4.15). Note that the contributions of the non-conservative products are included inside $\underline{\underline{\mathbf{C}}}_0$. As a consequence, five eigenvalues

$$\lambda_1^0 = u_2^0,\ \lambda_2^0 = (u_1 + c_1)^0,\ \lambda_3^0 = (u_1 - c_1)^0,\ \lambda_4^0 = (u_2 + c_2)^0,\ \lambda_5^0 = (u_2 - c_2)^0, \tag{5.103}$$

associated with five contact discontinuities are linked to $\underline{\underline{\mathbf{C}}}_0$. Besides, the constant speed u_{I}^*, associated with the Dirac mass function is chosen such that:

$$\max\left((u_1 - c_1)^0, (u_2 - c_2)^0\right) \ll u_2^0 \ll u_{\mathrm{I}}^* < \min\left((u_1 + c_1)^0, (u_2 + c_2)^0\right). \tag{5.104}$$

Hence, the Dirac measure adds a sixth discontinuous front in the computational domain which, in this case, is completely independent from the five linearized Baer-Nunziato contact waves. Nevertheless, for the sake of coherence, the constant mass $\mathbf{b}_0$ of the Dirac measure has the same structure as the non-conservative terms of the Baer-Nunziato isentropic system:

$$\mathbf{b}_0 = \begin{bmatrix} -u_{\mathrm{I}}^* \\ 0 \\ +p_{\mathrm{I}}^0 \\ 0 \\ -p_{\mathrm{I}}^0 \end{bmatrix} \left((\alpha_1)_{\mathrm{R}}^0 - (\alpha_1)_{\mathrm{L}}^0\right), \tag{5.105}$$

with,

$$p_{\mathrm{I}}^0 = \mathrm{Y}_2^0\, p_1^0 + \mathrm{Y}_1^0\, p_2^0,\ \mathrm{Y}_k^0 = \frac{m_k^0}{m^0},\ m^0 = m_1^0 + m_2^0, \tag{5.106}$$

the masses m_k^0 and the pressures p_k^0 being calculated from the state $\mathbf{U}^0$. In (5.101), the equilibrium state writes $\mathbf{U}^{\mathrm{eq}} = \mathbf{U}\left(\mathbf{W}^{\mathrm{eq}}\right)$, with $\mathbf{W}^{\mathrm{eq}}$ given in Table 5.2.

	α_1	$u_1\ (m.s^{-1})$	p_1 (bar)	$u_2\ (m.s^{-1})$	p_2 (bar)
$\mathbf{W}^{eq}$	0.5	3	3	3	3

Table 5.2 – Linear Riemann problem with dirac mass: equilibrium state

For both phases, the isentropic EOS reads:

$$\begin{aligned} &\forall k \in \{1,2\},\ p_k = \kappa_k \left(\rho_k\right)^{\gamma_k}, \\ &\kappa_1 = 10^3\ \mathrm{J}\,(kg)^{-1}\,\mathrm{K}^{-1},\ \gamma_1 = 5, \\ &\kappa_2 = 10^3\ \mathrm{J}\,(kg)^{-1}\,\mathrm{K}^{-1},\ \gamma_2 = 4. \end{aligned} \tag{5.107}$$

Finally, the time of the simulation is $\mathrm{T_{end}} = 3\times 10^{-4}\,s$ and $u_{\mathrm{I}}^* = 10^2\,m.s^{-1}$.

For the sake of completeness, the numerical scheme used to solve the above hand-made problem is provided below. Let us first introduce the function

$$\chi_{\frac{\Delta x}{2}}(x) = \begin{cases} 1 & \text{if } x \in \left]-\frac{\Delta x}{2}, \frac{\Delta x}{2}\right[, \\ 0 & \text{otherwise,} \end{cases} \tag{5.108}$$

and $x_0 = 0.5\,m$, the center of the computational domain. Noting $\mathbf{H}_{i+1/2}^n = \left(\mathbf{U}_{i+1}^n + \mathbf{U}_i^n\right)/2$, the first step writes:

$$\begin{cases} \mathbf{H}_{i+1/2}^{n+1/2} = \mathbf{H}_{i+1/2}^n + (\Delta t/2)\,\Phi_\tau\left(\mathbf{H}_{i+1/2}^n, \Delta t/2\right) \\ \qquad -\dfrac{\Delta t}{2\Delta x}\underline{\underline{\mathbf{C}}}_0\left(\mathbf{U}_{i+1}^{n+1/2} - \mathbf{U}_i^{n+1/2}\right) + \dfrac{\Delta t}{2\Delta x}\mathbf{b}_0\,\chi_{\frac{\Delta x}{2}}\left(x_{i+1/2} - x_0 - u_{\mathrm{I}}^*\,t^n\right), \\ \quad \forall j \in \{i, i+1\}: \\ \mathbf{U}_j^{n+1/2} = \mathbf{U}_j^n + (\Delta t/2)\,\Phi_\tau\left(\mathbf{U}_j^n, \Delta t/2\right). \end{cases} \tag{5.109}$$

Then, the primal mesh update being defined as $\mathbf{U}_i^{n+1/2} = \left(\mathbf{H}_{i+1/2}^{n+1/2} + \mathbf{H}_{i-1/2}^{n+1/2}\right)/2$, the second step reads:

$$\begin{cases} \mathbf{U}_i^{n+1} = \mathbf{U}_i^{n+1/2} + (\Delta t/2)\,\Phi_\tau\left(\mathbf{U}_i^{n+1/2}, \Delta t/2\right) \\ \qquad -\dfrac{\Delta t}{2\Delta x}\underline{\underline{\mathbf{C}}}_0\left(\mathbf{H}_{i+1/2}^{n+1} - \mathbf{H}_{i-1/2}^{n+1}\right) + \dfrac{\Delta t}{2\Delta x}\mathbf{b}_0\,\chi_{\frac{\Delta x}{2}}\left(x_i - x_0 - u_{\mathrm{I}}^*\,t^{n+1/2}\right), \\ \quad \forall j \in \{i-1/2, i+1/2\}: \\ \mathbf{H}_j^{n+1} = \mathbf{H}_j^{n+1/2} + (\Delta t/2)\,\Phi_\tau\left(\mathbf{H}_j^{n+1/2}, \Delta t/2\right). \end{cases} \tag{5.110}$$

The above scheme is thus very similar to the one presented in (5.39), (5.41). The only difference is that the frozen Dirac mass contribution $\mathbf{b}_0$ is only active in the dual or primal cells crossed by the front line $t \to u_{\mathrm{I}}^*\,t$.

Let us end this paragraph by saying that in the two following verification test cases the time-step is determined using the classical Baer-Nunziatio CFL condition (5.65) with $\mathscr{C} = 0.45$.

In the sequel, convergence curves and variable profiles are displayed in the case where relaxation source terms are not present in the hand-made system (5.101).

Case with no linear relaxation

Consider the configuration where the relaxation effects are canceled: $\underline{\underline{\tau}}^{-1} = \underline{\underline{\mathbf{0}}}$. Thus, attention is paid to the effect of the presence of the Dirac measure in system (5.101). Recall that according to the analytical solution derived in (5.23), after having imposed $\forall k \in [1,5]\ \ \mu_k = 0$, one can write:

$$\begin{aligned} \mathbf{U}^{\mathrm{exact}}(x,t) = &\sum_{k=1}^{5}\left\{\mathbf{a}_k^0(x,t) - [\mathbf{a}_k]_{u_{\mathrm{I}}^*}\,\mathrm{H}\left(x - \lambda_k^0\,t\right)\right\}\mathbf{r}_k^0 \\ &+\left\{\sum_{k=1}^{5}[\mathbf{a}_k]_{u_{\mathrm{I}}^*}\,\mathbf{r}_k^0\right\}\mathrm{H}\left(x - u_{\mathrm{I}}^*\,t\right), \end{aligned} \tag{5.111}$$

with,

$$\mathbf{a}_k^0(x,\,t) = \left[(\mathbf{a}_{\mathrm{L}}^0)_k + (\mathbf{a}_{\mathrm{R}}^0 - \mathbf{a}_{\mathrm{L}}^0)_k\,\mathrm{H}\left(x - \lambda_k^0\,t\right)\right]. \tag{5.112}$$

The analytical solution is thus self-similar and jumps through the additional discontinuous front line $t \to u_{\mathrm{I}}^*\,t$.

Figure 5.2 displays the convergence curves of $[\alpha_1,\,p_1,\,u_1,\,p_2,\,u_2]$ for meshes varying from 10^2 to 10^4 cells.

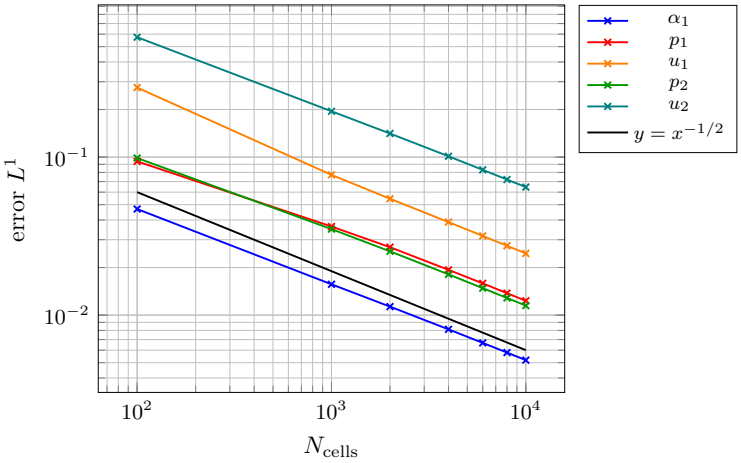

Figure 5.2 – Convergence curve: linear Riemann problem with Dirac mass

It turns out that the numerical scheme (5.109), (5.110) converges towards the analytical solution (5.111). Besides, one can observe that the rate of convergence is not modified by the presence of the Dirac measure. Indeed, the measured order is 1/2 which is the expected order when contact discontinuities are present in the computational domain.

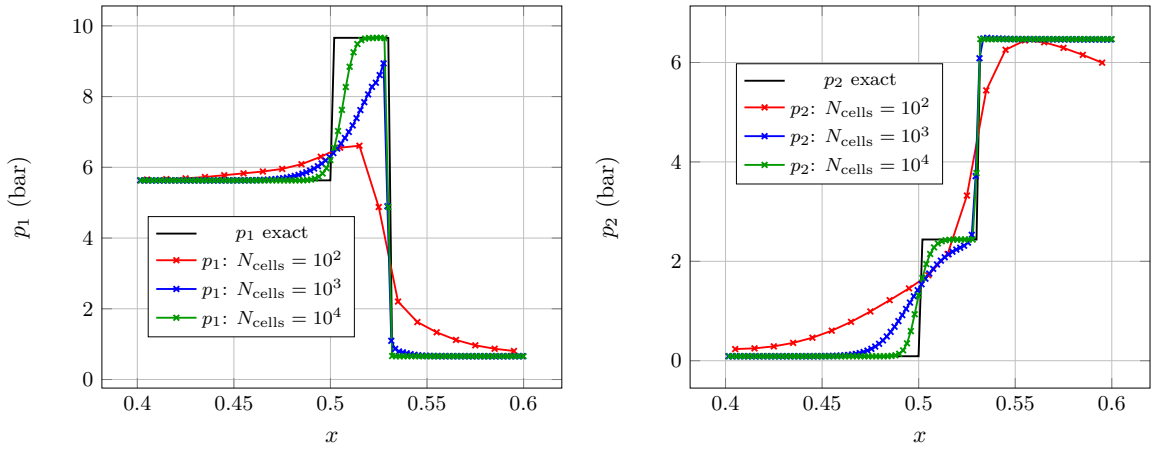

(a) p_1 (b) p_2

Figure 5.3 – Pressure profiles, linear Riemann problem with Dirac mass

Figure 5.3, Figure 5.4 and Figure 5.5 show the pressure, velocity and volume fraction profiles obtained with the present scheme. The computed profiles are provided for three different meshes: 10^2 cells (red), 10^3 cells (blue) and 10^4 cells (green). Pictures are centered in the region $]0.4,\,0.6[$ in which only the u_2^0-contact wave and the u_{I}^*-discontinuity can be seen. Since $u_2^0 \ll u_{\mathrm{I}}^*$, the contact wave corresponds to the discontinuity very close to $x = 0.5\,m$.

It can be observed that the computed solution related to the coarse mesh of 10^2-cells presents some non-monotonous trends in the vicinity of the u_{I}^*-discontinuous front. This is due to the sudden activation of the function $\chi_{\frac{\Delta x}{2}}(x)$ which injects the Dirac mass $\mathbf{b}_0$ into the appropriate cell. Subsequently, as the mesh is refined, these non-monotonous patterns tend to vanish. The

scheme manages to catch the new intermediate plateau between the u_2^0-contact wave and the u_1^*-discontinuous front.

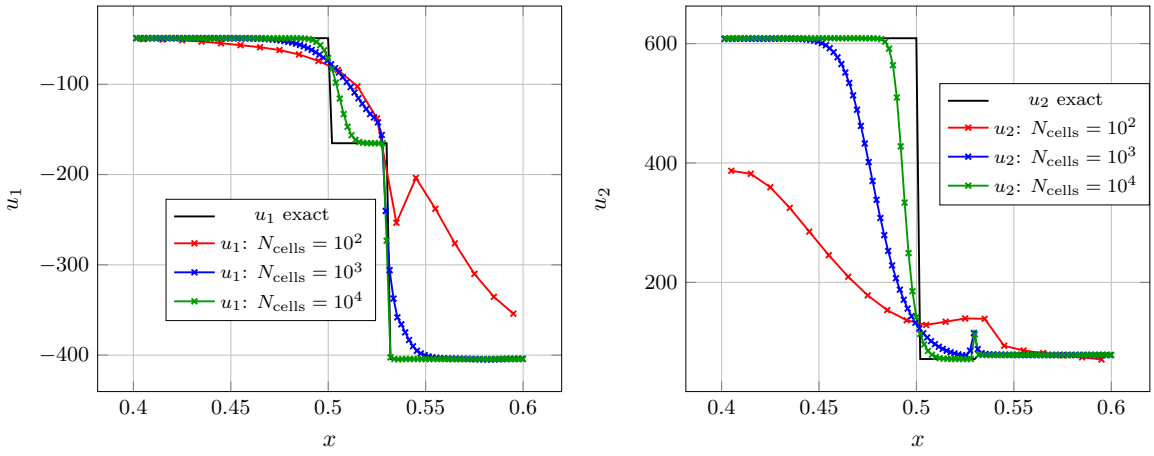

(a) u_1 (b) u_2

Figure 5.4 – Velocity profiles, linear Riemann problem with Dirac mass

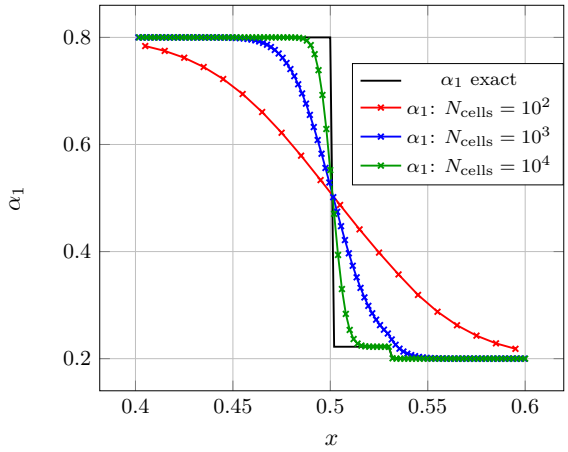

(a) α_1

Figure 5.5 – α_1 profile, linear Riemann problem with Dirac mass

In the next verification test case linear relaxation effects are added in the hand-made model.

Case with linear relaxations

Linear relaxation terms are now active. The time-relaxation matrix reads:

$$\underline{\underline{\tau}}^{-1} = \frac{1}{\tau}\mathbf{I}, \tag{5.113}$$

with $\tau = 3 \times 10^{-4}\, s$. Recall that the analytical solution is the one provided in (5.23). The self-similarity is lost because of the time-relaxation effects. What is more, interactions between the Dirac measure and the linear relaxation operator entail that exponentially decreasing profiles in space are expected in the intermediate region between a given λ_k^0-contact wave and the u_1^*-discontinuous front. The convergence curves presented in Figure 5.6 suggest that the proposed numerical scheme converges towards the analytical solution.

Once again, Figure 5.7, Figure 5.8 and Figure 5.9 display the pressure, the velocity and the volume fraction profiles in the vicinity of $x = 0.5\, m$. Let us mention that the profile of α_1 in Figure 5.9 is

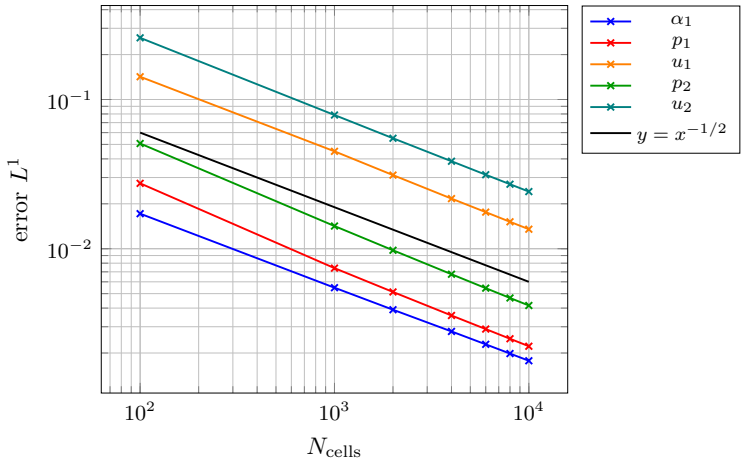

Figure 5.6 – Convergence curve: linear Riemann problem with Dirac mass and linear relaxation

the easiest to study because it corresponds to the first right eigenvector coordinate $\mathbf{a}_1(x,t)$ whose expression writes:

$$\alpha_1(x,t) = \mathbf{a}_1(x,t) = \begin{cases} (\alpha_1)_{\mathrm{L}}(t) & \text{if} \quad x < u_2^0\, t, \\ (\alpha_1)_{\mathrm{R}}(t) - e^{-(1/\tau)\left(\frac{u_{\mathrm{I}}^* t - x}{u_{\mathrm{I}}^* - u_2^0}\right)} \frac{\mathbf{l}_1^0 \cdot \mathbf{b}_0}{u_2^0 - u_{\mathrm{I}}^*} & \text{if} \quad u_2^0\, t < x < u_{\mathrm{I}}^*\, t, \\ (\alpha_1)_{\mathrm{R}}(t) & \text{if} \quad x > u_{\mathrm{I}}^*\, t, \end{cases} \tag{5.114}$$

with,

$$\begin{cases} (\alpha_1)_{\mathrm{L}}(t) = (\alpha_1)_{\mathrm{L}}^0\, e^{-t/\tau} + \alpha_1^{\mathrm{eq}}\left(1 - e^{-t/\tau}\right), \\ (\alpha_1)_{\mathrm{R}}(t) = (\alpha_1)_{\mathrm{R}}^0\, e^{-t/\tau} + \alpha_1^{\mathrm{eq}}\left(1 - e^{-t/\tau}\right). \end{cases} \tag{5.115}$$

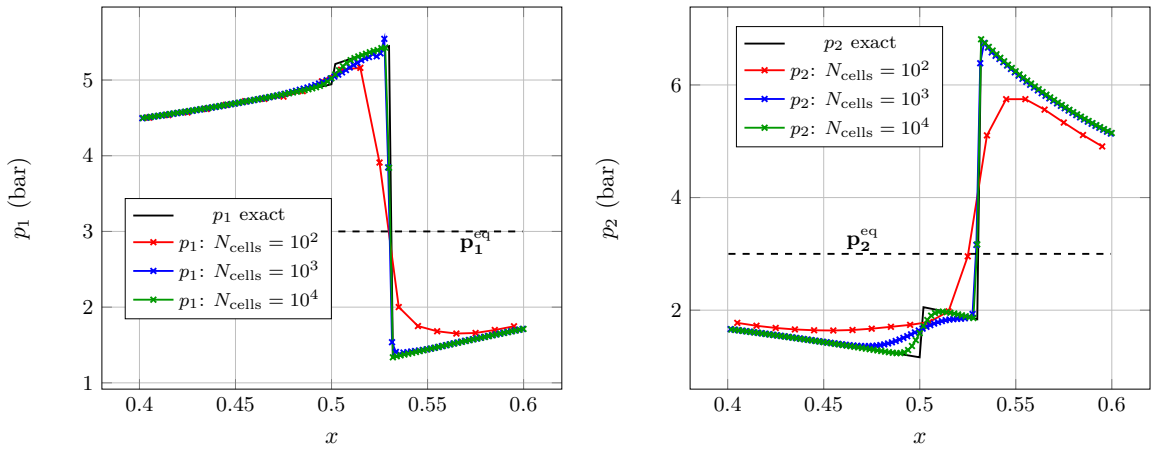

(a) p_1 (b) p_2

Figure 5.7 – Pressure profiles, linear Riemann problem with Dirac mass and linear relaxation

In Figure 5.9, the relaxation effect can be observed as the left final plateau of α_1 is located around 0.6 on the y-axis whereas the initial condition was 0.8. Besides the exponentially decreasing area for $x \in \left]u_2^0\, t,\, u_{\mathrm{I}}^*\, t\right[$ is captured as the mesh is refined.

The profiles of the other variables are more difficult to understand as each of them is a linear combination of the different eigenvector coordinates $\mathbf{a}_k(x,t)$, $k \in [1,5]$. Similarly to the case with no relaxation effect, for coarse meshes, the computed velocity profiles display steep non-monotonous behaviors around the u_{I}^*-discontinuity. However, for finer meshes, the present numerical scheme manages to retrieve the analytical exponential plateaus as well as the right location of the discontinuities.

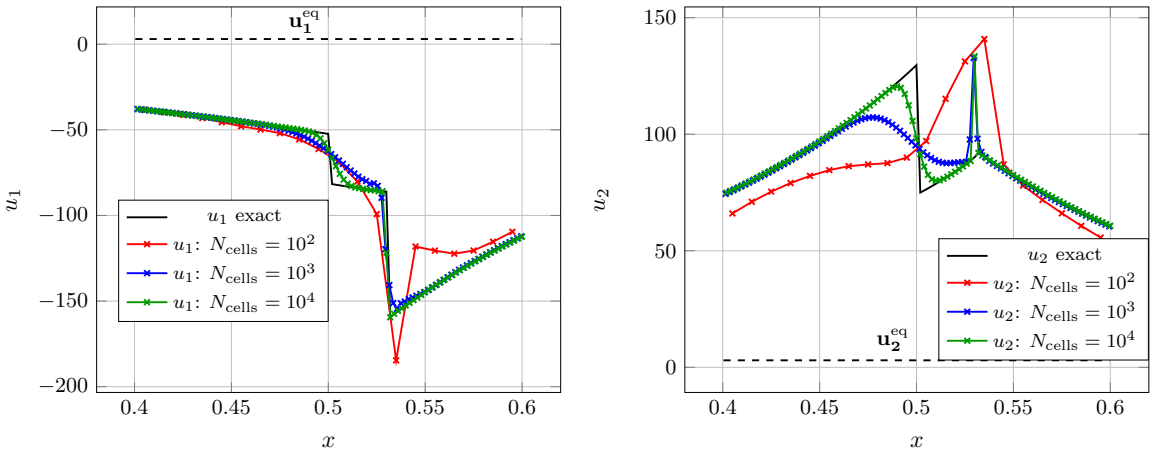

(a) u_1 (b) u_2

Figure 5.8 – Velocity profiles, linear Riemann problem with Dirac mass and linear relaxation

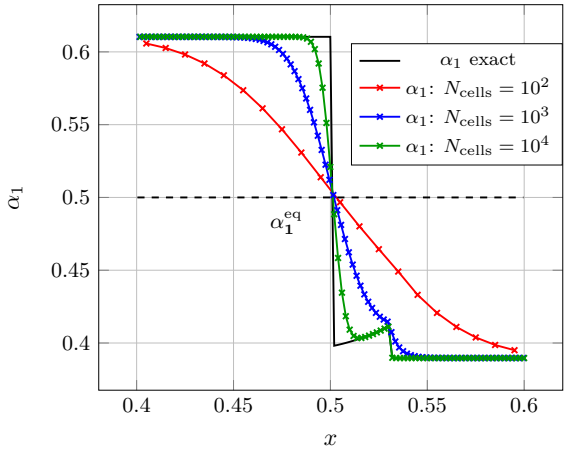

(a) α_1

Figure 5.9 – α_1 profile, linear Riemann problem with Dirac mass and linear relaxation

Let us end this verification test case by simply showing in Figure 5.10, Figure 5.11 the profiles of the pressure and velocity variables throughout the overall computational domain.

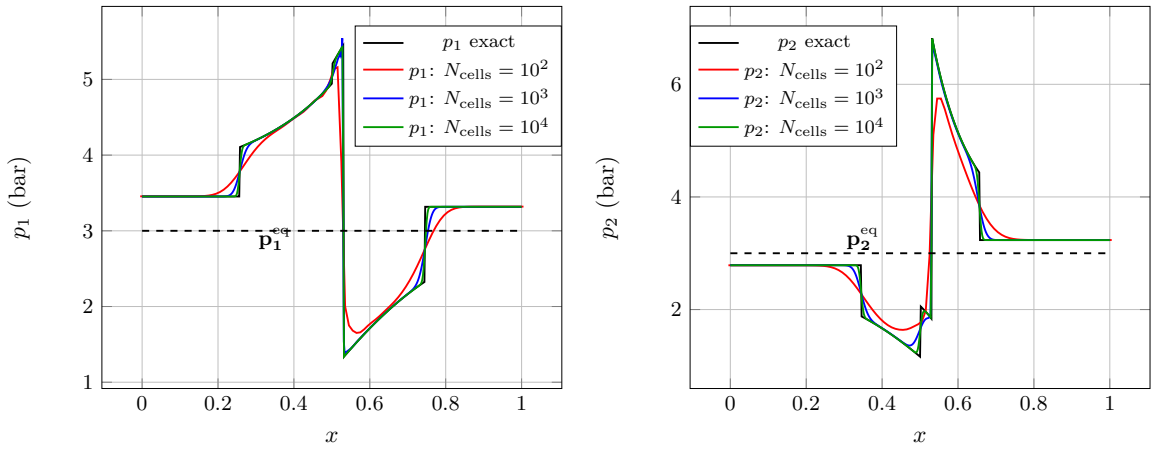

(a) p_1 (b) p_2

Figure 5.10 – Pressure profiles, linear Riemann problem with Dirac mass and linear relaxation

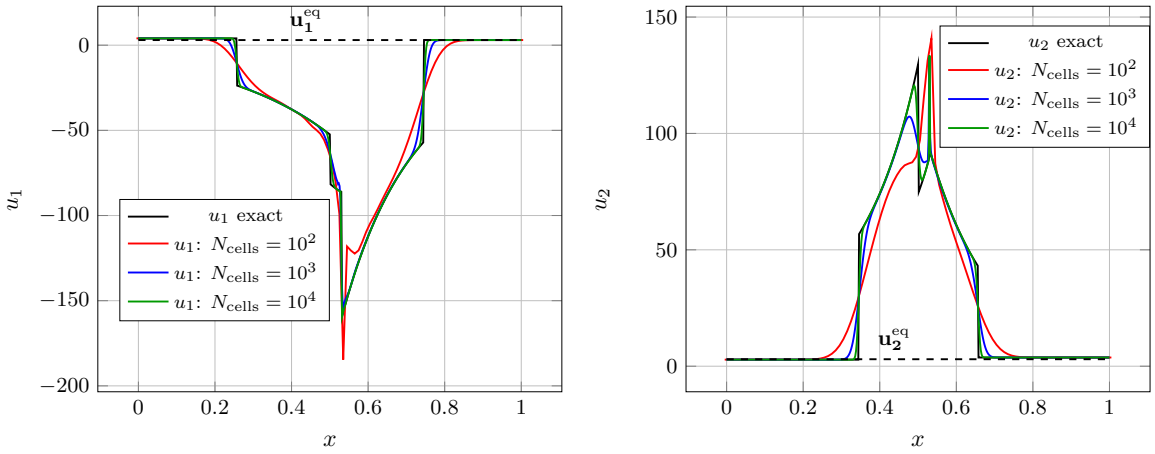

(a) u_1 (b) u_2

Figure 5.11 – Velocity profiles, linear Riemann problem with Dirac mass and linear relaxation

In the above verification test cases, the convergence of the hand-made scheme (5.109), (5.110) suggests that the proposed extension of the Bereux-Sainsaulieu staggered scheme (5.39), (5.41) might be a potential candidate to solve the isentropic Baer-Nunziato system with pressure and velocity relaxations. Before testing the present scheme on this intricate model, a last intermediate verification step proposes to test it against an *homogeneous* isentropic Baer-Nunziato Riemann problem.

5.4.2 Homogeneous isentropic Baer-Nunziato system

Here, the system at stake is the one written in (5.34) with $\mathbf{S}(\mathbf{U}) = \mathbf{0}$. The computational domain is $\Omega = [0, \mathrm{L}]$ with $\mathrm{L} = 1\,m$. Consider the initial conditions written in Table 5.3. For $\left(p_k, u_k\right)$, $k \in \{1, 2\}$, the analytical solution is made of $(u_k - c_k)$-shock wave propagating to the left followed by a non-stationary u_2-contact discontinuity. The EOS of both phases is similar to the ones written in (5.107). The intermediate analytical state between the shock waves and the contact discontinuity is given by:

Eventually, the time of the simulation is $\mathrm{T_{end}} = 2 \times 10^{-4}\,s$ and the time-step is determined by the classical CFL condition (5.65) with a Courant number $\mathscr{C} = 0.45$.

	Left cell	Right cell
α_1	0.8	0.2
u_1 $(m.s^{-1})$	8.33444149645988652	8.00004159069419529
p_1 (bar)	4.90242785728564020	4.99974006626945105
u_2 $(m.s^{-1})$	7.20241600910508240	4
p_2 (bar)	2.92896681753376033	4.49996101026474556

Table 5.3 – Initial conditions

	Intermediate state
α_1	0.8
u_1 $(m.s^{-1})$	5
p_1 (bar)	5
u_2 $(m.s^{-1})$	4
p_2 (bar)	3

Table 5.4 – Analytical intermediate state

In the following, the present approach, noted BS in the sequel, is compared with Rusanov and HLLAC schemes presented in subsection 5.3.4.

Figure 5.12, Figure 5.13 and Figure 5.14 display the pressure, velocity and volume fraction convergence curves associated with the different schemes.

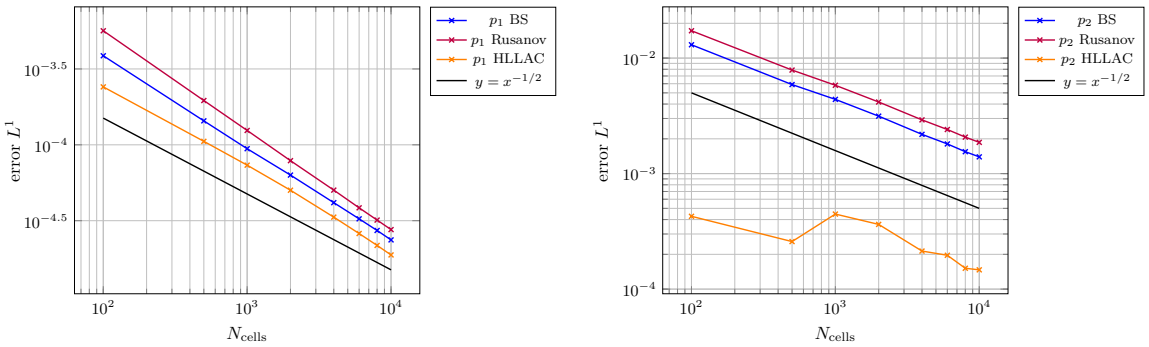

(a) p_1 (b) p_2

Figure 5.12 – Convergence curves, pressure: BS, Rusanov, HLLAC

As expected, for every variable, the HLLAC scheme is by far the most accurate with respect to the proposed approach and the Rusanov scheme. Note that even for a 10^4-cell mesh, the trend for the HLLAC-convergence curve of p_2 has not yet reached the asymptotic behavior corresponding to a straight line of slope $-1/2$. This might be due to the fact that the amplitude of the jump of p_2 through the u_2-contact wave is considerably bigger than the one corresponding to the u_2-c_2-shock wave. A similar slowness of the convergence process can also be observed for the variable u_2 which only jumps through the u_2-contact wave. One can finally observe that for every variable, the present is scheme is always slightly more accurate than the Rusanov scheme.

The profiles of the variables are shown in Figure 5.15, Figure 5.16 and Figure 5.17. Let us first underline that the jump of variable p_1 through the u_2-contact wave is almost invisible. Thus, for this test case, it justifies *a posteriori* the Riemann invariants approximation proposed in (5.48).

Besides, the profiles are in agreement with the results observed on the convergence curves. The profile of the solutions computed with the HLLAC scheme is steeper than those obtained with the BS or the Rusanov schemes. One can also note that, the u_2 profile computed with the BS and the Rusanov schemes exhibits a non-monotonous behavior which does not appear for the HLLAC scheme. However, it can be stressed that the trace of spurious ghost waves, which can be observed in the right part of the computational domain, is less pronounced for the BS scheme than for the

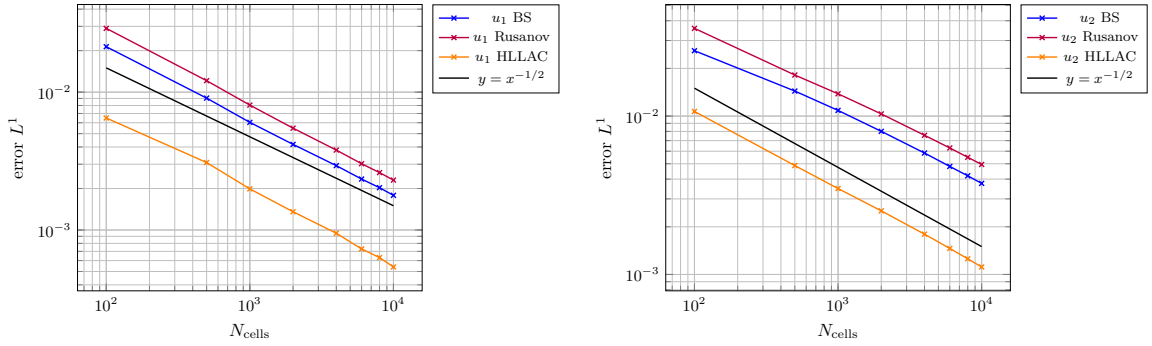

(a) u_1 (b) u_2

Figure 5.13 – Convergence curves, velocity: BS, Rusanov, HLLAC

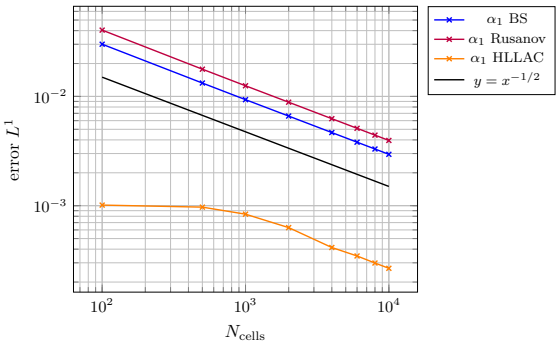

(a) α_1

Figure 5.14 – Convergence curve of α_1: BS, Rusanov, HLLAC

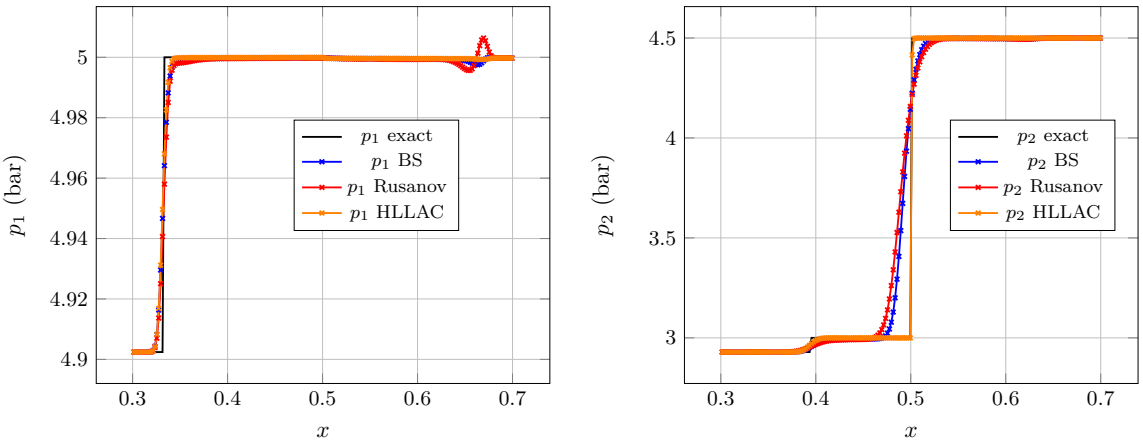

(a) p_1 (b) p_2

Figure 5.15 – Pressure profiles, Baer-Nunziato shock-contact, $N_{cells} = 5 \times 10^2$

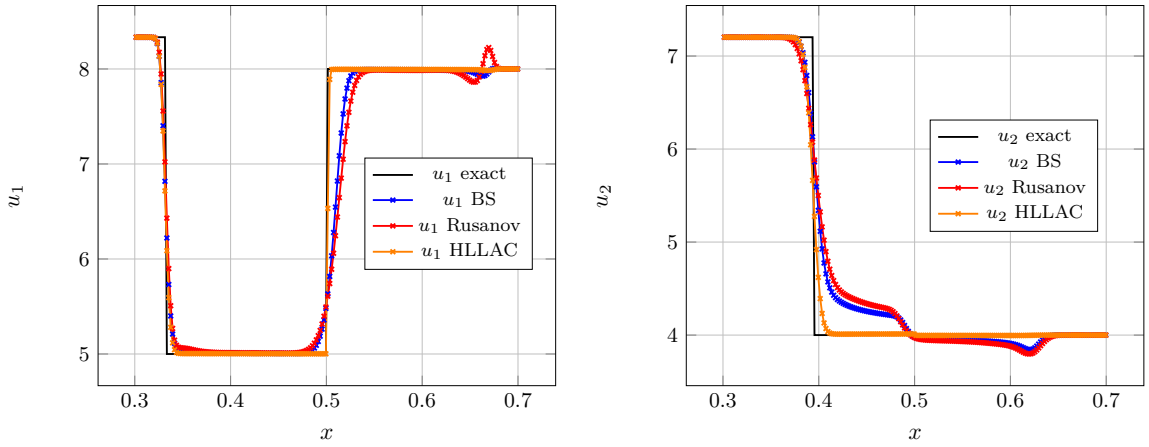

(a) u_1 (b) u_2

Figure 5.16 – Velocity profiles, Baer-Nunziato shock-contact, $N_{cells} = 5 \times 10^2$

Rusanov one.

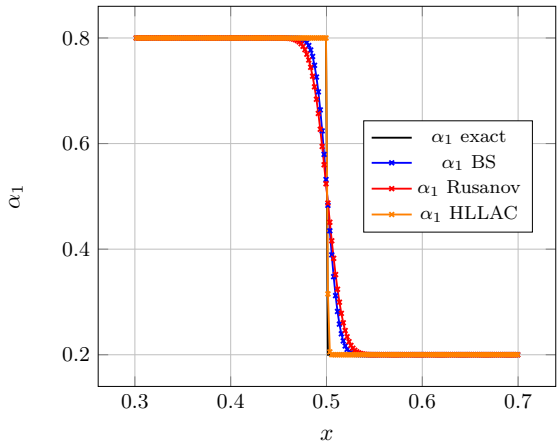

(a) α_1

Figure 5.17 – α_1 profile, Baer-Nunziato shock-contact, $N_{cells} = 5 \times 10^2$

The above test case has assessed the ability of the present numerical approach to capture the analytical solution of an homogeneous Riemann problem. Subsequently, pressure and velocity relaxations are no longer omitted, and we focus on generalized non-linear Riemann problems associated with the isentropic Baer-Nunziato system.

5.4.3 Isentropic Baer-Nunziato system with pressure and velocity relaxations

In this section, the problem at stake is given by:

$$\begin{aligned} &\partial_t \mathbf{U} + \partial_x \mathbf{F}(\mathbf{U}) + \underline{\underline{\mathbf{E}}}(\mathbf{U})\, \partial_x \mathbf{U} = \mathbf{S}(\mathbf{U}), \\ &\mathbf{U}(., t=0) = \begin{cases} \mathbf{U}_{\mathrm{L}}^0 \text{ if } x < 0.5, \\ \mathbf{U}_{\mathrm{R}}^0 \text{ if } x > 0.5. \end{cases} \end{aligned} \tag{5.116}$$

Formulas related to $\mathbf{F}(\mathbf{U})$, $\underline{\underline{\mathbf{E}}}(\mathbf{U})$ and $\mathbf{S}(\mathbf{U})$ are given in (5.34). The setting of this test case is similar to the one presented in subsection 4.5.3 of the previous chapter. Let us recall that for both phases, EOS is determined using vapor or liquid saturation values:

	p (bar)	$\rho\ (kg.m^{-3})$	γ	$\kappa\ (\mathrm{J}.kg^{-1}.\mathrm{K}^{-1})$
Liquid	$p^{\mathrm{sat}} = 150$	$\rho_{\mathrm{liq}}^{\mathrm{sat}} = 603.52$	$\gamma_{\mathrm{liq}}^{\mathrm{sat}} = 2.76$	$\kappa_{\mathrm{liq}}^{\mathrm{sat}} = 0.32$
Vapor	$p^{\mathrm{sat}} = 150$	$\rho_{\mathrm{vap}}^{\mathrm{sat}} = 97.73$	$\gamma_{\mathrm{vap}}^{\mathrm{sat}} = 3.62$	$\kappa_{\mathrm{vap}}^{\mathrm{sat}} = 0.94$

Table 5.5 – Saturation parameters

with $\kappa_{\mathrm{liq}}^{\mathrm{sat}} = p^{\mathrm{sat}} \left(\rho_{\mathrm{liq}}^{\mathrm{sat}}\right)^{-\gamma_{\mathrm{liq}}^{\mathrm{sat}}}$, $\kappa_{\mathrm{vap}}^{\mathrm{sat}} = p^{\mathrm{sat}} \left(\rho_{\mathrm{vap}}^{\mathrm{sat}}\right)^{-\gamma_{\mathrm{vap}}^{\mathrm{sat}}}$. The EOS write:

$$\begin{cases} p_1 = \kappa_{\mathrm{vap}}^{\mathrm{sat}} \left(\rho_1\right)^{\gamma_{\mathrm{vap}}^{\mathrm{sat}}}, \\ p_2 = \kappa_{\mathrm{liq}}^{\mathrm{sat}} \left(\rho_2\right)^{\gamma_{\mathrm{liq}}^{\mathrm{sat}}}. \end{cases} \tag{5.117}$$

Initial conditions are recalled in Table 5.6.

	α_1	$u_1\ (m.s^{-1})$	p_1 (bar)	$u_2\ (m.s^{-1})$	p_2 (bar)
$\mathbf{W}_{\mathrm{L}}^0$	0.8	1.5	110	-2	170
$\mathbf{W}_{\mathrm{R}}^0$	0.2	2	158	-1.5	120

Table 5.6 – Generalized non-linear Riemann problem: initial conditions

The complexity of problem (5.116) entails that, so far, no analytical solution can be found. As a consequence, the comparisons performed below are only based on the variable profiles. Besides, the proposed approach is tested with the modified discretization for the volume fraction equation provided in **Property 5.3.2**. Recall that such a choice ensures the discrete volume fraction maximum principle under the classical CFL condition (5.65). Besides, the Courant number in (5.65) is fixed to $\mathscr{C} = 0.45$. In this test case, the unsplit BS-type scheme is compared with two fractional step methods: the one using the Rusanov scheme for the convective part of the isentropic Baer-Nunziato model, and the other using the HLLAC solver.

In the paragraph below, a non-stiff relaxation regime is considered.

Non-stiff relaxation

The pressure and velocity relaxation time-scales are set equal to

$$\tau_{\mathrm{p}} = \tau_{\mathrm{u}} = 10^{-4}\, s. \tag{5.118}$$

For a mesh made of 5×10^2 cells, the approximated value of the discrete time-step related to (5.65) is $\Delta t \approx 3 \times 10^{-6}\, s$. Hence, the generalized non-linear Riemann problem is not stiff in that case. Figure 5.18, Figure 5.19 and Figure 5.20 display the pressure, velocity and volume fraction profiles obtained with the BS, Rusanov and HLLAC schemes with a mesh made of 5×10^2 cells. These profiles are compared with a grid-converged solution computed thanks to a Rusanov fractional step approach using a 10^5-cell mesh. Let us underline that the other grid-converged solutions obtained with the BS or the HLLAC schemes are similar to the Rusanov one.

As a first general remark, let us point out that the discontinuity associated with the u_2-contact wave can be observed on the p_2 and u_1 profiles but not on the p_1 profile. In the context where velocity relaxation forces $|u_1 - u_2|$ to tend to zero, this is coherent with the approximated Riemann invariants (5.48) obtained in the subsonic flow configurations.

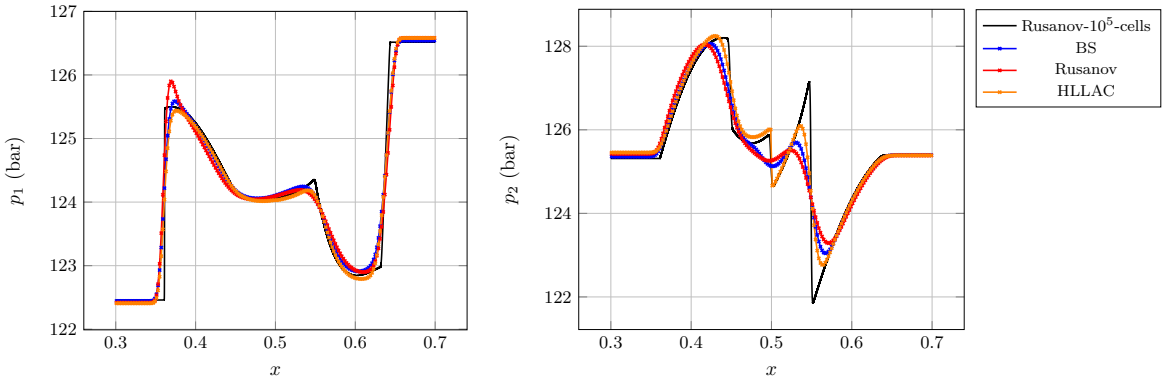

(a) p_1 (b) p_2

Figure 5.18 – Pressure profiles, Baer-Nunziato non-stiff generalized Riemann problem, $N_{cells} = 5 \times 10^2$

Whatever the variable examined, the Rusanov scheme is the numerical method which has the most important difficulty to capture the variations of the grid-converged solution. The profile comparison is thus oriented between the fractional step method involving the HLLAC scheme and the proposed approach.

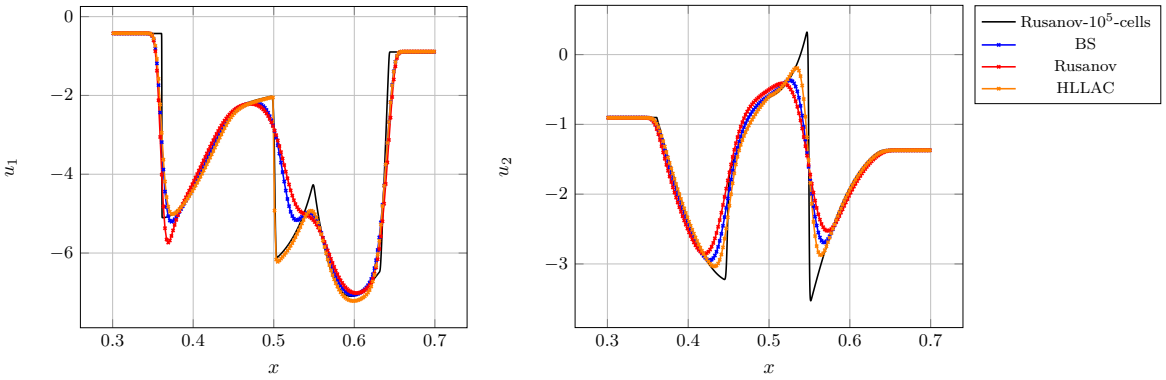

(a) u_1 (b) u_2

Figure 5.19 – Velocity profiles, Baer-Nunziato non-stiff generalized Riemann problem, $N_{cells} = 5 \times 10^2$

From a general point of view, the HLLAC method manages to be more accurate than the BS scheme. This is notably true in regions close to $x = 0.5\,m$ where the u_2-contact wave is supposed to be. Those good results for the HLLAC solver might have been fostered by the fact that relaxation is not stiff in this test case. Indeed, the structure of the grid-converged profiles could formally still contain some remains of solutions related to the homogeneous version of the generalized Riemann problem (5.116). Those remaining patterns are supposed to be captured by the HLLAC Riemann solver.

Nevertheless, we may have a closer look to the left and right regions of the computational domain which only undergo the velocity and pressure relaxation processes. In the latter regions, the p_1 and p_2 plateaus obtained with the BS scheme are closer to the grid-converged solution than the ones produced by the HLLAC fractional step method.

The next generalized Riemann problem is identical to the one presented above. The only difference is that the relaxation time-scales are chosen such that the problem becomes stiff.

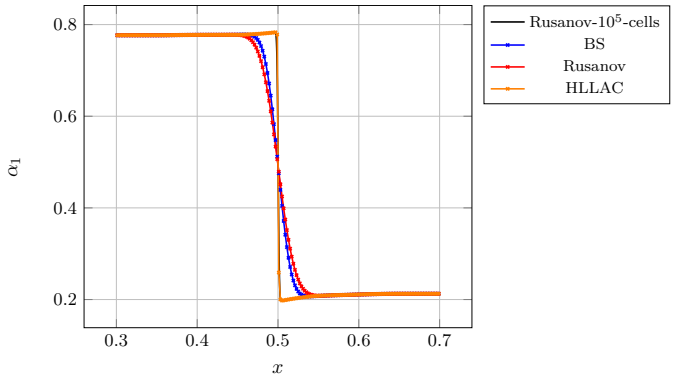

(a) α_1

Figure 5.20 – α_1 profile, Baer-Nunziato non-stiff generalized Riemann problem, $N_{cells} = 5 \times 10^2$

Stiff relaxation

The pressure and velocity relaxation time-scales are now equal to:

$$\tau_p = \tau_u = 10^{-8}\, s. \tag{5.119}$$

Thus, they are a hundred times faster than the discrete time-step obtained using the eigenvalues of the isentropic Baer-Nunziato system. Since the relaxation process takes place almost instantaneously, one focuses on the profiles of the mixture variables: $P = \alpha_1 p_1 + \alpha_2 p_2$, $U = Y_1 u_1 + Y_2 u_2$, $m = m_1 + m_2$; as well as the relaxation variables Δp and Δu.

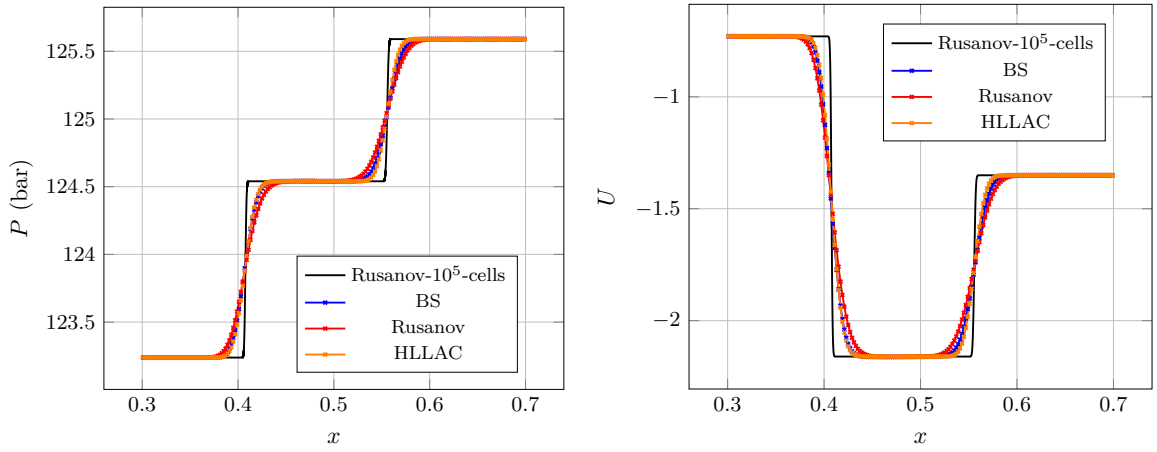

(a) P (b) U

Figure 5.21 – U, P profiles, Baer-Nunziato stiff generalized Riemann problem, $N_{cells} = 5 \times 10^2$

These profiles are displayed in Figure 5.21, Figure 5.22, Figure 5.23 and Figure 5.24. Let us first consider the structure of the grid-converged solution. Looking at the P, U and m profiles, it seems that the computed solution is composed of three discontinuities. Similarly to the Euler system, the mixture pressure and velocity only jump across two of them which propagate at the fastest speeds. Although it cannot be easily seen, the mixture density m jumps through the three discontinuities.

The three numerical methods manage to capture the appropriate intermediate states as well as the right locations associated with the fastest discontinuous fronts. The Rusanov scheme seems to be slightly more diffusive than the two other approaches. Besides, it turns out that the HLLAC fractional step is more accurate than the two other methods to capture the slowest discontinuity whose structure has been inherited from the u_2-contact wave. However, it can be observed that the profiles of the relaxation variables computed thanks to the proposed method are considerably closer to the ones of the grid-converged solution in comparison with those computed with the fractional step methods.

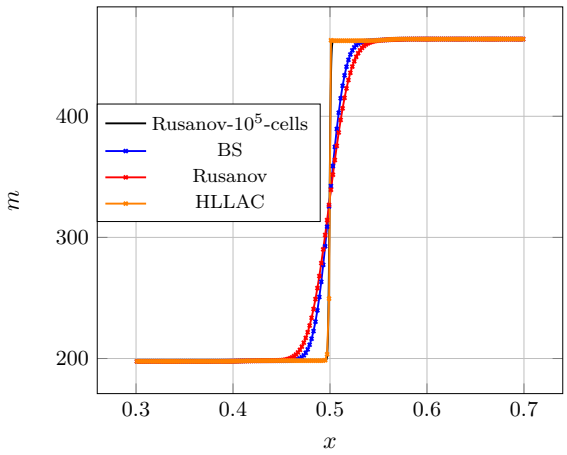

(a) m

Figure 5.22 – m profile, Baer-Nunziato stiff generalized Riemann problem, $N_{cells} = 5 \times 10^2$

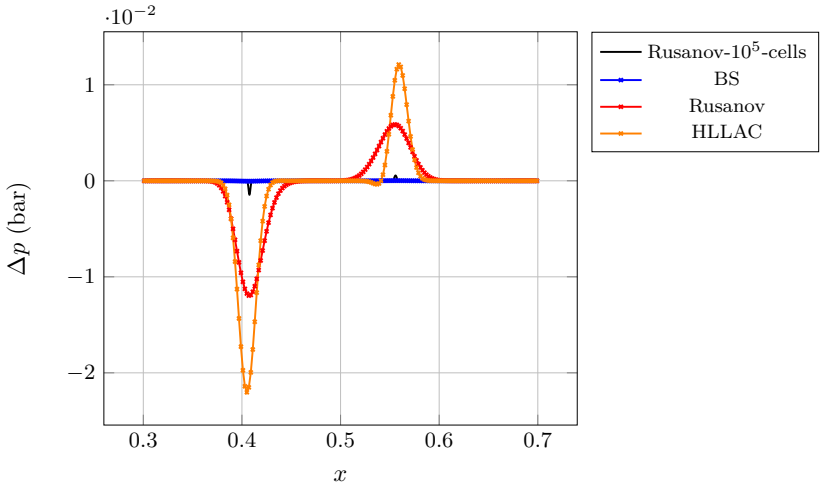

(a) Δp

Figure 5.23 – Δp profile, Baer-Nunziato stiff generalized Riemann problem, $N_{cells} = 5 \times 10^2$

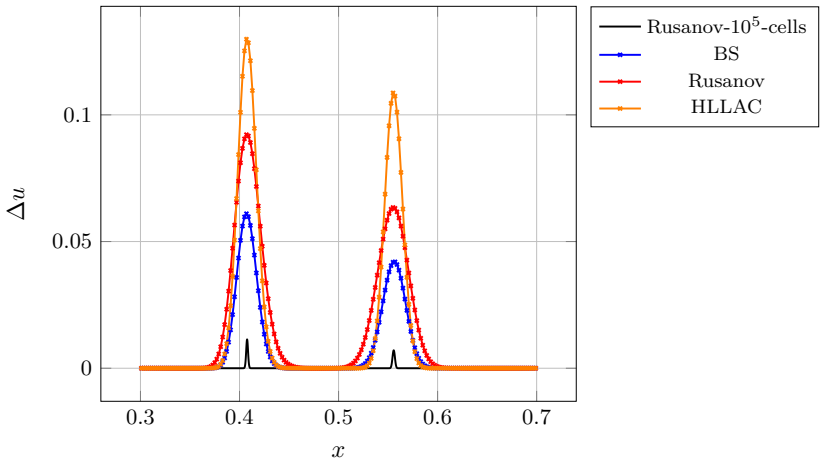

(a) Δu

Figure 5.24 – Δu profile, Baer-Nunziato stiff generalized Riemann problem, $N_{cells} = 5 \times 10^2$

Even if, in that case, the amplitude of such relaxation variables is considerably small, the ability for a two-phase flow numerical solver to correctly compute these quantities is crucial.

Indeed, the velocity relaxation variable Δu is used to determine the magnitude of the shear stress that both phases apply to each other [13]. More generally, in more complicated scenarios, the relaxation time scales can vary. Then, the local generalized Riemann problem to be solved might switch from stiff to non-stiff regimes. Hence, from one time-step to another, a surge of the small amplitude relaxation variables can potentially be triggered by strong pressure gradients related to the convective part of the Baer-Nunziato model. The accuracy of the increasing relaxation variables thus depends on the accuracy of their initial small values.

5.5 Conclusions

Based on the time-implicit staggered scheme derived by Bereux and Sainsaulieu for hyperbolic systems with relaxation in the sense of Liu, the present work proposes to extend this strategy to the isentropic Baer-Nunziato system with pressure and velocity relaxations.

The origin of such an extension comes from the weak formulation of the non-conservative products arising in this two-fluid two-pressure system. Indeed, one can assimilate such terms to a Dirac measure weighted by appropriate masses extracted from the Rankine-Hugoniot relations.

Subsequently, one can analyze the solution structure related to a new kind of generalized Riemann problem including linear relaxations and a frozen version of such a singular Dirac measure. In the specific case where the relaxation matrix is diagonal, the analytical solution can be found and provides a simple extension of the ODEs system verified by the space-averaged solution state.

The present numerical method stems from this extended time dynamics and proposes a time-implicit staggered scheme which conserves the partial masses as well as the momentum mixture of the Baer-Nunziato system. Furthermore, the discretization of the volume fraction equation involving initially the linearization of the pressure relaxation operator can be replaced by the resolution of a non-linear system. The latter system guarantees that a maximum principle holds for the discrete volume fraction update under classical CFL conditions.

Numerical results composed of homogeneous and generalized non-linear Riemann problems linked to the isentropic Baer-Nunziato system have assessed the accuracy of the proposed method with respect to the Rusanov and HLLAC schemes as well as their related fractional step versions.

In this comparison, one has to recall that, contrary to the HLLAC approximate Riemann solver, the space-averaging process of the present method voluntarily blurs the precious information stemming from the exact intermediate states created by homogeneous or generalized Riemann problems. Such a strategy has been adopted to circumvent one's inability to find the analytical solution of Riemann problems in which source terms are present.

It turns out that, for both homogeneous and generalized Riemann problems, the present time-implicit staggered scheme is more accurate than the Rusanov fractional step method. Moreover, though the proposed scheme is unable to be as accurate as the HLLAC scheme for homogeneous Riemann problems, it offers interesting elements of comparison when pressure and velocity relaxation effects are no longer omitted. One can notably stress that, in stiff regimes, the present approach better resolves the pressure and velocity relaxation variables.

In any case many perspectives exist for the improvement of the present method. One of them could be to progressively release the linear assumptions holding on the generalized linear Riemann problem proposed by Bereux-Sainsaulieu which is the starting point of this work. This suggestion is all the more motivating when one observes the proximity between the analytical solutions obtained in the case of linear generalized Riemann problems (see Figure 5.10b) and the grid-converged solutions based on the isentropic Baer-Nunziato system with pressure and velocity relaxations (see Figure 5.18b).

Another difficulty is the extension of the proposed staggered scheme to the multi-dimensional flows computed on unstructured meshes. Eventually one could also study the *asymptotically preserving* property of the present approach towards some given reduced models. However, this

would require to define exactly what is the asymptotic limit of the isentropic Baer-Nunziato system.

5.6 Appendices

A Adaptation of the HLLAC scheme for the isentropic Baer-Nunziato system

In this section, the exact forms of the contributions $\mathbf{F}_{\mathrm{L}}(\mathbf{U}_{\mathrm{R}}, \mathbf{U}_{\mathrm{L}})$ and $\mathbf{F}_{\mathrm{R}}(\mathbf{U}_{\mathrm{R}}, \mathbf{U}_{\mathrm{L}})$ introduced in (5.95) will be specified in the case of the HLLAC scheme. One can start by rewriting them as:

$$\begin{cases} \mathbf{F}_{\mathrm{L}}(\mathbf{U}_{\mathrm{R}}, \mathbf{U}_{\mathrm{L}}) = \mathbf{F}_f(\mathbf{U}_{\mathrm{R}}, \mathbf{U}_{\mathrm{L}}) - \mathbf{H}_{\mathrm{L}}(\mathbf{U}_{\mathrm{R}}, \mathbf{U}_{\mathrm{L}}), \\ \\ \mathbf{F}_{\mathrm{R}}(\mathbf{U}_{\mathrm{R}}, \mathbf{U}_{\mathrm{L}}) = \mathbf{F}_f(\mathbf{U}_{\mathrm{R}}, \mathbf{U}_{\mathrm{L}}) + \mathbf{H}_{\mathrm{R}}(\mathbf{U}_{\mathrm{R}}, \mathbf{U}_{\mathrm{L}}). \end{cases} \tag{5.120}$$

In equation (5.120), $\mathbf{F}_f(\mathbf{U}_{\mathrm{R}}, \mathbf{U}_{\mathrm{L}})$ stands for a numerical flux whereas $\mathbf{H}_j(\mathbf{U}_{\mathrm{R}}, \mathbf{U}_{\mathrm{L}})$, $j \in \{\mathrm{L}, \mathrm{R}\}$ are non-conservative contributions. In the sequel, these two kinds of discrete quantities are determined.

Conservative flux

The adaptation of the HLLAC scheme can be understood by looking at Figure 5.25. For $k \in$

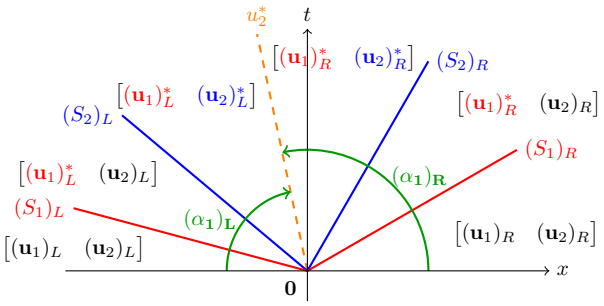

Figure 5.25 – HLLAC waves and states

$\{1, 2\}$, define the left and right wave speed estimates as

$$\begin{aligned} (\mathrm{S}_k)_{\mathrm{L}} &= \min\left((u_k - c_k)_{\mathrm{L}}, (u_k - c_k)_{\mathrm{R}}, \hat{u}_k - \hat{c}_k\right), \\ (\mathrm{S}_k)_{\mathrm{R}} &= \max\left((u_k + c_k)_{\mathrm{L}}, (u_k + c_k)_{\mathrm{R}}, \hat{u}_k + \hat{c}_k\right), \end{aligned} \tag{5.121}$$

with,

$$\hat{u}_k = \frac{\sqrt{(\rho_k)_{\mathrm{L}}}(u_k)_{\mathrm{L}} + \sqrt{(\rho_k)_{\mathrm{R}}}(u_k)_{\mathrm{R}}}{\sqrt{(\rho_k)_{\mathrm{L}}} + \sqrt{(\rho_k)_{\mathrm{R}}}}, \quad \hat{c}_k = \frac{\sqrt{(\rho_k)_{\mathrm{L}}}(c_k)_{\mathrm{L}} + \sqrt{(\rho_k)_{\mathrm{R}}}(c_k)_{\mathrm{R}}}{\sqrt{(\rho_k)_{\mathrm{L}}} + \sqrt{(\rho_k)_{\mathrm{R}}}}. \tag{5.122}$$

Let us also define a contact wave velocity u_2^* whose expression will be determined later on. Currently it is only assumed that $\forall k \in \{1, 2\}$:

$$(\mathrm{S}_k)_{\mathrm{L}} < u_2^* < (\mathrm{S}_k)_{\mathrm{R}}, \tag{5.123}$$

which means that the flow is subsonic. Similarly to the real isentropic Baer-Nunziato system, it is assumed that the volume fraction α_1 does not jump through the $(\mathrm{S}_k)_j$-waves, $j \in \{\mathrm{L}, \mathrm{R}\}$ which models the genuinely non-linear wave fronts. As a consequence, across those fronts both phase PDEs behave as two decoupled Euler systems. The intermediate states produced behind those fronts are thus approximated using HLLC-like jump conditions [12] applied to the Euler system of both phases:

$$\forall j \in \{\mathrm{L}, \mathrm{R}\}, \ \mathbf{F}\left((\mathbf{U}_k)_j^*\right) - \mathbf{F}\left((\mathbf{U}_k)_j\right) = (\mathrm{S}_k)_j \left((\mathbf{U}_k)_j^* - (\mathbf{U}_k)_j\right), \tag{5.124}$$

with $\mathbf{F}(\mathbf{U}_k) = \left[m_k u_k, m_k u_k^2 + \alpha_k p_k\right]^{\mathrm{T}}$. Equality related to the mass component of equation (5.124) yields:

$$(m_k)_j^* = (m_k)_j \frac{(u_k)_j - (\mathrm{S}_k)_j}{(u_k)_j^* - (\mathrm{S}_k)_j}. \tag{5.125}$$

Using equation (5.125), the momentum component of equation (5.124) gives:

$$(p_k)_j^* = p_k\left((u_k)_j^*\right) = (p_k)_j - (\rho_k)_j\left[(u_k)_j - (S_k)_j\right]\left[(u_k)_j^* - (u_k)_j\right]. \tag{5.126}$$

Let us stress that equation (5.125) *will not* be used to derive the expression of $(\rho_k)_j^*$ since this quantity is related to $(p_k)_j^*$ through the EOS. Hence, considering *only* equation (5.126), one can notice that there are four remaining unknowns that need to be determined in order to close the system:

$$(u_1)_L^*, (u_1)_R^*, (u_2)_L^*, (u_2)_R^*, \tag{5.127}$$

or equivalently,

$$(p_1)_L^*, (p_1)_R^*, (u_2)_L^*, (u_2)_R^*. \tag{5.128}$$

One can find these unknowns using equalities between the *approximated* Riemann invariants (5.48) through the u_2^*-contact wave. It simply reads:

$$(u_2)_L^* = (u_2)_R^* = u_2^*, \tag{5.129a}$$
$$(\alpha_1)_L\left((u_1)_L^* - u_2^*\right) = (\alpha_1)_R\left((u_1)_R^* - u_2^*\right), \tag{5.129b}$$
$$(\alpha_1)_L(p_1)_L^* + (\alpha_2)_L(p_2)_L^* = (\alpha_1)_R(p_1)_R^* + (\alpha_2)_R(p_2)_R^*, \tag{5.129c}$$
$$(p_1)_L^* = (p_1)_R^* = p_1^*. \tag{5.129d}$$

Thus, equalities (5.129b) and (5.129c) are used to find the couple $\{u_2^*, p_1^*\}$. For $k \in \{1,2\}$, define the quantities:

$$\begin{aligned}(q_k)_R &= (\rho_k)_R\left[(S_k)_R - (u_k)_R\right],\\ (q_k)_L &= (\rho_k)_L\left[(u_k)_L - (S_k)_L\right].\end{aligned} \tag{5.130}$$

Equalities (5.129b), (5.129c) can be rewritten as a linear system to be solved:

$$\begin{bmatrix} \frac{(\alpha_1)_R}{(q_1)_R} + \frac{(\alpha_1)_L}{(q_1)_L} & -\Delta\alpha_1 \\ \Delta\alpha_1 & (\alpha_2)_R(q_2)_R + (\alpha_2)_L(q_2)_L \end{bmatrix} \cdot \begin{bmatrix} p_1^* \\ u_2^* \end{bmatrix} = \mathbf{S}_{1,2}, \tag{5.131}$$

with,

$$\begin{aligned}\Delta\alpha_1 &= (\alpha_1)_R - (\alpha_1)_L,\\ \mathbf{S}_{1,2} &= \begin{bmatrix} (\alpha_1)_L\left[(u_1)_L + \frac{(p_1)_L}{(q_1)_L}\right] - (\alpha_1)_R\left[(u_1)_R - \frac{(p_1)_R}{(q_1)_R}\right] \\ (\alpha_2)_L\left[(p_2)_L + (q_2)_L(u_2)_L\right] - (\alpha_2)_R\left[(p_2)_R - (q_2)_R(u_2)_R\right] \end{bmatrix}.\end{aligned} \tag{5.132}$$

If one assumes that volume fractions belong to the open interval $]0,1[$ and according to the definition (5.121) of the wave estimates, there exists a unique solution to linear system (5.131). Indeed the determinant of its matrix reads:

$$\det = \left(\frac{(\alpha_1)_R}{(q_1)_R} + \frac{(\alpha_1)_L}{(q_1)_L}\right) \times \left((\alpha_2)_R(q_2)_R + (\alpha_2)_L(q_2)_L\right) + (\Delta\alpha_1)^2 > 0. \tag{5.133}$$

For a given state $\mathbf{U} \in \mathbb{R}^5$, let us introduce the notations:

$$\mathbf{U} = \begin{bmatrix} \alpha_1 \\ \mathbf{u}_1 \\ \mathbf{u}_2 \end{bmatrix}, \ \forall k \in \{1,2\}, \ \mathbf{u}_k = \begin{bmatrix} m_k \\ m_k u_k. \end{bmatrix}, \ \mathbf{f}_k(\alpha_k, \mathbf{u}_k) = \begin{bmatrix} m_k u_k \\ m_k u_k^2 + \alpha_k p_k \end{bmatrix}. \tag{5.134}$$

The conservative part of the scheme can be written:

$$\mathbf{F}_f(\mathbf{U}_R, \mathbf{U}_L) = \begin{bmatrix} 0 \\ (\mathbf{F}_1)_f(\mathbf{U}_R, \mathbf{U}_L) \\ (\mathbf{F}_2)_f(\mathbf{U}_R, \mathbf{U}_L) \end{bmatrix}, \tag{5.135}$$

with $\forall k \in \{1,2\}$,

$$(\mathbf{F}_k)_f(\mathbf{U}_R,\mathbf{U}_L)=\begin{cases}\mathbf{f}_k((\alpha_k)_L,(\mathbf{u}_k)_L) & \text{if} \quad (S_k)_L>0,\\ \mathbf{f}_k((\alpha_k)_L,(\mathbf{u}_k)_L)+(S_k)_L\left((\mathbf{u}_k)_L^*-(\mathbf{u}_k)_L\right) & \text{if} \quad (S_k)_L\le 0<u_2^*,\\ \mathbf{f}_k((\alpha_k)_R,(\mathbf{u}_k)_R)+(S_k)_R\left((\mathbf{u}_k)_R^*-(\mathbf{u}_k)_R\right) & \text{if} \quad u_2^*\le 0<(S_k)_R,\\ \mathbf{f}_k((\alpha_k)_R,(\mathbf{u}_k)_R) & \text{if} \quad (S_k)_R\le 0.\end{cases} \tag{5.136}$$

The intermediate states $(\mathbf{u}_k)_L^*$ and $(\mathbf{u}_k)_R^*$ are defined by:

$$(\mathbf{u}_1)_L^*=\begin{bmatrix}(m_1)_L^*\\(m_1)_L^*(u_1)_L^*\end{bmatrix},\ (\mathbf{u}_1)_R^*=\begin{bmatrix}(m_1)_R^*\\(m_1)_R^*(u_1)_R^*\end{bmatrix},\ (\mathbf{u}_2)_L^*=\begin{bmatrix}(m_2)_L^*\\(m_2)_L^*u_2^*\end{bmatrix},\ (\mathbf{u}_2)_R^*=\begin{bmatrix}(m_2)_R^*\\(m_2)_R^*u_2^*\end{bmatrix}, \tag{5.137}$$

with,

$$\begin{aligned}(m_1)_L^*&=(\alpha_1)_L\rho_1\left(p_1^*\right),\\(m_1)_R^*&=(\alpha_1)_R\rho_1\left(p_1^*\right),\\(m_2)_L^*&=(\alpha_2)_L\rho_2\left((p_2)_L^*\right),\\(m_2)_R^*&=(\alpha_2)_R\rho_2\left((p_2)_R^*\right).\end{aligned} \tag{5.138}$$

In (5.137), (5.138), the expressions of $(u_1)_j^*$ and $(p_2)_j^*$, $j\in\{L,R\}$ are given by equality (5.126) combined with the couple $\{p_1^*,u_2^*\}$.

Non-conservative contributions

Following the *thin boundary layer approximation* described in [10], the non-conservative contributions write:

$$\mathbf{H}_L(\mathbf{U}_R,\mathbf{U}_L)=\begin{cases}\begin{bmatrix}u_2^*\left[(\alpha_1)_R-(\alpha_1)_L\right]\\0\\\left[(\alpha_2)_R(p_2)_R^*-(\alpha_2)_L(p_2)_L^*\right]\\0\\-\left[(\alpha_2)_R(p_2)_R^*-(\alpha_2)_L(p_2)_L^*\right]\end{bmatrix} & \text{if} \quad u_2^*<0,\\ \mathbf{0} & \text{if} \quad u_2^*\ge 0,\end{cases} \tag{5.139}$$

and

$$\mathbf{H}_R(\mathbf{U}_R,\mathbf{U}_L)=\begin{cases}\mathbf{0} & \text{if} \quad u_2^*<0,\\ \begin{bmatrix}u_2^*\left[(\alpha_1)_R-(\alpha_1)_L\right]\\0\\\left[(\alpha_2)_R(p_2)_R^*-(\alpha_2)_L(p_2)_L^*\right]\\0\\-\left[(\alpha_2)_R(p_2)_R^*-(\alpha_2)_L(p_2)_L^*\right]\end{bmatrix} & \text{if} \quad u_2^*\ge 0.\end{cases} \tag{5.140}$$

5.7 References

[1] A. Ambroso, C. Chalons, F. Coquel, and T. Galié. Relaxation and numerical approximation of a two-fluid two-pressure diphasic model. *ESAIM: Mathematical Modelling and Numerical Analysis*, 43:1063–1097, 2009. 157, 159, 166

[2] F. Bereux and L. Sainsaulieu. A Roe-type Riemann solver for hyperbolic systems with relaxation based on time-dependent wave decomposition. *Numerische Mathematik*, 2:143–185, 1997. 157, 159, 164

[3] F. Coquel, J. M. Hérard, K. Saleh, and N. Seguin. A robust entropy-satisfying finite volume scheme for the isentropic Baer-Nunziato model. *ESAIM: Mathematical Modelling and Numerical Analysis*, 48:165–206, 2014. 157, 159, 166

[4] G. Dal Maso, P. G. LeFloch, and F. Murat. Definition and weak stability of nonconservative products. *Journal de mathématiques pures et appliquées*, 74:483–548, 1995. 167

[5] C. Demay, C. Bourdarias, B. D. L. De Meux, S. Gerbi, and J. M. Hérard. A fractional step method adapted to the two-phase simulation of mixed flows in pipes with a compressible two-layer model. *ESAIM: Mathematical Modelling and Numerical Analysis*, Accepted for publication, 2018. 157, 159, 173

[6] T. Gallouët, J-M Hérard, and N. Seguin. Numerical modeling of two-phase flows using the two-fluid two-pressure approach. *Mathematical Models and Methods in Applied Sciences*, 14: 663–700, 2004. 157, 159, 166, 174

[7] H. Lochon, F. Daude, P. Galon, and J. M. Hérard. HLLC-type Riemann solver with approximated two-phase contact for the computation of the Baer-Nunziato two-fluid model. *Journal of Computational Physics*, 326:733–762, 2016. 157, 159, 167, 175

[8] K. Saleh. *Analyse et simulation numérique par relaxation d'écoulements diphasiques compressibles. Contribution au traitement des phases evanescentes.* PhD thesis, Université Pierre et Marie Curie-Paris VI, 2012. URL https://tel.archives-ouvertes.fr/tel-00761099. 157, 159, 173

[9] R. Saurel and R. Abgrall. A multiphase Godunov method for compressible multifluid and multiphase flows. *Journal of Computational Physics*, 150:425–467, 1999. 157, 175

[10] D. W. Schwendeman, C. W. Wahle, and A. K. Kapila. The Riemann problem and a high-resolution Godunov method for a model of compressible two-phase flow. *Journal of Computational Physics*, 212:490–526, 2006. 157, 159, 175, 194

[11] S. Tokareva and E. F. Toro. HLLC-type Riemann solver for the Baer–Nunziato equations of compressible two-phase flow. *Journal of Computational Physics*, 229:3573–3604, 2010. 157, 175

[12] E. Toro, M. Spruce, and W. Speares. Restoration of the contact surface in the HLL-Riemann solver. *Shock waves*, 4:25–34, 1994. 175, 192

[13] N. Zuber and J. Findlay. Average volumetric concentration in two-phase flow systems. *Journal of Heat Transfer*, 87:453–468, 1965. 190

Conclusions et perspectives

Le contexte industriel de ces travaux de thèse se focalise sur deux configurations d'écoulements diphasiques eau-vapeur rencontrées dans certaines conduites des réacteurs à eau pressurisée. La première est initiée par la fermeture soudaine d'une vanne d'arrêt présente sur le circuit. L'écoulement monophasique liquide voit alors brutalement apparaître et se propager un front d'onde associé à un saut de pression de grande amplitude. Un tel front est appelé coup de bélier hydraulique [7, 13]. L'impact de ce dernier sur la structure mécanique de la conduite peut potentiellement engendrer des déformations, des fissures ou même des brèches.

La seconde configuration correspond à un régime d'écoulement stratifié [15] entre une phase d'eau liquide et une phase de vapeur circulant à contre courant l'une de l'autre. Sous l'effet des forces de cisaillement, l'interface entre les deux phases se déforme et l'écoulement évolue peu à peu vers un régime de type "slug" [15]. Des poches de vapeur se retrouvent alors piégées au sein de l'écoulement d'eau liquide. Le passage de ces poches à travers les systèmes de pompage du circuit peut engendrer une baisse du débit ainsi que des dégâts matériels. De plus, leur condensation brutale peut générer des coups de bélier dont l'impact sur les structures présente également un danger.

La première partie de cette thèse aborde la première configuration présentée ci-dessus. Si aucun phénomène de cavitation n'apparaît, l'écoulement est par nature monophasique liquide. Aussi, une modélisation diphasique par approche homogène [8] a été retenue. Le système d'équations à résoudre correspond alors au système d'Euler compressible. Au cours de la transition entre le régime nominal et la propagation du coup de bélier, la vitesse matérielle de l'écoulement reste très faible devant la célérité des ondes acoustiques. La particularité de cet écoulement compressible à faible nombre de Mach résulte alors de la soudaine apparition de sauts de pression de grande amplitude. En effet, le modèle asymptotique porté par le système d'Euler incompressible, pertinent pour le régime nominal, doit être remplacé par le modèle d'Allievi [1], plus adapté pour estimer ces sauts de pression.

Afin de traiter cette problématique d'écoulements multi-régimes, une méthode à pas fractionnaires, basée sur un splitting inspiré des travaux de Baraille *et al.* [5] entre un opérateur convectif et un opérateur acoustique a été proposée. L'originalité de l'approche tient à ce que le splitting est évolutif en temps à travers la donnée d'un unique paramètre $\mathscr{E}_0(t)$ à valeur dans l'intervalle $]0, 1]$. Cet aspect dynamique du splitting est crucial dans la mesure où il permet de sélectionner une résolution numérique adaptée à la nature de l'écoulement rencontré. En effet, pour des lois d'état de type gaz raide et sous réserve de positivité de la pression, ce splitting définit, dynamiquement, deux sous-systèmes hyperboliques conservatifs. Le premier est appelé sous-système convectif, noté $\mathcal{C}$. Lorsque le paramètre $\mathscr{E}_0$ tend vers un, ce sous-système tend formellement vers le système d'Euler complet. Cependant lorsque $\mathscr{E}_0$ tend vers zéro les termes associés au gradient de pression disparaissent de son jeu d'équations.

La résolution de ce sous-système s'appuie sur le comportement asymptotique du paramètre $\mathscr{E}_0$ dont la définition constitue un objectif de cette première partie de thèse. On souhaite notamment que $\mathscr{E}_0$ tende vers un pour des écoulements compressibles à haut nombre de Mach ou pour des écoulements compressibles basse vitesse admettant des sauts de pression de grande amplitude. Aussi, un solveur de Riemann approché dont l'intégration en temps est explicite a été proposé pour construire le flux numérique de ce sous-système. Combinée à un pas de temps basé sur

la célérité des ondes acoustiques les plus rapides, la résolution du sous-système $\mathcal{C}$ permet, lorsque $\mathscr{E}_0$ tend vers un, de capturer précisément les ondes de choc, ondes de raréfaction ainsi que les coups bélier potentiellement présents dans l'écoulement.

Le second sous-système, noté $\mathcal{A}$, est dit sous-système acoustique. Par complémentarité avec le sous-système $\mathcal{C}$, son flux s'annule quand $\mathscr{E}_0$ tend vers un. En revanche, dans le cas contraire où $\mathscr{E}_0$ tend vers zéro, son flux contient l'ensemble des contributions liées au gradient de pression. Le choix de discrétisation de ce sous-système est motivé par le fait que les petites valeurs de $\mathscr{E}_0$ correspondent à un régime d'écoulement à faible vitesse, admettant des sauts de pression de faible amplitude et dont l'importance est secondaire relativement à la dynamique des ondes matérielles. Aussi, le flux numérique du sous-système $\mathcal{A}$ est construit à partir d'une intégration implicite en temps de la dynamique associée à certains invariants de Riemann forts. Ce faisant, on espère pouvoir relaxer la contrainte de stabilité de l'approche à pas fractionnaires proposée et utiliser des pas de temps discrets adaptés à la propagation des ondes matérielles. Une analyse heuristique basée sur la propagation d'une onde de contact isolée suggère que la méthode numérique reste stable, pour tout nombre de Mach, pour des nombres de Courant basés sur les vitesses matérielles de l'ordre de 0.5.

La capacité de la méthode proposée à s'adapter aux transitions entre différents régimes d'écoulement repose donc sur la définition du paramètre $\mathscr{E}_0$. Au cours de ces travaux de thèse, $\mathscr{E}_0$ a été initialement construit sur la base du nombre de Mach maximal instantané de l'écoulement. Une telle définition permet alors de traiter des écoulements soniques ou supersoniques mais aussi des écoulements subsoniques au sein desquels les gradients de pression sont de faible amplitude.

Dans ce dernier cas de figure, on peut s'interroger sur l'aptitude du schéma numérique développé à approcher des solutions asymptotiques issues du système d'Euler incompressible mono ou multidimensionnel.

Face à cette problématique tout un pan de la littérature [11, 14, 19] met en garde quant aux difficultés rencontrées par les schémas de type Godunov approchés pour approximer, sur maillages grossiers, les solutions du système d'Euler incompressible multidimensionnel. Un traitement numérique préconisé consiste à introduire un terme correctif θ, proportionnel au nombre de Mach, afin de recentrer le flux de pression dans l'équation de quantité de mouvement du système.

Une telle correction a été introduite dans le deuxième chapitre de cette thèse afin de répondre à une problématique *différente* de précision sur les sauts de pression pour un écoulement monodimensionnel à faible nombre de Mach. Elle a néanmoins révélé une grande sensibilité du couple $(\mathscr{E}_0, \theta)$ sur la production d'oscillations artificielles venant polluer la qualité de la solution numérique. Des cas tests multidimensionnels non présentés dans cette thèse montrent que cette sensibilité perdure lors de la simulation d'écoulements incompressibles à densité variable. Dans tous les cas une étude plus approfondie sur la donnée du couple $(\mathscr{E}_0, \theta)$ afin de garantir la stabilité et la précision du schéma numérique proposé dans un régime proche de l'asymptotique du système d'Euler incompressible devrait être menée.

Afin de traiter le régime d'écoulement basse vitesse dans lequel un coup de bélier apparaît et se propage, la définition du paramètre $\mathscr{E}_0$ a été enrichie afin d'inclure un détecteur de sauts de pression. La construction d'un tel détecteur constitue un défi en soi. En effet, ce dernier doit distinguer d'une part les ondes de choc parasites de faible amplitude produites par l'écoulement à faible nombre de Mach d'un fluide très compressible, et d'autre part les sauts de pression très importants associés au passage d'un coup de bélier dans de l'eau très peu compressible. Dans le troisième chapitre de cette thèse, une approche naïve basée sur les relations de Rankine-Hugoniot appliquées à l'équation de la masse a été proposée. Une autre idée, non présentée dans ces travaux, consiste à construire ce détecteur de sauts de pression sur la base des relations de saut de Joukowski (1.17) [16]. Rappelons que ces relations sont obtenues dans le cadre du modèle asymptotique d'Allievi adapté à la modélisation des coups de bélier mécaniques à température constante. Malheureusement, les premières analyses basées sur des solutions de type ondes de choc isolées montrent que ce nouveau détecteur s'active même à travers les sauts de pression de faible amplitude d'un fluide de type gaz parfait s'écoulant à faible vitesse. Un travail de recherche sur l'inclu-

sion de la notion de compressibilité dans ce détecteur de sauts de pression devrait être mené à l'avenir.

Les idées présentées dans la deuxième partie de cette thèse ont été développées autour de la problématique liée à la transition entre l'écoulement stratifié eau-vapeur et le régime de type "slug". La modélisation diphasique choisie est construite sur la base d'une approche bifluide à deux pressions réprésentée à l'aide d'une version isentropique du système de Baer-Nunziato [4] avec termes sources de relaxation en pression et en vitesse. Lorsque ces derniers sont absents, une grande variété de solveurs de type Godunov approchés a déjà été proposée pour ce type de modèle [3, 10, 21]. Cependant, les preuves d'existence et d'unicité, ainsi que la construction d'une solution pour des problèmes de Riemann généralisés où les termes sources sont actifs, restent encore aujourd'hui hors d'atteinte. La construction d'un schéma numérique pour approximer la solution de ce type de problème se base alors souvent sur une approche à pas fractionnaires séparant la résolution de l'opérateur convectif de la résolution des termes de relaxation [12, 18, 20].

Ce travail prend le parti de renoncer à cette séparation, et entreprend la construction d'un schéma numérique où les effets de relaxation sont couplés à la convection. Pour ce faire, les travaux de Bereux et Sainsaulieu [6] sur les problèmes de Riemann linéaires généralisés sont repris et étendus. Les auteurs y présentent notamment le système d'EDO vérifié par la solution, moyennée en espace, d'un système linéaire hyperbolique et symmétrisable dans lequel des termes sources linéaires sont également présents. Le système d'EDO proposé tient compte des effets de convection et de relaxation à travers une différence de flux de bord, construits sur la base d'états soumis à la relaxation. Par la suite, le système d'EDO obtenu constitue la pierre d'angle d'une méthode numérique monodimensionnelle à maillage décalé.

L'extension des travaux de Bereux et Sainsaulieu se situe au niveau de la prise en compte des termes non-conservatifs inhérents au système de type Baer-Nunziato isentropique. Au sein du problème de Riemann linéaire généralisé, ces derniers sont modélisés par l'ajout d'une mesure de Dirac, de masse constante, portée par la trajectoire d'une onde matérielle dont la vitesse est gelée. En étudiant la structure de la solution dans le cas particulier où les effets de relaxation peuvent être découplés, ce travail propose une actualisation simple du système d'EDO introduit précédemment. Le schéma numérique proposé est alors conservatif pour les masses partielles ainsi que pour la quantité de mouvement de mélange. La positivité des masses partielles est également garantie sous-réserve d'une condition CFL *seulement* basée sur les valeurs propres de la partie convective du système étudié. Enfin, la positivité des masses partielles entraîne également le fait que le schéma préserve le principe du maximum sur le taux de présence statistique.

La méthode développée est comparée à des approches à pas fractionnaires construites à partir du schéma de Rusanov ou du solveur de Riemann approché HLLAC [17, 22]. La comparaison s'effectue sur des problèmes de Riemann généralisés basés sur le système de Baer-Nunziato isentropique avec relaxation en pression et en vitesse. Quelles que soient les échelles de temps de relaxation, les profils obtenus par la méthode non splittée proposée sont plus proches des solutions convergées en maillage que ceux issus de l'approche à pas fractionnaires basée sur le flux de Rusanov. Cependant, dans les régions où évoluent les discontinuités associées à l'onde de couplage du modèle, la méthode à pas fractionnaires de type HLLAC parvient à mieux saisir les détails de la solution obtenue sur maillages fins. Cependant, pour des échelles de temps de relaxation très petites relativement aux échelles de temps de l'opérateur convectif, le schéma proposé semble mieux approcher les variables d'écart en vitesse et en pression que les méthodes à pas fractionnaires.

Il convient de rappeler que, contrairement aux solveurs de Riemann approchés de type HLLAC, le schéma numérique proposé occulte l'estimation fine de l'ensemble des ondes et des états intermédiaires produits par la partie hyperbolique du modèle. Cette perte de détail intervient lors du processus de moyenne spatiale appliquée à la solution du problème de Riemann linéaire généralisé afin d'en extraire le système d'EDO mêlant convection et effets de relaxation. Cette moyenne spatiale est une solution de contournement face aux difficultés inhérentes à la prise en compte des effets de relaxation au sein d'un problème de Riemann, dans le cas du système Baer-Nunziato

isentropique.

Toujours est-il qu'une proximité troublante peut être observée entre les profils de solution analytique obtenus pour des problèmes de Riemann linéaires généralisés avec effets de relaxation découplés (voir FIGURE 5.10b du chapitre 5) et ceux calculés pour des problèmes de Riemann généralisés de type Baer-Nunziato isentropique avec relaxation en pression-vitesse (voir FIGURE 5.18b du chapitre 5). Aussi, pourrait-on s'interroger quant aux hypothèses de linéarisation suffisantes pour construire des solutions exactes d'un problème de Riemann généralisé basé sur un modèle bifluide convection-source relativement proche du système de Baer-Nunziato isentropique avec relaxation en pression et en vitesse. Ces solutions seraient alors utilisées afin de construire un schéma numérique. Reprenant les idées décrites à la FIGURE 5.1 du chapitre 5, les termes non-conservatifs du modèle de Baer-Nunziato seraient remplacés, dans le modèle approché, par une mesure de Dirac portée par la demi-droite $x = u_{\mathrm{I}}^{*}\, t$, avec u_{I}^{*} une vitesse *a priori* donnée. On chercherait alors à mettre en évidence des invariants de Riemann forts dont on pourrait intégrer les effets de relaxation le long de leur unique courbe caractéristique, et ce jusqu'au pied du front discontinu introduit par la mesure de Dirac. Pour exhiber de tels invariants, une technique pourrait consister à geler artificiellement le taux de présence statistique afin de pouvoir ré-écrire le système, dans les régions où la solution est régulière, comme deux systèmes d'Euler découplés. La construction d'un modèle de relaxation pour le système d'Euler décrite dans [9] montre alors que $u_k \pm \Pi_k / a_k$ (Π_k et a_k étant respectivement une pression et une constante de relaxation) sont des invariants de Riemann forts de ce modèle.

Une autre piste de réflexion est motivée par le fait que pour des conditions initiales uniformément à l'équilibre en pression et en vitesse dans tout le domaine, $p_2 = p_1 = \mathrm{P}$, $u_2 = u_1 = \mathrm{U}$, le schéma proposé préserve ces équilibres dans le temps. On pourrait alors étudier sa capacité à préserver certains autres équilibres physiques plus complexes qui peuvent potentiellement émerger du modèle de Baer-Nunziato isentropique en fonction des lois de fermeture et des échelles de temps de relaxation des termes sources. Ces équilibres s'écrivent généralement sous la forme d'une égalité liant les termes de relaxation algébriques à des termes différentiels d'ordre un construits à partir des gradients en espace de certaines quantités de mélange. Comme présenté dans [2], la construction formelle de certains de ces équilibres peut s'appuyer sur des développements de Chapman-Enskog appliqués aux EDP des variables de relaxation $\Delta p = p_2 - p_1$ et $\Delta u = u_2 - u_1$. Une démarche similaire moins spécifique présentée en Annexe A propose une description de l'ensemble des équilibres rencontrés en fonction du rapport des temps de relaxation en pression et en vitesse. Afin que ces équilibres transparaissent dans le schéma numérique construit, il nous semble primordial de baser ce dernier sur une ré-écriture du système de Baer-Nunziato isentropique en variables :

$$\begin{bmatrix} \mathcal{U} \\ \Delta \end{bmatrix} = \begin{bmatrix} [m_1,\, m,\, m\mathrm{U}]^{\mathrm{T}} \\ [\Delta u,\, \Delta p]^{\mathrm{T}} \end{bmatrix}, \qquad m = m_1 + m_2,\ m\mathrm{U} = m_1 u_1 + m_2 u_2. \tag{5.141}$$

Dans cette ré-écriture, seules les EDP associées à la variable Δ sont soumises à des effets de relaxation. Ayant au préalable gelé les contributions en $\mathcal{U}$ et $\partial_x \mathcal{U}$ dans les équations associées à Δ, les idées de Bereux-Sainsaulieu pourrait être appliquées à ce sous-système. On obtiendrait alors un système d'EDO en temps associées à la moyenne spatiale de Δ autour d'une face du maillage. Pour des temps de relaxation très petits devant les échelles de temps liées à la convection, ce système d'EDO projetterait la moyenne de Δ sur les équilibres attendus.

On pourrait alors s'intéresser au système conservatif associé à la variable $\mathcal{U}$ après avoir *gelé*, à l'aide des valeurs actualisées par le système d'EDO précédent, les contributions en Δ présentes dans le flux de cet autre sous-système. Sous-réserve d'hyperbolicité, on pourrait alors essayer de construire une solution exacte au problème de Riemann défini à une face du maillage. Pour des temps de relaxation très courts, l'idée serait de construire un schéma de Godunov associé à la variable $\mathcal{U}$ au sein duquel les contributions en variables Δ joueraient le rôle de loi de fermeture.

Références

[1] L. Allievi. *Teoria del colpo d'ariete*. Atti del Collegio degli Ingegneri ed Architetti Italiani, Milan, Italy (in Italian), 1913. 197

[2] A. Ambroso, C. Chalons, F. Coquel, T. Galié, E. Godlewski, P. A. Raviart, and N. Seguin. The drift-flux asymptotic limit of barotropic two-phase two-pressure models. *Communications in Mathematical Sciences*, 6 :521–529, 2008. 200

[3] A. Ambroso, C. Chalons, F. Coquel, and T. Galié. Relaxation and numerical approximation of a two-fluid two-pressure diphasic model. *ESAIM : Mathematical Modelling and Numerical Analysis*, 43 :1063–1097, 2009. 199

[4] M. R. Baer and J. W. Nunziato. A two-phase mixture theory for the deflagration-to-detonation transition (DDT) in reactive granular materials. *International Journal of Multiphase Flow*, 12 : 861–889, 1986. 199

[5] R. Baraille, G. Bourdin, F. Dubois, and A. Y. Le Roux. Une version à pas fractionnaires du schéma de Godunov pour l'hydrodynamique. *Compte Rendu de l'Académie des Sciences*, 314 : 147–152, 1992. 197

[6] F. Bereux and L. Sainsaulieu. A Roe-type Riemann solver for hyperbolic systems with relaxation based on time-dependent wave decomposition. *Numerische Mathematik*, 2 :143–185, 1997. 199

[7] A. Bergant, A. R. Simpson, and A. S. Tijsseling. Water hammer with column separation : A historical review. *Journal of Fluids and Structures*, 22 :135–171, 2006. 197

[8] S. Clerc. Numerical simulation of the homogeneous equilibrium model for two-phase flows. *Journal of Computational Physics*, 161 :354–375, 2000. 197

[9] F. Coquel, Q. L. Nguyen, M. Postel, and Q. H. Tran. Entropy-satisfying relaxation method with large time-steps for Euler IBVPS. *Mathematics of Computation*, 79 :1493–1533, 2010. 200

[10] F. Coquel, J. M. Hérard, K. Saleh, and N. Seguin. A robust entropy-satisfying finite volume scheme for the isentropic Baer-Nunziato model. *ESAIM : Mathematical Modelling and Numerical Analysis*, 48 :165–206, 2014. 199

[11] S. Dellacherie, P. Omnes, J. Jung, and P.A. Raviart. Construction of modified Godunov type schemes accurate at any Mach number for the compressible Euler system. *Mathematical Models and Methods in Applied Science*, 26 :2525–2615, 2016. 198

[12] T. Gallouët, J-M Hérard, and N. Seguin. Numerical modeling of two-phase flows using the two-fluid two-pressure approach. *Mathematical Models and Methods in Applied Sciences*, 14 :663–700, 2004. 199

[13] M. S. Ghidaoui, M. Zhao, D. A. McInnis, and D. H. Axworthy. A review of water hammer theory and practice. *Applied Mechanics Reviews*, 58 :49, 2005. 197

[14] H. Guillard and C. Viozat. On the behavior of upwind schemes in the low Mach number limit. *Computers and Fluids*, 28 :63–86, 1999. 198

[15] M. Ishii. *Thermo-Fluid Dynamic Theory of Two-Phase Flow*. Eyrolles, 1975. 197

[16] N. E. Joukowski. Memoirs of the Imperial Academy Society of St. Petersburg. *Proceedings of the American Water Works Association*, 24 :341–424, 1898. 198

[17] H. Lochon, F. Daude, P. Galon, and J. M. Hérard. HLLC-type Riemann solver with approximated two-phase contact for the computation of the Baer-Nunziato two-fluid model. *Journal of Computational Physics*, 326 :733–762, 2016. 199

[18] H. Lochon, F. Daude, P. Galon, and J. M. Hérard. Computation of fast depressurization of water using a two-fluid model : revisiting Bilicki modelling of mass transfer. *Computers & Fluids*, 156 :162–174, 2017. 199

[19] F. Rieper. A low-Mach number fix for Roe's approximate Riemann solver. *Journal of Computational Physics*, 230 :5263–5287, 2011. 198

[20] R. Saurel and R. Abgrall. A multiphase Godunov method for compressible multifluid and multiphase flows. *Journal of Computational Physics*, 150 :425–467, 1999. 199

[21] D. W. Schwendeman, C. W. Wahle, and A. K. Kapila. The Riemann problem and a high-resolution Godunov method for a model of compressible two-phase flow. *Journal of Computational Physics*, 212 :490–526, 2006. 199

[22] S. Tokareva and E. F. Toro. HLLC-type Riemann solver for the Baer–Nunziato equations of compressible two-phase flow. *Journal of Computational Physics*, 229 :3573–3604, 2010. 199

Annexe A

Équilibres convection-source pour le système Baer-Nunziato isentropique avec relaxation pression-vitesse

Le cadre de travail de cette annexe est la version isentropique d'un modèle de type Baer-Nunziato avec relaxation en pression-vitesse. Un tel modèle est présenté en (4.2). Dans ce système, l'expression des termes sources reste volontairement générale. Dans le jeu de variable $\mathbf{U} = [\alpha_1, m_1, m_1 u_1, m_2, m_2 u_2]^{\mathrm{T}}$, les effets de relaxation en pression et en vitesse s'écrivent en effet comme suit :

$$\left[-\frac{\widetilde{\mathrm{K}}_{\mathrm{p}}}{\tau_{\mathrm{p}}}\Delta p/p_{\mathrm{ref}}, 0, \frac{\widetilde{\mathrm{K}}_{\mathrm{u}}}{\tau_{\mathrm{u}}}\rho_{\mathrm{ref}}\Delta u, 0, -\frac{\widetilde{\mathrm{K}}_{\mathrm{u}}}{\tau_{\mathrm{u}}}\rho_{\mathrm{ref}}\Delta u\right]^{\mathrm{T}}. \tag{A.1}$$

Dans (A.1), τ_{p} et τ_{u} représentent des échelles de temps de relaxation qui sont *a priori* supposées très petites devant celles construites à partir des valeurs propres de la partie convective du système. Par ailleurs les co-facteurs $\widetilde{\mathrm{K}}_{\mathrm{p}}$ et $\widetilde{\mathrm{K}}_{\mathrm{u}}$ sont des termes en O(1) vis à vis des temps de relaxation.

Cette annexe se focalise principalement sur l'obtention de relations d'équilibre entre les termes sources algébriques de relaxation et certains gradients spatiaux liés à la convection. Pour cela, une ré-écriture du système est nécessaire. Elle s'appuie sur le jeu de variables

$$\mathbf{V} = \left[\alpha_1, \mathrm{P}, \mathrm{U}, \Delta u, \Delta p\right]^{\mathrm{T}}, \tag{A.2}$$

où P et U sont respectivement une pression et une vitesse de mélange du système. La construction des équilibres convection-source se base sur un développement de type Chapman-Enskog impliquant un rescaling des variables de relaxation. Une multitude d'équilibres peut alors être construite suivant la valeur du rapport $\tau_{\mathrm{p}}/\tau_{\mathrm{u}}$.

Par la suite une étude plus approfondie est menée lorsque les relations d'équilibre de la configuration $\tau_{\mathrm{p}}/\tau_{\mathrm{u}} = \mathrm{O}(1)$ sont "injectées" au sein de la matrice Jacobienne de convection. L'hyperbolicité, les valeurs propres ainsi que la structure des champs dans la limite $\Delta u \to 0$, $\Delta p \to 0$ sont notamment étudiées. On met alors en évidence l'existence d'une nouvelle célérité, c_{star}, dont l'ordre de grandeur est supérieur à la célérité de Wood propre aux mélanges diphasiques. Cette nouvelle célérité est reliée à la propagation des ondes non-linéaires de faible amplitude des variables de relaxation.

Cette annexe se termine par une dernière ré-écriture du système en variables

$$\mathbf{Z} = \left[m_1, m, m\mathrm{U}, \Delta u, \Delta p\right]^{\mathrm{T}}. \tag{A.3}$$

Ce choix est motivé par un objectif de construction d'un schéma numérique qui intégrerait les relations d'équilibre convection-source établies dans cette annexe dans le flux numérique lié aux variables conservatives $\mathcal{U} = [m_1, m, m\mathrm{U}]$.

A.1 Re-writing of the system in equilibrium-relaxation variables

As previously introduced, consider the vector of conservative variables related to the isentropic Baer-Nunziato system (4.14): $\mathbf{U} = [\alpha_1, m_1, m_1 u_1, m_2, m_2 u_2]^{\mathrm{T}}$. It belongs to the phase-space $\Phi^{\mathscr{C}}$ defined by:

$$\Phi^{\mathscr{C}} = \left\{ \mathbf{U} \in \mathbb{R}^5, \text{ s. t. } \alpha_1 \in]0,1[,\ m_1 > 0,\ m_2 > 0 \right\}. \tag{A.4}$$

Let us introduce the change of variable involving the non-conservative mixture variables completed by the velocity and pressure differences:

$$\mathbf{U} \to \mathbf{V}(\mathbf{U}) = \begin{bmatrix} \alpha_1 \\ \mathrm{U} \\ \mathrm{P} \\ \Delta u \\ \Delta p \end{bmatrix}, \tag{A.5}$$

with,

$$\left\{ \begin{array}{lcl} \alpha_2 & = & 1 - \alpha_1, \\ m & = & m_1 + m_2, \\ m\,\mathrm{U} & = & m_1 u_1 + m_2 u_2, \\ \mathrm{P} & = & \alpha_1 p_1\left(\frac{m_1}{\alpha_1}\right) + \alpha_2 p_2\left(\frac{m_2}{\alpha_2}\right), \\ \Delta u & = & \frac{m_2 u_2}{m_2} - \frac{m_1 u_1}{m_1}, \\ \Delta p & = & p_2\left(\frac{m_2}{\alpha_2}\right) - p_1\left(\frac{m_1}{\alpha_1}\right). \end{array} \right. \tag{A.6}$$

Remark A.1.1 (Admissibility of the change of variable $\mathbf{U} \to \mathbf{V}(\mathbf{U})$)
The change of variable (A.5) is admissible in the sense that,

$$\forall \mathbf{U} \in \Phi^{\mathscr{C}},\ \det\left(\partial_{\mathbf{U}} \mathbf{V}\right) = \frac{c_1^2 c_2^2}{\alpha_1 \alpha_2} \frac{1}{m_1 m_2} > 0, \tag{A.7}$$

and,

$$\begin{array}{ccc} \Phi^{\mathscr{C}} & \longmapsto & \mathbf{V}\left(\Phi^{\mathscr{C}}\right) \\ \mathbf{U} & \to & \mathbf{V}(\mathbf{U}) \end{array} \tag{A.8}$$

is bijective.

Proof 10
The derivation of the determinant results from classical manipulations on the differentials $\mathrm{d}(\mathrm{U})$, $\mathrm{d}(\mathrm{P})$, $\mathrm{d}(\Delta u)$ *and* $\mathrm{d}(\Delta p)$. *Let us show that function (A.8) is injective. Assume that there exist two states* $\mathbf{U}^-$ *and* $\mathbf{U}^+$ *of* $\Phi^{\mathscr{C}}$ *such that* $\mathbf{V}(\mathbf{U}^-) = \mathbf{V}\left(\mathbf{U}^+\right)$. *Thus,* $\forall k \in \{1,2\}$, $\alpha_k^- = \alpha_k^+$. *Besides one can write:*

$$\begin{aligned} p_1 &= \mathrm{P} - \alpha_2 \Delta p, \\ p_2 &= \mathrm{P} + \alpha_1 \Delta p. \end{aligned} \tag{A.9}$$

Then,

$$p_1\left(\frac{m_1^+}{\alpha_1^+}\right) = \mathrm{P}^+ - \alpha_2^+ \Delta p^+ = \mathrm{P}^- - \alpha_2^- \Delta p^- = p_1\left(\frac{m_1^-}{\alpha_1^-}\right) = p_1\left(\frac{m_1^-}{\alpha_1^+}\right). \tag{A.10}$$

Recall that according to the EOS properties written in (4.4), $\rho_k \to p_k^{EOS}(\rho_k)$ *is bijective from* $\mathbb{R}_+$ *to* $\mathbb{R}_+$. *One can deduce that* $m_1^+ = m_1^-$ *and* $m_2^+ = m_2^-$. *Finally, one can notice that,*

$$\begin{aligned} m_1 u_1 &= m_1 \mathrm{U} - \frac{m_1 m_2}{m} \Delta u, \\ m_2 u_2 &= m_2 \mathrm{U} + \frac{m_1 m_2}{m} \Delta u, \end{aligned} \tag{A.11}$$

from which one obtains $(m_1 u_1)^+ = (m_1 u_1)^-$ *and* $(m_2 u_2)^+ = (m_2 u_2)^-$.

In the following the isentropic Baer-Nunziato system (4.14) is rewritten using the new set of variables $\mathbf{V}$. Let us first re-write the isentropic Baer-Nunziatio system using the non-conservative set of variables $\mathbf{W} = \left[\alpha_1,\, u_1,\, p_1,\, u_2,\, p_2\right]^{\mathrm{T}}$. For smooth solutions, it reads $\forall k \in \{1,2\}$:

$$\begin{array}{lllllllll}
\partial_t \alpha_k & + & u_{\mathrm{I}}\,\partial_x \alpha_k & & & & & = & (-1)^k\,\mathrm{K_p}\,\Delta p, \\
\partial_t u_k & + & u_k\,\partial_x u_k & + & \tau_k\,\partial_x p_k & + & \frac{p_k - p_{\mathrm{I}}}{m_k}\,\partial_x \alpha_k & = & (-1)^{k+1}\,\frac{\mathrm{K_u}}{m_k}\,\Delta u, \\
\partial_t p_k & + & u_k\,\partial_x p_k & + & \mathrm{C}_k\,\partial_x u_k & + & \frac{\mathrm{C}_k}{\alpha_k}\,(u_k - u_{\mathrm{I}})\,\partial_x \alpha_k & = & (-1)^{k+1}\,\mathrm{K_p}\,\frac{\mathrm{C}_k}{\alpha_k}\,\Delta p.
\end{array} \tag{A.12}$$

Recall that C_k is equal to $\rho_k\, c_k^2$ and that closure laws are such that $u_{\mathrm{I}} = u_2$, $p_{\mathrm{I}} = p_1$. What is more, define $\mathrm{Y}_k = m_k/m$.

The PDEs of U, P, Δu and Δp are obtained by manipulating system (A.12) and using the differential relations written below:

$$\partial_x \mathrm{Y}_1 = \mathrm{W}^{\alpha}\,\partial_x \alpha_1 + \mathrm{W}^{\mathrm{P}}\,\partial_x \mathrm{P} + \mathrm{W}^{\Delta p}\,\partial_x \Delta p, \tag{A.13}$$

with,

$$\begin{cases}
\mathrm{W}^{\alpha} = \mathrm{Y}_1\mathrm{Y}_2\left[\dfrac{1}{\alpha_1\alpha_2} + \Delta p\left(\dfrac{1}{\mathrm{C}_1} - \dfrac{1}{\mathrm{C}_2}\right)\right], \\
\mathrm{W}^{\mathrm{P}} = \mathrm{Y}_1\mathrm{Y}_2\left(\dfrac{1}{\mathrm{C}_1} - \dfrac{1}{\mathrm{C}_2}\right), \\
\mathrm{W}^{\Delta p} = \mathrm{Y}_1\mathrm{Y}_2\left(\dfrac{\alpha_2}{\mathrm{C}_1} + \dfrac{\alpha_1}{\mathrm{C}_2}\right).
\end{cases} \tag{A.14}$$

$$\begin{cases}
\partial_x p_1 = \partial_x \mathrm{P} + \Delta p\,\partial_x \alpha_1 - \alpha_2\,\partial_x \Delta p, \\
\partial_x p_2 = \partial_x \mathrm{P} + \Delta p\,\partial_x \alpha_1 + \alpha_1\,\partial_x \Delta p, \\
\\
\partial_x u_1 = \partial_x \mathrm{U} + \Delta u\,\partial_x \mathrm{Y}_1 - \mathrm{Y}_2\,\partial_x \Delta u, \\
\partial_x u_2 = \partial_x \mathrm{U} + \Delta u\,\partial_x \mathrm{Y}_1 + \mathrm{Y}_1\,\partial_x \Delta u.
\end{cases} \tag{A.15}$$

After tedious calculations, the isentropic Baer-Nunziato system, expressed in variable $\mathbf{V}$, reads:

$$\partial_t \mathbf{V} \quad + \quad \underline{\underline{\mathbf{C}}}(\mathbf{V})\,\partial_x \mathbf{V} \quad = \quad \mathbf{G}(\mathbf{V}), \tag{A.16}$$

the Jacobian matrix $\underline{\underline{\mathbf{C}}}(\mathbf{V})$ being equal to,

$$\begin{bmatrix}
\mathrm{U} + \mathrm{Y}_1\,\Delta u & 0 & 0 & 0 & 0 \\
\omega_{\mathrm{U},\alpha_1}\,(\Delta u)^2 & \mathrm{U} & \frac{1}{m}\left(1 + \omega_{\mathrm{U,P}}\,(\Delta u)^2\right) & 2\mathrm{Y}_1\mathrm{Y}_2\,\Delta u & \omega_{\mathrm{U},\Delta p}\,(\Delta u)^2 \\
\omega_{\mathrm{P},\alpha_1}\,\Delta u & \alpha_1\mathrm{C}_1 + \alpha_2\mathrm{C}_2 & \mathrm{U} + \omega_{\mathrm{P,P}}\,\Delta u & \omega_{\mathrm{P},\Delta u} & \omega_{\mathrm{P},\Delta p}\,\Delta u \\
\mathrm{W}^{\alpha}\,(\Delta u)^2 + \omega_{\Delta u,\alpha_1}\,\Delta p & \Delta u & \mathrm{W}^{\mathrm{P}}\,(\Delta u)^2 + \tau_2 - \tau_1 & \mathrm{U} + \omega_{\Delta u,\Delta u}\,\Delta u & \alpha_2\tau_1 + \alpha_1\tau_2 + \mathrm{W}^{\Delta p}\,(\Delta u)^2 \\
\omega_{\Delta p,\alpha_1}\,\Delta u & \mathrm{C}_2 - \mathrm{C}_1 & \omega_{\Delta p,\mathrm{P}}\,\Delta u & \mathrm{Y}_2\mathrm{C}_1 + \mathrm{Y}_1\mathrm{C}_2 & \mathrm{U} + \omega_{\Delta p,\Delta p}\,\Delta u
\end{bmatrix}, \tag{A.17}$$

with,

$$\begin{cases}
\omega_{\mathrm{U},\alpha_1} = \mathrm{Y}_1\mathrm{Y}_2\left[\left(\dfrac{\mathrm{Y}_2}{\mathrm{C}_1} + \dfrac{\mathrm{Y}_1}{\mathrm{C}_2}\right)\Delta p + \left(\dfrac{\mathrm{Y}_2}{\alpha_1} - \dfrac{\mathrm{Y}_1}{\alpha_2}\right)\right], \\
\omega_{\mathrm{U,P}} = m\mathrm{Y}_1\mathrm{Y}_2\left[\dfrac{\mathrm{Y}_2}{\mathrm{C}_1} + \dfrac{\mathrm{Y}_1}{\mathrm{C}_2}\right], \\
\omega_{\mathrm{U},\Delta p} = -\mathrm{Y}_1\mathrm{Y}_2\left[\dfrac{\mathrm{Y}_2\alpha_2}{\mathrm{C}_1} - \dfrac{\mathrm{Y}_1\alpha_1}{\mathrm{C}_2}\right],
\end{cases} \tag{A.18}$$

$$\begin{cases}
\omega_{\mathrm{P},\alpha_1} = -\left[\alpha_1\Delta p + \mathrm{C}_1 - (\alpha_1\mathrm{C}_1 + \alpha_2\mathrm{C}_2)\,\mathrm{W}^{\alpha}\right], \\
\omega_{\mathrm{P,P}} = -\alpha_1\mathrm{Y}_2 + \alpha_2\mathrm{Y}_1 + (\alpha_1\mathrm{C}_1 + \alpha_2\mathrm{C}_2)\,\mathrm{W}^{\mathrm{P}}, \\
\omega_{\mathrm{P},\Delta u} = -\left[\mathrm{Y}_2(\alpha_1\mathrm{C}_1) - \mathrm{Y}_1(\alpha_2\mathrm{C}_2)\right], \\
\omega_{\mathrm{P},\Delta p} = \alpha_1\alpha_2 + (\alpha_1\mathrm{C}_1 + \alpha_2\mathrm{C}_2)\,\mathrm{W}^{\Delta p},
\end{cases} \tag{A.19}$$

$$\begin{cases} \omega_{\Delta u,\alpha_1} = -\left(\dfrac{1}{m_2} + \tau_1 - \tau_2\right), \\ \omega_{\Delta u,\Delta u} = (2Y_1 - 1)\,, \end{cases} \tag{A.20}$$

$$\begin{cases} \omega_{\Delta p,\alpha_1} = \Delta p + \dfrac{C_1}{\alpha_1} + (C_2 - C_1)\,W^{\alpha}, \\ \omega_{\Delta p,P} = 1 + (C_2 - C_1)\,W^{P}, \\ \omega_{\Delta p,\Delta p} = -\alpha_2 Y_2 + \alpha_1 Y_1 + (C_2 - C_1)\,W^{\Delta p}, \end{cases} \tag{A.21}$$

and,

$$\mathbf{G} = \begin{bmatrix} -K_p\,\Delta p \\ 0 \\ K_p\left(\Delta p - (C_2 - C_1)\right)\Delta p \\ -K_u\,\frac{m}{m_1 m_2}\,\Delta u \\ -K_p\left(\frac{C_1}{\alpha_1} + \frac{C_2}{\alpha_2}\right)\Delta p \end{bmatrix}. \tag{A.22}$$

Let us notice that the coefficients $\omega_{X,Y}$ are zeroth-order term with respect to Δu or Δp. Inside the Jacobian matrix (A.17), most of those terms are multiplied by these relaxation variables. Thus, the remaining zeroth-order terms with respect to Δu, Δp in (A.17) have been highlighted in green.

In the next section, formal Chapman-Enskog expansions on the relaxation-variable equations are performed so that to deduce important information about the conversion of algebraic relaxation source terms into spatial gradients at equilibrium.

A.2 Conversion of algebraic source terms into spatial gradients

The expressions of relaxation source term cofactors K_u and K_p are not specified in this section. Following formulas given in (4.11b) and (4.13b), one can rewrite them as:

$$K_p = \frac{\widetilde{K}_p}{\tau_p\, p_{ref}},\ K_u = \frac{\widetilde{K}_u}{\tau_u}\rho_{ref}. \tag{A.23}$$

Recall that, τ_p (respectively τ_u) is a pressure (respectively a velocity) relaxation time-scale. What is more, p_{ref} (respectively ρ_{ref}) is a reference pressure (respectively a reference density). Finally $\widetilde{K}_p$ and $\widetilde{K}_u$ are non-specified non-dimensional cofactors tending towards zero as α_1 tends towards zero or one. Let us also stress that both $\widetilde{K}_p$ and $\widetilde{K}_u$ are O(1) with respect to τ_p and τ_u. In many works [1, 2, 5], the pressure relaxation process is assumed to be much faster than the velocity relaxation. As a result, $\tau_p \ll \tau_u$ is generally imposed when performing the derivation of an asymptotic equilibrium sub-system. In this work, no assumption is made *a priori* about the order of τ_p/τ_u. Indeed, leaning on the work of Gavrilyuk [6], a large variety of physical phenomena can influence the pressure relaxation time-scale. Besides, the order of magnitude of each of them depends on external parameters as well as flow configurations. Hence, one could assume the existence of two-phase flow patterns such that $\tau_p \approx \tau_u$.

In order to preserve symmetry between pressure and velocity relaxation time-scales, let us introduce τ, η_p, η_u such that:

$$\tau = \min\left(\tau_p, \tau_u\right),\ \eta_p = \frac{\tau}{\tau_p},\ \eta_u = \frac{\tau}{\tau_u}. \tag{A.24}$$

Similarly to chapter 4 and chapter 5, stiff hyperbolic relaxation systems are considered herein. Thus, $\tau \ll \tau_{conv}$, where τ_{conv} is a time-scale based on the eigenvalues of the convective Jacobian

matrix. Hence, three different sub-regimes can be identified in the limit $\tau \to 0$:

$$\frac{\eta_p}{\eta_u} \approx 1 \Leftrightarrow \tau_p \approx \tau_u, \tag{A.25a}$$

$$\frac{\eta_p}{\eta_u} \gg 1 \Leftrightarrow \tau_p \ll \tau_u,\ \tau = \tau_p, \tag{A.25b}$$

$$\frac{\eta_p}{\eta_u} \ll 1 \Leftrightarrow \tau_p \gg \tau_u,\ \tau = \tau_u. \tag{A.25c}$$

In the first case, pressure and velocity relaxation processes occur at the same rate. The formal equilibrium model is made of a single pressure and a single velocity. Starting from seven-equation models, the work of Kapila *et al.* [7, 8] describes a five-equation model resulting from successive velocity-pressure asymptotic relaxations. Let us also mention the work of Kreeft and Koren [10] which provides a new conservative formulation of the above five-equation model.

In the formal asymptotic sub-regime (A.25b), both phases should be endowed with the same pressure and two distinct velocities. Such a configuration might be associated with two-fluid single-pressure models. It is known that those models lack of good mathematical properties. Indeed, the eigenvalues of their Jacobian matrix may take complex values and thus threaten the hyperbolicity of the system at stake.

Eventually, in the limit of sub-regime (A.25c), both phases have the same velocity but different pressures. As a consequence, this configuration might correspond to two-fluid two-pressure six-equation models as the one proposed by Saurel *et al.* [15].

In the sequel, a formal Chapman-Enskog expansion is applied to the relaxation-variable equations (A.16), (A.17). Considering state values close to the equilibrium manifold,

$$\left\{\mathbf{V} \in \mathbb{R}^5,\ \text{s. t. } \Delta u = 0,\ \Delta p = 0\right\}, \tag{A.26}$$

the relaxation variables are reformulated as:

$$\begin{cases} \Delta u = 0 + \tau_u \Delta u' + O(\tau_u^2), \\ \Delta p = 0 + \tau_p \Delta p' + O(\tau_p^2). \end{cases} \tag{A.27}$$

What is more, the remaining equilibrium variables α_1, U and P are supposed to contain a zeroth-order contribution with respect to $\max(\tau_u, \tau_p)$. Thus, no expansion in powers of τ_u or τ_p is introduced for these variables. We now try to identify the terms of similar order of magnitude in the relaxation-variable equations according to the different asymptotic regimes presented in (A.25).

A.2.1 Equilibrium in the case: $\tau_p \approx \tau_u$

When the above re-scaling is injected into the equations of Δu and Δp, one can identify differential and algebraic expressions weighted by η_p/τ or η_u/τ. If one keeps only these leading-order terms, one can extract two equilibrium relations namely:

$$-K_u \frac{m}{m_1 m_2} \Delta u = (\tau_2 - \tau_1)\, \partial_x P, \tag{A.28a}$$

$$-K_p \left(\frac{C_1}{\alpha_1} + \frac{C_2}{\alpha_2}\right) \Delta p = (C_2 - C_1)\, \partial_x U. \tag{A.28b}$$

Equilibrium (A.28a) says that velocity relaxation acts actually as a mixture pressure gradient weighted by the specific volume difference of both phases. On the contrary, pressure relaxation effects can be related to the gradient of a velocity mixture balanced by the difference $C_2 - C_1$. One can mention that the equilibrium relations (A.28) have already been obtained in [12, 13] by performing the same simultaneous pressure-velocity relaxation assumption. The trace of these equilibriums is also present in the single-velocity and single-pressure five-equation model derived in [8] and [11] where pressure and velocity relaxations are performed successively.

A.2.2 Equilibrium in the case: $\tau_p \ll \tau_u$

In this sub-regime three additional contributions can be added into equality (A.28b) if it is assumed that $\tau_u/\tau_p = O(1/\tau_p)$ with $\tau_p \to 0$. The new pressure equilibrium then reads:

$$-K_u \frac{m}{m_1 m_2} \Delta u = (\tau_2 - \tau_1)\, \partial_x P, \tag{A.29a}$$

$$-K_p \left(\frac{C_1}{\alpha_1} + \frac{C_2}{\alpha_2}\right) \Delta p = (C_2 - C_1)\, \partial_x U + \omega_{\Delta p, P} \Delta u \partial_x P + \hat{\omega}_{\Delta p, \alpha_1} \Delta u \partial_x \alpha_1 + [Y_2 C_1 + Y_1 C_2]\, \partial_x \Delta u, \tag{A.29b}$$

with,

$$\begin{cases} \omega_{\Delta p, P} = 1 + (C_2 - C_1)\, W^P, \\ \hat{\omega}_{\Delta p, \alpha_1} = \dfrac{C_1}{\alpha_1} + (C_2 - C_1)\, \dfrac{Y_1 Y_2}{\alpha_1 \alpha_2}. \end{cases} \tag{A.30}$$

One can notice that $\tau_u/\tau_p = O(1/\tau_p)$ is equivalent to $\tau_u = O(1)$. Thus, the stiffness of the velocity relaxation process might vanish. If it is the case, equality (A.29a) does not hold anymore.

A.2.3 Equilibrium in the case: $\tau_p \gg \tau_u$

Supposing that $\tau_p/\tau_u = O(1/\tau_u)$ with $\tau_u \to 0$, The equilibrium relation (A.28a) is completed by the differential terms weighted by τ_p/τ_u. It gives:

$$-K_u \frac{m}{m_1 m_2} \Delta u = (\tau_2 - \tau_1)\, \partial_x P + [\alpha_2 \tau_1 + \alpha_1 \tau_2]\, \partial_x \Delta p + \omega_{\Delta u, \alpha_1} \Delta p \partial_x \alpha_1, \tag{A.31a}$$

$$-K_p \left(\frac{C_1}{\alpha_1} + \frac{C_2}{\alpha_2}\right) \Delta p = (C_2 - C_1)\, \partial_x U, \tag{A.31b}$$

with,

$$\omega_{\Delta u, \alpha_1} = -\left(\frac{1}{m_2} + \tau_1 - \tau_2\right). \tag{A.32}$$

Once again, $\tau_p/\tau_u = O(1/\tau_u)$ is equivalent to $\tau_p = O(1)$. Thus, the stiffness of the pressure relaxation process might vanish. If it is the case, equality (A.31b) does no longer hold.

A.2.4 Global equilibrium formulation

It is possible to summarize relations (A.28), (A.29) and (A.31) in a more compact form. Indeed, consider a smooth (at least continuous) function $\Phi : \mathbb{R}_+ \to [0, 1]$ such that $\forall X \in \mathbb{R}_+$:

$$\Phi(X) = \begin{cases} 1 \text{ if } X \ll 1\ (\to 0), \\ 0 \text{ if } X \in [1, +\infty[. \end{cases} \tag{A.33}$$

Then, the equilibriums can be formally rewritten as:

$$\begin{aligned} -K_u \frac{m}{m_1 m_2} \Delta u &= (\tau_2 - \tau_1)\, \partial_x P + \Phi\left(\frac{\tau_u}{\tau_p}\right) \left([\alpha_2 \tau_1 + \alpha_1 \tau_2]\, \partial_x \Delta p + \omega_{\Delta u, \alpha_1} \Delta p \partial_x \alpha_1\right), \\ -K_p \left(\frac{C_1}{\alpha_1} + \frac{C_2}{\alpha_2}\right) \Delta p &= (C_2 - C_1)\, \partial_x U \\ &\quad + \Phi\left(\frac{\tau_p}{\tau_u}\right) \left(\omega_{\Delta p, P} \Delta u \partial_x P + \hat{\omega}_{\Delta p, \alpha_1} \Delta u \partial_x \alpha_1 + [Y_2 C_1 + Y_1 C_2]\, \partial_x \Delta u\right). \end{aligned} \tag{A.34}$$

The above section has allowed to define three different relaxation sub-regimes. For each of them, one can turn the algebraic source terms into first-order differential expressions. Therefore, at equilibrium, relaxation acts as a sum of gradients which can be integrated into the initial Jacobian matrix of the isentropic Baer-Nunziato system. In the following, attention is paid to the influence of those new gradients in terms of hyperbolicity for the asymptotic system obtained under the sub-regime $\tau_p \approx \tau_u$, $\tau \to 0$.

A.3 Isentropic Baer-Nunziato system at equilibrium

Formulas (A.28) are now injected into system (A.16). Let us define the pressure $\mathcal{P}^{\text{eq}}$ as:

$$\mathcal{P}^{\text{eq}} = \frac{\mathrm{C}_1}{\alpha_1} + \frac{\mathrm{C}_2}{\alpha_2}. \tag{A.35}$$

For smooth solutions, the resulting system reads:

$$\partial_t \mathbf{V} \quad + \quad \underline{\underline{\mathbf{C}}}^{\text{eq}}(\mathbf{V})\, \partial_x \mathbf{V} \quad = \quad \mathbf{G}^{\text{eq}}(\mathbf{W}), \tag{A.36}$$

with $\underline{\underline{\mathbf{C}}}^{\text{eq}}$:

$$\begin{bmatrix} \mathrm{U} + \mathrm{Y}_1 \Delta u & -\frac{\mathrm{C}_2 - \mathrm{C}_1}{\mathcal{P}^{\text{eq}}} & 0 & 0 & 0 \\ \omega_{\mathrm{U},\alpha_1} (\Delta u)^2 & \mathrm{U} & \frac{1}{m}\left(1 + \omega_{\mathrm{U},\mathrm{P}} (\Delta u)^2\right) & 2\mathrm{Y}_1\mathrm{Y}_2 \Delta u & \omega_{\mathrm{U},\Delta p} (\Delta u)^2 \\ \omega_{\mathrm{P},\alpha_1} \Delta u & m c_{\mathrm{w}}^2 & \mathrm{U} + \omega_{\mathrm{P},\mathrm{P}} \Delta u & \omega_{\mathrm{P},\Delta u} & \omega_{\mathrm{P},\Delta p} \Delta u \\ \mathrm{W}^{\alpha} (\Delta u)^2 + \omega_{\Delta u,\alpha_1} \Delta p & \Delta u & \mathrm{W}^{\mathrm{P}} (\Delta u)^2 + 0 & \mathrm{U} + \omega_{\Delta u,\Delta u} \Delta u & \alpha_2\tau_1 + \alpha_1\tau_2 + \mathrm{W}^{\Delta p} (\Delta u)^2 \\ \omega_{\Delta p,\alpha_1} \Delta u & 0 & \omega_{\Delta p,\mathrm{P}} \Delta u & \mathrm{Y}_2\mathrm{C}_1 + \mathrm{Y}_1\mathrm{C}_2 & \mathrm{U} + \omega_{\Delta p,\Delta p} \Delta u \end{bmatrix}, \tag{A.37}$$

and,

$$\mathbf{G}^{\text{eq}} = \begin{bmatrix} 0 \\ 0 \\ \mathrm{K}_{\mathrm{p}} (\Delta p)^2 \\ 0 \\ 0 \end{bmatrix}. \tag{A.38}$$

In matrix (A.37), the coefficients written in red result from the injection of the pressure equilibrium relation (A.28b) into the Jacobian matrix while the blue coefficients refer to the injection of the velocity equilibrium (A.28a). As already observed in [8, 11, 13, 14], the pressure relaxation source term provides an additional non-conservative term $-(\mathrm{C}_2 - \mathrm{C}_1)/\mathcal{P}^{\text{eq}}\, \partial_x \mathrm{U}$ in the equation of α_1. Besides, the Wood [17] or Wallis [16] celerity pops up in the equation of P. Recall that it is defined as:

$$\frac{1}{m c_{\mathrm{w}}^2} = \frac{\alpha_1}{\mathrm{C}_1} + \frac{\alpha_2}{\mathrm{C}_2}. \tag{A.39}$$

It replaces the initial frozen celerity $m\, c_{\text{froz}}^2 = \alpha_1 \mathrm{C}_1 + \alpha_2 \mathrm{C}_2$. In Figure A.1, the Wood celerity (red curve) and the frozen celerity (green curve) are displayed as a function of α_1 for thermodynamical parameters corresponding to saturated liquid and vapor phases. One can also notice that the integration of relations (A.34) in the relaxation variables dynamics allows to remove two zeroth-order terms with respect to Δu and Δp.

In many works dealing with the derivation of reduced equation models stemming from two-phase hyperbolic systems with relaxation, the relaxation-variable equations are in the end discarded and replaced by algebraic equilibrium relations. Following [3], in the present work, we conjecture that it is important for the accuracy of the numerical method to capture the dynamics of the relaxation variables whatever the stiffness of the relaxation time-scales is. Therefore, in the sub-regime $\tau_{\mathrm{u}} \approx \tau_{\mathrm{p}}$, $\tau \to 0$, it is assumed that even if the amplitudes of Δu and Δp vanish almost immediately towards zero, the dynamics of these variables can be potentially crossed by fast non-linear waves. As a result, the gradients $\partial_x \Delta u$ and $\partial_x \Delta p$ are not dropped off, and the asymptotic Jacobian is still a matrix belonging to $\mathbb{R}^{5\times 5}$.

A.3.1 Asymptotic Jacobian matrix

In the limit $\Delta u \to 0$ and $\Delta p \to 0$, the convection matrix $\underline{\underline{\mathbf{C}}}^{\text{eq}}$ can be simplified as:

$$\underline{\underline{\mathbf{C}}}^{\text{eq}}_{\Delta \to 0} = \begin{bmatrix} \mathrm{U} & -\frac{\mathrm{C}_2 - \mathrm{C}_1}{\mathcal{P}^{\text{eq}}} & 0 & 0 & 0 \\ 0 & \mathrm{U} & \frac{1}{m} & 0 & 0 \\ 0 & \mathbf{m c_{\mathrm{w}}^2} & \mathrm{U} & \omega_{\mathrm{P},\Delta u} & 0 \\ 0 & 0 & \mathbf{0} & \mathrm{U} & \alpha_2\tau_1 + \alpha_1\tau_2 \\ 0 & \mathbf{0} & 0 & \mathrm{Y}_2\mathrm{C}_1 + \mathrm{Y}_1\mathrm{C}_2 & \mathrm{U} \end{bmatrix}. \tag{A.40}$$

It can be observed that the injection of relations (A.28) into the relaxation-variable dynamics allows to obtain an asymptotic Jacobian matrix that is block upper triangular. The dynamics of Δu and Δp do no longer depend on $\partial_x \alpha_1$, $\partial_x \mathrm{U}$ and $\partial_x \mathrm{P}$. Besides, the dynamics of the equilibrium variables is only coupled with the relaxation-variable equations through the term $\omega_{\mathrm{P},\Delta u} \partial_x \Delta u$. The simple stucture of the above asymptotic matrix (A.40) allows to derive its eigenvalues as well as its fields composition. The eigenvalues are:

$$\lambda_1^{\mathrm{eq}} = \mathrm{U},\ \lambda_2^{\mathrm{eq}} = \mathrm{U} + c_{\mathrm{w}},\ \lambda_3^{\mathrm{eq}} = \mathrm{U} - c_{\mathrm{w}},\ \lambda_4^{\mathrm{eq}} = \mathrm{U} + c_{\mathrm{star}},\ \lambda_5^{\mathrm{eq}} = \mathrm{U} - c_{\mathrm{star}}, \tag{A.41}$$

with,

$$c_{\mathrm{star}}^2 = (\alpha_2\tau_1 + \alpha_1\tau_2) \times (\mathrm{Y}_2\mathrm{C}_1 + \mathrm{Y}_1\mathrm{C}_2) = \alpha_2 c_1^2 + \alpha_1 c_2^2. \tag{A.42}$$

One can point out that the first three eigenvalues are related to the block of equilibrium variables. They have already been found in [8]. However the emergence of c_{star} results from the fact that the relaxation variable dynamics has been maintained in the asymptotic approach. To the best of our knowledge c_{star} is a new celerity associated with the relaxation variables.

In Figure A.1, a comparison between the frozen celerity c_{froz}, the Wood celerity c_{w} and the new celerity c_{star} seen as functions of α_1 is conducted. For this purpose the phase 1 (respectively the phase 2) is assimilated to a saturated vapor phase (respectively a saturated liquid phase) whose density $\rho_{\mathrm{vap}}^{\mathrm{sat}}(p^{\mathrm{sat}})$, $\rho_{\mathrm{liq}}^{\mathrm{sat}}(p^{\mathrm{sat}})$ and sound speed $c_{\mathrm{vap}}^{\mathrm{sat}}(p^{\mathrm{sat}})$ and $c_{\mathrm{liq}}^{\mathrm{sat}}(p^{\mathrm{sat}})$ are given in Table A.1.

	Pressure (bar)	Density $(kg.m^{-3})$	Sound speed $(m.s^{-1})$
Phase 1	$p^{\mathrm{sat}} = 50$	$\rho_{\mathrm{vap}}^{\mathrm{sat}} = 25.351$	$c_{\mathrm{vap}}^{\mathrm{sat}} = 498.043$
Phase 2	$p^{\mathrm{sat}} = 50$	$\rho_{\mathrm{liq}}^{\mathrm{sat}} = 777.369$	$c_{\mathrm{liq}}^{\mathrm{sat}} = 1087.810$

Table A.1 – Phase densities and celerities

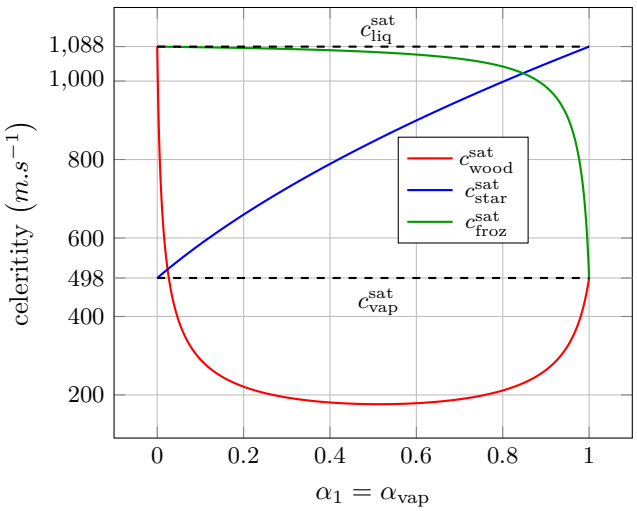

Figure A.1 – Celerity comparison for saturated liquid and vapor phases

As already observed [4, 16, 17], the expression of the Wood celerity allows to retrieve a property measured experimentally [9]: the value of sound speed in liquid-vapor mixtures is lower than both liquid or vapor sound speeds. Such a feature is not shared by c_{froz} and c_{star}. However recall that c_{star} is related to the relaxation variable waves which have to be distinguished from the mixture pressure acoustic waves.

Besides, c_{star} displays a rather surprising behavior which is quite different from c_{w} or c_{star}. Indeed, when one of the phases vanishes, c_{star} takes the value of the vanishing phase celerity. One can notably observe that for a wide range of α_1, c_{star} takes higher values than c_{w}. Consequently, even if the amplitude of the relaxation variables Δu and Δp is close to zero, their dynamics triggers waves that propagate considerably faster than the waves linked to the equilibrium-variable dynamics.

The following subsection is dedicated to a brief study of the fields related to the asymptotic Jacobian matrix $\underset{=\Delta\to 0}{\mathbf{C}^{\mathrm{eq}}}$.

A.3.2 Fields structure

The eigenvectors related to the equilibrium variables can be calculated easily and write:

$$\mathbf{r}_{\mathrm{U}\pm c_{\mathrm{w}}} = \begin{bmatrix} -\frac{\mathrm{C}_2-\mathrm{C}_1}{\mathcal{P}^{\mathrm{eq}}} \\ \pm c_{\mathrm{w}} \\ m\, c_{\mathrm{w}}^2 \\ 0 \\ 0 \end{bmatrix}, \ \mathbf{r}_{\mathrm{U}} = \begin{bmatrix} 1 \\ 0 \\ 0 \\ 0 \\ 0 \end{bmatrix}. \tag{A.43}$$

Thus, $\nabla(\mathrm{U}\pm c_{\mathrm{w}})\cdot\mathbf{r}_{\mathrm{U}\pm c_{\mathrm{w}}} \neq 0$ and $\nabla(\mathrm{U}\pm)\cdot\mathbf{r}_{\mathrm{U}} = 0$. Thus, the fields related to $\left\{\mathrm{U}\pm c_{\mathrm{w}}, \mathbf{r}_{\mathrm{U}\pm c_{\mathrm{w}}}\right\}$ are genuinely non-linear while the one associated with $\left\{\mathrm{U}, \mathbf{r}_{\mathrm{U}}\right\}$ is linearly degenerate.

In the case of the relaxation eigenvalues $\{\mathrm{U}\pm c_{\mathrm{star}}\}$, the effect of the coupling term $\omega_{\mathrm{P},\Delta u}\,\partial_x \Delta u$ can be measured through the complexity of the expression of $\mathbf{r}_{\mathrm{U}\pm c_{\mathrm{star}}}$. Indeed, if $c_{\mathrm{w}} \neq c_{\mathrm{star}}$:

$$\mathbf{r}_{\mathrm{U}\pm c_{\mathrm{star}}} = \begin{bmatrix} \frac{1}{m\left(c_{\mathrm{w}}^2-c_{\mathrm{star}}^2\right)}\frac{\mathrm{C}_2-\mathrm{C}_1}{\mathcal{P}^{\mathrm{eq}}}\,\omega_{\mathrm{P},\Delta u} \\ \mp\frac{c_{\mathrm{star}}}{m\left(c_{\mathrm{w}}^2-c_{\mathrm{star}}^2\right)}\,\omega_{\mathrm{P},\Delta u} \\ -\frac{c_{\mathrm{star}}^2}{\left(c_{\mathrm{w}}^2-c_{\mathrm{star}}^2\right)}\,\omega_{\mathrm{P},\Delta u} \\ c_{\mathrm{star}} \\ \pm\frac{\rho_1\rho_2}{m}\,c_{\mathrm{star}}^2 \end{bmatrix}. \tag{A.44}$$

In that case the field $\left\{\mathrm{U}\pm c_{\mathrm{star}}, \mathbf{r}_{\mathrm{U}\pm c_{\mathrm{star}}}\right\}$ is *a priori* genuinely non-linear. What is more, the set $\left\{\mathbf{r}_{\mathrm{U}\pm c_{\mathrm{w}}}, \mathbf{r}_{\mathrm{U}}, \mathbf{r}_{\mathrm{U}\pm c_{\mathrm{star}}}\right\}$ maps $\mathbb{R}^5$ and the asymptotic system

$$\partial_t \mathbf{V} \quad + \quad \underset{=\Delta\to 0}{\mathbf{C}^{\mathrm{eq}}}(\mathbf{V})\,\partial_x \mathbf{V} \quad = \quad \mathbf{0}, \tag{A.45}$$

is hyperbolic. However, a new resonant configuration comes up when $c_{\mathrm{w}} = c_{\mathrm{star}}$. Indeed, in this specific case, $\mathbf{r}_{\mathrm{U}\pm c_{\mathrm{w}}} = \mathbf{r}_{\mathrm{U}\pm c_{\mathrm{star}}}$ and the set of eigenvectors only maps $\mathbb{R}^3$.

The following section is dedicated to another re-writing of the isentropic Baer-Nunziato model. When discretized numerically, the new set of equations will potentially allow to take into account the equilibrium relations obtained in (A.34) while guaranteeing the conservativity of mixture variables.

A.4 Re-writing of the system using conserved-mixture variables and relaxation variables

Let us define the new set of variables $\mathbf{Z}$ composed of three conservative quantities completed by velocity and pressure differences:

$$\mathbf{U} \to \mathbf{Z}(\mathbf{U}) = \begin{bmatrix} m_1 \\ m \\ m\mathrm{U} \\ \Delta u \\ \Delta p \end{bmatrix}. \tag{A.46}$$

Remark A.4.1 (Admissibility of the change of variable $\mathbf{U}\to\mathbf{Z}(\mathbf{U})$)
The change of variable (A.46) *is admissible in the sense that,*

$$\forall \mathbf{U}\in\Phi^{\mathscr{C}},\ \det\left(\partial_{\mathbf{U}}\mathbf{Z}\right) = -\left(\frac{\mathrm{C}_2}{\alpha_2}+\frac{\mathrm{C}_1}{\alpha_1}\right)\times\left(\frac{1}{m_1}+\frac{1}{m_2}\right) < 0, \tag{A.47}$$

and,

$$\begin{array}{ccc} \Phi^{\mathscr{C}} & \longmapsto & \mathbf{Z}\left(\Phi^{\mathscr{C}}\right) \\ \mathbf{U} & \to & \mathbf{Z}(\mathbf{U}) \end{array} \tag{A.48}$$

is bijective.

Proof 11

Consider $\mathbf{U}^+$ *and* $\mathbf{U}^-$ *such that* $\mathbf{Z}(\mathbf{U}^+) = \mathbf{Z}(\mathbf{U}^-)$. *Equalities related to the first and the second components of* $\mathbf{Z}$ *give* $\forall k \in \{1,2\}: \; m_k^+ = m_k^-$. *By using formulas* (A.11) *and the fact that* $\Delta u^+ = \Delta u^-$, *one also obtains* $(m_k u_k)^+ = (m_k u_k)^-$. *Finally, since the function* $\alpha_1 \to p_2\left(\frac{m_2}{1-\alpha_1}\right) - p_1\left(\frac{m_1}{\alpha_1}\right)$ *is bijective (strictly increasing from* $]0,1[$ *to* $\mathbb{R}$*):*

$$\begin{aligned} \Delta p^+ = \Delta p^- &\Leftrightarrow p_2\left(\frac{m_2^+}{1-\alpha_1^+}\right) - p_1\left(\frac{m_1^+}{\alpha_1^+}\right) = p_2\left(\frac{m_2^+}{1-\alpha_1^-}\right) - p_1\left(\frac{m_1^+}{\alpha_1^-}\right) \\ &\Leftrightarrow \alpha_1^+ = \alpha_1^-. \end{aligned} \tag{A.49}$$

As mentioned in the proof, provided that $m_1 > 0$, $m > 0$ and Δp are given, the variable α_1 is always implicitly defined, by:

$$p_2\left(\frac{m_2}{1-\alpha_1}\right) - p_1\left(\frac{m_1}{\alpha_1}\right) = \Delta p. \tag{A.50}$$

In the sequel the isentropic version of the Baer-Nunziato system with pressure and velocity relaxations is rewritten using the new set of variables $\mathbf{Z}$. Let us split this vector between the conservative mixture variables and the relaxation variables:

$$\mathbf{Z} = \begin{bmatrix} \mathcal{U} \\ \Delta \end{bmatrix} = \begin{bmatrix} [m_1, m, m\mathrm{U}]^{\mathrm{T}} \\ [\Delta u, \Delta p]^{\mathrm{T}} \end{bmatrix}. \tag{A.51}$$

The subsystem related to $\mathcal{U}$ is conservative by definition and reads:

$$\partial_t \mathcal{U} + \partial_x \mathcal{F}(\mathcal{U}, \Delta) = \mathbf{0}, \tag{A.52}$$

with,

$$\begin{aligned} \mathcal{F}(\mathcal{U}, \Delta) &= \begin{bmatrix} m_1 u_1 \\ m\mathrm{U} \\ m_1 (u_1)^2 + m_2 (u_2)^2 + \alpha_1 p_1 + \alpha_2 p_2 \end{bmatrix} \\ &= \begin{bmatrix} \mathrm{Y}_1 (m\mathrm{U} - (m - m_1)\Delta u) \\ m\mathrm{U} \\ m\mathrm{U}^2 + \mathrm{Y}_1 (m - m_1)(\Delta u)^2 + \alpha_1 p_1\left(\frac{m_1}{\alpha_1}\right) + (1-\alpha_1) p_2\left(\frac{m-m_1}{1-\alpha_1}\right) \end{bmatrix}. \end{aligned} \tag{A.53}$$

After tedious calculations and in the case of smooth solutions, the PDEs verified by the relaxation variable vector Δ is given by:

$$\partial_t \Delta \quad + \quad \underline{\underline{\mathbf{C}}}_{\Delta,\mathcal{U}} \partial_x \mathcal{U} \quad + \quad \underline{\underline{\mathbf{C}}}_{\Delta,\Delta} \partial_x \Delta \quad = \quad \begin{bmatrix} -\mathrm{K_u} \frac{m}{m_1 m_2} \Delta u \\ \\ -\mathrm{K_p}\left(\frac{\mathrm{C}_1}{\alpha_1} + \frac{\mathrm{C}_2}{\alpha_2}\right) \Delta p \end{bmatrix}, \tag{A.54}$$

with,

$$\underline{\underline{\mathbf{C}}}_{\Delta,\mathcal{U}} = \begin{bmatrix} \omega_{\Delta u, m_1} & \omega_{\Delta u, m} & \frac{\Delta u}{m} \\ \omega_{\Delta p, m_1} & -u_2 \frac{\mathrm{C}_2 - \mathrm{C}_1}{m} & \frac{\mathrm{C}_2 - \mathrm{C}_1}{m} \end{bmatrix}, \; \underline{\underline{\mathbf{C}}}_{\Delta,\Delta} = \begin{bmatrix} \mathrm{U} + (2\mathrm{Y}_1 - 1)\Delta u & \omega_{\Delta u, \Delta p} \\ \mathrm{Y}_1 \mathrm{C}_2 + \mathrm{Y}_2 \mathrm{C}_1 & u_2 \end{bmatrix}, \tag{A.55}$$

and,

$$\begin{cases} \omega_{\Delta u, m_1} = \dfrac{(\Delta u)^2}{m} - (\tau_2 - \tau_1)^2 m c_{\mathrm{w}}^2 - \dfrac{\Delta p}{m_2} \dfrac{c_{\mathrm{star}}^2}{\alpha_1 \alpha_2 \mathcal{P}^{\mathrm{eq}}}, \\ \omega_{\Delta u, m} = -u_2 \dfrac{\Delta u}{m} + \tau_2 (\tau_2 - \tau_1) m c_{\mathrm{w}}^2 + \dfrac{\Delta p}{m_2} \dfrac{c_2^2}{\alpha_2 \mathcal{P}^{\mathrm{eq}}}, \\ \omega_{\Delta p, m_1} = \Delta u \left(\dfrac{\mathrm{C}_2 - \mathrm{C}_1}{m} - (\tau_2 - \tau_1) m c_{\mathrm{w}}^2 + \dfrac{\mathrm{C}_1}{\alpha_1} \dfrac{c_{\mathrm{star}}^2}{\alpha_1 \alpha_2 \mathcal{P}^{\mathrm{eq}}} \right), \\ \omega_{\Delta u, \Delta p} = \dfrac{1}{\alpha_1 \alpha_2 \mathcal{P}^{\mathrm{eq}}} \left[c_{\mathrm{star}}^2 - \dfrac{\alpha_1}{\rho_2} \Delta p \right]. \end{cases} \tag{A.56}$$

A.5 References

[1] A. Ambroso, C. Chalons, F. Coquel, T. Galié, E. Godlewski, P. A. Raviart, and N. Seguin. The drift-flux asymptotic limit of barotropic two-phase two-pressure models. *Communications in Mathematical Sciences*, 6:521–529, 2008. 206

[2] A. Ambroso, C. Chalons, and P. A. Raviart. A Godunov-type method for the seven-equation model of compressible two-phase flow. *Computers and Fluids*, 54:67–91, 2012. 206

[3] F. Bereux and L. Sainsaulieu. A Roe-type Riemann solver for hyperbolic systems with relaxation based on time-dependent wave decomposition. *Numerische Mathematik*, 2:143–185, 1997. 209

[4] C. E. Brennen. *Fundamentals of Multiphase Flow*. Cambridge University Press, 2005. 210

[5] T. Gallouët, J-M Hérard, and N. Seguin. Numerical modeling of two-phase flows using the two-fluid two-pressure approach. *Mathematical Models and Methods in Applied Sciences*, 14: 663–700, 2004. 206

[6] S. Gavrilyuk. The structure of pressure relaxation terms: one-velocity case. EDF internal report, H-I83-2014-00276-EN, 2014. 206

[7] A. K. Kapila, S. F. Son, J. B. Bdzil, R. Menikoff, and D. S. Stewart. Two-phase modeling of DDT: Structure of the velocity-relaxation zone. *Physics of Fluids*, 9:3885–3897, 1997. 207

[8] A. K. Kapila, R. Menikoff, J. B. Bdzil, S. F. Son, and D. S. Stewart. Two-phase modeling of deflagration-to-detonation transition in granular materials: Reduced equations. *Physics of Fluids*, 13:3002–3024, 2001. 207, 209, 210

[9] H. B. Karplus. The velocity of sound in a liquid containing gas bubbles. Technical Report COO-248, Illinois Inst. Tech., 1958. 210

[10] J. J. Kreeft and B. Koren. A new formulation of Kapila's five-equation model for compressible two-fluid flow, and its numerical treatment. *Journal of Computational Physics*, 229:6220–6242, 2010. 207

[11] M. Labois. *Modélisation des deséquilibres mécaniques dans les écoulements diphasiques: Approches par relaxation et par modèle réduit*. PhD thesis, Université de Provence, 2008. URL https://tel.archives-ouvertes.fr/tel-00338818. 207, 209

[12] A. Murrone. *Modèles bi-fluides à six et sept équations pour les écoulements diphasiques à faible nombre de Mach*. PhD thesis, Université de Provence-Aix-Marseille I, 2003. 207

[13] A. Murrone and H. Guillard. A five equation reduced model for compressible two phase flow problems. *Journal of Computational Physics*, 202:664–698, 2005. 207, 209

[14] F. Petitpas, E. Franquet, R. Saurel, and O. Le Metayer. A relaxation-projection method for compressible flows. Part II: Artificial heat exchanges for multiphase shocks. *Journal of Computational Physics*, 225:2214–2248, 2007. 209

[15] R. Saurel, F. Petitpas, and R. A. Berry. Simple and efficient relaxation methods for interfaces separating compressible fluids, cavitating flows and shocks in multiphase mixtures. *Journal of Computational Physics*, 228:1678–1712, 2009. 207

[16] G. B. Wallis. *One Dimensional Two-Phase Flow*. Mcgraw-Hill, 1969. 209, 210

[17] A. B. Wood. *A Testbook of Sound*. G. Bell and Sons Ltd., London, 1930. 209, 210

Bibliographie générale

Références

[1] R. Abgrall and R. Saurel. Discrete equations for physical and numerical compressible multiphase mixtures. *Journal of Computational Physics*, 186 :361–396, 2003.

[2] L. Allievi. *Teoria del colpo d'ariete*. Atti del Collegio degli Ingegneri ed Architetti Italiani, Milan, Italy (in Italian), 1913.

[3] A. Ambroso, C. Chalons, F. Coquel, T. Galié, E. Godlewski, P. A. Raviart, and N. Seguin. The drift-flux asymptotic limit of barotropic two-phase two-pressure models. *Communications in Mathematical Sciences*, 6 :521–529, 2008.

[4] A. Ambroso, C. Chalons, F. Coquel, and T. Galié. Relaxation and numerical approximation of a two-fluid two-pressure diphasic model. *ESAIM : Mathematical Modelling and Numerical Analysis*, 43 :1063–1097, 2009.

[5] A. Ambroso, C. Chalons, and P. A. Raviart. A Godunov-type method for the seven-equation model of compressible two-phase flow. *Computers and Fluids*, 54 :67–91, 2012.

[6] N. Andrianov, R. Saurel, and G. Warnecke. A simple method for compressible multiphase mixtures and interfaces. *International Journal for Numerical Methods in Fluids*, 41 :109–131, 2003.

[7] M. R. Baer and J. W. Nunziato. A two-phase mixture theory for the deflagration-to-detonation transition (DDT) in reactive granular materials. *International Journal of Multiphase Flow*, 12 :861–889, 1986.

[8] W. F. Ballhaus and P. M. Goorjian. Implicit finite-difference computations of unsteady transonic flows about airfoils. *AIAA Journal*, 15 :1728–1735, 1977.

[9] W. F. Ballhaus and P. M. Goorjian. Implicit methods of second-order accuracy for the Euler equations. *AIAA Journal*, 23 :33–40, 1985.

[10] R. Baraille, G. Bourdin, F. Dubois, and A. Y. Le Roux. Une version à pas fractionnaires du schéma de Godunov pour l'hydrodynamique. *Compte Rendu de l'Académie des Sciences*, 314 :147–152, 1992.

[11] T. Barberon and P. Helluy. Finite volume simulation of cavitating flows. *Computers and Fluids*, 34 :832–858, 2005.

[12] F. Barre and M. Bernard. The CATHARE code strategy and assessment. *Nuclear Engineering and Design*, 124 :257–284, 1990.

[13] M. Baudin, C. Berthon, F. Coquel, R. Masson, and Q. H. Tran. A relaxation method for two-phase flow models with hydrodynamic closure laws. *Numerische Mathematik*, 99 :411–440, 2005.

[14] M. Baudin, F. Coquel, and Q. H. Tran. A semi-implicit relaxation scheme for modelling two-phase flow in a pipeline. *SIAM Journal of Scientific Computing*, 27 :914–936, 2005.

[15] F. Bereux and L. Sainsaulieu. A Roe-type Riemann solver for hyperbolic systems with relaxation based on time-dependent wave decomposition. *Numerische Mathematik*, 2 :143–185, 1997.

[16] A. Bergant, A. R. Simpson, and A. S. Tijsseling. Water hammer with column separation : A historical review. *Journal of Fluids and Structures*, 22 :135–171, 2006.

[17] R. A. Berry, L. Zou, H. Zhao, H. Zhang, J. W. Peterson, R. C. Martineau, and D. Andrs. *Relap-7 theory manual*. Idaho National Engineering Laboratory, Idaho Falls, United States, 2016.

[18] D. Bestion. The physical closure laws in the CATHARE code. *Nuclear Engineering and Design*, 124 :229–245, 1990.

[19] Z. Bilicki and J. Kestin. Physical aspects of the relaxation model in two-phase flow. *Proceedings of the Royal Society of London A : Mathematical, Physical and Engineering Sciences*, 428 :379–397, 1990.

[20] F. Bouchut. *Nonlinear Stability of Finite Volume Methods for Hyperbolic Conservation Laws*. Birkäser, 2004.

[21] A. Bourlioux. *Analysis of numerical methods in a simplified detonation model*. PhD thesis, Princeton University, 1991.

[22] C. E. Brennen. *Fundamentals of Multiphase Flow*. Cambridge University Press, 2005.

[23] T. Buffard and J-M. Hérard. A conservative fractional step method to solve non-isentropic Euler equations. *Computer Methods in Applied Mechanics and Engineering*, 144 :199–225, 1996.

[24] T. Buffard, T. Gallouët, and J-M. Hérard. A sequel to a rough Godunov scheme : application to real gases. *Computer & Fluids*, 29 :813–847, 2000.

[25] H. B. Callen. *Thermodynamics and an Introduction to Thermostatistics*. John Wiley & sons, 1985.

[26] C. Chalons and J. F. O. Coulombel. Relaxation approximation of the Euler equations. *Journal of Mathematical Analysis and Applications*, 348 :872–893, 2008.

[27] C. Chalons, M. Girardin, and S. Kokh. An all-regime Lagrange-Projection like scheme for the gas dynamics equations on unstructured meshes. *Communications in Computational Physics*, 20 :188–233, 2016.

[28] C. Chalons, M. Girardin, and S. Kokh. An all-regime Lagrange-Projection like scheme for 2D homogeneous models for two-phase flows on unstructured meshes. *Journal of Computational Physics*, 335 :885–904, 2016.

[29] G. Q. Chen, C. D. Levermore, and T.-P. Liu. Hyperbolic conservation laws with stiff relaxation terms and entropy. *Communications on Pure and Applied Mathematics*, 47 :787–830, 1994.

[30] S. Clerc. Numerical simulation of the homogeneous equilibrium model for two-phase flows. *Journal of Computational Physics*, 161 :354–375, 2000.

[31] F. Coquel, T. Gallouët, J-M Hérard, and N. Seguin. Closure laws for a two-fluid two-pressure model. *Comptes Rendus de l'Académie des Sciences : Mathematique*, 334 :927–932, 2002.

[32] F. Coquel, Q. L. Nguyen, M. Postel, and Q. H. Tran. Entropy-satisfying relaxation method with large time-steps for Euler IBVPS. *Mathematics of Computation*, 79 :1493–1533, 2010.

[33] F. Coquel, E. Godlewski, and N. Seguin. Relaxation of fluid systems. *Mathematical Models and Methods in Applied Science*, 22 :43–95, 2012.

[34] F. Coquel, J. M. Hérard, K. Saleh, and N. Seguin. A robust entropy-satisfying finite volume scheme for the isentropic Baer-Nunziato model. *ESAIM : Mathematical Modelling and Numerical Analysis*, 48 :165–206, 2014.

[35] F. Coquel, J. M. Hérard, K. Saleh, and N. Seguin. Two properties of two-velocity two-pressure models for two-phase flows. *Communications in Mathematical Sciences*, 12 :593–600, 2014.

[36] R. Courant and K. O. Friedrichs. *Supersonic Flow and Shock Waves (Vol. 21)*. Springer Science & Business Media, 1999.

[37] F. Crouzet, F. Daude, P. Galon, J. M. Hérard, O. Hurisse, and Y. Liu. Validation of a two-fluid model on unsteady liquid–vapor water flows. *Computers and Fluids*, 119 :131–142, 2015.

[38] G. Dal Maso, P. G. LeFloch, and F. Murat. Definition and weak stability of nonconservative products. *Journal de mathématiques pures et appliquées*, 74 :483–548, 1995.

[39] S. Dallet. *Simulation numérique d'écoulements diphasiques en régime compressible ou à faible nombre de Mach*. PhD thesis, Aix-Marseille Université, 2017.

[40] F. Daude and P. Galon. On the computation of the Baer–Nunziato model using ALE formulation with HLL-and HLLC-type solvers towards fluid–structure interactions. *Journal of Computational Physics*, 304 :189–230, 2016.

[41] F. Daude, I. Mary, and P. Comte. Self-adaptative Newton-based iteration strategy for the LES of turbulent multi-scale flows. *Computers and Fluids*, 100 :278–290, 2014.

[42] P. Degond and M. Tang. All speed scheme for the low Mach number limit of the isentropic Euler equation. *Communications in Computational Physics*, 10 :1–31, 2011.

[43] S. Dellacherie. Relaxation schemes for the multicomponent Euler system. *ESAIM : Mathematical Modelling and Numerical Analysis*, 37 :909–936, 2003.

[44] S. Dellacherie. Analysis of Godunov type schemes applied to the compressible Euler system at low Mach number. *Journal of Computational Physics*, 229 :978–1016, 2009.

[45] S. Dellacherie, P. Omnes, and F. Rieper. The influence of cell geometry on the Godunov scheme applied to the linear wave equation. *Journal of Computational Physics*, 229 :5315–5338, 2010.

[46] S. Dellacherie, P. Omnes, J. Jung, and P.A. Raviart. Construction of modified Godunov type schemes accurate at any Mach number for the compressible Euler system. *Mathematical Models and Methods in Applied Science*, 26 :2525–2615, 2016.

[47] C. Demay, C. Bourdarias, B. D. L. De Meux, S. Gerbi, and J. M. Hérard. A fractional step method adapted to the two-phase simulation of mixed flows in pipes with a compressible two-layer model. *ESAIM : Mathematical Modelling and Numerical Analysis*, Accepted for publication, 2018.

[48] G. Dimarco, R. Loubère, and M-H. Vignal. Study of a new asymptotic preserving scheme for the Euler system in the low Mach number limit. *SIAM : Journal of Scientific Computing*, 39 : 2099–2128, 2017.

[49] P. Downar-Zapolski, Z. Bilicki, L. Bolle, and J. Franco. The non-equilibrium relaxation model for one-dimensional flashing liquid flow. *International journal of multiphase flow*, 22 :473–483, 1996.

[50] D. A. Drew. Mathematical modeling of two-phase flow. *Annual review of fluid mechanics*, 15 :261–291, 1983.

[51] D. A. Drew and S. L. Passman. *Theory of Multicomponent Fluids*. Springer Science & Business Media, 2006.

[52] F. Drui. *Modélisation et simulation Eulériennes des écoulements diphasiques à phases séparées et dispersées : développement d'une modélisation unifiée et de méthodes numériques adaptées au calcul massivement parallèle*. PhD thesis, Université Paris-Saclay, 2017. URL https://tel.archives-ouvertes.fr/tel-01618320.

[53] P. Embid and M. R. Baer. Mathematical analysis of a two-phase continuum mixture theory. *Continuum Mechanics and Thermodynamics*, 4 :279–312, 1992.

[54] I. Faille and E. Heintzé. A rough finite volume scheme for modeling two-phase flow in a pipeline. *Computers and Fluids*, 28 :213–241, 1999.

[55] T. Fåtten and H. Lund. Relaxation two-phase flow models and the subcharacteristic condition. *Mathematical Models and Methods in Applied Sciences*, 21 :2379–2407, 2011.

[56] P. Fillion, A. Chanoine, S. Dellacherie, and A. Kumbaro. FLICA-OVAP : A new platform for core thermal–hydraulic studies. *Nuclear Engineering and Design*, 241 :4348–4358, 2011.

[57] T. Gallouët, J-M Hérard, and N. Seguin. Some recent finite volume schemes to compute Euler equations using real gas EOS. *International Journal for Numerical Methods in Fluids*, 39 :1073–1138, 2002.

[58] T. Gallouët, J-M Hérard, and N. Seguin. A hybrid scheme to compute contact discontinuities in one-dimensional Euler systems. *ESAIM : Mathematical Modelling and Numerical Analysis*, 36 :1133–1159, 2002.

[59] T. Gallouët, J-M Hérard, and N. Seguin. Numerical modeling of two-phase flows using the two-fluid two-pressure approach. *Mathematical Models and Methods in Applied Sciences*, 14 :663–700, 2004.

[60] S. Gavrilyuk. The structure of pressure relaxation terms : one-velocity case. EDF internal report, H-I83-2014-00276-EN, 2014.

[61] S. Gavrilyuk and R. Saurel. Mathematical and numerical modeling of two-phase compressible flows with micro-inertia. *Journal of Computational Physics*, 175 :326–360, 2002.

[62] M. S. Ghidaoui, M. Zhao, D. A. McInnis, and D. H. Axworthy. A review of water hammer theory and practice. *Applied Mechanics Reviews*, 58 :49, 2005.

[63] M. Girardin. *Asymptotic preserving and all-regime Lagrange-Projection like numerical schemes : application to two-phase flows in low Mach regime*. PhD thesis, Université Pierre et Marie Curie, 2015. URL https://tel.archives-ouvertes.fr/tel-01127428.

[64] J. Glimm, D. Saltz, and D. H. Sharp. Renormalization group solution of two-phase flow equations for Rayleigh-Taylor mixing. *Physics Letters*, 222 :171–176, 1996.

[65] J. Glimm, D. Saltz, and D. H. Sharp. Two-phase modelling of a fluid mixing layer. *Journal of Fluid Mechanics*, 378 :119–143, 1999.

[66] P. Goatin and P. G. LeFloch. The Riemann problem for a class of resonant hyperbolic systems of balance laws. *Annales de l'Institut Henri Poincaré (C) Non Linear Analysis*, 21 :881–902, 2004.

[67] E. Godlewski and P.A. Raviart. *Numerical Approximation of Hyperbolic Systems of Conservation Laws*. Springer, 1996.

[68] A. Guelfi, D. Bestion, M. Boucker, P. Boudier, P. Fillion, M. Grandotto, and P. Péturaud. NEPTUNE : a new software platform for advanced nuclear thermal hydraulics. *Nuclear Science and Engineering*, 156 :281–324, 2007.

[69] H. Guillard and F. Duval. A Darcy law for the drift velocity in a two-phase flow model. *Journal of Computational Physics*, 224 :288–313, 2007.

[70] H. Guillard and A. Murrone. On the behavior of upwind schemes in the low Mach number limit : II Godunov type schemes. *Computers and Fluids*, 33 :655–675, 2004.

[71] H. Guillard and C. Viozat. On the behavior of upwind schemes in the low Mach number limit. *Computers and Fluids*, 28 :63–86, 1999.

[72] V. Guillemaud. *Modélisation et simulation numérique des écoulements diphasiques par une approche bifluide à deux pressions*. PhD thesis, Université de Provence-Aix-Marseille I, 2007. URL https://tel.archives-ouvertes.fr/tel-00169178/.

[73] J. Haack, S. Jin, and J. G. Liu. An all-speed asymptotic-preserving method for the isentropic Euler and Navier-Stokes equations. *Communications in Computational Physics*, 12 :955–980, 2012.

[74] L. Haar, J. S. Gallagher, and G. S. Kell. *NBS/NRC Steam Tables : Thermodynamic and Transport Properties and Computer Programs for Vapor and Liquid States of Water in SI Units*. Taylor & Francis, 1984.

[75] E. Hairer and G. Wanner. *Solving Ordinary Differential Equations II : Stiff and Differential-algebraic Problems*. Springer, 1991.

[76] A. Harten, P. D. Lax, and B. Van Leer. On upstream differencing and Godunov-type schemes for hyperbolic conservation laws. *SIAM Review*, 25 :35–61, 1983.

[77] J. M. Hérard and Y. Liu. Une approche bifluide statistique de modélisation des écoulements diphasiques à phases compressibles. EDF internal report, H-I81-2013-01162-FR, 2013.

[78] C. W. Hirt, A. A. Amsden, and J. L. Cook. An arbitrary lagrangian-eulerian computing method for all flow speeds. *Journal of Computational Physics*, 14 :227–253, 1974.

[79] R. A. Horn and C. R. Johnson. *Matrix Analysis*. Cambridge university press, 1990.

[80] D. Iampietro, F. Daude, P. Galon, and J. M. Hérard. A Mach-sensitive implicit-explicit scheme adapted to compressible multi-scale flows. *Journal of Computational and Applied Mathematics*, 340 :122–150, 2018.

[81] D. Iampietro, F. Daude, P. Galon, and J. M. Hérard. A Mach-sensitive splitting approach for Euler-like systems. *ESAIM : Mathematical Modelling and Numerical Analysis*, 52 :207–253, 2018.

[82] Electric Power Research Institute. *Water Hammer Handbook for Nuclear Plants Engineers and Operators*. EPRI, 1996.

[83] E. Isaacson and B. Temple. Nonlinear resonance in systems of conservation laws. *SIAM Journal on Applied Mathematics*, 52 :1260–1278, 1992.

[84] M. Ishii. *Thermo-Fluid Dynamic Theory of Two-Phase Flow*. Eyrolles, 1975.

[85] M. Ishii and T. Hibiki. *Thermo-Fluid Dynamics of Two-Phase Flow*. Springer, 2006.

[86] M. Ishii and N. Zuber. Drag coefficient and relative velocity in bubbly, droplet or particulate flows. *AIChE Journal*, 25 :843–855, 1979.

[87] S. Jin. Runge-Kutta methods for hyperbolic conservation laws with stiff relaxation terms. *Journal of Computational Physics*, 122 :51–67, 1995.

[88] S. Jin. Efficient asymptotic-preserving (AP) schemes for some multiscale kinetic equations. *SIAM Journal on Scientific Computing*, 21 :441–454, 1999.

[89] S. Jin and Z.-P. Xin. The relaxation schemes for systems of conservation laws in arbitrary dimensions. *Communications on Pure and Applied Mathematics*, 48 :235–276, 1995.

[90] N. E. Joukowski. Memoirs of the Imperial Academy Society of St. Petersburg. *Proceedings of the American Water Works Association*, 24 :341–424, 1898.

[91] A. K. Kapila, S. F. Son, J. B. Bdzil, R. Menikoff, and D. S. Stewart. Two-phase modeling of DDT : Structure of the velocity-relaxation zone. *Physics of Fluids*, 9 :3885–3897, 1997.

[92] A. K. Kapila, R. Menikoff, J. B. Bdzil, S. F. Son, and D. S. Stewart. Two-phase modeling of deflagration-to-detonation transition in granular materials : Reduced equations. *Physics of Fluids*, 13 :3002–3024, 2001.

[93] H. B. Karplus. The velocity of sound in a liquid containing gas bubbles. Technical Report COO-248, Illinois Inst. Tech., 1958.

[94] L. Kelvin. Hydrokinetic solutions and observations. *Philosophical Magazine*, 42 :362–377, 1871.

[95] S. Klainerman and A. Majda. Singular limits of quasilinear hyperbolic systems with large parameters and the incompressible limit of compressible fluids. *Communications on Pure and Applied Mathematics*, 34 :481–524, 1981.

[96] S. Klainerman and A. Majda. Compressible and incompressible fluids. *Communications on Pure and Applied Mathematics*, 35 :629–651, 1981.

[97] R. Klein. Semi-implicit extension of a Godunov-type scheme based on low Mach number asymptotics I : One-dimensional flow. *Journal of Computational Physics*, 121 :213–237, 1995.

[98] J. J. Kreeft and B. Koren. A new formulation of Kapila's five-equation model for compressible two-fluid flow, and its numerical treatment. *Journal of Computational Physics*, 229 :6220–6242, 2010.

[99] M. Labois. *Modélisation des deséquilibres mécaniques dans les écoulements diphasiques : Approches par relaxation et par modèle réduit*. PhD thesis, Université de Provence, 2008. URL https://tel.archives-ouvertes.fr/tel-00338818.

[100] Idaho National Engineering Laboratory. *RELAP5/MOD3 code manual volume I*. Lockheed Idaho Technologies Company, 2001.

[101] J. LaSalle. Some extensions of Liapunov's second method. *IRE Transactions on Circuit Theory*, 7 :520–527, 1960.

[102] G. Le Coq, S. Aubry, J. Cahouet, P. Lequesne, G. Nicolas, and S. Pastorini. Le logiciel THYC. modélisation en volume finis des écoulements tridimensionnels diphasiques dans les faisceaux de tubes. *Bulletin de la Direction des études et recherches-Electricité de France. Série A, nucléaire, hydraulique, thermique*, 1 :61–76, 1989.

[103] R. J. LeVeque and H. C. Yee. A study of numerical methods for hyperbolic conservation laws with stiff source terms. *Journal of Computational Physics*, 86 :187–210, 1987.

[104] G. Linga. A hierarchy of non-equilibrium two-fluid models. *SIAM Journal on Applied Mathematics*, 2015. Submitted.

[105] M. S. Liou. A sequel to AUSM, Part II : AUSM+-up for all speeds. *Journal of Computational Physics*, 74 :137–170, 2006.

[106] T.-P. Liu. Hyperbolic conservation laws with relaxation. *Communications in Mathematical Physics*, 108 :153–175, 1987.

[107] H. Lochon. *Modélisation et simulation d'écoulements transitoires eau-vapeur en approche bifluide*. PhD thesis, Université d'Aix-Marseille, 2016. URL https://tel.archives-ouvertes.fr/tel-01379453/.

[108] H. Lochon, F. Daude, P. Galon, and J. M. Hérard. HLLC-type Riemann solver with approximated two-phase contact for the computation of the Baer-Nunziato two-fluid model. *Journal of Computational Physics*, 326 :733–762, 2016.

[109] H. Lochon, F. Daude, P. Galon, and J. M. Hérard. Comparison of two-fluid models on steam-water transients. *ESAIM : Mathematical Modelling and Numerical Analysis*, 50 :1631–1657, 2016.

[110] H. Lochon, F. Daude, P. Galon, and J. M. Hérard. Computation of fast depressurization of water using a two-fluid model : revisiting Bilicki modelling of mass transfer. *Computers & Fluids*, 156 :162–174, 2017.

[111] H. Lund. A hierarchy of relaxation models for two-phase flow. *SIAM Journal on Applied Mathematics*, 72 :1713–1741, 2012.

[112] M. P. Martín and G. V. Candler. A parallel implicit method for the direct numerical simulation of wall-bounded compressible turbulence. *Journal of Computational Physics*, 215 :153–171, 2006.

[113] G. R. McGuire and J. L. Morris. A class of implicit, second-order accurate, dissipative schemes for solving systems of conservation laws. *Journal of Computational Physics*, 14 : 126–147, 1974.

[114] G. R. McGuire and J. L. Morris. Explicit-implicit schemes for the numerical solution of non-linear hyperbolic systems. *Mathematics of Computation*, 29 :407–424, 1975.

[115] G. Métivier and S. Schochet. The incompressible limit of the non-isentropic Euler equations. *Archive for Rational Mechanics and Analysis*, 158 :61–90, 2001.

[116] S. T. Munkejord. Comparison of Roe-type methods for solving the two-fluid model with and without pressure relaxation. *Computers and Fluids*, 36 :1061–1080, 2007.

[117] A. Murrone. *Modèles bi-fluides à six et sept équations pour les écoulements diphasiques à faible nombre de Mach*. PhD thesis, Université de Provence-Aix-Marseille I, 2003.

[118] A. Murrone and H. Guillard. A five equation reduced model for compressible two phase flow problems. *Journal of Computational Physics*, 202 :664–698, 2005.

[119] A. Murrone and H. Guillard. Behavior of upwind scheme in the low Mach number limit : III. Preconditioned dissipation for a five equation two phase model. *Computers and Fluids*, 37(10) :1209–1224, 2008.

[120] S. Noelle, G. Bispen, K. R. Arun, M. Lukáčová-Medvid'ová, and C. D. Munz. A weakly asymptotic preserving low Mach number scheme for the Euler equations of gas dynamics. *SIAM Journal on Scientific Computing*, 36 :B989–B1024, 2014.

[121] M. Papin and R. Abgrall. Fermetures entropiques pour les systèmes bifluides à sept équations. *Comptes Rendus de l'Académie des Sciences : Mécanique*, 333 :838–842, 2005.

[122] L. Pareschi and G. Russo. Implicit–explicit Runge–Kutta schemes and applications to hyperbolic systems with relaxation. *SIAM Journal of Scientific Computing*, 25 :129–155, 2005.

[123] M. Pelanti and K. M. Shyue. A mixture-energy-consistent six-equation two-phase numerical model for fluids with interfaces, cavitation and evaporation waves. *Journal of Computational Physics*, 259 :331–357, 2014.

[124] R. B. Pember. Numerical methods for hyperbolic conservation laws with stiff relaxation I. Spurious solutions. *SIAM Journal on Applied Mathematics*, 53 :1293–1330, 1993.

[125] R. B. Pember. Numerical methods for hyperbolic conservation laws with stiff relaxation II. Higher-order Godunov methods. *SIAM Journal on Scientific Computing*, 14 :824–859, 1993.

[126] F. Petitpas, E. Franquet, R. Saurel, and O. Le Metayer. A relaxation-projection method for compressible flows. Part II : Artificial heat exchanges for multiphase shocks. *Journal of Computational Physics*, 225 :2214–2248, 2007.

[127] V. H. Ransom and D. L. Hicks. Hyperbolic two-pressure models for two-phase flow. *Journal of Computational Physics*, 53 :124–151, 1984.

[128] F. Rieper. A low-Mach number fix for Roe's approximate Riemann solver. *Journal of Computational Physics*, 230 :5263–5287, 2011.

[129] K. Saleh. *Analyse et simulation numérique par relaxation d'écoulements diphasiques compressibles. Contribution au traitement des phases evanescentes*. PhD thesis, Université Pierre et Marie Curie-Paris VI, 2012. URL https://tel.archives-ouvertes.fr/tel-00761099.

[130] R. Saurel and R. Abgrall. A multiphase Godunov method for compressible multifluid and multiphase flows. *Journal of Computational Physics*, 150 :425–467, 1999.

[131] R. Saurel, F. Petitpas, and R. A. Berry. Simple and efficient relaxation methods for interfaces separating compressible fluids, cavitating flows and shocks in multiphase mixtures. *Journal of Computational Physics*, 228 :1678–1712, 2009.

[132] S. Schochet. The compressible Euler equations in a bounded domain : existence of solutions and the incompressible limit. *Communications in Mathematical Physics*, 104 :49–75, 1986.

[133] J. Schütz and S. Noelle. Flux splitting for stiff equations : a notion on stability. *Journal of Scientific Computing*, 64 :522–540, 2015.

[134] D. W. Schwendeman, C. W. Wahle, and A. K. Kapila. The Riemann problem and a high-resolution Godunov method for a model of compressible two-phase flow. *Journal of Computational Physics*, 212 :490–526, 2006.

[135] A. R. Simpson. *Large water hammer pressures due to column separation in sloping pipes*. PhD thesis, Diss. University of Michigan, 1986.

[136] A. R. Simpson and E. B. Wylie. Large water-hammer pressures for column separation in pipelines. *Journal of Hydraulic Engineering*, 117 :1310–1316, 1991.

[137] J. Smoller. *Shock Waves and Reaction-Diffusion Equations*. Springer-Verlag, 1994.

[138] G. A. Sod. *Numerical Methods in Fluid Dynamics, Initial and Initial-boundary Value Problems*. Cambridge University Press, 1985. (English translation by E. E. Halmos 1925, *The theory of waterhammer*, Trans. ASME).

[139] H. B. Stewart and B. Wendroff. Two-phase flow : models and methods. *Journal of Computational Physics*, 56 :363–409, 1984.

[140] I. Suliciu. On the thermodynamics of fluids with relaxation and phase transitions. *International Journal of Engineering Science*, 36 :921–947, 1998.

[141] S. Tokareva and E. F. Toro. HLLC-type Riemann solver for the Baer–Nunziato equations of compressible two-phase flow. *Journal of Computational Physics*, 229 :3573–3604, 2010.

[142] E. Toro, M. Spruce, and W. Speares. Restoration of the contact surface in the HLL-Riemann solver. *Shock waves*, 4 :25–34, 1994.

[143] E. F. Toro, M. Spruce, and W. Spears. Restoration of the contact surface in the HLL-Riemann solver. *Shock Waves*, 4 :25–34, 1994.

[144] E.F. Toro. *Riemann Solvers and Numerical Methods for Fluid Dynamics*. Springer, 1999.

[145] I. Toumi, A. Bergeron, D. Gallo, E. Royer, and D. Caruge. FLICA-4 : a three-dimensional two-phase flow computer code with advanced numerical methods for nuclear applications. *Nuclear Engineering and Design*, 1-2 :139–155, 2000.

[146] E. Turkel. Preconditioned methods for solving the incompressible and low speed compressible equations. *Journal of Computational Physics*, 72 :277–298, 1987.

[147] W. Wagner and H. J. Kretzschmar. IAPWS industrial formulation 1997 for the thermodynamic properties of water and steam. *International Steam Tables : Properties of Water and Steam Based on the Industrial Formulation IAPWS-IF97*, pages 7–150, 2008.

[148] G. B. Wallis. *One Dimensional Two-Phase Flow*. Mcgraw-Hill, 1969.

[149] J. B. Whitham. *Linear and Non Linear Waves*. John Wiley & Sons Inc, 1974.

[150] A. B. Wood. *A Testbook of Sound*. G. Bell and Sons Ltd., London, 1930.

[151] H. Zakerzadeh. On the Mach-uniformity of the Lagrange-Projection scheme. *ESAIM : Mathematical Modelling and Numerical Analysis*, 51 :1343–1366, 2017.

[152] H. Zakerzadeh and S. Noelle. A note on the stability of implicit-explicit flux splittings for stiff hyperbolic systems. Preprint, 2016. URL https://www.igpm.rwth-aachen.de/forschung/preprints/449.

[153] N. Zuber and J. Findlay. Average volumetric concentration in two-phase flow systems. *Journal of Heat Transfer*, 87 :453–468, 1965.